Constant Stress and Pressure Rheology of Dense Colloidal Suspensions

Thesis by
Mu Wang

In Partial Fulfillment of the Requirements for the
degree of
Doctor of Philosophy

CALIFORNIA INSTITUTE OF TECHNOLOGY
Pasadena, California

2017
Defended November 18, 2016

Mu Wang
ORCID: 0000-0001-6090-6187

ACKNOWLEDGEMENTS

Pursuing a doctoral degree at Caltech is a great experience. I am fortunate enough to enjoy the privilege of working with the best scientists and educators of our times in beautiful Southern California. At this point I realize that I owe a debt of gratitude to many people.

The thesis would not have been possible without my advisor, Professor Brady. Under his guidance, I grew from a novice engineer to an independent researcher. Professor Brady is always a great source of scientific insights and inspiration. He is the model researcher and educator that I will always aspire to be.

I want to express deepest gratitude to my family. My wife, Ning Sun, has sacrificed so much for me to fulfill my dream. She is always supportive and keeps me positive. My son, Nicholas, who was so eager to see the world early, taught me great lessons on preservation, survival, and optimism.

I wish to thank the companionship and friendship of members of the Brady group and the Wang group. I always enjoyed our conversations and discussions on many topics .

I also would like to acknowledge the financial supports from the Natural Sciences and Engineering Research Council of Canada (NSERC) by a Postgraduate Scholarship (PGS), and the National Science Foundation (NSF) grant CBET-1337097.

ABSTRACT

This thesis is a computational investigation on several aspects of the constant stress and pressure rheology of dense polydisperse colloidal suspensions. Using bidisperse suspensions as a model, we first study the influences of size polydispersity on short-time transport properties. The hydrodynamic interactions are calculated using a polydisperse implementation of Stokesian Dynamics (SD) via a Monte-Carlo approach. We carefully compare the SD computations with existing theoretical and numerical results, and critically assess the strengths and weaknesses of the SD algorithm. For suspensions, we find that the Pairwise Additive (PA) approximations with the Percus-Yevick structural input is valid up to volume fraction $\phi = 0.1$. We also develop an semi-analytical approximation scheme to predict the wavenumber-dependent partial hydrodynamic functions based on the $\delta\gamma$-scheme of Beenakker & Mazur [Physica 120A (1983) 388 & 126A (1984) 349], which is shown to be valid up to $\phi = 0.4$.

To meet the computation requirements of dynamic simulations, we then developed the Spectral Ewald Accelerated Stokesian Dynamics (SEASD) based on the framework of SD with extension to compressible solvents. The SEASD uses the Spectral Ewald (SE) method [Lindbo & Tornberg, J. Comput. Phys. 229 (2010) 8994] for mobility computation with flexible error control, a novel block-diagonal preconditioner for the iterative solver, and the Graphic Processing Units (GPU) acceleration. For further speedup, we developed the SEASD-nf, a polydisperse extension of the mean-field Brownian approximation of Banchio & Brady [J. Chem. Phys. 118 (2003) 10323]. The SEASD and SEASD-nf are extensively validated with static and dynamic computations, and are found to scale as $O(N \log N)$ with N the system size. The SEASD and SEASD-nf agree satisfactorily over a wide range of parameters for dynamic simulations.

Next, we investigate the colloidal film drying processes to understand the structural and mechanical implications when the constant pressure constraint is imposed by confining boundaries. The suspension is sandwiched between a stationary substrate and an interface moving either at a constant velocity or with constant imposed stress. Using Brownian Dynamics (BD) simulations without hydrodynamic interactions, we find that both fast and slow interface movement promote crystallization via distinct mechanisms. The most amorphous suspension structures occur when the interface moves at a rate comparable to particle Brownian motion. Imposing constant normal

stresses leads to similar suspension behaviors, except that the interface stops moving when the suspension osmotic pressure matches the imposed stress. We also compare the simulation results with a continuum model. This work reveals the critical role of interface movement on the stress and structure of the suspension.

Finally, we study the constant shear stress and pressure rheology of dense colloidal suspensions using both BD and SEASD-nf to identify the role of hydrodynamic interactions. The constant pressure constraint is imposed by introducing a compressible solvent. We focus on the rheological, structural, and dynamical characteristics of flowing suspensions. Although hydrodynamic interactions profoundly affect the suspension structure and dynamics, they only quantitatively influence the behaviors of amorphous suspensions. The suspension becomes glassy, i.e., exhibits flow-arrest transitions, when the imposed pressure is high, and reveals the Shear Arrest Point (SAP) in the non-Brownian limit. From a granular perspective, we find that the suspensions move away from the arrested state in a universal fashion regardless of the imposed pressure, suggesting the critical role of the jamming physics. The hydrodynamic simulations quantitatively agree with the experiments of Boyer et al. [Phys. Rev. Lett. 107 (2011) 188301] with a volume fraction shift. The results at all imposed stresses and pressures reveal a generalized Stokes-Einstein-Sutherland relation with an effective temperature proportional to the pressure. We develop a model that accurately describes the rheology and diffusion of glassy suspensions. Our results show the critical role of pressure on the behaviors of dense colloidal suspensions.

PUBLISHED CONTENT AND CONTRIBUTIONS

[1] M. Wang and J. F. Brady, "Short-time transport properties of bidisperse suspensions and porous media: a Stokesian Dynamics study", the Journal of Chemical Physics **142**, 094901 (2015) doi:10.1063/1.4913518,
M.W. participated in the conception of the project, developed the algorithm, performed simulations, analyzed the data, and wrote the manuscript.

[2] M. Wang, M. Heinen, and J. F. Brady, "Short-time diffusion in concentrated bidisperse hard-sphere suspensions", the Journal of Chemical Physics **142**, 064905 (2015) doi:10.1063/1.4907594,
M.W. participated in the conception of the project, performed Stokesian Dynamics simulations, analyzed the data, and participated in the writing of the manuscript.

[3] M. Wang and J. F. Brady, "Spectral Ewald Acceleration of Stokesian Dynamics for polydisperse suspensions", Journal of Computational Physics **306**, 443 (2016) doi:10.1016/j.jcp.2015.11.042,
M.W. participated in the conception of the project, design, developed, and validated the algorithm, and wrote the manuscript.

[4] M. Wang and J. F. Brady, "Constant stress and pressure rheology of colloidal suspensions", Physical Review Letters **115**, 158301 (2015) doi:10.1103/PhysRevLett.115.158301,
M.W. participated in the conception of the project, performed simulations and analyzed the data, and wrote the manuscript.

CONTENTS

LIST OF FIGURES

LIST OF TABLES

Chapter 1

INTRODUCTION

Colloidal suspensions are widely present in nature and in industry from biological fluids to advanced materials, with examples as diverse as cytoplasm, milk, and ink. They have attracted extensive research interests dating back to Einstein [1]. Despite almost 110 years of extensive experimental, computational, and theoretical investigations, the behaviors of dense colloidal suspensions remain poorly understood [2, 3]. Even the most elementary form—the hard-sphere colloidal suspensions that are mixtures of submicron rigid particles in a viscous solvent—exhibit rich and surprising behaviors such as glass and jamming transitions [4, 5], shear thinning and shear thickening, i.e., a decrease and increase of suspension viscosity with increasing strain rate [6], and particle migration [7, 8]. These behaviors arise from the complex interplay among interparticle forces, hydrodynamic interactions, and Brownian motion. A thorough understanding is critical for developing new materials and improving existing processes.

This thesis is a comprehensive computational investigation on the rheology of dense colloidal suspensions. By dense we refer to suspensions that exhibit flow-arrest transitions, i.e., that are unable to flow unless the imposed stress exceeds the yield stress. The volume fraction is therefore above the glass transition $\phi_G \approx 0.58$ but below the jamming transition $\phi_J \approx 0.64$ for hard-sphere systems. The current standard method for rheology simulations of colloidal suspensions is Stokesian Dynamics (SD) [9], which exploits both the mobility and the resistance formalism of Stokes flow to accurately capture the hydrodynamic interactions that are non-pairwise-additive and long-range in the far field and diverging in the near field. The monodisperse implementation of SD has been used to study suspension rheology up to the monodisperse fluid-solid transition $\phi_F \approx 0.494$ with fixed volume fraction ϕ and strain rate $\dot{\gamma}$ [10, 11]. However, we cannot directly use the standard SD or the Accelerated Stokesian Dynamics(ASD), the Particle-Mesh-Ewald (PME) variation of the SD [12], to study the rheology of dense suspensions for several reasons: (1) The monodisperse suspensions spontaneously crystallize when $\phi > \phi_F$. The crystallization process qualitatively alters the suspension behaviors compared to the amorphous state; (2) With constant imposed strain rate $\dot{\gamma}$ we implicitly assume the suspensions flow like a fluid, and therefore we are unable to accurately probe the

dynamics near the flow-arrest transitions; (3) We assume that the prescribed volume fraction ϕ is given and fixed. This assumption is valid for suspensions far from the jamming transitions. However, near the jamming point, the exact value of ϕ_J is strongly protocol dependent and therefore unknown, and the prescribed ϕ may not be reached.

The solution to the challenges above is the constant stress and pressure rheology of polydisperse suspensions. Introducing a small particle size polydispersity significantly suppresses the crystallization process [13]. This ensures that the suspensions are amorphous at least in the arrested state. Imposing a constant shear stress σ and measuring the resulting responses can probe both the flowing state, where the suspension continuously deforms with $\dot{\gamma} > 0$, and the arrested state, where the suspension behaves like a solid with $\dot{\gamma} = 0$. When the imposed stress is close to the yield stress, we can observe the dynamics of the flow-arrest transitions. Finally, imposing a constant pressure Π allows the suspension volume fractions to adjust accordingly, and to reach a maximum value in the $\Pi \to \infty$ limit. In this way, we can properly study the rheology of dense suspensions.

Introducing particle size polydispersity in colloidal suspensions not only suppresses the crystallization at ϕ_F, but also alters the hydrodynamic interactions among particles, and consequently, the suspension transport properties. Particle size differences can introduce qualitative changes in hydrodynamic interactions. For example, the trajectories of two sedimenting particles can become periodic if their sizes are different [14]. On the other hand, although there are extensive studies on the transport properties of hard-sphere and charge-stabilized monodisperse equilibrium colloidal suspensions [15–17], the influences of particle size differences have not been addressed. Here, the transport properties are measured at a time scale much smaller than the time scale of configuration change, and therefore they only depend on the instantaneous (equilibrium) configurations.

Experimentally, the constant stress and pressure rheology was first introduced by Prasad and Kytömaa [18] for non-Brownian suspensions using a concentric cylinder geometry with pressure control in the vorticity direction. They observed that ϕ changes with the imposed stress and pressure. Recently, Boyer et al. [19] introduced a different experimental setup based on the cone and plate geometry with pressure control in the velocity gradient direction. They successfully collapsed the results from different samples, and constructed the flow curve of non-Brownian suspensions. However, there is no corresponding computational investigations for

overdamped colloidal suspensions.

In addition to introducing physical boundaries, another way of keeping the pressure constant is to introduce a compressible solvent with a bulk viscosity κ_0 and adjust the uniform compressive flow in unconfined suspensions. In a compressible solvent, a rigid particle can not expand or contract with the uniform compressive flow and thus generates a flow disturbance satisfying the Stokes equation, which, in turn, generates a pressure moment [20, 21]. In this way, the normal stress of hard-sphere suspensions is proportional to the compressible flow. This approach eliminates the structural anisotropy due to confining boundaries.

The thesis consists of four parts. In the first part, we investigate the effects of particle size differences on the short-time transport properties of equilibrium colloidal suspensions. We extend the conventional SD method for infinite suspensions [22] to polydisperse systems. Since hydrodynamic interactions do not affect the equilibrium properties, these transport properties are computed using a Monte-Carlo approach. We address suspension properties including the short-time translational and rotational self-diffusivities, the instantaneous sedimentation velocity, the wavenumber-dependent partial hydrodynamic functions, and the high-frequency shear and bulk viscosities; and porous media properties including the permeability and the translational and rotational hindered diffusivities. The computational results are compared with existing theoretical and numerical results. For suspensions, we also explore the range of validity of various approximation schemes, notably the Pairwise Additive (PA) approximations with the Percus-Yevick structural input. We critically assess the strengths and weaknesses of the SD algorithm for various transport properties. For very dense systems, we discuss the interplay between the hydrodynamic interactions and the structures due to the presence of a second species of a different size.

In this part, we also develop an approximation scheme for the bidisperse partial hydrodynamic functions based on the $\delta\gamma$-scheme for monodisperse suspensions [23, 24] with partial static structure factors as the input and a rescaling law for the mixture. The so-modified $\delta\gamma$ scheme predicts hydrodynamic functions in good agreement with the SD computations up to $\phi = 0.4$.

The polydisperse SD has an unfavorable $O(N^3)$ computation scaling, with N the number of particles in the system, which effectively restricts the algorithm to static computations of equilibrium systems, where hydrodynamic interactions do not affect the structural evolution, and to dynamic simulations with small N. This limitation

necessitates developing a new algorithm for dynamic simulations of dense suspensions.

The second part of the thesis is devoted to the development of a computational method designed for dynamic simulations of polydisperse suspensions with full hydrodynamic interactions, Spectral Ewald Accelerated Stokesian Dynamics (SEASD). Based on the framework of Stokesian Dynamics (SD) with extension to compressible solvents, the SEASD uses the Spectral Ewald (SE) method [25] for mobility computation, a far-field block-diagonal preconditioner for the iterative solver, and Graphic Processing Units (GPU) acceleration. For further speedup, we develop SEASD-nf, a polydisperse extension of the mean-field Brownian approximation of Banchio and Brady [26]. We extensively discuss implementation and parameter selection strategies in the SEASD, and demonstrate the spectral accuracy in the mobility evaluation and the overall $O(N \log N)$ computation scaling. The algorithm is rigorously validated using three computational examples in monodisperse and bidisperse suspensions: the short-time transport properties, the equilibrium osmotic pressure and viscoelastic moduli, and the steady shear Brownian rheology. The results show that the SEASD and SEASD-nf agree satisfactorily over a wide range of parameters, and provide insight to the dynamics of polydisperse colloidal suspensions.

The third part of the thesis shifts the attention from hydrodynamic interactions to the constant pressure constraint. We consider the structural and mechanical influences of the confining boundary motion if the constant pressure constraint is imposed. This problem is formulated as the film drying process by confining colloidal suspensions between a moving interface and a stationary substrate, with only excluded volume interactions among the particles and walls.

In this part, we develop a new variant of the Brownian Dynamics simulations, the Energy Minimization Potential-Free (EMPF) algorithm for confined systems and for stress profile measurement. The interface moves either at a constant velocity or with a constant imposed normal stress. For constant interface velocity U_w, comparing the rate of interface movement U_w/a to the rate of diffusion d_0/a^2 defines a Péclet number, $\mathrm{Pe}_U = U_w a/d_0$, with a the particle radius and d_0 the single-particle diffusivity. In the $\mathrm{Pe}_U \ll 1$ limit, Brownian motion dominates and the suspensions are driven by thermodynamics. In the $\mathrm{Pe}_U \gg 1$ limit, a particle front emerges next to the moving interface and promotes localized, epitaxial crystallization. The stress profile becomes step-like and has a boundary layer next to the moving interface. The

most amorphous structures at a given gap width occur at moderate Pe_U. We also develop a continuum model for the drying process and compare the model prediction with the simulation results. With constant imposed normal stress, the suspension shows similar behaviors, except that the interface stops moving when the suspension osmotic pressure matches the imposed stress. This part shows the critical role of interface movement on the resulting suspension structures and mechanics.

The fourth part of the thesis focuses on the constant stress and pressure rheology of colloidal suspensions without and with hydrodynamic interactions. We use the Potential-Free Brownian Dynamics (PFBD) [27] for computations without hydrodynamic interactions, and use SEASD-nf for hydrodynamic simulations. As the confinement strongly affects the suspension behaviors even without hydrodynamic interactions, we impose the constant pressure constraint by introducing a compressible solvent.

We first study the flow behaviors using PFBD. Expressing the flow behavior in terms of the macroscopic friction coefficient $\mu = \sigma/\Pi$, with σ the shear stress and Π the osmotic pressure, reveals a Shear Arrest Point (SAP) from the collapse of the rheological data in the non-Brownian limit. The flow curves agree quantitatively (when scaled) with the experiments of Boyer et al. [19]. Near suspension arrest, both the shear and the incremental normal viscosities display a universal power law divergence, demonstrating the important role of jamming on the arrest of colloidal suspensions and illustrating the care needed when conducting and analyzing experiments and simulations near the flow-arrest transition.

We then investigate the constant stress and pressure rheology with and without hydrodynamic interactions by focusing on the rheological, structural, and dynamical characteristics of the flowing suspensions. Hydrodynamic interactions, for example, lead to the preferential alignment of particles in the vorticity direction at high imposed stresses, and the shear-melting of the string-order structures at moderate stresses.

For suspensions without hydrodynamic interactions, we also explore the suspension instability near flow-arrest transitions. Through temporal coarse graining, the stationary strain rate distribution near flow-arrest transitions shows two peaks, with one in the arrested state and one in the flowing state. The stress-scaled self-diffusivities at different stresses collapse, and depend only on Π and $\dot{\gamma}$. The results lead to a diffusion-rheology flow map for Brownian suspensions. Spatially, the fast-moving particles move collectively when the suspensions change from an arrested state to a

flowing state.

Adopting a granular perspective that characterizes the suspension dynamics using the viscous number $I_v = \eta_0\dot{\gamma}/\Pi$ with η_0 the solvent viscosity, we find that the rheology, the structural features, and the diffusive dynamics collapse in the high pressure limit. For glassy suspensions, μ and ϕ approach the arrest point (ϕ_m, μ_m) as $I_v \to 0$, which approaches the SAP in the $\Pi \to \infty$ limit. Away from the flow-arrest transitions, $\delta\phi = \phi_m - \phi$ and $\delta\mu = \mu - \mu_m$ exhibit universal power law behavior with respect to I_v, suggesting that the jamming physics dominates the flow behavior, and that thermal fluctuations only change the arrest locations. With this insight, we also develop a simple rheology model that accurately captures the behaviors of glassy suspensions. Hydrodynamic interactions only quantitatively alter this behavior. Moreover, the results from hydrodynamic simulations in the non-Brownian limit agrees quantitatively with the experiments of Boyer et al. [19] with a shift in ϕ.

In addition, the interaction friction coefficient $\mu^{\mathrm{I}} = \mu - (1 + \frac{5}{2}\phi)I_v$ collapse for *all* flowing suspensions as functions of $\dot{\gamma}a^2/d^s_\infty$, with d^s_∞ the long-time self-diffusivity, as $\mu^{\mathrm{I}} \propto \dot{\gamma}a^2/d^s_\infty$. The data collapse suggests a generalized Stokes-Einstein-Sutherland relation with an effective temperature proportional to the imposed pressure. The structural distortions also collapse with $\dot{\gamma}a^2/d^s_\infty$ for all the flowing suspensions, suggesting that the shear stresses are only proportional to the product of structural distortion and osmotic pressure near flow-arrest transitions. These universal behaviors are valid regardless of hydrodynamic interactions, suggesting that a mean-field description is possible for the diffusion and rheology of Brownian suspensions.

The thesis is arranged as follows: the first part contains Chapters 2 and 3, with Chapter 2 focusing on the short-time transport properties and Chapter 3 on the modified $\delta\gamma$-scheme for approximating the bidisperse diffusion properties. The second part is Chapter 4, presenting details of the SEASD algorithm. The third part is presented in Chapter 5 as the structure and mechanical properties in the colloidal film drying process. The fourth part is in Chapters 6, 7, and 8. Chapter 6 presents a short study on the mechanical aspects of the constant stress and pressure rheology of colloidal suspensions without hydrodynamic interactions. Chapter 7 significantly expands the previous chapter with additional focus on the dynamical and structural aspects. Chapter 8 thoroughly investigate the influences of hydrodynamic interactions. We finish this thesis with a conclusion and outlook in Chapter 9.

Finally, we note that Chapters 2–8 are presented in a form suitable for publication, with Chapters 2, 3, 4, and 6 already published.

References

[1] A. Einstein, "Eine neue bestimmung der moleküldimensionen", Annalen der Physik **19**, 289 (1906).

[2] R. J. Hunter, *Foundations of colloid science* (Oxford University Press, 2001).

[3] W. B. Russel, D. A. Saville, and W. R. Schowalter, *Colloidal dispersions* (Cambridge University Press, 1991).

[4] M. C. Miguel and J. M. Rubi, eds., *Jamming, yielding, and irreversible deformation in condensed matter* (Springer, 2006).

[5] L. Berthier, G. Biroli, L. Bouchaud J.-P.and Cipelletti, and W. van Saarloos, eds., *Dynamical heterogeneities in glasses, colloids, and granular media* (Oxford University Press, 2011).

[6] J. Mewis and N. J. Wagner, *Colloidal suspension rheology* (Cambridge University Press, 2013).

[7] D. Leighton and A. Acrivos, "The shear-induced migration of particles in concentrated suspensions", J. Fluid Mech. **181**, 415 (1987).

[8] T. Dbouk, E. Lemaire, L. Lobry, and F. Moukalled, "Shear-induced particle migration: predictions from experimental evaluation of the particle stress tensor", J. Non-Newtonian Fluid Mech. **198**, 78 (2013).

[9] J. F. Brady and G. Bossis, "Stokesian dynamics", Annu. Rev. Fluid Mech. **20**, 111 (1988).

[10] T. N. Phung, J. F. Brady, and G. Bossis, "Stokesian dynamics simulation of brownian suspensions", J. Fluid Mech. **313**, 181 (1996).

[11] D. R. Foss and J. F. Brady, "Structure, diffusion and rheology of brownian suspensions by stokesian dynamics simulation", J. Fluid Mech. **407**, 167 (2000).

[12] A. Sierou and J. F. Brady, "Accelerated stokesian dynamics simulations", J. Fluid Mech. **448**, 115 (2001).

[13] W. C. K. Poon, E. R. Weeks, and C. P. Royall, "On measuring colloidal volume fractions", Soft Matter **8**, 21 (2012).

[14] E. Wacholder and N. F. Sather, "The hydrodynamic interaction of two unequal spheres moving under gravity through quiescent viscous fluid", J. Fluid Mech. **65**, 417 (1974).

[15] R. J. Phillips, J. F. Brady, and G. Bossis, "Hydrodynamic transport properties of hard-sphere dispersions. i. suspensions of freely mobile particles", Phys. Fluids **31**, 3462 (1988).

[16] R. J. Phillips, J. F. Brady, and G. Bossis, "Hydrodynamic transport properties of hard-sphere dispersions. ii. porous media", Phys. Fluids **31**, 3473 (1988).

[17] A. J. Banchio and G. Nägele, "Short-time transport properties in dense suspensions: from neutral to charge-stabilized colloidal spheres", J. Chem. Phys. **128**, 104903 (2008).

[18] D. Prasad and H. K. Kytömaa, "Particle stress and viscous compaction during shear of dense suspensions", Int. J. Multiphase Flow **21**, 775 (1995).

[19] F. Boyer, E. Guazzelli, and O. Pouliquen, "Unifying suspension and granular rheology", Phys. Rev. Lett. **107**, 188301 (2011).

[20] J. F. Brady, A. S. Khair, and M. Swaroop, "On the bulk viscosity of suspensions", J. Fluid Mech. **554**, 109 (2006).

[21] A. S. Khair, M. Swaroop, and J. F. Brady, "A new resistance function for two rigid spheres in a uniform compressible low-reynolds-number flow", Phys. Fluids **18**, 043102 (2006).

[22] J. F. Brady, R. J. Phillips, J. C. Lester, and G. Bossis, "Dynamic simulation of hydrodynamically interacting suspensions", J. Fluid Mech. **195**, 257 (1988).

[23] C. W. J. Beenakker and P. Mazur, "Self-diffusion of spheres in a concentrated suspension", Physica A **120**, 388 (1983).

[24] C. W. J. Beenakker and P. Mazur, "Diffusion of spheres in a concentrated suspension ii", Physica A **126**, 349 (1984).

[25] D. Lindbo and A.-K. Tornberg, "Spectrally accurate fast summation for periodic Stokes potentials", J. Comput. Phys. **229**, 8994 (2010).

[26] A. J. Banchio and J. F. Brady, "Accelerated stokesian dynamics: brownian motion", J. Chem. Phys. **118**, 10323 (2003).

[27] D. R. Foss and J. F. Brady, "Brownian Dynamics simulation of hard-sphere colloidal dispersions", J. Rheol. **44**, 629 (2000).

Chapter 2

SHORT-TIME TRANSPORT PROPERTIES OF BIDISPERSE COLLOIDAL SUSPENSIONS AND POROUS MEDIA

[1] M. Wang and J. F. Brady, "Short-time transport properties of bidisperse suspensions and porous media: a Stokesian Dynamics study", the Journal of Chemical Physics **142**, 094901 (2015) doi:10.1063/1.4913518,

2.1 Introduction

Understanding the short-time transport properties of colloidal suspensions has been a lasting pursuit of researchers for over a century, dating back to Einstein's inquiry to the effective viscosity of dilute suspensions [1]. Such understanding has important scientific and technological implications due to colloidal suspensions' rich and complex behaviors—their applications encompass virtually every aspect of our lives.

The principal challenges in investigating colloidal suspensions are (*i*) the long-range and non-pairwise-additive hydrodynamic interactions (HIs) mediated by the solvent, which exhibit sharp transitions when two particles are close, and (*ii*) their sensitive response to the particle configurations, *e.g.*, their shape, size, and physico-chemical environments. To overcome these difficulties, a wide range of computational techniques have been developed: Lattice Boltzmann simulations [2, 3], Dissipative Particle Dynamics [4, 5], Smoothed Particle Hydrodynamics [6, 7], hydrodynamic multipole methods [8–10], boundary integral methods[11, 12], the Force Coupling Method [13–15], and (Accelerated) Stokesian Dynamics [16–19], to name a few. Despite significant advancement, substantial gaps remain in the vast parameter space, which leads to the versatility of colloidal suspensions.

In this work we present a comprehensive simulation study of the short-time transport properties of bidisperse colloidal systems, exploring the effects of particle size. Size polydispersity arises naturally in colloidal systems [20] and is known to affect their phase and packing behaviors [21] and transport properties [22–24], particularly at high density. However, the majority of existing theoretical and simulation works focuses on monodisperse systems. For polydisperse systems, with a few exceptions [25], earlier studies were restricted to dilute systems [26–30], or imposed

simplifications on HIs [31, 32].

To the best of our knowledge, the present work is the first study for polydisperse suspensions with full HIs covering the entire concentration range up to close packing. Specifically, the following species and mixture properties will be addressed: (1) the short-time translational self-diffusivity, (2) the short-time rotational self-diffusivity, (3) the instantaneous sedimentation velocity, (4) the hydrodynamic functions, (5) the high-frequency dynamic shear viscosity, and (6) the high-frequency dynamic bulk viscosity.

From a hydrodynamic perspective, flows in porous media are closely related to those in colloidal suspensions. In both cases, the fluid motions are governed by the Stokes equation, and, for a given particle configuration, the distinction is that in suspensions the particles are free to move, while in porous media the particles are fixed in space. Compared to suspensions, the immobile particles give rise to much stronger HIs and qualitatively different behaviors in their transport properties. Here, we present the following transport properties of bidisperse porous media: (1) the translational drag coefficient, which is related to the permeability, (2) the translational hindered diffusivity, and (3) the rotational hindered diffusivity.

We chose the Stokesian Dynamics (SD) [16, 17, 33] as the computational tool due to the simplicity and effectiveness of its formalism in treating the hydrodynamic interactions. For monodisperse systems, SD has been used to study the short-time transport properties of hard-sphere suspensions [34] and porous media [35], and its Particle Mesh Ewald (PME) variation, known as Accelerated Stokesian Dynamics (ASD), has been used to study the transport properties of charged colloidal suspensions [36, 37]. For polydisperse systems, only partial extensions of SD exist. Chang & Powell [31, 38, 39] extended SD to polydisperse systems without the far-field mobility Ewald summation. Consequently, their extension is only appropriate for monolayers. Ando & Skolnick [40] developed a force-torque level polydisperse SD to investigate the effect of molecular crowding on protein diffusion. Since stresslet order moments were ignored, their implementation is unsuitable for rheological studies. In this work, we implemented the SD algorithm for polydisperse systems to the stresslet level with Ewald summed periodic boundary conditions.

The simplicity of the SD framework unfortunately comes at a cost of accuracy for certain transport properties. However, the errors associated with SD cannot be estimated *a priori* and have to be understood by comparing with existing results from other computational techniques. This leads to the second objective of this

work: a careful assessment of the accuracy and effectiveness of SD.

Computing hydrodynamic interactions using conventional SD requires $O(N^3)$ operations, where N is the number of particles in the system. This makes SD computationally expensive and imposes severe restrictions on the system size accessible to dynamic simulations [41]. The time limiting step is the explicit inversion of the mobility and resistance tensors. The scaling can be reduced to $O(N^2)$ by taking advantage of iterative solvers [42–44], to $O(N \log N)$ in ASD through PME techniques [18], and further down to $O(N)$ using fast multipole methods [45]. However, for computing short-time transport properties in this work, the choice of the $O(N^3)$ algorithm is deliberate. Here, hydrodynamic computations are performed for independent configurations using a Monte-Carlo approach, and each $O(N^3)$ matrix inversion straightforwardly yields *all* the short-time transport properties associated with the configuration for both the suspension and the porous medium. In addition, the conventional SD incorporates a mean-field quadrupole contribution in the mobility computation [33], improving its accuracy.

The transport properties of colloidal suspensions can also be approximated via (semi-) analytical expressions. These approximations are often preferred over full hydrodynamic computations since they are easier to access. There are two approaches to treat HIs: One is akin to the diagrammatic methods in liquid state theories [46]. For example, the $\delta\gamma$-scheme developed by Beenakker & Mazur [47–49] incorporates many-body HIs by resumming an infinite subset of the hydrodynamic scattering series from all particles in the suspension. In a companion paper [50], we introduced a semi-empirical extension of the original monodisperse $\delta\gamma$-scheme to approximate the partial hydrodynamic functions of polydisperse suspensions. The other approach is similar to the virial expansions: Explicit computations of the two-body, three-body, *etc.*, HIs lead to polynomial expressions of transport properties in powers of concentration. Its simplest form considers only the two-body HIs and is known as the Pairwise Additive (PA) approximation [51]. It is asymptotically exact for dilute suspensions, and can conveniently incorporate size polydispersity since the two-body HIs can be computed to arbitrary precision. At higher concentrations, the many-body HIs become important and the PA approximations break down. The third objective of this work is to assess the validity of the PA approximations for polydisperse suspensions by comparing to the SD results.

The remainder of the chapter is arranged as follows: in Sec. 2.2 we define the bidisperse systems under study and their various transport properties. Sec. 2.3

describes the polydisperse SD algorithm and the simulation procedure. In Sec. 2.4 we summarize the equations for the PA approximations, and in Sec 2.5 we review the existing analytical results beyond the PA level. We present and discuss the SD results for bidisperse suspensions and porous media in Sec. 2.6 and 2.7, respectively. We conclude this chapter with a few comments in Sec. 2.8.

2.2 Bidisperse suspensions and porous media

Static structures

We consider an unbounded homogeneous isotropic mixture of hard-sphere particles of different radii. For two particles with radii a_α and a_β, their interaction potential $u_{\alpha\beta}(r)$ can be written as

$$u_{\alpha\beta}(r) = \begin{cases} 0 & \text{if } r > a_\alpha + a_\beta \\ \infty & \text{otherwise,} \end{cases} \tag{2.1}$$

where r is the center-center distance between the two particles, and $\alpha, \beta \in \{1, 2\}$ are the species indices for bidisperse systems. We choose the following dimensionless parameters to describe the configuration:

$$\lambda = a_2/a_1, \tag{2.2}$$

$$\phi = \phi_1 + \phi_2, \text{ and} \tag{2.3}$$

$$y_1 = \phi_1/\phi, \tag{2.4}$$

where λ is the size ratio, ϕ is the total volume fraction, $\phi_\alpha = \frac{4}{3}\pi a_\alpha^3 n_\alpha$ is the species volume fraction, and y_α is the volume composition of species α. The species number density $n_\alpha = N_\alpha/V$ with N_α the number of α particles in the system and V the system size. The total number of particles in the system is $N = N_1 + N_2$, and the total number density is $n = n_1 + n_2$. The thermodynamic limit corresponds to increasing both N and V to infinity while keeping their ratio constant. Obviously the volume composition $0 \le y_1 \le 1$. For convenience, and without loss of generality, we assume $a_1 < a_2$ and thus $\lambda \ge 1$.

The structure of bidisperse systems can be characterized by the partial static strcture factors

$$S_{\alpha\beta}(q) = \left\langle n^\alpha_{-\boldsymbol{q}} n^\beta_{\boldsymbol{q}} \right\rangle, \tag{2.5}$$

where q is the orientation-averaged wavenumber, and $\langle\cdot\rangle$ is the average operator in the thermodynamic limit over all configurations. The species density fluctuation $n^\alpha_{\boldsymbol{q}}$ is defined as

$$n^\alpha_{\boldsymbol{q}} = \frac{1}{\sqrt{N_\alpha}} \sum_{j\in\alpha} e^{-\imath \boldsymbol{q}\cdot\boldsymbol{r}_j}, \tag{2.6}$$

with $\imath = \sqrt{-1}$, $\boldsymbol{r}_j$ the position of particle j, and $j \in \alpha$ means summing over all particle j in species α. One way to capture the overall structure of the mixture is the number-number static structure factor

$$S_{NN}(q) = \sum_{\alpha,\beta} \sqrt{x_\alpha x_\beta} S_{\alpha\beta}(q), \tag{2.7}$$

with $x_\alpha = N_\alpha/N$ the species molar or number fraction. However, measurements from scattering experiments are often different from $S_{NN}(q)$, and correspond to a weighted average of $S_{\alpha\beta}(q)$,

$$S_M(q) = \frac{1}{\overline{f^2}(q)} \sum_{\alpha,\beta} \sqrt{x_\alpha x_\beta} f_\alpha(q) f_\beta(q) S_{\alpha\beta}(q), \tag{2.8}$$

where $f_\alpha(q)$ is the species scattering amplitude, and $\overline{f^2}(q) = \sum_\alpha x_\alpha f_\alpha^2(q)$ is the square mean scattering amplitude [52]. Unless different species have constant scattering amplitude and $f_\alpha = f_\beta$, we generally have $S_{NN}(q) \neq S_M(q)$, making the interpretation of experiments with polydisperse systems difficult.

The real space characterization of the homogeneous and isotropic mixture structure is described by the partial radial distribution functions $g_{\alpha\beta}(r)$. It is the probability of finding a particle of species β with distance r for a given particle of species α. Accordingly, we have [51]

$$g_{\alpha\beta}(r) = \frac{1}{n_\alpha n_\beta} \left\langle \sum_{\substack{i\in\alpha \\ j\in\beta}}{}' \frac{1}{V} \delta(\boldsymbol{r} - \boldsymbol{r}_i + \boldsymbol{r}_j) \right\rangle, \tag{2.9}$$

where $\delta(x)$ is the Dirac delta function, and the prime on the summation sign excludes the case of $i = j$. The radial distribution function is related to the inverse Fourier transform of $S_{\alpha\beta}$ as [46]

$$g_{\alpha\beta}(r) = 1 + \frac{1}{2\pi^2 r \sqrt{n_\alpha n_\beta}} \int_0^\infty [S_{\alpha\beta}(q) - \delta_{\alpha\beta}] q \sin(qr) \mathrm{d}q, \tag{2.10}$$

where $\delta_{\alpha\beta}$ is the Kronecker delta. Accordingly, the mixture total radial distribution function is

$$g(r) = \sum_{\alpha,\beta} x_\alpha x_\beta g_{\alpha\beta}(r). \tag{2.11}$$

The short-time hydrodynamics

Colloidal suspensions and porous media exhibit different behaviors depending on the time scale [53], and in this work we are interested in the short-time properties.

For a Newtonian solvent with shear viscosity η_0 and density ρ_0, by "short-time" we mean a coarse grained time scale t satisfying

$$\tau_H \sim \tau_I \ll t \ll \tau_D, \tag{2.12}$$

where τ_H is the hydrodynamic time, τ_I is the inertia time, and τ_D is the diffusion time.

The hydrodynamic time $\tau_H = \rho_0 a_2^2/\eta_0$ characterizes the time required for the fluid momentum to diffuse a length scale of the (larger) particle. With $\tau_H \ll t$, the Reynolds number $\mathrm{Re} = \tau_H/t \ll 1$, and therefore the HIs are dominated by the viscous stresses. Consequently, the fluid motion is governed by the Stokes equation and the incompressibility constraint,

$$\boldsymbol{\nabla} p(\boldsymbol{x}) = \eta_0 \nabla^2 \boldsymbol{v}(\boldsymbol{x}) \;\text{ and } \boldsymbol{\nabla} \cdot \boldsymbol{v}(\boldsymbol{x}) = 0, \tag{2.13}$$

where $p(\boldsymbol{x})$ and $\boldsymbol{v}(\boldsymbol{x})$ are the fluid pressure and velocity field, respectively. We further supplement the above equations with the no-slip boundary condition on the particle surfaces.

The particle inertia time, $\tau_I = \frac{2}{9}\rho_2 a_2^2/\eta_0$, where ρ_2 is the density of the (larger) particle, describes the time required for the *particle* momentum to dissipate by interacting with the solvent. The consequence of $\tau_I \ll t$ is that the particle momentum dissipates almost instantaneously and the particle dynamics are completely overdamped in the time scale we are interested in. Therefore, the HIs in the suspension are solely determined by the instantaneous particle configurations $\boldsymbol{r}^N = \{\boldsymbol{r}_1, \boldsymbol{r}_2, \ldots, \boldsymbol{r}_N\}$. This allows the use of Monte-Carlo type approaches to study the short-time transport properties, as each independent configuration is equivalent.

The diffusion time $\tau_D = 6\pi\eta_0 a_1^3/k_\mathrm{B}T$, where $k_\mathrm{B}T$ is the thermal energy scale, sets the upper limit of the short-time regime. It characterizes the time for a smaller particle to move a distance of its own size when driven by thermal fluctuations, *i.e.*, $\tau_D = a_1^2/d_{0,1}^t$, where $d_{0,1}^t = k_\mathrm{B}T/(6\pi\eta_0 a_1)$ is the Stokes-Einstein-Sutherland (SES) translational diffusivity of a single particle with radius a_1. In dense suspensions, the particles are close to each other, and the mean interparticle gap spacing $\xi a_1 \ll a_1$. In this case, the relative mobility for the nearly touching particles scales as ξ, and the relative diffusivity scales as $\xi d_{0,1}^t$. As a result, the characteristic time for a particle of size a_1 to move a distance of ξa_1 remains τ_D. Therefore, τ_D is a valid diffusion time scale at any suspension volume fraction. At the time scale $t \sim \tau_D$, the (smaller) particles wander far from their original positions and directly interact with

the neighboring particles. Such interactions change the suspension configuration, and lead to subdiffusive particle behaviors. At a much longer time scale $t \gg \tau_D$, the memory effects associated with changes in the particle configuration begin to decorrelate, and the particle motion becomes diffusive again. For the moderate size ratios considered in this work, the time scale τ_D is always several orders of magnitude larger than τ_I and τ_H, leaving a well-defined short-time regime as shown in Eq. (2.12).

The Stokes equation in Eq. (2.13) governs the HIs in the suspension. Its linearity gives rise to the linear dependence between the forces $\boldsymbol{F}$, torques $\boldsymbol{T}$, and stresslets $\boldsymbol{S}$ and the linear and angular velocities $\boldsymbol{U}$ and $\boldsymbol{\Omega}$, respectively. For all particles in the suspension, we have [54]

$$\begin{pmatrix} \boldsymbol{\mathcal{F}} \\ \boldsymbol{S} \end{pmatrix} = -\boldsymbol{\mathcal{R}} \cdot \begin{pmatrix} \boldsymbol{\mathcal{U}} - \boldsymbol{\mathcal{U}}^{\infty} \\ -\boldsymbol{e}^{\infty} \end{pmatrix}, \tag{2.14}$$

where $\boldsymbol{\mathcal{R}}$ is the grand resistance tensor, $\boldsymbol{\mathcal{F}} = \{\boldsymbol{F}, \boldsymbol{T}\}$ is the generalized force, $\boldsymbol{\mathcal{U}} - \boldsymbol{\mathcal{U}}^{\infty} = \{\boldsymbol{U} - \boldsymbol{u}^{\infty}, \boldsymbol{\Omega} - \boldsymbol{\omega}^{\infty}\}$ is the generalized velocity disturbance, and $\boldsymbol{u}^{\infty}$, $\boldsymbol{\omega}^{\infty}$, and $\boldsymbol{e}^{\infty}$ are the imposed linear velocity, angular velocity, and strain rate, respectively. The unsubscripted symbols suggest all particles are involved, *e.g.*, $\boldsymbol{F} = \{\boldsymbol{F}_1, \boldsymbol{F}_2, \ldots, \boldsymbol{F}_N\}$. Each element of the grand resistance tensor depends on the configuration of the entire system, *i.e.*, $\boldsymbol{\mathcal{R}} = \boldsymbol{\mathcal{R}}(\boldsymbol{r}^N)$, and the minimum dissipation theorem of Stokes flow requires $\boldsymbol{\mathcal{R}}$ to be symmetric and positive definite [54]. We can partition the grand resistance tensor $\boldsymbol{\mathcal{R}}$ as

$$\boldsymbol{\mathcal{R}}(\boldsymbol{r}^N) = \begin{pmatrix} \boldsymbol{R}_{FU} & \boldsymbol{R}_{FE} \\ \boldsymbol{R}_{SU} & \boldsymbol{R}_{SE} \end{pmatrix}, \tag{2.15}$$

where, for example, $\boldsymbol{R}_{FU}$ describes the coupling between the generalized force and the generalized velocity. The resistance tensor $\boldsymbol{R}_{FU}$ and its inverse $\boldsymbol{R}_{FU}^{-1}$ play a particularly important role in the short-time transport properties of suspensions and porous media, and can be further partitioned as

$$\boldsymbol{R}_{FU} = \begin{pmatrix} \boldsymbol{\zeta}^{tt} & \boldsymbol{\zeta}^{tr} \\ \boldsymbol{\zeta}^{rt} & \boldsymbol{\zeta}^{rr} \end{pmatrix}, \tag{2.16}$$

$$\boldsymbol{R}_{FU}^{-1} = \begin{pmatrix} \boldsymbol{\mu}^{tt} & \boldsymbol{\mu}^{tr} \\ \boldsymbol{\mu}^{rt} & \boldsymbol{\mu}^{rr} \end{pmatrix}, \tag{2.17}$$

where each sub-matrix contains coupling between the translational (t) and rotational (r) velocities and forces.

Suspension transport properties

The dynamic structural evolution of a colloidal mixture can be described by the dynamic partial structure factors

$$S_{\alpha\beta}(q,t) = \left\langle n^{\alpha}_{-\boldsymbol{q}}(0) n^{\beta}_{\boldsymbol{q}}(t) \right\rangle, \tag{2.18}$$

where $n^{\beta}_{\boldsymbol{q}}(t)$ is the density fluctuations measured at time t from Eq. (2.5), and thus $S_{\alpha\beta}(q) = S_{\alpha\beta}(q,0)$. The dynamics of $S_{\alpha\beta}(q,t)$ are governed by the Smoluchowski equation [51, 55], and one can show that in the short time limit,

$$\boldsymbol{S}(q,t) \approx \exp[-tq^2 \boldsymbol{D}(q)] \cdot \boldsymbol{S}(q), \tag{2.19}$$

where $\boldsymbol{S}(q,t)$ for bidisperse suspensions is a 2×2 matrix with elements of $S_{\alpha\beta}(q,t)$, and $\boldsymbol{D}(q)$ is the q-dependent diffusivity matrix depending on the suspension structure and HIs. The hydrodynamic contribution to diffusivity matrix $\boldsymbol{D}(q)$ is extracted as

$$\boldsymbol{H}(q) = \boldsymbol{D}(q) \cdot \boldsymbol{S}(q)/(k_{\mathrm{B}}T), \tag{2.20}$$

and $\boldsymbol{H}(q)$ is known as the hydrodynamic matrix with elements $H_{\alpha\beta}(q)$, the partial hydrodynamic functions. The microscopic definition of $H_{\alpha\beta}(q)$ is

$$H_{\alpha\beta}(q) = \frac{1}{\sqrt{N_\alpha N_\beta}} \left\langle \sum_{\substack{i\in\alpha \\ j\in\beta}} \hat{\boldsymbol{q}} \cdot \boldsymbol{\mu}^{tt}_{ij}(\boldsymbol{r}^N) \cdot \hat{\boldsymbol{q}} e^{\imath \boldsymbol{q}\cdot(\boldsymbol{r}_i - \boldsymbol{r}_j)} \right\rangle, \tag{2.21}$$

where $\hat{\boldsymbol{q}} = \boldsymbol{q}/|\boldsymbol{q}|$ is the unit vector of $\boldsymbol{q}$. The mobility tensors $\boldsymbol{\mu}^{tt}_{ij}$ are elements of the tensor $\boldsymbol{\mu}^{tt}$ in Eq. (2.17), and describe the coupling between the linear velocity disturbance of the particle i due to an imposed force on the particle j.

It is convenient to split $H_{\alpha\beta}(q)$ as

$$H_{\alpha\beta}(q) = \delta_{\alpha\beta} d^t_{s,\alpha}/(k_{\mathrm{B}}T) + H^d_{\alpha\beta}(q), \tag{2.22}$$

where $H^d_{\alpha\beta}(q)$ is the q-dependent distinct part of the partial hydrodynamic function, and $d^t_{s,\alpha}$ is the short-time translational self-diffusivity of species α. Note that we use the lowercase symbol to signify its q-independence. The microscopic definition of $d^t_{s,\alpha}$ is

$$d^t_{s,\alpha} = \frac{k_{\mathrm{B}}T}{N_\alpha} \left\langle \sum_{i\in\alpha} \hat{\boldsymbol{q}} \cdot \boldsymbol{\mu}^{tt}_{ii} \cdot \hat{\boldsymbol{q}} \right\rangle, \tag{2.23}$$

and it describes the short-time mean-square displacement of species α in a Brownian suspension

$$d^t_{s,\alpha} = \lim_{t\to0} \frac{\mathrm{d}}{\mathrm{d}t} \left\langle \tfrac{1}{6}[\boldsymbol{r}_i(t) - \boldsymbol{r}_i(0)]^2 \right\rangle, i \in \alpha. \tag{2.24}$$

Comparing Eq. (2.21) and (2.23), we see that in the short wave-length limit,

$$d^t_{s,\alpha} = \lim_{q\to\infty} k_B T H_{\alpha\alpha}(q). \tag{2.25}$$

The suspension hydrodynamic functions can be obtained by dynamic scattering experiments, but $H_{\alpha\beta}(q)$ is often difficult to access directly unless special techniques such as selective index of refraction matching are employed [56]. Otherwise, the measured hydrodynamic function $H_M(q)$ is related to $H_{\alpha\beta}(q)$ as [52]

$$H_M(q) = \frac{1}{\overline{f^2}(q)} \sum_{\alpha,\beta} \sqrt{x_\alpha x_\beta} f_\alpha(q) f_\beta(q) H_{\alpha\beta}(q), \tag{2.26}$$

where $f_\alpha(q)$, $f_\beta(q)$ and $\overline{f^2}(q)$ are defined in Eq. (2.8). In the hypothetical case of constant and equal f_α, the number-number mixture hydrodynamic function is

$$H_{NN}(q) = \sum_{\alpha,\beta} \sqrt{x_\alpha x_\beta} H_{\alpha\beta}(q). \tag{2.27}$$

The rotational Brownian motion of colloidal suspensions can be observed by introducing optical anisotropy to the otherwise spherical particles using depolarized dynamic light scattering techniques [30, 57]. The optical anisotropy is characterized by the orientation unit vector $\hat{\boldsymbol{n}}_i(t)$ for particle i at time t. The short-time decay of the rotational correlation function of particles of species α,

$$S^\alpha_r(t) = \langle P_2[\hat{\boldsymbol{n}}_i(t) \cdot \hat{\boldsymbol{n}}_i(0)] \rangle, i \in \alpha, \tag{2.28}$$

where $P_2(x)$ is the Legendre polynomial of the second order, defines the short-time rotational self-diffusivity

$$d^r_{s,\alpha} = -\tfrac{1}{6} \lim_{t\to 0} \frac{\mathrm{d}}{\mathrm{d}t} \ln[S^\alpha_r(t)]. \tag{2.29}$$

Microscopically, $d^r_{s,\alpha}$ is defined as

$$d^r_{s,\alpha} = \frac{k_B T}{N_\alpha} \left\langle \sum_{i\in\alpha} \hat{\boldsymbol{q}} \cdot \boldsymbol{\mu}^{rr}_{ii} \cdot \hat{\boldsymbol{q}} \right\rangle, \tag{2.30}$$

where $\boldsymbol{\mu}^{rr}_{ij}$ are elements of $\boldsymbol{\mu}^{rr}$ in Eq. (2.17), and describe the angular velocity disturbance on particle i due to an imposed torque on particle j.

Sedimentation occurs when the particle density ρ_α is different from the solvent density ρ_0. The net body force exerted on species α depends on the species radius a_α and the density difference $\Delta\rho_\alpha = \rho_\alpha - \rho_0$. In bidisperse suspensions, the

instantaneous sedimentation velocities depend on the size ratio λ and the density ratio [28, 58]

$$\gamma = \Delta\rho_2/\Delta\rho_1. \tag{2.31}$$

The ratio of the mean forces between the two species is $F_2/F_1 = \lambda^3\gamma$. Examination of Eq. (2.21) reveals that the species instantaneous sedimentation velocities, $U_{s,1}$ and $U_{s,2}$, can be expressed in terms of $H_{\alpha\beta}(0) = \lim_{q\to 0} H_{\alpha\beta}(q)$ as

$$\frac{U_{s,1}}{U_{0,1}} = \frac{1}{\mu_{0,1}}\left[H_{11}(0) + \lambda^3\gamma\sqrt{\frac{x_2}{x_1}}H_{12}(0)\right], \tag{2.32}$$

$$\frac{U_{s,2}}{U_{0,2}} = \frac{1}{\mu_{0,2}}\left[\frac{1}{\lambda^3\gamma}\sqrt{\frac{x_1}{x_2}}H_{21}(0) + H_{22}(0)\right], \tag{2.33}$$

where, for species α, $\mu_{0,\alpha} = (6\pi\eta_0 a_\alpha)^{-1}$ is the single particle mobility and $U_{0,\alpha} = \mu_{0,\alpha}F_\alpha$ is the single particle sedimentation velocity. For simplicity, we only consider the case $\gamma = 1$.

A distinguishing feature of sedimentation in polydisperse suspensions is that $U_{s,\alpha}$ can be negative. The motion of one species can give rise to a strong back flow that reverses the sedimentation velocity of the second species, *i.e.*, the particles move in a direction opposite to the imposed body force, especially when the body force is weak [28]. For monodisperse suspensions, on the other hand, the positive definiteness of the mobility tensor $\boldsymbol{\mu}$ requires the sedimentation velocity to be positive.

Eq. (2.32) and (2.33) also reveal the close connection between $U_{s,\alpha}$ and $H_{\alpha\beta}(q)$. At different wavenumber q, $H_{\alpha\beta}(q)$ probes the suspension HIs at different length scales: single particle behaviors as $q \to \infty$, and collective dynamics as $q \to 0$. The wavenumber corresponding to the maximum of $H_{\alpha\beta}(q)$ is closely related to the size of the structures that dominate the suspension short-time dynamics [36].

The suspension rheological properties are obtained from the volume average of the Cauchy stress [59, 60],

$$\langle\boldsymbol{\sigma}\rangle = -\langle p\rangle_f\boldsymbol{I} + 2\eta_0\langle\boldsymbol{e}^\infty\rangle + (\kappa_0 - \tfrac{2}{3}\eta_0)\langle\boldsymbol{\nabla}\cdot\boldsymbol{u}^\infty\rangle\boldsymbol{I} + n\langle\boldsymbol{S}^H\rangle, \tag{2.34}$$

where p is the solvent pressure, $\langle\cdot\rangle_f$ is the fluid phase averaging operator, $\boldsymbol{I}$ is the idem tensor, κ_0 is the solvent bulk viscosity, and $\langle\boldsymbol{S}^H\rangle$ is the stresslet due to the presence of particles. In the short-time limit and without the interparticle forces,

$$\langle\boldsymbol{S}^H\rangle = -\langle\boldsymbol{R}_{SU}\cdot\boldsymbol{R}_{FU}^{-1}\cdot\boldsymbol{R}_{FE} - \boldsymbol{R}_{SE}\rangle : \langle\boldsymbol{e}^\infty\rangle. \tag{2.35}$$

Eq. (2.34) ignores the stress contributions from the Brownian motion, and therefore is strictly valid in the short-time limit. To measure the transport properties associated with $\langle \boldsymbol{\sigma} \rangle$ defined in Eq. (2.34) and (2.35), rheological experiments have to be performed with high-frequency, low-amplitude deformations, such that the suspension microstructures are only slightly perturbed from the equilibrium hard-sphere structures, and the Brownian stress contribution is out of phase with the applied oscillating deformation [34]. In a high-frequency shear experiment with an imposed strain rate of amplitude $\dot{\gamma}$, the suspension high-frequency dynamic shear viscosity is

$$\eta_s = \eta_0 + n\langle S^H \rangle_{12}/\dot{\gamma}, \tag{2.36}$$

where the subscript 12 denotes the velocity-velocity gradient component of the stresslet. In a high-frequency expansion experiment with an imposed expansion rate of amplitude $\dot{e}$, the high-frequency dynamic bulk viscosity is

$$\kappa_s = \kappa_0 + \tfrac{1}{3} n\langle \boldsymbol{S}^H \rangle : \boldsymbol{I}/\dot{e}. \tag{2.37}$$

Note that for solvent with a finite bulk viscosity κ_0, the incompressibility condition of the Stokes equation is violated. However, as is shown in Ref. [60], the fluid velocity disturbance remains incompressible and satisfies the Stokes equation. The rigid colloidal particles, unable to expand with the fluid, therefore contribute to the suspension bulk viscosity.

Porous medium transport properties

When a fluid passes through a porous medium, which is frequently modeled as a matrix of stationary particles, the particles resist the flow, creating a pressure drop across the material. The resistance behavior is often characterized by the dimensionless drag coefficient F_α [25], defined through

$$6\pi\eta_0 a_\alpha F_\alpha \boldsymbol{V} = \boldsymbol{F}_{d,\alpha}, \tag{2.38}$$

where $\boldsymbol{V}$ is the superficial fluid velocity and $\boldsymbol{F}_{d,\alpha}$ is the mean drag force for particle species α including the back pressure gradient contribution from the fluid. A force balance considering both the fluid and the particles shows that the average force for each particle is

$$\boldsymbol{F}_{d,\alpha} = \frac{1-\phi}{N_\alpha} \left\langle \sum_{i\in\alpha} \sum_{j=1}^{N} \boldsymbol{\zeta}_{ij}^{tt} \right\rangle \cdot \boldsymbol{V}, \tag{2.39}$$

where $\boldsymbol{\zeta}_{ij}^{tt}$ is from the resistance tensor $\boldsymbol{\zeta}^{tt}$ in Eq. (2.16), and describes the force-linear velocity coupling between particles i and j.

For a porous medium containing particles of different sizes, the average drag coefficient is defined as

$$\langle F\rangle = \sum_{\alpha} \frac{y_\alpha}{z_\alpha^2} F_\alpha, \tag{2.40}$$

where the diameter fraction $z_\alpha = a_\alpha/\langle a\rangle$ and $\langle a\rangle = (\sum_\alpha y_\alpha/a_\alpha)^{-1}$. As is shown in Ref. [25], Eq. (2.40) allows convenient extension of the Darcy's equation to polydisperse systems. The porous medium permeability $\langle K\rangle$ is closely related to $\langle F\rangle$ in Eq. (2.40) as

$$\langle K\rangle = \frac{\langle F\rangle}{1-\phi}. \tag{2.41}$$

The diffusive behaviors of particles in porous media are characterized by the translational and rotational hindered diffusivities, denoted as $d^t_{\mathrm{HD},\alpha}$ and $d^r_{\mathrm{HD},\alpha}$, respectively. They describe the short-time Brownian motions of a *single* mobile particle in a matrix of fixed particles. In terms of the resistance tensors, we have [35]

$$d^t_{\mathrm{HD},\alpha} = \frac{k_\mathrm{B}T}{N_\alpha}\left\langle \sum_{i\in\alpha} \hat{\boldsymbol{q}}\cdot(\boldsymbol{\zeta}^{tt}_{ii})^{-1}\cdot\hat{\boldsymbol{q}}\right\rangle, \tag{2.42}$$

$$d^r_{\mathrm{HD},\alpha} = \frac{k_\mathrm{B}T}{N_\alpha}\left\langle \sum_{i\in\alpha} \hat{\boldsymbol{q}}\cdot(\boldsymbol{\zeta}^{rr}_{ii})^{-1}\cdot\hat{\boldsymbol{q}}\right\rangle, \tag{2.43}$$

where $\boldsymbol{\zeta}^{rr}_{ij}$ are elements of $\boldsymbol{\zeta}^{rr}$ in Eq. (2.16), and describe the torque-angular velocity coupling between particles i and j.

2.3 The polydisperse Stokesian Dynamics

The framework of Stokesian Dynamics (SD) has been extensively discussed elsewhere [16, 17, 19, 33, 61] and here we only present the aspects pertinent to the extension to polydisperse systems. The grand resistance tensor $\boldsymbol{\mathcal{R}}$ in Eq. (2.15) is computed in SD as

$$\boldsymbol{\mathcal{R}} = (\boldsymbol{\mathcal{M}}^\infty)^{-1} + \boldsymbol{\mathcal{R}}_{2B} - \boldsymbol{\mathcal{R}}^\infty_{2B}, \tag{2.44}$$

where the far-field mobility tensor $\boldsymbol{\mathcal{M}}^\infty$ is constructed pairwisely from the multipole expansions and Faxén's laws of Stokes equation up to the stresslet level, and its inversion captures the long-range many-body HIs. The near-field lubrication correction $(\boldsymbol{\mathcal{R}}_{2B} - \boldsymbol{\mathcal{R}}^\infty_{2B})$ is based on the exact two-body solutions with the far-field contributions removed, and it accounts for the singular HIs when particles are in close contact. The SD recovers the exact solutions of two-particle problems and was shown to agree well with the exact solution of three-particle problems [62].

Extending SD to polydisperse systems retains the computational framework above. The far-field polydisperse mobility tensor $\boldsymbol{\mathcal{M}}^\infty$ is computed using multipole expan-

sions as Ref. [38] and the results are extended to infinite periodic systems using Beenakker's technique [63, 64]. The lubrication corrections $(\mathcal{R}_{2B} - \mathcal{R}^{\infty}_{2B})$ for a particle pair with radii a_α and a_β are based on the exact solutions of two-body problems in series form [65–68] up to s^{-300}, where $s = 2r/(a_\alpha + a_\beta)$ is the scaled center-center particle distance. Note that in Ref. [68] there is an extra $(n + 1)$ that should be removed in the denominator of the fraction in front of $P_{s(q-s)(p-n-1)}$ for the expression of P_{npq}. In the simulations, the lubrication corrections are invoked when $r < 2(a_\alpha + a_\beta)$, and the analytic lubrication expressions are used when $r < 1.05(a_\alpha + a_\beta)$. To avoid singularities in the grand resistance tensor due to particle contact, we enforced a minimum separation of $10^{-6}(a_i + a_j)$ between particles.

Our polydisperse SD program treats the solvent as a compressible fluid and computes the fluid velocity disturbance due to the presence of rigid particles. As a result, the trace of the particle stresslet is no longer zero and has to be computed. The solvent compressibility allows the quantities related the pressure moment to be directly incorporated to the grand resistance tensor $\mathcal{R}$, augmenting its size from $11N \times 11N$ to $12N \times 12N$. This is more convenient compared to the earlier approaches, where the pressure related quantities are treated as a separate problem and sometimes require iterations [67, 69, 70].

A subtlety in incorporating the fluid compressibility is that in the mobility problem, a compressible flow disturbance can only be generated by the trace of the stresslet. As a result, the pairwisely constructed far-field grand mobility tensor $\mathcal{M}^{\infty}$ is not symmetric. This asymmetry is necessary to eliminate the spurious hydrodynamic reflections upon its inversion and ensure the elements of $(\mathcal{M}^{\infty})^{-1}$ corresponding to the incompressible problem remain the same as the original SD. However, the symmetry of $\mathcal{R}$ is restored by copying the missing components in $\boldsymbol{R}_{SU}$ and the lower triangular part of $\boldsymbol{R}_{SE}$ from the transpose of $\boldsymbol{R}_{FE}$ and the upper triangular part of of $\boldsymbol{R}_{SE}$, respectively [61].

As pointed out by Cichocki *et al.* [10], the pairwise additive lubrication correction $(\mathcal{R}_{2B} - \mathcal{R}^{\infty}_{2B})$ contains both the relative and collective motions of the particle pair. When computing the three-body contributions to the suspension short-time self-diffusivity, the lubrication corrections corresponding to the collective motion destroy the convergence and should be eliminated [10]. In this work, however, we have verified that removing the pair collective motion part of the lubrication corrections has limited quantitative effect (on average less than 1% difference) on the resulting

transport properties. Therefore, the results in Sec. 2.6 and 2.7 are based on the full lubrication corrections that reproduce the exact pair results. Note that the force-torque level SD implementation of Ando & Skolnick [40] removed the pair collective motion in the lubrication corrections.

Our simulations proceed as follows. First, a random bidisperse hard-sphere packing at the desired composition is generated using the event-driven Lubachevsky-Stillinger algorithm [71, 72] with high compression rate. After the desired volume fraction ϕ is reached, the system is equilibrated for a short time (10 events per particle) without compression. This short equilibration stage is necessary as the compression pushes particles closer to each other, and prolonging this equilibration stage does not alter the resulting suspension structure significantly. After the grand resistance tensor $\boldsymbol{\mathcal{R}}$ is constructed based on the particle configuration $\boldsymbol{r}^N$, the short-time transport properties presented in section 2.2 are extracted.

The simulations were performed for bidisperse systems of size ratio $\lambda = 2$ and 4 as well as monodisperse systems. To scan the parameter space, we first fix the mixture composition to $y_1 = 0.5$ and vary the total volume fraction ϕ. We then study the effects of y_1 with fixed ϕ at $\lambda = 2$. Typically each configuration contains 800 particles and at least 500 independent configurations are studied for each composition. For systems with disparate size ratios, we ensure at least 10 large particles are presented in the simulations.

Fig. 2.1 shows the structural characterizations, $g_{\alpha\beta}(r)$ and $S_{\alpha\beta}(q)$, measured from the above simulation protocol for a bidisperse suspension of $\lambda = 4$, $y_1 = 0.5$, and $\phi = 0.4$. The measurements from the simulations are compared with the Percus-Yevick (PY)[73, 74] integral equation solutions. Note that at $y_1 = 0.5$, the mixture number composition is highly asymmetric, *i.e.*, $x_1 = 0.985$. For $g_{\alpha\beta}(r)$ in Fig. 2.1a, the simulation measurements can be accurately described by the PY solutions [75, 76] despite the small underestimation of the contact values for $g_{12}(r)$ and $g_{22}(r)$. Although semi-empirical corrections [76, 77] exist for this well-known symptom of the PY solutions [46], they are not applicable for dense mixtures with large size ratios. In Fig. 2.1b, $S_{\alpha\beta}(q)$ directly measured from the simulations agree well with the analytical PY solutions [78, 79] except at small wavenumbers. Note that the PY $S_{\alpha\beta}(q)$ was shown to be valid for polydisperse mixtures at ϕ even beyond the monodisperse close packing [80]. Fig. 2.1 validates the PY solution as a satisfactory description of the suspension structures in both the real and the wave spaces.

The transport properties extracted from $\boldsymbol{\mu}^{tt}$, *i.e.*, $d^t_{s,\alpha}$, $U_{s,\alpha}$, and $H_{\alpha\beta}(q)$, exhibit a

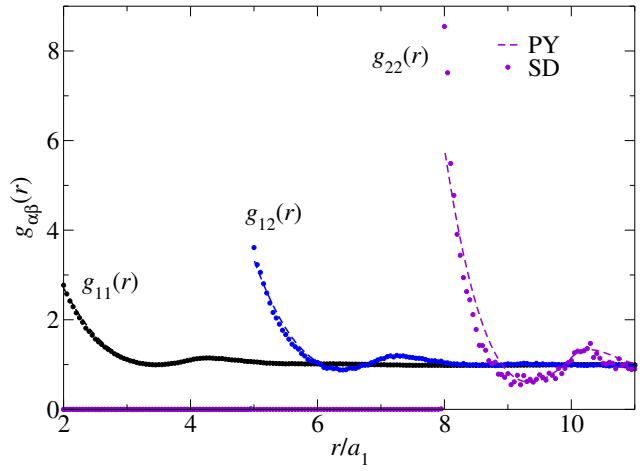

(a)

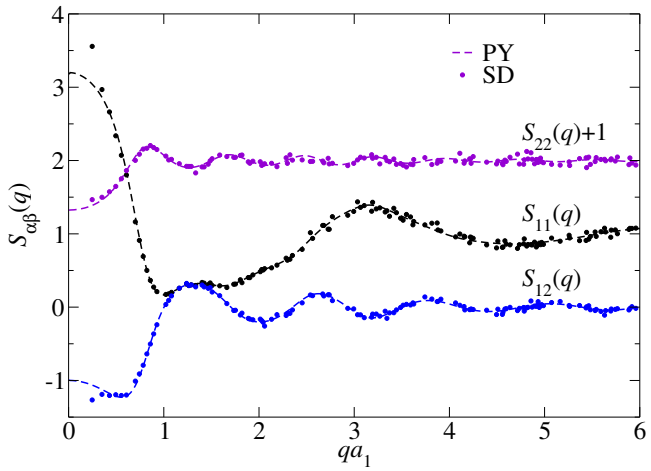

(b)

Figure 2.1: (Color online) The structures of bidisperse suspensions with $\lambda = 4$, $\phi = 0.4$, and $y_1 = 0.5$ directly measured from the SD simulations (dots) and computed from the Percus-Yevick (PY) integral equation (dashed lines): (a) the partial radial distribution functions $g_{\alpha\beta}(r)$, and (b) the partial static structure factors $S_{\alpha\beta}(q)$. Note that $S_{22}(q)$ for the larger particles is shifted up by 1 for clarity.

strong $\sqrt[3]{N}$ size dependence in the simulations due to the imposed periodic boundary conditions [34, 36, 81, 82]. The finite size effect can be eliminated by considering $H_{\alpha\beta}(q)$ as a generalized sedimentation velocity with contributions from random suspensions and cubic lattices [34, 82]. For bidisperse suspensions, the finite size correction $\Delta_N H_{\alpha\beta}(q)$ for partial hydrodynamic functions from an N-particle system, $H_{\alpha\beta,N}(q)$, is

$$\Delta_N H_{\alpha\beta}(q) = \frac{1.76\mu_{0,1}S_{\alpha\beta}(q)}{(x_1 + x_2\lambda^3)^{\frac{1}{3}}}\frac{\eta_0}{\eta_s}\left(\frac{\phi}{N}\right)^{\frac{1}{3}}, \tag{2.45}$$

so that in the thermodynamic limit the partial hydrodynamic function $H_{\alpha\beta}(q) = \Delta_N H_{\alpha\beta}(q) + H_{\alpha\beta,N}(q)$. In Eq. (2.45), η_s/η_0 is the suspension high-frequency dynamic shear viscosity obtained from the same simulations, and the static structure factors $S_{\alpha\beta}(q)$ are taken from the analytical PY solution [78, 79]. Note the scaling for $\Delta_N H_{\alpha\beta}(q)$ is $\mu_{0,1}$ regardless of the choice of α and β. The corrections for $d^t_{s,\alpha}$ and $U_{s,\alpha}$ correspond to the large and small q limit of Eq. (2.45), respectively. We checked that other transport properties, including the shear viscosity η_s/η_0, change little with the system size.

The effectiveness of Eq. (2.45) is demonstrated in Fig. 2.2 for all three partial hydrodynamic functions. Without the correction, simulations at different N produce distinct $H_{\alpha\beta}(q)$ and the finite size effect is significant. After applying Eq. (2.45), the data at different N collapse for all q. Note that the finite size collapse of $H_{22}(q)$ in Fig. 2.2c for small N is slightly scattered due to the limited number of large particles, *e.g.*, at $N = 100$, there are only 11 large particles in the mixture. The corrected results for $N = 400$ and 800 do agree with each other satisfactorily. Eq. (2.45) spares us from extrapolating multiple simulations to eliminate the finite size effect, and we apply it for all the presented results.

2.4 The pairwise additive approximation

The pairwise additive (PA) approximation is convenient for estimating suspension transport properties at low volume fractions [51]. It explicitly takes the mixture structures into account by incorporating the radial distribution functions (RDF) $g_{\alpha\beta}(r)$ into its formulation. As is evident from Fig. 2.1, the PY solution satisfactorily captures the suspension structures, and is therefore used in this work.

The PA approximations of the short-time translational and rotational self-diffusivities,

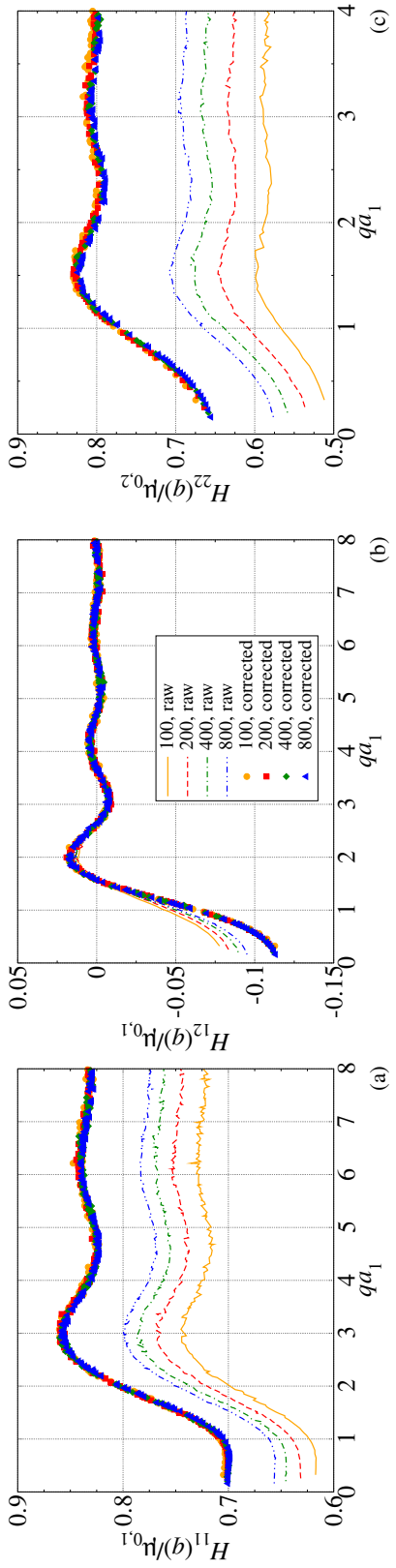

Figure 2.2: (Color online) The raw and corrected partial hydrodynamic functions with different simulation system sizes, (a): $H_{11}(q)$, (b): $H_{12}(q)$, and (c): $H_{22}(q)$, for a bidisperse suspension at $\lambda = 2$, $\phi = 0.1$, and $y_1 = 0.5$.

$d^t_{s,\alpha}$ and $d^r_{s,\alpha}$ respectively, for species α are [27, 30]

$$\frac{d^t_{s,\alpha}}{d^t_{0,\alpha}} = 1 + \sum_\beta I^t_{\alpha\beta}\phi_\beta, \tag{2.46}$$

$$\frac{d^r_{s,\alpha}}{d^r_{0,\alpha}} = 1 + \sum_\beta I^r_{\alpha\beta}\phi_\beta, \tag{2.47}$$

where $d^t_{0,\alpha} = k_\mathrm{B}T\mu_{0,\alpha}$ is the single particle translational diffusivity, $d^r_{0,\alpha} = k_\mathrm{B}T/(8\pi\eta_0 a^3_\alpha)$ is the single particle rotational self-diffusivity. The integrals $I^t_{\alpha\beta}$ and $I^r_{\alpha\beta}$ are

$$I^t_{\alpha\beta} = \frac{(1+\lambda_{\beta\alpha})^3}{8\lambda^3_{\beta\alpha}} \int_2^\infty s^2 g_{\alpha\beta}(s)(x^a_{11} + 2y^a_{11} - 3)\mathrm{d}s, \tag{2.48}$$

$$I^r_{\alpha\beta} = \frac{(1+\lambda_{\beta\alpha})^3}{8\lambda^3_{\beta\alpha}} \int_2^\infty s^2 g_{\alpha\beta}(s)(x^c_{11} + 2y^c_{11} - 3)\mathrm{d}s, \tag{2.49}$$

where $s = 2r/(a_\alpha + a_\beta)$ and $\lambda_{\beta\alpha} = a_\beta/a_\alpha$. Note that the RDF $g_{\alpha\beta}(s) = g_{\alpha\beta}(s, \lambda, \phi)$ depends on the mixture composition. The mobility couplings of the dimensionless hydrodynamic functions x^a, y^a, x^c, *etc.*, are described in Kim & Karrila [54], and we adopt the scaling of Jeffrey & Onishi [65].

The PA approximation of the sedimentation velocity is a natural extension of Batchelor [28]:

$$\frac{U_{s,\alpha}}{U_{0,\alpha}} = 1 + \sum_\beta S_{\alpha\beta}\phi_\beta, \tag{2.50}$$

and the integral [83]

$$\begin{aligned} S_{\alpha\beta} = &\left(\frac{1+\lambda_{\beta\alpha}}{2\lambda_{\beta\alpha}}\right)^3 \int_2^\infty s^2 g_{\alpha\beta}(s)(x^a_{11} + 2y^a_{11} - 3)\mathrm{d}s \\ &- \gamma(\lambda^2_{\beta\alpha} + 3\lambda_{\beta\alpha} + 1) + \tfrac{3}{4}\gamma(1+\lambda_{\beta\alpha})^2 \int_2^\infty s h_{\alpha\beta}(s)\mathrm{d}s \\ &+ \gamma\left(\frac{1+\lambda_{\beta\alpha}}{2}\right)^2 \int_2^\infty s^2 g_{\alpha\beta}(s)(\hat{x}^a_{12} + 2\hat{y}^a_{12})\mathrm{d}s, \end{aligned} \tag{2.51}$$

where $h_{\alpha\beta}(s) = g_{\alpha\beta}(s) - 1$. The far field hydrodynamic functions take the form

$$\hat{x}^a_{12}(\lambda_{\beta\alpha}, s) = x^a_{12}(\lambda_{\beta\alpha}, s) - \tfrac{3}{2}s^{-1} + \frac{2(1+\lambda^2_{\beta\alpha})}{(1+\lambda_{\beta\alpha})^2}s^{-3}, \tag{2.52}$$

$$\hat{y}^a_{12}(\lambda_{\beta\alpha}, s) = y^a_{12}(\lambda_{\beta\alpha}, s) - \tfrac{3}{4}s^{-1} - \frac{1+\lambda^2_{\beta\alpha}}{(1+\lambda_{\beta\alpha})^2}s^{-3}. \tag{2.53}$$

The PA approximation of the distinct part of the partial hydrodynamic function, $H^d_{\alpha\beta}$, is [52]

$$\begin{aligned} H^d_{\alpha\beta}(q) =& \mu_{0,\alpha}\lambda_{\beta\alpha}^{-\frac{3}{2}}\sqrt{\phi_\alpha\phi_\beta}\left[\tfrac{9}{8}(1+\lambda_{\beta\alpha})^2 H^{d,1}_{\alpha\beta}\right. \\ &\left. +\tfrac{3}{2}(1+\lambda_{\beta\alpha}^2)H^{d,2}_{\alpha\beta} + \tfrac{3}{4}(1+\lambda_{\beta\alpha})^2 H^{d,3}_{\alpha\beta}\right], \end{aligned} \tag{2.54}$$

with

$$\begin{aligned} H^{d,1}_{\alpha\beta} =& -2\frac{j_1(2\bar{q})}{\bar{q}} + \int_2^\infty s h_{\alpha\beta}(s)\left(j_0(\bar{q}s) - \frac{j_1(\bar{q}s)}{\bar{q}s}\right)\mathrm{d}s, \\ H^{d,2}_{\alpha\beta} =& \frac{j_1(2\bar{q})}{2\bar{q}} + \int_2^\infty h_{\alpha\beta}(s)\frac{j_2(\bar{q}s)}{\bar{q}s}\mathrm{d}s, \\ H^{d,3}_{\alpha\beta} =& \int_2^\infty s^2 g_{\alpha\beta}(s)\times \\ & \left[\hat{y}^a_{12} j_0(\bar{q}s) + (\hat{x}^a_{12} - \hat{y}^a_{12})\left(j_0(\bar{q}s) - 2\frac{j_1(\bar{q}s)}{\bar{q}s}\right)\right]\mathrm{d}s, \end{aligned}$$

where $\bar{q} = \frac{1}{2}(a_\alpha + a_\beta)q$ is the rescaled wavenumber, and $j_0(x)$, $j_1(x)$, and $j_2(x)$ are spherical Bessel functions of the first kind.

The shear viscosity for polydisperse suspensions is computed as [26, 84]

$$\frac{\eta_s}{\eta_0} = 1 + \tfrac{5}{2}\phi + \tfrac{5}{2}\phi^2 + \sum_{\alpha,\beta} I^\eta_{\alpha\beta}\phi_\alpha\phi_\beta, \tag{2.55}$$

where $\frac{5}{2}\phi$ is the Einstein viscosity correction and $\frac{5}{2}\phi^2$ is the sum of force dipoles in the suspension. The integral $I^\eta_{\alpha\beta}$ is

$$I^\eta_{\alpha\beta} = \tfrac{15}{32}(1+\lambda_{\beta\alpha})^3(1+\lambda_{\beta\alpha}^{-3})\int_2^\infty s^2 g_{\alpha\beta}(s)\hat{J}(s,\lambda_{\beta\alpha})\mathrm{d}s, \tag{2.56}$$

and the expression for $\hat{J}$ is presented Ref. [26].

The PA approximation of the suspension bulk viscosity is [60]

$$\frac{\kappa_s}{\eta_0} = \frac{\kappa_0}{\eta_0} + \frac{4\phi}{3(1-\phi)} + \sum_{\alpha,\beta} I^\kappa_{\alpha\beta}\phi_\alpha\phi_\beta, \tag{2.57}$$

where the integral

$$I^\kappa_{\alpha\beta} = \frac{(1+\lambda_{\beta\alpha})^6}{32\lambda_{\beta\alpha}^3}\int_2^\infty s^2 g_{\alpha\beta}(s)\hat{J}_Q(s,\lambda_{\beta\alpha})\mathrm{d}s. \tag{2.58}$$

The definition of $\hat{J}_Q$ and its asymptotic forms are presented in Appendix 2.A.

Table 2.1: The PA approximation coefficients computed with $g_{\alpha\beta} = 1$. For the sedimentation velocity coefficient $S_{\alpha\beta}$, the density ratio $\gamma = 1$.

$\lambda_{\beta\alpha}$	$-I^t_{\alpha\beta}$	$-I^r_{\alpha\beta}$	$-S_{\alpha\beta}$	$I^\eta_{\alpha\beta}$	$I^\kappa_{\alpha\beta}$
1/16	2.4152	2.2345	3.6033	1.8237	1.6412
1/8	2.3464	1.9952	3.7252	1.8661	1.6059
1/4	2.2424	1.6101	4.0146	2.0388	1.5716
1/2	2.0876	1.1083	4.7167	2.3312	1.5683
1	1.8315	0.63102	6.5464	2.5023	1.5835
2	1.4491	0.30980	11.966	2.3312	1.5683
4	1.0365	0.14186	29.392	2.0388	1.5716
8	0.68904	0.064479	88.930	1.8661	1.6059
16	0.43484	0.030028	304.60	1.8237	1.6412

The integrals for the PA approximations are evaluated numerically using Gauss-Kronrod quadrature over the entire integration domain. The integrands are calculated using twin-multipole expansions up to s^{-300} for $2 \le s \le 30$ and far-field asymptotes, presented in Appendix 2.A, for $s > 30$. At $s = 30$, the difference between the exact and the asymptotic solutions is sufficiently small.

Table 2.1 presents the PA approximation coefficients for suspension properties with $g_{\alpha\beta} = 1$ and for the sedimentation velocities the density ratio $\gamma = 1$. Note that $I^\eta_{\alpha\beta}$ and $I^\kappa_{\alpha\beta}$ are symmetric with respect to $\lambda_{\beta\alpha}$ and $\lambda^{-1}_{\beta\alpha}$ in the table. The PA computations agree well with the published results for monodisperse and polydisperse systems [26, 27, 29, 30, 57, 60]. As far as we are aware, the values of $I^r_{\alpha\beta}$ and $I^\kappa_{\alpha\beta}$ are presented for the first time using the exact two-body problem solutions.

2.5 Analytical results beyond the PA level

Suspension properties

The short-time diffusive behaviors of monodisperse hard-sphere colloidal suspensions have been extensively studied in the past. The short-time translational self-diffusivity, d^t_s, can be accurately estimated by the following semi-empirical expression for $\phi \le 0.5$ [37, 85]

$$\frac{d^t_s}{d^t_0} \approx 1 - 1.8315\phi \times (1 + 0.1195\phi - 0.70\phi^2), \tag{2.59}$$

where $d^t_0 = k_B T/(6\pi\eta_0 a)$ is the SES translational diffusivity for particles of radius a. The quadratic term in Eq. (2.59) recovers the three-body coefficients with lubrication [10], and the cubic term is fitted from the computation results of ASD [36] and the hydrodynamic multipole method [85]. The short-time rotational self-diffusivity,

d_s^r, has been calculated up to ϕ^2 by including the three-body HIs with lubrication effects[10],

$$\frac{d_s^r}{d_0^r} \approx 1 - 0.631\phi - 0.726\phi^2, \tag{2.60}$$

where $d_0^r = k_B T/(8\pi\eta_0 a^3)$ is the SES rotational diffusivity.

Extending the monodisperse results above to polydisperse colloidal suspensions is a non-trivial undertaking and the results beyond the PA level are limited to the case of bidisperse suspensions with one species presented in trace amount [30]. Alternatively, inspired by the form of Eq. (2.59), we propose the following hybrid scheme for the polydisperse self-diffusivities:

$$\frac{d_{s,\alpha}^t}{d_{0,\alpha}^t} \approx 1 + \Big(\sum_\beta I_{\alpha\beta}^t \phi_\beta\Big) \times (1 + 0.1195\phi - 0.70\phi^2), \tag{2.61}$$

$$\frac{d_{s,\alpha}^r}{d_{0,\alpha}^r} \approx 1 + \Big(\sum_\beta I_{\alpha\beta}^r \phi_\beta\Big) \times (1 + 1.1505\phi), \tag{2.62}$$

with the coefficients $I_{\alpha\beta}^t$ and $I_{\alpha\beta}^r$ from Table 2.1. Eq. (2.61) and (2.62) are designed in such a way that, for monodisperse suspensions, we recover Eq. (2.59) and (2.60), and for dilute polydisperse suspensions, we recover the PA approximation results with $g_{\alpha\beta} = 1$. Moreover, it assumes that the particle size only affects the HIs on the pair level, and the many-body HIs are of a mean-field nature, depending only on the total volume fraction. A similar decoupling idea was used for studying the translational and rotational diffusivities of permeable particle suspensions [85]. In the companion paper [50], we have successfully applied Eq. (2.61) to approximate the bidisperse partial hydrodynamic functions $H_{\alpha\beta}(q)$ with the monodisperse $\delta\gamma$ scheme [47, 48] up to $\phi = 0.4$.

The analytical expression of the monodisperse sedimentation velocity including the three-body HIs is [86]

$$\frac{U_s}{U_0} \approx 1 - 6.546\phi + 21.918\phi^2, \tag{2.63}$$

where $U_0 = F/(6\pi\eta_0 a)$ is the single particle sedimentation velocity. A semi-empirical approximation of the polydisperse sedimentation velocities was proposed by Davis & Gecol [87], and for bidisperse suspensions it is

$$\frac{U_{s,\alpha}}{U_{0,\alpha}} = (1-\phi)^{-S_{\alpha\alpha}}[1 + (S_{\alpha\beta} - S_{\alpha\alpha})\phi_\beta], \tag{2.64}$$

with the coefficients from Table 2.1. Eq. (2.64) recovers the PA approximation results with $g_{\alpha\beta} = 1$ in the dilute limit.

For the monodisperse hydrodynamic function $H(q)$, the principal peak occurs close to the wavenumber q_m corresponding to the static structure factor peak. The value $H(q_m)$ is well represented by a linear fit [36, 88]

$$H(q_m)/\mu_0 = 1 - 1.35\phi. \tag{2.65}$$

The analytical approximation for monodisperse suspension shear viscosity including the three-body HIs is [89]

$$\frac{\eta_s}{\eta_0} \approx 1 + 2.5\phi + 5.0023\phi^2 + 9.09\phi^3. \tag{2.66}$$

Presently, we are not aware of any approximations of the suspension bulk viscosity beyond the PA approximation level. Note that in Ref. [60], the quadratic term in the suspension bulk viscosity is 1.57, and agrees with 1.58 in Table 2.1 for $\lambda_{\beta\alpha} = 1$.

Porous medium properties

For monodisperse porous media, the following expression agreed with the Lattice Boltzmann simulation results within a 3% error up to $\phi = 0.6$ [25]:

$$F(\phi) = 10\frac{\phi}{(1-\phi^2)} + (1-\phi)^2(1 + 1.5\sqrt{\phi}). \tag{2.67}$$

For polydisperse porous media, the species drag coefficient is well represented by the following equation [25],

$$F_\alpha = [(1-\phi)z_\alpha + \phi z_\alpha^2 + 0.064(1-\phi)z_\alpha^3]F(\phi), \tag{2.68}$$

where z_α is the species diameter fraction defined in Sec. 2.2, and $F(\phi)$ is from Eq. (2.67).

Few studies have been performed on the hindered diffusion in porous media. As far as we are aware, only the translational hindered diffusivity for monodisperse porous media has been investigated, and it can be obtained by solving the following self-consistent equation [90]:

$$(d^t_{\rm HD})^{-1} = 1 + \sqrt{\tfrac{9}{2}\phi}(d^t_{\rm HD})^{-\frac{1}{2}} + \tfrac{3}{2}\phi(d^t_{\rm HD})^{-1} + \dots \tag{2.69}$$

2.6 Results for suspensions

Short-time translational self-diffusivity

Fig. 2.3 presents the short-time translational self-diffusivity $d^t_{s,\alpha}$ for both species as a function of the total volume fraction ϕ for bidisperse suspensions with $y_1 = 0.5$ and

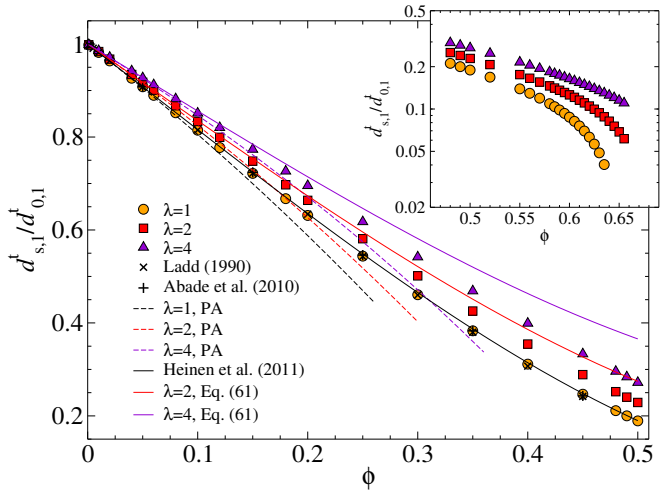

(a)

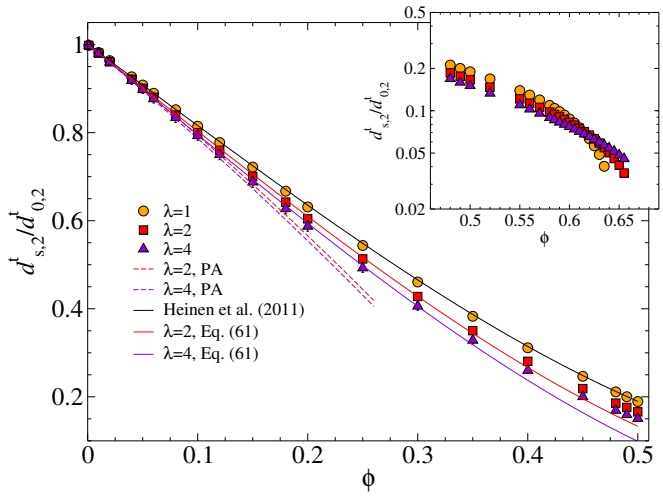

(b)

Figure 2.3: (Color online) The short-time translational self-diffusivity (a): $d^t_{s,1}$ and (b): $d^t_{s,2}$ as a function of ϕ for bidisperse suspensions with $y_1 = 0.5$ and $\lambda = 1$, 2, and 4 [bottom to top in (a) and top to bottom in (b), respectively]. The monodisperse simulation results from Ladd [81] and Abade *et al.*[91] are also presented in (a). The PA approximations are shown in dashed lines and Eq. (2.61), which reduces to the expression of Heinen *et al.*[37] at $\lambda = 1$, is shown in solid lines. The insets show the results at higher ϕ.

$\lambda = 2$ and 4, as well as for monodisperse suspensions. In the same figure we also present the monodisperse computations of Ladd [81] and Abade *et al.* [91], which are in excellent agreement with the SD results. The semi-empirical expression of Heinen *et al.* [37], Eq. (2.59), accurately captures the monodisperse data up to $\phi = 0.5$. The PA approximations, however, are valid only for $\phi < 0.1$, and begin to deviate from the simulation data afterwards. At very high ϕ, as is shown in the inset of Fig. 2.3a, the monodisperse d_s^t decreases drastically when $\phi > 0.60$, and vanishes as the volume fraction approaches $\phi \sim 0.64$ [18].

In a bidisperse suspension ($\lambda > 1$), the relative short-time translational self-diffusivities of the smaller species is always higher than that of the larger species, *i.e.*, $d_{s,1}^t/d_{0,1}^t > d_{s,2}^t/d_{0,2}^t$. The diffusivity difference between the small and the large particles increases with the increasing suspension size ratio λ. At a fixed ϕ, for the smaller particles $d_{s,1}^t/d_{0,1}^t$ can be much higher than the monodisperse value d_s^t/d_0^t, particularly at high λ, as is shown in Fig. 2.3a, but $d_{s,2}^t/d_{0,2}^t$ does not differ significantly from d_s^t/d_0^t even with a large size ratio, as is shown in Fig. 2.3b. This suggests that the HIs for the two species are distinct: intuitively, the larger particles, which can be surrounded by multiple smaller particles, experience mean-field-like HIs, as if they were suspended in an effective medium formed by the solvent and the smaller particles. The HIs for the smaller particles, on the other hand, are expected to be strongly affected by the presence of the large particles.

The PA approximations of $d_{s,\alpha}^t$, shown in dashed lines in Fig. 2.3, agree with the SD computations up to $\phi \approx 0.1$. At higher volume fractions, the HIs beyond the two-body level begin to dominate and the PA approximations underestimate the diffusivities for both species. The decoupling approximations of Eq. (2.61), shown in solid lines, exhibit superior agreement. For the small particles in Fig. 2.3a, Eq. (2.61) is accurate up to $\phi \approx 0.25$ and 0.15 for $\lambda = 2$ and 4, respectively. The decoupling approximation works much better for the large particles, and remains valid for $\phi = 0.4$ and 0.35 for $\lambda = 2$ and 4, respectively, as is shown in Fig. 2.3b. Beyond their range of validity, the decoupling approximation overestimates the small particle diffusivity and underestimates the large particle diffusivity.

The SD calculations for very dense suspensions up to and beyond the monodisperse close packing volume fraction ($\phi \sim 0.64$) are shown in the insets of Fig. 2.3. For the smaller particles in Fig. 2.3a, the reduction of $d_{s,1}^t$ with increasing ϕ is slower for $\lambda > 1$ compared to the monodisperse case. In particular, at $\phi = 0.655$, the highest volume fractions we studied in this work, the diffusivity $d_{s,1}^t/d_{0,1}^t$ remains higher

than 0.1 at $\lambda = 4$. More interestingly, for the larger particles shown in Fig. 2.3b, $d^t_{s,2}/d^t_{0,2}$ for $\lambda > 1$ crosses the monodisperse values near $\phi \approx 0.61$. At higher ϕ, the diffusivities $d^t_{s,2}/d^t_{0,2}$ for $\lambda = 4$ is higher than those for $\lambda = 2$. This is simply because the size polydispersity improves the particle packing and increases the suspension maximum packing density [21], where the diffusivity $d^t_{s,\alpha}$ reduces to zero due to particle contact. At a fixed y_1, increasing λ increases the maximum packing density. As a result, at sufficiently high ϕ, the diffusivities of both species can exceed the monodisperse value, and the apparent diffusivity enhancement increases with λ.

Fig. 2.4 examines the ratio of the species diffusivity to the monodisperse value at the same volume fraction ϕ, $d^t_{s,\alpha}/d^t_s$, as a function of the suspension composition y_1 at several ϕ for bidisperse suspensions of $\lambda = 2$. The ratio $d^t_{s,\alpha}/d^t_s$ highlights the influence of suspension composition on the diffusivities, such that it recovers 1 when $y_1 \to 0$ for the large species and $y_1 \to 1$ for the small species. At low to moderate ϕ, as is shown in the insets of Fig. 2.4, the PA approximation and the decoupling approximation of Eq. (2.61) are also presented in dashed and solid lines, respectively. Both approximation schemes capture the SD calculations up to $\phi = 0.25$ at all y_1 except overestimating $d^t_{s,1}/d^t_s$ at $\phi = 0.25$. Within this volume fraction range, $d^t_{s,\alpha}/d^t_s$ for both species decreases almost linearly with increasing y_1, with $d^t_{s,1}/d^t_s$ towards and $d^t_{s,2}/d^t_s$ away from unity, respectively. Physically, replacing smaller particles with larger particles at a fixed ϕ (decreasing y_1) increases the diffusivities of both species. Moreover, at a given ϕ, the tracer diffusivity is the maximum diffusivity for the smaller particles and the minimum diffusivity for the larger particles. At $\phi = 0.25$, the maximum diffusivity enhancement for the smaller particles is 15% as $y_1 \to 0$, while the maximum reduction for the larger particles is 10% as $y_1 \to 1$.

The ratio $d^t_{s,\alpha}/d^t_s$ exhibits more intriguing behaviors for dense suspensions. For small particles, as is shown in Fig. 2.4a, $d^t_{s,1}/d^t_s$ increases significantly with decreasing y_1. In particular, at $\phi = 0.635$, $d^t_{s,1}/d^t_s \to 2.9$ as $y_1 \to 0$. Moreover, the ratio $d^t_{s,1}/d^t_s$ is no longer linear with y_1 when ϕ is close to 0.635, particularly when y_1 is small. For the larger particles in Fig. 2.4b, the ratio $d^t_{s,2}/d^t_s$ is more surprising. Contrary to the dilute behaviors shown in the inset, $d^t_{s,2}/d^t_s$ increases with increasing ϕ when $\phi > 0.5$. Moreover, with $\phi > 0.6$, $d^t_{s,2}/d^t_s$ exceeds unity, and a maximum $d^t_{s,2}/d^t_s$ emerges at a non-trivial y_1. For $\phi = 0.635$, the maximum occurs between $y_1 = 0.2$ and 0.3, and corresponds to a 150% diffusivity enhancement relative to the monodisperse value. These peculiar behaviors correspond to the approaching and crossing of the monodisperse diffusivities in the inset of Fig. 2.3b, and are

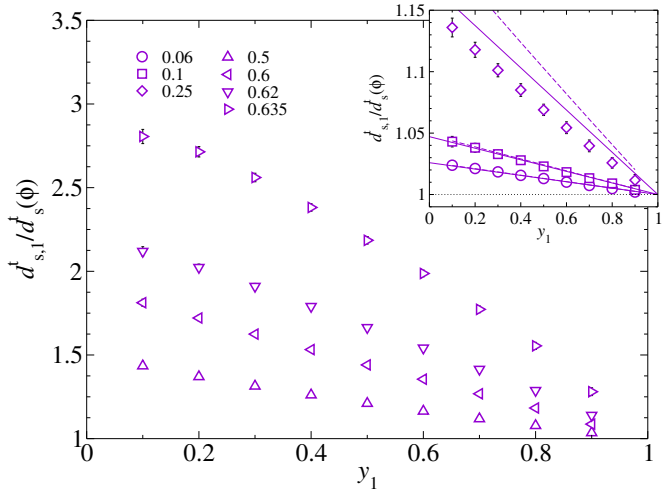

(a)

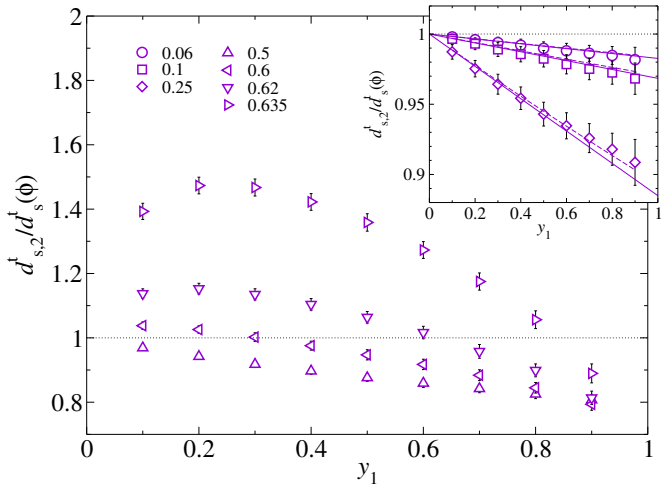

(b)

Figure 2.4: The normalized translational diffusivity (a): $d^t_{s,1}/d^t_s$ and (b): $d^t_{s,2}/d^t_s$ as a function of y_1 at different ϕ for bidisperse suspensions of $\lambda = 2$. The monodisperse short-time translational self-diffusivity at the corresponding ϕ is d^t_s. The insets also show the PA approximations (dashed lines) and Eq. (2.61) (solid lines).

due to changes in both the HIs and the bidisperse particle packing. A particularly interesting aspect of Fig. 2.4 is that for a dense monodisperse suspension near closing packing, replacing a small amount of large particles with small particles promotes diffusivities $d^t_{s,\alpha}$ of *both* species.

Short-time rotational self-diffusivity

Fig. 2.5 shows the short-time rotational self-diffusivity for both species, $d^r_{s,\alpha}$, as a function of ϕ for bidisperse suspensions with $\lambda = 2$ and 4 at $y_1 = 0.5$, as well as for monodisperse suspensions. The Lattice-Boltzmann (LB) computations of Hagen *et al.*[92] and the hydrodynamic multipole calculations of Abade *et al.*[85] for monodisperse suspensions are also presented. The monodisperse d^r_s/d^r_0 shows a much weaker ϕ dependence compared to its translational counterpart d^t_s/d^t_0. Up to $\phi = 0.2$, the monodisperse SD results agree well with the hydrodynamic multipole results. At higher volume fractions, the SD results lie between the LB and the hydrodynamic multipole results. The PA approximation agrees with the SD d^r_s/d^r_0 only up to $\phi = 0.1$, and underestimates the diffusivity at higher ϕ. The analytical expression of Cichocki *et al.*[10], Eq. (2.60), exhibits remarkable agreement with the simulations up to $\phi = 0.5$. Moreover, for very dense suspensions, as is shown in the inset of Fig. 2.5a, the diffusivity d^r_s/d^r_0 does not drop as rapidly as d^t_s/d^t_0, and retains a large value (~ 0.25) even close to the maximum packing, undoubtedly owning to the weak logarithm singularity of the rotational lubrication interactions.

For bidisperse suspensions, the small and the large particle rotational diffusivities $d^r_{s,\alpha}/d^r_{0,\alpha}$ are shown in Fig. 2.5a and 2.5b, respectively. Compared to the monodisperse results, $d^r_{s,1}/d^r_{0,1}$ are higher and $d^r_{s,2}/d^r_{0,2}$ are lower. Unlike their translational counterparts, the rotational diffusivities of both species are noticeably different from the monodisperse values, and are sensitive to the size ratio λ, particularly at moderate to high ϕ. On the other hand, they display less sensitivity to ϕ compared to $d^t_{s,\alpha}/d^t_{0,\alpha}$, as rotation is always easier than translation in a crowded environment. At very high ϕ, as shown in the inset of Fig. 2.5a and 2.5b, the diffusivities $d^r_{s,2}/d^r_{0,2}$ at higher λ do not cross the monodisperse values even at $\phi = 0.635$. Therefore, the suspension packing plays a less significant role on the rotational diffusivities. Note that the weak ϕ and the strong λ dependence of $d^r_{s,\alpha}/d^r_{0,\alpha}$ exhibited in Fig. 2.5 can be exploited experimentally as a structural probe for dense suspensions [30, 57].

The PA approximations, shown in dashed lines in Fig. 2.5 in respective colors, agree reasonably well with the polydisperse SD results up to $\phi = 0.15$, and then

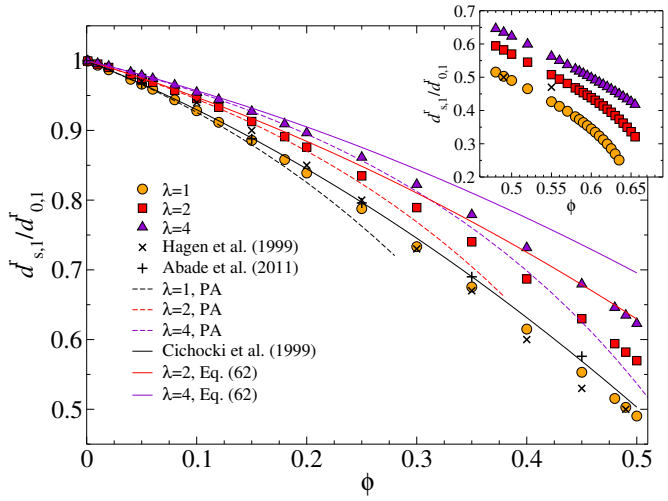

(a)

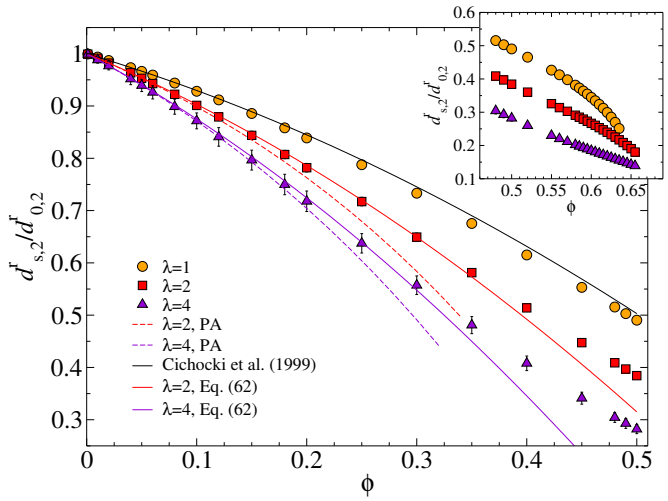

(b)

Figure 2.5: (Color online) The short-time rotational self-diffusivity (a): $d^r_{s,1}$ and (b): $d^r_{s,2}$ as a function of ϕ for bidisperse suspensions with $y_1 = 0.5$ and $\lambda = 1$, 2, and 4 [bottom to top in (a) and top to bottom in (b), respectively]. The monodisperse simulation results from Hagen *et al.*[92] and Abade *et al.*[85] are also presented in (a). The PA approximations are shown in dashed lines and Eq. (2.62), which reduces to the results of Cichocki *et al.* [10] at $\lambda = 1$, is shown in solid lines. The insets show the results at higher ϕ.

significantly underestimate the diffusivities due to the HIs beyond the pairwise level. The decoupling approximation of Eq. (2.62), plotted as solid lines in respective colors in Fig. 2.5, shows a better agreement, and, similarly to the translational case, works better for the larger particles. In particular, the decoupling approximation is valid up to $\phi = 0.2$ for the smaller particles with $\lambda = 2$ and 4; for the larger particles, it is valid up to $\phi = 0.4$ for $\lambda = 2$ and up to $\phi = 0.3$ for $\lambda = 4$. The success of the decoupling approximation again demonstrates that the HIs for the larger particles are mean-field-like. For the smaller particles, the size effect is more complex and is beyond the decoupling approximation.

The influences of the composition y_1 on the ratio $d^r_{s,\alpha}/d^r_s$, with d^r_s at the same ϕ, are presented in Fig. 2.6 for bidisperse suspensions with $\lambda = 2$. The effect of y_1 at low and moderate ϕ are shown in the insets of Fig. 2.6a and 2.6b for the smaller and the larger particles, respectively. Increasing the small particle composition y_1 with a fixed ϕ decreases $d^r_{s,\alpha}$ of both species almost linearly, with the smaller particles towards the monodisperse value and the larger particles away from it. The ratio $d^r_{s,1}/d^r_{0,1}$ exhibits a maximum for trace amount of smaller particles and $d^r_{s,2}/d^r_{0,2}$ exhibits a minimum for trace amount of larger particles. As is shown in the insets of Fig. 2.6, increasing ϕ increases the maximum of $d^r_{s,1}/d^r_{0,1}$ for the smaller particles and reduces the minimum of $d^r_{s,2}/d^r_{0,2}$ for the larger particles. The PA approximation and the decoupling expression, Eq. (2.62), are presented as dashed and solid lines, respectively, in the insets of Fig. 2.6. Both approximation schemes capture the composition y_1 dependence of $d^r_{s,\alpha}/d^r_s$ up to $\phi = 0.10$ for both species. At $\phi = 0.25$, Eq. (2.62) also captures the y_1 dependence for both species, but the PA approximations overestimate the effect of composition change.

The ratio $d^r_{s,\alpha}/d^r_s$ at higher ϕ differ significantly from its translational counterpart. For the smaller particles in Fig. 2.6a, $d^r_{s,1}/d^r_s$ increases with increasing ϕ and remains linear with y_1 with fixed ϕ. At $\phi = 0.635$, the tracer diffusivity of the small particles is almost 190% of the monodisperse values. For the larger particles in Fig. 2.6b, with $\phi \geq 0.5$, increasing ϕ also *increases* $d^r_{s,2}/d^r_s$ altogether, and this is qualitatively different from the dilute behaviors in the inset. At $\phi \geq 0.62$, the ratio $d^r_{s,2}/d^r_s$ can exceed unity, suggesting the rotational diffusivities of both species are enhanced due to the change in the particle packing. Moreover, the ratio $d^r_{s,2}/d^r_s$ is very sensitive to y_1, and with the presented data, it appears almost linear with y_1. This means $d^r_{s,2}/d^r_s$ must exhibit a maximum at $y_1 \ll 0.1$. Therefore, for a dense monodisperse suspension near close packing, replacing trace amount of large particles with small

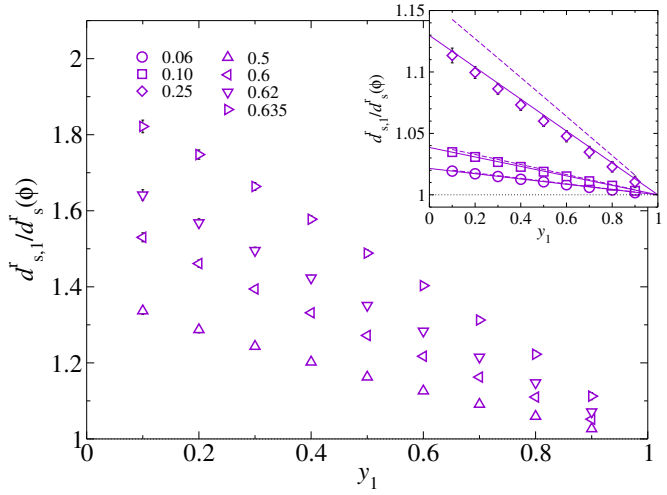

(a)

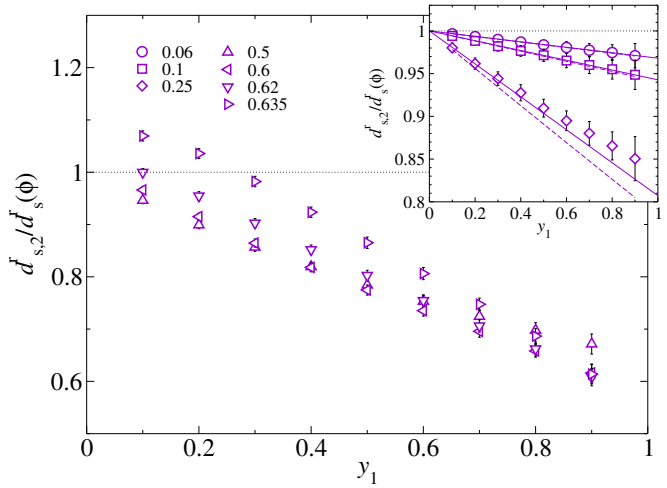

(b)

Figure 2.6: The normalized rotational diffusivity (a): $d^r_{s,1}/d^r_s$ and (b): $d^r_{s,2}/d^r_s$ as a function of y_1 at different ϕ for bidisperse suspensions of $\lambda = 2$. The monodisperse short-time rotational self-diffusivity at the corresponding ϕ is d^r_s. The insets also show the PA approximations (dashed lines) and Eq. (2.62) (solid lines).

particles can increase the rotational diffusivities of the both species. Together with Fig. 2.4, Fig. 2.6 illustrates the distinctive behaviors of the HIs for translational and rotational motions.

Instantaneous sedimentation velocity

The instantaneous sedimentation velocities $U_{s,\alpha}/U_{0,\alpha}$ of bidisperse suspensions with equal density materials at $\lambda = 2$ and 4 and $y_1 = 0.5$, as well as monodisperse suspensions, are presented in Fig. 2.7. For monodisperse suspensions, U_s/U_0 from Ladd [81] and Abade *et al.* [91] are also shown in Fig. 2.7a for comparison. The SD results agree with the earlier computational studies [81, 91] up to $\phi = 0.2$, and then yield higher values. Although the absolute magnitude of the differences appears to be small, the relative difference is significant, up to 36% at $\phi = 0.45$. The origin of the discrepancy, as pointed out by Brady & Durlofsky [83], is that the multipole expansions up to the mean-field quadrupole level used in SD is not sufficient to capture the collective HIs in sedimentation problems. On the other hand, SD closely captures the qualitative aspects of U_s/U_0, and remains positive over the entire volume fraction range. As mentioned earlier, the incorporation of the mean-field quadrupole in the mobility tensor construction improves the accuracy of the conventional SD compared to ASD [18].

The monodisperse PA approximations and the analytical results of Cichocki *et al.* [86], Eq. (2.63), are shown in dashed and solid lines in Fig. 2.7a, respectively. The agreement between the simulations and the analytical expressions is unsatisfactory. The PA approximation is valid only up to $\phi = 0.05$, and Eq. (2.63), which incorporates three-body effect, shows a minor improvement and agrees with the simulations only up to $\phi = 0.08$. Such lack of agreement at higher ϕ clearly illustrates the challenges in developing theories for sedimentation problems.

For bidisperse suspensions, the species sedimentation velocities are shown in Fig. 2.7a and 2.7b for the small and the large particles, respectively. With equal densities for both species, $U_{s,1}/U_{0,1}$ of the smaller particles is lower than the monodisperse values, and $U_{s,2}/U_{0,2}$ of the larger particles is higher. Interestingly, at $\lambda = 4$, the small particle sedimentation velocity $U_{s,1}$ changes sign when $\phi \geq 0.08$. In this case, the fall of large particles generates a strong upward backflow that offsets the effects of the downward force on the small particles, making them move with the fluid in the opposite direction. The small particle $U_{s,1}$ first reaches a minimum, then increases with increasing ϕ. At $\lambda = 2$, $U_{s,1}$ approaches zero for $\phi > 0.35$,

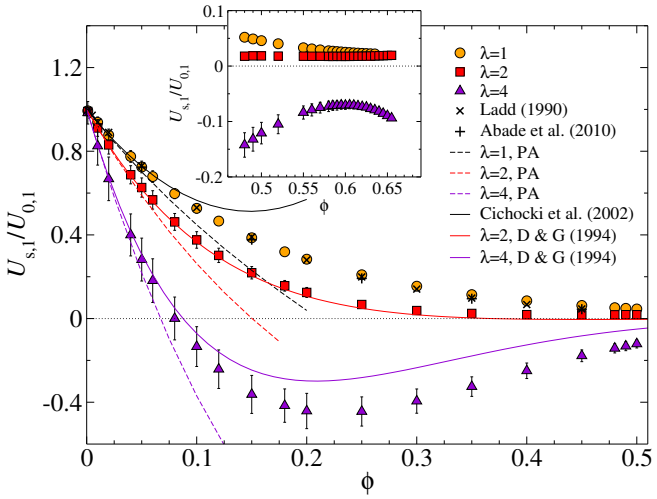

(a)

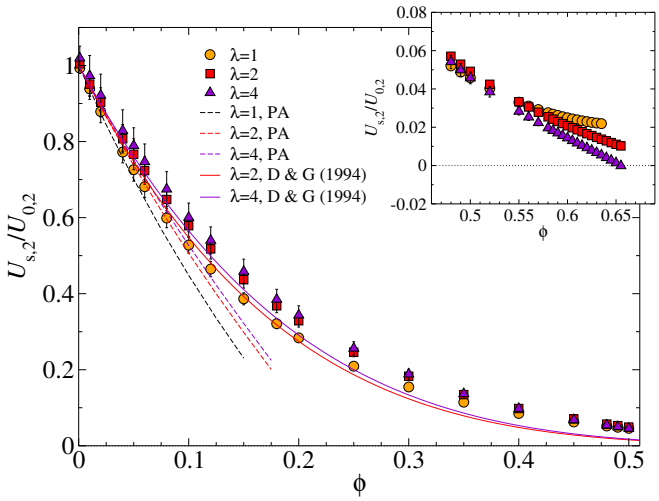

(b)

Figure 2.7: (Color online) The instantaneous sedimentation velocity (a): $U_{s,1}$ and (b): $U_{s,2}$ as a function of ϕ for bidisperse suspensions with $y_1 = 0.5$ and $\lambda = 1$, 2, and 4 [top to bottom in (a) and bottom to top in (b), respectively]. The monodisperse simulation results from Ladd [81] and Abade *et al.*[91] are also presented in (a). The PA approximations are shown in dashed lines. The theoretical results of Cichocki *et al.*[86] for $\lambda = 1$, and the semi-empirical expression of Davis & Gecol [87], Eq. (2.64), for $\lambda = 2$ and 4 are presented in solid lines. The insets show the results at higher ϕ.

suggesting that the combination of the imposed force and the back flow makes the particles almost stationary. Apparently, the HIs for the small particles are strongly affected by ϕ and λ. On the other hand, for the larger particles, $U_{s,2}$ closely follows the monodisperse values, and shows little variation with different λ.

The SD results of the sedimentation velocity $U_{s,\alpha}/U_{0,\alpha}$ for very dense systems are shown in the insets of Fig. 2.7. For the smaller particles near close packing, $U_{s,1}$ is positive for $\lambda = 1$ and 2, and remains negative for $\lambda = 4$. For the larger particles, the sedimentation velocities $U_{s,2}$ cross each other. As a result, at $\phi > 0.6$, the monodisperse sedimentation velocity is the highest, and the magnitude of $U_{s,2}/U_{0,2}$ decreases with increasing λ, an opposite trend compared to the dilute suspensions.

The polydisperse PA approximation and the semi-empirical expression of Davis & Gecol[87], Eq. (2.64), are presented in dashed and solid lines in respective colors in Fig. 2.7, respectively. The PA approximations capture $U_{s,\alpha}$ of both species up to $\phi = 0.05$ for $\lambda = 2$ and 4, and then underestimate the SD results. In Fig. 2.7a, the semi-empirical approximation of Eq. (2.64) shows a remarkable overall agreement with the SD results for $\lambda = 2$ at all ϕ, and for $\lambda = 4$, it captures the velocity direction change but overestimates the sedimentation velocity at higher ϕ. For the larger particles in Fig. 2.7b, Eq. (2.64) captures the qualitative trend in the SD results of $U_{s,2}$. However, at higher ϕ, the quantitative difference becomes apparent.

Fig. 2.8 presents the effect of composition y_1 on the ratio $U_{s,\alpha}/U_s$, where U_s is the the monodisperse value at the same ϕ, for bidisperse suspensions with $\lambda = 2$ at various volume fractions. For volume fractions up to $\phi = 0.25$, the data are shown in the insets of Fig. 2.8a and 2.8b for the small and the large species, respectively. At low and moderate ϕ, increasing y_1 increases the ratio $U_{s,\alpha}/U_s$ for both species almost linearly. For the smaller particles the ratio moves towards unity and for the larger particles away from unity. The ratio $U_{s,\alpha}/U_s$ exhibits a minimum as $y_1 \to 0$ for the smaller particles and a maximum as $y_1 \to 1$ for the larger particles. Increasing the total volume fraction ϕ reduces the minimum in $U_{s,1}/U_s$ and increases the maximum in $U_{s,2}/U_s$ due to stronger HIs. When ϕ is large enough, the small particle velocity ratio $U_{s,1}/U_s$ can change sign as the backflow from the other species becomes strong enough to reverse the particle motion. On the other hand, the enhancement of $U_{s,2}/U_s$ for the larger particles as $y_1 \to 1$ is more modest. In this limit, a large particle sees the small particles and the solvent as an effective medium with a higher viscosity, leading to the sedimentation velocity enhancement relative to the monodisperse case. The PA approximations, shown as the dashed lines in Fig. 2.8,

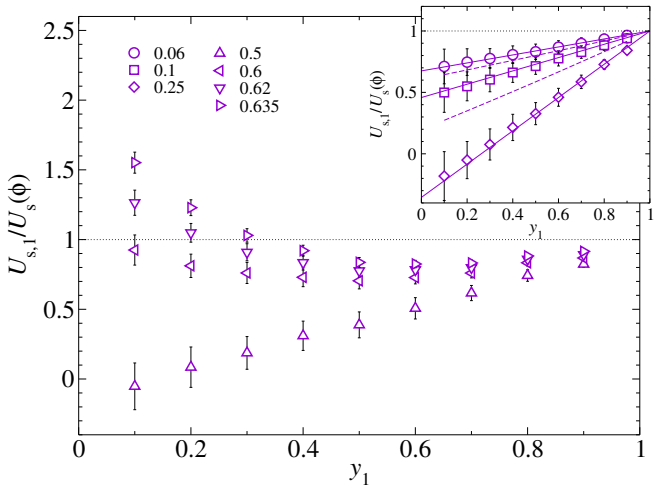

(a)

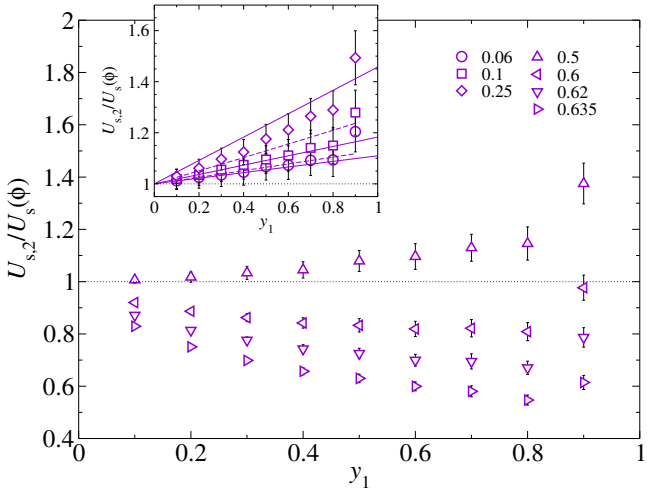

(b)

Figure 2.8: The normalized instantaneous sedimentation velocity (a): $U_{s,1}/U_s$ and (b): $U_{s,2}/U_s$ as a function of y_1 at different ϕ for bidisperse suspensions of $\lambda = 2$. The monodisperse instantaneous sedimentation velocity at the corresponding ϕ is U_s. The insets also show the PA approximations (dashed lines) and the approximations of Davis & Gecol [87], Eq. (2.64) (solid lines).

capture the effect of y_1 on $U_{s,\alpha}/U_s$ only up to $\phi = 0.06$ and then overestimate the effect of suspension composition. On the other hand, the semi-empirical expression of Davis & Gecol [87] works up to $\phi = 0.25$ for the smaller particles and $\phi = 0.1$ for the larger particles.

At higher ϕ, the sedimentation behaviors are different from the dilute limit. For example, in Fig. 2.8a, the ratio $U_{s,1}/U_s$ in the dilute limit $y_1 \to 0$ *increases* with increasing ϕ when $\phi \geq 0.5$. When $\phi \geq 0.6$, $U_{s,1}/U_s$ is no longer monotonic in y_1, and exceeds unity for small y_1. In Fig. 2.8b, the $y_1 \to 1$ limit of $U_{s,2}/U_s$ exhibits a trend opposite to dilute suspensions, and decreases with increasing ϕ. At $\phi \geq 0.6$, the ratio $U_{s,2}/U_s$ becomes less than 1 and also exhibits non-linear behaviors with respect to y_1, most likely due to changes in the suspension packing.

Hydrodynamic functions

The q-dependent partial hydrodynamic functions $H_{\alpha\beta}(q)$ for bidisperse suspensions with $\lambda = 2$ at various ϕ are presented in Fig. 2.9. The interspecies partial hydrodynamic function $H_{12}(q)$ in Fig. 2.9b are shifted for clarity. Physically, the partial hydrodynamic function $H_{\alpha\beta}(q)$ corresponds to the wave space component of a generalized sedimentation velocity of species α in response to a spatially periodic external force on species β. Therefore, at small q, the species hydrodynamic functions $H_{11}(q)$ and $H_{22}(q)$ are always positive since the other species remains force-free. This interpretation also explains the negative interspecies $H_{12}(q)$ at small q: the external force on species 2 generates a backflow that moves the force-free species 1 in an opposite direction.

The partial hydrodynamic functions $H_{11}(q)$ and $H_{22}(q)$, shown in Fig. 2.9a and 2.9c respectively, are always less than unity for all q and decrease with increasing ϕ. At $\phi = 0.01$ and 0.1, $H_{11}(q)$ and $H_{22}(q)$ are similar to each other for the scaled wavenumber qa_α. At higher ϕ, $H_{11}(q)$ exhibits a minimum ahead of the dominant peak at the wavenumber corresponding to the principal peak of $H_{22}(q)$. The modulations of $H_{11}(q)$ and $H_{22}(q)$ are the strongest at moderate ϕ, where the HIs are the most sensitive to the suspension structures. At $\phi \geq 0.6$, the magnitude and the q-modulations of $H_{\alpha\alpha}(q)$ become small. Therefore, for very dense suspensions, the HIs are mean-field-like and are insensitive to different length scales. Note that the peak of $H_{11}(q)$ at $qa_1 \approx 3.5$ develops a cusp-shape, most likely due to the packing of particles.

The interspecies hydrodynamic functions $H_{12}(q)$, shown in Fig. 2.9b, exhibit the

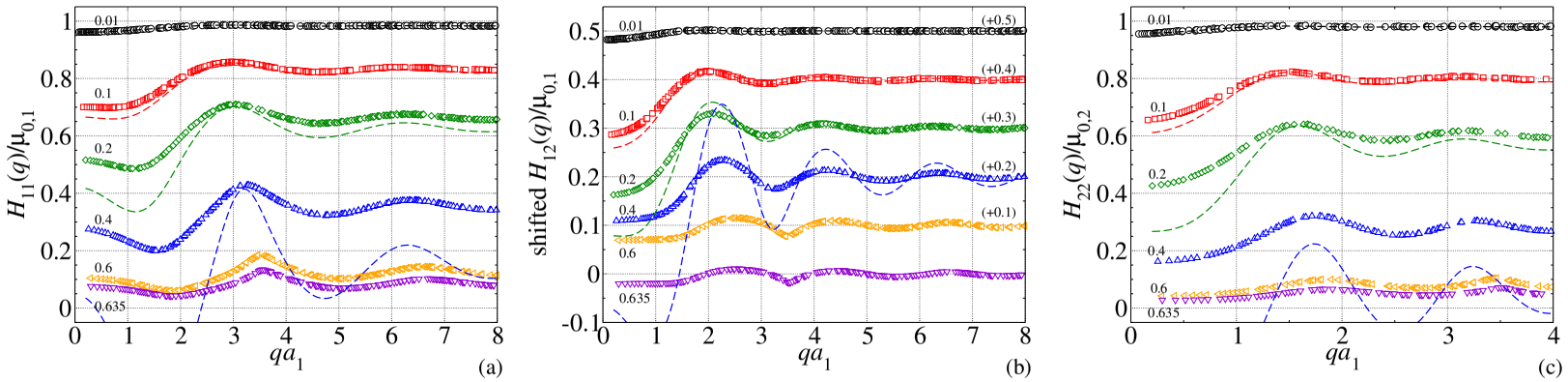

Figure 2.9: (Color online) The partial hydrodynamic functions (a): $H_{11}(q)$, (b): $H_{12}(q)$, and (c): $H_{22}(q)$ for bidisperse suspensions with $\lambda = 2$ and $y_1 = 0.5$ at $\phi = 0.01$ (◯), 0.1 (□), 0.2 (◇), 0.4 (△), 0.6 (◁), and 0.635 (▽). In (b) the interspecies partial hydrodynamic functions $H_{12}(q)$ are shifted by the amount indicated in the parentheses for clarity. The PA approximations up to $\phi = 0.4$ are shown in dashed lines with the same color as the simulation results.

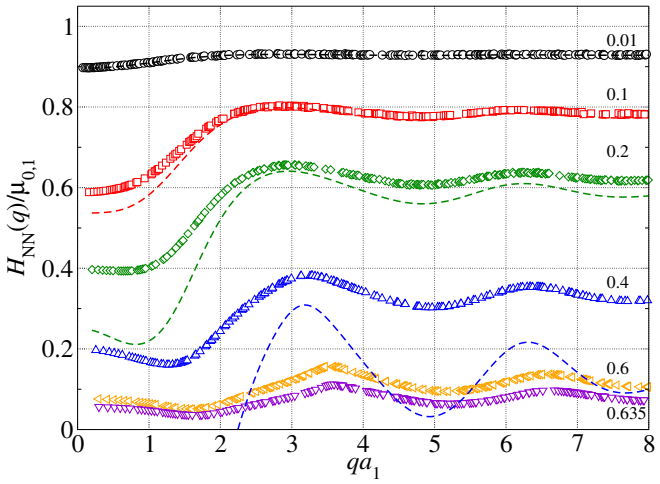

Figure 2.10: (Color online) The number-number mixture hydrodynamic functions $H_{NN}(q)$ for bidisperse suspensions with $\lambda = 2$ and $y_1 = 0.5$ at $\phi = 0.01$ (◯), 0.1 (□), 0.2 (◇), 0.4 (△), 0.6 (◁), and 0.635 (▽). The PA approximations up to $\phi = 0.4$ are shown in dashed lines with the same color as the simulation results.

most significant modulation at moderate volume fractions between $\phi = 0.1$ and 0.4. Comparing to that of $H_{11}(q)$ and $H_{22}(q)$, however, the modulation is relatively weak. When $\phi \geq 0.6$, $H_{12}(q)$ becomes almost constant in q.

The PA approximations of $H_{\alpha\beta}(q)$, shown as dashed lines in respective colors in Fig. 2.9, capture the SD results satisfactorily up to $\phi = 0.1$. The largest difference between the PA approximation and the SD results is in the low q limit. At $\phi = 0.2$, the PA approximations capture the shape of $H_{\alpha\beta}(q)$, but are quantitatively inaccurate. The method completely fails at $\phi = 0.4$, where the estimated $H_{\alpha\beta}(q)$ becomes negative and exhibits too much modulations. Note that, for $H_{11}(q)$ at $\phi = 0.4$, the value of the dominant peak from the PA approximation coincides the SD results.

Fig. 2.10 presents the number-number mixture hydrodynamic function $H_{NN}(q)$ constructed from $H_{\alpha\beta}(q)$ in Fig. 2.9. The corresponding PA approximations up to $\phi = 0.4$ are also shown in respective colors, and exhibit a similar degree of agreement as in Fig. 2.9. Note that $H_{NN}(q)$ is the simplest form of the mixture hydrodynamic function $H_M(q)$, and treats the bidisperse suspension as a single entity with equal and constant scattering intensities for both species. Evidently, $H_{NN}(q)$ is strongly affected by $H_{11}(q)$ since the number composition corresponding to $y_1 = 0.5$ is $x_1 = 0.889$. The mobility of the most mobile structures in the suspension corresponds to the principal peak of $H_{NN}(q)$, and the respective wavenumber q_m identifies the

length scale of such structure. In Fig. 2.10, the length scale corresponding to q_m, $\ell_m \sim 2\pi/q_m$, approximately reflects the average spacing between neighboring small particles in the mixture. It suggests that collective particle motions on the length scale of the nearest neighbor cage experience the least hydrodynamic resistance. The wavenumber q_m increases with ϕ, suggesting the cage shrinks. Moreover, a minimum appears ahead of $H_{NN}(q)$ principal peak when $\phi > 0.2$. Such a minimum is a unique feature of polydisperse mixture hydrodynamic functions.

Fig. 2.11 illustrates the influence of y_1 on $H_{\alpha\beta}(q)$ for bidisperse suspensions at $\phi = 0.4$ and $\lambda = 2$. Note that the corresponding monodisperse hydrodynamic functions are presented as dashed lines in Fig. 2.11a and 2.11c, and $H_{12}(q)$ is shifted for different y_1 in Fig. 2.11b. When present in small quantity, $H_{11}(q)$ at $y_1 = 0.1$ is distinct from $H_{22}(q)$ at $y_1 = 0.9$ in several aspects. First, the average magnitude of $H_{11}(q)/\mu_{0,1}$ is almost 60% higher than that of $H_{22}(q)/\mu_{0,2}$, suggesting a higher intrinsic mobility of the smaller particles. Meanwhile, the modulation of $H_{11}(q)/\mu_{0,1}$ is stronger: $H_{11}(q)$ at $y_1 = 0.1$ exhibits distinct maximum and minimum with respect to q, but $H_{22}(q)$ at $y_2 = 0.9$ is almost flat. Therefore, the smaller particles are sensitive to the local suspension environment, while the larger ones experience mean-field-like HIs. The transition of $H_{\alpha\alpha}(q)$ towards the monodisperse $H(q)$ also illustrates the distinct HIs for the small and the large particles. In essence, the large wavenumber limit of $H_{11}(q)$ reduces with increasing y_1, but the limiting value of $H_{22}(q)$ grows with decreasing y_1, *i.e.*, increased presence of the larger particles. For the interspecies partial hydrodynamic function $H_{12}(q)$, the modulation reaches a maximum at $y_1 = 0.5$, but the magnitude of the modulation remains small compared to $H_{\alpha\alpha}(q)$.

The principal peak of $H_{NN}(q_m)$ as a function of ϕ for bidisperse suspensions with $\lambda = 2$ and 4 and $y_1 = 0.5$, as well as for monodisperse suspensions, is shown in Fig. 2.12. The peak wavenumber q_m is directly measured from the computed $H_{NN}(q)$, and using q_m corresponding to the principal peak of the number-number static structure factor $S_{NN}(q)$ of the PY closure yields virtually the same results. Note that we scale the results with $(x_1\mu_{0,1} + x_2\mu_{0,2})$ for proper dilute behaviors. The monodisperse SD results agree well with the computations of Abade *et al.* [91], also presented in Fig. 2.12. For $\phi < 0.5$, the monodisperse data are well described by the linear expression of Eq. (2.65) [36]. For bidisperse suspensions, the ϕ evolution of the principal peak value $H_{NN}(q_m)$ follows closely the monodisperse results, with the data for $\lambda = 2$ below and the data for $\lambda = 4$ above, and is also almost linear. The PA

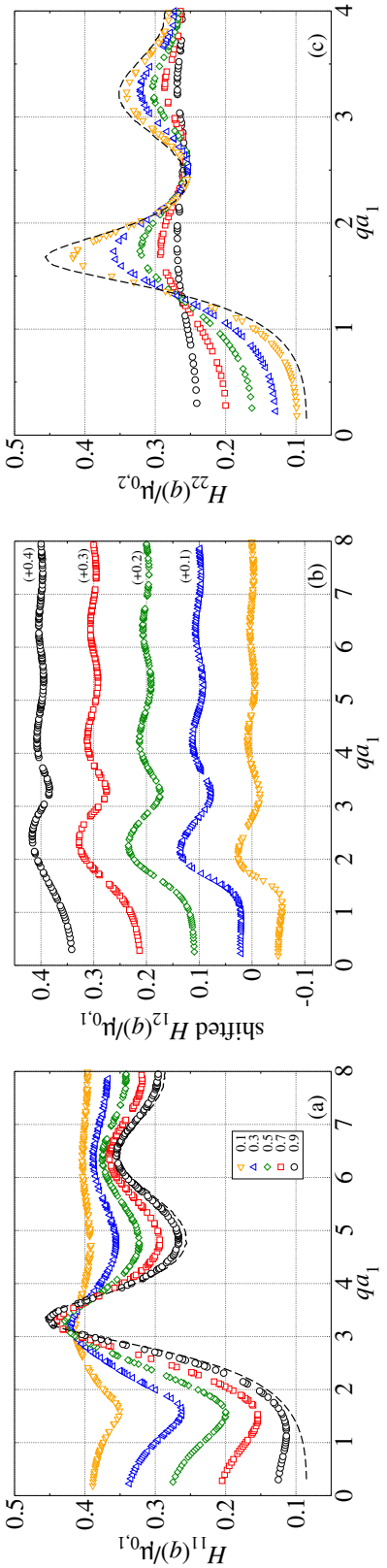

Figure 2.11: (Color online) The partial hydrodynamic functions (a): $H_{11}(q)$, (b): $H_{12}(q)$, and (c): $H_{22}(q)$ for bidisperse suspensions with $\lambda = 2$ and $\phi = 0.4$ at different y_1, with the legends shown in (a). The monodisperse results are shown in dashed lines. In (b) the interspecies partial hydrodynamic functions $H_{12}(q)$ are shifted by the amount indicate in the parentheses for clarity.

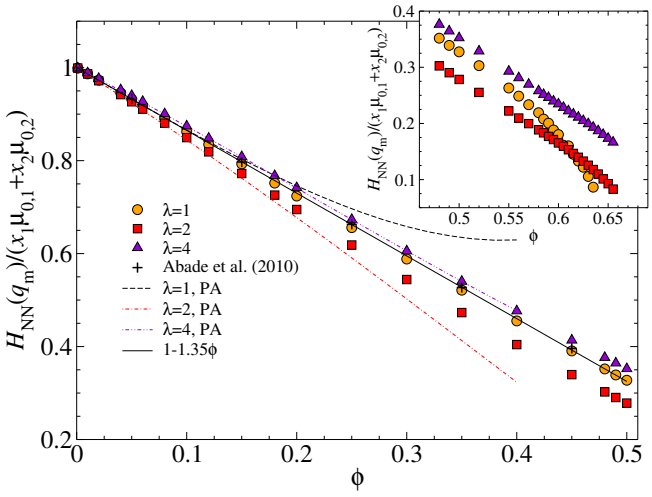

Figure 2.12: (Color online) The peak value of the rescaled number-number mixture hydrodynamic function $H_{NN}(q_m)/(x_1\mu_{0,1} + x_2\mu_{0,2})$ as a function of ϕ for bidisperse suspensions with $\lambda = 1$, 2, and 4 at composition $y_1 = 0.5$. The monodisperse simulation results from Abade *et al.*[91] and the analytical fitting of Banchio & Nägele [36] are also presented. The PA approximations are shown in dashed line for $\lambda = 1$, dash-dotted line for $\lambda = 2$, and dash-double-dotted line for $\lambda = 4$. The inset shows the results at higher ϕ.

approximations exhibit varying degrees of agreement with the SD computations: they are valid up to $\phi = 0.15$ for $\lambda \leq 2$, and show exceptional agreement up to $\phi = 0.4$ for $\lambda = 4$. This agreement, however, is incidental and similar to the peak value agreement observed in Fig. 2.9a for $H_{11}(q)$. For very dense suspensions ($\phi > 0.45$) shown in the inset of Fig. 2.12, the peak value drops drastically near close packing, and the $\lambda = 2$ data cross the monodisperse results at $\phi \approx 0.61$ due to changes in the suspension packing structure.

The effects of the composition y_1 on the normalized peak of the hydrodynamic function are shown in Fig. 2.13 at various ϕ for bidisperse suspensions with $\lambda = 2$. The peak values and the corresponding wavenumbers are directly measured from the computed $H_{NN}(q)$, and the scaling $H_{NN}(q_m)/H_{\max}/(x_1 + x_2\lambda^{-1})$ ensures the ratio goes to 1 as $y_1 \to 0$ or 1. The inset of Fig. 2.13 shows normalized peaks for $\phi \leq 0.4$. In this range, the presence of the second species always reduces the peak value relative to the monodisperse suspensions, and the reduction increases with increasing ϕ, *e.g.*, at $\phi = 0.4$ the maximum reduction is 20%. The corresponding composition is $y_1 = 0.2$, suggesting an asymmetric influence on $H_{NN}(q)$ for different species. For more dense suspensions, shown in the main figure of Fig. 2.13, increasing the

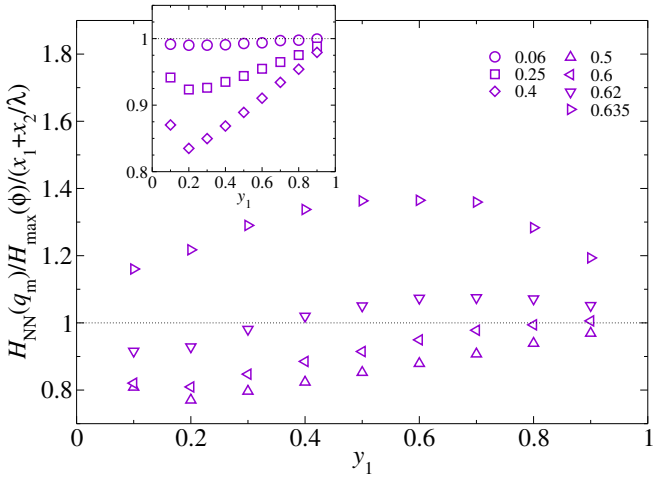

Figure 2.13: The normalized number-number mixture hydrodynamic function peaks $[H_{NN}(q_m)/H_{\max}]/(x_1 + x_2\lambda^{-1})$ as a function of y_1 at different ϕ for bidisperse suspensions with $\lambda = 2$. The q_m is directly measured from the simulations. The monodisperse peak value at the corresponding ϕ is $H_{\max}$.

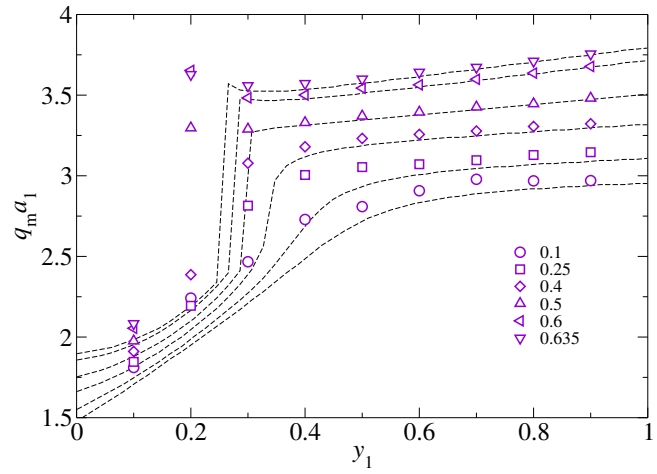

Figure 2.14: The scaled wavenumber $q_m a_1$ corresponding to the maximum of $H_{NN}(q)$ measured from the simulations (symbols) as a function of y_1 at different ϕ for bidisperse suspensions with $\lambda = 2$. The q_m from the PY number-number mixture static structure factor $S_{NN}(q)$ are shown in dashed lines, with increasing ϕ indicated in the legend from bottom to top.

volume fraction ϕ lessens the extent of the normalized peak reduction, and when $\phi \geq 0.6$, introducing a second species into the suspension can bring the normalized peak beyond unity. Here, the particle packing at different y_1 clearly plays a vital role in the behavior of the mixture hydrodynamic function principal peak.

The wavenumbers q_m corresponding to the principal peak of $H_{NN}(q)$ in Fig. 2.13 are shown in Fig. 2.14. Also plotted as dashed lines are the wavenumbers corresponding to the principal peak of $S_{NN}(q)$ from the PY closure. For very dense suspensions up to $\phi = 0.635$, we have verified that the bidisperse PY static structure factor $S_{NN}(q)$ adequately describes suspension structures at finite wavenumbers [80]. For monodisperse suspensions, the maximum of $H(q)$ is practically at the maximum of the static structure factor [36]. However, as shown in Fig. 2.14, this is not the always the case for bidisperse suspensions. For y_1 close to 1, q_m for the principal peak of $H_{NN}(q)$ and $S_{NN}(q)$ indeed coincide. However, with decreasing y_1, the peak locations for $H_{NN}(q)$ and $S_{NN}(q)$ begin to deviate from each other, and the most significant difference is found at $y_1 = 0.2$ at high ϕ. Here, the $S_{NN}(q)$ peak corresponds to the mean distance between large particles, while the $H_{NN}(q)$ peak corresponds to the mean distance between small particles. The decoupling of the hydrodynamic and structural descriptions of dense suspensions illustrates the care needed when treating the HIs of dense mixtures.

High-frequency dynamic shear viscosity

The high-frequency dynamic shear viscosities η_s for volume fractions up to $\phi = 0.5$ of bidisperse suspensions with $\lambda = 2$ and 4 and $y_1 = 0.5$, as well as monodisperse suspensions, are shown in Fig. 2.15. The monodisperse SD results exhibit excellent agreement with the computations of Ladd [81], also shown in the figure. The analytical expression of Cichocki *et al.* [89], Eq. (2.66), is valid up to $\phi = 0.25$. The bidisperse η_s closely follows the monodisperse results, and is almost indistinguishable from the monodisperse results until $\phi > 0.45$. The weak size dependence of η_s is also evident from the weak $\lambda_{\beta\alpha}$ dependence of $I^{\eta}_{\alpha\beta}$ in Table 2.1. The PA approximations with proper suspension structures, also shown in Fig. 2.15, exhibit very weak λ dependence for $\lambda < 4$, and agree with the SD computations up to $\phi = 0.2$. The inset of Fig. 2.15 examines the pairwise HI contributions to the high-frequency dynamic shear viscosity, $\eta_s/\eta_0 - 1 - \frac{5}{2}\phi$, in the dilute limit. Here, the SD results closely follow the PA approximations, and grow as $\sim \phi^2$ when $\phi \ll 1$.

The results for dense suspensions with $\phi > 0.45$ are shown in Fig. 2.16. When $\phi >$

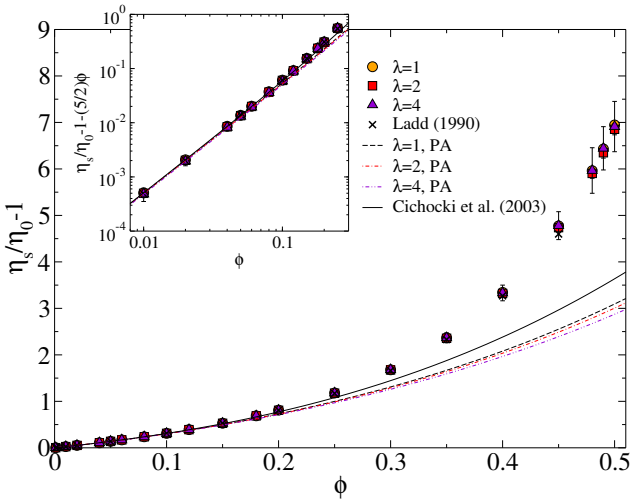

Figure 2.15: (Color online) The particle shear viscosity $\eta_s/\eta_0 - 1$ as a function of ϕ, up to $\phi = 0.5$, for bidisperse suspensions with $y_1 = 0.5$ and $\lambda = 1$, 2, and 4. The monodisperse results from Ladd [81] and the analytical result of Cichocki *et al.*[89] are also shown. The PA approximations for $\lambda = 1$ (dashed), 2 (dash-dotted), and 4 (dash-double-dotted) are also presented. The inset shows the interaction contribution to the suspension shear viscosity, $\eta_s/\eta_0 - 1 - \frac{5}{2}\phi$, in the dilute limit.

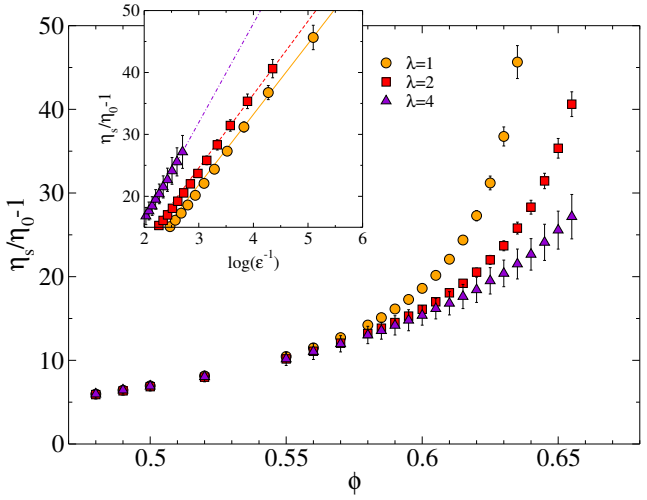

Figure 2.16: (Color online) The particle shear viscosity $\eta_s/\eta_0 - 1$ as a function of ϕ for very dense bidisperse suspensions with $y_1 = 0.5$ and $\lambda = 1$, 2, and 4. The inset shows the logarithmic shear viscosity divergence, with $\varepsilon = 1 - \phi/\phi_m$. Also presented in lines are the asymptotic behaviors, Eq. (2.70), with fitted constants from Table 2.2 for $\lambda = 1$(solid), 2(dashed), and 4(dash-dotted).

Table 2.2: The limiting volume fraction ϕ_m in $\varepsilon = 1 - \phi/\phi_m$, and the constants in Eq. (2.70) and (2.71), characterizing the asymptotic divergences of η_s and κ_s, respectively, fitted from the SD computations for bidisperse suspensions with $y_1 = 0.5$.

λ	ϕ_m	B_η	$-C_\eta$	B_κ	$-C_\kappa$
1	0.639	11.38	12.37	32.69	71.86
2	0.664	11.84	10.93	31.29	61.46
4	0.702	15.98	16.00	–	–

0.55, the viscosity η_s increases drastically, and increasing λ reduces η_s significantly. As revealed by experiments [22, 23, 93] and simulations [31], the viscosity reduction is primarily due to the improved packing for polydisperse suspensions, *i.e.*, the average particle spacing increases with λ, leading to a viscosity reduction. The divergent behavior of η_s is well represented by the asymptotic expression [18],

$$\frac{\eta_s}{\eta_0} \approx B_\eta \log(\varepsilon^{-1}) + C_\eta + \cdots, (\varepsilon \ll 1), \tag{2.70}$$

where B_η and C_η are constants, and $\varepsilon = 1 - \phi/\phi_m$, with ϕ_m the limiting volume fraction. The parameter ε characterizes the mean interparticle gap spacing relative to the particle size. Note that B_η, C_η, and ϕ_m depend on the bidisperse suspension composition [18, 94], and the fitted values from the SD computations are shown in Table 2.2. The inset of Fig. 2.16 shows the η_s asymptotic behaviors based on Eq. (2.70), and that the SD results and the fitted expression agree well. However, the numerical values of B_η and C_η for monodisperse suspensions differ from earlier ASD results [18]. This is likely because the asymptotic behaviors near close packing are very sensitive to the suspension structures, and any differences in the packing generation protocol, or even different parameters within the same protocol, can lead to quantitative differences. However, the asymptotic form suggested by Eq. (2.70) remains valid.

The effects of composition y_1 on the normalized shear viscosity $\eta_s(\phi, y_1)/\eta_s(\phi)$, where $\eta_s(\phi)$ is the monodisperse shear viscosity at the same ϕ, are shown in Fig. 2.17 for bidisperse suspensions at $\lambda = 2$. For the moderate λ studied here, the effect of size ratio is not apparent until $\phi = 0.4$. At higher ϕ near the monodisperse close packing, the presence of a second species with a different size leads to significant viscosity reduction. Moreover, the normalized shear viscosity in Fig. 2.17 is not symmetric for y_1: the smaller particles are more effective at viscosity reduction. For example, at $\phi = 0.635$, at $y_1 = 0.1$ and 0.9 the viscosity is 66% and 80% of the

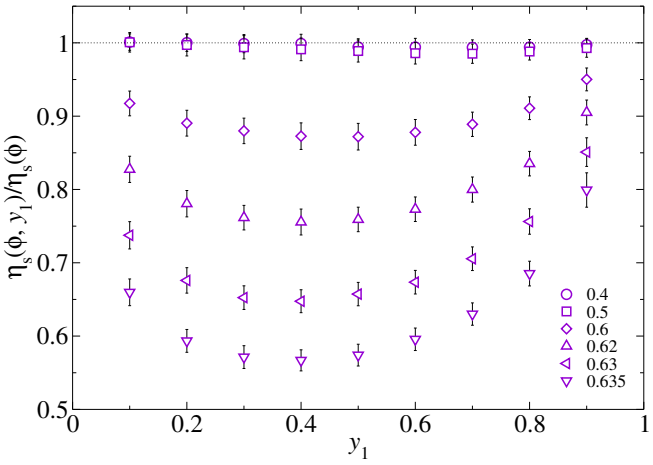

Figure 2.17: The normalized high-frequency dynamic shear viscosity $\eta_s(\phi, y_1)/\eta_s(\phi)$ as a function of y_1 at different ϕ for bidisperse suspensions with $\lambda = 2$. The monodisperse high-frequency dynamic shear viscosity at the corresponding ϕ is $\eta_s(\phi)$.

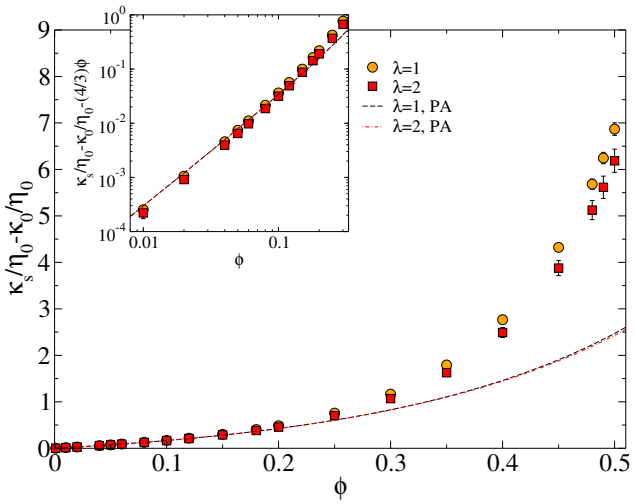

Figure 2.18: (Color online) The particle bulk viscosity $(\kappa_s - \kappa_0)/\eta_0$ as a function of ϕ, up to $\phi = 0.5$, for bidisperse suspensions with $y_1 = 0.5$ and $\lambda = 1$ and 2. The PA approximations for $\lambda = 1$ (dashed) and 2 (dash-dotted) are also presented. The inset shows the interaction contribution to the suspension bulk viscosity, $(\kappa_s - \kappa_0)/\eta_0 - \frac{4}{3}\phi$, in the dilute limit.

monodisperse value, respectively.

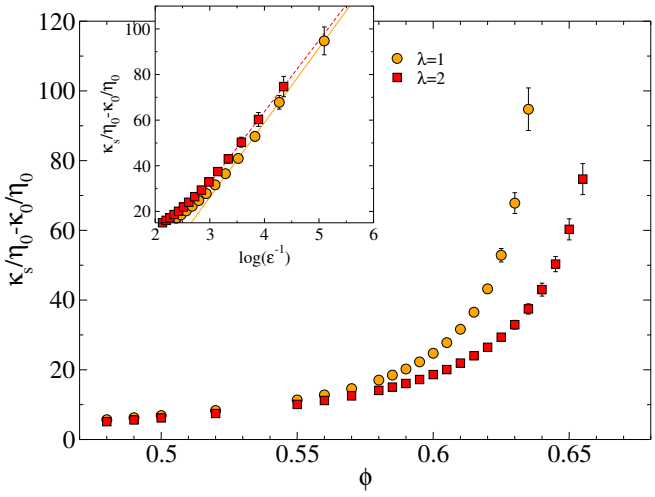

Figure 2.19: (Color online) The particle bulk viscosity $(\kappa_s - \kappa_0)/\eta_0$ as a function of ϕ for very dense bidisperse suspensions with $y_1 = 0.5$ and $\lambda = 1$ and 2. The inset shows the logarithmic bulk viscosity divergence, with $\varepsilon = 1 - \phi/\phi_m$. Also presented in lines are the asymptotic behaviors, Eq. (2.71), with fitted constants from Table 2.2 for $\lambda = 1$(solid) and 2(dashed).

High-frequency dynamic bulk viscosity

Fig. 2.18 presents the the high-frequency dynamic bulk viscosity κ_s as a function of ϕ for monodisperse and bidisperse suspensions with $\lambda = 2$ and $y_1 = 0.5$. Note that the level of approximation in SD is insufficient for the bulk viscosity at large size ratios, and therefore the results for $\lambda = 4$ are not shown. For monodisperse suspensions, the SD results agree with earlier studies [61]. The bulk viscosity of bidisperse suspensions are slightly smaller than the monodisperse values. The particle size ratio λ weakly affects κ_s, but the influence is stronger compared to η_s. At $\phi = 0.3$, differences in λ can be found between $\lambda = 2$ and 1, while for η_s, this is not apparent until $\phi = 0.45$. The PA approximations, also presented in Fig. 2.18, show little size dependence, as also indicated in Table 2.1, and agree with the SD computations up to $\phi = 0.2$. The inset of Fig. 2.18 presents the dilute behaviors of pairwise HI contribution to the bulk viscosity, $(\kappa_s - \kappa_0)/\eta_0 - \frac{4}{3}\phi$. The results show quadratic growth with ϕ, and agree well with the PA approximations.

The results of κ_s for $\phi > 0.45$ are presented in Fig. 2.19. At $\phi > 0.55$, significant differences emerge between the monodisperse and bidisperse results. To identify the divergent behavior of κ_s, we fitted the SD results for dense suspensions ($\phi > 0.6$) with asymptotic terms ε^{-1} and $\log(\varepsilon^{-1})$ using the same ϕ_m in Table 2.2 for ε, since

both η_s and κ_s are computed from the same configurations. It was consistently found that the coefficient of the ε^{-1} terms are orders of magnitudes smaller than those of the $\log(\varepsilon^{-1})$ terms. Therefore, we conclude from the SD data that the κ_s divergence is best described by

$$\frac{\kappa_s}{\eta_0} - \frac{\kappa_0}{\eta_0} \approx B_\kappa \log(\varepsilon^{-1}) + C_\kappa + \cdots, (\varepsilon \ll 1), \tag{2.71}$$

where the constants B_κ and C_κ are functions of the suspension compositions and packing generation protocol, and their fitted values are presented in Table 2.2. Eq. (2.71) and the SD data agree well, as shown in the inset of Fig. 2.19. The weak logarithmic divergence of κ_s first appears odd given the inverse gap spacing ($\sim \xi^{-1}$) divergence of the hydrodynamic function T^Q [68]. In the $\varepsilon \ll 1$ limit, the HIs are dominated by the lubrication forces, and η_s and κ_s can be estimated from the HIs between nearest neighbors with appropriate geometric information [95–97]. This approach is particularly useful for estimating the divergence behavior of colloidal lattices [94, 98]. For random suspensions, however, such divergence behavior also depends on the geometric statistics such as the nearest neighbor gap spacing distribution $P(\xi)\mathrm{d}\xi$ [99]. If the probability density function $P(\xi)$ is somewhat uniformly distributed [100], with a lower bound proportional to ε, properties dominated by ξ^{-1} HIs can show logarithm asymptotic behavior since $\int_\varepsilon \xi^{-1} P(\xi)\mathrm{d}\xi \sim \log(\varepsilon^{-1})$. This simple argument explains the logarithm divergence of κ_s despite the ξ^{-1} divergence of T^Q. The same argument also explains the logarithm divergence of the high-frequency dynamic shear viscosity η_s, shown in Eq. (2.70) and in Fig. 2.16, since for two nearly touching spheres, η_s is dominated by the two-body resistance function $X^M \sim \xi^{-1}$. We defer the formal study involving structural analysis of hard-sphere packings to a future work.

Fig. 2.20 shows the influence of composition y_1 on the ratio $[\kappa_s(\phi, y_1) - \kappa_0]/[\kappa_s(\phi) - \kappa_0]$, where $\kappa_s(\phi)$ in the denominator is the monodisperse bulk viscosity at ϕ, for bidisperse suspensions with $\lambda = 2$. At moderate volume fraction $\phi = 0.25$, the effect of introducing a differently sized species on κ_s is slight. At higher volume fraction, particularly near the monodisperse close packing, the bulk viscosity reduces significantly due to the introduction of a second species. For example, at $\phi = 0.635$, the mixture κ_s can be as low as 39% of the monodisperse value at $y_1 = 0.4$. The shape of the curve is asymmetric to $y_1 = 0.5$, indicating that the larger and the smaller particles affect κ_s differently.

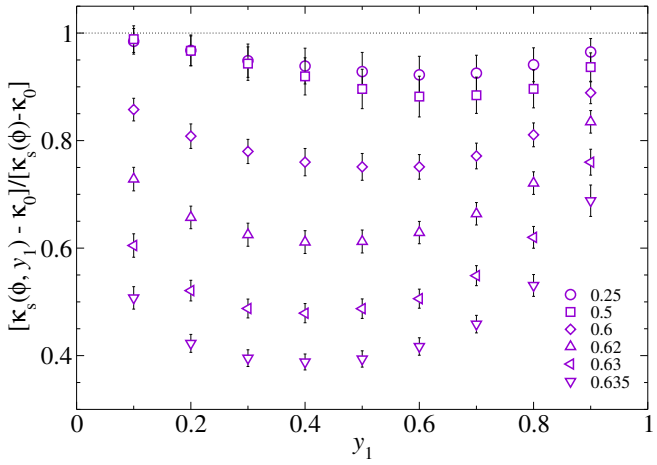

Figure 2.20: The normalized high-frequency dynamic bulk viscosity $[\kappa_s(\phi, y_1) - \kappa_0]/[\kappa_s(\phi) - \kappa_0]$ as a function of y_1 at different ϕ for bidisperse suspensions with $\lambda = 2$. The monodisperse high-frequency dynamic bulk viscosity at the corresponding ϕ is $\kappa_s(\phi)$.

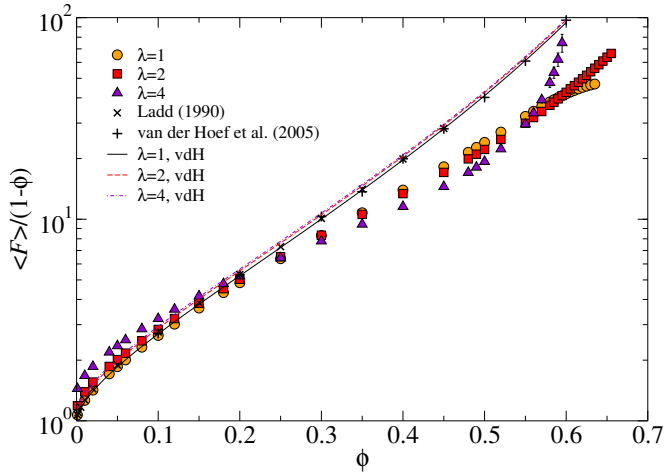

Figure 2.21: (Color online) The mean drag coefficient $\langle F \rangle / (1 - \phi)$ as a function of ϕ for bidisperse porous media with $y_1 = 0.5$ and size ratios $\lambda = 1$, 2, and 4. The monodisperse results from Ladd [81] and van der Hoef *et al.*[25] are also shown. The semi-empirical correlations [25], Eq. (2.67) and (2.68), are also presented for comparison.

2.7 Results for porous media

Permeability (mean drag coefficient)

The permeability, presented in terms of the mean particle drag coefficient $\langle F \rangle$ in Eq. (2.40), is shown in Fig. 2.21 for bidisperse porous media of $\lambda = 2$ and 4 and $y_1 = 0.5$, as well as for monodisperse media. The monodisperse results of Ladd [81] and van der Hoef *et al.* [25] are also shown in the figure. Note that near close packing, $\langle F \rangle$ does not diverge as the fluid can pass through the interstitial spaces between particles. The SD results agree with earlier studies for $\phi < 0.25$, and underestimate $\langle F \rangle$ at higher ϕ. At $\phi = 0.6$, the drag coefficient from SD is only 40% of the LB computations of van der Hoef *et al.* [25] in Fig. 2.21. This is because $\langle F \rangle$ is strongly affected by the many-body HIs, and the lubrication interactions only play a limited role. As a result, the computation of $\langle F \rangle$ relies on the accurate estimation of the grand mobility tensor. The multipole expansion to the mean-field quadrupole level used in SD is insufficient to capture the HIs between stationary particles, similar to the errors associated with the sedimentation velocity $U_{s,\alpha}$ in Sec. 2.6.

For bidisperse suspensions, SD remains valid for $\phi < 0.25$, and at higher ϕ it is expected to capture the qualitative aspect of the particle size effects. Since each stationary particle in a porous medium acts as a force monopole, the particle size plays a relatively minor role. This is confirmed in Fig. 2.21, where the bidisperse $\langle F \rangle$ closely follows the monodisperse data. At low ϕ, the mean drag coefficient increases slightly with the size ratio λ. The behavior for $\phi > 0.25$ arises from the complex interplay between the HIs and the particles configurations.

The semi-empirical expressions for the drag coefficient, Eq. (2.67) and (2.68), are also plotted in Fig. 2.21. For monodisperse porous media, Eq. (2.67) accurately captures earlier simulation results [25, 81] even in the dense limit. For bidisperse porous media, comparing to the SD results at low ϕ, the empirical expressions work well for $\lambda = 2$, but underestimate the size effects for $\lambda = 4$. This may be because in constructing Eq. (2.68), van der Hoef *et al.* [25] did not consider the case of $\lambda = 4$ at low to moderate ϕ in their simulations.

The effects of composition y_1 on the drag coefficient ratio $\langle F \rangle / F(\phi)$, where $F(\phi)$ is the monodisperse drag coefficient, for bidisperse mixtures at $\lambda = 2$, are presented in Fig. 2.22. The empirical expressions Eq. (2.67) and (2.68) are not shown because they do not recover to the correct limit when $y_1 \to 0$ or 1. Over the wide range of ϕ presented, except when $\phi > 0.62$, the mean drag coefficient $\langle F \rangle$ for the mixture differs from the monodisperse results by at most 10%. Introducing a second

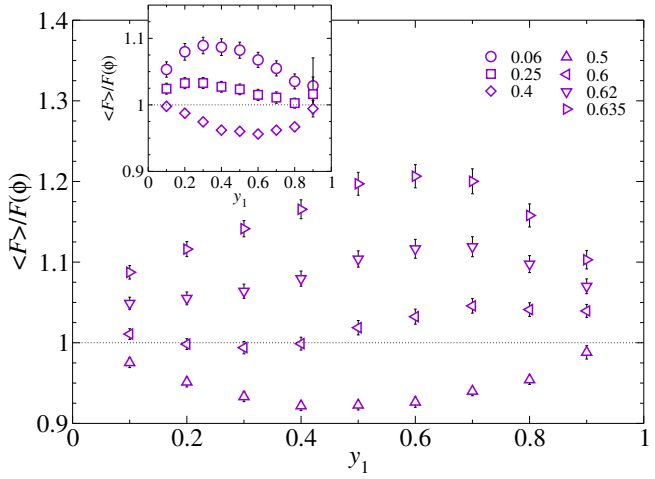

Figure 2.22: The normalized mean drag coefficient $\langle F \rangle / F(\phi)$ as a function of y_1 at different ϕ for bidisperse porous media with $\lambda = 2$. The monodisperse drag coefficient at the corresponding ϕ is $F(\phi)$.

species of a different size to a monodisperse porous medium first increases the mean drag coefficient for $\phi < 0.4$, while at higher volume fractions, the second species reduces $\langle F \rangle$ for $\phi < 0.6$ and then increases the mean drag coefficient again near the monodisperse close packing. At $\phi = 0.635$, $\langle F \rangle$ is merely 21% higher than the monodisperse drag coefficient $F(\phi)$. The relative insensitivity of $\langle F \rangle$ to y_1 suggests that the particle size plays a minor role in the permeability of porous media. Fig. 2.21 and 2.22 show that SD remains a useful tool [101] to assess qualitative aspects of polydisperse porous media.

Translational hindered diffusivity

Fig. 2.23 presents the translational hindered diffusivity, $d^t_{\mathrm{HD},\alpha}$, as a function of the volume fraction ϕ for bidisperse porous media with $y_1 = 0.5$ and $\lambda = 2$ and 4, as well as for monodisperse porous media. The self-consistent expression of Eq. (2.69) [90], also presented in the figure, agrees with the SD computation for $\phi < 0.05$ and underestimate the results at higher ϕ. Note that the hindered diffusive properties describe particle relative motions in a stationary matrix, and therefore the lubrication effects are important.

Compared to the suspension short-time translational self-diffusivity $d^t_{s,\alpha}$ in Sec. 2.6, the hindered diffusivity $d^t_{\mathrm{HD},\alpha}$ exhibits a stronger ϕ and λ dependence due to stronger HIs in porous media. In particular, $d^t_{\mathrm{HD},\alpha}$ decreases quickly with ϕ with an initial $\sim$

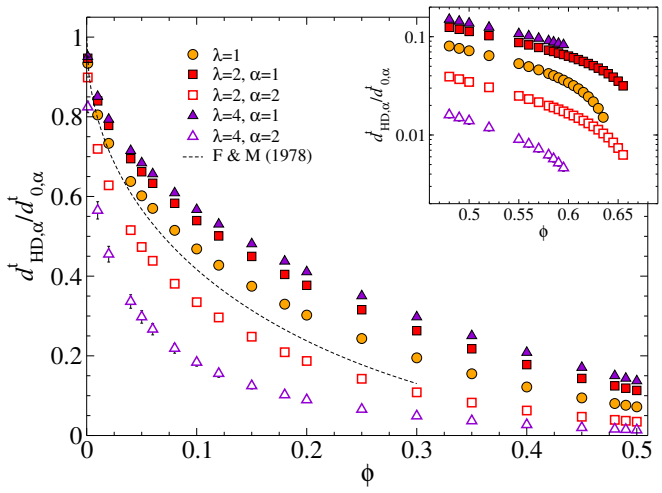

Figure 2.23: (Color online) The translational hindered diffusivity $d^t_{\mathrm{HD},\alpha}$, with $\alpha \in \{1, 2\}$ for both species, as a function of ϕ for bidisperse porous media with $y_1 = 0.5$ and $\lambda = 1$, 2, and 4. The result of Freed & Muthukumar [90], Eq. (2.69), is shown in dashed line. The inset shows the results at high ϕ.

$\sqrt{\phi}$ reduction. The hindered diffusivity for small particles, $d^t_{\mathrm{HD},1}$, exhibits moderate enhancement relative to the monodisperse systems similar to $d^t_{s,1}$. Moreover, at a fixed ϕ, the large particle hindered diffusivity $d^t_{\mathrm{HD},2}$ reduces appreciably with increasing λ, in contrast to the λ-insensitive $d^t_{s,2}$ in suspensions. The increased sensitivity is simply because the fixed particle matrix exerts much stronger HIs on a mobile particle inside. For very dense systems shown in Fig. 2.23 inset, the hindered diffusivities for both species display dramatic reductions at $\phi > 0.6$ as the nearby stationary particles get closer, and the reduction is most pronounced near the close packing volume fraction. Moreover, the large particle $d^t_{\mathrm{HD},2}$ approaches the monodisperse value at $\phi \approx 0.63$, suggesting an enhancement of $d^t_{\mathrm{HD},2}$ due to more efficient particle packing in bidisperse systems.

The effects of porous media composition y_1 on the diffusivity ratio $d^t_{\mathrm{HD},\alpha}/d^t_{\mathrm{HD}}$ are shown in Fig. 2.24. The translational hindered diffusivity for monodisperse porous media at the same ϕ is d^t_{HD}. At any ϕ, the diffusivities $d^t_{\mathrm{HD},\alpha}$ for both species decreases monotonically with increasing y_1, towards the monodisperse results for the smaller particles and away from it for the larger particles. When presented in trace amount at a fixed ϕ, $d^t_{\mathrm{HD},1}/d^t_{\mathrm{HD}}$ reaches a maximum for small particles while $d^t_{\mathrm{HD},2}/d^t_{\mathrm{HD}}$ reaches a minimum for large particles. Compared to the suspension $d^t_{s,1}/d^t_s$, the maximum of $d^t_{\mathrm{HD},1}/d^t_{\mathrm{HD}}$ is significantly higher due to stronger HIs.

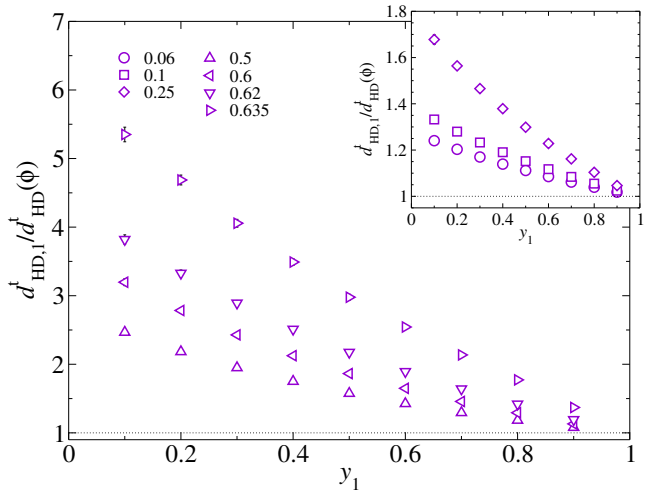

(a)

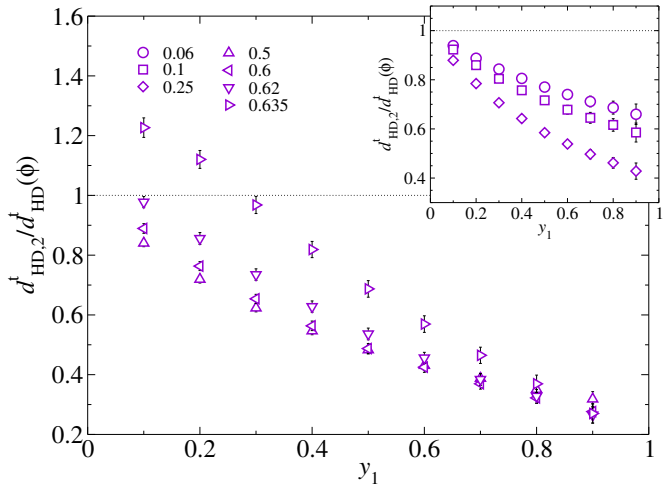

(b)

Figure 2.24: The normalized translational hindered diffusivity (a): $d^t_{\mathrm{HD},1}/d^t_{\mathrm{HD}}$ and (b): $d^t_{\mathrm{HD},2}/d^t_{\mathrm{HD}}$ as a function of y_1 at different ϕ for bidisperse porous media of $\lambda = 2$. The monodisperse translational hindered diffusivity at the corresponding ϕ is d^t_{HD}.

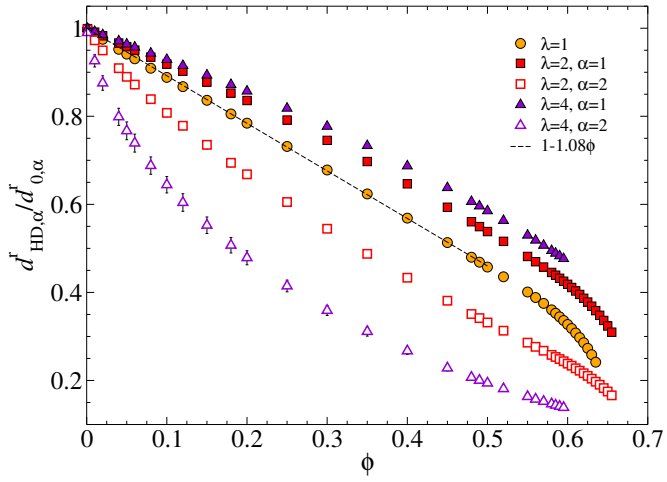

Figure 2.25: (Color online) The rotational hindered diffusivity $d^r_{\mathrm{HD},\alpha}$, with $\alpha \in \{1, 2\}$ for both species, as a function of ϕ for bidisperse porous media with $y_1 = 0.5$ and $\lambda = 1$, 2, and 4. The linear fit of Eq. (2.72) is presented in dashed line.

Moreover, the increase of $d^t_{\mathrm{HD},1}/d^t_{\mathrm{HD}}$ with decreasing y_1 is clearly stronger than linear when $y_1 \to 0$. For the larger particles, at low to moderate ϕ, as shown in the inset of Fig. 2.24b, introducing the smaller particles to the system reduces its hindered diffusivity, and the reduction enhances with increasing ϕ. However, for dense porous medium, particularly when $\phi > 0.5$, increasing ϕ at fixed y_1 increases $d^t_{\mathrm{HD},2}$. For $\phi > 0.6$, the hindered diffusivity for the larger particles $d^t_{\mathrm{HD},2}$ becomes extremely sensitive to the small particles. In Fig. 2.24b at $\phi = 0.635$, the maximum of $d^t_{\mathrm{HD},2}/d^t_{\mathrm{HD}}$ occurs at $y_1 \ll 0.1$. In contrast, the suspension ratio $d^t_{s,2}/d^t_s$ exhibits less sensitivity. Note that only at $\phi = 0.635$, the presence of the smaller particles enhances the hindered diffusivities of both species in the porous medium.

Rotational hindered diffusivity

Finally, the ϕ dependence of the rotational hindered diffusivities $d^r_{\mathrm{HD},\alpha}$ for bidisperse porous media with $y_1 = 0.5$ at $\lambda = 2$ and 4 and for monodisperse porous media is shown in Fig. 2.25. The monodisperse rotational hindered diffusivity d^r_{HD} agrees with the earlier study [35] and decreases much slower with ϕ compared to its translational counterpart d^t_{HD}. The SD results up to $\phi = 0.5$ can be satisfactorily described by a linear fit,

$$\frac{d^r_{\mathrm{HD}}}{d^r_0} = 1 - 1.08\phi, \tag{2.72}$$

also shown in Fig. 2.25. This is a stronger dependence on ϕ compared to the suspension short-time rotational self-diffusivity d_s^r in Sec. 2.6. Approaching the close packing volume fraction, the diffusivity d_{HD}^r decreases but largely remains finite, as the nearby stationary particles can only weakly affect the rotation of the mobile particle.

In bidisperse porous media, $d_{\mathrm{HD},\alpha}^r$ for both species is highly sensitive to the size ratio λ. The bidisperse $d_{\mathrm{HD},\alpha}^r$ differs significantly from the monodisperse results, and no longer displays the almost linear relation with ϕ. For the smaller particles, the diffusivity $d_{\mathrm{HD},1}^r$ is higher than the monodisperse results, while the for the larger particles $d_{\mathrm{HD},2}^r$ is always lower. The deviation from the monodisperse results grows with increasing particle size ratio λ, and is more significant for the larger particles. This is because the average number of neighboring particles, which produces the most significant HI to the mobile particle, scales as λ^3 for the larger particles.

The effects of the medium composition y_1 on the ratio $d_{\mathrm{HD},\alpha}^r/d_{\mathrm{HD}}^r$ for $\lambda = 2$, where d_{HD}^r is the monodisperse data at the same ϕ, are shown in Fig. 2.26. The results are qualitatively similar to $d_{s,\alpha}^r/d_s^r$ in Fig. 2.6. Quantitatively, the effect of y_1 at fixed ϕ on $d_{\mathrm{HD},\alpha}^r$ is slightly stronger. At low to moderate ϕ, $d_{\mathrm{HD},\alpha}^r/d_{\mathrm{HD}}^r$ for both species decreases monotonically with increasing y_1. At a fixed ϕ, a trace amount of small particles yields the maximum of $d_{\mathrm{HD},1}^r/d_{\mathrm{HD}}^r$, while a trace amount of large particles leads to the minimum of $d_{\mathrm{HD},2}^r/d_{\mathrm{HD}}^r$. At very high ϕ, the most notable feature is the mutual enhancement of $d_{\mathrm{HD},1}^r$ and $d_{\mathrm{HD},2}^r$ with a small amount of small particles, *e.g.*, at $y_1 = 0.1$ and $\phi = 0.635$. The extent of the enhancement, however, is much weaker than the translational counterpart $d_{\mathrm{HD},\alpha}^t$, but is similar to the suspension counterpart $d_{s,\alpha}^r$. The similarity between $d_{\mathrm{HD},\alpha}^r$ and $d_{s,\alpha}^r$ suggests that the HIs of rotational motions are weak but sensitive to the environment through ϕ and λ.

2.8 Concluding remarks

In this work we presented a comprehensive study of the short-time transport properties of bidisperse suspensions and porous media over a wide range of parameter space using conventional Stokesian Dynamics. For suspensions, our study includes the short-time translational and rotational self-diffusivities, the instantaneous sedimentation velocity, the partial hydrodynamic functions, and the high-frequency dynamic shear and bulk viscosities, and for porous media, our study includes the mean drag coefficient (permeability) and the translational and rotational hindered diffusivities.

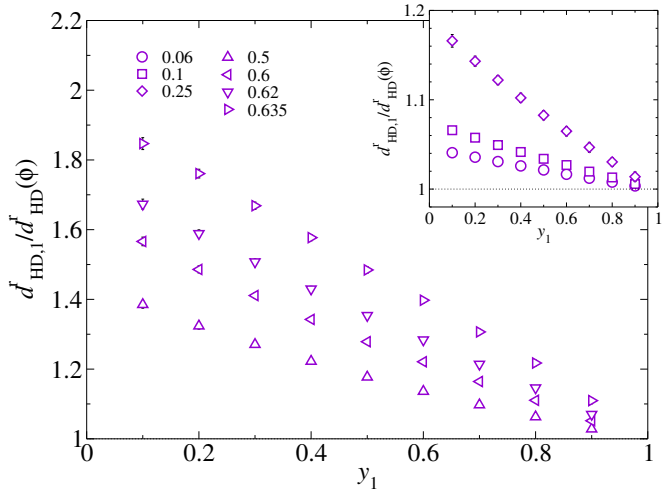

(a)

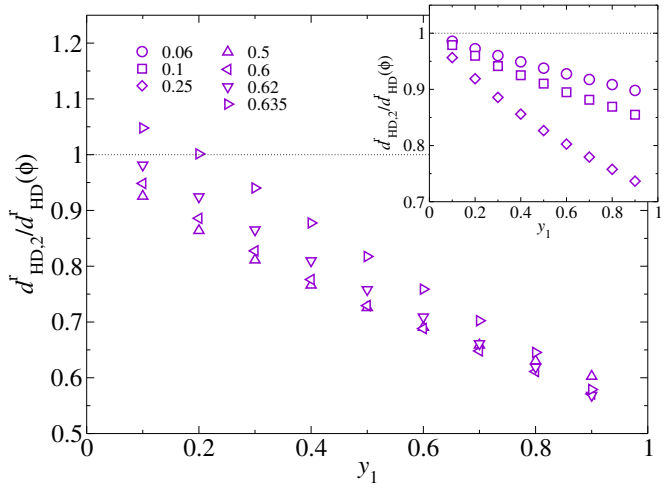

(b)

Figure 2.26: The normalized rotational hindered diffusivity (a): $d^r_{\mathrm{HD},1}/d^r_{\mathrm{HD}}$ and (b): $d^r_{\mathrm{HD},2}/d^r_{\mathrm{HD}}$ as a function of y_1 at different ϕ for bidisperse porous media of $\lambda = 2$. The monodisperse rotational hindered diffusivity at the corresponding ϕ is d^r_{HD}.

Our computational survey shows that introducing a second species of different size to a monodisperse suspension or porous medium leads to significant changes in the hydrodynamic interactions, and different transport properties respond differently. For dense suspensions, the changes in particle structures can significantly affect the HIs, leading to surprising mutual enhancement of diffusivities and reduction of viscosities. The peak locations of the mixture hydrodynamic function $H_{NN}(q)$ differ from those of the mixture static structure factor $S_{NN}(q)$, suggesting great care is needed when studying the HIs of dense systems. The $\log(\varepsilon^{-1})$ divergences of both the shear and bulk viscosities, where $\varepsilon = 1-\phi/\phi_m$ with ϕ_m the limiting volume fraction, show the subtle and complex interplay between the lubrication interactions and the suspension structures.

To estimate suspension properties, the PA approximations can reliably predict various transport properties up to $\phi = 0.15$. The method breaks down at higher volume fractions, even with proper suspension structural input. For diffusivities, we found that the decoupling approximations in Eq. (2.61) and (2.62) work better than the PA approximations. They are particularly effective in estimating the diffusivities of the larger particles up to $\phi = 0.4$, but the range of validity for the smaller particles is more restricted, indicating the HIs for the two species are different. For polydisperse sedimentation velocities, the approximation of Davis & Gecol [87] is quantitatively accurate at low to moderate ϕ.

The limitation of the Stokesian Dynamics algorithm is also assessed in this work. The low moment multipole expansions in SD cannot accurately capture the HIs corresponding to collective particle motions and with very large size ratios. As a result, the SD computations of the suspension sedimentation velocity and porous media permeability are significantly different from other methods for $\phi > 0.25$. However, even in this range, SD is expected to capture qualitative aspects of the size effects.

The present work can serve as a concrete starting point for future experimental and computational investigations of polydisperse systems. Extension of this work includes improved approximation scheme for various transport properties [50], investigations of systems with different interaction potentials, *e.g.*, screened electrostatic interactions, and long-time dynamic studies.

2.A Additional expressions for the PA approximations

The PA approximation of the polydisperse bulk viscosity requires first defining the functions $x^p_{\alpha\beta}$, which are the mobility counterpart of the resistance functions $X^P_{\alpha\beta}$ in Ref. [67]:

$$\begin{pmatrix} x^p_{11} & \frac{1}{2}(1+\lambda_{\beta\alpha})x^p_{12} \\ \frac{1}{2}(1+\lambda_{\beta\alpha})x^p_{21} & \lambda_{\beta\alpha}x^p_{22} \end{pmatrix} = \frac{1}{3}\begin{pmatrix} x^a_{11} & \frac{2}{1+\lambda_{\beta\alpha}}x^a_{12} \\ \frac{2}{1+\lambda_{\beta\alpha}}x^a_{12} & \frac{1}{\lambda_{\beta\alpha}}x^a_{22} \end{pmatrix} \times \begin{pmatrix} X^P_{11} & \frac{1}{4}(1+\lambda_{\beta\alpha})^2 X^P_{21} \\ \frac{1}{4}(1+\lambda_{\beta\alpha})^2 X^P_{12} & \lambda^2_{\beta\alpha}X^P_{22} \end{pmatrix}. \tag{2.73}$$

With the definition of particle stresslet in Eq. (2.35), we have the function $J_Q(s,\lambda_{\beta\alpha})$, which is essential for the suspension bulk viscosity,

$$\begin{aligned} J_Q =& \frac{8}{(1+\lambda_{\beta\alpha})^3}\Big[\Big(T^Q_{11} + \tfrac{1}{8}(1+\lambda_{\beta\alpha})^3 T^Q_{12}\Big) - \Big(X^P_{11}x^p_{11} \\ &+ \tfrac{1}{8}(1+\lambda_{\beta\alpha})^3 X^P_{12}x^p_{21} + \tfrac{1}{2}(1+\lambda_{\beta\alpha})X^P_{11}x^p_{12} \\ &+ \tfrac{1}{4}\lambda_{\beta\alpha}(1+\lambda_{\beta\alpha})^2 X^P_{12}x^p_{22}\Big)\Big], \end{aligned} \tag{2.74}$$

where $T^Q_{\alpha\beta}$ are computed in Ref. [68]. Finally, we have

$$\hat{J}_Q(s,\lambda_{\beta\alpha}) = \tfrac{1}{2}[J_Q(s,\lambda_{\beta\alpha}) + J_Q(s,\lambda^{-1}_{\beta\alpha})] \tag{2.75}$$

for computing the integral in Eq. (2.58).

We use the following asymptotic expressions for $s \to \infty$ in the PA approximations:

$$x^a_{11} + 2y^a_{11} - 3 \approx -\frac{60\lambda^3_{\beta\alpha}}{(1+\lambda_{\beta\alpha})^4}s^{-4} + \frac{480\lambda^3_{\beta\alpha} - 264\lambda^5_{\beta\alpha}}{(1+\lambda_{\beta\alpha})^6}s^{-6}, \tag{2.76}$$

$$x^c_{11} + 2y^c_{11} - 3 \approx -\frac{480\lambda^3_{\beta\alpha}}{(1+\lambda_{\beta\alpha})^6}s^{-6} - \frac{5760\lambda^3_{\beta\alpha}}{(1+\lambda_{\beta\alpha})^8}s^{-8}, \tag{2.77}$$

$$\hat{x}^a_{12} + 2\hat{y}^a_{12} \approx \frac{1200\lambda^3}{(1+\lambda)^6}s^{-5}, \tag{2.78}$$

$$\hat{J} \approx \frac{480\lambda^3_{\beta\alpha}}{(1+\lambda_{\beta\alpha})^6}s^{-6}, \tag{2.79}$$

$$\hat{J}_Q \approx \frac{1280\lambda^3_{\beta\alpha}(1-\lambda_{\beta\alpha}+\lambda^2_{\beta\alpha})}{(1+\lambda_{\beta\alpha})^8}s^{-6}. \tag{2.80}$$

References

[1] A. Einstein, "Eine neue bestimmung der moleküldimensionen", Annalen der Physik **19**, 289 (1906).

[2] A. J. C. Ladd, "Short-time motion of colloidal particles: numerical simulation via a fluctuating lattice-boltzmann equation", Phys. Rev. Lett. **70**, 1339 (1993).

[3] B. Dünweg and A. J. C. Ladd, "Lattice boltzmann simulations of soft matter systems", Adv. Polym. Sci. **221**, 89 (2009).

[4] P. J. Hoogerbrugge and J. M. V. A. Koelman, "Simulating microscopic hydrodynamic phenomena with dissipative particle dynamics", Europhys. Lett. **19**, 155 (1992).

[5] Z. Li and G. Drazer, "Hydrodynamic interactions in dissipative particle dynamics", Phys. Fluids **20**, 103601 (2008).

[6] G. R. Liu and M. B. Liu, *Smoothed particle hydrodynamics: a meshfree particle method* (World Scientific, 2003).

[7] L. B. Lucy, "A numerical approach to the fission hypothesis", Astronomical Journal **82**, 1013 (1977).

[8] A. J. C. Ladd, "Hydrodynamic interactions in a suspension of spherical particles", J. Chem. Phys. **88**, 5051 (1988).

[9] B. Cichocki, B. U. Felderhof, K. Hinsen, E. Wajnryb, and J. Blawzdziewicz, "Friction and mobility of many spheres in stokes flow", J. Chem. Phys. **100**, 3780 (1994).

[10] B. Cichocki, M. L. Ekiel-Jeżewska, and E. Wajnryb, "Lubrication corrections for three-particle contribution to short-time self-diffusion coefficients in colloidal dispersions", J. Chem. Phys. **111**, 3265 (1999).

[11] C. Pozrikidis, *Boundary integral and singularity methods for linearized viscous flow* (Cambridge University Press, 1992).

[12] A. Kumar and M. D. Graham, "Accelerated boundary integral method for multiphase flow in non-periodic geometries", J. Comput. Phys. **231**, 6682 (2012).

[13] M. R. Maxey and B. K. Patel, "Localized force representations for particles sedimenting in stokes flows", Int. J. Multiphase Flow **27**, 1603 (2001).

[14] S. Lomholt and M. R. Maxey, "Force-coupling method for particulate two-phase flow stokes flow", J. Comput. Phys. **184**, 381 (2003).

[15] S. Lomholt, B. Stenum, and M. R. Maxey, "Experimental verification of the force coupling method for particulate flows", Int. J. Multiphase Flow **28**, 225 (2002).

[16] L. Durlofsky, J. F. Brady, and G. Bossis, "Dynamic simulation of hydrodynamically interacting particles", J. Fluid Mech. **180**, 21 (1987).

[17] J. F. Brady and G. Bossis, "Stokesian dynamics", Annu. Rev. Fluid Mech. **20**, 111 (1988).

[18] A. Sierou and J. F. Brady, "Accelerated stokesian dynamics simulations", J. Fluid Mech. **448**, 115 (2001).

[19] A. J. Banchio and J. F. Brady, "Accelerated stokesian dynamics: brownian motion", J. Chem. Phys. **118**, 10323 (2003).

[20] W. C. K. Poon, E. R. Weeks, and C. P. Royall, "On measuring colloidal volume fractions", Soft Matter **8**, 21 (2012).

[21] A. B. Hopkins, F. H. Stillinger, and S. Torquato, "Disordered strictly jammed binary sphere packings attain an anomalously large range of densities", Phys. Rev. E **88**, 022205 (2013).

[22] T. Shikata, H. Niwa, and Y. Morishima, "Viscoelastic behavior of bimodal suspensions", J. Rheo. **42**, 765 (1998).

[23] B. E. Rodriguez, E. W. Kaler, and M. S. Wolfe, "Binary mixtures of monodisperse latex dispersions. 2. viscosity", Langmuir **8**, 2382 (1992).

[24] A. T. J. M. Woutersen and C. G. de Kruif, "The viscosity of semidilute, bidisperse suspensions of hard spheres", J. Rheo. **37**, 681 (1993).

[25] M. A. van der Hoef, R. Beetstra, and J. A. M. Kuipers, "Lattice-boltzmann simulations of low-reynolds-number flow past mono- and bidisperse array of spheres: results for the permeability and drag force", J. Fluid Mech. **528**, 233 (2005).

[26] N. J. Wagner and A. T. J. M. Woutersen, "The viscosity of bimodal and polydisperse suspensions of hard spheres in the dilute limit", J. Fluid Mech. **278**, 267 (1994).

[27] G. K. Batchelor, "Diffusion in a dilute polydisperse system of interacting spheres", J. Fluid Mech. **131**, 155 (1983).

[28] G. K. Batchelor, "Sedimentation in a dilute polydisperse system of interacting spheres. part 1. general theory", J. Fluid Mech. **119**, 379 (1982).

[29] G. K. Batchelor and C.-S. Wen, "Sedimentation in a dilute polydisperse system of interacting spheres. part 2. numerical results", J. Fluid Mech. **124**, 495 (1982).

[30] H. Zhang and G. Nägele, "Tracer-diffusion in binary colloidal hard-sphere suspensions", J. Chem. Phys. **117**, 5908 (2002).

[31] C. Chang and R. L. Powell, "The rheolgy of bimodal hardsphere dispersions", Phys. Fluids **6**, 1628 (1994).

[32] R. Seto, R. Mari, J. F. Morris, and M. M. Denn, "Discontinuous shear thickening of frfriction hard-sphere suspensions", Phys. Rev. Lett. **111**, 218301 (2013).

[33] J. F. Brady, R. J. Phillips, J. C. Lester, and G. Bossis, "Dynamic simulation of hydrodynamically interacting suspensions", J. Fluid Mech. **195**, 257 (1988).

[34] R. J. Phillips, J. F. Brady, and G. Bossis, "Hydrodynamic transport properties of hard-sphere dispersions. i. suspensions of freely mobile particles", Phys. Fluids **31**, 3462 (1988).

[35] R. J. Phillips, J. F. Brady, and G. Bossis, "Hydrodynamic transport properties of hard-sphere dispersions. ii. porous media", Phys. Fluids **31**, 3473 (1988).

[36] A. J. Banchio and G. Nägele, "Short-time transport properties in dense suspensions: from neutral to charge-stabilized colloidal spheres", J. Chem. Phys. **128**, 104903 (2008).

[37] M. Heinen, A. J. Banchio, and G. Nägele, "Short-time rheology and diffusion in suspensions of yukawa-type colloidal particles", J. Chem. Phys. **135**, 154504 (2011).

[38] C. Chang and R. L. Powell, "Dynamic simulation of bimodal suspensions of hydrodynamically interacting spherical particles", J. Fluid Mech. **253**, 1 (1993).

[39] C. Chang and R. L. Powell, "Self-diffusion of bimodal suspensions of hydrodynamically interacting spherical particles in shearing flow", J. Fluid Mech. **281**, 51 (1994).

[40] T. Ando and J. Skolnick, "Crowding and hydrodynamic interactions likely dominate in vivo macromolecular motion", Proc. Natl. Acad. Sci. U. S. A. **107**, 18457 (2010).

[41] D. R. Foss and J. F. Brady, "Structure, diffusion and rheology of brownian suspensions by stokesian dynamics simulation", J. Fluid Mech. **407**, 167 (2000).

[42] Y. Saad, *Iterative methods for sparse linear systems* (SIAM, 2003).

[43] M. Kopp and F. Höfling, "Gpu-accelerated simulation of colloidal suspensions with direct hydrodynamic interactions", Eur. Phys. J.-Spec. Top. **210**, 101 (2012).

[44] F. Bülow, P. Hamberger, H. Nirschl, and W. Döfler, "A parallel implementation of the stokesian dynamics method applied to the simulation of colloidal suspensions", Compt. Fluids **103**, 156 (2014).

[45] K. Ichiki, "Improvement of the stokesian dynamics method for systems with a finite number of particles", J. Fluid Mech. **452**, 231 (2002).

[46] J. P. Hansen and I. R. McDonald, *Theory of simple liquids* (Academic Press, 2006).

[47] C. W. J. Beenakker and P. Mazur, "Self-diffusion of spheres in a concentrated suspension", Physica A **120**, 388 (1983).

[48] C. W. J. Beenakker and P. Mazur, "Diffusion of spheres in a concentrated suspension ii", Physica A **126**, 349 (1984).

[49] C. W. J. Beenakker, "The effective viscosity of a concentrated suspension of spheres (and its relation to diffusion)", Physica A **128**, 48 (1984).

[50] M. Wang, M. Heinen, and J. F. Brady, "Short-time diffusion in concentrated bidisperse hard-sphere suspensions", J. Chem. Phys. **142**, 064905 (2015).

[51] G. Nägele, "On the dynamics and structure of charge-stabilized suspensions", Phys. Rep. **272**, 215 (1996).

[52] G. Nägele, O. Kellerbauer, R. Krause, and R. Klein, "Hydrodynamic effects in polydisperse charged colloidal suspensions at short times", Phys. Rev. E **47**, 2562 (1993).

[53] W. B. Russel, D. A. Saville, and W. R. Schowalter, *Colloidal dispersions* (Cambridge University Press, 1991).

[54] S. Kim and S. J. Karrila, *Microhydrodynamics* (Dover, 2005).

[55] J. K. G. Dhont, *An introduction to dynamics of colloids* (Elsevier, Amsterdam, 1996).

[56] S. R. Williams and W. van Megen, "Motions in binary mixtures of hard colloidal spheres: melting of the glass", Phys. Rev. E **64**, 041502 (2001).

[57] G. H. Koenderink, H. Zhang, D. G. A. Aarts, M. P. Lettinga, A. P. Philipse, and G. Nägele, "On the validity of stokes-einstein-debye relations for rotational diffusion in colloidal suspensions", Faraday Discuss. **123**, 335 (2003).

[58] G. K. Batchelor and R. W. Janse Van Rensburg, "Structure formation in bidisperse sedimentation", J. Fluid Mech. **66**, 379 (1986).

[59] J. F. Brady, "The rheological behavior of concentrated colloidal dispersions", J. Chem. Phys. **99**, 567 (1993).

[60] J. F. Brady, A. S. Khair, and M. Swaroop, "On the bulk viscosity of suspensions", J. Fluid Mech. **554**, 109 (2006).

[61] M. Swaroop, "The bulk viscosity of suspensions", PhD thesis (California Institute of Technology, 2010).

[62] H. J. Wilson, "Stokes flow past three spheres", J. Comput. Phys. **245**, 302 (2013).

[63] C. W. J. Beenakker, "Ewald sum of the rotne-prager tensor", J. Chem. Phys. **85**, 1581 (1986).

[64] K. R. Hase and R. L. Powell, "Calculation of the ewald summed far-field mobility functions for arbitrarily size spherical particles in stokes flow", Phys. Fluids **13**, 32 (2001).

[65] D. J. Jeffrey and Y. Onishi, "Calculation of the resistance and mobility functions for two unequal rigid spheres in low-reynolds-number flow", J. Fluid Mech. **139**, 261 (1984).

[66] D. J. Jeffrey, "The calculation of the low reynolds number resistance functions for two unequal spheres", Phys. Fluids A **4**, 16 (1992).

[67] D. J. Jeffrey, J. F. Morris, and J. F. Brady, "The pressure moments for two rigid spheres in low-reynolds-number flow", Phys. Fluids A **5**, 10 (1993).

[68] A. S. Khair, M. Swaroop, and J. F. Brady, "A new resistance function for two rigid spheres in a uniform compressible low-reynolds-number flow", Phys. Fluids **18**, 043102 (2006).

[69] Y. Yurkovetsky and J. F. Morris, "Particle pressure in sheared brownian suspensions", J. Rheo. **52**, 141 (2008).

[70] A. Sierou and J. F. Brady, "Rheology and microstructure in concentrated noncolloidal suspensions", J. Rheo. **46**, 1031 (2002).

[71] B. D. Lubachevsky and F. H. Stillinger, "Geometric properties of random disk packings", J. Stat. Phys. **60**, 561 (1990).

[72] M. Skoge, A. Donev, F. H. Stillinger, and S. Torquato, "Packing hyperspheres in high-dimensional euclidean spaces", Phys. Rev. E **74**, 041127 (2006).

[73] J. K. Percus and G. J. Yevick, "Analysis of classical statistical mechanics by means of collective coordinates", Phys. Rev. **110**, 1 (1958).

[74] J. L. Lebowitz, "Exact solution of generalized percus-yevick efluation for a mixture of hard spheres", Phys. Rev. **133**, A895 (1964).

[75] W. R. Smith, D. J. Henderson, P. J. Leonard, J. A. Barker, and E. W. Grundke, "Fortran codes for the correlation functions of hard sphere fluids", Mol. Phys. **106**, 3 (2008).

[76] E. W. Grundke and D. Henderson, "Distribution functions of multi-component fluid mixtures of hard spheres", Mol. Phys. **24**, 269 (1972).

[77] L. Verlet and J.-J. Weis, "Equilibrium theory of simple liquids", Phys. Rev. A **5**, 939 (1972).

[78] N. W. Ashcroft and D. C. Langreth, "Structure of binary liquid mixtures. i", Phys. Rev. **156**, 685 (1967).

[79] N. W. Ashcroft and D. C. Langreth, "Errata", Phys. Rev. **166**, 934 (1968).

[80] F. Scheffold and T. G. Mason, "Scattering from highly packed disordered colloids", J. Phys.: Condens. Matter **21**, 332102 (2009).

[81] A. J. C. Ladd, "Hydrodynamic transport coefficients of random dispersions of hard spheres", J. Chem. Phys. **93**, 3484 (1990).

[82] A. J. C. Ladd, H. Gang, J. X. Zhu, and D. A. Weitz, "Temporal and spatial dependence of hydrodynamic correlations: simulation and experiment", Phys. Rev. E **52**, 6550 (1995).

[83] J. F. Brady and L. Durlofsky, "The sedimentation rate of disordered suspensions", Phys. Fluids **31**, 717 (1988).

[84] G. K. Batchelor and J. T. Green, "The determination of the bulk stress in a suspension of spherical particles to order c2", J. Fluid Mech. **56**, 401 (1972).

[85] G. C. Abade, B. Cichocki, M. L. Ekiel-Jeżewska, G. Nägele, and E. Wajnryb, "Rotational and translational self-diffusion in concentrated suspensions of permeable particles", J. Chem. Phys. **134**, 244903 (2011).

[86] B. Cichocki, M. L. Ekiel-Jeźewska, P. Szymczak, and E. Wajnryb, "Three-particle contribution to sedimentation and collective diffusion in hard-sphere suspensions", J. Chem. Phys. **117**, 1231 (2002).

[87] R. H. Davis and H. Gecol, "Hindered settling function with no empirical parameters for polydisperse suspensions", AIChE J. **40**, 570 (1994).

[88] A. J. Banchio, G. Nägele, and J. Bergenholtz, "Viscoelasticity and generalized stokes–einstein relations of colloidal dispersions", J. Chem. Phys. **111**, 8721 (1999).

[89] B. Cichocki, M. L. Ekiel-Jeźewska, and E. Wajnryb, "Three-particle contribution to effective viscosity of hard-sphere suspensions", J. Chem. Phys. **119**, 606 (2003).

[90] K. F. Freed and M. Muthukumar, "On the stokes problem for a suspension of spheres at finite concentrations", J. Chem. Phys. **68**, 2088 (1978).

[91] G. C. Abade, B. Cichocki, M. L. Ekiel-Jeżewska, G. Nägele, and E. Wajnryb, "Short-time dynamics of permeable particles in concentrated suspensions", J. Chem. Phys. **132**, 014503 (2010).

[92] M. H. J. Hagen, D. Frenkel, and C. P. Lowe, "Rotational diffusion in dense suspensions", Physica A **272**, 376 (1999).

[93] J. S. Chong, E. B. Christiansen, and A. D. Baer, "Rheology of concentrated suspensions", J. Appl. Polym. Sci. **15**, 2007 (1971).

[94] J. M. A. Hofman, H. J. H. Clercx, and P. P. J. M. Schram, "Effective viscosity of dense colloidal crystals", Phys. Rev. E **62**, 8212 (2000).

[95] N. A. Frankel and A. Acrivos, Chem. Eng. Sci. **2**, 847 (1967).

[96] G. Marrucci and M. M. Denn, "On the viscosity of a concentrated solid spheres", Rheol. Acta **24**, 317 (1985).

[97] B. H. A. A. van den Brule and R. J. J. Jongschaap, "Modeling of concentrated suspensions", J. Stat. Phys. **62**, 1225 (1991).

[98] K. C. Nunan and J. B. Keller, "Effective viscosity of a periodic suspension", J. Fluid Mech. **142**, 269 (1984).

[99] S. A. Patlazhan, "Effective viscosity theory of a random concentrated suspension of polydisperse hard spheres", Physica A **198**, 385 (1993).

[100] A. Donev, S. Torquato, and F. H. Stillinger, "Pair correlation function characteristics of nearly jammed and ororder hard-sphere packings", Phys. Rev. E **71**, 011105 (2005).

[101] R. Otomo and S. Harada, "Fluid permeability in stratified unconsolidated particulate bed", Transport Porous Med. **96**, 439 (2013).

Chapter 3

SHORT-TIME DIFFUSION OF COLLOIDAL SUSPENSIONS

[1] M. Wang, M. Heinen, and J. F. Brady, "Short-time diffusion in concentrated bidisperse hard-sphere suspensions", the Journal of Chemical Physics **142**, 064905 (2015) doi:10.1063/1.4907594,

3.1 Introduction

Short-time diffusion in Brownian suspensions has been a topic of extensive research for many years, which has pushed forward the development of various computer simulation methods including Lattice Boltzmann simulations [1–3], Dissipative Particle Dynamics [4, 5], Stochastic Rotation / Multiparticle Collision Dynamics [6–8], hydrodynamic force multipole methods [9, 10], boundary integral methods [11, 12], and (Accelerated) Stokesian Dynamics [13–15]. Each of these simulation methods is rather involved, which is one reason for the on-going development of approximate (semi-) analytical theoretical schemes for colloidal short-time dynamics [16–25].

In spite of extensive simulations and analytical theoretical studies, substantial gaps remain in the colloidal suspension parameter space that has yet been explored, which is due both to the large number of tunable parameters in soft matter systems, and the complexity of the salient hydrodynamic interactions (HIs) among the suspended particles. The purpose of this chapter is to assess the short-time diffusive dynamics in *mixtures* of hard spheres with two different hard-core diameters using a generalization of Stokesian Dynamics (SD) simulations and an analytical-theoretical scheme. While similar theoretical studies have so far been limited to suspensions in which at least one of the species is very dilute [16, 19, 22, 26], in the present chapter we cover a large range of packing fractions including both dilute and dense bidisperse hard-sphere fluids. All results presented here can be straightforwardly generalized to suspensions of more than two particle species.

Experiments on polydisperse suspensions have so far been limited to very high densities [27–29], where polydispersity suppresses crystallization and facilitates studies of the glass transition, or to fluid mixtures of charged particles which exhibit strong pair correlations already at low volume fractions [30]. Moderately dense,

polydisperse equilibrium suspensions are experimentally underattended to date, despite their resemblance of many substances handled in industrial, biological, and medical applications. Polydispersity is the rule rather than the exception in naturally occurring suspensions and should therefore receive more attentions in experimental, theoretical, and computational studies. One reason for the lack of experimental studies may be the poor theoretical understanding of diffusion in polydisperse fluid suspensions. Providing a semi-analytical theoretical scheme that applies in a wide range of volume fractions and compositions, the present chapter should help to close this gap in the theory of suspensions and facilitate future experiments.

In addition to the steric no-overlap constraint, the suspended hard spheres interact via solvent-mediated HIs. Accurate inclusion of HIs into theory and simulation is essential, since the linear transport coefficients for colloidal suspensions are governed entirely by the HIs in the colloidal short-time regime. However, the peculiar properties of HIs render their computation a formidable task. In particular, HIs are long-ranged, non-pairwise-additive, and exhibit steep divergences in case of lubrication, *i.e.*, when particles move in close contact configurations.

A semi-analytical theoretical scheme for short-time suspension dynamics, with multi-body HIs included in an approximate fashion, has been devised by Beenakker and Mazur [17, 18, 20], and has quite recently been re-assessed by Makuch and Cichocki [25]. This method, commonly referred to as the $\delta\gamma$ scheme, makes use of resummation techniques by which an infinite subset of the hydrodynamic scattering series [31] is computed, including all particles in suspension. Nevertheless, a complementary infinite subset of scattering diagrams is omitted in the $\delta\gamma$ scheme which, moreover, fails to include the correct lubrication limits of particle mobilities. Comparisons of the original $\delta\gamma$-scheme predictions to experimental and computer simulation data have revealed a shortcoming of the $\delta\gamma$ scheme in its prediction of self-diffusion coefficients [23, 24, 32–34], which can be largely overcome by resorting to a modified $\delta\gamma$ scheme in which the computation of the self-diffusion coefficients is carried out by a more accurate method [23, 24, 33]. To date the (modified) $\delta\gamma$ scheme remains the only analytical-theoretical approach that captures the essential physics of diffusion in dense suspensions, making predictions at an acceptable accuracy level. Unfortunately, the $\delta\gamma$ scheme has so far been formulated for monodisperse suspensions only, and a stringent generalization to mixtures poses a tedious task.

Here we propose a simple rescaling rule that allows the application of the numer-

ically efficient, easy to implement standard $\delta\gamma$-scheme expressions to mixtures of bidisperse hard spheres. The rescaling rule is based on the notion of describing either species as an effective, structureless host medium for the other species to move in. By comparing to our SD simulation results we show that the rescaled, modified $\delta\gamma$ scheme predicts both species' partial hydrodynamic functions with a surprisingly good accuracy, for suspension volume fractions as high as 40%. The proposed, rescaled $\delta\gamma$ scheme can be particularly useful in the analysis of scattering experiments, where only a limited part of the hydrodynamic function can be measured due to the limited range of accessible wave vectors.

The remaining part of this chapter is organized as follows: In Sec. 3.2 we define the hard-sphere mixtures under study, and discuss the prevailing interactions among the particles. Section 3.3 contains a discussion of colloidal short-time diffusion and the partial hydrodynamic functions that are calculated in this chapter. Our SD simulations are outlined in Sec. 3.4, which is followed by a a discussion of the static pair correlation functions in Sec. 3.5. The proposed, rescaled $\delta\gamma$ scheme is outlined in Sec. 3.6. In Sec. 3.7 we present our results for partial hydrodynamic functions of various suspensions, and we draw our finalizing conclusions in Sec. 3.8.

3.2 Bidisperse hard-sphere suspensions

We study unbounded homogeneous equilibrium suspensions of non-overlapping Brownian hard spheres with hard-core radii a_α and a_β. The pairwise additive direct interaction potentials between the particles can be written as

$$u_{\alpha\beta}(r) = \begin{cases} \infty & \text{for } r < a_\alpha + a_\beta, \\ 0 & \text{otherwise} \end{cases} \tag{3.1}$$

in terms of the particle-center separation distance r and the particle species indices $\alpha, \beta \in \{1, 2\}$. The suspensions' thermodynamic equilibrium state, studied in this chapter, is entirely described by the three non-negative dimensionless parameters

$$\lambda = a_2/a_1, \tag{3.2}$$

$$\phi = \phi_1 + \phi_2, \text{ and} \tag{3.3}$$

$$y = \phi_1/\phi, \tag{3.4}$$

where λ is the size ratio and $\phi_\alpha = (4/3)\pi n_\alpha a_\alpha^3$ is the volume fraction of species α in terms of the partial number concentration $n_\alpha = N_\alpha/V$. In taking the thermodynamic limit both the number, N_α, of particles of species α, and the system volume V diverge to infinity while their ratio n_α is held fixed. The remaining parameters in Eq. (3.3)

and (3.4) are the total volume fraction ϕ and the composition ratio y, which satisfies $0 \leq y \leq 1$. Without loss of generality, we assume $a_2 \geq a_1$ in the following. We denote the total number of particles as N, and obviously, $N = N_1 + N_2$.

All particles are assumed neutrally buoyant in an infinite quiescent, structureless Newtonian solvent of shear viscosity η_0. No external forces or torques act on the suspended particles. The solvent is assumed to be incompressible, and the Reynolds number for particle motion is assumed to be very small, such that the solvent velocity field $\boldsymbol{v}(\boldsymbol{r})$ and dynamic pressure field $p(\boldsymbol{r})$ satisfy the stationary Stokes equation with incompressibility constraint,

$$\eta_0 \Delta \boldsymbol{v}(\boldsymbol{r}) = \nabla p(\boldsymbol{r}), \tag{3.5}$$

$$\nabla \cdot \boldsymbol{v}(\boldsymbol{r}) = 0, \tag{3.6}$$

at every point $\boldsymbol{r}$ inside the solvent. Equations (3.5) and (3.6) are supplemented with hydrodynamic no-slip boundary conditions on the surface of each suspended sphere. The linearity of Eqs. (3.5) and (3.6) suggests a linear coupling between the translational velocity of particle l, $\boldsymbol{U}_l$, and the force exerted on particle j, $\boldsymbol{F}_j$:

$$\boldsymbol{U}_l = -\sum_{j=1}^{N_j} \boldsymbol{\mu}_{lj}^{tt} \cdot \boldsymbol{F}_j, \tag{3.7}$$

where the mobility tensor $\boldsymbol{\mu}_{lj}^{tt}$ has a size of 3×3. By placing the tensor $\boldsymbol{\mu}_{ij}^{tt}$ as elements of a larger, generalized matrix, we construct the suspension grand mobility tensor $\boldsymbol{\mu}^{tt}$ of size $3N \times 3N$. The minimum dissipation theorem [35] requires $\boldsymbol{\mu}^{tt}$ to be symmetric and positive definite.

3.3 Short-time diffusion

Here we are interested in diffusive dynamics at a coarse-grained scale of times t that satisfy the two strong inequalities [36]

$$\tau_H \sim \tau_I \ll t \ll \tau_D, \tag{3.8}$$

defining the colloidal *short-time* regime. The hydrodynamic time scale $\tau_H = a_2^2 \rho_0 / \eta_0$, involving the solvent mass density ρ_0, quantifies the time at which solvent shear waves traverse typical distances between (the larger) colloidal particles. The criterion $t \gg \tau_H$ implies that HIs, being transmitted by solvent shear waves, act effectively instantaneously at the short-time scale. Therefore, the elements of the grand mobility matrix $\boldsymbol{\mu}^{tt}$ depend on the instantaneous positions $\boldsymbol{r}^N = \{\boldsymbol{r}_1, \boldsymbol{r}_2, \cdots, \boldsymbol{r}_N\}$ of

all particles, but not on their positions at earlier times. The momentum relaxation time $\tau_I = m_2/(6\pi\eta_0 a_2)$ in terms of the mass, m_2 of a particle of species 2, is similar in magnitude to τ_H. At times $t \gg \tau_I$, many random collisions of a colloidal particle with solvent molecules have taken place, the particle motion is diffusive, and inertia plays no role. The colloidal short time regime is bound from above by the (diffusive) interaction time scale $\tau_D = a_1^2/d_0^1$, given in terms of the Stokes-Einstein-Sutherland (SES) translational free diffusion coefficient, $d_0^1 = k_B T \mu_0^1$ of the smaller particle species. Here, $\mu_0^\alpha = (6\pi\eta_0 a_\alpha)^{-1}$ is the single particle mobility of species α, k_B is the Boltzmann constant and T is the absolute temperature. During times $t \gtrsim \tau_D$, diffusion causes the spatial configuration of the (smaller) particles to deviate appreciably from their initial configuration, and in addition to the HIs, rearrangements of the cage of neighboring particles start to influence particle dynamics. This results in a sub-diffusive particle motion at times $t \gtrsim \tau_D$ preceding the ultimate diffusive long-time regime $t \gg \tau_D$ at which a particle samples many independent local neighborhoods. Unless the particle size-ratio λ is very large, τ_D is some orders of magnitude larger than both τ_H and τ_I, and the colloidal short-time regime in Eq. (3.8) is well defined [36].

Scattering experiments on bidisperse colloidal suspensions, including the most common small angle light scattering [37] and x-ray scattering [38, 39] techniques, allow the extraction of the measurable dynamic structure factor [21]

$$S_M(q,t) = \frac{1}{\overline{f^2}(q)} \sum_{\alpha,\beta=1}^{2} \sqrt{x_\alpha x_\beta}\, f_\alpha(q) f_\beta(q)\, S_{\alpha\beta}(q,t), \tag{3.9}$$

which contains the scattering amplitudes, $f_\alpha(q)$, for particles of either species, the mean squared scattering amplitude $\overline{f^2}(q) = x_1 f_1^2(q) + x_2 f_2^2(q)$ in terms of the molar fractions $x_\alpha = N_\alpha/N$, and the partial dynamic structure factors $S_{\alpha\beta}(q,t)$. In the case of scattering experiments, N_α is the mean number of α-type particles in the scattering volume. The microscopic definition of the partial dynamic structure factors reads

$$S_{\alpha\beta}(q,t) = \lim_{\infty} \left\langle \frac{1}{\sqrt{N_\alpha N_\beta}} \sum_{\substack{l\in\alpha \\ j\in\beta}} \exp\left\{ i\mathbf{q}\cdot[\boldsymbol{r}_l^\alpha(0) - \boldsymbol{r}_j^\beta(t)] \right\} \right\rangle, \tag{3.10}$$

with the summation carried out over all particles l that belong to species α and all particles j that belong to species β, with $i = \sqrt{-1}$ denoting the imaginary unit, $\lim_\infty$ indicating the thermodynamic limit, the brackets $\langle \ldots \rangle$ standing for the ensemble average, and $\boldsymbol{r}_k^\gamma(t)$ denoting the position of particle number k (which

belongs to species γ) at time t. From the microscopic definition it follows that $S_{\alpha\beta}(q) = S_{\beta\alpha}(q)$, and that the functions $S_{\alpha\alpha}(q)$ are non-negative, while the $S_{\alpha\beta}(q)$ for $\alpha \neq \beta$ can assume either sign. In the special case of $t = 0$, the partial dynamic structure factors reduce to the partial static structure factors $S_{\alpha\beta}(q) = S_{\alpha\beta}(q, 0)$ and, likewise, $S_M(q, 0) = S_M(q)$ is the measurable static structure factor.

A useful approximation in the analysis of experimental scattering data for suspensions with a small degree of particle polydispersity (typically 10% or less relative standard deviation in the particle-size distribution) is the decoupling approximation [21, 33] in which all functions $S_{\alpha\beta}(q, t)$ in Eq. (3.9) are approximated by a monodisperse, mean structure factor $S(q, t)$. For the strongly size-asymmetric hard-sphere mixtures studied here, the $S_{\alpha\beta}(q, t)$ show distinct mutual differences, which rules out the application of the decoupling approximation.

In some experiments, the $f_\alpha(q)$ for different species α may be tuned independently. An example is the selective refractive index matching of solvent and particles in light scattering experiments [40]. Under such circumstances, the three independent functions $S_{\alpha\beta}(q)$ for $\alpha, \beta \in \{1, 2\}$ may be singled out individually. When all functions $S_{\alpha\beta}(q, t)$ are known, the dynamic number-number structure factor

$$S_{NN}(q, t) = \sum_{\alpha,\beta=1}^{2} \sqrt{x_\alpha x_\beta}\, S_{\alpha\beta}(q, t), \tag{3.11}$$

can be determined, which reduces, for $t = 0$, to the static number-number structure factor $S_{NN}(q)$. In computer simulations, the $S_{\alpha\beta}(q, t)$ and $S_{NN}(q, t)$ are easily extracted once that all the time-dependent particle positions $\boldsymbol{r}_k^\gamma(t)$ are known, but the challenge lies in the accurate computation of the latter.

Colloidal dynamics at times $t \gg \tau_H \sim \tau_B$ are governed by the Smoluchowski diffusion equation [36] which quantifies the temporal evolution for the probability density function $P(t, \boldsymbol{r}^N)$ of the particle configuration $\boldsymbol{r}^N$ at time t. It can be shown [41] that the 2×2 correlation matrix $\boldsymbol{S}(q, t)$ with elements $S_{\alpha\beta}(q, t)$ decays at short times as

$$\boldsymbol{S}(q, t) \approx e^{-q^2 \boldsymbol{D}(q) t} \cdot \boldsymbol{S}(q), \tag{3.12}$$

with a diffusivity matrix $\boldsymbol{D}(q)$ that can be split as

$$\boldsymbol{D}(q) = k_\mathrm{B} T \boldsymbol{H}(q) \cdot \boldsymbol{S}^{-1}(q), \tag{3.13}$$

into a product of the matrix $\boldsymbol{H}(q)$ of partial hydrodynamic functions $H_{\alpha\beta}(q)$ and the inverse partial static structure factor matrix $\boldsymbol{S}^{-1}(q)$.

The functions $H_{\alpha\beta}(q)$ can be interpreted as generalized wavenumber-dependent short-time sedimentation velocities: In a homogeneous suspension, the value of $H_{\alpha\beta}(q)$ quantifies the spatial Fourier components of the initial velocity attained by particles of species α, when a weak force field is switched on that acts on particles of species β only, dragging them in a direction parallel to $\mathbf{q}$ with a magnitude that oscillates harmonically as $\cos(\mathbf{q}\cdot\boldsymbol{r})$. The microscopic definition of the partial hydrodynamic functions reads [21]

$$H_{\alpha\beta}(q) = \lim_{\infty}\left\langle \frac{1}{\sqrt{N_\alpha N_\beta}} \sum_{\substack{l\in\alpha \\ j\in\beta}} \hat{\mathbf{q}}\cdot\boldsymbol{\mu}^{tt}_{lj}(\boldsymbol{r}^N)\cdot\hat{\mathbf{q}}\,\exp\left\{i\mathbf{q}\cdot[\boldsymbol{r}^\alpha_l - \boldsymbol{r}^\beta_j]\right\}\right\rangle, \tag{3.14}$$

where $\hat{\mathbf{q}} = \mathbf{q}/q$ is the normalized wave vector, and the summation ranges are the same as Eq. (3.10). Note that the positive definiteness of the $\boldsymbol{\mu}^{tt}$ implies that the functions $H_{\alpha\alpha}(q)$ are non-negative, whereas the functions $H_{\alpha\beta}(q)$ can assume both positive and negative values for $\alpha \neq \beta$. In particular, the latter functions assume negative values at small values of q due to the solvent backflow effect: when a weak spatially homogeneous external force acts on particles of species β only, it causes the β-type particles to sediment in a direction parallel to the applied force, which corresponds to $H_{\beta\beta}(q\to 0) > 0$. Mass conservation requires the collective motion of β-type particles to be compensated by an opposing backflow of solvent, which drags the α-type particles in the direction anti-parallel to the applied force. Hence, $H_{\alpha\beta}(q\to 0) < 0$ for $\alpha \neq \beta$.

By splitting the sum in Eq. (3.14) into the self ($l = j$) and the complementary distinct contributions, the functions $H_{\alpha\beta}(q)$ can each be decomposed, according to

$$H_{\alpha\beta}(q) = \delta_{\alpha\beta}\frac{d^\alpha_s}{k_B T} + H^d_{\alpha\beta}(q), \tag{3.15}$$

into a sum of a wavenumber-independent self-part and the wavenumber-dependent distinct part of the partial hydrodynamic function, $H^d_{\alpha\beta}(q)$, which tends to zero for large values of q. In case of infinite dilution, or in the (purely hypothetical) case of vanishing hydrodynamic forces, $H_{\alpha\beta}(q)/\mu^\alpha_0$ reduces to the Kronecker delta symbol $\delta_{\alpha\beta}$. The short-time translational self diffusion coefficient d^α_s is equal to the time derivative of the mean squared displacement $W_\alpha(t) = \frac{1}{6}\left\langle[\boldsymbol{r}^\alpha_l(t) - \boldsymbol{r}^\alpha_l(0)]^2\right\rangle$ of a particle of species α at short times. At infinite dilution, $d^\alpha_s = d^\alpha_0$.

If all functions $H_{\alpha\beta}(q)$ are known, then the number-number hydrodynamic function

$$H_{NN}(q) = \sum_{\alpha,\beta=1}^{2} \sqrt{x_\alpha x_\beta}\, H_{\alpha\beta}(q) \tag{3.16}$$

and the measurable hydrodynamic function

$$H_M(q,t) = \frac{1}{\overline{f^2}(q)} \sum_{\alpha,\beta=1}^{2} \sqrt{x_\alpha x_\beta}\, f_\alpha(q) f_\beta(q)\, H_{\alpha\beta}(q), \tag{3.17}$$

can be computed, which quantify the short-time decay of the dynamic number-number structure factor

$$S_{NN}(q,t) \approx S_{NN}(q) e^{-q^2 D_{NN}(q) t} \tag{3.18}$$

and the measurable dynamic structure factor

$$S_M(q,t) \approx S_M(q) e^{-q^2 D_M(q) t}, \tag{3.19}$$

through the number-number diffusion function $D_{NN}(q) = k_B T H_{NN}(q)/S_{NN}(q)$ and the measurable diffusion function $D_M(q) = k_B T H_M(q)/S_M(q)$.

3.4 Stokesian Dynamics simulations

The framework of the Stokesian Dynamics (SD) has been extensively discussed elsewhere [13, 15, 42, 43] and here we only present the aspects pertinent to this chapter. For rigid particles in a suspension, the generalized particle forces $\boldsymbol{\mathcal{F}}$ and stresslets $\boldsymbol{S}$ are linearly related to the generalized particle velocities $\boldsymbol{\mathcal{U}}$ through the grand resistance tensor $\boldsymbol{\mathcal{R}}$ as [35]

$$\begin{pmatrix} \boldsymbol{\mathcal{F}} \\ \boldsymbol{S} \end{pmatrix} = -\boldsymbol{\mathcal{R}} \cdot \begin{pmatrix} \boldsymbol{\mathcal{U}} - \boldsymbol{\mathcal{U}}^\infty \\ -\boldsymbol{e}^\infty \end{pmatrix}, \tag{3.20}$$

where $\boldsymbol{\mathcal{U}}^\infty$ and $\boldsymbol{e}^\infty$ are the imposed generalized velocity and strain rate, respectively. The generalized force $\boldsymbol{\mathcal{F}}$ represents the forces and torques of all particles in the suspension, and the generalized velocity $\boldsymbol{\mathcal{U}}$ contains the linear and angular velocities for all particles. The grand resistance tensor $\boldsymbol{\mathcal{R}}$ is partitioned as

$$\boldsymbol{\mathcal{R}} = \begin{pmatrix} \boldsymbol{R}_{FU} & \boldsymbol{R}_{FE} \\ \boldsymbol{R}_{SU} & \boldsymbol{R}_{SE} \end{pmatrix}, \tag{3.21}$$

where, for example, $\boldsymbol{R}_{FU}$ describes the coupling between the generalized force and the generalized velocity, $\boldsymbol{R}_{FE}$ describes the coupling between the generalized force and the strain rate, *etc.*. In the SD method the grand resistance is approximated as

$$\boldsymbol{\mathcal{R}} = (\boldsymbol{\mathcal{M}}^\infty)^{-1} + \boldsymbol{\mathcal{R}}_{2B} - \boldsymbol{\mathcal{R}}_{2B}^\infty, \tag{3.22}$$

where the far field mobility tensor $\boldsymbol{\mathcal{M}}^\infty$ is constructed pairwisely from the multipole expansions and the Faxén's laws of the Stokes equation up to the stresslet level,

and its inversion captures the long-range many-body hydrodynamic interactions. The near-field lubrication correction $(\boldsymbol{\mathcal{R}}_{2B} - \boldsymbol{\mathcal{R}}_{2B}^{\infty})$ is based on the exact two-body solutions with the far field contributions removed, and it accounts for the singular HIs when particles are in close contact. The SD method recovers the exact solutions of two-particle problems and was shown to agree well with the exact solution of three-particle problems [44].

Extending the SD method to polydisperse systems retains the computational framework above. The far-field polydisperse mobility tensor $\boldsymbol{\mathcal{M}}^{\infty}$ is computed using the multipole expansions as in Ref. [45] and the resulting expressions are extended to infinite periodic systems using Beenakker's technique [46, 47]. The lubrication correction $(\boldsymbol{\mathcal{R}}_{2B} - \boldsymbol{\mathcal{R}}_{2B}^{\infty})$ for particle pair with radii a_α and a_β are based on the exact solution of two-body problems in Ref. [48–51] up to s^{-300}, where $s = 2r/(a_\alpha + a_\beta)$ is the scaled center-to-center particle distance. In our simulations, the lubrication corrections are invoked when $r < 2(a_\alpha + a_\beta)$, and the analytic lubrication expressions are used when $r < 1.05(a_\alpha + a_\beta)$.

Our simulations proceed as follows. First, a random bimodal hard-sphere packing at the desired composition is generated using the event-driven Lubachevsky-Stillinger algorithm [52, 53] with high compression rate. After the desired volume fraction ϕ is reached, the system is equilibrated for a short time (10 events per particle) at zero compression rate. This short equilibration stage is necessary as the compression pushes particles closer to each other than in thermodynamic equilibrium. Prolonging the equilibration stage does not alter the resulting suspension structure significantly.

To avoid singularities in the grand resistance tensor due to particle contact, we enforce a minimum separation of $10^{-6}(a_i + a_j)$ between particles in our simulations. The resistance tensor $\boldsymbol{\mathcal{R}}$ is then constructed based on the particle configuration $\boldsymbol{r}^N$. The partial hydrodynamic functions are extracted from $\boldsymbol{\mu}^{tt}$, a submatrix of the grand mobility tensor

$$\boldsymbol{R}_{FU}^{-1} = \begin{pmatrix} \boldsymbol{\mu}^{tt} & \boldsymbol{\mu}^{tr} \\ \boldsymbol{\mu}^{rt} & \boldsymbol{\mu}^{rr} \end{pmatrix}, \tag{3.23}$$

which contains coupling between the translational (t) and rotational (r) velocities and forces of a freely-mobile particle suspension. Typically each configuration contains 800 particles and at least 500 independent configurations are studied for each composition.

The partial hydrodynamic functions $H_{\alpha\beta}(q)$ extracted from the simulations exhibit a strong $\sqrt[3]{N}$ size dependence due to the imposed periodic boundary conditions [9,

23, 54, 55]. The finite size effect can be eliminated by considering $H_{\alpha\beta}(q)$ as a generalized sedimentation velocity. The sedimentation velocity from a finite size system with periodic boundary conditions is a superposition of the velocities from random suspensions and cubic lattices [54, 55]. This argument is straightforwardly extended to bidisperse suspensions, where the size correction, $\Delta_N H_{\alpha\beta}(q)$, for the partial hydrodynamic functions computed from the N-particles system, $H_{\alpha\beta,N}(q)$, is

$$\Delta_N H_{\alpha\beta}(q) = \frac{1.76\mu_0^1[1+(\lambda^3-1)y]^{\frac{1}{3}}S_{\alpha\beta}(q)}{\lambda}\frac{\eta_0}{\eta_s}\left(\frac{\phi}{N}\right)^{\frac{1}{3}}. \tag{3.24}$$

In Eq. (3.24), $\Delta_N H_{\alpha\beta}(q) = H_{\alpha\beta}(q) - H_{\alpha\beta,N}(q)$, $H_{\alpha\beta}(q)$ is the hydrodynamic function in the thermodynamic limit, and η_s/η_0 is the high frequency shear viscosity of the suspension, which is obtained from the same simulation. Note that the shear viscosity η_s/η_0 changes little with system size, and that the scaling for $H_{\alpha\beta}(q)$ in Eq. (3.24) is chosen to be μ_0^1 regardless of the choice of α and β.

3.5 Static pair correlations

Fig. 3.1 features the partial radial distribution functions $g_{\alpha\beta}(r)$ (upper panel) and the partial static structure factors $S_{\alpha\beta}(q)$ (lower panel) generated by the simulation protocol described in the previous section for a bidisperse suspension of $\lambda = 2$, $y = 0.5$, and $\phi = 0.5$, the highest volume fraction studied in this chapter. The function $g_{\alpha\beta}(r)$ quantifies the probability of finding a particle of species β at a center-to-center distance r from a particle of species α [56]. The measured functions $g_{\alpha\beta}(r)$ and $S_{\alpha\beta}(q)$ (open circles in both panels of Fig. 3.1) are compared with the solutions of the Percus-Yevick (PY)[57–59] and the Rogers-Young (RY)[60] integral equations at the same system parameters. We solve the polydisperse RY scheme as described in Ref. [61] with a single mixing parameter that ensures the partial thermodynamic self-consistency with respect to the total isothermal osmotic compressibility of the mixture in the virial and the fluctuation routes[56]. The RY-scheme equations are solved numerically by means of a spectral solver that has been comprehensively outlined in Refs. [62, 63]. The PY scheme is simpler, but it is thermodynamically inconsistent. It predicts the static pair-correlations of particles with repulsive pair interactions less accurately than the RY scheme [64]. Differences between the PY- and RY-scheme solutions are most prominent in the functions $g_{\alpha\beta}(r)$, in particular around the contact values $g_{\alpha\beta}(r = a_\alpha + a_\beta)$. Nevertheless, observing the lower panel Fig. 3.1 we note that the PY scheme predicts the partial static structure factors accurately, and in nearly perfect agreement with the RY-scheme and the simulations, even at the high volume fraction $\phi = 0.5$. We have checked that the nearly perfect

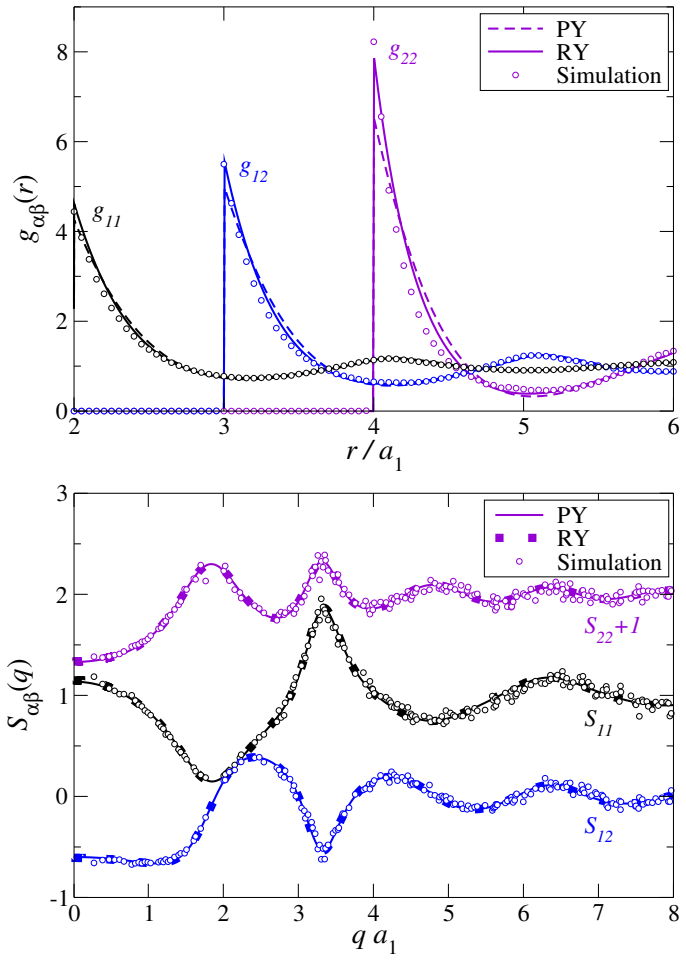

Figure 3.1: The bidisperse suspension partial radial distribution functions $g_{\alpha\beta}(r)$ (upper panel) and partial static structure factors $S_{\alpha\beta}(q)$ (lower panel) for $\phi = 0.5$, $y = 0.5$, and $\lambda = 2$, directly measured from the simulations (open circles), and computed via the Percus-Yevick (PY) and Rogers-Young (RY) integral equation schemes. Note that the function $S_{22}(q)$ has been shifted upwards by one unit along the vertical axis for clarity.

agreement between the PY- and RY-scheme predictions for the functions $S_{\alpha\beta}(q)$ remains for other composition parameters (from $y = 0.1$ to $y = 0.9$), and that the final predictions of our combined, semi-analytical theoretical scheme (*i.e.*, the hydrodynamic functions plotted in Fig. 3.3, 3.4 and 3.6) do not change significantly when the RY-scheme functions $S_{\alpha\beta}(q)$ are used instead of the PY-scheme solutions.

Therefore, the simple, analytically solvable PY scheme is sufficiently accurate to generate the static structure input for the rescaled $\delta\gamma$ scheme described in the following sections. The main source of error of our method is from the various approximations made in the $\delta\gamma$ scheme and its modifications, rather than the slight inaccuracy of the structural input. Consequently, we have used the PY-scheme static structure factors in generating all results presented further down this article. In future applications of our method, the reader may use the RY-scheme or other more accurate integral equation schemes, particularly when studying systems with different pair potentials. In addition, a related line of research is concerned with tests and improvements of the different $\delta\gamma$-scheme approximations (for monodisperse suspensions) [34]. Such assessment relies critically on an accurate static structure input and hence the RY-scheme is used there.

3.6 Rescaled $\delta\gamma$ scheme

The $\delta\gamma$ scheme, originally introduced by Beenakker and Mazur [18, 20] and quite recently revised by Makuch *et al.* [25, 34] predicts short-time linear transport coefficients of monodisperse colloidal suspensions with an overall good accuracy, for volume fractions of typically less than 40%. A modified version of the $\delta\gamma$ scheme with an improved accuracy has been proposed in Ref. [23, 24, 32, 33]. The modification consists of replacing the rather inaccurate, microstructure-independent $\delta\gamma$-scheme expression for the self-diffusion coefficient d_s by a more accurate expression. The hydrodynamic function for a monodisperse suspension is then calculated as the sum of this more accurate self-term and the distinct part of the hydrodynamic function, with the latter retained from the original $\delta\gamma$ scheme (*c.f.*, the special case of Eq. (3.15) for monodisperse suspensions). This replacement of the self-diffusion coefficient does not only result in an improved accuracy of the predicted hydrodynamic functions for hard spheres, but also allows computation of hydrodynamic functions of charge-stabilized colloidal particles with mutual electrostatic repulsion of variable strength.

There are several possibilities for choosing the self-diffusion coefficient in the mod-

ified $\delta\gamma$ scheme. It can be treated as a fitting parameter [32], calculated by computer simulation [23], or in the approximation of pairwise additive HIs, which is specially well-suited for charge-stabilized suspensions [24, 33]. In case of monodisperse hard-sphere suspensions,

$$\frac{d_s}{d_0} \approx 1 - 1.8315\phi(1 + 0.1195\phi - 0.70\phi^2), \tag{3.25}$$

where $d_0 = k_B T \mu_0$ and $\mu_0 = (6\pi\eta_0 a)^{-1}$, is a highly accurate approximation provided that $\phi \lesssim 0.5$ [24]. Expression (3.25) coincides with the known truncated virial expression [10] to quadratic order in ϕ. The prefactor of the cubic term has been determined as an optimal fit value that reproduces numerically precise computer simulation results for d_s/d_0 [23, 65].

The distinct part of the monodisperse hydrodynamic function is approximated in the $\delta\gamma$-scheme as:

$$\begin{aligned} \frac{H^d(q)}{\mu_0} = \frac{3}{2\pi} \quad & \int_0^\infty dy' \left[\frac{\sin(y')}{y'}\right]^2 \cdot \left[1 + \phi S_{\gamma_0}(\phi, y')\right]^{-1} \\ \times \quad & \int_{-1}^{1} d\mu (1-\mu^2) \left[S(|\mathbf{q} - \mathbf{q}'|) - 1\right]. \end{aligned} \tag{3.26}$$

In Eq. (3.26), $y = 2qa$ is a dimensionless wavenumber, $\mu = \mathbf{q} \cdot \mathbf{q}'/(qq')$ is the cosine of the angle between $\mathbf{q}$ and $\mathbf{q}'$, and the volume-fraction and wavenumber-dependent function $S_{\gamma_0}(\phi, y)$ (not to be confused with a static structure factor) has been specified in Ref. [20, 32].

For monodisperse suspensions, the $\delta\gamma$ scheme requires only the static structure factor $S(q)$ and the suspension volume fraction ϕ as the input for calculating the hydrodynamic functions, namely,

$$\frac{H(q)}{\mu_0} \approx H_{\delta\gamma}[S(q), \phi], \tag{3.27}$$

where $H_{\delta\gamma}[\cdot, \cdot]$ denotes the modified $\delta\gamma$-scheme result based on Eq. (3.15), (3.25) and (3.26).

Extending the $\delta\gamma$ scheme to the more general case of bidisperse suspensions is a non-trivial task. The size polydispersity affects (*i*) the structural input through the partial static structure factors $S_{\alpha\beta}(q)$, and (*ii*) the hydrodynamic scattering series [31], upon which the $\delta\gamma$ scheme is constructed [25]. For bidisperse suspensions,

the structural input in (i) can be computed by liquid integral equations, *e.g.*, the PY scheme [57–59, 66] which we use in the present study. However, the evaluation of the bidisperse hydrodynamic scattering series is more difficult since each scattering diagram for monodisperse suspensions has to be replaced by multiple diagrams describing the scattering in particle clusters containing particles of both species. Even if the resummation of the bidisperse hydrodynamic scattering series can be achieved, the accuracy of the results remains unknown without a direct comparison to experiments or computer simulations.

Here we bypass the difficult task of bidisperse hydrodynamic scattering series resummation and adopt a simpler idea based on the existing (modified) $\delta\gamma$ scheme for monodisperse particle suspensions. The partial hydrodynamic functions $H_{\alpha\alpha}(q)$ can always be written as

$$\frac{H_{\alpha\alpha}(q)}{\mu_0^\alpha} = f_\alpha H_{\delta\gamma}[S_{\alpha\alpha}(q), \phi_\alpha], \tag{3.28}$$

where the factor

$$f_\alpha = f_\alpha(q; \lambda, \phi, y) \tag{3.29}$$

describes the wave-number dependent HIs due to the other species β not captured in the $\delta\gamma$ scheme, and also depends on the suspension composition.

For the interspecies partial hydrodynamic functions $H_{\alpha\beta}(q)$ ($\alpha \neq \beta$), the limiting value at $q \to \infty$, like $S_{\alpha\beta}(q)$, goes to zero. Therefore, only the distinct part in the $\delta\gamma$ scheme is relevant, and to maintain consistency with Eq. (3.26), a shifted distinct static structure factor $S_{\alpha\beta}(q) + 1$ ($\alpha \neq \beta$) is used as the input. Similar to Eq. (3.28), a scaling factor $f_{\alpha\beta} = f_{\alpha\beta}(q; \lambda, \phi, y)$ provides the connection to the $\delta\gamma$ scheme by

$$\frac{H_{\alpha\beta}(q)}{\mu_0^\alpha} = f_{\alpha\beta} H^d_{\delta\gamma}[S_{\alpha\beta}(q) + 1, \phi], (\alpha \neq \beta), \tag{3.30}$$

when $H^d_{\delta\gamma}[S_{\alpha\beta}(q)+1, \phi]$ is computed according to Eq. (3.26). Note that in Eq. (3.30) the total volume fraction ϕ is used in the $\delta\gamma$ scheme. This is motivated by the physics of $H_{\alpha\beta}(q)$ ($\alpha \neq \beta$)—from a generalized sedimentation perspective, it describes the q-dependent velocity response of species α due to an application of q-dependent forces on the β species. Since both species are present, the total volume fraction ϕ should be used. For monodisperse suspensions with artificially labeled particles, we expect $f_{\alpha\beta} \sim 1$. In bidisperse suspensions the deviation from unity in $f_{\alpha\beta}$ is due to the size effects in HIs.

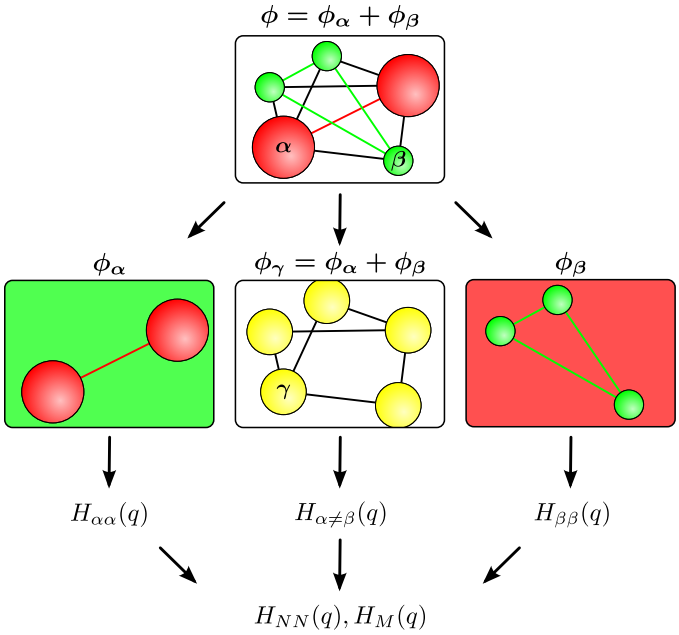

Figure 3.2: Schematic representation of the effective medium concept. Straight red, green and black lines indicate the $\alpha\alpha$, $\beta\beta$ and $\alpha \neq \beta$ correlations, respectively. Either species α, β is approximated as an effective structureless fluid for the other species to move in (left and right panels). The distinct species contributions ($\alpha \neq \beta$, central panel) are approximated by those of a hydrodynamically monodisperse fluid of fictitious γ-type particles in pure solvent. The size of γ-type particles is chosen such that $\phi_\gamma = \phi = \phi_\alpha + \phi_\beta$, and their center of mass positions coincide with those of the $\alpha-$ and $\beta-$ type particles in the bidisperse suspension (top panel).

A simplification for the hydrodynamic interactions in bidisperse suspensions is to assume that the HIs are of a mean-field nature, and consequently the factors in Eq. (3.28) and (3.30) become q-independent, *i.e.*,

$$f_\alpha(q;\lambda,\phi,y) \approx f_\alpha(\lambda,\phi,y) \tag{3.31}$$

$$f_{\alpha\beta}(q;\lambda,\phi,y) \approx f_{\alpha\beta}(\lambda,\phi,y). \tag{3.32}$$

In this way, the monodisperse $\delta\gamma$ scheme is extended to bidisperse suspensions by introducing composition dependent scaling constants. We call the resulting approximation scheme the rescaled $\delta\gamma$ scheme. As we will see in Sec. 3.7, this simplification describes the SD measurement surprisingly well—providing an *a posteriori* justification for Eq. (3.31) and (3.32). Note that the rescaling rules in Eq. (3.28) and (3.30) can be straightforwardly generalized to the polydisperse case with more than two different particle species.

Fig. 3.2 succinctly illustrates the rescaled $\delta\gamma$ scheme. In computing the functions

$H_{\alpha\alpha}(q)$, we ignore the particulate nature of species β which is replaced by an effective medium for species α to move in (left and right panels in Fig. 3.2). The effective translational free diffusion coefficient is therefore $f_\alpha d_0^\alpha$, and is expected to be smaller than the SES diffusion coefficient d_0^α for diffusion in the pure solvent, leading to $f_\alpha < 1$. The distinct species partial hydrodynamic function $H_{\alpha\beta}(q)$ for $\alpha \neq \beta$ is approximated by the corresponding function in a hydrodynamically monodisperse suspension of fictitious particles (γ-type particles in Fig. 3.2) in pure solvent, which occupy the same center of mass positions as the α- and β- type particles in the bidisperse suspension. The size of the γ-type particles is chosen such that $\phi_\gamma = \phi = \phi_\alpha + \phi_\beta$. We stress again that the fidelity of our approach cannot be easily estimated, but rather is validated *a posteriori* by comparing with the SD simulation results.

For our rescaled $\delta\gamma$ scheme to be useful, estimations of the scaling factors f_α and $f_{\alpha\beta}$ are required. To estimate the factor f_α, recall that $f_\alpha d_0^\alpha$ describes the translational free diffusivity of one particle of species α in an effective medium of many β particles. Equivalently, for many α particles, $f_\alpha d_s(\phi_\alpha)/d_0$, where $d_s(\phi_\alpha)/d_0$ is the self-diffusivity of monodisperse suspensions at volume fraction ϕ_α, represents the species self-diffusivity $d_s^\alpha(\phi, \lambda, y)/d_0^\alpha$ in the bidisperse mixture, *i.e.*,

$$f_\alpha = \frac{d_s^\alpha(\phi, \lambda, y)/d_0^\alpha}{d_s(\phi_\alpha)/d_0}, \tag{3.33}$$

where the monodisperse self-diffusivity $d_s(\phi)/d_0$ is given in Eq. (3.25), and the estimation of the species self-diffusivity is discussed next. For the interspecies factor $f_{\alpha\beta}$, we assume the mean-field description of HIs is sufficient and the size effect is weak, *i.e.*,

$$f_{\alpha\beta} = 1. \tag{3.34}$$

Note that both Eq. (3.33) and (3.34) are physically motivated and are validated by the SD measurements in Section 3.7.

The estimation of f_α in Eq. (3.33) requires an approximation of the species short-time self-diffusivity d_s^α/d_0^α in the mixture. For dilute systems where HIs can be decomposed into sums of pairwise additive contributions, d_s^α/d_0^α can be calculated to linear order in the volume fractions as [19, 22]

$$\frac{d_s^\alpha}{d_0^\alpha} = 1 + \sum_{\beta=1,2} I_{\alpha\beta}\phi_\beta + O(\phi_1^2, \phi_2^2), \tag{3.35}$$

with the integrals

$$I_{\alpha\beta} = \frac{(1+\lambda_{\beta\alpha})^3}{8\lambda_{\beta\alpha}^3} \int_2^\infty s^2 \left[x_{11}^a(s) + 2y_{11}^a(s) - 3\right] ds \tag{3.36}$$

in terms of $s = 2r/(a_\alpha + a_\beta)$ and $\lambda_{\beta\alpha} = a_\beta/a_\alpha$. The scalar hydrodynamic two-body mobility functions $x_{11}^a(s)$ and $2y_{11}^a(s)$ describe the relative motions of two spheres in the direction parallel and orthogonal to a line that connects the sphere centers, respectively, and can be calculated with arbitrary precision [35, 48, 67]. A series expansion in the inverse particle separation yields the leading order far-field terms of the integrand

$$x_{11}^a + 2y_{11}^a - 3 = \frac{-60\lambda_{\beta\alpha}^3}{[s(1+\lambda_{\beta\alpha})]^4} + \frac{480\lambda_{\beta\alpha}^3 - 264\lambda_{\beta\alpha}^5}{[s(1+\lambda_{\beta\alpha})]^6} + O(s^{-8}). \tag{3.37}$$

Here, we employ the two-body mobility coefficients from ref. [48] up to s^{-300} to ensure a smooth crossover to the analytically known close-contact (lubrication) expressions [68]. For particle size-ratio $\lambda = 2$, numerical integration of Eq. (3.36) yields the values $I_{11} = I_{22} = -1.8315$, $I_{12} = -1.4491$ and $I_{21} = -2.0876$.

Computation of the quadratic and higher order terms of the virial expansion in Eq. (3.35) is an elaborate task, even when three-body HIs are included in their leading-order far-field asymptotic form only [22]. In place of such cumbersome computation of the d_s^α/d_0^α, we propose a simple Ansatz

$$\frac{d_s^\alpha}{d_0^\alpha} \approx 1 + \left(\sum_{\beta=1,2} I_{\alpha\beta}\phi_\beta\right) \times \left(1 + 0.1195\phi - 0.70\phi^2\right) \tag{3.38}$$

which reduces to the accurate expression in Eq. (3.25) for $\lambda = 1$, and is correct to linear order in the volume fractions for all values of λ. In Eq. (3.38), the effects of different particle sizes are incorporated in the linear term while the effects of different volume fractions are treated in a mean-field way, *i.e.*, independent of the size ratio. It is important to note here that Eq. (3.38) is merely an educated guess for the quadratic and cubic terms in the virial expansions of the d_s^α/d_0^α. The accuracy of (3.38) will be tested by comparison to our SD results in Sec. 3.7. With Eqs. (3.25), (3.34), and (3.38), the analytical estimation for f_α is

$$f_\alpha = \frac{1 + \left(\sum_{\beta=1,2} I_{\alpha\beta}\phi_\beta\right) \times \left(1 + 0.1195\phi - 0.70\phi^2\right)}{1 - 1.8315\phi_\alpha\left(1 + 0.1195\phi_\alpha - 0.70\phi_\alpha^2\right)}. \tag{3.39}$$

3.7 Results and discussions

In this section we compare results of the rescaled $\delta\gamma$ scheme described in Sec. 3.6 to the results of the SD simulations outlined in Sec. 3.4. For each suspension composition, the SD simulations typically take a few days, while computations using the rescaled $\delta\gamma$ scheme only require at most a few minutes. This great performance incentive renders the rescaled $\delta\gamma$ scheme more convenient for many applications.

The rescaled $\delta\gamma$ scheme relies on the monodisperse $\delta\gamma$ scheme to capture the structural features in the hydrodynamic functions of bidisperse suspensions, using bidisperse static structure factors as input. The validity of this Ansatz can be directly validated by studying a bidisperse suspension where one of the species, say, species β, only influences the suspension structurally but not hydrodynamically, *i.e.*, $f_\alpha = 1$ in Eq. (3.28). An experimental realization of such system would be a mixture of hard-sphere particles and highly permeable porous but rigid particles of different size. In the SD simulations, we generate a bidisperse suspension configuration and then exclude the inactive species β from the hydrodynamic computations. The resulting hydrodynamically monodisperse, but structurally bidisperse suspension's function $H(q)$ is influenced by the partial static structure factor $S_{\alpha\alpha}(q)$.

Fig. 3.3 compares the partial hydrodynamic functions $H_{\alpha\alpha}(q)$ of bidisperse suspensions containing hydrodynamically inactive particles from the rescaled $\delta\gamma$ scheme [Eq. (3.28) with $f_\alpha = 1$] and the SD simulations. Recall that, for example, $H_{11}(q)$ corresponds to suspensions with hydrodynamically inactive large particles. Comparing to the SD measurements, the monodisperse $\delta\gamma$ scheme accurately captures the structural features in the hydrodynamic functions with structural input $S_{11}(q)$, including in particular the minimum in $H_{11}(q)$ for $qa_1 \approx 1.7$ due to cages formed by the large particles. However, the monodisperse $\delta\gamma$ scheme systematically overestimates the magnitude of the hydrodynamic functions at all wave-numbers, since the species self-diffusivity in this case is different from the self-diffusivity in Eq. (3.25) for monodisperse suspensions, due to the different suspension structures.

Turning now to the true (structurally and hydrodynamically) bidisperse suspensions where both species are hydrodynamically active, Fig. 3.4 features the SD measurements (symbols) of the partial hydrodynamic functions $H_{\alpha\beta}(q)$ for bidisperse suspensions with $\lambda = 2$ over a wide range of the compositions y and total volume fractions ϕ, covering both the dilute ($\phi = 0.1$) and the concentrated ($\phi = 0.5$) regimes. The qualitative and quantitative aspects of the functions $H_{\alpha\beta}(q)$ are ex-

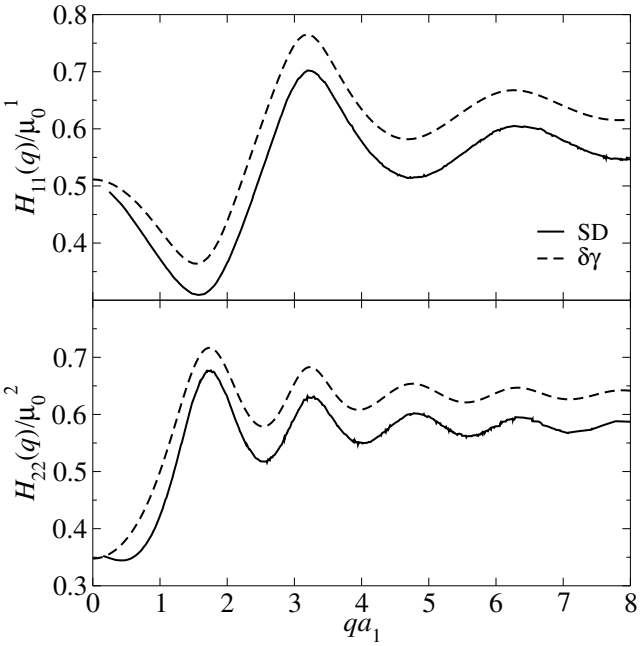

Figure 3.3: The partial hydrodynamic functions $H_{11}(q)$ and $H_{22}(q)$ for a bidisperse suspension of $\phi = 0.4$, $y = 0.5$, and $\lambda = 2$ with the respective other species being hydrodynamically inactive. The hydrodynamic functions are scaled with the single particle mobility $\mu_0^\alpha = (6\pi\eta_0 a_\alpha)^{-1}$ and the wave number is scaled with a_1, the radius of the smaller particles.

tensively examined and discussed in a companion paper [69], and here we focus on the performance of the rescaled $\delta\gamma$ scheme.

We first discuss the central assumptions of the rescaled $\delta\gamma$ scheme: the wave-number independence of the fitting parameters f_α and $f_{\alpha\beta}$ in Eq. (3.31) and (3.32), respectively. The q-independent parameters f_α and $f_{\alpha\beta}$ were computed by least-square fitting the SD measurements and the rescaled $\delta\gamma$ scheme as in Eq. (3.28) and (3.30). The fitted partial hydrodynamic functions are presented as solid curves in Fig. 3.4. For $H_{\alpha\alpha}(q)$, the fitted data capture all the qualitative and most quantitative features in the SD measurements at all q for both species. The best agreement is found at $y = 0.5$, where both species are present in large enough amounts for the mean-field description of the HIs to be valid. For more asymmetric compositions, such as at $y = 0.1$ and $y = 0.9$, the agreement deteriorates slightly at low q with increasing ϕ. For the dilute suspensions at $\phi = 0.1$, we find excellent agreement between the fitted functions and the SD measurements. At $\phi = 0.25$, despite the excellent overall agreement for both species, the discrepancies are slightly more pronounced for the smaller species. The mean-field description is more appropriate for the

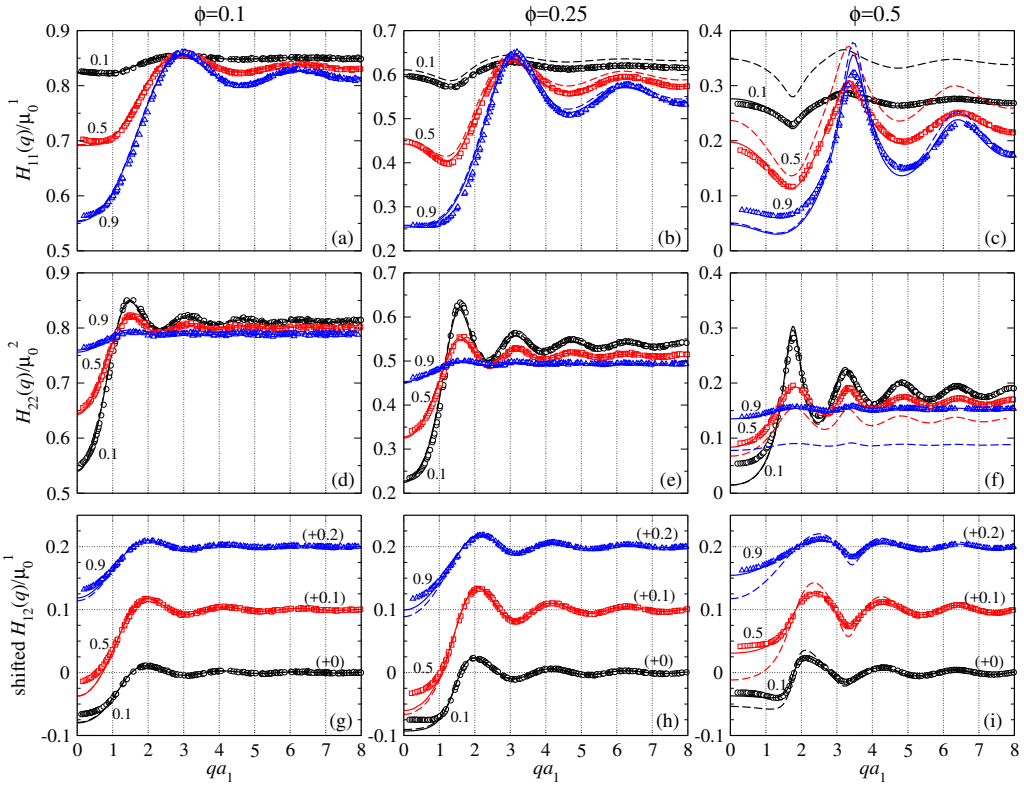

Figure 3.4: The partial hydrodynamic functions $H_{\alpha\beta}(q)$ of bidisperse suspensions with full hydrodynamics. The size ratio is $\lambda = 2$. The top, middle, and bottom rows are $H_{11}(q)$ and $H_{22}(q)$, and $H_{12}(q)$, respectively. The interspecies partial hydrodynamic functions $H_{12}(q)$ are shifted by 0.1 for $y = 0.5$ and by 0.2 for $y = 0.9$ for clarity (also indicated in the figure). The left, middle, and right columns correspond to volume fractions $\phi = 0.1$, 0.25, and 0.5, respectively. For each ϕ we show the SD measurements for composition $y = 0.1$ (◯), $y = 0.5$ (□), and $y = 0.9$ (△). The results for the fitted $\delta\gamma$ scheme are shown as solid curves, and results of the parameter-free rescaled $\delta\gamma$ scheme with f_α from Eq. (3.39) and $f_{\alpha\beta}$ from Eq. (3.34) are shown as dashed curves.

hydrodynamic environment of the large particles, as each of them is surrounded by multiple small particles. On the other hand, the small particles are strongly affected by the presence of large particles, and the respective hydrodynamic environment exhibits more fluctuations. This leads to the slight differences in $H_{11}(q)$ at $y = 0.9$ in Fig. 3.4(b). At $\phi = 0.5$, the accuracy of the $\delta\gamma$ scheme breaks down since the unaccounted hydrodynamic scattering diagrams become important. However, despite some disagreements the fitted scheme still captures many qualitative features of $H_{\alpha\alpha}(q)$. The discrepancies are particularly apparent in the low q limit with asymmetric compositions, *e.g.*, $H_{11}(q)$ at $y = 0.9$ in Fig. 3.4(c) and $H_{22}(q)$ at $y = 0.1$ in Fig. 3.4(f). In these cases, the q-independent scaling factor f_α is not sufficient to describe the hydrodynamic interactions from the minority species β. For $H_{\alpha\beta}(q)$ ($\alpha \neq \beta$) shown in Fig. 3.4(g)–(i), the agreement between the measured and fitted $H_{12}(q)$ is excellent for all ϕ except at small q. Note that the modulations of $H_{12}(q)$ first increase from $\phi = 0.1$ to $\phi = 0.25$ due to the enhancement of hydrodynamic interactions, and then decrease from $\phi = 0.25$ to $\phi = 0.5$, possibly due to hydrodynamic shielding effects. The q-modulations in $H_{12}(q)$ are small compared to $H_{11}(q)$ and $H_{22}(q)$. Overall, the agreement between the SD measurement and the fitted scheme validates the assumption of q-independence of f_α and $f_{\alpha\beta}$, up to relatively high volume fractions.

It seems appropriate to discuss the role of the near-field lubrication interactions on the partial hydrodynamic functions $H_{\alpha\beta}(q)$ here. In many cases, the lubrication effects play a critical role in transport properties of bidisperse hard-sphere suspensions. For example, when computing the pairwise additive shear viscosity of dilute bidisperse suspensions, neglecting the lubrication effects can lead to quantitatively and qualitatively wrong results on the composition dependence of the viscosity [70]. To assess the influences of lubrication here, we recomputed $H_{\alpha\beta}(q)$ of bidisperse suspensions at $\lambda = 2$ and $\phi = 0.5$ using SD without the lubrication corrections. Relative to the full results in Fig. 3.4, the resulting $H_{\alpha\beta}(q)$ are much larger in magnitude and exhibit more pronounced modulation with respect to q. However, unlike the pairwise additive shear viscosity, the $H_{\alpha\beta}(q)$ without the lubrication effects are qualitatively similar to the results in Fig. 3.4, *i.e.*, the shape of the curve at each composition and the relative features with different compositions remain unchanged. In fact, the $H_{\alpha\beta}(q)$ results with and without the lubrication correction can be brought to quantitative agreement with a q-independent factor. For this reason, the results without the lubrication corrections are not presented. Apparently, the lubrication effects only play a quantitative, rather than qualitative, role in the determination of

$H_{\alpha\beta}(q)$ for bidisperse hard-sphere suspensions.

The fitted q-independent scaling factors f_1, f_2, and f_{12} as a function of the composition y for bidisperse suspensions with $\lambda = 2$ at different volume fractions ϕ are presented in Fig. 3.5. As expected, at a fixed volume fraction ϕ, f_α decreases monotonically from 1 with the increasing presence of the other species β. At a fixed value of y, f_α also decreases from 1 when the volume fraction ϕ is increased. Both decreasing trends in f_α are due to the enhanced HIs from the other species. The scaling factor f_{12} for the interspecies hydrodynamic interactions exhibits more peculiar behaviors. For $\phi = 0.1$ and 0.25, the factor f_{12} is close to unity, suggesting that the mean-field hydrodynamic interaction assumption in the rescaled $\delta\gamma$-scheme is valid. However, f_{12} does become smaller with increasing y, *i.e.*, for $H_{12}(q)$, adding larger particles to the suspension is not equivalent to adding smaller particles, which becomes particularly clear for $\phi \geq 0.25$ in Fig. 3.5(c). For $\phi = 0.4$ and 0.5, f_{12} becomes much smaller than unity and decreases monotonically with increasing y. At these volume fractions, it appears that f_{12} is extremely sensitive to the presence of the other species in the mixture, as we expect f_{12} to recover to unity when $y \to 0$ or $y \to 1$.

The f_1 and f_2 predicted by Eq. (3.39) are shown in Fig. 3.5(a) and (b) as curves. The predicted f_1 agrees well with the fitted value up to $\phi = 0.25$, and at higher volume fractions, the equation overestimates f_1 by 10% at $\phi = 0.35$ and $y = 0.1$ and by 20% at $\phi = 0.45$ and $y = 0.1$. The predicted f_2 for the larger species, however, agrees well with the fitted value up to $\phi = 0.4$ at all compositions except when y is close to unity. Since Eq. (3.39) is motivated by a mean-field model of d_s^α/d_0^α, Eq. (3.38), Fig. 3.5 again suggests that the larger particles in bidisperse suspensions experience the mean field from the small particles, while the hydrodynamic environment of the smaller particles shows stronger fluctuations. Specifically, since Eqs. (3.38) and (3.39) are exact in the dilute limit when the pairwise HIs dominate, the error must come from the many-body HI term which is based on the monodisperse results. Both the near-field and far-field effects contribute to the many-body HI, and both depend on the bidisperse suspension compositions. For dense suspensions, it is difficult to separate one contribution from another, and any improvements must consider both in tandem. Based on Fig. 3.4 and 3.5, any improvement of the rescaled $\delta\gamma$ scheme requires a better estimation of d_s^α by explicitly considering the composition dependence of the many-body HIs. For practical purposes here, from Fig. 3.5 we note that the parameter-free analytical estimation of f_α and $f_{\alpha\beta}$ is satisfactory up to

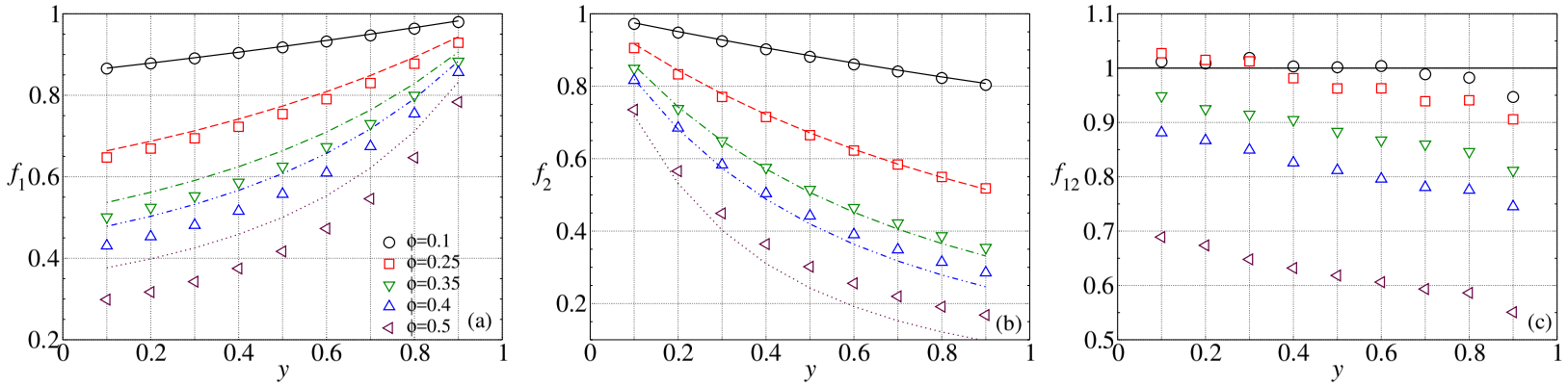

Figure 3.5: The fitted q-independent scaling factors (a): f_1, (b): f_2, and (c): f_{12} in the rescaled $\delta\gamma$ scheme for the bidisperse suspensions with $\lambda = 2$. The curves are calculated according to Eq. (3.39) for f_α with $\phi = 0.1$ (solid), 0.25 (dashed), 0.35 (dash-dotted), 0.4 (dash-double-dotted), and 0.5 (dotted).

$\phi \sim 0.35$–0.4 at all compositions, for $\lambda = 2$.

The parameter-free partial hydrodynamic functions, predicted by the rescaled $\delta\gamma$ scheme with factors f_α from Eq. (3.39) and f_{12} from Eq. (3.34), are presented in Fig. 3.4 as dashed curves. The agreement with the SD measurements is satisfactory for $H_{\alpha\beta}(q)$ at all compositions at $\phi = 0.1$ and 0.25. In Fig. 3.4(b) the predicted f_1 slightly overestimates $H_{11}(q)$ at $y = 0.1$ at $\phi = 0.25$, primarily due to the overestimation of the small particle diffusivity in Eq. (3.38). At $\phi = 0.5$, the prediction breaks down, and the discrepancy is most pronounced at $y = 0.1$ for the overestimation of $H_{11}(q)$ in Fig. 3.4(c) and at $y = 0.9$ for the underestimation of $H_{22}(q)$ in Fig. 3.4(f). Moreover, Eq. (3.34) overestimates the q-modulations in $H_{12}(q)$ in all compositions at $\phi = 0.5$ in Fig. 3.4(i), as the hydrodynamic shielding in dense systems cannot be captured by $f_{12} = 1$.

In practice, individual partial hydrodynamic functions $H_{\alpha\beta}(q)$ cannot be conveniently measured in scattering experiments and the measured quantity $H_M(q)$ is a weighted average of the $H_{\alpha\beta}(q)$. Note from Eq. (3.16) and (3.17), that $H_M(q)$ differs from the similar number-number hydrodynamic function $H_{NN}(q)$ only trough its dependence on the particle-specific scattering amplitudes $f_\alpha(q)$. To test the accuracy of the rescaled $\delta\gamma$ scheme, it is sufficient to test its predictions of $H_{NN}(q)$. In Fig. 3.6 we compare the $H_{NN}(q)$ from the SD measurements and from the rescaled $\delta\gamma$ scheme, with factors f_α and $f_{\alpha\beta}$ obtained from optimal least square fittings (solid curves) and from the parameter-free analytic Eq. (3.39) and (3.34) (dashed curves). Results for the same bidisperse suspensions are depicted in Fig. 3.6 and 3.4. For $\phi = 0.1$, the rescaled $\delta\gamma$ scheme captures the SD results with high precision in the entire q-range, at all studied compositions y. Small discrepancies occur most noticeably in the $q \to 0$ limit. At $\phi = 0.25$, the difference in $H_{NN}(q)$ from both the fitted and the parameter-free analytical expression is less than 5% in the entire q-range, which demonstrates the validity of our proposed rescaling rules for the $\delta\gamma$ scheme. For the very dense suspensions, $\phi = 0.5$, we see how the rescaled $\delta\gamma$ scheme breaks down. With the fitted f_α and $f_{\alpha\beta}$, the scheme is only capable of capturing the qualitative features in the measured $H_{NN}(q)$. With the f_α and $f_{\alpha\beta}$ from Eq. (3.39) and (3.34), the scheme exhibits significant differences from the SD measurements with decreasing y.

The performance of the rescaled $\delta\gamma$ scheme for size ratios $\lambda \neq 2$ (and in particular for $\lambda > 2$) remains to be explored. In representative tests for $\lambda = 4$ we found that the scaling approximation of Eq. (3.33) remains valid, but Eq. (3.39) breaks

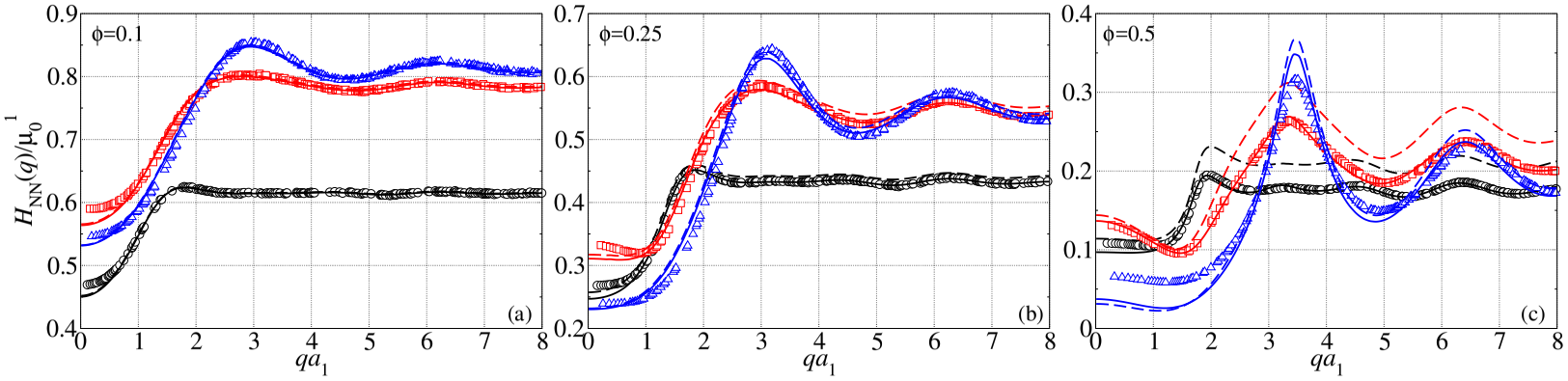

Figure 3.6: The number-number hydrodynamic functions $H_{NN}(q)$ for bidisperse suspensions with $\lambda = 2$ and full hydrodynamics for volume fractions (a): $\phi = 0.1$, (b):$\phi = 0.25$, and (c): $\phi = 0.5$. For each ϕ, we show the SD measurements for composition $y = 0.1$ (◯), $y = 0.5$ (□), and $y = 0.9$ (△). The $H_{NN}(q)$ from the $\delta\gamma$ scheme with fitted f_α and $f_{\alpha\beta}$ are shown as solid curves, and the results of the parameter-free theory with f_α according to Eq. (3.39) and $f_{\alpha\beta}$ according to Eq. (3.34) are shown as dashed curves.

down around $\phi = 0.25$ and $y = 0.5$, particularly for the smaller particles. This is due to the breakdown of Eq. (3.38) for the short-time self-diffusivity d_s^α/d_0^α. Note that Eqs. (3.38) and (3.39) are exact in the dilute limit $\phi \to 0$, and that they remain valid in a decreasing ϕ-range with increasing size ratio. At a given λ and ϕ, the approximations are expected to be better for the larger particles than for the smaller particles, due to the more mean-field-like HIs among the larger particles. However, establishing an accuracy measure of the rescaled $\delta\gamma$ scheme in the full suspension parameter range requires direct comparison with accurate hydrodynamic computations. Unfortunately, this is a very elaborate and computationally expensive task because of the system size that increases with increasing values of λ, and because of accuracy limitations of the SD method. In future, obtaining an accurate expression of d_s^α/d_0^α for dense suspensions with arbitrary values of λ will be the key to further improvement of the rescaled $\delta\gamma$ scheme.

3.8 Conclusions

In this chapter we have proposed a rescaled $\delta\gamma$ scheme to compute approximations of the partial hydrodynamic functions $H_{\alpha\beta}(q)$ in colloidal mixtures. We found that the $H_{\alpha\beta}(q)$ from the Stokesian Dynamics measurements differs from the $\delta\gamma$ scheme with appropriate structural input by a q-independent factor, suggesting that the hydrodynamic environment for one species can be described as a mean field due to the HIs from the other species and the solvent. This constitutes the fundamental assumption of the rescaled $\delta\gamma$ scheme.

We extensively tested the rescaled $\delta\gamma$ scheme with the SD simulation measurements for bidisperse suspensions over a wide range of volume fractions ϕ and compositions y, and provided approximate analytical estimates for the scaling factors f_α, and $f_{\alpha\beta}$. Comparing with the SD measurements, the rescaled $\delta\gamma$ scheme with analytical scaling factors can accurately predict the number-number hydrodynamic function $H_{NN}(q)$ up to $\phi \approx 0.4$ at all studied composition ratios y, for a particle-size ratio as high as $\lambda = 2$.

The proposed rescaled $\delta\gamma$ scheme is the first semi-analytical method for estimating the bidisperse hydrodynamic functions up to $\phi = 0.4$, and it can be readily extended to polydisperse and charged systems. It will be a valuable tool for interpreting dynamic scattering experiments of moderately dense bidisperse systems.

References

[1] A. J. C. Ladd, "Short-time motion of colloidal particles: numerical simulation via a fluctuating lattice-boltzmann equation", Phys. Rev. Lett. **70**, 1339 (1993).

[2] V. Lobaskin and B. Dünweg, "A new model for simulating colloidal dynamics", New J. Phys. **6**, 54 (2004).

[3] B. Dünweg and A. J. C. Ladd, "Lattice boltzmann simulations of soft matter systems", Adv. Polym. Sci. **221**, 89 (2009).

[4] P. J. Hoogerbrugge and J. M. V. A. Koelman, "Simulating microscopic hydrodynamic phenomena with dissipative particle dynamics", Europhys. Lett. **19**, 155 (1992).

[5] Z. Li and G. Drazer, "Hydrodynamic interactions in dissipative particle dynamics", Phys. Fluids **20**, 103601 (2008).

[6] A. Malevanets and R. Kapral, "Mesoscopic model for solvent dynamics", J. Chem. Phys. **110**, 8605 (1999).

[7] T. Ihle and D. M. Kroll, "Stochastic rotation dynamics: a galilean-invariant mesoscopic model for fluid flow", Phys. Rev. E **63**, 020201 (2001).

[8] A. Wysocki, C. P. Royall, R. G. Winkler, G. Gompper, H. Tanaka, A. van Blaaderen, and H. Löwen, "Multi-particle collision dynamics simulations of sedimenting colloidal dispersions in confinement", Faraday Discuss. **144**, 245 (2010).

[9] A. J. C. Ladd, "Hydrodynamic transport coefficients of random dispersions of hard spheres", J. Chem. Phys. **93**, 3484 (1990).

[10] B. Cichocki, M. Ekiel-Jezewska, and E. Wajnryb, "Lubrication corrections for three-particle contribution to short-time self-diffusion coefficients in colloidal dispersions", J. Chem. Phys. **111**, 3265 (1999).

[11] C. Pozrikidis, *Boundary integral and singularity methods for linearized viscous flow* (Cambridge University Press, 1992).

[12] A. Kumar and M. D. Graham, "Accelerated boundary integral method for multiphase flow in non-periodic geometries", J. Comput. Phys. **231**, 6682 (2012).

[13] J. F. Brady and G. Bossis, "Stokesian dynamics", Annu. Rev. Fluid Mech. **20**, 111 (1988).

[14] A. Sierou and J. F. Brady, "Accelerated stokesian dynamics simulations", J. Fluid Mech. **448**, 115 (2001).

[15] A. J. Banchio and J. F. Brady, "Accelerated stokesian dynamics: brownian motion", J. Chem. Phys. **118**, 10323 (2003).

[16] R. B. Jones, "Diffusion of tagged interacting spherically symmetric polymers", Physica A **97**, 113 (1979).

[17] C. W. J. Beenakker and P. Mazur, "Self-diffusion of spheres in a concentrated suspension", Physica A **120**, 388 (1983).

[18] C. W. J. Beenakker and P. Mazur, "Diffusion of spheres in a concentrated suspension: resummation of many-body hydrodynamic interactions", Phys. Lett. A **98**, 22 (1983).

[19] G. K. Batchelor, "Diffusion in a dilute polydisperse system of interacting spheres", J. Fluid Mech. **131**, 155 (1983).

[20] C. W. J. Beenakker and P. Mazur, "Diffusion of spheres in a concentrated suspension ii", Physica A **126**, 349 (1984).

[21] G. Nägele, "On the dynamics and structure of charge-stabilized suspensions", Phys. Rep. **272**, 216 (1996).

[22] H. Y. Zhang and G. Nägele, "Tracer-diffusion in binary colloidal hard-sphere suspensions", J. Chem. Phys. **117**, 5908 (2002).

[23] A. J. Banchio and G. Nägele, "Short-time transport properties in dense suspensions: from neutral to charge-stabilized colloidal spheres", J. Chem. Phys. **128**, 104903 (2008).

[24] M. Heinen, A. J. Banchio, and G. Nägele, "Short-time rheology and diffusion in suspensions of yukawa-type colloidal particles", J. Chem. Phys. **135**, 154504 (2011).

[25] K. Makuch and B. Cichocki, "Transport properties of suspensions–critical assessment of beenakker-mazur method", J. Chem. Phys. **137**, 184902 (2012).

[26] M. Krüger and M. Rauscher, "Diffusion of a sphere in a dilute solution of polymer coils", J. Chem. Phys. **131**, 094902 (2009).

[27] T. Narumi, S. V. Franklin, K. W. Desmond, M. Tokuyama, and E. R. Weeks, "Spatial and temporal dynamical heterogeneities approaching the binary colloidal glass transition†", Soft Matter **7**, 1472 (2011).

[28] M. Laurati, K. J. Mutch, N. Koumakis, J. Zausch, C. P. Amann, A. B. Schofield, G. Petekidis, J. F. Brady, J. Horbach, M. Fuchs, and S. U. Egelhaaf, "Transient dynamics in dense colloidal suspensions under shear: shear rate dependence", J. Phys.-Condes. Matter **24**, 464104 (2012).

[29] T. Sentjabrskaja, M. Hermes, W. C. K. Poon, C. D. Estrada, R. Castañeda-Priego, S. U. Egelhaaf, and M. Laurati, "Transient dynamics during stress overshoots in binary colloidal glasses", Soft Matter **10**, 6546 (2014).

[30] G. Nägele, O. Kellerbauer, R. Krause, and R. Klein, "Hydrodynamic effects in polydisperse charged colloidal suspensions at short times", Phys. Rev. E **47**, 2562 (1993).

[31] K. Makuch, "Scattering series in the mobility problem for suspensions", J. Stat. Mech.-Theory Exp. **2012**, P11016 (2012).

[32] U. Genz and R. Klein, "Collective diffusion of charged spheres in the presence of hydrodynamic interaction", Physica A **171**, 26 (1991).

[33] F. Westermeier, B. Fischer, W. Roseker, G. Grübel, G. Nägele, and M. Heinen, "Structure and short-time dynamics in concentrated suspensions of charged colloids", J. Chem. Phys. **137**, 114504 (2012).

[34] K. Makuch, M. Heinen, G. C. Abade, and G. Nägele, "Rotational self-diffusion in suspensions of charged particles: simulations and revised beenakker-mazur and pairwise additivity methods.", Soft Matter **11**, 5313 (2015).

[35] S. Kim and S. J. Karrila, *Microhydrodynamics: principles and selected applications* (Butterworth-Heinemann, 1991).

[36] J. K. G. Dhont, *An introduction to dynamics of colloids* (Elsevier, 1996).

[37] B. J. Berne and R. Pecora, *Dynamic light scattering: with applications to chemistry, biology, and physics*, 1st ed. (Wiley, New York, 1976).

[38] A. Guinier and G. Fournet, *Small-angle scattering of x-rays* (Wiley, 1955).

[39] O. Glatter and O. Kratky, *Small angle x-ray scattering* (Academic Press, 1982).

[40] S. R. Williams and W. van Megen, "Motions in binary mixtures of hard colloidal spheres: melting of the glass", Phys. Rev. E **64**, 041502 (2001).

[41] A. Z. Akcasu, M. Benmouna, and B. Hammouda, "On the dynamics of polyelectrolyte solutions", J. Chem. Phys. **80**, 2762 (1984).

[42] L. Durlofsky, J. F. Brady, and G. Bossis, "Dynamic simulation of hydrodynamically interacting particles", J. Fluid Mech. **180**, 21 (1987).

[43] J. F. Brady, R. J. Phillips, J. C. Lester, and G. Bossis, "Dynamic simulation of hydrodynamically interacting suspensions", J. Fluid Mech. **195**, 257 (1988).

[44] H. J. Wilson, "Stokes flow past three spheres", J. Comput. Phys. **245**, 302 (2013).

[45] C. Chang and R. L. Powell, "Dynamic simulation of bimodal suspensions of hydrodynamically interacting spherical particles", J. Fluid Mech. **253**, 1 (1993).

[46] C. W. J. Beenakker, "Ewald sum of the rotne-prager tensor", J. Chem. Phys. **85**, 1581 (1986).

[47] K. R. Hase and R. L. Powell, "Calculation of the ewald summed far-field mobility functions for arbitrarily sized spherical particles in stokes flow", Phys. Fluids **13**, 32 (2001).

[48] D. J. Jeffrey and Y. Onishi, "Calculation of the resistance and mobility functions for two unequal rigid spheres in low-reynolds-number flow", J. Fluid Mech. **139**, 261 (1984).

[49] D. J. Jeffrey, "The calculation of the low reynolds number resistance functions for two unequal spheres", Phys. Fluids A **4**, 16 (1992).

[50] D. J. Jeffrey, J. F. Morris, and J. F. Brady, "The pressure moments for two rigid spheres in low-reynolds-number flow", Phys. Fluids A **5**, 2317 (1993).

[51] A. S. Khair, M. Swaroop, and J. F. Brady, "A new resistance function for two rigid spheres in a uniform compressible low-reynolds-number flow", Phys. Fluids **18**, 043102 (2006).

[52] B. D. Lubachevsky and F. H. Stillinger, "Geometric properties of random disk packings", J. Stat. Phys. **60**, 561 (1990).

[53] M. Skoge, A. Donev, F. H. Stillinger, and S. Torquato, "Packing hyperspheres in high-dimensional euclidean spaces", Phys. Rev. E **74**, 041127 (2006).

[54] R. J. Phillips, J. F. Brady, and G. Bossis, "Hydrodynamic transport properties of hard-sphere dispersions. i. suspensions of freely mobile particles", Phys. Fluids **31**, 3462 (1988).

[55] A. Ladd, H. Gang, Z. J. X., and D. A. Weitz, "Temporal and spatial dependence of hydrodynamic correlations: simulation and experiment", Phys. Rev. E **52**, 6550 (1995).

[56] J.-P. Hansen and I. R. McDonald, *Theory of simple liquids*, 2nd ed. (Academic Press, 1986).

[57] J. K. Percus and G. J. Yevick, "Analysis of classical statistical mechanics by means of collective coordinates", Phys. Rev. **110**, 1 (1958).

[58] N. W. Ashcroft and D. C. Langreth, "Structure of binary liquid mixtures. i", Phys. Rev. **156**, 685 (1967).

[59] N. W. Ashcroft and D. C. Langreth, "Structure of binary liquid mixtures. i", Phys. Rev. **166**, 934 (1968).

[60] F. J. Rogers and D. A. Young, "New, thermodynamically consistent, integral equation for simple fluids", Phys. Rev. A **30**, 999 (1984).

[61] T. Biben and J.-P. Hansen, "Phase separation of asymmetric binary hard-sphere fluids", Phys. Rev. Lett. **66**, 2215 (1991).

[62] M. Heinen, E. Allahyarov, and H. Löwen, "Highly asymmetric electrolytes in the primitive model: hypernetted chain solution in arbitrary spatial dimensions", J. Comput. Chem. **35**, 275 (2014).

[63] M. Heinen, J. Horbach, and H. Löwen, "Liquid pair correlations in four spatial dimensions: theory versus simulation", Mol. Phys. **113**, 1164 (2015).

[64] J. M. Méndez-Alcaraz, M. Chávez-Páez, B. D'Aguanno, and R. Klein, "Structural properties of colloidal suspensions", Physica A **220**, 173 (1995).

[65] G. C. Abade, B. Cichocki, M. L. Ekiel-Jeżewska, G. Nägele, and E. Wajnryb, "Rotational and translational self-diffusion in concentrated suspensions of permeable particles", J. Chem. Phys. **134**, 244903 (2011).

[66] J. L. Lebowitz, "Exact solution of generalized percus-yevick equation for a mixture of hard spheres", Phys. Rev. **133**, A895 (1964).

[67] R. Schmitz and B. U. Felderhof, "Mobility matrix for two spherical particles with hydrodynamic interaction", Physica A **116**, 163 (1982).

[68] D. J. Jeffrey, "Low-reynolds-number flow between converging spheres", Mathematika **29**, 58 (1982).

[69] M. Wang and J. F. Brady, "Short-time transport properties of bidisperse suspensions and porous media: a stokesian dynamics study", J. Chem. Phys. **142**, 094901 (2015).

[70] N. J. Wagner and A. T. J. M. Woutersen, "The viscosity of bimodal and polydisperse suspensions of hard spheres in the dilute limit", J. Fluid Mech. **278**, 267 (1994).

Chapter 4

SPECTRAL EWALD ACCELERATION OF STOKESIAN DYNAMICS FOR POLYDISPERSE COLLOIDAL SUSPENSIONS

[1] M. Wang and J. F. Brady, "Spectral Ewald Acceleration of Stokesian Dynamics for polydisperse suspensions", Journal of Computational Physics **306**, 443 (2016) doi:10.1016/j.jcp.2015.11.042,

4.1 Introduction

Colloidal suspensions are dispersions of small particles in a viscous solvent, and are found in almost every aspect of our life, ranging from dairy milk to printer ink. They have two distinguishing features: (*i*) Brownian motion of the particles due to thermal fluctuations, and (*ii*) the long-range, non-pairwise-additive hydrodynamic interactions (HIs) mediated by the solvent. As a result of these features, dispersions exhibit many surprising behaviors such as non-Newtonian rheology, glass transitions, phase transitions, *etc.*, and have attracted extensive scientific and engineering interests [1]. Using monodisperse colloidal suspensions as a model system, significant understanding has been achieved through theoretical, simulation, and experimental studies.

However, naturally occurring colloidal suspensions are seldom monodisperse, and particle size differences are often unavoidable. In addition, particle size disparity introduces phenomena otherwise not observed in monodisperse suspensions. For example, size polydispersity reduces suspension viscosity [2–4], softens and even melts colloidal glasses [5], and promotes particle segregation in pressure driven flows [6]. Apparently, these behaviors can only be understood by studying dynamics of polydisperse colloidal suspensions.

In this work we develop a computational method based on the framework of Stokesian Dynamics [7] (SD) for fast and realistic dynamic simulations of dense, polydisperse colloidal suspensions, with a focus on suspension rheology. Presently, theoretical and computational studies on polydisperse colloidal suspensions, even for the simplest case of neutrally buoyant hard-sphere particles, are scarce, and heavily focus on the dilute or the short-time limits [8–12]: the former restricts HIs to the two- or three-body level, and the latter ignores suspension dynamic evolution,

particularly the influence of Brownian motion. Beyond these limiting cases, we are only aware of the work of Ando & Skolnick [13], who studied particle diffusion in dense polydisperse colloidal suspensions using conventional SD in the context of biological molecular crowding. Their implementation limits HIs to the force-torque level, and therefore is unsuitable for rheological investigations.

A difficulty in dynamic simulations of dense colloidal suspensions is the singular HIs due to the lubrication interactions between close particle pairs. To directly resolve HIs, a computational method must capture the flow details in the small gap between particles. For multipole expansion based methods [7, 14, 15], a large number of expansion terms are necessary to achieve convergence, and for methods based on surface or spatial discretization, such as the boundary element method [16, 17] or direct numerical simulations [18–21], very fine meshing is needed in the gap. Directly resolving lubrication interactions drastically increases the computational cost and limits many studies to low volume fractions. For example, the force coupling method study of Abbas *et al.* [22] on the dynamics of non-Brownian bidisperse suspensions is limited to particle volume fractions below 20%.

A solution to the above difficulty is the SD framework [7], which exploits the local and pairwise additive nature of lubrication interactions. In SD, the long-range, non-pairwise-additive HIs are computed from the mobility perspective using low-order multipole expansions, and for particles in close contact, lubrication corrections are added pairwise to the corresponding resistance formalism. The corrections are based on the solutions of two-body problems with the far-field contributions removed. In this way, SD avoids directly resolving the singular lubrication interactions. The idea of lubrication correction in SD is general enough for incorporation to other computational methods. For example, similar lubrication corrections has been developed for hydrodynamic multipole methods [14, 15, 23, 24], the force coupling method [25], the lattice Boltzmann method [26], and the fictitious domain method [27]. Moreover, with an appropriate fluid solver, the lubrication corrections can be improved beyond the pairwise level [28]. We feel that, by incorporating the lubrication corrections, many recent computational techniques can significantly extend their accessible parameter range without increasing the computational burden. This point is demonstrated in the present work, which essentially combines the lubrication corrections and the Spectral Ewald (SE) method of Lindbo & Tornberg [29, 30] for dynamic simulations of dense polydisperse suspensions.

The Spectral Ewald (SE) method is a new particle mesh technique for computing

long-range electrostatic [30] or hydrodynamic [29] interactions, and has recently been incorporated into the boundary integral method for spheroidal particles [31]. Particle mesh techniques including the Particle Mesh Ewald (PME) method [32] and the Smooth Particle Mesh Ewald (SPME) method [33] have been extensively used for calculating HIs with $O(N \log N)$ computation scaling. Note that, although algorithms based on the fast multipole method [34] can achieve a better computation scaling–down to $O(N)$, they often have significant computation overheads, and require large system sizes to justify the complexity [35]. Therefore, for many dynamic simulations, the particle mesh techniques remain the practical choice. Notable examples are Accelerated Stokesian Dynamics (ASD) [36] which uses the PME method for the far-field mobility evaluation, and the work of Saintillan *et al.* [37], where the SPME method is employed to study fiber sedimentation. Compared to other particle mesh techniques, the SE method is spectrally accurate, and can separate errors from the mesh interpolation and the wave-space truncation. Both features are essential for capturing the complicated HIs in polydisperse suspensions.

Another challenge in dynamic simulations of colloidal suspensions is Brownian motion, which is configuration dependent due to the fluctuation-dissipation relation. When Euler-Maruyama time integration is used, the deterministic particle drift due to the Brownian motion must also be included [38]. As a result, computing Brownian-related quantities requires the gradient and the square root of the mobility tensor. Fortunately, these quantities can be evaluated in a matrix-free manner under the framework of ASD, making dynamic studies on hundreds of colloidal particles possible [39, 40]. Moreover, the mean-field Brownian approximation, which estimates the mobility tensor based on the near-field HIs, is able to further speed up the computations [39, 41]. In this work, these developments are fully incorporated for the dynamic simulation of Brownian polydisperse suspensions. Note that a different approach to treat the Brownian motion is based on fluctuating hydrodynamics [42], where the thermal fluctuations are directly incorporated in the governing fluid equations. It has been applied to the lattice Boltzmann method [43], the force coupling method [44], and the immersed boundary method [45].

The emergence of the General Purpose Graphic Processing Unit (GPGPU) programming often brings significant, sometimes orders of magnitude, speed improvements for many existing algorithms. Recently, Kopp & Höfling [46] implemented the conventional SD for infinite solvent using GPGPU with direct HI summation. Despite the $O(N^2)$ scaling, they achieved impressive speedup over the CPU implementation.

However, to study the dynamics of homogeneous suspensions, further extension to periodic systems are necessary. On the other hand, GPU acceleration of the SPME method [47, 48] in molecular dynamics provides access to millisecond-scale dynamics on personal computers. These acceleration techniques are applicable to particle mesh techniques in general, and inspired the present work. In particular, we used GPGPU programming to compute the HIs with the SE method in homogeneous suspensions, and realized almost an order of magnitude speedup in dynamic simulations.

Furthermore, our computation method extends SD to compressible suspensions, allowing dynamic simulations of constant pressure rheology [49] without introducing geometric confinement. This is possible because the flow disturbances due to rigid particles in a compressible solvent are incompressible and satisfy the Stokes equation [50]. Another benefit of such extension is that the suspension normal stress, which is essential for particle migration in sheared suspensions [51–53], can be directly evaluated.

The remainder of the chapter is arranged as follows: Sec. 4.2 establishes the basic formalism for HIs in compressible Stokes flow. In Sec. 4.3, various aspects of mobility computations with the SE method are presented. Here, we also discuss different approaches to incorporate particle size polydispersity and the GPGPU implementation. In Sec. 4.4, we present the Spectral Ewald Accelerated Stokesian Dynamics (SEASD) and its mean-field Brownian approximation, SEASD-nf, for dynamic simulations of Brownian polydisperse suspensions. In Sec. 4.5 we carefully discuss the accuracy and parameter selections for the SE method, and the computation scaling of various SEASD implementations. Sec. 4.6 presents a series of validation calculations for monodisperse and bidisperse suspensions with SEASD and SEASD-nf: Sec. 4.6 addresses the short-time transport properties, Sec. 4.6 evaluates the equilibrium osmotic pressure and viscoelastic moduli, and Sec. 4.6 presents various aspects of the steady shear rheology of Brownian suspensions. The results also reveal the role of particle sizes in the dynamics of bidisperse suspensions. Finally, we conclude this work with a few comments in Sec. 4.7.

4.2 Hydrodynamic interactions in (compressible) Stokes flow

The mobility and resistance formalism

We first consider a suspension of N spherical rigid particles, each with radius a_i and position $\boldsymbol{r}_i$, in an *incompressible* solvent of viscosity η_0 and density ρ_0, occupying

a volume V. For the special case of bidisperse suspensions with particle sizes a_1 and a_2, the suspension composition is fully characterized by three dimensionless parameters,

$$\lambda = a_2/a_1,\ \phi = \phi_1 + \phi_2, \text{ and } y_2 = \phi_2/\phi, \tag{4.1}$$

where λ is the size ratio, ϕ is the total volume fraction, and y_2 is the volume ratio of species 2. The species volume fraction is $\phi_\alpha = \frac{4}{3}\pi a_\alpha^3 n_\alpha$, $\alpha \in \{1, 2\}$, and the species number density is n_α. The total number density satisfies $n = n_1 + n_2$, and the species number fraction is $x_\alpha = n_\alpha/n$. Without loss of generality, we take $a_2 > a_1$.

If the particles are sufficiently small, the particle Reynolds number $\mathrm{Re}_{\mathrm{p},\alpha} = \rho_0 a_\alpha U_\alpha/\eta_0 \ll 1$, where U_α is the species characteristic velocity. In this limit, the velocity field $\boldsymbol{v}(\boldsymbol{r})$ and the pressure field $p(\boldsymbol{r})$ of the solvent satisfy the Stokes equation,

$$\boldsymbol{\nabla} p = \eta_0 \nabla^2 \boldsymbol{v},\ \boldsymbol{\nabla} \cdot \boldsymbol{v} = 0, \tag{4.2}$$

supplemented by no-slip boundary conditions on particle surfaces. Due to the linearity of Eq. (4.2), there is a linear relation between the velocity disturbance on the surface of a particle i, $\boldsymbol{u}_i'$, and the surface force density of another particle j, $\boldsymbol{f}_j$,

$$\boldsymbol{u}_i'(\boldsymbol{r}) = -\int \mathrm{d}\boldsymbol{r}' \sum_j \mathbf{M}_{ij}(\boldsymbol{r}, \boldsymbol{r}'; X) \cdot \boldsymbol{f}_j(\boldsymbol{r}'), \tag{4.3}$$

where $\mathbf{M}_{ij}(\boldsymbol{r}, \boldsymbol{r}'; X)$ is a mobility operator depending on positions $\boldsymbol{r}$ and $\boldsymbol{r}'$ and the suspension configuration $X = \{\boldsymbol{r}_1, \boldsymbol{r}_2, \ldots\}$. The surface force density is localized on the particle surface, *i.e.*, $\boldsymbol{f}_j(\boldsymbol{r}) = \boldsymbol{\sigma}(\boldsymbol{r}) \cdot \boldsymbol{n}_j \delta(\|\boldsymbol{r} - \boldsymbol{r}_j\| - a_j)$, where $\boldsymbol{\sigma}$ is the stress tensor, $\boldsymbol{n}_j$ is the surface normal of particle j, and $\delta(x)$ is the Dirac delta function. The stress tensor $\boldsymbol{\sigma} = -p\mathbf{I} + \eta_0[\boldsymbol{\nabla}\boldsymbol{v} + (\boldsymbol{\nabla}\boldsymbol{v})^\dagger]$, with $\dagger$ indicating transposition and $\mathbf{I}$ is the idem tensor. The velocity disturbance $\boldsymbol{u}_i'(\boldsymbol{r}) = \boldsymbol{U}_i + \boldsymbol{\Omega}_i \times (\boldsymbol{r} - \boldsymbol{r}_i) - \boldsymbol{v}^\infty(\boldsymbol{r})$, where $\boldsymbol{v}^\infty(\boldsymbol{r})$ is the ambient flow satisfying $\boldsymbol{\nabla} \cdot \boldsymbol{v}^\infty = 0$, and $\boldsymbol{U}_i$ and $\boldsymbol{\Omega}_i$ are respectively the linear and angular velocities of particle i. By stacking the force density vectors $\boldsymbol{f} = (\boldsymbol{f}_1, \boldsymbol{f}_2, \ldots)^\dagger$ and the velocity disturbance vectors $\boldsymbol{u}' = (\boldsymbol{u}_1', \boldsymbol{u}_2', \ldots)^\dagger$ the grand mobility operator $\mathbf{M}$ is constructed from elements $\mathbf{M}_{ij}$ in Eq. (4.3), such that

$$\boldsymbol{u}'(\boldsymbol{r}) = -\int \mathrm{d}\boldsymbol{r}' \mathbf{M}(\boldsymbol{r}, \boldsymbol{r}'; X) \cdot \boldsymbol{f}(\boldsymbol{r}'), \tag{4.4}$$

for the N particles in the suspension. Eqs. (4.3) and (4.4) are known as the mobility formalism, and the inverse relation is the resistance formalism,

$$\boldsymbol{f}(\boldsymbol{r}) = -\int \mathrm{d}\boldsymbol{r}' \mathbf{R}(\boldsymbol{r}, \boldsymbol{r}'; X) \cdot \boldsymbol{u}'(\boldsymbol{r}'), \tag{4.5}$$

where $\mathbf{R}(\boldsymbol{r}, \boldsymbol{r}'; X)$ is the grand resistance operator.

The integral representations in Eqs. (4.4) and (4.5) can be equivalently expressed as multipole expansions of $\boldsymbol{f}(\boldsymbol{r})$ and $\boldsymbol{u}'(\boldsymbol{r})$, $\mathfrak{f}$ and $\mathfrak{u}'$ respectively, around the particle centers, *i.e.*,

$$\boldsymbol{f}(\boldsymbol{r}) \to \mathfrak{f} = \begin{bmatrix} \mathcal{F}^{\mathrm{H}} \\ \mathbf{S}^{\mathrm{H}} \\ \vdots \end{bmatrix} \text{ and } \boldsymbol{u}'(\boldsymbol{r}) \to \mathfrak{u}' = \begin{bmatrix} \mathcal{U}' \\ -\mathbf{E}^{\infty} \\ \vdots \end{bmatrix}, \tag{4.6}$$

where $\mathcal{F}^{\mathrm{H}}$ is the generalized hydrodynamic force, $\mathbf{S}^{\mathrm{H}}$ is the hydrodynamic stresslet, $\mathcal{U}'$ is the generalized velocity disturbance, and $\mathbf{E}^{\infty}$ is the rate of strain tensor for the ambient flow. Note that $\mathcal{F}^{\mathrm{H}} = (\boldsymbol{F}^{\mathrm{H}}, \boldsymbol{T}^{\mathrm{H}})^{\dagger}$, where $\boldsymbol{F}^{\mathrm{H}}$ and $\boldsymbol{T}^{\mathrm{H}}$ are respectively the particle hydrodynamic force and torque for all particles, and $\mathcal{U}' = (\boldsymbol{U} - \boldsymbol{U}^{\infty}, \boldsymbol{\Omega} - \boldsymbol{\Omega}^{\infty})^{\dagger}$, where $\boldsymbol{U} - \boldsymbol{U}^{\infty}$ and $\boldsymbol{\Omega} - \boldsymbol{\Omega}^{\infty}$ are respectively the linear and angular velocity disturbances. The hydrodynamic force, torque, and stresslet for particle i are defined as integrals of the localized surface force density $\boldsymbol{f}_i$,

$$\boldsymbol{F}_i^{\mathrm{H}} = -\int \mathrm{d}\boldsymbol{r}\, \boldsymbol{f}_i(\boldsymbol{r}), \tag{4.7}$$

$$\boldsymbol{T}_i^{\mathrm{H}} = -\int \mathrm{d}\boldsymbol{r}\, (\boldsymbol{r} - \boldsymbol{r}_i) \times \boldsymbol{f}_i(\boldsymbol{r}), \tag{4.8}$$

$$\mathbf{S}_i^{\mathrm{H}} = -\int \mathrm{d}\boldsymbol{r}\, \tfrac{1}{2}[(\boldsymbol{r} - \boldsymbol{r}_i)\boldsymbol{f}_i(\boldsymbol{r}) + \boldsymbol{f}_i(\boldsymbol{r})(\boldsymbol{r} - \boldsymbol{r}_i)]. \tag{4.9}$$

In Eq. (4.6) the ambient velocities are evaluated at particle centers, *i.e.*, $\boldsymbol{U}_i^{\infty} = \boldsymbol{v}^{\infty}(\boldsymbol{r}_i)$, $\boldsymbol{\Omega}_i^{\infty} = \frac{1}{2}\boldsymbol{\nabla} \times \boldsymbol{v}^{\infty}|_{\boldsymbol{r}_i}$, and $\mathbf{E}^{\infty} = \frac{1}{2}[\boldsymbol{\nabla}\boldsymbol{v}^{\infty} + (\boldsymbol{\nabla}\boldsymbol{v}^{\infty})^{\dagger}]_{\boldsymbol{r}_i}$. The expansions in Eqs. (4.4) and (4.5) lead to the following infinite dimension linear relation,

$$\mathfrak{u}' = -\mathfrak{M}(X) \cdot \mathfrak{f} \text{ and } \mathfrak{f} = -\mathfrak{R}(X) \cdot \mathfrak{u}', \tag{4.10}$$

where $\mathfrak{M}(X)$ and $\mathfrak{R}(X)$ are the multipole grand mobility and resistance tensors of operators $\mathbf{M}(\boldsymbol{r}, \boldsymbol{r}'; X)$ and $\mathbf{R}(\boldsymbol{r}, \boldsymbol{r}'; X)$, respectively. Evidently, $\mathfrak{M} = \mathfrak{R}^{-1}$, and from the Lorentz reciprocal theorem [54], both are positive definite.

The infinite dimension vectors $\mathfrak{f}$ and $\mathfrak{u}'$ can be reduced to finite dimensions by projection [55]. To the stresslet level of $\mathfrak{f}$ and the strain rate level of $\mathfrak{u}'$, we introduce projection matrices $\mathcal{P}$ and $\mathcal{Q}$, such that $\mathcal{P} \cdot \mathfrak{f} = (\mathcal{F}^{\mathrm{H}}, \mathbf{S}^{\mathrm{H}})^{\dagger}$ and $\mathcal{Q} \cdot \mathfrak{u}' = (\mathcal{U}', -\mathbf{E}^{\infty})^{\dagger}$. Moreover, $\mathcal{P} \cdot \mathcal{P}^{\dagger} = \mathcal{Q} \cdot \mathcal{Q}^{\dagger} = \mathcal{I}$, where $\mathcal{I}$ is an identity matrix. The following linear relation holds:

$$\begin{bmatrix} \mathcal{U}' \\ -\mathbf{E}^{\infty} \end{bmatrix} = -\mathcal{M} \cdot \begin{bmatrix} \mathcal{F}^{\mathrm{H}} \\ \mathbf{S}^{\mathrm{H}} \end{bmatrix}, \text{ and } \mathcal{R} = \mathcal{M}^{-1}, \tag{4.11}$$

where $\mathcal{M} = \mathcal{Q}\mathfrak{M}\mathcal{P}^\dagger$ is the grand mobility tensor and $\mathcal{R} = \mathcal{P}\mathfrak{R}\mathcal{Q}^\dagger$ is the grand resistance tensor. Both $\mathcal{M}$ and $\mathcal{R}$ are exact as the projections $\mathcal{P}$ and $\mathcal{Q}$ ensure that all the scattering of hydrodynamic interactions among the particles are captured. For convenience, the grand resistance tensor is partitioned as

$$\mathcal{R} = \begin{bmatrix} \boldsymbol{R}_{\mathcal{FU}} & \boldsymbol{R}_{\mathcal{F}\mathrm{E}} \\ \boldsymbol{R}_{\mathrm{S}\mathcal{U}} & \boldsymbol{R}_{\mathrm{SE}} \end{bmatrix}, \tag{4.12}$$

where, for example, $\boldsymbol{R}_{\mathcal{FU}}$ describes the coupling between the generalized force and the generalized velocity. The linear relation in Eq. (4.11) can also be deduced from the linearity of Eq. (4.2) without appealing to the multipole expansion, but here we establish a connection with other works, particularly the multipole methods of Cichocki and coworkers [15, 56]. Note that for rigid spherical particles, external flows can only affect the first two moments of $\mathfrak{f}$ and $\mathfrak{u}'$ due to symmetry and the no-slip boundary condition.

Elements of $\mathfrak{M}$ and $\mathfrak{R}$ can be computed from, for example, the induced force multipole [57, 58], eigenfunction expansions [15, 24, 59], and multipole expansions [7]. To the stresslet level, $\mathfrak{M}$ can be conveniently evaluated by combining the Faxén formulae and the multipole expansions. For a rigid particle i in an incompressible solvent, the Faxén formulae are [7],

$$\boldsymbol{U}_i - \boldsymbol{U}^\infty = -\frac{\boldsymbol{F}_i^{\mathrm{H}}}{6\pi\eta_0 a_i} + \left(1 + \tfrac{1}{6}a_i^2\nabla^2\right)\boldsymbol{v}'\big|_{\boldsymbol{r}_i} \tag{4.13}$$

$$\boldsymbol{\Omega}_i - \boldsymbol{\Omega}^\infty = -\frac{\boldsymbol{T}_i^{\mathrm{H}}}{8\pi\eta_0 a_i^3} + \tfrac{1}{2}\boldsymbol{\nabla}\times\boldsymbol{v}'\big|_{\boldsymbol{r}_i} \tag{4.14}$$

$$-\mathsf{E}^\infty = -\frac{\overline{\mathsf{S}_i^{\mathrm{H}}}}{\frac{20}{3}\pi\eta_0 a_i^3} + \left(1 + \tfrac{1}{10}a_i^2\nabla^2\right)\tfrac{1}{2}[\boldsymbol{\nabla}\boldsymbol{v}' + (\boldsymbol{\nabla}\boldsymbol{v}')^\dagger]\big|_{\boldsymbol{r}_i}, \tag{4.15}$$

where the overline indicates the traceless part of the symmetric tensor, and $\boldsymbol{v}'(\boldsymbol{r})$ is the velocity field in the absence of particle i. With the fundamental solution of Stokes equation $\mathsf{J}(\boldsymbol{r})$ and the force density $\boldsymbol{f}$, the velocity field $\boldsymbol{v}'(\boldsymbol{r})$ can be computed as [54],

$$\boldsymbol{v}(\boldsymbol{r}) = -\frac{1}{8\pi\eta_0}\int \mathrm{d}\boldsymbol{r}'\mathsf{J}(\boldsymbol{r}-\boldsymbol{r}')\cdot\boldsymbol{f}(\boldsymbol{r}'). \tag{4.16}$$

Expanding the force density around particle centers, we have

$$\boldsymbol{v}'(\boldsymbol{r}) = \frac{1}{8\pi\eta_0}\sum_j{}' \left(1 + \tfrac{1}{6}a_j^2\nabla^2\right)\mathsf{J}\cdot\boldsymbol{F}_j^{\mathrm{H}} + \mathsf{R}\cdot\boldsymbol{T}_j^{\mathrm{H}} - \left(1 + \tfrac{1}{10}a_j^2\nabla^2\right)\mathsf{K} : \overline{\mathsf{S}_j^{\mathrm{H}}} + \cdots, \tag{4.17}$$

where the prime on the summation excludes the case $i = j$, and the functions $\mathbf{J}$, $\mathbf{R}$, and $\mathbf{K}$ are evaluated at $\boldsymbol{r} - \boldsymbol{r}_j$. In the Cartesian tensor form, $\mathbf{R} = R_{\alpha\beta} = \frac{1}{4}\epsilon_{\delta\gamma\beta}(\nabla_\gamma J_{\alpha\delta} - \nabla_\delta J_{\alpha\gamma})$ and $\mathbf{K} = K_{\alpha\beta\gamma} = \frac{1}{2}[\nabla_\gamma J_{\alpha\beta} + \nabla_\beta J_{\alpha\gamma}]$, with $\epsilon_{\alpha\beta\gamma}$ the Levi-Civita symbol. With Eqs. (4.13)–(4.15) and (4.17), the grand mobility tensor $\mathfrak{M}$ for incompressible solvents can be constructed in a pairwise fashion.

The fundamental solutions

The formalism in Sec. 4.2 relies on $\mathbf{J}(\boldsymbol{r})$, the fundamental solution of Stokes equation. Different boundary conditions such as periodicity [60, 61], confinement [24, 62], or a combination of both [63], can be incorporated to $\mathbf{J}(\boldsymbol{r})$. For an infinite expanse of fluid, we have the well-known Oseen tensor,

$$\mathbf{J}(\boldsymbol{r}) = \frac{1}{r}(\mathbf{I} + \hat{\boldsymbol{r}}\hat{\boldsymbol{r}}), \tag{4.18}$$

where $r = \|\boldsymbol{r}\|$ and $\hat{\boldsymbol{r}} = \boldsymbol{r}/r$.

To study dynamics of homogeneous suspensions, periodic boundary conditions are necessary to assess the HIs. In this case, the proper fundamental solution $\mathbf{J}(\boldsymbol{r})$ describes the fluid velocity disturbance due to an array of periodic forces $\boldsymbol{F}\sum_{\boldsymbol{p}}\delta(\boldsymbol{r} - \boldsymbol{R}_{\boldsymbol{p}})$, where $\boldsymbol{R}_{\boldsymbol{p}} = \sum_{d=1}^{3} p_d \mathbf{a}_d$ is the location of the periodic forcing. Here, $\boldsymbol{p} = (p_1, p_2, p_3) \in \mathbb{Z}^3$, $\delta(\boldsymbol{r})$ is the 3D Dirac delta function, and $\mathbf{a}_1$, $\mathbf{a}_2$, and $\mathbf{a}_3$ are the Bravais lattice vectors describing the spatial periodicity. From a Fourier expansion of the Stokes equation [Eq. (4.2)], we have for the periodic $\mathbf{J}(\boldsymbol{r})$:

$$\mathbf{J}(\boldsymbol{r}) = -\frac{8\pi}{V}(\mathbf{I}\nabla^2 - \boldsymbol{\nabla}\boldsymbol{\nabla})\sum_{\boldsymbol{k}\neq 0}\frac{1}{k^4}\exp(-\imath\boldsymbol{k}\cdot\boldsymbol{r}), \tag{4.19}$$

where $\imath = \sqrt{-1}$, the unit cell volume $V = \mathbf{a}_1\cdot(\mathbf{a}_2\times\mathbf{a}_3)$, the wave vector $\boldsymbol{k} = \sum_{d=1}^{3} j_d \mathbf{b}_d$ is defined by the reciprocal vectors $\mathbf{b}_1$, $\mathbf{b}_2$, and $\mathbf{b}_3$, $\boldsymbol{j} = (j_1, j_2, j_3) \in \mathbb{Z}^3$, and $k^2 = \boldsymbol{k}\cdot\boldsymbol{k}$. Writing the lattice and the reciprocal vectors as column vectors and defining matrices $\mathbf{A} = [\mathbf{a}_1\mathbf{a}_2\mathbf{a}_3]$ and $\mathbf{B} = [\mathbf{b}_1\mathbf{b}_2\mathbf{b}_3]$, we have $\mathbf{B}^\dagger = 2\pi\mathbf{A}^{-1}$ and $\exp(\imath\boldsymbol{k}\cdot\boldsymbol{R}_{\boldsymbol{p}}) = 1$. By requiring $\boldsymbol{k} \neq 0$ in Eq. (4.19), the external forces are balanced by the pressure gradient [60], a necessary condition for convergent HIs [64].

A difficulty associated with HIs is the long range nature of $\mathbf{J}(\boldsymbol{r})$, *i.e.*, Eq. (4.18) decays as r^{-1} in the real space and Eq. (4.19) as k^{-2} in the wave space. For periodic systems, however, the conditionally converging sum in Eq. (4.19) can be split into two exponentially fast converging series, *i.e.*,

$$\mathbf{J}(\boldsymbol{r}) = \mathbf{J}_R(\boldsymbol{r}) + \mathbf{J}_W(\boldsymbol{r}), \tag{4.20}$$

where $\mathbf{J}_R(\boldsymbol{r})$ is the real-space sum, $\mathbf{J}_W(\boldsymbol{r})$ is the wave-space sum. Although the splitting in Eq. (4.20) is not unique [29], a particularly efficient scheme by Hasimoto [60] utilizes the integral

$$\frac{1}{k^4} = \pi^2 \int_0^\infty \beta \exp(-\pi k^2 \beta) \mathrm{d}\beta, \, (k \neq 0), \tag{4.21}$$

and the Poisson summation formula. The result is

$$\mathbf{J}_R(\boldsymbol{r}) = \sum_{\boldsymbol{p}\neq 0} (\mathbf{I}\nabla^2 - \boldsymbol{\nabla}\boldsymbol{\nabla}) \left[r\mathrm{Erfc}(r\xi) - \frac{1}{\xi\sqrt{\pi}} e^{-r^2\xi^2} \right], \tag{4.22}$$

$$\mathbf{J}_W(\boldsymbol{r}) = \frac{8\pi}{V} \sum_{\boldsymbol{k}\neq 0} (\mathbf{I}\nabla^2 - \boldsymbol{\nabla}\boldsymbol{\nabla}) \left(-1 - \frac{k^2}{4\xi^2} \right) \frac{1}{k^4} e^{-\frac{1}{4}k^2\xi^{-2}} e^{-\imath \boldsymbol{k}\cdot\boldsymbol{r}}, \tag{4.23}$$

where ξ is the splitting parameter and $\mathrm{Erfc}(x)$ is the complementary error function. Eqs. (4.20), (4.22), and (4.23) are referred to as the Ewald summation of the Oseen tensor. The real-space sum $\mathbf{J}_R$ only covers the *neighboring* periodic cells. The parameter ξ is consistent with the convention of Beenakker[61] and satisfies $4\pi\alpha\xi^2 = 1$, where α is the splitting parameter introduced by Hasimoto [60].

Extension to compressible fluid

The formalism in Sec. 4.2 is limited to an incompressible fluid, *i.e.*, the imposed flow must satisfy $\boldsymbol{\nabla}\cdot\boldsymbol{v}^\infty = 0$. This requirement is relaxed by imposing a *uniform* rate of expansion everywhere in the fluid, such that $\boldsymbol{\nabla}\cdot\boldsymbol{v}^\infty = E^\infty$, and the fluid is assumed compressible with a bulk viscosity κ_0. The rigid particles, unable to expand with the compressible fluid, generate a velocity disturbance that satisfies the incompressible Stokes equation [50]. From the linearity of Stokes flow, this velocity disturbance can be superimposed with other flows in the suspension, extending the existing formalism to compressible fluids.

For a rigid particle of radius a_i located at $\boldsymbol{r}_i = 0$, the velocity disturbance $\boldsymbol{v}_s$ due to a compressible flow with an expansion rate E^∞ is

$$\boldsymbol{v}_s(\boldsymbol{r}) = -\tfrac{1}{3} a_i^3 E^\infty \frac{\boldsymbol{r}}{r^3}. \tag{4.24}$$

This isotropic flow disturbance generates an isotropic stress contribution. Introducing the pressure moment as the trace of the stresslet in Eq. (4.9), *i.e.*,

$$S_i^{\mathrm{H}} = -\int \mathrm{d}\boldsymbol{r}\, (\boldsymbol{r} - \boldsymbol{r}_i)\cdot \boldsymbol{f}_i(\boldsymbol{r}), \tag{4.25}$$

we have $S_i^{\mathrm{H}} = -\frac{16}{3}\pi\eta_0 a_i^3 E^\infty$ from Eq. (4.24). Therefore, the velocity disturbance due to a pressure moment S_i^{H} at the origin is

$$\boldsymbol{v}_s(\boldsymbol{r}) = \frac{1}{16\pi\eta_0} \frac{\boldsymbol{r}}{r^3} S_i^{\mathrm{H}} = \boldsymbol{Q}(\boldsymbol{r}) S_i^{\mathrm{H}}. \tag{4.26}$$

Adding the compressible velocity disturbances $\boldsymbol{v}_s(\boldsymbol{r})$ from other particles to the incompressible velocity disturbance $\boldsymbol{v}'(\boldsymbol{r})$ in Eq. (4.17), the general velocity disturbance in a compressible suspension is

$$\boldsymbol{v}_c'(\boldsymbol{r}) = \boldsymbol{v}'(\boldsymbol{r}) + \sum_j{}' \boldsymbol{Q}(\boldsymbol{r} - \boldsymbol{r}_j) S_j^{\mathrm{H}}. \tag{4.27}$$

When applying the Faxén formulae [Eqs. (4.13)–(4.15)] in compressible suspensions, the velocity disturbance $\boldsymbol{v}_c'$, instead of $\boldsymbol{v}'$, is used.

In addition to Eqs. (4.13)–(4.15), the Faxén relation for the pressure moment in a compressible fluid is [65, 66]

$$S_i^{\mathrm{H}} = -\tfrac{16}{3}\pi\eta_0 a_i^3 E^{\infty} + 4\pi a_i^3 p'(\boldsymbol{r}_i), \tag{4.28}$$

where p' is the pressure disturbance without the particle at $\boldsymbol{r}_i$. The pressure disturbance can be obtained from the pressure fundamental solution of Stokes equation,

$$\boldsymbol{P}(\boldsymbol{r}) = \frac{\boldsymbol{r}}{r^3}, \tag{4.29}$$

such that the pressure distribution due to a force density is

$$p(\boldsymbol{r}) = -\frac{1}{4\pi}\int \mathrm{d}\boldsymbol{r}'\boldsymbol{P}(\boldsymbol{r} - \boldsymbol{r}')\cdot\boldsymbol{f}(\boldsymbol{r}'). \tag{4.30}$$

For the pressure disturbance p' in Eq. (4.28), expanding the surface force densities leads to

$$p'(\boldsymbol{r}) = \frac{1}{4\pi}\sum_j{}' \boldsymbol{P}(\boldsymbol{r} - \boldsymbol{r}_j)\cdot\boldsymbol{F}_j^{\mathrm{H}} - \boldsymbol{\nabla}\boldsymbol{P} : \mathbf{S}_j^{\mathrm{H}}|_{(\boldsymbol{r}-\boldsymbol{r}_j)} + \cdots. \tag{4.31}$$

Eq. (4.28) is different from the Faxén formulae in Eqs. (4.13)–(4.15) as it presents the pressure moment or the trace of the stresslet on the left hand side. This subtle difference highlights a distinct feature of the compressible flow disturbances: in a compressible fluid, the pressure moment can cause particle movement satisfying the incompressible Stokes equation, but the incompressible force moments cannot generate compressible disturbances. As a result, the interaction part of the pressure moment can only be evaluated after $\boldsymbol{F}_i^{\mathrm{H}}$, $\boldsymbol{T}_i^{\mathrm{H}}$, and $\overline{\mathbf{S}_i^{\mathrm{H}}}$ are known. Otherwise, the resulting hydrodynamic interactions contain spurious contributions due to the unphysical coupling between the incompressible force moments and the compressible flow disturbances.

To extend the above results for $\boldsymbol{v}_s$ and S_i^{H} to periodic boundary conditions, we note that the divergence of $\boldsymbol{Q}$ in Eq. (4.26) satisfies

$$\boldsymbol{\nabla}\cdot\boldsymbol{Q} = \frac{1}{4\eta_0}\delta(\boldsymbol{r}), \tag{4.32}$$

since $\nabla^2 r^{-1} = -4\pi\delta(\boldsymbol{r})$. Therefore, for uniform expansion in compressible suspensions, the particles act as fluid sources, each with a strength proportional to its pressure moment. In a periodic system, the velocity disturbance corresponding to an array of sources is obtained by replacing the delta function in Eq. (4.32) with $\sum_{\boldsymbol{p}} \delta(\boldsymbol{r} - \boldsymbol{R}_{\boldsymbol{p}})$. From Fourier transform, the solution is

$$\boldsymbol{Q}(\boldsymbol{r}) = \frac{1}{4\eta_0 V} \boldsymbol{\nabla} \sum_{\boldsymbol{k}\neq 0} \frac{1}{k^2} e^{-\imath \boldsymbol{k}\cdot\boldsymbol{r}}. \tag{4.33}$$

The above wave-space sum can be split to two exponentially converging series [30, 60] using

$$\sum_{\boldsymbol{k}\neq 0} \frac{1}{k^2} e^{-\imath \boldsymbol{k}\cdot\boldsymbol{r}} = \frac{V}{4\pi} \sum_{\boldsymbol{p}\neq 0} \frac{1}{r} \mathrm{Erfc}(r\xi) + \sum_{\boldsymbol{k}\neq 0} \frac{1}{k^2} e^{-\frac{1}{4}k^2\xi^{-2}} e^{-\imath \boldsymbol{k}\cdot\boldsymbol{r}}. \tag{4.34}$$

Similar to $\boldsymbol{Q}(\boldsymbol{r})$, the pressure fundamental solution $\boldsymbol{P}(\boldsymbol{r})$ in Eq. (4.29) can also be extended to periodic systems.

4.3 The mobility computation

The mobility problem seeks the action of the grand mobility tensor $\mathfrak{M}$ on the force moments such as $\mathcal{F}^{\mathrm{H}}$ and $\mathbf{S}^{\mathrm{H}}$. It can be constructed in a pairwise fashion using the formalism in Sec. 4.2 for compressible suspensions. Naïvely, this is an $O(N^2)$ operation for an N-particle system since the long-range HIs necessitate considerations of all particle pairs. However, with the Ewald summation that splits the fundamental solutions $\mathbf{J}(\boldsymbol{r})$, $\boldsymbol{Q}(\boldsymbol{r})$, and $\boldsymbol{P}(\boldsymbol{r})$ into exponentially fast converging wave-space and real-space series, the particle mesh techniques can improve the computation scaling to $O(N \log N)$. In the following, our implementation of the mobility computation is discussed.

Wave-space computation: the Spectral Ewald (SE) method

The wave-space computation concerns the part of grand mobility tensor associated with $\mathbf{J}_W(\boldsymbol{r})$ of Eq. (4.23) and the wave-space sum of Eq. (4.34) in $\boldsymbol{P}(\boldsymbol{r})$ and $\boldsymbol{Q}(\boldsymbol{r})$. Using the Fast Fourier Transform (FFT) algorithm, the computation cost can be reduced to $O(N \log N)$. To illustrate this, let us consider the wave-space velocity disturbance $\boldsymbol{U}_i^W$ on particle i at the Rotne-Prager level, obtained by combining Eqs. (4.13), (4.17), and (4.23), *i.e.*,

$$\boldsymbol{U}_i^W = \frac{1}{\eta_0 V} \sum_{\boldsymbol{k}\neq 0} e^{-\imath \boldsymbol{k}\cdot\boldsymbol{r}_i} \left(1 - \tfrac{1}{6}a_i^2 k^2\right) \mathbf{g}_1(\boldsymbol{k}) \cdot \sum_j \left(1 - \tfrac{1}{6}a_j^2 k^2\right) e^{\imath \boldsymbol{k}\cdot\boldsymbol{r}_j} \boldsymbol{F}_j^{\mathrm{H}}, \tag{4.35}$$

and the wave-space kernel

$$\mathbf{g}_1(\boldsymbol{k}) = \left(1 + \tfrac{1}{4}k^2\xi^{-2}\right) k^{-4} e^{-\frac{1}{4}k^2\xi^{-2}} (\mathbf{I}k^2 - \boldsymbol{k}\boldsymbol{k}). \tag{4.36}$$

Different from Eq. (4.17), the summation over particle j in Eq. (4.35) is unrestricted and includes the case of $i = j$. Therefore, the self interaction term for $i = j$, which is from the inverse transform of Eq. (4.35) with $\boldsymbol{r}_i = \boldsymbol{r}_j$ [61],

$$\frac{1}{8\eta_0\pi^3} \int \left(1 - \tfrac{1}{6}a_i^2k^2\right)^2 \mathbf{g}_1(\boldsymbol{k}) \mathrm{d}\boldsymbol{k} \cdot \boldsymbol{F}_i^{\mathrm{H}} = \frac{\xi(9 - 10a_i^2\xi^2 + 7a_i^4\xi^4)}{18\eta_0\pi^{3/2}} \boldsymbol{F}_i^{\mathrm{H}}, \tag{4.37}$$

should be removed. Eq. (4.35) exposes the basic idea behind many particle mesh techniques including the PME method and the SPME method. From an inverse Fourier transform, the real-space force distribution corresponding to the summation over j in Eq. (4.35) is

$$\sum_j (1 + \tfrac{1}{6}a_j^2\nabla^2) \boldsymbol{F}_j^{\mathrm{H}} \delta(\boldsymbol{r} - \boldsymbol{r}_j). \tag{4.38}$$

The force distribution in Eq. (4.38) is assigned to a regular spatial grid by approximating the delta functions by Lagrangian polynomials in the PME method [67] or Cardinal B-splines in the SPME method [33]. The interpolated forces are then transformed to the wave space by FFT and the wave-space computation in Eq. (4.35) is performed. The wave-space results is then brought back to the real space by inverse FFTs. Subsequently, the velocity on each particle, $\boldsymbol{U}_i^W$, is interpolated back from the grid, preferably using the same interpolation scheme for the force assignment [68]. Here, the action of the mobility tensor on the force $\boldsymbol{F}^{\mathrm{H}}$, rather than the tensor itself, is computed. The kernel $\mathbf{g}_1(\boldsymbol{k})$ in Eq. (4.36) is effectively a low-pass filter that cuts off the spatial signals at high k. Computationally, for M^3 grid points the FFT scales as $O(M^3 \log M^3)$. In FFT-based particle mesh methods, it is necessary to have $M \propto N^{1/3}$ to ensure the overall accuracy in the mobility evaluation as the number of near neighbors in the real-space computation is kept constant. Consequently, the wave-space computation scales as $O(N \log N)$.

There are two sources of error affecting the accuracy of particle mesh techniques. The first is associated with the truncation of the wave-space sum (k-summation) in Eq. (4.35). This is only affected by the number of grid points M in the simulation box. The second error is the interpolation error, and arises from polynomial approximation of the δ-functions in Eq. (4.38). For a simulation box of size L, this error scales as $(L/M)^p$, where p is the polynomial order of the approximation scheme. Since both errors are associated with M, we cannot separate the two error sources.

Consequently, to maintain a satisfactory overall accuracy, a large M is often used in the wave-space computations to keep the interpolation error small, resulting in unnecessary FFT computations.

In addition, for polydisperse suspensions, different particle sizes introduce additional complications to traditional particle mesh techniques. If the Laplacian in Eq. (4.38) is computed in the real space in the SPME method, the interpolation error increases to $(L/M)^{p-2}$, which further increases the M requirement. For the PME method, real-space differentiation is unsuitable due to the discontinuity of Lagrangian polynomials, and all the computations have to be carried out in the wave space. This significantly increases the total number of FFTs. In addition, different particle sizes increase the complexity in the algorithm implementation. Therefore, a simple method with flexible error control is crucial for accurate and efficient wave-space computation in polydisperse systems.

To address these concerns, we use a new particle mesh technique, the Spectral Ewald (SE) method [29–31] for the wave-space mobility computation. The SE method decouples the k-space truncation and interpolation errors, and is accurate, efficient, and flexible for polydisperse systems. To show this, we use Eq. (4.35) again as an example and consider the general case of non-orthogonal lattice vectors. We first introduce the fractional coordinate $\boldsymbol{t} = (t_1, t_2, t_3)^\dagger \in [0, 1)^3$. For each point $\boldsymbol{r}$ in the simulation box, $\boldsymbol{r} = t_1\mathbf{a}_1 + t_2\mathbf{a}_2 + t_3\mathbf{a}_3 = \mathbf{A}\cdot\boldsymbol{t}$. Accordingly, defining $\boldsymbol{q} = (q_1, q_2, q_3)^\dagger$ such that $\boldsymbol{k} = q_1\mathbf{b}_1 + q_2\mathbf{b}_2 + q_3\mathbf{b}_3 = \mathbf{B}\cdot\boldsymbol{q}$, $\exp(\imath\boldsymbol{k}\cdot\boldsymbol{r}) = \exp(2\pi\imath\boldsymbol{q}\cdot\boldsymbol{t})$, and $k^2 = \boldsymbol{q}^\dagger\cdot\mathbf{B}^\dagger\cdot\mathbf{B}\cdot\boldsymbol{q}$. Eq. (4.35) is rewritten in $\boldsymbol{t}$ and $\boldsymbol{q}$ as

$$\begin{aligned}\boldsymbol{U}_i^W =& \frac{1}{\eta_0 V}\sum_{\boldsymbol{q}\neq 0} e^{-2\pi\imath\boldsymbol{q}\cdot\boldsymbol{t}_i - \frac{1}{8}\theta q^2\xi^{-2}}\left(1 - \tfrac{1}{6}a_i^2\boldsymbol{q}^\dagger\cdot\mathbf{B}^\dagger\cdot\mathbf{B}\cdot\boldsymbol{q}\right)e^{\frac{1}{4}\theta q^2\xi^{-2}}\mathbf{g}_1(\mathbf{B}\cdot\boldsymbol{q})\\ &\cdot\sum_j\left(1 - \tfrac{1}{6}a_j^2\boldsymbol{q}^\dagger\cdot\mathbf{B}^\dagger\cdot\mathbf{B}\cdot\boldsymbol{q}\right)e^{2\pi\imath\boldsymbol{q}\cdot\boldsymbol{t}_j - \frac{1}{8}\theta q^2\xi^{-2}}\boldsymbol{F}_j^{\mathrm{H}},\end{aligned} \tag{4.39}$$

with two $e^{-\frac{1}{8}\theta q^2\xi^{-2}}$ multiplied after particle positions and one $e^{\frac{1}{4}\theta q^2\xi^{-2}}$ before $\mathbf{g}_1$, and θ is a parameter. Introducing the Fourier transform pair

$$\hat{f}_{\boldsymbol{q}} = \int \mathrm{d}\boldsymbol{t}\, f(\boldsymbol{t})e^{2\pi\imath\boldsymbol{q}\cdot\boldsymbol{t}} \text{ and } f(\boldsymbol{t}) = \int \mathrm{d}\boldsymbol{q}\,\hat{f}_{\boldsymbol{q}}e^{-2\pi\imath\boldsymbol{q}\cdot\boldsymbol{t}}, \tag{4.40}$$

the basic idea of SE is to note that

$$h(\boldsymbol{t}) = \int \mathrm{d}\boldsymbol{q}\, e^{-2\pi\imath\boldsymbol{q}\cdot\boldsymbol{t} - \frac{1}{8}\theta q^2\xi^{-2}} = \left(\frac{8\pi\xi^2}{\theta}\right)^{\frac{3}{2}}\exp\left(-\frac{8\pi^2\xi^2}{\theta}\|\boldsymbol{t}\|_*^2\right), \tag{4.41}$$

i.e., the Fourier transform of a Gaussian remains a Gaussian, and the shape of the Gaussian is controlled by θ. Here, $\|\cdot\|_*$ indicates distance computation using the

minimum image convention for periodic systems. The inverse Fourier transform of the second line of Eq. (4.39) with respect to $\boldsymbol{q}$ is

$$\boldsymbol{H}(\boldsymbol{t}) = \sum_j \left(1 + \tfrac{1}{24} a_j^2 \pi^{-2} \boldsymbol{\nabla}_t^\dagger \cdot \mathbf{B}^\dagger \cdot \mathbf{B} \cdot \boldsymbol{\nabla}_t\right) h|_{(\boldsymbol{t}-\boldsymbol{t}_j)} \boldsymbol{F}_j^{\mathrm{H}}, \tag{4.42}$$

where $\boldsymbol{\nabla}_t = (\partial/\partial t_1, \partial/\partial t_2, \partial/\partial t_3)^\dagger$. Eq. (4.42) facilitates interpolation of a discrete force distribution onto a uniform grid of coordinate $\boldsymbol{t}$ via the Gaussian shape function $h(\boldsymbol{t})$ in Eq. (4.41). The effect of particle size is automatically incorporated in the grid assignment scheme in the real space. After converting the real-space $\boldsymbol{H}(\boldsymbol{t})$ to the wave-space $\hat{\boldsymbol{H}}_{\boldsymbol{q}}$ using FFTs, the wave-space computation produces

$$\hat{\boldsymbol{G}}_{\boldsymbol{q}} = \begin{cases} e^{\frac{1}{4}\theta q^2 \xi^{-2}} \mathbf{g}_1(\mathbf{B} \cdot \boldsymbol{q}) \cdot \hat{\boldsymbol{H}}_{\boldsymbol{q}}, & \boldsymbol{q} \neq 0 \\ 0 & \text{otherwise.} \end{cases} \tag{4.43}$$

From Parseval's theorem,

$$\int_{\mathrm{T}} \mathrm{d}\boldsymbol{t}\, f(\boldsymbol{t}) g^*(\boldsymbol{t}) = \sum_{\boldsymbol{q}} \hat{f}_{\boldsymbol{q}} \hat{g}^*_{\boldsymbol{q}}, \tag{4.44}$$

where T is a periodic lattice and $(\cdot)^*$ indicates complex conjugation, Eq. (4.39) becomes a convolution integral with the Gaussian shape function,

$$\boldsymbol{U}_i^W = \frac{1}{\eta_0 V} \int_{\mathrm{T}} \mathrm{d}\boldsymbol{t} \boldsymbol{G}(\boldsymbol{t}) \left(1 + \tfrac{1}{24} a_i^2 \pi^{-2} \boldsymbol{\nabla}_t^\dagger \cdot \mathbf{B}^\dagger \cdot \mathbf{B} \cdot \boldsymbol{\nabla}_t\right) h|_{(\boldsymbol{t}-\boldsymbol{t}_i)}, \tag{4.45}$$

where $\boldsymbol{G}(\boldsymbol{t})$ is the inverse Fourier transform of $\hat{\boldsymbol{G}}_{\boldsymbol{q}}$. Extending the SE method to couplings beyond Rotne-Prager level is straightforward, with adjusted $\boldsymbol{H}(\boldsymbol{t})$ and $\boldsymbol{G}(\boldsymbol{t})$ based on the Faxén laws and multipole expansions in Sec. 4.2. In this work, we have implemented the mobility computation to the stresslet and the strain rate level.

Unlike other particle mesh techniques, the SE formulation in Eqs. (4.39)–(4.45) is exact and therefore the errors are entirely from the numerical implementations. Since the FFT algorithm is accurate to machine precision, the sources of error include the discretization and truncation of the shape function [Eq. (4.41)], and the numerical integration in Eq. (4.45). Practically, the evaluation of each shape function is limited to P^3 points ($P \leq M$) around the particle. Due to the exponential decay of $h(\boldsymbol{t})$, the truncation error decreases exponentially with increasing P. Meanwhile, the integral in Eq. (4.45) is evaluated using trapezoidal quadrature [29, 30], which also exhibits exponential error decay with increasing P. Therefore, the interpolation error in SE

method depends exclusively on P for sufficiently large M, and can be separately controlled from the k-space truncation error. The rapid, exponential error decay is known as spectral accuracy [29, 30], and this is the namesake of the SE method.

The computation cost of the SE method also becomes apparent with the truncation of $h(\boldsymbol{t})$. The grid assignment in Eq. (4.42) and the convolution Eq. (4.45) are $O(NP^3)$ for an N-particle system, and the FFTs to and from the wave space are $O[M^3 \log(M^3)]$. With $M^3 \propto N$, the time limiting step is the FFT, and the SE method also scales as $O(N \log N)$ as other particle mesh techniques.

The Gaussian shape in $h(\boldsymbol{t})$ of Eq. (4.41) is controlled by θ, which is parameterized as

$$\theta = \left(\frac{2\pi P\xi}{Mm}\right)^2, \tag{4.46}$$

on a regular grid of M^3 points with P^3 points for each shape function evaluation. The shape parameter m in Eq. (4.46) ensures that at the edge of the $h(\boldsymbol{t})$ evaluation, *i.e.*, $t^2 = P^2/(2M)^2$, $h \propto e^{-m^2/2}$. Therefore, with fixed M and P, m describes the truncation of $h(\boldsymbol{t})$ on the discretized grid and is consistent with the original SE method of Lindbo & Tornberg [29, 30].

The computation efficiency of the SE method relies on rapidly computing the $O(NP^3)$ different Gaussian shape functions $h(\boldsymbol{t})$, which involves expensive exponential evaluations. To reduce these expensive operations, Lindbo & Tornberg [29, 30] introduced the fast Gaussian gridding (FGG) technique [69] to the SE method. In essence, the FGG technique evaluates the exponential function on a regular grid as

$$e^{-\alpha(\delta t + i\Delta t)^2} = e^{-\alpha(\delta t)^2} \times \left(e^{-2\alpha\delta t\Delta t}\right)^i \times \left[e^{-\alpha(\Delta t)^2}\right]^{i^2}, \tag{4.47}$$

where α is a constant, δt is the off-grid value, Δt is the spacing of the regular grid, and i is an integer within the range $[-P/2, P/2]$. It reduces the P exponential evaluations in each direction in the SE method to 3 exponential computations and at most $2P$ multiplications. In addition, the last term of Eq. (4.47) is independent of δt, and therefore only needs to be computed once.

Wave-space computation: the particle size effect

In Sec. 4.3 the terms associated with finite particle sizes in the Faxén laws and the multipole expansions are incorporated in the real-space derivatives of the shape function $h(\boldsymbol{t})$. For example, in a simple shear flow with lattice vectors $\mathbf{a}_1 = (L, 0, 0)$, $\mathbf{a}_2 = (\gamma L, L, 0)$, and $\mathbf{a}_3 = (0, 0, L)$, where γ is the strain, the relevant term in

Eqs. (4.42) and (4.45) is

$$\left(\tfrac{1}{24}a_i^2\pi^{-2}\boldsymbol{\nabla}_t^\dagger\cdot\mathbf{B}^\dagger\cdot\mathbf{B}\cdot\boldsymbol{\nabla}_t\right)h(\boldsymbol{t})=$$
$$\tfrac{8}{3}\left(\frac{\pi\xi a_i}{\theta L}\right)^2\left\{-\theta(3+\gamma^2)+16\pi^2\xi^2[(1+\gamma^2)t_1^2+t_2^2+t_3^2-2\gamma t_1t_2]\right\}h(\boldsymbol{t}). \tag{4.48}$$

The finite particle sizes introduce additional features to the shape function, and for non-orthogonal simulation boxes, non-trivial anisotropy. As a result, compared to the case of point forces, more points P are needed to resolve the details in Eq. (4.48). On the other hand, the benefit of evaluating the particle size effects in the real space is that fewer FFTs are involved. To compute the mobility problem of compressible suspensions to the stresslet and the strain rate levels, only four pairs of FFTs are necessary: three are associated with $\mathbf{J}_W$ in Eq. (4.23), and one is associated with the $\boldsymbol{Q}$ in Eq. (4.26).

Alternatively, the particle size effect can be completely accounted in the wave space. This requires, for each particle j, $\boldsymbol{F}_j^{\mathrm{H}}$, $\boldsymbol{T}_j^{\mathrm{H}}$, and $\mathbf{S}_j^{\mathrm{H}}$, as well as $a_j^2\boldsymbol{F}_j^{\mathrm{H}}$ and $a_j^2\mathbf{S}_j^{\mathrm{H}}$, to be separately interpolated to the grid via $h(\boldsymbol{t})$ and brought to the wave space for computation. The derivatives associated with the Faxén laws and multipole expansions in Sec. 4.2 are carried out in the wave space as multiplication of wave vectors. The final results are then combined from different convolutions and weighted by the particle sizes. To demonstrate this, we again take the wave-space Rotne-Prager velocity, Eq. (4.39), as an example. In this approach, the grid assignment is split into two parts:

$$\boldsymbol{H}'(\boldsymbol{t})=\sum_j h(\boldsymbol{t}-\boldsymbol{t}_j)\boldsymbol{F}_j^{\mathrm{H}}\text{ and }\boldsymbol{H}''(t)=\sum_j h(\boldsymbol{t}-\boldsymbol{t}_j)a_j^2\boldsymbol{F}_j^{\mathrm{H}}. \tag{4.49}$$

The wave-space computation for $\boldsymbol{q}\neq 0$ is also split as

$$\hat{\boldsymbol{G}}'_{\boldsymbol{q}}=e^{\frac{1}{4}\theta q^2\xi^{-2}}\mathbf{g}_1(\mathbf{B}\cdot\boldsymbol{q})\cdot\left[\hat{\boldsymbol{H}}'_{\boldsymbol{q}}-(\tfrac{1}{6}\boldsymbol{q}^\dagger\cdot\mathbf{B}^\dagger\cdot\mathbf{B}\cdot\boldsymbol{q})\hat{\boldsymbol{H}}''_{\boldsymbol{q}}\right], \tag{4.50}$$
$$\hat{\boldsymbol{G}}''_{\boldsymbol{q}}=(-\tfrac{1}{6}\boldsymbol{q}^\dagger\cdot\mathbf{B}^\dagger\cdot\mathbf{B}\cdot\boldsymbol{q})e^{\frac{1}{4}\theta q^2\xi^{-2}}\mathbf{g}_1(\mathbf{B}\cdot\boldsymbol{q})\cdot\left[\hat{\boldsymbol{H}}'_{\boldsymbol{q}}-(\tfrac{1}{6}\boldsymbol{q}^\dagger\cdot\mathbf{B}^\dagger\cdot\mathbf{B}\cdot\boldsymbol{q})\hat{\boldsymbol{H}}''_{\boldsymbol{q}}\right], \tag{4.51}$$

and $\hat{\boldsymbol{G}}'_{\boldsymbol{q}}=\hat{\boldsymbol{G}}''_{\boldsymbol{q}}=0$ when $\boldsymbol{q}=0$. The wave-space velocity disturbance is a sum of two convolutions:

$$\boldsymbol{U}_i^W=\frac{1}{\eta_0 V}\int_{\mathrm{T}}\mathrm{d}\boldsymbol{t}\boldsymbol{G}'(\boldsymbol{t})h(\boldsymbol{t}-\boldsymbol{t}_i)+\frac{a_i^2}{\eta_0 V}\int_{\mathrm{T}}\mathrm{d}\boldsymbol{t}\boldsymbol{G}''(\boldsymbol{t})h(\boldsymbol{t}-\boldsymbol{t}_i). \tag{4.52}$$

Note that the convolution associated with $\boldsymbol{G}''(\boldsymbol{t})$ is weighted by the particle size a_i. Compared to the other approach, the wave-space computation is rather straightforward for the force interpolation and convolution. With the same P, the accuracy

is expected to be higher as the derivatives are calculated in the wave space [68]. However, the computation burden is shifted to the FFTs: for the mobility problem to the $\mathbf{S}$ and $\mathbf{E}$ level, a total of 20 pairs of FFTs are necessary: 12 for $\boldsymbol{F}_j^{\mathrm{H}}$, $\boldsymbol{T}_j^{\mathrm{H}}$, and $\mathbf{S}_j^{\mathrm{H}}$, three for $a_j^2\boldsymbol{F}_j^{\mathrm{H}}$, and five for the traceless part of $a_j^2\mathbf{S}_j^{\mathrm{H}}$.

A third approach, a hybridization between the wave- and the real-space approaches above, aims to reduce the errors associated with the high order derivatives of $h(\boldsymbol{t})$ in the real space. It retains the real-space derivatives in the force interpolation step, but when evaluating the Faxén laws, the second order derivatives are computed in the wave space for improved accuracy. The first order derivatives are computed in the real space to keep the total number of FFTs low. As a result, this hybrid approach requires 12 FFTs: four to the wave space and eight from the wave space. Taking Eq. (4.39) again for example, the most significant error in Sec. 4.3 is due to applying the operator $(\boldsymbol{\nabla}_t^{\dagger}\cdot\mathbf{B}^{\dagger}\cdot\mathbf{B}\cdot\boldsymbol{\nabla}_t)$ twice to $h(\boldsymbol{t})$, once during the force interpolation, and another time during the convolution. The hybrid approach retains the real-space grid assignment using $\boldsymbol{H}(\boldsymbol{t})$ in Eq. (4.42), but evaluates the convolution using Eq. (4.52) with modified $\hat{\boldsymbol{G}}'(\boldsymbol{t})$ and $\hat{\boldsymbol{G}}''(\boldsymbol{t})$: in the wave-space computations, the content in the square bracket on the right hand side of Eqs. (4.50) and (4.51) is replaced with $\hat{\boldsymbol{H}}_{\boldsymbol{q}}$ in Eq. (4.42). We adopted this hybrid approach in this work to compute the HIs, and discuss the accuracy of various approaches in Sec. 4.5.

Real-space computation

The real-space contributions to the grand mobility tensor $\mathfrak{M}$ are computed pairwise using the formalism in Sec. 4.2. Since $\mathbf{J}_R(\boldsymbol{r})$ [Eq. (4.22)] decays exponentially fast with distance, when the parameter ξ is sufficiently large, only particle pairs within a cutoff distance r_c need to be evaluated. If each particle has on average N_{nnb} near neighbors within the cutoff distance r_c, the scaling for the real-space computation is $O(NN_{\mathrm{nnb}})$, and by keeping N_{nnb} constant, the real-space computation scales as $O(N)$. Here, fast neighbor search algorithms such as the linked list [70] or the chaining mesh [71] are used. These methods divide the simulation box into cells of size slightly larger than r_c and sort the particles into the cells. To find the neighbors of a particle, only particles in the residing cell and its 26 neighboring cells are searched.

To accommodate the iterative scheme for HI computations in Sec. 4.4, the real-space grand mobility tensor is constructed as a sparse matrix at each time step. After the matrix construction, the action of the real-space contributions to $\mathfrak{M}$ is

simply a matrix-vector multiplication. Otherwise, neighbor searching and pairwise HI evaluations need to be carried out at every iteration. Note that we also include the self-contributions from the wave-space computations, *e.g.*, Eq. (4.37), and the self-part of the pressure Faxén law [Eq. (4.28)], in the real-space grand mobility tensor.

GPGPU acceleration of the mobility computation

The mobility computation with the SE method was first implemented on CPU and the performance was unsatisfactory for dynamic simulations. The bottlenecks are the force interpolation step and the convolution step. These are common speed limiting steps in particle mesh techniques due to ineffective memory caching between the particle and the grid data. For polydisperse systems in this work, the situation is aggravated as more interpolation points P are needed for satisfactory HI resolution. After a few optimization iterations on CPU, we realized that the key to the performance is the memory bandwidths. Since modern GPUs typically have significantly higher memory bandwidths compared to CPUs, in this work the entire mobility computation is carried out on GPU using CUDA C, a popular GPGPU programming model with a relatively mature environment for scientific computations.

The GPU mobility computations are carried out in Single Precision (SP) for the highest GPU performance. The cost of the performance in SP computation is the accuracy, as the SP arithmetics can be severely limited by the number of significant digits compared to the Double Precision (DP). However, this is not a problem in this work for at least three reasons: (*i*) For dynamic simulations with iterative solvers, the SP accuracy is often sufficient; (*ii*) The SE method is able to reach the round-off error of the SP arithmetics with proper parameter selection due to its spectral accuracy; and (*iii*) The far-field HIs captured by the mobility computations are more smooth compared to the near-field interactions, which are evaluated in DP on CPUs. Note that the near-field interactions have to be evaluated in DP as they change rapidly for close particles and become singular at particle contact. The split of the near- and the far-field HIs in SD allows a natural mixed precision HI computation that captures the most significant contributions from each part.

The GPGPU computations exploit the massively parallel structure of modern GPUs by simultaneously executing a large number of similar tasks, or threads, on the data. To maintain performance, data dependencies and communications between threads should be minimized. This makes the GPU implementation of the SE method differ-

ent from its CPU counterpart. Inspired by earlier GPU implementations of particle mesh techniques, this work combines the grid-based method of Ganesan *et al.* [47] for force interpolation and the particle-based approach of Harvey & De Fabritiis [48] for convolution. The grid-based force interpolation keeps a list of contributing particles for each grid point, and the list is updated when the particle configurations are changed. The grid values are computed in parallel using M^3 threads: with the particle list, each thread sums the force, torque, and stresslet contributions independently for each grid point. On the other hand, the particle-based convolution is a weighted summation on P^3 grid points for each particle. To maximize parallelization, the summation for each particle is performed by a group of P threads cooperatively. Each thread in the group first sums P^2 grid points on the transverse plane, and for the final result, the first thread in the group adds up the values from other threads using the shared memory of the GPU. Moreover, on the GPU we use the `cufft` package for the FFTs and the `cusparse` package for the sparse matrix-vector multiplication.

4.4 Dynamic simulation with Stokesian Dynamics

The framework of SD [7, 64] approximates the projected grand resistance tensor $\mathcal{R}$ in Eq. (4.12) as

$$\mathcal{R} = \mathfrak{M}^{-1} + \mathcal{R}^{\mathrm{nf}}, \tag{4.53}$$

where $\mathfrak{M}$ is the multipole grand mobility tensor, and $\mathcal{R}^{\mathrm{nf}}$ is the pairwise additive lubrication correction without the far-field contributions. Recall that the inversion of $\mathfrak{M}$ captures the many-body aspect of HIs, and the short-range correction $\mathcal{R}^{\mathrm{nf}}$ captures the lubrication effects. The SD recovers the exact result for two-body problems and agrees well with the exact solutions of three-body problems [72]. It can provide significant insights to the HIs of dense suspensions [73, 74].

Iterative computation of hydrodynamic interactions

We incorporate the SE mobility computation into the framework of SD using the iterative scheme of Swan & Brady [63], and call the resulting method the Spectral Ewald Accelerated Stokesian Dynamics (SEASD). Here, a matrix-free iterative scheme is necessary as the grand mobility tensor $\mathfrak{M}$ is not explicitly constructed. The iterative scheme splits the overall hydrodynamic force,

$$\mathcal{F}^{\mathrm{H}} = -\boldsymbol{R}_{\mathcal{F}\mathcal{U}} \cdot \mathcal{U}^{\mathrm{H}} + \boldsymbol{R}_{\mathcal{F}\mathrm{E}} \cdot \mathbf{E}^{\infty}, \tag{4.54}$$

where $\mathcal{U}^{\mathrm{H}}$ is the velocity disturbances due to HIs, into a near-field part and a far-field part. The near-field part satisfies

$$0 = -\boldsymbol{R}^{\mathrm{nf}}_{\mathcal{F}\mathcal{U}} \cdot \mathcal{U}^{\mathrm{H}} + \mathcal{F}^{\mathrm{H,ff}} + \widetilde{\mathcal{F}}^{\mathrm{P}}, \tag{4.55}$$

where $\boldsymbol{R}^{\mathrm{nf}}_{\mathcal{F}\mathcal{U}}$ is the $\mathcal{F}\mathcal{U}$ coupling in $\mathcal{R}^{\mathrm{nf}}$ and is stored as a sparse matrix, $\widetilde{\mathcal{F}}^{\mathrm{P}} = \mathcal{F}^{\mathrm{P}} + \boldsymbol{R}^{\mathrm{nf}}_{\mathcal{F}\mathrm{E}} \cdot \mathbf{E}^{\infty}$ contains the interparticle force $\mathcal{F}^{\mathrm{P}}$ and the near-field contributions from $\mathbf{E}^{\infty}$. The far-field hydrodynamic force $\mathcal{F}^{\mathrm{H,ff}}$ satisfies

$$\begin{bmatrix} \mathcal{U}^{\mathrm{H}} \\ -\mathbf{E}^{\infty} \end{bmatrix} = -\mathfrak{M} \cdot \begin{bmatrix} \mathcal{F}^{\mathrm{H,ff}} \\ \mathbf{S}^{\mathrm{H,ff}} \end{bmatrix}, \tag{4.56}$$

where $\mathbf{S}^{\mathrm{H,ff}}$ is the far-field stresslet from HIs. Solving Eqs. (4.55) and (4.56), the far-field hydrodynamic forces and stresslets are

$$\begin{bmatrix} \widetilde{\mathcal{F}}^{\mathrm{H,ff}} \\ \mathbf{S}^{\mathrm{H,ff}} \end{bmatrix} = \widetilde{\mathfrak{M}}^{-1} \cdot \left((\lambda_R \mathfrak{M} - \mathcal{I}) \cdot \begin{bmatrix} (\widetilde{\boldsymbol{R}}^{\mathrm{nf}}_{\mathcal{F}\mathcal{U}})^{-1} \cdot \widetilde{\mathcal{F}}^{\mathrm{P}} \\ \mathbf{0} \end{bmatrix} + \begin{bmatrix} \mathbf{0} \\ \mathbf{E}^{\infty} \end{bmatrix} \right), \tag{4.57}$$

where

$$\widetilde{\mathfrak{M}} = \left((\mathcal{I} - \lambda_R \mathfrak{M}) \cdot \begin{bmatrix} (\widetilde{\boldsymbol{R}}^{\mathrm{nf}}_{\mathcal{F}\mathcal{U}})^{-1} & \mathbf{0} \\ \mathbf{0} & \mathbf{0} \end{bmatrix} + \mathfrak{M} \right). \tag{4.58}$$

To ensure invertibility, a diagonal matrix $\lambda_R \boldsymbol{I}$, with λ_R a parameter, is added to $\boldsymbol{R}^{\mathrm{nf}}_{\mathcal{F}\mathcal{U}}$, *i.e.*, $\widetilde{\boldsymbol{R}}^{\mathrm{nf}}_{\mathcal{F}\mathcal{U}} = \boldsymbol{R}^{\mathrm{nf}}_{\mathcal{F}\mathcal{U}} + \lambda_R \boldsymbol{I}$, and accordingly $\widetilde{\mathcal{F}}^{\mathrm{H,ff}} = \mathcal{F}^{\mathrm{H,ff}} + \lambda_R \mathcal{U}^{\mathrm{H}}$. A convenient choice for λ_R is $6\pi\eta_0 a$, where a is the reference particle radius [63].

Solving Eq. (4.57) requires nested iteration as each evaluation of $\widetilde{\mathfrak{M}}$ contains the solution of the near-field problem with $\widetilde{\boldsymbol{R}}^{\mathrm{nf}}_{\mathcal{F}\mathcal{U}}$. The near-field problem is efficiently solved by the Generalized Minimum Residual (GMRES) method with an Incomplete Cholesky preconditioner with zero fill-in (IC0) [75]. To reduce the IC0 breakdown, prior to applying the preconditioner the particles are reordered using the reverse Cuthill-McKee algorithm. For isotropic suspensions, the near-field problem typically converges to an error of 10^{-4} within 10 iterations [36]. For suspensions with strong structural anisotropy, however, the convergence becomes more difficult and the IC0 preconditioner breaks down even with the reordering. This is resolved by increasing λ_R in $\widetilde{\boldsymbol{R}}^{\mathrm{nf}}_{\mathcal{F}\mathcal{U}}$, or introducing a threshold value λ_{IC} during the IC0 preconditioner computation [75]. Increasing λ_R in $\widetilde{\boldsymbol{R}}^{\mathrm{nf}}_{\mathcal{F}\mathcal{U}}$ does not change the convergence of the near-field problem, but increases the number of expensive $\widetilde{\mathfrak{M}}$ iterations. On the other hand, increasing λ_{IC} deteriorates the quality of the IC0 preconditioner and increases the iterations required for the near-field problem, but has little effect on the far-field evaluations. In dynamic simulations, both λ_R and λ_{IC} are adjusted for

optimal computation efficiency. The current SEASD implementation uses the fact that the near-field evaluation is faster than the far-field evaluation. In the event of an IC0 breakdown, the algorithm tries to recalculate the IC0 preconditioner with an increased λ_{IC} until the ratio $\lambda_{\text{IC}}/\lambda_R$ exceeds a threshold. After that, the algorithm also increases the parameter λ_R and regenerates $\widetilde{\boldsymbol{R}}^{\text{nf}}_{\mathcal{FU}}$ for further calculations. This process is repeated until a successful IC0 preconditioner generation. Presently, the $\lambda_{\text{IC}}/\lambda_R$ threshold is 7 and the increments for λ_{IC} and λ_R are 5.

The pressure moment computation in SEASD also follows the near- and far-field splitting scheme in Eqs. (4.55) and (4.56). Due to the special coupling between the pressure moments and other force moments in compressible suspensions (Sec. 4.2), the interaction contribution to the far-field pressure moment is evaluated after $\boldsymbol{F}^{\text{H,ff}}$ and the traceless part of $\mathbf{S}^{\text{H,ff}}$ are solved in Eq. (4.57). On the other hand, the near-field part of the pressure moment is evaluated along with other parts of the stresslets using the near-field resistance functions.

The near-field pairwise lubrication corrections $\mathcal{R}^{\text{nf}}$ are based on the exact solutions of two-body problems in series form [65, 66, 76, 77] up to s^{-300}, where $s = 2r/(a_i+a_j)$, with a_i and a_j the radii of the pair, is the scaled particle center-center distance. In the simulations, the lubrication corrections are activated when $s < 4$: for $s > 2.1$ the interpolation of tabulated data and for $s \leq 2.1$ the analytical expressions are used. Note that $\mathcal{R}^{\text{nf}}$ constructed from two-body problems contains both the relative and the collective motions of the particle pair and, as pointed out by Cichocki *et al.* [23], the lubrication corrections corresponding to the collective motion can destroy the far-field asymptotes beyond the pair level. However, for dense suspensions, this only leads to a minor quantitative difference on the suspension static properties [11] in conventional SD. Therefore, we retain the full lubrication correction here for consistency with the existing SD framework. The SD implementations of Ando & Skolnick [13] removed the pair collective motion in the lubrication corrections.

Far-field preconditioner

Here we introduce a preconditioner for $\widetilde{\mathfrak{M}}$ to reduce the number of expensive far-field mobility evaluations when solving Eq. (4.57). Since $\widetilde{\mathfrak{M}}$ is not explicitly constructed, the preconditioner needs to be built from a suitable approximation. For mobility problems without the lubrication corrections, Saintillan *et al.* [37] and Keaveny [44] found substantial iteration improvement even with the diagonal mobility approximation. Unfortunately, the approximation of $\widetilde{\mathfrak{M}}$ is more involved due to the presence

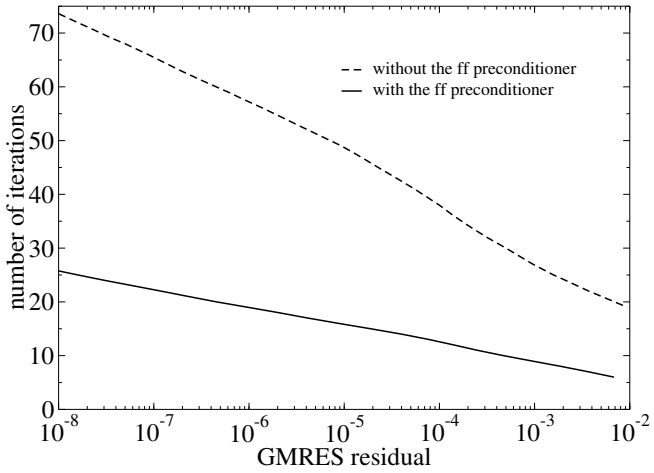

Figure 4.1: The number of far-field iterations, *i.e.*, the number of the grand mobility tensor $\widetilde{\mathfrak{M}}$ evaluations, as a function of the GMRES residual with (solid line) and without (dashed line) the far-field preconditioner for a bidisperse suspension of $N = 200$, $\lambda = 2$, $x_2 = 0.3$, and $\phi = 0.2$.

of $(\widetilde{\boldsymbol{R}}^{\mathrm{nf}}_{\mathcal{FU}})^{-1}$. In this work, a block diagonal approximation of $\widetilde{\mathfrak{M}}$ for the far-field preconditioner is adopted. First, the near-field resistance tensor $\widetilde{\boldsymbol{R}}^{\mathrm{nf}}_{\mathcal{FU}}$ is approximated by N blocks of 6×6 submatrices along its diagonal. Using the direct sum notation, this is $\bigoplus_{i=1}^{N} (\widetilde{\boldsymbol{R}}^{\mathrm{nf}}_{\mathcal{FU}})_{ii}$, where $\bigoplus$ is the direct sum, and $(\widetilde{\boldsymbol{R}}^{\mathrm{nf}}_{\mathcal{FU}})_{ij}$ is the block submatrix between particles i and j in $\widetilde{\boldsymbol{R}}^{\mathrm{nf}}_{\mathcal{FU}}$. To approximate $\widetilde{\mathfrak{M}}$, we use

$$(\widetilde{\boldsymbol{R}}^{\mathrm{nf}}_{\mathcal{FU}})^{-1} \approx \bigoplus_{i=1}^{N} [(\widetilde{\boldsymbol{R}}^{\mathrm{nf}}_{\mathcal{FU}})_{ii}]^{-1}, \tag{4.59}$$

which only involves N inversion of 6×6 matrices. The mobility tensor $\mathfrak{M}$ is approximated by its block-diagonal components using direct Ewald summation, *i.e.*, for each particle, the approximation only considers the interactions with its periodic images. To obtain the preconditioner, we apply the Incomplete LU decomposition with zero fill-in (ILU0) [75] on the approximated $\widetilde{\mathfrak{M}}$, which is constructed following Eq. (4.58) with the approximated $(\widetilde{\boldsymbol{R}}^{\mathrm{nf}}_{\mathcal{FU}})^{-1}$ and $\mathfrak{M}$. Unlike Saintillan *et al.* [37], including close pair interactions has an adverse effect on the preconditioner due to the diagonal approximation of $\widetilde{\boldsymbol{R}}^{\mathrm{nf}}_{\mathcal{FU}}$.

The effectiveness of this preconditioner on the far-field iteration is demonstrated in Fig. 4.1 and Table 4.1. In this case, the HIs corresponding to random forces and strain rates are solved for a random bidisperse suspension of 200 particles with $\lambda = 2$, $x_2 = 0.3$, and $\phi = 0.2$, and the SE parameters are $\xi = 0.5$, $(M, P) = (64, 15)$,

Table 4.1: The wall time (in seconds) for solving Eq. (4.57) at different GMRES residuals with and without the far-field preconditioner using the CPU and the GPU mobility computation. The second column includes the time for constructing the approximate $\widetilde{\mathfrak{M}}$ and its ILU0 decomposition. The configurations and parameters are the same as Fig. 4.1.

	ILU0	GMRES residual						
		10^{-8}	10^{-7}	10^{-6}	10^{-5}	10^{-4}	10^{-3}	10^{-2}
CPU, direct	–	4.16	3.66	3.19	2.71	2.14	1.54	1.12
CPU, ff precond.	0.0146	1.56	1.32	1.13	0.977	0.845	0.632	0.466
GPU, direct	–	–	–	–	0.190	0.144	0.101	0.0724
GPU, ff precond.	0.0154	–	–	–	0.0683	0.0541	0.0395	0.0286

$r_c = 4(a_i + a_j)$, and $m = 8$. For these parameters, the far-field preconditioner substantially reduces the number of GMRES iterations and the computation time by a factor between 2.5 and 3, depending on the GMRES residual. The time required for constructing the approximate $\widetilde{\mathfrak{M}}$ and its ILU0 decomposition is far less than the GMRES computation time, even with the GPU acceleration at a residual of 10^{-2}. Therefore, for the parameters in Fig. 4.1, using the far-field preconditioner is always justified. Generally speaking, however, the preconditioner is preferred for small GMRES residual, and the exact break-even point depends on the SE parameters such as M, P, and r_c. Moreover, since the preconditioner construction is an $O(N)$ operation and the $\widetilde{\mathfrak{M}}$ evaluation scales as $O(N \log N)$, preconditioning is always justified for large systems. In addition, in dynamic simulations, further time saving is possible by updating the preconditioner every few time steps.

Dynamic simulation of Brownian suspensions

Particle dynamics in a suspension are described by the generalized N-body Langevin equation,

$$\mathbf{m} \cdot \frac{\mathrm{d}\mathcal{U}}{\mathrm{d}t} = \mathcal{F}^{\mathrm{H}} + \mathcal{F}^{\mathrm{P}} + \mathcal{F}^{\mathrm{B}}, \tag{4.60}$$

where $\mathbf{m}$ is the generalized mass/moment of inertial matrix, $\mathcal{U}$ is the generalized particle velocity and $\mathcal{F}^{\mathrm{H}}$, $\mathcal{F}^{\mathrm{P}}$, and $\mathcal{F}^{\mathrm{B}}$ are the forces on particles. The hydrodynamic force $\mathcal{F}^{\mathrm{H}}$ arises from the HIs and can be computed from Eq. (4.54). The interparticle force $\mathcal{F}^{\mathrm{P}}$ originates from the interparticle potentials. The Brownian force $\mathcal{F}^{\mathrm{B}}$ is due to thermal fluctuations in the solvent, and from the fluctuation-dissipation theorem [78], $\mathcal{F}^{\mathrm{B}}$ satisfies

$$\overline{\mathcal{F}^{\mathrm{B}}(t)} = 0 \text{ and } \overline{\mathcal{F}^{\mathrm{B}}(0)\mathcal{F}^{\mathrm{B}}(t)} = 2k_{\mathrm{B}}T\delta(t)\boldsymbol{R}_{\mathcal{F}\mathcal{U}}. \tag{4.61}$$

Here, the overline denotes an average over the solvent fluctuations and $k_{\mathrm{B}}T$ is the thermal energy scale.

The configuration evolution is obtained by integrating Eq. (4.60) twice over an appropriate time scale Δt, and the result is [38, 79]

$$\Delta X = \left[\mathcal{U}^{\infty} + \boldsymbol{R}^{-1}_{\mathcal{F}\mathcal{U}} \cdot \left(\boldsymbol{R}_{\mathcal{F}\mathrm{E}} \cdot \mathbf{E}^{\infty} + \mathcal{F}^{\mathrm{P}}\right)\right]\Delta t + k_{\mathrm{B}}T\boldsymbol{\nabla} \cdot \boldsymbol{R}^{-1}_{\mathcal{F}\mathcal{U}}\Delta t + \Delta X^{\mathrm{B}}, \tag{4.62}$$

where ΔX is the suspension configuration change over time Δt, $\mathcal{U}^{\infty}$ is the generalized velocity from the imposed flow, and ΔX^{B} is the Brownian displacement which satisfies

$$\overline{\Delta X^{\mathrm{B}}} = 0 \text{ and } \overline{\Delta X^{\mathrm{B}}\Delta X^{\mathrm{B}}} = 2k_{\mathrm{B}}T\Delta t\boldsymbol{R}^{-1}_{\mathcal{F}\mathcal{U}}. \tag{4.63}$$

The second term on the right hand side of Eq. (4.62) is the deterministic drift due to the configuration dependent Brownian force $\mathcal{F}^{\mathrm{B}}$, and the divergence operator is acting on the last index of $\boldsymbol{R}^{-1}_{\mathcal{F}\mathcal{U}}$. The divergence can be numerically evaluated following Banchio & Brady [39].

The suspension bulk stress is obtained by spatially averaging the Cauchy stress [50, 51], *i.e.*,

$$\langle \boldsymbol{\Sigma} \rangle = -\langle p \rangle_{\mathrm{f}} \mathbf{I} + 2\eta_0 \left\langle \overline{\mathbf{E}^{\infty}} \right\rangle + (\kappa_0 - \tfrac{2}{3}\eta_0) E^{\infty} \mathbf{I} - n k_{\mathrm{B}} T \mathbf{I} + n(\langle \mathbf{S}^{\mathrm{E}} \rangle + \langle \mathbf{S}^{\mathrm{P}} \rangle + \langle \mathbf{S}^{\mathrm{B}} \rangle), \quad (4.64)$$

where $\langle p \rangle_{\mathrm{f}}$ is the average solvent pressure, $\langle \cdot \rangle$ is the volume average over the entire suspension, κ_0 is the fluid bulk viscosity, and n is the particle number density. The particle stresslets $\mathbf{S}^{\mathrm{H}}$ are broken down as $\mathbf{S}^{\mathrm{H}} = \mathbf{S}^{\mathrm{E}} + \mathbf{S}^{\mathrm{P}} + \mathbf{S}^{\mathrm{B}}$, where $\mathbf{S}^{\mathrm{E}}$ is the contributions from the imposed flow, $\mathbf{S}^{\mathrm{P}}$ from the interparticle potential, and $\mathbf{S}^{\mathrm{B}}$ from the Brownian motion. Their suspension averages are expressed in resistance tensors

$$\langle \mathbf{S}^{\mathrm{E}} \rangle = -\langle \boldsymbol{R}_{\mathrm{S}\mathcal{U}} \cdot \boldsymbol{R}^{-1}_{\mathcal{F}\mathcal{U}} \cdot \boldsymbol{R}_{\mathcal{F}\mathrm{E}} - \boldsymbol{R}_{\mathrm{SE}} \rangle : \langle \mathbf{E}^{\infty} \rangle, \quad (4.65)$$

$$\langle \mathbf{S}^{\mathrm{P}} \rangle = -\langle (\boldsymbol{R}_{\mathrm{S}\mathcal{U}} \cdot \boldsymbol{R}^{-1}_{\mathcal{F}\mathcal{U}} + \boldsymbol{r}\mathbf{I}) \cdot \boldsymbol{F}^{\mathrm{P}} \rangle, \quad (4.66)$$

$$\langle \mathbf{S}^{\mathrm{B}} \rangle = -k_{\mathrm{B}} T \langle \boldsymbol{\nabla} \cdot (\boldsymbol{R}_{\mathrm{S}\mathcal{U}} \cdot \boldsymbol{R}^{-1}_{\mathcal{F}\mathcal{U}}) \rangle, \quad (4.67)$$

where the divergence in Eq. (4.67) is applied to the last index in the bracket. For hard-sphere suspensions, $\langle \mathbf{S}^{\mathrm{P}} \rangle = 0$ as the HI and the interparticle force contributions exactly cancel each other [51]. The Brownian stresslet $\langle \mathbf{S}^{\mathrm{B}} \rangle$ can also be computed using the modified mid-point scheme [39].

In dynamic simulations, the Brownian displacement ΔX^{B} is evaluated from the Brownian force $\mathcal{F}^{\mathrm{B}}$ in Eq. (4.61) as

$$\Delta X^{\mathrm{B}} = \boldsymbol{R}^{-1}_{\mathcal{F}\mathcal{U}} \cdot \mathcal{F}^{\mathrm{B}} \Delta t. \quad (4.68)$$

Following Banchio & Brady [39], the Brownian force can be split into a near-field part and a far-field part,

$$\mathcal{F}^{\mathrm{B}} = \mathcal{F}^{\mathrm{B,nf}} + \mathcal{F}^{\mathrm{B,ff}}. \quad (4.69)$$

Both $\mathcal{F}^{\mathrm{B,nf}}$ and $\mathcal{F}^{\mathrm{B,ff}}$ have zero mean and satisfy

$$\overline{\mathcal{F}^{\mathrm{B,nf}} \mathcal{F}^{\mathrm{B,nf}}} = \frac{2k_{\mathrm{B}}T}{\Delta t} \boldsymbol{R}^{\mathrm{nf}}_{\mathcal{F}\mathcal{U}}, \quad (4.70)$$

$$\overline{\mathcal{F}^{\mathrm{B,ff}} \mathcal{F}^{\mathrm{B,ff}}} = \frac{2k_{\mathrm{B}}T}{\Delta t} (\mathfrak{M}^{-1})_{\mathcal{F}\mathcal{U}}, \quad (4.71)$$

$$\overline{\mathcal{F}^{\mathrm{B,ff}} \mathcal{F}^{\mathrm{B,nf}}} = 0, \quad (4.72)$$

where $(\mathfrak{M}^{-1})_{\mathcal{FU}}$ is the $\mathcal{FU}$ block of the inverted far-field grand mobility tensor. The pairwise-additive lubrication corrections allow pairwise evaluation of the near-field Brownian force $\mathcal{F}^{\mathrm{B,nf}}$ [39]. Since $\mathfrak{M}$ is not explicitly constructed, to compute $\mathcal{F}^{\mathrm{B,ff}}$, it is necessary to solve

$$\begin{bmatrix} \mathcal{F}^{\mathrm{B,ff}} \\ \Delta \mathbf{S}^{\mathrm{B}} \end{bmatrix} = \frac{2k_{\mathrm{B}}T}{\Delta t} (\mathfrak{M}^{-1/2}) \cdot \mathbf{\Psi}, \tag{4.73}$$

where $\mathbf{\Psi}$ is a Gaussian noise of zero mean and unit variance, and $\Delta \mathbf{S}^{\mathrm{B}}$ is the fluctuation part of the Brownian stress in Eq. (4.67). The inverse square root of the grand mobility tensor $\mathfrak{M}^{-1/2}$ in Eq. (4.73) can be approximated using Chebychev polynomials with eigenvalue estimations [39, 80], or solved as an Initial Value Problem (IVP) [40, 81], which was first used by Swan & Brady [40] in ASD. The solution of the following IVP [82] with matrix $\boldsymbol{A}$,

$$\frac{\mathrm{d}\boldsymbol{x}}{\mathrm{d}\tau} = -\tfrac{1}{2} \left[\tau \boldsymbol{I} + (1-\tau)\boldsymbol{A}\right]^{-1} \cdot (\boldsymbol{A} - \boldsymbol{I}) \cdot \boldsymbol{x}, \ \boldsymbol{x}(0) = \boldsymbol{c}, \tag{4.74}$$

at $\tau = 1$ satisfies $\boldsymbol{x}(1) = \boldsymbol{A}^{-1/2} \cdot \boldsymbol{c}$. Swan & Brady [40] devised a numerical scheme to solve Eq. (4.74) in ASD: at each time step with step size $\Delta\tau$, Eq. (4.74) is marched first with a Euler forward half-step then a Euler backward half-step, *i.e.*,

$$\frac{\boldsymbol{x}_{i+\frac{1}{2}} - \boldsymbol{x}_i}{\Delta\tau/2} = -\tfrac{1}{2} \left[\tau_i \boldsymbol{I} + (1-\tau_i)\boldsymbol{A}\right]^{-1} \cdot (\boldsymbol{A} - \boldsymbol{I}) \cdot \boldsymbol{x}_i, \tag{4.75}$$

$$\frac{\boldsymbol{x}_{i+1} - \boldsymbol{x}_{i+\frac{1}{2}}}{\Delta\tau/2} = -\tfrac{1}{2} \left[\tau_{i+1} \boldsymbol{I} + (1-\tau_{i+1})\boldsymbol{A}\right]^{-1} \cdot (\boldsymbol{A} - \boldsymbol{I}) \cdot \boldsymbol{x}_{i+1}. \tag{4.76}$$

With $\boldsymbol{A} = \mathfrak{M}$ and $\boldsymbol{c} = (2k_{\mathrm{B}}T/\Delta t)\mathbf{\Psi}$, Eq. (4.73) is solved at $\tau = 1$. In SEASD, both Eqs. (4.75) and (4.76) are solved iteratively, usually with a smaller tolerance compared to $\Delta\tau$. The results with $\Delta\tau = 0.1$ are often satisfactory.

For dynamic simulation of Brownian suspensions under a simple shear flow with strain rate $\dot{\gamma}$, the ratio of the convective transport rate $\dot{\gamma}$ and the diffusive transport rate $k_{\mathrm{B}}T/(6\pi\eta_0 a_{\mathrm{p}}^3)$ defines the Péclet number,

$$\mathrm{Pe} = \frac{6\pi\eta_0 a_{\mathrm{p}}^3 \dot{\gamma}}{k_{\mathrm{B}}T}. \tag{4.77}$$

Small Pe indicates Brownian motion dominance, and large values suggest negligible Brownian influences. For bidisperse suspensions, we define Pe based on the size of the small particles to capture the dynamics of the most rapid changes, *i.e.*, $a_{\mathrm{p}} = a_1$. In dynamic simulations, the time in Eq. (4.62) is scaled according to the Péclet number: when $\mathrm{Pe} \leq 1$, it is scaled with the diffusive time scale of the small particles, $6\pi\eta_0 a_1^3/(k_{\mathrm{B}}T)$, and when $\mathrm{Pe} > 1$, the convective time scale $\dot{\gamma}^{-1}$.

The mean-field Brownian approximation

The most time-consuming step in dynamic simulations of Brownian suspensions is computing $\mathcal{F}^{\mathrm{B,ff}}$ from Eq. (4.73) due to the large number of $\mathfrak{M}$ evaluations, although the IVP approach in Sec. 4.4 is expected to be faster than the Chebychev approximation [40]. Further speed improvement is possible by introducing a mean-field approximation of the Brownian-related quantities [39]. In this approach, the far-field grand mobility tensor $\mathfrak{M}$ is approximated as a diagonal matrix for all Brownian-related computations, and the full HI computations are retained for the flow-related quantities such as $\mathbf{S}^{\mathrm{E}}$. As a result, this method retains the $O(N \log N)$ scaling, but with an order of magnitude smaller prefactor for monodisperse suspensions [39]. The diagonal approximation of $\mathfrak{M}$ uses the single particle result for the ES coupling, and the far-field translational and rotational short-time self-diffusivities for the $\mathcal{UF}$ coupling. These far-field values are from Monte-Carlo computations of equilibrium configurations at the same volume fraction *without* the lubrication corrections. Extending this approach to polydisperse suspensions is trivial: the suspension far-field diffusivities in the diagonal elements are replaced by the far-field diffusivities for each species. The mean-field Brownian approximation is especially suitable for studying dense suspension rheology, where the HIs are dominated by the near-field lubrication interactions. Following Brady & Banchio [39], we designate this approximation scheme SEASD-nf.

4.5 Accuracy and performance

Mobility computation accuracy

The accuracy of the mobility computation is characterized by the relative ∞-norm of the strain rate, *i.e.*,

$$e_{\infty,r}(E) = \max_{i\in\{1,\dots,N\}} \frac{\|\mathbf{E}_i^{\mathrm{SE}} - \mathbf{E}_i^{*}\|}{\|\mathbf{E}_i^{*}\|}, \tag{4.78}$$

where $\mathbf{E}_i^{\mathrm{SE}}$ is the particle strain rate from the SE method and $\mathbf{E}_i^{*}$ is a well-converged value from direct Ewald summation. Other error measurements can be similarly defined. For example, $e_{\infty,r}(U)$ for the linear velocity was used by Lindbo & Tornberg [29] to characterize the accuracy of the SE method for point forces. For the stresslet-strain rate level mobility computation here, we found $e_{\infty,r}(E)$ the most stringent error criteria, possibly because more derivatives are involved in Eq. (4.15).

To facilitate quantitative discussions, in this section we focus on a random bidisperse hard-sphere system of $N = 50$, $\phi = 0.05$, $\lambda = 2$, and $x_2 = 0.3$. The imposed force,

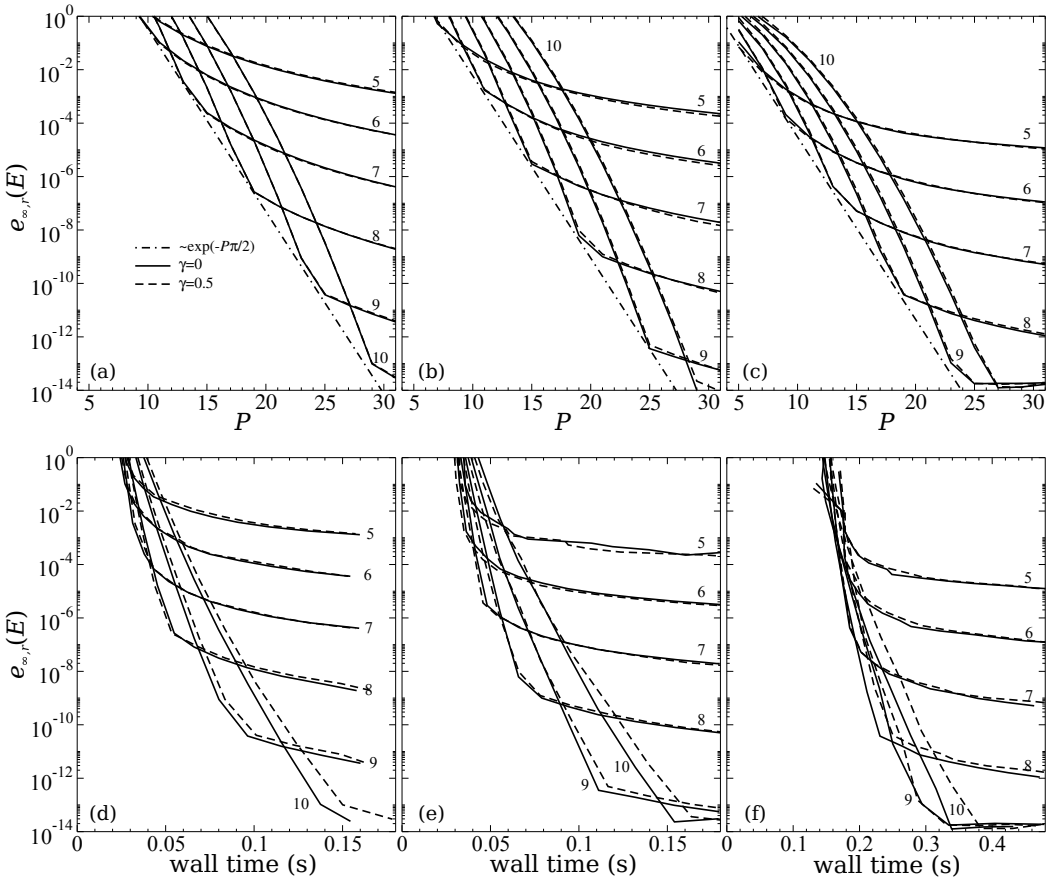

Figure 4.2: The wave-space accuracy measured by $e_{\infty,r}(E)$ [Eq. (4.78)] as a function of the interpolation point P (a–c) and the CPU wall time in seconds (d–f) with various shape parameter m at $M = 64$ and $\xi a_1 = 0.1$. The particle size effects are incorporated using (a), (d): the real-space, (b), (e): the hybrid, and (c), (f): the wave-space approaches in Sec. 4.3. The values of m are annotated in each figure. The solid and dashed lines represent the case of $\gamma = 0$ and 0.5, respectively. The dashed dotted lines show the exponential minimum error decay, $e_{\infty,r}(E) \sim \exp(-P\pi/2)$.

torque, and stresslet on each particle are randomly drawn from a normal distribution, and scaled to ensure $\|\boldsymbol{F}_i\| = 1$, $\|\boldsymbol{T}_i\| = 1$, and $\|\mathbf{S}_i\| = 1$. The simulation box lattice vectors are $\mathbf{a}_1 = (L, 0, 0)$, $\mathbf{a}_2 = (\gamma L, L, 0)$, and $\mathbf{a}_3 = (0, 0, L)$, with γ the strain. The computations are carried out in DP accuracy on CPU.

Wave-space accuracy

Fig. 4.2 presents the accuracy of wave-space computations using different SE implementations with orthogonal ($\gamma = 0$) and sheared ($\gamma = 0.5$) simulation boxes in solid and dashed lines, respectively. The error $e_{\infty,r}(E)$ is shown as functions of the

interpolation point P and the CPU wall time (in seconds) with various shape parameter m at $M = 64$ and $\xi a_1 = 0.1$. Different particle size incorporation approaches discussed in Sec. 4.3 are presented: in Fig. 4.2a and 4.2d the real-space approach, in Fig. 4.2b and 4.2e the hybrid approach, and in Fig. 4.2c and 4.2f the wave-space approach.

There are several key observations in Fig. 4.2a–4.2c. First of all, the errors associated with orthogonal and sheared simulation boxes are almost identical. This validates the general formalism for non-orthogonal simulation boxes in Sec. 4.3. Secondly, the SE method is sensitive to P and m, which respectively correspond to the discretization and truncation of the shape function $h(\boldsymbol{t})$. At a given m, $e_{\infty,r}(E)$ first decreases exponentially, followed by a much slower reduction with increasing P. The two-stage reduction of $e_{\infty,r}(E)$ is well understood for point forces [29]: the exponential decrease is due to the improved resolution of the shape function, and the slower reduction is associated with the Gaussian truncation from the shape parameter m. Therefore, at large P and m the result is expected to be accurate; indeed, in Fig. 4.2 the minimum errors are all close to the machine precision. Such accuracy is inaccessible using the PME or the SPME method at this grid number ($M = 64$) due to the inherent coupling between the interpolation and the wave-space truncation errors. Moreover, for a given P, $e_{\infty,r}(E)$ first decreases to a minimum and then increases with increasing m. At the minimum, $e_{\infty,r}(E)$ is transitioning from exponential to slower decay, and the errors from the shape resolution are about the same as the errors from the Gaussian truncation. From the error estimation of Lindbo & Tornberg [29, 30], at a given P, the minimum wave-space error $e_{\infty,r}(E)$ and the corresponding shape parameter m are

$$e_{\infty,r}(E) \sim \exp(-P\pi/2) \text{ and } m \sim \sqrt{\pi P}, \tag{4.79}$$

respectively. The asymptotic exponential decay of the minimum $e_{\infty,r}(E)$ is also shown as dash-dotted lines in Fig. 4.2. The exponential decay of the minimum error with respect to P to the round-off precision at large P and m clearly demonstrate the spectral accuracy [83] of the SE method.

In Fig. 4.2a–4.2c, different particle size incorporation approaches exhibit similar qualitative behaviors with quantitative differences. For example, to achieve an accuracy of $e_{\infty,r}(E) \sim 10^{-4}$ at the optimal m, in Fig. 4.2a, 4.2b, and 4.2c the required P are respectively 15, 13, and 9, corresponding to the real-space, hybrid, and wave-space approaches discussed in Sec. 4.3. The latter two approaches reduce

the $h(\boldsymbol{t})$ evaluations by 35% and 78% compared to the real-space approach at a cost of the number of required FFTs. Therefore, there is a subtle balance between the number of interpolation points P and the number of FFTs in the SE method implementation. This balance is quantified in Fig. 4.2d–4.2f. In terms of the wall times, the real-space and the hybrid approaches are comparable, and both are much faster than the wave-space approach, which involves extensive FFT computations. Clearly, the accuracy gain in the wave-space approach cannot justify the large wall time over the entire P range. Meanwhile, for a given accuracy, the hybrid approach is slower than the real-space approach when $e_{\infty,r}(E) \gtrsim 10^{-4}$, and becomes faster when $e_{\infty,r}(E) \lesssim 10^{-4}$. Since fast computations with high accuracy are more relevant for dynamic simulations, the hybrid approach in Fig. 4.2b and 4.2e is adopted in SEASD.

Finally, Fig. 4.2 shows that, in addition to the spectral accuracy and the ease of implementation, the SE method also allows flexible error control by adjusting P and m without changing the grid points M. As a result, the errors from the wave-space summation and the interpolation can be separated, and this permits more flexible error control when computing HIs in polydisperse systems. On the other hand, such error separation is not possible in other particle mesh techniques such as the PME and the SPME methods.

Overall mobility accuracy

Both the wave-space and the real-space computations affect the overall mobility accuracy, and the controlling parameters are the grid point M, the interpolation point P, the Gaussian shape parameter m, the real-space cutoff radius r_c, and the splitting parameter ξ. Out of the five parameters, only changes in ξ and m do not affect the computational cost since adjusting M affects the FFT size, changing r_c influences the number of near neighbors, *etc.* With a fixed computation cost, *i.e.*, fixed M, P, and r_c, it is desirable to find the combination of m and ξ that minimizes the overall error. Alternatively, with accurate error estimations, the parameter selection can start from a desired tolerance [30]. However, error estimations for hydrodynamic interactions beyond the point force level are unavailable and difficult to obtain. Therefore, the simple and pragmatic approach with fixed computational costs is adopted here.

Fig. 4.3 and 4.4 present the effects of m and ξ on the overall mobility accuracy with various P and r_c for $M = 64$ and 32, respectively. The wave-space computation uses

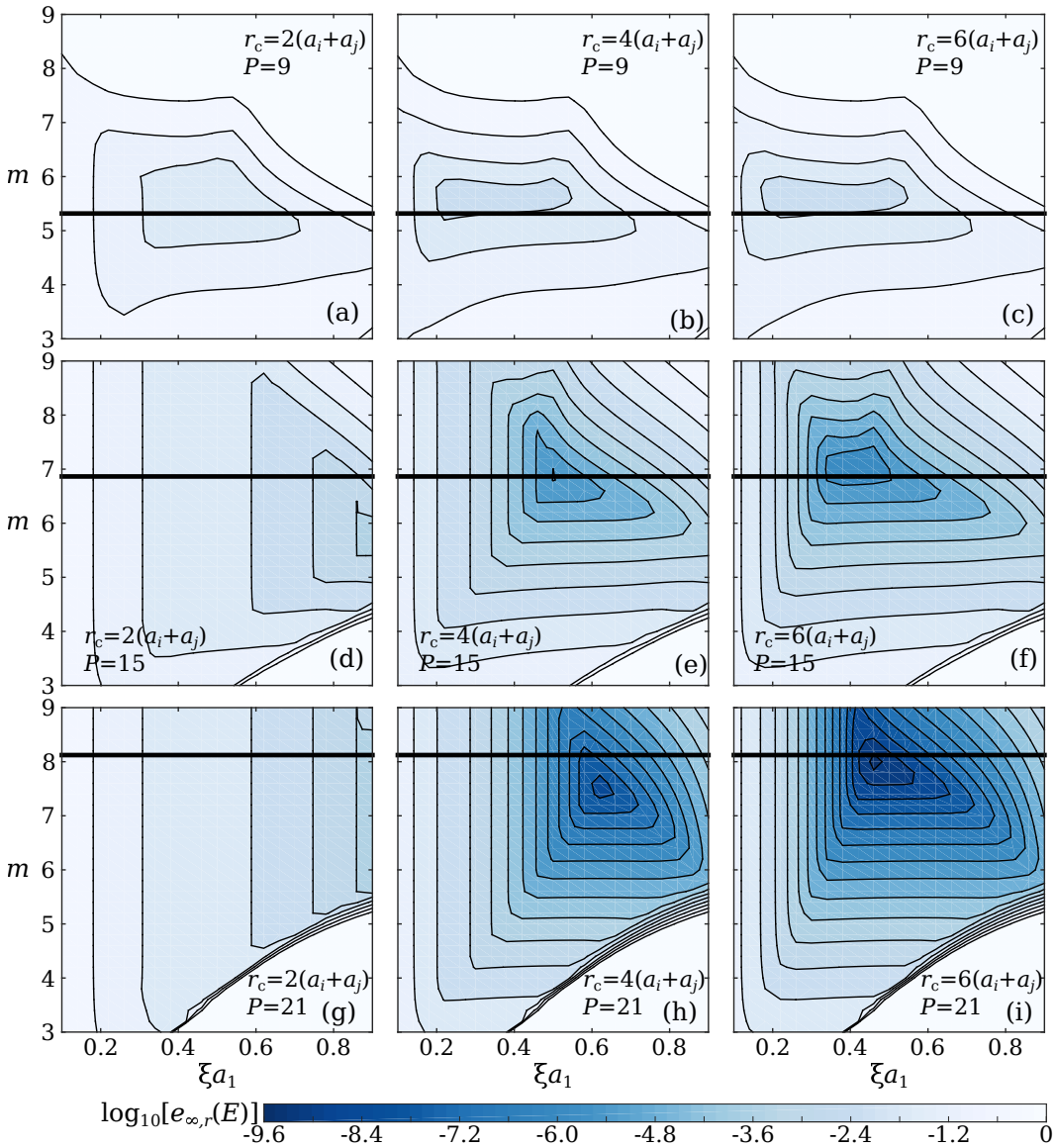

Figure 4.3: (Color online) The overall accuracy measured in $e_{\infty,r}(E)$ as a function of the splitting parameter ξa_1 and the shape parameter m at $M = 64$ for a real-space cutoff radius $r_c = 2(a_i+a_j)$ (left column), $4(a_i+a_j)$ (middle column), and $6(a_i+a_j)$ (right column), and the interpolation point $P = 9$ (top row), 15 (middle row), and 21 (bottom row). The thick black lines represent $m = \sqrt{\pi P}$. The simulation cell is orthogonal ($\gamma = 0$), and the particle size effects are accounted using the hybrid approach.

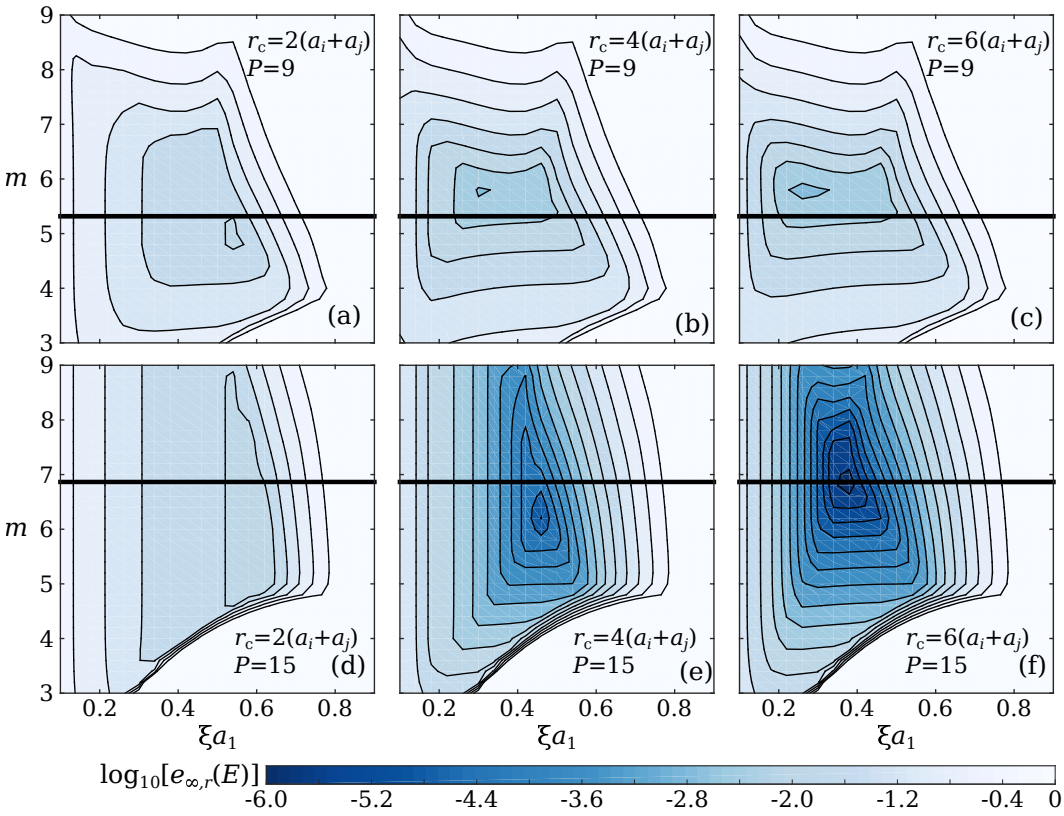

Figure 4.4: (Color online) The overall accuracy measured in $e_{\infty,r}(E)$ as a function of the splitting parameter ξa_1 and the shape parameter m with $M = 32$ for a real-space cutoff radius $r_c = 2(a_i+a_j)$ (left column), $4(a_i+a_j)$ (middle column), and $6(a_i+a_j)$ (right column), and the interpolation point $P = 9$ (top row) and 15 (bottom row). The thick black lines represent $m = \sqrt{\pi P}$. The simulation cell is orthogonal ($\gamma = 0$), and the particle size effects are accounted using the hybrid approach.

the hybrid approach in Sec. 4.3, and the simulation box is orthogonal ($\gamma = 0$). The thick black lines in these figures represent the optimal shape parameter $m = C\sqrt{\pi P}$ with $C = 1$. Although Lindbo & Tornberg [29, 30] established that the optimal m for the wave-space accuracy takes place with C slightly below unity, here the choice of $C = 1$ is for simplicity. Note that in our implementation, the cutoff radius r_c depends on the particle pair radii a_i and a_j.

It proves revealing to discuss Fig. 4.3 and 4.4 from the perspective of error sources. As mentioned earlier, the SE method allows separate controls in the real-space and wave-space truncation errors and the wave-space interpolation error. Earlier investigations of the SE method [29, 30] showed that the wave-space truncation errors for both the electrostatic and the hydrodynamic interactions decay as $e^{-[\pi\kappa_\infty/(\xi L)]^2}$ with $\kappa_\infty = \frac{1}{2}(M-1)$, and the real-space truncation errors decay as $e^{-\xi^2 r_c^2}$. The same

results should hold for the mobility computations here. The interpolation error, controlled by P and m, also affects the overall accuracy.

Parameters M (through κ_∞) and ξ influence the wave-space truncation errors. Comparing Fig. 4.3 and 4.4 shows the effects of M. Note that the color scales in these figures are different, and the minimum $e_{\infty,r}(E)$ in Fig. 4.3f and 4.4f is approximately the same. The qualitative features the two figures are similar. Quantitatively, decreasing M increases the wave space truncation error, and it shrinks the parameter space corresponding to $e_{\infty,r}(E) < 1$. Consequently, at $M = 32$, the accuracy of the mobility evaluation is more sensitive to ξa_1 compared to the case of $M = 64$. On the other hand, the wave-space truncation error grows with ξ. For all plots in Fig. 4.3 and 4.4, the overall error $e_{\infty,r}(E)$ increases with ξa_1 after it reaches a minimum. Apparently, the wave-space truncation error dominates the accuracy at large ξa_1.

The real-space truncation errors are directly affected by ξ and r_c. Contrary to the wave-space truncation error, increasing ξ improves the real-space accuracy in Fig. 4.3 and 4.4. The real-space truncation error dominates the overall accuracy at small ξa_1. The overall error $e_{\infty,r}(E)$ reaches a minimum at intermediate ξa_1 when the wave- and the real-space errors are approximately the same. Comparing rows in Fig. 4.3 and 4.4 illustrates that reducing r_c increases the real-space truncation error and shifts the $e_{\infty,r}(E)$ minimum towards larger ξa_1, *e.g.*, Fig. 4.3g–4.3i. It also shows a lesser reduction in $e_{\infty,r}(E)$ with increasing ξ at small ξa_1. With the small r_c in Fig. 4.3g, the minimum in $e_{\infty,r}(E)$ takes place at $\xi a_1 > 1$.

The SE interpolation error, controlled by m and P, also affects the overall accuracy. Consistent with observations in Fig. 4.2, the overall error $e_{\infty,r}(E)$ reaches a minimum with increasing m. The influences of m on $e_{\infty,r}(E)$ are less obvious when the overall accuracy is dominated by the real-space truncation error, *e.g.*, when $\xi a_1 < 0.46$ in Fig. 4.3i. Comparing columns in Fig. 4.3 and 4.4, *e.g.*, Fig. 4.3i, 4.3f, and 4.3c, shows that reducing P increases the interpolation error due to poor Gaussian resolution and shifts the $e_{\infty,r}(E)$ minimum towards lower m. Moreover, the overall accuracy deteriorates at large m and small P, *e.g.*, in Fig. 4.3c, $e_{\infty,r}(E) > 1$ when $m > 8$. In addition, the thick black lines representing $m = \sqrt{\pi P}$ provide a good approximation to the regions of the highest accuracy in both Fig. 4.3 and 4.4. This approximation, although not exact, substantially simplifies the search for the optimal ξ.

The influences of the particle number N on the overall mobility accuracy is presented in Fig. 4.5 for $M = 32$ and 64. The simulation box size is fixed at $L/a_1 = 23.5$ in

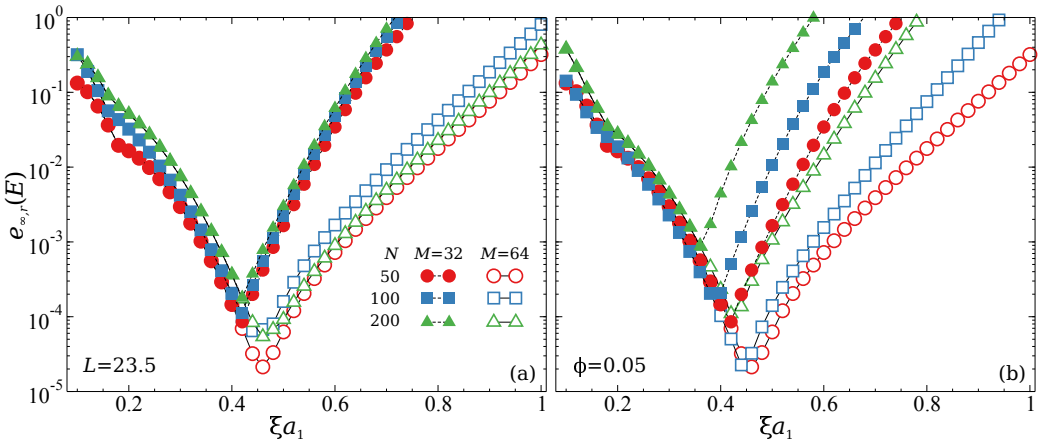

Figure 4.5: (Color online) The overall mobility accuracy measured in $e_{\infty,r}(E)$ as a function of the splitting parameter ξ with $N = 50$, 100, and 200, and $M = 32$ (filled symbols) and 64 (open symbols) for (a): constant box size $L/a_1 = 23.5$ and (b): constant volume fraction $\phi = 0.05$. Changes are based on the baseline case in Sec. 4.5. Other parameters are $P = 13$, $m = 6.7$, and $r_c = 4(a_i + a_j)$.

Fig. 4.5a, and the suspension volume fraction is fixed at $\phi = 0.05$ in Fig. 4.5b. Other parameters remain unchanged from the baseline case, and the mobility computation parameters are $P = 13$, $m = 6.7$, and $r_c = 4(a_i + a_j)$. The mobility accuracy is more sensitive to changes in L than changes in ϕ. In Fig. 4.5a, $e_{\infty,r}(E)$ changes little, but in Fig. 4.5b, the $e_{\infty,r}(E)$ minimum increases drastically with different N. The almost identical reduction in $e_{\infty,r}(E)$ at small ξa_1 suggests that the real-space error are not significantly affected by N in either case. The different $e_{\infty,r}(E)$ at higher ξa_1 in Fig. 4.5b shows that the wave-space computation is sensitive to the box size at fixed P and m. This is well-known for particle mesh techniques in general [29, 68]. Therefore, to retain the computational accuracy with larger systems at the same volume fraction, it is necessary to increase the grid point M or the interpolation point P. Note that the same qualitative error behaviors are found in the pressure moment computations.

Accuracy of the GPGPU implementation

The accuracy of the GPU mobility computation discussed in Sec. 4.3 is presented in Fig. 4.6. The GPU computations are clearly accurate enough for dynamic simulations. Fig. 4.6a shows the GPU wave-space accuracy as a function of the interpolation point P for various shape parameters m in orthogonal ($\gamma = 0$) and sheared ($\gamma = 0.5$) simulation boxes. Here, the particle size effects are incorporated using the hybrid approach in Sec. 4.3, and the SE method parameters are identical to those

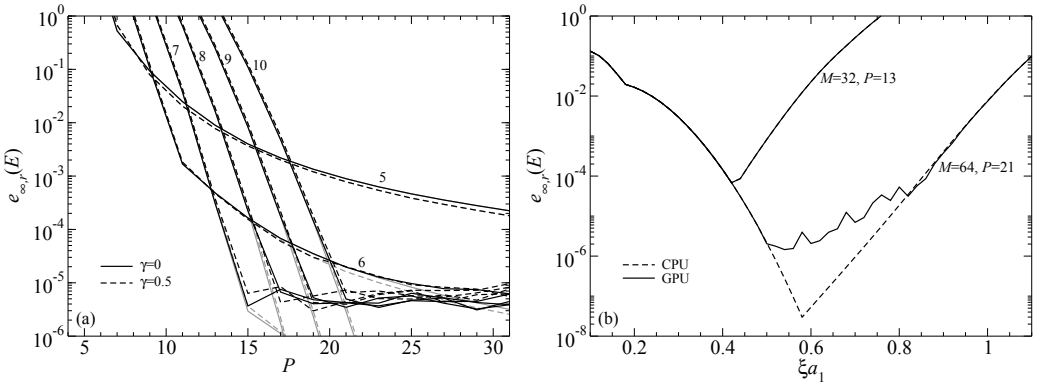

Figure 4.6: The accuracy of GPGPU mobility computation measured in $e_{\infty,r}(E)$. (a): the wave-space accuracy as a function of P for various m with the same parameters in Fig. 4.2b. The GPU results are shown in black lines, and the CPU results in Fig. 4.2b are reproduced in gray lines. The values of m are annotated in the figure. The solid and dashed lines represent the case of $\gamma = 0$ and 0.5, respectively. (b): The overall mobility accuracy from the GPU (solid lines) and the CPU (dashed lines) computations as a function ξa_1 with $r_c = 4(a_i + a_j)$ and $m = \sqrt{\pi P}$. The corresponding M and P are annotated in the figure.

of Fig. 4.2b. Moreover, for comparison the data in Fig. 4.2b are reproduced in gray. In Fig. 4.6a, the GPU results in black are indistinguishable from the CPU results in gray when $e_{\infty,r}(E) > 10^{-5}$ for all m and γ, indicating that the GPU computations are only limited by the SP arithmetics. When the error $e_{\infty,r}(E)$ reaches 10^{-5}, increasing the interpolation point P does not improve the accuracy on GPUs, while the error from the DP arithmetics on CPU continues to decrease until $e_{\infty,r}(E) \sim 10^{-14}$. In addition, the wave-space errors remain $e_{\infty,r}(E) \sim 10^{-5}$ after reaching the SP limit, *i.e.*, increasing P does not adversely affect the wave-space accuracy.

The overall GPU mobility accuracy as a function of ξa_1 is presented in Fig. 4.6b for two M and P combinations with $m = \sqrt{\pi P}$ and $r_c = 4(a_i + a_j)$ in orthogonal simulation boxes. The errors $e_{\infty,r}(E)$ are computed using the baseline case of Sec. 4.5. The GPU results are shown in solid lines and the CPU results in dashed lines. When the overall error $e_{\infty,r}(E) > 10^{-4}$, *i.e.*, the case of $(M, P) = (32, 13)$ in Fig. 4.6b, the GPU and the CPU results are indistinguishable from each other. However, the differences are evident for the case of $(M, P) = (64, 21)$. When $0.5 < \xi a_1 < 0.85$, the GPU computations deviate from the CPU results with larger errors due to the SP arithmetics. Beyond this range, the CPU and the GPU results overlap again. In both cases, the accuracy achieved by the GPU mobility computation is sufficient for dynamic simulations, where the error tolerance is typically set at

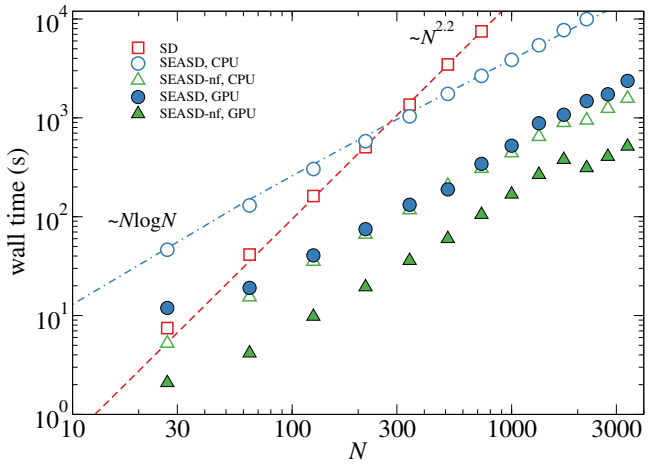

Figure 4.7: (Color online) The wall times (in second) of 100 time steps in dynamic simulations at Pe = 1 as functions of the particle number N using the conventional SD, SEASD, and SEASD-nf. The open symbols represent the CPU mobility computation and the filled symbols the GPU mobility computation. The dashed line show the $O(N^{2.2})$ scaling, and the dash-dotted line show the $O(N \log N)$ scaling. The suspension is bidisperse with $\lambda = 2$, $y_2 = 0.5$, and $\phi = 0.45$ starting from equilibrium configurations.

10^{-3}. The results in Fig. 4.6 dispel any concerns over the SP accuracy in the GPU mobility computations for dynamic simulations.

Overall performance

To assess the performances of various SEASD implementations, we measure the wall time to march 100 steps in a dynamic simulation of Brownian suspensions at Pe = 1, starting from an equilibrium bidisperse configuration with $\lambda = 2$, $y_2 = 0.5$, and $\phi = 0.45$. This composition is different from the baseline case in Sec. 4.5, and is selected to reflect the SEASD performance in dense systems. The mobility parameters are fixed at $P = 11$, $r_c = 4(a_i + a_j)$, $\xi = 0.35$ and $m = 5.8$, and the grid point M changes as $M \propto N^{1/3}$ starting from $M = 24$ at $N = 27$. These parameters are adequate for dynamic simulations, as is demonstrated in Sec. 4.6 and 4.6. The tolerances of the iterative solvers are 10^{-3}. In the SEASD, the far-field Brownian forces are calculated using Eqs. (4.75) and (4.76) with $\Delta\tau = 0.2$, and in the SEASD-nf, the far-field diffusivities are from Table 4.3. All the timing results are collected from a workstation with Intel i7-3770K CPU and NVIDIA GeForce GTX 680 GPU.

Fig. 4.7 presents the overall performance in terms of the wall time as a function of

Table 4.2: The GPU/CPU speedup of various parts of a mobility computation with different system size N. The CPU baseline time (in seconds) is shown in parenthesis.

N	GPU/CPU speedup (CPU baseline time in seconds)			
	wave-space setup	wave-space evaluation	real-space setup	real-space evaluation
64	13.0 (0.00319)	9.5 (0.00604)	3.9 (0.00222)	8.2 (0.00059)
512	72.6 (0.0338)	16.1 (0.0514)	2.7 (0.0543)	10.0 (0.00921)
1728	77.4 (0.126)	13.4 (0.191)	2.6 (0.217)	10.8 (0.0353)
4096	83.6 (0.329)	23.1 (0.607)	2.6 (0.543)	9.9 (0.0801)

the system size N for various SEASD implementations. The open symbols represent the CPU results and the filled symbols represent the GPU results. For comparison, Fig. 4.7 also shows the wall time from the conventional SD [11, 12, 84] in red squares. Various SEASD implementations show the expected $O(N \log N)$ asymptotic scaling, highlighted by the dash dotted line in Fig. 4.7. On the other hand, the conventional SD scales as $O(N^{2.2})$, highlighted by the dashed line. This scaling is due to the combined effect of the pairwise grand mobility tensor construction and the explicit matrix inversion, and should recover $O(N^3)$ at higher N. Comparing the wall times between the GPU and CPU implementations demonstrates the power of GPGPU programming in dynamic suspension simulations. At large N, the GPU/CPU speedup can reach 7 for SEASD and on average 3 for SEASD-nf. Therefore, by combining the GPGPU programming and the SEASD-nf algorithm, a total speedup of ~ 20 can be achieved. Such speedup makes studying suspension dynamics in larger systems and at longer times feasible. Compared to SEASD, SEASD-nf benefits less from the GPGPU programming because the algorithm has fewer far-field mobility evaluations. Moreover, in Fig. 4.7, the wall time for the GPU SEASD-nf at large N does not grow monotonically with N, and this is because the FFT computation in `cufft` strongly depends on the grid point M, which follows $M \propto N^{1/3}$. Finally, at $N \approx 216$, the wall time between the CPU SEASD and SD breaks even, and at $N \approx 50$, and wall times among the GPU SEASD, the CPU SEASD-nf, and SD are about the same. For all the system sizes studied here, the GPU SEASD-nf is always faster than the conventional SD.

To complement the overall time measurements in Fig. 4.7, Table 4.2 presents the

corresponding GPU/CPU speedup and the baseline CPU time for various parts in a mobility evaluation at different N. Both the wave-space and the real-space evaluations require a setup step that only needs to run once for each configuration. The table demonstrates that the GPGPU programming significantly improves the wave-space computations. At $N = 4096$ the wave-space GPU/CPU speedup for the setup step is 83.6 and for the evaluation step is 23.1. In contrast, the GPU performance for the real-space evaluation is less impressive. For $N = 4096$, the speedup for the real-space setup and evaluation are 2.6 and 9.9, respectively. The data from Table 4.2 show that the bottleneck for the GPU mobility evaluation is the real-space setup. Moreover, the near-field computations, which are carried out on CPU, reduce the overall speedup in dynamic simulations.

4.6 Static and dynamic simulation results

Short-time transport properties

In this section we present static SEASD simulation results on the short-time transport properties of monodisperse and bidisperse hard-sphere suspensions. With the iterative computation scheme in Sec. 4.4, the short-time translational and rotational self-diffusivities, instantaneous sedimentation velocities, and high-frequency dynamic shear and bulk viscosities can be straightforwardly evaluated. Other transport properties can also be calculated with an appropriate computation scheme.

The suspension short-time limit refers to a time scale t satisfying $\tau_I \ll t \ll \tau_D$, where τ_I is the inertial time and τ_D is the diffusion time. The inertia time $\tau_I = \frac{2}{9}\rho_{\mathrm{p}} a_{\mathrm{p}}^2/\eta_0$, where ρ_{p} and a_{p} are the characteristic particle density and radius, describes the time required for the *particle* momentum to dissipate by interacting with the solvent. When $\tau_I \ll t$, the particle momentum dissipates almost instantaneously and the particle dynamics are completely overdamped. The diffusion time $\tau_D = 6\pi\eta_0 a_{\mathrm{p}}^3/k_{\mathrm{B}}T$ characterizes the time scale of suspension configuration change and $t \ll \tau_D$ ensures that the transport properties entirely arise from the (instantaneous) HIs. Therefore, they are only determined by the configuration X, and can be calculated by sampling independent but equivalent configurations. In this work we use the Monte-Carlo procedure of Wang & Brady [11]: the hard-sphere configurations are first generated by an event-driven Lubachesky-Stillinger algorithm [85, 86], followed by a short equilibration. The transport properties are then computed statically. Here we compare the results from the SEASD with CPU mobility computation with our recent conventional SD results [11]. Although the SEASD and the SD are based on the same formalism, the grand mobility tensor $\mathfrak{M}$ constructed from SD includes

an additional mean-field quadrupole term [64], which can have quantitative consequences. For bidisperse hard-sphere suspensions, we focus on the composition with $\lambda = 2$ and $y_2 = 0.5$. In the SEASD computations, the system size is $N = 800$, and the results are averaged over 500 independent configurations. Note that for simple cubic array of monodisperse particles, SEASD produces identical results as those of Sierou & Brady [36].

Short-time translational and rotational self-diffusivities

The microscopic definition of the short-time translational and rotational self-diffusivities, $d^t_{s,\alpha}$ and $d^r_{s,\alpha}$ respectively, for homogeneous suspensions are,

$$d^t_{s,\alpha} = \frac{k_B T}{N_\alpha}\Big\langle \sum_{i\in\alpha} \hat{\boldsymbol{q}} \cdot \boldsymbol{\mu}^{tt}_{ii} \cdot \hat{\boldsymbol{q}} \Big\rangle, \text{ and } d^r_{s,\alpha} = \frac{k_B T}{N_\alpha}\Big\langle \sum_{i\in\alpha} \hat{\boldsymbol{q}} \cdot \boldsymbol{\mu}^{rr}_{ii} \cdot \hat{\boldsymbol{q}} \Big\rangle, \tag{4.80}$$

where $\hat{\boldsymbol{q}}$ is a vector of unit length for the averaging process and $\boldsymbol{\mu}^{tt}_{ii}$ and $\boldsymbol{\mu}^{rr}_{ii}$ are respectively the diagonal blocks of the linear velocity-force and angular velocity-torque couplings in $\boldsymbol{R}^{-1}_{\mathcal{FU}}$. Note that $i \in \alpha$ in Eq. (4.80) suggests the summation is restricted to particles of species α. The diffusivities are computed using the matrix-free approach of Sierou & Brady [36]: the velocity disturbance $\mathcal{U}^R$ corresponding to a stochastic external force $\mathcal{F}^R$ satisfying $\langle \mathcal{F}^R \rangle = 0$ and $\langle \mathcal{F}^R \mathcal{F}^R \rangle = \mathcal{I}$ is evaluated. It is straightforward to show that the ensemble average $\left\langle \mathcal{U}^R \mathcal{F}^R \right\rangle = \text{diag}(\boldsymbol{R}^{-1}_{\mathcal{FU}})$, allowing extraction of the diffusivities in Eq. (4.80).

The computed short-time translational self-diffusivities $d^t_{s,\alpha}$ exhibit a strong $N^{-1/3}$ size dependence due to the periodic boundary conditions. The size dependence from an N-particle system can be eliminated by adding the following quantity to the results,

$$\Delta_N d^t_{s,\alpha} = \frac{1.76 d^t_{0,1}}{(x_1 + x_2\lambda^3)^{\frac{1}{3}}} \frac{\eta_0}{\eta_s} \left(\frac{\phi}{N}\right)^{\frac{1}{3}}, \tag{4.81}$$

where $d^t_{0,1} = k_B T/(6\pi\eta_0 a_1)$ is Stokes-Einstein-Sutherland diffusivity for species 1, and η_s is the high-frequency dynamic shear viscosity from the same configurations. The shear viscosity exhibits little size dependence, and can be directly used. The effectiveness of Eq. (4.81) has been demonstrated by Wang & Brady [11] in the wave-number-dependent hydrodynamic functions. The results here always contain this finite size N correction.

Fig. 4.8a and Fig. 4.8b respectively present $d^t_{s,\alpha}/d^t_{0,\alpha}$ and $d^r_{s,\alpha}/d^r_{0,\alpha}$ of monodisperse and bidisperse suspensions, where the single particle translational and rotational

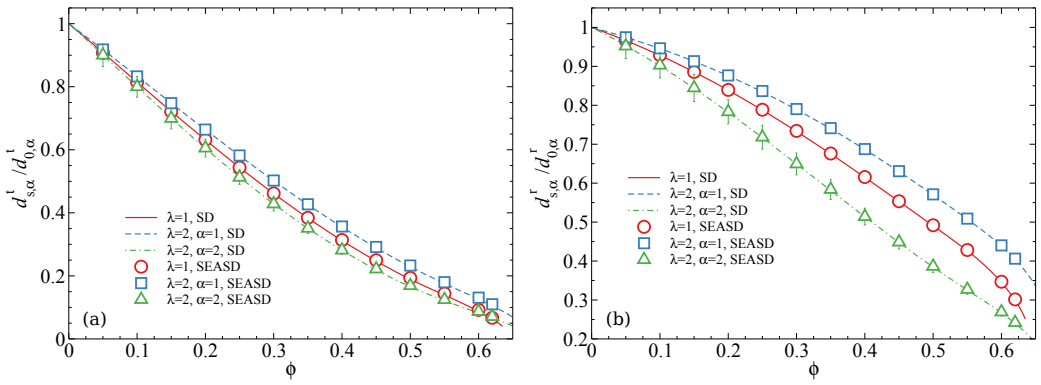

Figure 4.8: (Color online) The species short-time (a): translational and (b): rotational self-diffusivities, $d^t_{s,\alpha}$ and $d^r_{s,\alpha}$ respectively, as functions of the total volume fraction ϕ for monodisperse and bidisperse hard-sphere suspensions with $\lambda = 2$, $y_2 = 0.5$. The results are scaled with the single particle translation and rotational diffusivity, $d^t_{0,\alpha}$ and $d^r_{0,\alpha}$, respectively. The SEASD results are shown in symbols and the conventional SD results from Wang & Brady [11] are shown as lines.

Table 4.3: The polynomial coefficient fitted from the far-field diffusivities in Fig. 4.9. The data is for polydisperse suspensions with $\lambda = 2$ and $y_2 = 0.5$. The far-field self-diffusivity $d^{\rm ff}_s$ can be expressed as $d^{\rm ff}_s/d_0 = 1 + c_1\phi + c_2\phi^2 + c_3\phi^3$, where d_0 is the single particle diffusivity.

	$d^{t,\rm ff}_{s,1}$	$d^{t,\rm ff}_{s,2}$	$d^{r,\rm ff}_{s,1}$	$d^{r,\rm ff}_{s,2}$
c_1	−1.27	−1.70	−0.207	−0.538
c_2	0.536	1.005	−0.131	−0.312
c_3	−0.018	−0.12	−0.091	0.19

self-diffusivities are $d^t_{0,\alpha} = k_{\rm B}T/(6\pi\eta_0 a_\alpha)$ and $d^r_{0,\alpha} = k_{\rm B}T/(8\pi\eta_0 a^3_\alpha)$. The SEASD results, shown in symbols, agree well with the conventional SD results shown in lines. As expected, both $d^t_{s,\alpha}$ and $d^t_{s,\alpha}$ decrease with increasing volume fraction ϕ, and for bidisperse suspensions, the small particles show diffusivity enhancement while the large particles exhibit diffusivity supression. Compared to $d^t_{s,\alpha}$, $d^r_{s,\alpha}$ are less sensitive to the volume fractions ϕ, but more sensitive to the particle sizes λ. The SEASD results for large particles show larger error bars compared to the SD results [11], most likely due to the stochastic computation procedure.

We have also calculated the far-field short-time translational and rotational self-diffusivities $d^{t,\rm ff}_{s,\alpha}$ and $d^{r,\rm ff}_{s,\alpha}$, where "ff" suggests only the far-field HIs without the lubrication corrections are considered. They are the input for subsequent SEASD-nf computations in Sec. 4.6 and 4.6. The $N^{-1/3}$ size dependence in the far-field trans-

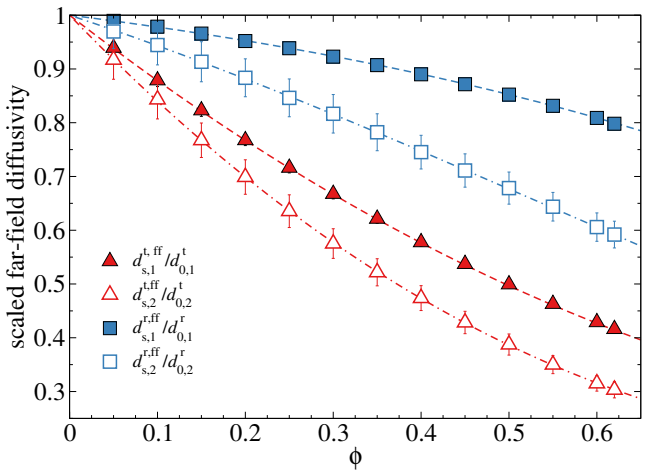

Figure 4.9: (Color online) The species far-field short-time translational and rotational self-diffusivities, $d_{s,\alpha}^{t,\mathrm{ff}}$ and $d_{s,\alpha}^{r,\mathrm{ff}}$, respectively, as functions of the total volume fraction ϕ for bidisperse hard-sphere suspensions with $\lambda = 2$ and $y_2 = 0.5$. The results are scaled with the single particle translation and rotational diffusivity, $d_{0,\alpha}^{t}$ and $d_{0,\alpha}^{r}$, respectively. The symbols are the computation results, and the dashed and the dash-dotted lines are polynomial fittings for the small and the large particles, respectively.

lational diffusivity $d_{s,\alpha}^{t,\mathrm{ff}}$ is corrected using Eq. (4.81) with the corresponding far-field viscosity. Fig. 4.9 shows $d_{s,\alpha}^{t,\mathrm{ff}}$ and $d_{s,\alpha}^{r,\mathrm{ff}}$ for bidisperse suspensions up to $\phi = 0.62$. Compared to Fig. 4.8, the far-field diffusivities exhibit weaker volume fraction dependence, and they do not have sharp reductions at high volume fractions. Consistent with Fig. 4.8, $d_{s,\alpha}^{r,\mathrm{ff}}$ also exhibits stronger particle size dependence compared to its translational counterpart. In general, the ϕ dependence of any scaled far-field diffusivity d_s^{ff}/d_0, with d_0 the corresponding single-particle data, can be adequately captured by a cubic polynomial $d_s^{\mathrm{ff}}/d_0 = 1 + c_1\phi + c_2\phi^2 + c_3\phi^3$, where the coefficients c_i, $i \in \{1, 2, 3\}$, only depend on the suspension composition. The fitting coefficients for bidisperse suspensions with $\lambda = 2$ and $y_2 = 0.5$ are presented Table 4.3. The polynomial fittings, also shown in Fig. 4.9 in dashed and dash-dotted lines for the small and the large particles, respectively, indeed describe the data. Not shown in Fig. 4.9 are the SEASD far-field diffusivities for monodisperse suspensions, which are identical to those of Banchio & Brady [39].

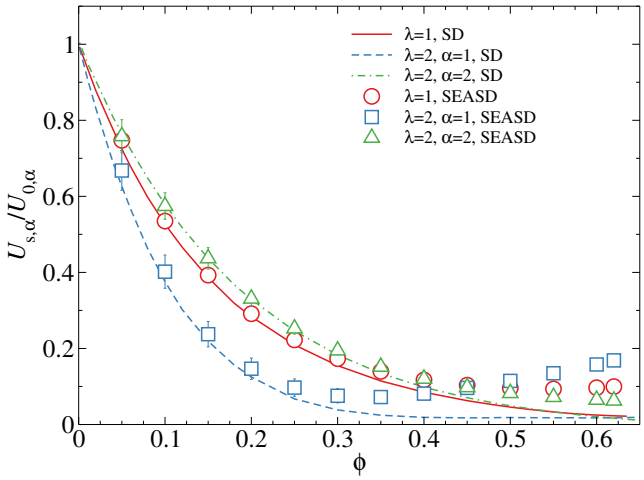

Figure 4.10: (Color online) The scaled species instantaneous sedimentation velocities, $U_{s,\alpha}/U_{0,\alpha}$, as functions of the total volume fraction ϕ for monodisperse and bidisperse hard-sphere suspensions with $\lambda = 2$ and $y_2 = 0.5$. The single particle sedimentation velocity is $U_{0,\alpha}$. The SEASD results are shown in symbols and the conventional SD results from Wang & Brady [11] are shown as lines.

Instantaneous sedimentation velocity

The species instantaneous sedimentation velocities $U_{s,\alpha}$ are computed by applying a uniform external force F_α to each species. For bidisperse suspensions, the sedimentation velocity $U_{s,\alpha}$ also depends on the species density ratio [8], $\gamma = \Delta\rho_2/\Delta\rho_1$, with $\Delta\rho_\alpha = \rho_\alpha - \rho_0$ the density difference of species α. The species force ratio satisfies $F_2/F_1 = \gamma\lambda^3$, and here we set $\gamma = 1$ to facilitate comparison with earlier results. To eliminate the $N^{-1/3}$ size dependence, the following corrections are added to the results:

$$\Delta_N U_{s,1} = \frac{1.76U_{0,1}}{(x_1 + x_2\lambda^3)^{\frac{1}{3}}}\frac{\eta_0}{\eta_s}\left(\frac{\phi}{N}\right)^{\frac{1}{3}}\left[S_{11}(0) + \lambda^3\gamma\sqrt{\frac{x_2}{x_1}}S_{12}(0)\right], \tag{4.82}$$

$$\Delta_N U_{s,2} = \frac{1.76U_{0,1}}{(x_1 + x_2\lambda^3)^{\frac{1}{3}}}\frac{\eta_0}{\eta_s}\left(\frac{\phi}{N}\right)^{\frac{1}{3}}\left[\sqrt{\frac{x_1}{x_2}}S_{21}(0) + \lambda^3\gamma S_{22}(0)\right], \tag{4.83}$$

where $U_{0,\alpha} = F_\alpha/(6\pi\eta_0 a_\alpha)$ is the single particle sedimentation velocity and $S_{\alpha\beta}(0)$ is the partial static structural factors in the zero wave number limit. Eqs. (4.82) and (4.83) are based on the finite-size correction for partial hydrodynamic functions [11]. Here, the partial static structural factors are computed from the polydisperse Percus-Yevic integral equations [87–90].

Fig. 4.10 presents the SEASD $U_{s,\alpha}/U_{0,\alpha}$ in symbols, which are not identical to the

conventional SD results shown in lines. The difference is especially pronounced at high volume fractions. For monodisperse suspensions, the SEASD and the conventional SD agree with each other satisfactorily up to $\phi \approx 0.3$, and at higher ϕ, the SEASD results become significantly higher. This difference is from the mean-field quadrupole term, which is absent in SEASD. Despite the quantitative differences, the SEASD monodisperse sedimentation velocity remain positive and physical. A similar overestimation of the sedimentation velocity is also found when comparing ASD results [36] and the conventional SD results [64] for simple cubic arrays.

The differences between the SEASD and the conventional SD results are more significant for bidisperse suspensions. For $U_{s,2}$ of the large particles, the differences are not evident until $\phi = 0.3$, and for $U_{s,1}$ of the small particles, the differences are obvious even at $\phi \approx 0.2$. Moreover, $U_{s,1}$ exhibits a minimum and increases with ϕ at higher volume fraction, leading to a crossing of $U_{s,1}$ and $U_{s,2}$ at $\phi = 0.45$. These unphysical behaviors are caused by inaccurate HI computations at the stresslet-strain rate level. Apparently, the HIs of the small particles, which are surrounded by many large particles, are more complex than those of the large particles and more difficult to capture accurately. Note that for sedimentation the lubrication interactions are not important and one must rely on the far-field mobility for all HIs.

Fig. 4.10 also illustrates that the sedimentation problems in dense bidisperse suspensions, even at $\lambda = 2$, is challenging for SEASD. Incorporating the mean-field quadrupole term [64], $(1 - \frac{1}{5}\phi)$, in the grand mobility tensor can significantly improve the results [11]. For the conventional SD, such incorporation involves multiplying $(1 - \frac{1}{5}\phi)$ to the quadrupole terms in the velocity-force coupling of the grand mobility tensor [64]. However, including this term in the SEASD, or any particle mesh approaches, is more involved due to the wave-space computation. One method is to multiply $(1 - \frac{1}{5}\phi)$ to the quadrupole term in the Faxén's law, Eq. (4.13). This modification produces undesired changes in the velocity-torque and velocity-stresslet couplings, and has to be corrected by a separate wave-space computation that applies $\frac{1}{30}\phi a_i^2 \nabla^2$ to the velocity disturbances from the torques and stresslets. Apparently, this additional wave-space correction increases the computational cost and the algorithm complexity, and therefore is not implemented in this work.

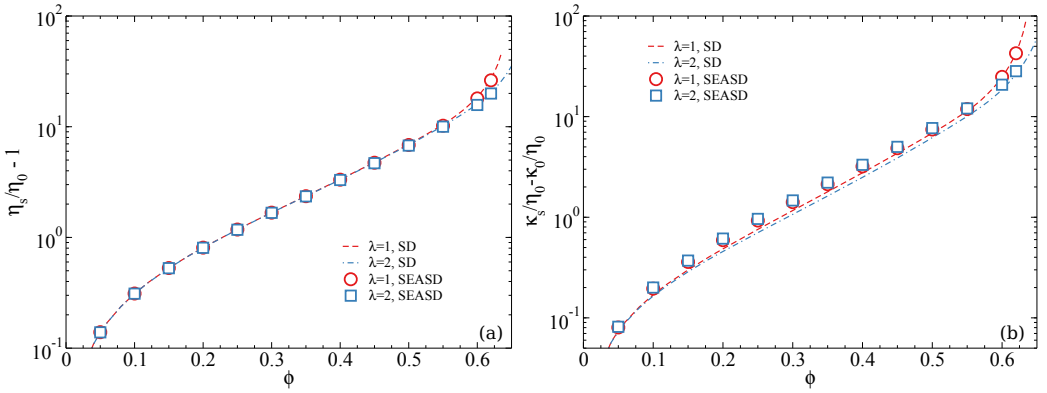

Figure 4.11: (Color online) The high-frequency dynamic (a): shear viscosity η_s and (b): bulk viscosity κ_s as functions of the total volume fraction ϕ for monodisperse and bidisperse hard-sphere suspensions with $\lambda = 2$ and $y_2 = 0.5$. The results are scaled with the solvent viscosity η_0, and only the particle contributions, $\eta_s/\eta_0 - 1$ and $(\kappa_s - \kappa_0)/\eta_0$ are presented. The SEASD results are shown as symbols and the conventional SD results [11] are shown as lines.

High-frequency dynamic shear and bulk viscosities

The high-frequency dynamic shear and bulk viscosities, η_s and κ_s, are respectively defined as,

$$\eta_s = \eta_0 + n\langle \mathbf{S}^{\mathrm{E}} \rangle_{xy}/\dot{\gamma}, \text{ and } \kappa_s = \kappa_0 + \tfrac{1}{3} n\langle \mathbf{S}^{\mathrm{E}} \rangle : \mathbf{I}/\dot{e}, \tag{4.84}$$

where $\dot{\gamma}$ is the imposed strain rate, $\dot{e}$ is the imposed uniform expansion rate, $\mathbf{S}^{\mathrm{E}}$ is the hydrodynamic stresslet in Eq. (4.65), and the subscript xy denotes the velocity-velocity gradient component. They are directly computed from SEASD and exhibit little size dependencies. Experimentally, η_s and κ_s are measured by imposing high-frequency, low-amplitude deformations, such that the suspension microstructures are only slightly perturbed, and the Brownian stress contributions are out of phase with the applied deformations [91].

Fig. 4.11a and 4.11b present the volume fraction ϕ dependence of the particle contributions to the high-frequency dynamic shear and bulk viscosities, $\eta_s/\eta_0 - 1$ and $(\kappa_s - \kappa_0)/\eta_0$, respectively. The SEASD calculations are shown in symbols, and the corresponding conventional SD results are shown in lines. For η_s, the SEASD and the conventional SD results agree well over the entire ϕ range. The results for monodisperse and bidisperse suspensions with $\lambda = 2$ are almost identical when $\phi < 0.55$. At higher volume fractions, the monodisperse η_s are more sensitive to ϕ compared to the bidisperse results, as introducing particles of difference sizes significantly alters the suspension hydrodynamic environment in this limit. Unlike

the sedimentation velocities, for the shear viscosity lubrication interactions are important at high ϕ.

For the high-frequency dynamics bulk viscosity κ_s in Fig. 4.11b, the SEASD and the conventional SD results show qualitative agreement with noticeable quantitative differences at moderate ϕ: the SEASD results are higher and less sensitive to the particle size ratio λ. The differences are caused by different pressure moment computation procedures. Recall that the far-field grand mobility tensor $\mathfrak{M}$ is not symmetric by construction, and the symmetry of $\mathfrak{M}^{-1}$ must be restored for subsequent calculations. This is done in the conventional SD by explicitly copying matrix elements after the matrix inversion [92]. This is not applicable for the matrix-free computation of $\mathfrak{M}$ in SEASD. Here, the pressure moment is computed from the far-field forces and stresses. Fig. 4.11b shows that the two conceptually equivalent approaches do lead to small quantitative differences. Moreover, for dense suspensions, such differences are masked by the dominance of lubrication interactions. Therefore, the SEASD and the conventional SD results agree well at low and high ϕ. Near the close packing limit, κ_s for bidisperse suspensions is significantly lower than that of the monodisperse case, since the particle size polydispersity improves the particle packing.

Equilibrium suspensions

Here we present the dynamic simulation results with SEASD and SEASD-nf for monodisperse and bidisperse Brownian suspensions at zero Péclet number. In particular, we are interested in the following equilibrium properties: the osmotic pressure Π, the high-frequency dynamic bulk modulus K'_∞, and the high-frequency dynamic shear modulus G'_∞. The dynamic simulations are carried out with 100 particles over 200 diffusive time units with a time step $\Delta t d^t_{0,1}/a_1^2 = 10^{-3}$. The mobility computation in SEASD is performed on GPUs with $M = 32$, $P = 11$, and $r_c = 4(a_i + a_j)$, and the far-field Brownian force is calculated using the IVP method in Sec. 4.4 with $\Delta\tau = 0.1$. The tolerance for the iterative solver is 10^{-3} and the tolerance for matrix inversion in Eqs. (4.75) and (4.76) is 0.02. The composition of bidisperse suspensions are $\lambda = 2$ and $y_2 = 0.5$. Therefore, for the SEASD-nf computations the coefficients in Table 4.3 are used. Note that with Pe = 0, SEASD-nf computations do not contain far-field mobility evaluations.

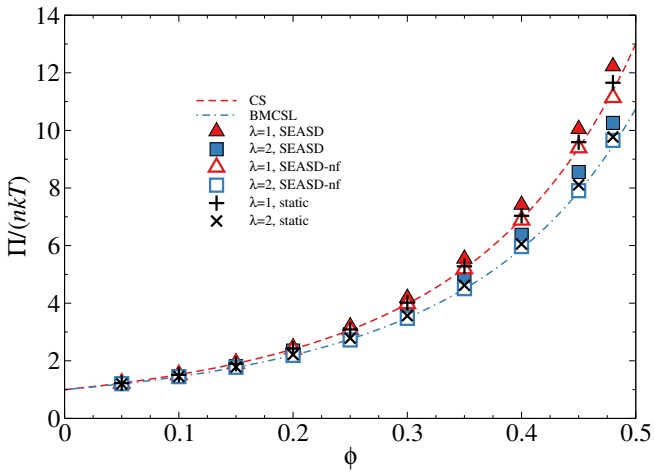

Figure 4.12: (Color online) The equilibrium osmotic pressure $\Pi/(nk_BT)$ of monodisperse and bidisperse Brownian suspensions with $\lambda = 2$ and $y_2 = 0.5$, as a function of volume fraction ϕ. The dashed line represents the CS equation of state, Eq. (4.86), and the dash-dotted line represents the BMCSL equation of state, Eq. (4.87).

Osmotic pressure

The osmotic pressure of an equilibrium suspension is defined as

$$\Pi = nk_BT - \tfrac{1}{3}n\langle \mathbf{S}^B \rangle : \mathbf{I}, \tag{4.85}$$

where $\langle \mathbf{S}^B \rangle$ is the Brownian stresslet in Eq. (4.67). For rigid particles with no-slip boundary conditions, Brady [51] showed that the osmotic pressure is purely hydrodynamic in origin, and is identical to that of a hard-sphere fluid. The osmotic pressure of monodisperse suspensions is well described by the Carnahan-Starling (CS) equation up to the fluid-solid transition,

$$\frac{\Pi}{nk_BT} = \frac{1 + \phi + \phi^2 - \phi^3}{(1-\phi)^3}. \tag{4.86}$$

The CS equation of state is extended to polydisperse suspensions as the Boublik-Mansoori-Carnahan-Starling-Leland (BMCSL) equation [93]:

$$\frac{\Pi}{nk_BT} = \frac{1 + \phi + \phi^2 - 3\phi(z_1 + z_2\phi) - z_3\phi^3}{(1-\phi)^3}, \tag{4.87}$$

where $z_1 = \Delta_{12}(1+\lambda)/\sqrt{\lambda}$, $z_2 = \Delta_{12}(y_1\lambda + y_2)/\sqrt{\lambda}$, and $z_3 = [(y_1^2 x_1)^{1/3} + (y_2^2 x_2)^{1/3}]^3$ with $\Delta_{12} = \sqrt{y_1 y_2}\sqrt{x_1 x_2}(\lambda - 1)^2/\lambda$.

Fig. 4.12 presents the equilibrium osmotic pressure of monodisperse and bidisperse suspensions with $\lambda = 2$ and $y_2 = 0.5$ as functions of ϕ using SEASD and SEASD-nf. The CS [Eq. (4.86)] and the BMCSL [Eq. (4.87)] equations of state at the corresponding bidisperse compositions are shown in dashed and dash-dotted lines, respectively. Also shown in Fig. 4.12 are the static computation results with $N = 200$, denoted "static". The static computations do not consider particle dynamics, and calculate the osmotic pressure by taking a full Brownian step from independent particle configurations in a Monte-Carlo fashion. In Fig. 4.12, at each volume fraction 500 independent configurations are used in the static computations.

The osmotic pressures from the SEASD, the SEASD-nf, and the static computations agree with the CS and BMCSL predictions in Fig. 4.12. The static computations show the best agreement over the entire ϕ range, and this directly validates the Brownian stress computation method in Sec. 4.4. The dynamic SEASD results are slightly higher than the theoretical predictions because the configuration evolution is affected by the finite $\Delta\tau$ in the far-field Brownian force computation. The slight difference is well within the discretization errors of Eqs. (4.75) and (4.76). Note that, as long as the tolerances for the iterative solution of Eqs. (4.75) and (4.76) are smaller than the discretization step size $\Delta\tau$, the principal source of error is the time discretization. We have verified that reducing the iterative solver tolerance with fixed $\Delta\tau$ does not improve the results. Finally, the agreement in the bidisperse osmotic pressures from SEASD-nf and the BMCSL equation validates the extension of the mean-field Brownian approximation to polydisperse systems. The SEASD-nf results are only slightly lower than the theoretical predictions, which is acceptable considering the substantial speedup offered by this approach.

High-frequency dynamic moduli

The suspension high-frequency dynamic bulk and shear moduli, K'_∞ and G'_∞ respectively, can be computed from the short-time limit of the pressure-pressure and stress-stress autocorrelation functions [92, 94, 95], *i.e.*,

$$K'_\infty = \lim_{t\to 0} \frac{V}{k_B T} \langle \delta\Pi(t)\delta\Pi(0)\rangle \,, \text{ and } G'_\infty = \lim_{t\to 0} \frac{V}{k_B T} \langle \sigma(t)\sigma(0)\rangle \,, \tag{4.88}$$

where $\delta\Pi$ is the osmotic pressure fluctuations and σ is the off-diagonal components of the bulk stress $\langle \boldsymbol{\Sigma} \rangle$ in Eq. (4.64). Note that the viscoelasticity of colloidal suspensions is entirely of hydrodynamic origin, and without HIs, *e.g.*, in hard-sphere fluids, these moduli are infinite.

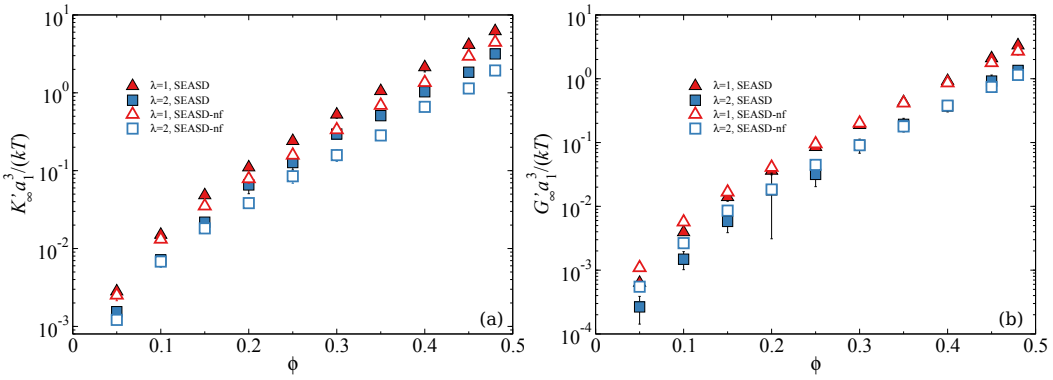

Figure 4.13: (Color online) The high-frequency dynamic moduli: (a) the bulk modulus $K'_\infty a_1^3/(k_BT)$, and (b) the shear modulus $G'_\infty a_1^3/(k_BT)$, as functions of volume fraction ϕ for equilibrium monodisperse and bidisperse Brownian suspensions with $\lambda = 2$ and $y_2 = 0.5$. The results are computed from SEASD (filled symbols) and SEASD-nf (open symbols).

Fig. 4.13a and 4.13b respectively present K'_∞ and G'_∞ of monodisperse and bidisperse suspensions as functions of ϕ from the same SEASD and SEASD-nf dynamic simulations of Fig. 4.12. Both K'_∞ and G'_∞ grow rapidly with ϕ, and at the same volume fraction, the monodisperse moduli are always higher. In Fig. 4.13a, the bulk modulus K'_∞ computed from SEASD and SEASD-nf share the same qualitative behaviors. However, the SEASD results are almost always higher than the SEASD-nf results except at small ϕ, and their differences grow with increasing ϕ. This is consistent with the growing differences in Π with increasing ϕ in Fig. 4.12. On the other hand, in Fig. 4.13b the differences in the shear modulus G'_∞ between the SEASD and the SEASD-nf results decrease with increasing ϕ, with the SEASD-nf data higher at low volume fractions. Note that the bidisperse SEASD results show large fluctuations when $\phi = 0.2 \sim 0.25$, most likely due to the small number of large particles at $N = 100$ and the particular particle spacing at this volume fraction. Finally, small differences in fluctuation quantities such as K'_∞ and G'_∞ are expected for SEASD and SEASD-nf because the Brownian stresses are computed differently. However, the same qualitative behaviors are followed in both methods.

Rheology of bidisperse suspensions

The final validation of SEASD and SEASD-nf is the steady shear rheology of Brownian suspensions at constant strain rate. Both monodisperse and bidisperse hard-spehre suspensions are considered: the volume fractions are fixed at $\phi = 0.45$ in both cases, and the bidisperse composition is $\lambda = 2$ and $y_2 = 0.5$. The

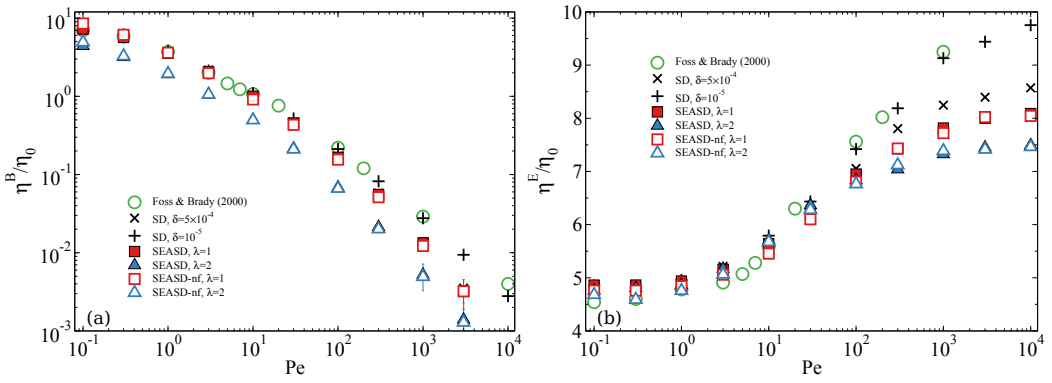

Figure 4.14: (Color online) Different viscosity contributions to the rheology of monodisperse and bidisperse hard-sphere suspensions: (a) the Brownian viscosity η^B/η_0 and (b) the flow viscosity η^E/η_0, as functions of Pe. The volume fraction $\phi = 0.45$ in both cases, and the bidisperse composition is $\lambda = 2$ and $y_2 = 0.5$.

results are extracted from the SEASD and the SEASD-nf simulations with GPU mobility computation over a wide range of Péclet number $\mathrm{Pe} = 6\pi\eta_0 a_1^3\dot{\gamma}/(k_\mathrm{B}T)$. Moreover, we introduce a small excluded volume on each particle to emulate the effects of surface asperities or polymer coating and to prevent particle overlap. It is characterized by,

$$\delta = 1 - a_i/b_i, \tag{4.89}$$

where b_i is the excluded volume radius for each particle. The SEASD and SEASD-nf simulations are carried out at $\delta = 5 \times 10^{-4}$ with $N = 200$ over 150 dimensionless time units with a step size 10^{-3}. Other simulation parameters are similar to those in Sec. 4.6. The data are averaged in segments after the steady state is reached, usually after 20 dimensionless time units. As is customary, the x-direction is the velocity direction, the y-direction is the velocity gradient direction, and the z-direction is the vorticity direction.

Shear viscosity

Fig. 4.14a and 4.14b respectively present the Brownian viscosity η^B and the flow viscosity η^E as functions of the Péclet number. These viscosities are defined as

$$\eta^B = n\langle \mathbf{S}^\mathrm{B}\rangle_{xy}/\dot{\gamma} \text{ and } \eta^E = n\langle \mathbf{S}^\mathrm{E}\rangle_{xy}/\dot{\gamma}, \tag{4.90}$$

with $\langle \mathbf{S}^\mathrm{B}\rangle$ in Eq. (4.67) and $\langle \mathbf{S}^\mathrm{E}\rangle$ in Eq. (4.65). In this figure, the monodisperse data are shown in squares and the bidisperse data in triangles, with the SEASD results in filled symbols and the SEASD-nf results in open symbols. For comparison,

the SD results of Foss & Brady [73] for monodisperse suspensions are presented in open circles. To clarify the effects of the excluded volume parameter δ on viscosities, another set of monodisperse SD simulations with $N = 30$ are performed at $\delta = 5\times10^{-4}$ and 10^{-5}, and the results are shown as crosses and pluses respectively. In all cases, the stress contributions from the inter-particle forces are negligible, and therefore are not shown.

In Fig. 4.14 both the Brownian viscosity η^B and the flow viscosity η^E exhibit the expected behaviors: with increasing Pe, η^B decreases (shear-thinning) and η^E grows (shear-thickening). In addition, there are several important observations. First of all, the excluded volume parameter δ introduces quantitative effects on the suspension rheology. Comparing the SD results with $\delta = 5 \times 10^{-4}$ and 10^{-5}, increasing δ enhances the shear-thinning of η^B and weakens the shear-thickening of η^E, especially at high Pe. At low Pe, the effect of δ is almost unnoticeable. The SD results at $\delta = 10^{-5}$ agree well with those of Foss & Brady [73], and the results at $\delta = 5\times10^{-4}$ are consistent with the monodisperse SEASD and SEASD-nf results, with larger differences shown in η^E. This difference is most likely due to the number of particles in the computations. Next, the bidisperse Brownian viscosity η^B is always lower than the monodisperse value at all Pe, and for the flow viscosity η^E, their difference is most apparent at high Pe. The large difference in η^E at high Pe suggests distinct HIs and structures between the monodisperse and the bidisperse suspensions, since Fig. 4.11a suggests η^E is insensitive to the equilibrium suspension structures at $\phi = 0.45$. Finally, the SEASD and SEASD-nf results in Fig. 4.14 almost always overlap each other, showing that the mean-field Brownian approximation is valid over the entire Péclet number range. At high Pe, the Brownian viscosity η^B from SEASD shows larger fluctuations compared to the SEASD-nf results as the Brownian stresses are difficult to compute with highly anisotropic structures. However, these fluctuations do not affect the overall viscosity since the Brownian contribution at high Pe is insignificant.

Non-equilibrium osmotic pressures

Fig. 4.15a and 4.15b present the Brownian and the flow contributions to the suspension osmotic pressure,

$$\Pi^B = nk_BT - \tfrac{1}{3}n\langle \mathbf{S}^B\rangle : \mathbf{I} \text{ and } \Pi^E = -\tfrac{1}{3}n\langle \mathbf{S}^E\rangle : \mathbf{I}, \tag{4.91}$$

respectively, as functions of Péclet number Pe. In these figures, the scaling for the Brownian contribution is nk_BT and the scaling for the flow contribution Π^E is

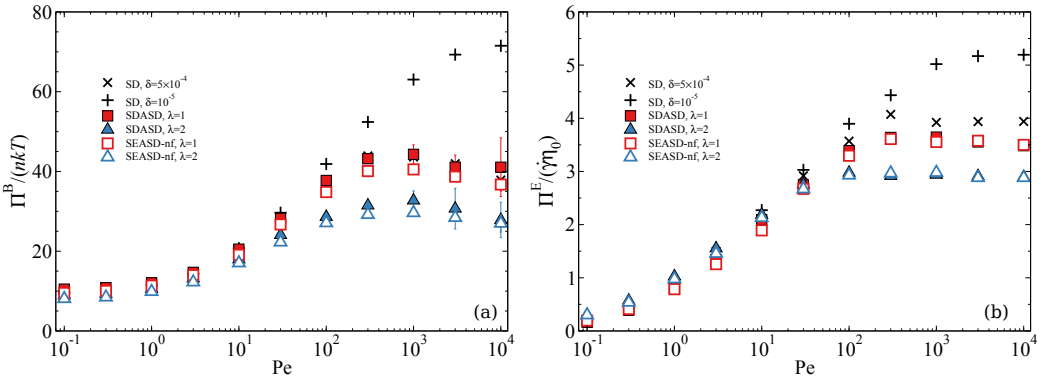

Figure 4.15: (Color online) Different contributions to the osmotic pressures of monodisperse and bidisperse hard-sphere suspensions: (a) the Brownian contribution scaled with nk_BT, $\Pi^B/(nk_BT)$, and (b) the flow contribution scaled with $\eta_0\dot{\gamma}$, $\Pi^H/(\dot{\gamma}\eta_0)$, as functions of Pe. The volume fraction is $\phi = 0.45$ in both cases, and the bidisperse composition is $\lambda = 2$ and $y_2 = 0.5$.

$\eta_0\dot{\gamma}$. Similar to Fig. 4.15, the monodisperse data are presented in squares and the bidisperse data in triangles, with the SEASD results in filled symbols and SEASD-nf results in open symbols. Fig. 4.15 also presents the $N = 30$ monodisperse SD results with $\delta = 5\times10^{-4}$ and 10^{-5} in crosses and pluses, respectively. Similarly to the shear stresses, the inter-particle contribution to the osmotic pressures is also negligible.

In Fig. 4.15, both $\Pi^B/(nk_BT)$ and $\Pi^E/(\dot{\gamma}\eta_0)$ grow with increasing Pe when Pe $<$ 100. The Brownian contribution $\Pi^B/(nk_BT)$ asymptotes the equilibrium value as Pe $\to$ 0. At higher Pe, the influence of the excluded volume parameter δ becomes apparent. For the Brownian osmotic pressure contribution $\Pi^B/(nk_BT)$, the SD results at $\delta = 10^{-5}$ continuously grow with Pe up to Pe $= 10^4$, the highest value in our study, while with $\delta = 5\times10^{-4}$, a maximum in $\Pi^B/(nk_BT)$ around Pe $= 10^3$ is apparent. After the maximum, $\Pi^B/(nk_BT)$ decreases slowly with growing Pe. In this case, the parameter δ not only brings quantitative, but also qualitative differences. On the other hand, the flow osmotic pressure contribution $\Pi^E/(\dot{\gamma}\eta_0)$ increases and reaches a plateau at high Pe. Comparing the SD results with $\delta = 5\times10^{-4}$ and 10^{-5}, increasing δ reduces the final plateau value of $\Pi^E/(\dot{\gamma}\eta_0)$ at a smaller Pe. Apparently, the high Pe osmotic pressure is very sensitive to the excluded volume parameter δ. In terms of the normal viscosity, *i.e.*, $\Pi/\dot{\gamma}$ with $\Pi = \Pi^B + \Pi^E$, increasing δ weakens the shear thickening of the normal viscosity. Furthermore, the SD results at $\delta = 10^{-5}$ agree qualitatively with the results of Yurkovetsky & Morris [53], with slight quantitative difference due to different osmotic pressure

computations. At $\delta = 5 \times 10^{-4}$, the Brownian osmotic pressures Π^B from SD and SEASD almost overlap each other in Fig. 4.15a, and Π^E from SEASD is lower than the SD results in Fig. 4.15b. Similarly to Fig. 4.14b, the difference is most likely due to the small system sizes in the SD computations. Moreover, the SEASD Π^B also exhibits larger error bars at high Pe due to the Brownian stress computation, but such errors are of little consequences on the suspension total osmotic pressures.

For the bidisperse results shown in triangles in Fig. 4.15, the Brownian osmotic pressure Π^B is always lower than its monodisperse counterpart, and the bidisperse Π^E is first slightly higher than the monodisperse results at low Pe and then lower at high Pe. The crossing of the monodisperse and bidisperse Π^E demonstrates the complex interplay between HIs and structures in polydisperse systems.

The SEASD-nf results in Fig. 4.15 agree qualitatively with the SEASD computations. However, for Π^B, there are quantitative differences at both $\lambda = 1$ and $\lambda = 2$, with the SEASD-nf results systematically lower. This difference is inherently associated with the far-field Brownian force computations in Sec. 4.4 and the mean-field Brownian approximations, and is also encountered in Fig. 4.12. However, the quantitative discrepancies in Π^B are still within the discretization errors of $\Delta\tau$ in Eqs. (4.75) and (4.76). On the other hand, for Π^E, the SEASD-nf and SEASD results almost always overlap each other over the entire Pe range for both bidisperse and monodisperse suspensions. SEASD-nf satisfactorily captures both contributions of the suspension osmotic pressures, Π^B and Π^E.

Normal stress differences

The first normal stress difference N_1 and the second normal stress difference N_2, defined as

$$N_1 = \langle \boldsymbol{\Sigma} \rangle_{xx} - \langle \boldsymbol{\Sigma} \rangle_{yy} \text{ and } N_2 = \langle \boldsymbol{\Sigma} \rangle_{yy} - \langle \boldsymbol{\Sigma} \rangle_{zz}, \tag{4.92}$$

describe the stress anisotropy in sheared suspensions, and are important for understanding phenomena such as the shear-induced particle migrations [52]. The normal stress differences N_1 and N_2 are respectively shown in Fig. 4.16a and Fig. 4.16b. The monodisperse data are shown in squares and the bidisperse data in triangles, with SEASD results in filled symbols and SEASD-nf results in open symbols. In addition, in Fig. 4.16, the SD results of Foss & Brady [73] are presented in circles, and the SD computations at $N = 30$ with $\delta = 5 \times 10^{-4}$ and 10^{-5} are respectively shown in crosses and pluses.

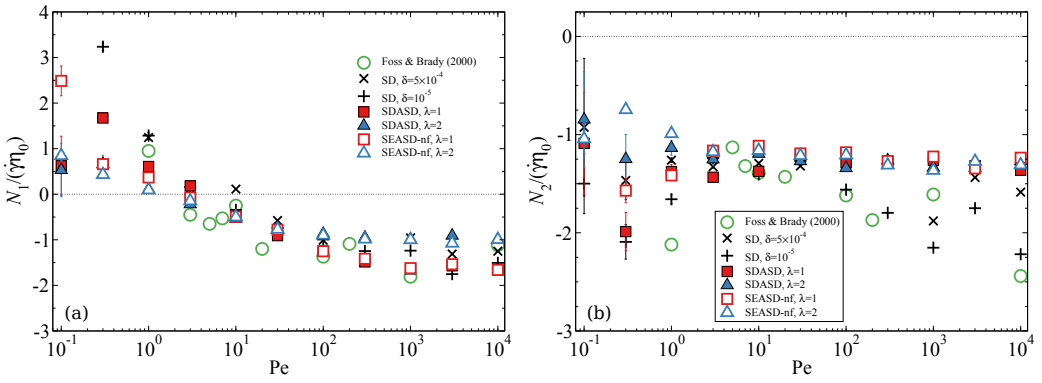

Figure 4.16: (Color online) The normal stress differences: (a) the first normal stress difference N_1 and (b) the second normal stress difference N_2 as functions of Péclet number Pe. The volume fraction is $\phi = 0.45$ in both cases and the bidisperse composition is $\lambda = 2$ and $y_2 = 0.5$.

In general, the first normal stress difference N_1 in Fig. 4.16a changes from positive to negative with increasing Pe, and the second normal stress N_2 in Fig. 4.16b remains negative for all Pe studied and exhibits weak Pe dependence. The data with small systems are strongly scattered, particularly at small Pe. For monodisperse suspensions, the excluded volume parameter δ has little effect on N_1 or N_2, as there lacks a qualitative difference for the SD results at $\delta = 5\times10^{-4}$ and 10^{-5} in Fig. 4.16. These SD results in general agree with the data of Foss & Brady [73] when Pe > 1. At smaller Pe, the data exhibit large errors due to fluctuations in Brownian stresses, making quantitative comparisons difficult.

In Fig. 4.16 the SEASD results at $\lambda = 1$ follow the SD data with the same qualitative behaviors. The differences at low Pe is likely associated with the difficulties in measuring the fluctuating Brownian normal stresses. In addition, the SEASD results show clearer trends at high Pe thanks to larger system sizes: both N_1 and N_2 asymptote toward constant values with increasing Pe. Particle size polydispersity weakens the influences of Pe on the first normal stress difference N_1. In Fig. 4.16a, the bidisperse N_1 are less sensitive to Pe compared to the monodisperse case, and as Pe $\to \infty$, the bidisperse N_1 asymptotes towards a negative value with a smaller magnitude. On the other hand, the size polydispersity has little effect on the second normal stress N_2, as the bidisperse N_2 almost overlaps the monodisperse N_2, especially at large Pe.

The SEASD-nf and the SEASD results agree satisfactorily when Pe ≥ 10 for both the monodisperse and bidisperse suspensions. As expected, larger differences are

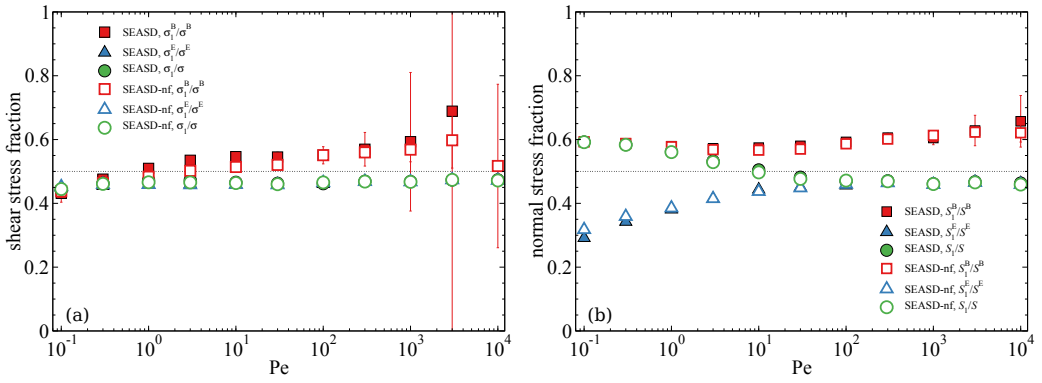

Figure 4.17: (Color online) The fraction of stresses taken up by the small particles (species 1) in a bidisperse suspension: (a) the fraction of the shear stress and (b) the fraction of the normal stress. The stress fractions are shown as functions of Pe. The composition of the bidisperse hard-sphere suspension is $\phi = 0.45$, $\lambda = 2$, and $y_2 = 0.5$.

found at low Pe, as the mean-field Brownian approximation in SEASD-nf explicitly removes the anisotropy in the far-field mobility tensor. However, the SEASD-nf results still capture the qualitative aspects of N_1 and N_2 even in the low Pe limit.

Finally, we note in passing that the shear-induced particle migration takes place in bounded suspensions with spatially varying strain rate, *e.g.*, the Poiseuille flow, and it can be computationally investigated by introducing confining boundaries. For the SEASD, this is conceptually straightforward: we only have to replace the unbounded fundamental solution to the one with the confining boundaries [63], and use the spectral Ewald method for doubly periodic systems [96].

Species stress distribution

Stress distributions across different species are key to understand the phenomena of particle migration and segregation in polydisperse suspensions [97], and are presently only accessible from simulations. Fig. 4.17 presents the stress distribution, expressed as the stress fraction taken up by the small particles (species 1), as functions of Pe for bidisperse suspensions with $\phi = 0.45$, $\lambda = 2$, and $y_2 = 0.5$. Fig. 4.17a shows various shear stress fractions. In terms of the definitions in Eqs. (4.64)–(4.67), σ_1/σ (circles), σ_1^B/σ^B (squares) , and σ_1^E/σ^E (triangles) in Fig. 4.17a are

$$\sigma_1/\sigma = x_1\langle\mathbf{\Sigma}\rangle_{1,xy}/\langle\mathbf{\Sigma}\rangle_{xy},$$

$$\begin{aligned}\sigma_1^B/\sigma^B &= x_1\langle \mathbf{S}^{\mathrm{B}}\rangle_{1,xy}/\langle \mathbf{S}^{\mathrm{B}}\rangle_{xy},\\ \sigma_1^E/\sigma^E &= x_1\langle \mathbf{S}^{\mathrm{E}}\rangle_{1,xy}/\langle \mathbf{S}^{\mathrm{E}}\rangle_{xy},\end{aligned} \tag{4.93}$$

where $\langle\cdot\rangle_\alpha$ indicates averaging with respect to species α. Fig. 4.17b presents various normal stress fractions. The normal stress fractions S_1/S (circles), S_1^B/S^B (squares), and S_1^E/S^E (triangles) in Fig. 4.17b are similarly defined as

$$\begin{aligned}S_1/S &= x_1(\mathbf{I}:\langle\boldsymbol{\Sigma}\rangle_1)/(\mathbf{I}:\langle\boldsymbol{\Sigma}\rangle),\\ S_1^B/S^B &= x_1(\mathbf{I}:\langle\mathbf{S}^{\mathrm{B}}\rangle_1)/(\mathbf{I}:\langle\mathbf{S}^{\mathrm{B}}\rangle),\\ S_1^E/S^E &= x_1(\mathbf{I}:\langle\mathbf{S}^{\mathrm{E}}\rangle_1)/(\mathbf{I}:\langle\mathbf{S}^{\mathrm{E}}\rangle).\end{aligned} \tag{4.94}$$

In both figures, the SEASD results are shown in filled symbols and the SEASD-nf results are shown in open symbols.

Fig. 4.17a illustrates that the total shear stress is roughly equally partitioned between the two species, and the fraction σ_1/σ is almost constant with respect to Pe. This is largely because the flow shear stress fraction σ_1^E/σ^E is insensitive to Pe. The Brownian shear stress fraction σ_1^B/σ^B, on the other hand, exhibits weak Pe dependence: the ratio σ_1^B/σ^B increases with Pe from less than 0.45 at Pe = 0.1 to close to 0.6 at Pe = 100. At higher Pe, the Brownian stress fraction shows large fluctuations, also due to the difficulties associated with the anisotropic structures. However, in this limit, the Brownian contribution to the total stress is small, and the large fluctuations in Fig. 4.17a is inconsequential. On the other hand, the total normal stress fraction S_1/S in Fig. 4.17b shows stronger Pe dependence, and it decreases from 0.6 at Pe = 0.1 to 0.45 at Pe = 10^4. Contrary to shear stress distributions in Fig. 4.17a, the Brownian normal stress distribution S_1^B/S^B is almost constant at 0.6, but S_1^E/S^E increases from 0.3 at Pe = 0.1 and asymptotes towards 0.45 as Pe $\to \infty$. Since the Brownian stresslet dominates at low Pe and the flow stresslet dominates at high Pe, the normal stress distributions in Fig. 4.17b are distinctively affected by both the flow and the Brownian contributions. Fig. 4.17 demonstrates that both the shear and the normal stresses in bidisperse suspensions are distributed based on the species volume and the distribution weakly depends on Pe. This is a useful insight for modelling polydisperse systems.

The stress distributions from SEASD-nf accurately capture the SEASD results except the Brownian shear stress distribution σ_1^B/σ^B at high Pe in Fig. 4.17a, where the SEASD-nf results is slightly lower. This difference, however, is expected since the mean-field Brownian approximation ignores the structural anisotropy in

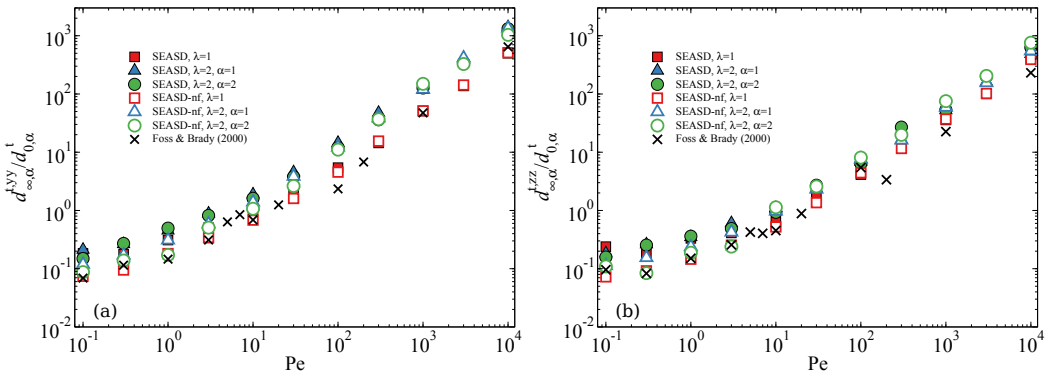

Figure 4.18: (Color online) The species long-time self-diffusivities: (a) the velocity gradient direction diffusivity $d^{t,yy}_{\infty,\alpha}$ and (b) the vorticity direction diffusivity $d^{t,zz}_{\infty,\alpha}$ of monodisperse and bidisperse hard-sphere suspensions as functions of Pe. The volume fraction is $\phi = 0.45$ for both cases, and the bidisperse composition is $\lambda = 2$ and $y_2 = 0.5$.

the suspension. Moreover, the discrepancies are only evident at Péclet numbers where the Brownian stress does not affect the overall suspension rheology. From this perspective, the overall quality of the SEASD-nf approximation is deemed satisfactory.

Long-time diffusion

An important characterization of the overall suspension dynamics is the translational long-time self-diffusivities. The long-time limit refers to a time scale $t \gg \tau_D$, where, recall that, $\tau_D = 6\pi\eta_0 a_p^3/k_B T$ is the single particle diffusive time scale. In this limit, the particle movement is diffusive due to extensive interactions with its neighbors. The corresponding diffusivities are obtained from the particle mean-square displacement. In the velocity gradient and the vorticity directions, these self-diffusivities are respectively defined as

$$d^{t,yy}_{\infty,\alpha} = \lim_{t\to\infty} \tfrac{1}{2}\mathrm{d}\langle(\Delta y)^2\rangle_\alpha/\mathrm{d}t \text{ and } d^{t,zz}_{\infty,\alpha} = \lim_{t\to\infty} \tfrac{1}{2}\mathrm{d}\langle(\Delta z)^2\rangle_\alpha/\mathrm{d}t, \tag{4.95}$$

where Δy and Δz are the particle trajectory fluctuations in y- and z-directions. Fig. 4.18a and 4.18b respectively present the long-time diffusivities $d^{t,yy}_{\infty,\alpha}$ and $d^{t,zz}_{\infty,\alpha}$ as functions of the Péclet number. The monodisperse results are shown in squares. For bidisperse suspensions, the small and the large particle long-time self-diffusivities are presented in triangles and circles, respectively. For comparison, Fig. 4.18 also shows the results from Foss & Brady [73] in crosses. Moreover, the SEASD and the SEASD-nf results are shown in filled and open symbols, respectively.

For monodisperse suspensions in Fig. 4.18, both $d_\infty^{t,yy}$ and $d_\infty^{t,zz}$ grow with Pe due to the imposed shear flow, with the velocity direction diffusivity $d_\infty^{t,yy}$ slightly higher. At low Pe, $d_\infty^{t,yy}$ and $d_\infty^{t,zz}$ grow weakly with Pe, and at large Pe, both diffusivities are proportional to Pe. The SEASD results are consistent with the SD results of Foss & Brady [73] at intermediate Pe. The differences at large and small Pe are most likely due to the system size, as in this work $N = 200$ while in Foss & Brady [73] $N = 27$. For bidisperse suspensions, the long-time self-diffusivities $d_{\infty,\alpha}^{t,yy}$ and $d_{\infty,\alpha}^{t,zz}$ for both species exhibit similar Pe dependencies as the monodisperse case. However, introducing a second species to the suspension apparently enhances the long-time self-diffusivities of both species, particularly at high Pe. This mutual diffusivity enhancement is in contrast to the short-time diffusivities in Fig. 4.8a, where at $\phi = 0.45$, the small particle diffusivity enhancement is always accompanied by the large particle diffusivity supression. Moreover, the diffusivity enhancement in y-direction is stronger than those in z-direction.

In Fig. 4.18 the diffusivities from SEASD-nf in general agree with the SEASD results for both monodisperse and bidisperse suspensions. At low Pe, the SEASD-nf diffusivity is lower, particularly for the large particles. The agreement between SEASD and SEASD-nf improves with increasing Pe due to the reduced influences of Brownian motion.

Suspension structures

Finally, we examine the structures of sheared bidisperse suspensions via the projections of the partial pair-distribution functions $g_{\alpha\beta}(\boldsymbol{r})$, which are defined as the conditional probability of finding another particle in species β given a particle of species α, *i.e.*,

$$g_{\alpha\beta}(\boldsymbol{r}) = \frac{1}{n_\alpha n_\beta}\left\langle \sum_{\substack{i\in\alpha,\\ j\in\beta}}{}' \frac{1}{V}\delta(\boldsymbol{r} - \boldsymbol{r}_i + \boldsymbol{r}_j)\right\rangle. \tag{4.96}$$

They are related to the pair-distribution function $g(\boldsymbol{r})$ through

$$g(\boldsymbol{r}) = \sum_{\alpha,\beta} x_\alpha x_\beta g_{\alpha\beta}(\boldsymbol{r}). \tag{4.97}$$

Fig. 4.19, 4.20, and 4.21 present projections of $g(\boldsymbol{r})$ and $g_{\alpha\beta}(\boldsymbol{r})$ on the velocity-velocity gradient (xy-) plane, the velocity-vorticity (xz-) plane, and the velocity gradient-vorticity (yz-) plane, respectively, at selected Péclet numbers. These figures are based on particle trajectories from SEASD simulation, and are indistinguishable from the SEASD-nf results.

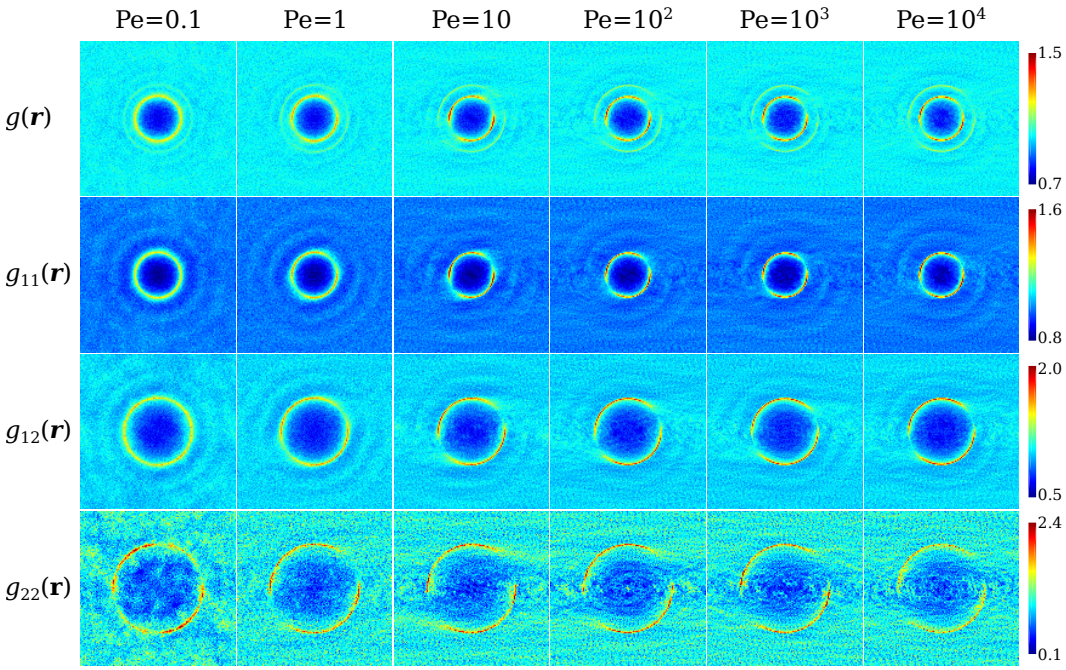

Figure 4.19: (Color online) The velocity-velocity gradient (xy-) plane projection of the pair-distribution function $g(\boldsymbol{r})$ and the partial pair-distribution functions $g_{\alpha\beta}(\boldsymbol{r})$ at various Pe for bidisperse suspensions with $\phi = 0.45$, $\lambda = 2$, and $y_2 = 0.5$.

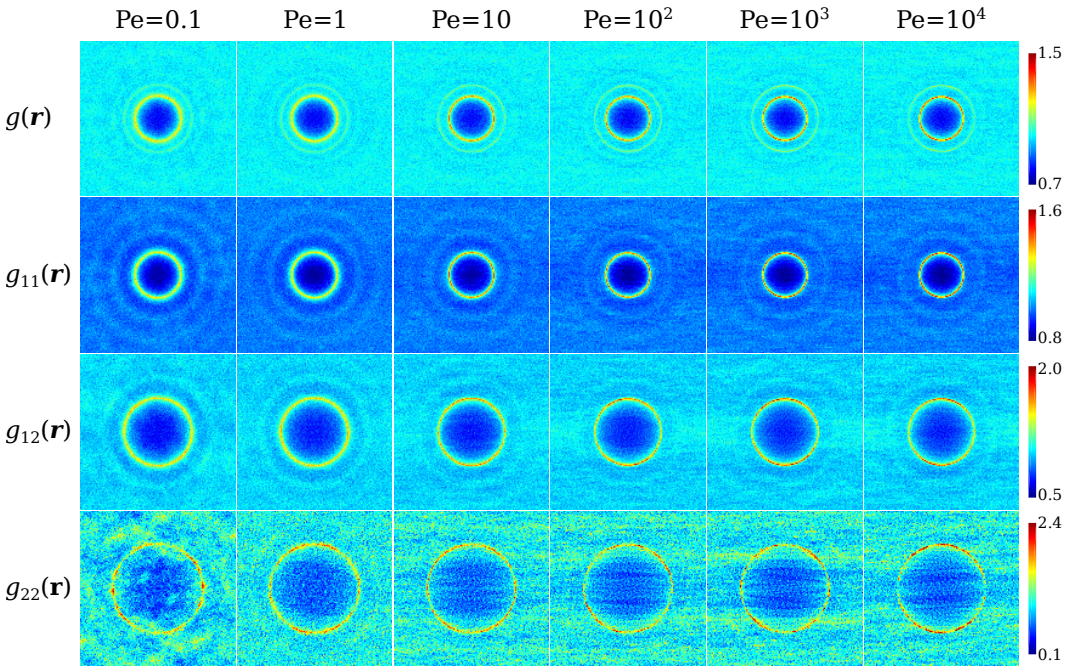

Figure 4.20: (Color online) The velocity-vorticity (xz-) plane projection of the pair-distribution function $g(\boldsymbol{r})$ and the partial pair-distribution functions $g_{\alpha\beta}(\boldsymbol{r})$ at various Pe for bidisperse suspensions with $\phi = 0.45$, $\lambda = 2$, and $y_2 = 0.5$.

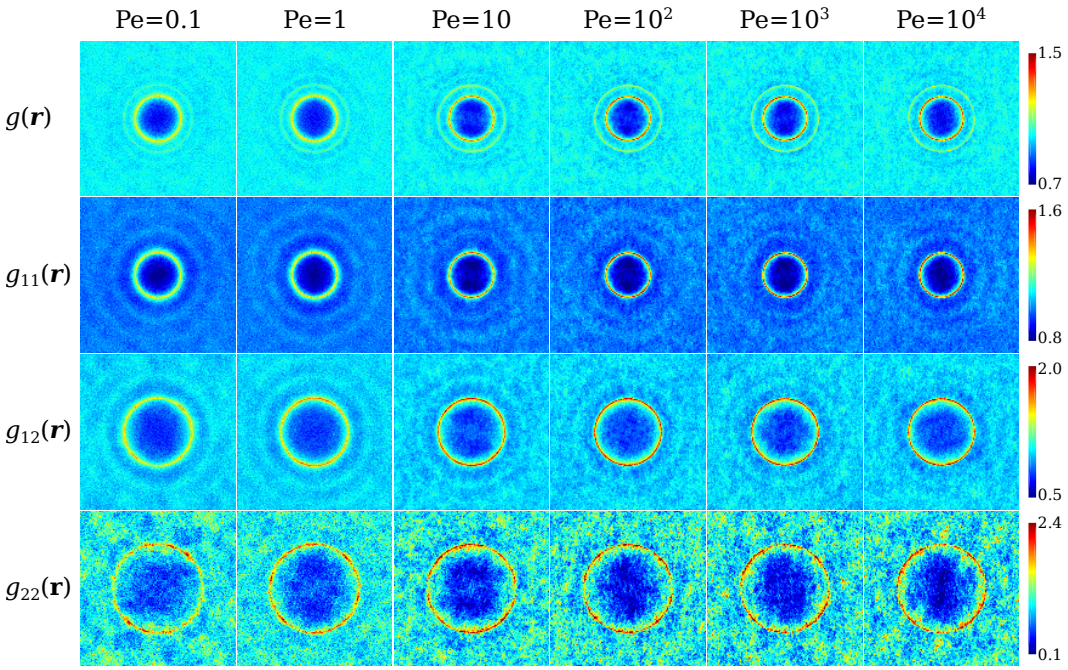

Figure 4.21: (Color online) The velocity gradient-vorticity (yz-) plane projection of the pair-distribution function $g(\boldsymbol{r})$ and the partial pair-distribution functions $g_{\alpha\beta}(\boldsymbol{r})$ at various Pe for bidisperse suspensions with $\phi = 0.45$, $\lambda = 2$, and $y_2 = 0.5$.

Fig. 4.19 clearly displays the structural anisotropy caused by the shear flow in the xy-plane, characterized by the distortion of the otherwise isotropic pair-distribution rings. With increasing Pe, the overall pair-distribution function $g(\boldsymbol{r})$ shows an accumulation of neighboring particles in the compressional quadrant. This is indicated by the brightening and thinning of the rings at $2a_1$, $a_1 + a_2$, and $2a_2$, corresponding to the particle pairs of two small particles, a large and a small particle, and two large particles, respectively. Meanwhile, the particle pairs are depleted in the extensional quadrant.

Specific changes in different particle pairs are revealed by examining the corresponding partial pair-distribution function $g_{\alpha\beta}(\boldsymbol{r})$ in Fig. 4.19. The distribution of the small-small particle pairs is presented in $g_{11}(\boldsymbol{r})$. Similarly to $g(\boldsymbol{r})$, $g_{11}(\boldsymbol{r})$ is increasingly distorted and compressed in the compressional quadrant with increasing Pe, forming a boundary layer. At higher Pe, the pair structure remain approximately unchanged. In the extensional quadrant, the pair breakup point shifts from the extensional axis towards the velocity (x-) direction due to the lubrication interactions, with a clear tail of high probability outlining the trajectory of small-small pair disengagement. The distribution of the small-large particle pairs in $g_{12}(\boldsymbol{r})$ shows a similar

structural distortion in the compressional quadrant with increasing Pe. Moreover, in the extensional quadrant, the trajectory of particle disengagement is more diffusive compared to $g_{11}(\boldsymbol{r})$ at the same Pe. This suggests that particle movement in bidisperse suspensions are facilitated by the breakup of small-large particle pairs, and partially explains the mutual enhancement of long-time self-diffusivity in Fig. 4.18. For the distribution of large-large particle pairs, $g_{22}(\boldsymbol{r})$ also exhibits anisotropy with increasing Pe in Fig. 4.19. However, due to the limited particle number, information beyond the first coordinate shell is difficult to analyze.

Fig. 4.20 displays the total and partial pair-distribution function projections in the xz-plane. Unlike the xy-plane projections in Fig. 4.19 which exhibits strong anisotropy, the suspension structures here are less sensitive to Pe. With increasing Pe, the particles are compressed towards each other, which is evidenced by the thinning and brightening of the first coordinate shells. More interestingly, at higher Pe $\geq$ 100, $g_{12}(\boldsymbol{r})$ shows a belt of particle enrichment along the flow direction, while $g_{11}(\boldsymbol{r})$ and $g_{22}(\boldsymbol{r})$ exhibit a corresponding particle depletion. This indicates that the small-large pairs are preferred in the xz-plane, and that the shear flow promotes species mixing in the flow direction.

Fig. 4.21 shows the projection of $g(\boldsymbol{r})$ and $g_{\alpha\beta}(\boldsymbol{r})$ in the yz-plane. With increasing Pe, the shear flow also compresses the particle pairs in this plane without apparent anisotropy. Note that even at Pe $= 10^4$, the suspension does not exhibit string ordering [98] due to the HIs. The lack of structural formation is also confirmed by the continuous increase of the long-time self-diffusivities $d^{t,yy}_{\infty,\alpha}$ and $d^{t,yy}_{\infty,\alpha}$ with Pe in Fig. 4.18.

4.7 Conclusions

In this chapter we presented the Spectral Ewald Accelerated Stokesian Dynamics (SEASD) for dynamic simulations of polydisperse colloidal suspensions. Using the framework of Stokesian Dynamics (SD), SEASD can accurately and rapidly compute HIs in dense polydisperse suspensions. Other features of SEASD include (*i*) direct inclusion of the solvent compressibility and pressure evaluations, (*ii*) the use of the Spectral Ewald (SE) method for accurate mobility computation with flexible error control, (*iii*) a far-field preconditioner to accelerate the convergence of the nested iterative scheme, (*iv*) GPGPU accelerated mobility evaluation for almost an order of magnitude speed improvement, and (*v*) the incorporation of SEASD-nf, an extension of the mean-field Brownian approximation of Banchio & Brady [39]

to polydisperse suspensions.

We extensively discussed the accuracy of mobility computation using the SE method, established the baseline for parameter selection, and demonstrated the adequate accuracy in the GPU single precision (SP) mobility computation. We found that compared to the full SEASD computations, SEASD-nf can achieve significant speedup without substantially sacrificing accuracy. Indeed, for all the dynamic simulations in this work, the SEASD and the SEASD-nf results agree satisfactorily. In addition, we verified the $\mathcal{O}(N \log N)$ computational scaling of SEASD and SEASD-nf in dynamic simulations.

We rigorously validated SEASD and SEASD-nf for monodisperse and bidisperse colloidal suspensions via: (*i*) the short-time transport properties, (*ii*) the equilibrium osmotic pressure and viscoelastic moduli, and (*iii*) the steady Brownian shear rheology at $\phi = 0.45$. For (*i*), the SEASD diffusivities and shear viscosity agree with the conventional SD calculations. The SEASD sedimentation velocity differ qualitatively from the SD results due to the absence of a mean-field quadrupole term in the mobility computation. For the bulk viscosity computation, different procedures to eliminate the spurious HIs lead to slight differences in the SEASD and the SD results. In (*ii*), SEASD and SEASD-nf reproduced the equilibrium suspension osmotic pressure for monodisperse and bidisperse suspensions within the error tolerance, with the SEASD data higher. For the steady shear rheology in (*iii*), the agreement between SEASD-nf and SEASD is satisfactory in the suspension mechanics, dynamics, and structures. Moreover, we found that the particle size polydispersity reduces the suspension viscosity and osmotic pressure, and enhances the long-time translational self-diffusivities of both species. Our rheological simulations also improve our understanding on the structure, dynamics, and rheology of polydisperse suspensions.

The SEASD and the SEASD-nf developed in this work are important tools for studying dynamics of dense, polydisperse colloidal suspensions, and have significantly extended the parameter space accessible to computational studies. For example, they can provide otherwise inaccessible details on a wide range of experimental observations including the yielding phenomena in glass rheology and the continuous and discontinuous shear-thickening. Furthermore, the computational framework can be conveniently extended to other systems, *e.g.*, with geometric confinement or with autonomous propulsion.

Finally, through SEASD and SEASD-nf we have demonstrated the generality and

versatility of the SD framework, particularly the splitting of the far- and near-field interactions: with a suitable far-field computation, the lubrication interactions can be added pairwise for free. We believe that many far-field HI computational methods can and should be used with the SD framework to expand their accessible parameter range, particularly for dense systems.

References

[1] W. B. Russel, D. A. Saville, and W. R. Schowalter, *Colloidal dispersions* (Cambridge University Press, 1991).

[2] J. S. Chong, E. B. Christiansen, and A. D. Baer, "Rheology of concentrated suspensions", J. Appl. Polym. Sci. **15**, 2007 (1971).

[3] B. E. Rodriguez, E. W. Kaler, and M. S. Wolfe, "Binary mixtures of monodisperse latex dispersions. 2. viscosity", Langmuir **8**, 2382 (1992).

[4] T. Shikata, H. Niwa, and Y. Morishima, "Viscoelastic behavior of bimodal suspensions", J. Rheo. **42**, 765 (1998).

[5] T. Sentjabrskaja, E. Babaliari, J. Hendricks, M. Laurati, G. Petekidis, and S. U. Egelhaaf, "Yielding of binary colloidal glasses", Soft Matter **9**, 4524 (2013).

[6] D. Semwogerere and E. R. Weeks, "Shear-induced particle migration in binary colloidal suspensions", Phys. Fluids **20**, 043306 (2008).

[7] L. Durlofsky, J. F. Brady, and G. Bossis, "Dynamic simulation of hydrodynamically interacting particles", J. Fluid Mech. **180**, 21 (1987).

[8] G. K. Batchelor, "Sedimentation in a dilute polydisperse system of interacting spheres. Part 1. General theory", J. Fluid Mech. **119**, 379 (1982).

[9] N. J. Wagner and A. T. J. M. Woutersen, "The viscosity of bimodal and polydisperse suspensions of hard spheres in the dilute limit", J. Fluid Mech. **278**, 267 (1994).

[10] H. Zhang and G. Nägele, "Tracer-diffusion in binary colloidal hard-sphere suspensions", J. Chem. Phys. **117**, 5908 (2002).

[11] M. Wang and J. F. Brady, "Short-time transport properties of bidisperse suspensions and porous media: a Stokesian Dynamics study", J. Chem. Phys. **142**, 094901 (2015).

[12] M. Wang, M. Heinen, and J. F. Brady, "Short-time diffusion in concentrated bidisperse hard-sphere suspensions", J. Chem. Phys. **142**, 064905 (2015).

[13] T. Ando and J. Skolnick, "Crowding and hydrodynamic interactions likely dominate in vivo macromolecular motion", Proc. Natl. Acad. Sci. U. S. A. **107**, 18457 (2010).

[14] A. J. C. Ladd, "Hydrodynamic transport coefficients of random dispersions of hard spheres", J. Chem. Phys. **93**, 3484 (1990).

[15] B. Cichocki, B. U. Felderhof, K. Hinsen, E. Wajnryb, and J. Blawzdziewicz, "Friction and mobility of many spheres in Stokes flow", J. Chem. Phys. **100**, 3780 (1994).

[16] G. K. Youngren and A. Acrivos, "Stokes flow past a particle of arbitrary shape: a numerical method of solution", J. Fluid Mech. **69**, 377 (1975).

[17] C. Pozrikidis, *Boundary integral and singularity methods for linearized viscous flow* (Cambridge University Press, 1992).

[18] L. B. Lucy, "A numerical approach to the fission hypothesis", Astronomical Journal **82**, 1013 (1977).

[19] G. R. Liu and M. B. Liu, *Smoothed particle hydrodynamics: a meshfree particle method* (World Scientific, 2003).

[20] P. J. Hoogerbrugge and J. M. V. A. Koelman, "Simulating microscopic hydrodynamic phenomena with Dissipative Particle Dynamics", Europhys. Lett. **19**, 155 (1992).

[21] B. Dünweg and A. J. C. Ladd, "Lattice Boltzmann simulations of soft matter systems", Adv. Polym. Sci. **221**, 89 (2009).

[22] M. Abbas, E. Climent, O. Simonin, and M. R. Maxey, "Dynamics of bidisperse suspensions under stokes flows: linear shear flow and sedimentation", Phys. Fluids **18**, 121504 (2006).

[23] B. Cichocki, M. L. Ekiel-Jeźewska, and E. Wajnryb, "Lubrication corrections for three-particle contribution to short-time self-diffusion coefficients in colloidal dispersions", J. Chem. Phys. **111**, 3265 (1999).

[24] B. Cichocki, R. B. Jones, R. Kutteh, and E. Wajnryb, "Friction and mobility for colloidal spheres in Stokes flow near a boundary: the multipole method and applications", J. Chem. Phys. **112**, 2548 (2000).

[25] K. Yeo and M. R. Maxey, "Simulation of concentrated suspensions using the force-coupling method", J. Comput. Phys. **229**, 2401 (2010).

[26] N.-Q. Nguyen and A. J. C. Ladd, "Lubrication corrections for lattice-Boltzmann simulations of particle suspensions", Phys. Rev. E **66**, 046708 (2002).

[27] S. Gallier, E. Lemaire, L. Lobry, and F. Peters, "A fictitious domain approach for the simulation of dense suspensions", J. Comput. Phys. **256**, 367 (2014).

[28] A. Lefebvre-Lepot, B. Merlet, and T. N. Nguyen, "An accurate method to include lubrication forces in numerical simulations of dense Stokesian suspensions", J. Fluid Mech. **769**, 369 (2015).

[29] D. Lindbo and A.-K. Tornberg, "Spectrally accurate fast summation for periodic Stokes potentials", J. Comput. Phys. **229**, 8994 (2010).

[30] D. Lindbo and A.-K. Tornberg, "Spectral accuracy in fast Ewald-based methods for particle simulations", J. Comput. Phys. **230**, 8744 (2011).

[31] L. af Klinteberg and A.-K. Tornberg, "Fast Ewald summation for Stokesian particle suspensions", Int. J. Numer. Methods Fluids **76**, 669 (2014).

[32] T. Darden, D. York, and L. Pedersen, "Particle mesh Ewald: an Nlog(N) method for Ewald sums in large systems", J. Chem. Phys. **98**, 10089 (1993).

[33] U. Essmann, L. Perera, M. L. Berkowitz, T. Darden, H. Lee, and L. G. Pedersen, "A smooth particle mesh Ewald method", J. Chem. Phys. **103**, 8577 (1995).

[34] L. Greengard and V. Rokhlin, "A fast algorithm for particle simulations", J. Comput. Phys. **73**, 325 (1987).

[35] K. Ichiki, "Improvement of the Stokesian Dynamics method for systems with a finite number of particles", J. Fluid Mech. **452**, 231 (2002).

[36] A. Sierou and J. F. Brady, "Accelerated Stokesian Dynamics simulations", J. Fluid Mech. **448**, 115 (2001).

[37] D. Saintillan, E. Darve, and E. S. G. Shaqfeh, "A smooth particle-mesh Ewald algorithm for Stokes suspension simulations: the sedimentation of fibers", Phys. Fluids **17**, 033301 (2005).

[38] D. L. Ermak and J. A. McCammon, "Brownian dynamics with hydrodynamic interactions", J. Chem. Phys. **69**, 1352 (1978).

[39] A. J. Banchio and J. F. Brady, "Accelerated Stokesian Dynamics: brownian motion", J. Chem. Phys. **118**, 10323 (2003).

[40] J. W. Swan and J. F. Brady, "Colloidal dispersions deformed by a steady shear stress", Submitted (2013).

[41] A. Kumar and J. J. L. Higdon, "Origins of the anomalous stress behavior in charged colloidal suspensions under shear", Phys. Rev. E **82**, 051401 (2010).

[42] L. D. Landau and E. M. Lifshitz, *Fluid mechanics* (Butterworth-Heinemann, 1987).

[43] A. J. C. Ladd, H. Gang, J. X. Zhu, and D. A. Weitz, "Temporal and spatial dependence of hydrodynamic correlations: Simulation and experiment", Phys. Rev. E **52**, 6550 (1995).

[44] E. E. Keaveny, "Fluctuating force-coupling method for simulations of colloidal suspensions", J. Comput. Phys. **269**, 61 (2014).

[45] S. Delong, F. B. Usabiaga, R. Delgado-Buscalioni, B. E. Griffith, and A. Donev, "Brownian dynamics without Green's functions", J. Chem. Phys. **140**, 134110, (2014).

[46] M. Kopp and F. Höfling, "GPU-accelerated simulation of colloidal suspensions with direct hydrodynamic interactions", Eur. Phys. J.-Spec. Top. **210**, 101 (2012).

[47] N. Ganesan, M. Taufer, B. Bauer, and S. Patel, "FENZI: gpu-enabled Molecular Dynamics simulations of large membrane regions based on the CHARMM force field and PME", in Ieee ipdpsw (2011), p. 472.

[48] M. J. Harvey and G. De Fabritiis, "An implementation of the smooth particle mesh Ewald method on GPU hardware", J. Chem. Theory Comput. **5**, 2371 (2009).

[49] F. Boyer, E. Guazzelli, and O. Pouliquen, "Unifying suspension and granular rheology", Phys. Rev. Lett. **107**, 188301 (2011).

[50] J. F. Brady, A. S. Khair, and M. Swaroop, "On the bulk viscosity of suspensions", J. Fluid Mech. **554**, 109 (2006).

[51] J. F. Brady, "Brownian motion, hydrodynamics, and the osmotic pressure", J. Chem. Phys. **98**, 3335 (1993).

[52] J. F. Morris and F. Boulay, "Curvilinear flows of noncolloidal suspensions: the role of normal stresses", J. Rheo. **43**, 1213 (1999).

[53] Y. Yurkovetsky and J. F. Morris, "Particle pressure in sheared Brownian suspensions", J. Rheo. **52**, 141 (2008).

[54] S. Kim and S. J. Karrila, *Microhydrodynamics* (Dover, 2005).

[55] K. Makuch and B. Cichocki, "Transport properties of suspensions–critical assessment of beenakker-mazur method", Journal of Chemical Physics **137**, 184902 (2012).

[56] P. Szymczak and B. Cichocki, "A diagrammatic approach to response problems in composite systems", J. Stat. Mech. Theor. Exp., P01025 (2008).

[57] W. van Saarloos and P. Mazur, "Many-sphere hydrodynamic interactions and mobilities in a suspension", Physica **115A**, 21 (1982).

[58] A. J. C. Ladd, "Hydrodynamic interactions in a suspension of spherical particles", J. Chem. Phys. **88**, 5051 (1988).

[59] R. Schmitz and B. U. Felderhof, "Creeping flow about a spherical particle", Physica **113A**, 90 (1982).

[60] H. Hasimoto, "On the periodic fundamental solutions of the Stokes equations and their application to viscous flow past a cubic array of spheres", J. Fluid Mech. **5**, 317 (1959).

[61] C. W. J. Beenakker, "Ewald sum of the Rotne-Prager tensor", J. Chem. Phys. **85**, 1581 (1986).

[62] J. W. Swan and J. F. Brady, "Particle motion between parallel walls: hydrodynamics and simulation", Phys. Fluids **22**, 103301 (2010).

[63] J. W. Swan and J. F. Brady, "The hydrodynamics of confined dispersions", J. Fluid Mech. **687**, 254 (2011).

[64] J. F. Brady, R. J. Phillips, J. C. Lester, and G. Bossis, "Dynamic simulation of hydrodynamically interacting suspensions", J. Fluid Mech. **195**, 257 (1988).

[65] D. J. Jeffrey, J. F. Morris, and J. F. Brady, "The pressure moments for two rigid spheres in low-Reynolds-number flow", Phys. Fluids A **5**, 10 (1993).

[66] A. S. Khair, M. Swaroop, and J. F. Brady, "A new resistance function for two rigid spheres in a uniform compressible low-Reynolds-number flow", Phys. Fluids **18**, 043102 (2006).

[67] H. G. Petersen, "Accuracy and efficiency of the particle mesh Ewald method", J. Chem. Phys. **103**, 3668 (1995).

[68] M. Deserno and C. Holm, "How to mesh up ewald sums. I.A theoretical and numerical comparison of various particle mesh routines", J. Chem. Phys. **109**, 7678 (1998).

[69] L. Greengard and J.-Y. Lee, "Accelerating the nonuniform Fast Fourier Transform", SIAM Rev. **46**, 443 (2004).

[70] M. P. Allen and D. J. Tildesley, *Computer simulation of liquids* (Clarendon Press, 1991).

[71] R. W. Hockney and J. W. Eastwood, *Computer simulation using particles* (Adam Hilger, 1989).

[72] H. J. Wilson, "Stokes flow past three spheres", J. Comput. Phys. **245**, 302 (2013).

[73] D. R. Foss and J. F. Brady, "Structure, diffusion and rheology of Brownian suspensions by Stokesian Dynamics simulation", J. Fluid Mech. **407**, 167 (2000).

[74] A. Sierou and J. F. Brady, "Rheology and microstructure in concentrated noncolloidal suspensions", J. Rheo. **46**, 1031 (2002).

[75] Y. Saad, *Iterative methods for sparse linear systems* (SIAM, 2003).

[76] D. J. Jeffrey and Y. Onishi, "Calculation of the resistance and mobility functions for two unequal rigid spheres in low-Reynolds-number flow", J. Fluid Mech. **139**, 261 (1984).

[77] D. J. Jeffrey, "The calculation of the low Reynolds number resistance functions for two unequal spheres", Phys. Fluids A **4**, 16 (1992).

[78] D. J. Evans and G. Morriss, *Statistical mechanics of nonequilibrium liquids* (Cambridge University Press, 2008).

[79] G. Bossis and J. F. Brady, "Self-diffusion of Brownian particles in concentrated suspensions under shear", J. Chem. Phys. **87**, 5437 (1987).

[80] R. M. Jendrejack, M. D. Graham, and J. J. de Pablo, "Hydrodynamic interactions in long chain polymers: Application of the Chebyshev polynomial approximation in stochastic simulations", J. Chem. Phys. **113**, 2894 (2000).

[81] N. J. Higham, *Functions of matrices: theory and computation* (SIAM, 2008).

[82] S. K. Boyd, J. Baglama, and E. J. Allen, "Numerical approximation of the product of the square root of a matrix with a vector", Linear Algebra Appl. **310**, 167 (2000).

[83] L. N. Trefethen, *Spectral methods in matlab* (SIAM, 2000).

[84] M. Wang and J. F. Brady, "The suspension balance model revisited: Revisited", In preparation (2015).

[85] B. D. Lubachevsky and F. H. Stillinger, "Geometric properties of random disk packings", J. Stat. Phys. **60**, 561 (1990).

[86] M. Skoge, A. Donev, F. H. Stillinger, and S. Torquato, "Packing hyperspheres in high-dimensional Euclidean spaces", Phys. Rev. E **74**, 041127 (2006).

[87] J. K. Percus and G. J. Yevick, "Analysis of classical statistical mechanics by means of collective coordinates", Phys. Rev. **110**, 1 (1958).

[88] J. L. Lebowitz, "Exact solution of generalized Percus-Yevick equation for a mixture of hard spheres", Phys. Rev. **133**, A895 (1964).

[89] N. W. Ashcroft and D. C. Langreth, "Structure of binary liquid mixtures. I", Phys. Rev. **156**, 685 (1967).

[90] N. W. Ashcroft and D. C. Langreth, "Errata", Phys. Rev. **166**, 934 (1968).

[91] R. J. Phillips, J. F. Brady, and G. Bossis, "Hydrodynamic transport properties of hard-sphere dispersions. I. Suspensions of freely mobile particles", Phys. Fluids **31**, 3462 (1988).

[92] M. Swaroop, "The bulk viscosity of suspensions", PhD thesis (California Institute of Technology, 2010).

[93] G. A. Mansoori, N. S. Carnahan, K. E. Starling, and T. W. Leland, "Equilibrium thermodynamic properties of the mixture of hard spheres", J. Chem. Phys. **54**, 1523 (1971).

[94] J. F. Brady, "The rheological behavior of concentrated colloidal dispersions", J. Chem. Phys. **99**, 567 (1993).

[95] G. Nägele and J. Bergenholtz, "Linear viscoelasticity of colloidal mixtures", J. Chem. Phys. **108**, 9893 (1998).

[96] D. Lindbo and A.-K. Tornberg, "Fast and spectrally accurate summation of 2-periodic Stokes potentials", arXiv:1111.1815 (2011).

[97] H. M. Vollebregt, R. G. M. van der Sman, and R. M. Boom, "Model for particle migration in bidisperse suspensions by use of effective temperature", Faraday Discuss. **158**, 89 (2012).

[98] D. R. Foss and J. F. Brady, “Brownian Dynamics simulation of hard-sphere colloidal dispersions”, J. Rheo. **44**, 629 (2000).

Chapter 5

SUSPENSION MICROSTRUCTURES AND MECHANICS IN THE COLLOIDAL FILM DRYING PROCESS

5.1 Introduction

Colloidal suspensions find widespread applications in science and technology. They are commonly applied as thin films on a substrate to modify or enhance its surface properties. An example is latex paint, which, by changing the corrosion resistance and color of the substrate, makes the material more durable and aesthetically appealing. In addition to chemistry, the thin film structure and mechanics also become increasingly important to the film's quality and functionality, especially for many novel materials. For instance, the optical properties of thin-film colloidal structures are strongly influenced by its long-range crystalline nature [1] or lack thereof [2]. On the other hand, the residual stresses in the film can lead to cracking and warping that adversely affect the film quality [3–5]. The thin film structural and mechanical properties largely depend on the film drying process, where the solvent is removed from the suspension, and the colloidal particles are compressed by the receding interface [6]. A thorough understanding of this process is clearly necessary for further innovations [7, 8].

The colloidal film drying process is complex: in addition to the interfacial phenomena from the continuously receding liquid-air interface, such as capillary pressure and Marangoni flow [6, 9], it is also affected by features inherent to the colloidal suspension [10, 11]: (*i*) Brownian motion, (*ii*) hydrodynamic interactions, and (*iii*) interparticle potential. Both (*i*) and (*ii*) originate from the disparate size difference between the colloidal particles and the solvent molecules. Examples of (*iii*) include screened electrostatic potentials, excluded volume effects, and the plastic/elastic deformation of the particles [9]. These features are also strongly affected by the confinement from the interface and the substrate [10, 12–15]. Clearly, the complexity necessitates simplifications to distill the essential physics.

In this work we use Brownian Dynamics (BD) simulations and continuum models to study the structural and mechanical evolution of the colloidal film drying process. We focus on the simplest non-trivial model system: the uniaxial compression of monondisperse hard-sphere Brownian particles between hard boundaries without

hydrodynamic interactions. This system captures the colloidal interactions among the moving boundary, the particle Brownian motion, and the excluded volume effect. Compared to earlier simulations of the film drying processes via kinetic Monte Carlo [16], soft potential BD [17], and multiscale methods [18–20], focusing on a simple model allows systematic investigation of key parameters. Indeed, our focus on simple systems is motivated by progress in the rheology of dense colloidal suspensions, which has come from in-depth investigations of hard-sphere Brownian systems [21–23].

In the colloidal film drying process, as the fluid evaporates, the liquid-air interface pushes the particles towards the stationary substrate, while the particle Brownian motion attempts to smooth out any local concentration fluctuations (see Fig. 5.1). With an interface velocity U_w, the competition between convection and diffusion defines Péclet number,

$$\mathrm{Pe}_U = aU_w/d_0, \tag{5.1}$$

where a is the particle radius and $d_0 = k_\mathrm{B}T/\zeta$ is the single-particle Stokes-Einstein-Sutherland diffusivity, with $k_\mathrm{B}T$ the thermal energy scale and $\zeta = 6\pi\eta_0 a$ the particle resistance in a solvent of viscosity η_0. Physically, $\mathrm{Pe}_U \ll 1$ suggests slow interface movement and Brownian motion dominated dynamics, while $\mathrm{Pe}_U \gg 1$ indicates fast interface movement and convection dominance. Experimentally, varying the drying rate changes Pe_U, which, in turn, alters the film structure. To obtain uniform and ordered film structures, conventional wisdom is that $\mathrm{Pe}_U \ll 1$ is necessary to allow time for the thermodynamic phase transition [24–26]. Surprisingly, recent experiments and simulations also found highly ordered structures with $\mathrm{Pe}_U \gg 1$ [27].

The first objective of this work is to characterize the film structures over a wide range of Pe_U. In the $\mathrm{Pe}_U \ll 1$ limit, the final film structure can be predicted from the equilibrium phase behaviors of confined suspensions, as the slow interface movement allows sufficient time for equilibration. The phase behavior of hard-sphere systems are well studied in experiments [28] and simulations [29, 30]. With confinement, the crystallization onset density is significantly reduced compared to bulk systems [31], and reducing the confinement (increasing the gap spacing) introduces a hierarchy of crystalline structures as $c\triangle \to c\square \to (c+1)\triangle$, where c is the number of crystalline layers, and $\triangle$ and $\square$ respectively represent crystalline structures of triangular and square symmetries (see Fig. 5.2). The behavior at finite Pe_U and large gap spacing may be inferred from the sedimentation process next to a confining boundary through a change of reference frame, assuming limited

influences of hydrodynamic interactions. Experiments [32–34] and simulations [35–37] show that crystal growth is initiated next to the confining boundary as a first order phase transition, and continues upwards epitaxially. With increasing sedimentation velocity—equivalent to increasing the interface velocity in the drying process—the competition between the particle settling and the crystal growth lead to stack faults and even glassy structures in crystalline domains. Similar structural evolution is expected for the drying process near the moving interface. Furthermore, at smaller gap spacing, the confinement can disrupt the crystallization process, leading to frustrated structures [38, 39]. However, we are not aware of any similar theoretical and simulation investigations in the $\mathrm{Pe}_U \gg 1$ limit.

We deliberately limit ourselves to systems without hydrodynamic interactions. With this simplification, compression, filtration, and sedimentation are equivalent when the gap spacing are sufficiently large. However, such equivalence does not hold with hydrodynamic interactions. For example, Rayleigh-Taylor instability [34] develops in sedimentation as particles are under constant forces, but not in compression or filtration as particles move with the imposed flow. In sedimentation, the back flow from the no-flux boundary conditions leads to strong particle velocity fluctuations [40]. However, the back flow is absent in filtration and compression due to solvent removal. Furthermore, the influences of hydrodynamic interactions on confined systems are profound [12, 15], and are beyond the scope of this work.

The second objective of this work is to study the stress distributions in the suspension during the drying process. The residual stress can cause unwanted deformation in the film product, such as cracking and warping [4, 5, 9]. Physically, they are attributed to the capillary pressure from the liquid menisci among the colloidal particles. However, stress balance alone can show that the deformation is inevitable regardless of the underlying mechanisms. The argument goes as follows: a stable film formed by the drying process with interface movement in the z direction must satisfy the steady state stress balance $\partial \Sigma_{zz}/\partial z = 0$, suggesting that the zz component of the stress, Σ_{zz}, must be constant across the film. If the Σ_{zz} distribution in the z-direction is not constant, other mechanisms including the lateral film deformation must step in to maintain the constant stress. Therefore, monitoring the stress distribution during the compression process provides a key indication on future film deformation. This often overlooked aspect of the compression process is also addressed in this work.

The film drying process is also affected by the interface movement profile: in addition to the constant velocity movement, the interface may also move in response to a

constant imposed normal stress Σ_e. The resulting film structural and mechanical evolution is also investigated in this work. Here, the competition between the external energy $a^3\Sigma_e$ and the thermal energy $k_\mathrm{B}T$ defines a stress Péclet number

$$\mathrm{Pe}_\Sigma = a^3\Sigma_e/(k_\mathrm{B}T). \tag{5.2}$$

With this drying process, the interface slows down as the suspension osmotic pressure grows due the increasing density, and eventually stops when the osmotic pressure matches Σ_e. Clearly, a single Pe_Σ corresponds to spectrum of Pe_U down to zero in the constant velocity drying process.

Experimentally, constant stress interface movement may be achieved by compressing the suspension using a rigid, porous substrate that is only permeable to the solvent with constant mechanical load. Although new for colloidal systems, this compression mode is common in the Surface Force Apparatus (SFA) experiments to characterize the molecular interactions in thin films [41]. These experiments lead to extensive molecular dynamics [42–45] and Monte Carlo [46, 47] investigations for interpreting the results. With the same principle of operation to SFA experiments, the constant normal stress compression is a promising method to characterize interactions in colloidal films. We hope this work serves as a first step for future investigations in this direction.

Another focus of this work is on continuum models, which are crucial for selecting parameters in the engineering and design of the drying process [26, 48]. Assuming local thermal equilibrium, these models are derived from the principle of mass conservation, and agree well with experiments with strong thermal fluctuations ($\mathrm{Pe}_U \ll 1$ or $\mathrm{Pe}_\Sigma \ll 1$). The same philosophy is used to model the sedimentation processes [10, 49, 50]. However, it is unclear if these continuum models remain valid when the thermal fluctuations are weak. In this limit, other physics also becomes important. For example, non-local effects are necessary to properly model the non-equilibrium flow of granular materials [51]. By developing continuum models for constant velocity and constant normal stress interface movement following the traditional approach [10], we compare the model predictions with the simulation results to elucidate the validity of the models, especially in the high Péclet number limit.

Finally, dynamic simulation of the drying process and the measurement of suspension stress profiles pose significant challenges for existing algorithms. Brownian dynamics algorithms for hard-sphere suspensions can be based on event-driven [52,

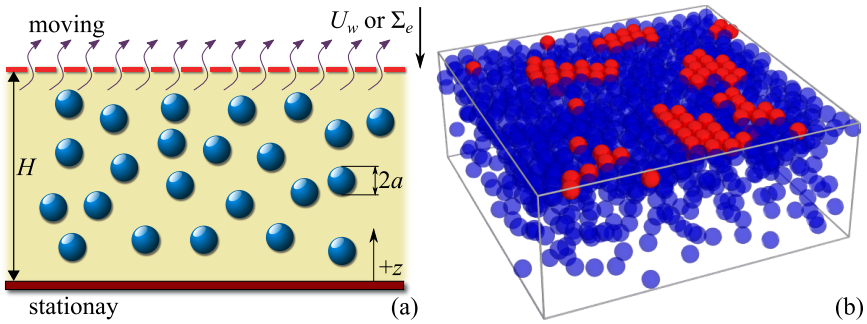

Figure 5.1: (Color online) (a): A sketch of the colloidal film drying process. Colloidal particles of radius a are sandwiched between a stationary substrate at $z = 0$ and an interface at $z = H$, moving either at constant velocity U_w or in response to a constant normal stress Σ_e in the $-z$ direction. The interface allows the solvent, but not the particles, to pass. (b): A snapshot of the simulation cell at $\mathrm{Pe}_U = 50$ and $H = 15a$. The blue particles are amorphous while the red particles are crystalline.

53] or time-discretization [21, 54–56]. Here, the complications due to the moving interface rules out the event-driven algorithms. On the other hand, time-discretization methods known as the "potential-free" algorithms are based on iterative overlap resolution. Unfortunately, they are unsuitable for accurate stress profile measurement, as the particle position changes in the overlap resolution process. Moreover, circular overlap resolution at high densities may halt the simulation. In this work, we address these challenges by developing a new Energy Minimization Potential-Free (EMPF) algorithm, which imposes the hard-sphere potential by simultaneously resolving the overlaps using the minimum energy principle.

This rest of the chapter is arranged as follows: in Sec. 5.2 we describe the problem setup, the energy minimization potential-free algorithm, and the continuum model. The simulation and numerical results are presented and discussed in Sec. 5.3. Finally, we summarize and conclude in Sec. 5.4.

5.2 Methods

We consider N neutrally buoyant colloidal particles of equal radius a suspended in a solvent of viscosity η_0, occupying a total volume of V. The position of particle i is at $\boldsymbol{x}_i = (x_i, y_i, z_i)$. The particle number density $n = N/V$ and the volume fraction $\phi = \frac{4}{3}\pi a^3 n$. The suspension is sandwiched between a stationary substrate at $z = 0$ and an interface at $z = H(t)$, moving towards the substrate in the $-z$ direction. The sketch of the colloidal film drying process is shown in Fig. 5.1a, and a snapshot of

the simulation cell is shown in Fig. 5.1b. In the transverse (x- and y-) directions, we set the simulation cell width to W, *i.e.*, $V = HW^2$, and impose periodic boundary conditions.

At the beginning of the film drying process, the initial volume fraction is ϕ_0 and the interface is located at $z = H_0$. The colloidal particles are randomly distributed without overlapping between the two boundaries. For constant velocity interface movement, the interface position changes according to

$$\frac{\mathrm{d}H}{\mathrm{d}t} = -U_w, \tag{5.3}$$

where U_w is the interface speed. When the interface is subject to an external normal stress of magnitude Σ_e, its position changes according to the force balance

$$\zeta \alpha_m \frac{\mathrm{d}H}{\mathrm{d}t} = a^2 \Sigma_m(t) - a^2 \Sigma_e, \tag{5.4}$$

where $\Sigma_m(t)$ is the instantaneous suspension normal stress on the moving interface, and α_m is the interface resistance coefficient, *i.e.*, $\alpha_m \zeta$ is the hydrodynamic resistance of the interface. Eq. (5.3) and (5.4) suggest that $\mathrm{Pe}_U = \mathrm{Pe}_\Sigma / \alpha_m$ when $\Sigma_m = 0$. However, as the suspension osmotic pressure grows with ϕ, the equivalence quickly breaks down during the drying the process.

Without hydrodynamic interactions, the time evolution of particle position $\boldsymbol{x}_i$ follows the overdamped Langevin equation [21, 54, 57],

$$\zeta \frac{\mathrm{d}\boldsymbol{x}_i}{\mathrm{d}t} = \boldsymbol{f}_i^{\mathrm{P}} + \boldsymbol{f}_i^{\mathrm{W}} + \boldsymbol{f}_i^{\mathrm{B}}, \tag{5.5}$$

where $\zeta = 6\pi\eta_0 a$, $\boldsymbol{f}_i^{\mathrm{P}}$ and $\boldsymbol{f}_i^{\mathrm{W}}$ are respectively the forces from the interparticle and the particle-wall potentials, and $\boldsymbol{f}_i^{\mathrm{B}}$ is the Brownian force satisfying $\overline{\boldsymbol{f}_i^{\mathrm{B}}(t)} = 0$ and $\overline{\boldsymbol{f}_i^{\mathrm{B}}(t)\boldsymbol{f}_j^{\mathrm{B}}(t')} = 2k_{\mathrm{B}}T\zeta^{-1}\delta_{ij}\delta(t-t')\mathbf{I}$ with δ_{ij} the Kronecker delta, $\delta(t-t')$ the Dirac delta, and $\mathbf{I}$ the idem tensor. The interparticle potential V_{ij}^{P} and the particle-wall potential V_i^{W} are respectively

$$V_{ij}^{\mathrm{P}} = \begin{cases} 0, & \text{if } r_{ij} > 2a \\ \infty, & \text{otherwise} \end{cases} \quad \text{and} \quad V_i^{\mathrm{W}} = \begin{cases} 0, & \text{if } a < z_i < H - a \\ \infty, & \text{otherwise} \end{cases}, \tag{5.6}$$

where $r_{ij} = \|\boldsymbol{x}_i - \boldsymbol{x}_j\|$. Computation of $\boldsymbol{f}_i^{\mathrm{P}}$ and $\boldsymbol{f}_i^{\mathrm{W}}$ via the EMPF algorithm for hard potentials is discussed next.

The Energy Minimization Potential-Free algorithm

The potential-free BD algorithm directly discretizes Eq. (5.5) with time step Δt for suspensions with singular hard-sphere potentials and advances the simulation following a predictor-corrector scheme. The position of particle i changes as

$$\boldsymbol{x}_i(t+\Delta t) = \boldsymbol{x}_i(t) + \Delta\boldsymbol{x}_i^{\mathrm{R}} + \Delta\boldsymbol{x}_i^{\mathrm{P}}. \tag{5.7}$$

In the predictor step, the particles are randomly displaced by $\Delta\boldsymbol{x}_i^{\mathrm{R}}$, drawn from a normal distribution with zero mean and a variance of $2d_0\Delta t$, with $d_0 = k_{\mathrm{B}}T/\zeta$. In the corrector step, the algorithm ensures that the suspension is free from any overlaps by moving particle i a distance $\Delta\boldsymbol{x}_i^{\mathrm{P}}$, such that for any $i \neq j$, $\|\boldsymbol{x}_i - \boldsymbol{x}_j\| \geq (a_i + a_j)$. The resulting interparticle force is $\boldsymbol{f}_i^{\mathrm{P}} = \zeta_i \Delta\boldsymbol{x}_i^{\mathrm{P}}/\Delta t$, with $\zeta_i = 6\pi\eta_0 a_i$. The stress tensor for homogeneous suspensions is simply the spatial moment of the interparticle force, $\boldsymbol{\Sigma} = -V^{-1}\sum_{i=1}^{N} \boldsymbol{x}_i \boldsymbol{f}_i^{\mathrm{P}}$.

In the original potential-free algorithm, the overlap-free condition is satisfied by repeatedly restoring the overlapping pairs back to contact along their line of centers until the system is free of overlaps. As soon as the algorithm identifies an overlapped pair $s = (p, q)$ with particles p and q, it moves each particle a distance $\Delta\boldsymbol{x}_{s,p}^{\mathrm{P}}$ and $\Delta\boldsymbol{x}_{s,q}^{\mathrm{P}}$ to meet the non-overlapping condition and Newton's third law, $\boldsymbol{f}_{s,p}^{\mathrm{P}} + \boldsymbol{f}_{s,q}^{\mathrm{P}} = 0$. The algorithm works efficiently for dilute suspensions. However, for dense suspensions, the original algorithm suffers several issues: (*i*) performance degradation. Resolving the overlap of one pair may cause secondary overlaps in adjacent particles. Therefore, computationally expensive iterative overlap resolution that scans the entire suspensions multiple times are necessary. In extreme cases, the simulation may be trapped by a repeating sequence of configurations and unable to advance in time. The confining boundaries in the film drying process further aggravate this problem. (*ii*) indeterminate terminal configurations. For particles with multiple overlaps with other particles, the final overlap-free configuration strongly depends on the order in which the overlap pairs are resolved. (*iii*) ambiguous local stress. As the stress is the spatial moment of the interparticle force, the local stress is ambiguous if a particle has multiple overlaps with other particles: it is unclear which particle position during the overlap resolution process should be used for stress measurement. This is especially problematic for measuring the stress profile in suspensions with large stress variations.

Here, we develop the Energy Minimization Potential-Free (EMPF) algorithm to address these issues. The motivation for the EMPF algorithm is the realization

that, for an overlapping pair, the particle movement from the original potential-free algorithm minimizes the energy cost. In other words, for an overlapping pair $s = (p, q)$, it minimizes

$$\epsilon_s = \epsilon_p + \epsilon_q = \boldsymbol{f}_p^{\mathrm{P}} \cdot \Delta\boldsymbol{x}_p^{\mathrm{P}} + \boldsymbol{f}_q^{\mathrm{P}} \cdot \Delta\boldsymbol{x}_q^{\mathrm{P}}, \tag{5.8}$$

subject to the non-overlapping and zero total force constraints,

$$\|(\boldsymbol{x}_p + \Delta\boldsymbol{x}_p^{\mathrm{P}}) - (\boldsymbol{x}_q + \Delta\boldsymbol{x}_q^{\mathrm{P}})\| - (a_p + a_q) = 0, \tag{5.9}$$

$$\boldsymbol{f}_p^{\mathrm{P}} + \boldsymbol{f}_q^{\mathrm{P}} = 0. \tag{5.10}$$

It can be shown that the $\Delta\boldsymbol{x}_p^{\mathrm{P}}$ and $\Delta\boldsymbol{x}_q^{\mathrm{P}}$ that minimize ϵ_s are unique—a manifestation of the minimization principle in classical mechanics [58]. The idea of energy minimization is also used by O'Hern et al. [59] to generate jammed packings.

The EMPF algorithm *simultaneously* removes multiple overlaps by generalizing the minimization argument for particles pairs, and therefore resolves the issues associated with the original potential-free algorithm. For a overlapped cluster with n particles and m overlapping pairs, the non-overlapping configuration can be found by minimizing the following cost function:

$$\begin{aligned} f_c(\boldsymbol{y}) = &\sum_{s=1}^{m} \lambda_s^p [\|(\boldsymbol{x}_p + \Delta\boldsymbol{x}_p^{\mathrm{P}}) - (\boldsymbol{x}_q + \Delta\boldsymbol{x}_q^{\mathrm{P}})\|^2 - (a_p + a_q)^2] \\ &+ \boldsymbol{\lambda}^f \cdot \sum_{i=1}^{n} \boldsymbol{f}_i^{\mathrm{P}} + \sum_{i=1}^{n} \epsilon_i, \end{aligned} \tag{5.11}$$

where $\epsilon_i = \boldsymbol{f}_i^{\mathrm{P}} \cdot \Delta\boldsymbol{x}_i^{\mathrm{P}}$ is the energy for moving particle i, λ_s^p is the Lagrange multiplier associated with the pair $s = (p, q)$, $\boldsymbol{\lambda}^f = (\lambda_x^f, \lambda_y^f, \lambda_z^f)$ is the three-component Lagrange multiplier vector associated with the zero total force constraint, and $\boldsymbol{y} = (\{\Delta\boldsymbol{x}_i^{\mathrm{P}}\}_n, \{\lambda_s^p\}_m, \boldsymbol{\lambda}^f)$ is the unknown vector. The minimum of f_c in Eq. (5.11) is found by solving the non-linear systems of equation $\boldsymbol{\nabla}_{\boldsymbol{y}} f_c = 0$ using Newton-Raphson iterations. The analytical Hessian matrix, $\mathbf{H}(f_c) = \boldsymbol{\nabla}_{\boldsymbol{y}} \boldsymbol{\nabla}_{\boldsymbol{y}} f_c$, is used as the Jacobian for the solver. The associated linear systems are solved using dense linear solvers for small clusters ($n < 50$), and sparse solvers otherwise.

In dynamic simulations with the EMPF algorithm, after applying the random displacement $\Delta\boldsymbol{x}_i^{\mathrm{R}}$, clusters with overlaps are first identified, and the overlaps in one cluster are then resolved simultaneously. At high density, particles from different clusters may create new overlaps after a resolution. In this case, these clusters are

merged into a new one for simultaneous overlap resolution based on the current configuration to ensure the overlap-free configuration. The cluster merge continues to ensure that all the overlaps in the current configuration are resolved simultaneously. In the case of solver failure, a new set of random displacements $\Delta \boldsymbol{x}_i^{\mathrm{R}}$ is applied for all particles from the last non-overlapping configuration. We stop after successive solver failures, providing an exist point for the simulations.

Several comments are in line for the EMPF algorithm. First, the simultaneous overlap resolution is consistent with pairwise interactions. Since the algorithm always lead to particle clusters in mechanical equilibrium, pairwise force decomposition is always possible [58]. Second, to resolve issues associated with the original potential-free algorithm, the EMPF algorithm requires solving a system of nonlinear equations. The computation efficiency may be improved by techniques such as parallelization, which are not available for sequential pairwise overlap resolution. The EMPF algorithm compared to the original algorithm is like the Newton-Raphson method compared to the successive substitution in root-finding problems: the former is always preferred due to its reliability and robustness. Finally, the EMPF algorithm, like many methods based on time discretization, overestimates the contact value in the singlet and pair distribution functions [52], and exhibits a slow $\sqrt{\Delta t}$ error convergence [60]. Therefore, small time steps are necessary for meaningful results. We have checked that the EMPF algorithm produces correct results in the pair distribution functions, osmotic pressure, and stress correlation functions in equilibrium bulk suspensions. The results are also insensitive to the system sizes.

Eq. (5.11) is valid for clusters not in contact with the confining boundaries. To study the film drying processes, cost functions that account for the particle-wall interactions under different interface movement profiles are also necessary. These are presented in the appendix. With constant velocity interface movement, Eq. (5.3) alone is sufficient. For constant normal stress interface movement, Eq. (5.4) becomes

$$H(t + \Delta t) = H(t) - a^2 \Sigma_e \Delta t / (\zeta \alpha_m) + \Delta H^{\mathrm{P}}, \tag{5.12}$$

where the second term in the right hand side accounts for the wall movement from the imposed stress, and ΔH^{P} is the interface's response to the suspension stresses. It is determined by minimizing the associated cost functions.

The continuum model

The continuum transport model for the film drying process is inspired by earlier colloidal theories [10, 26, 48, 50]. The influences of the solvent are ignored as

hydrodynamic interactions are not considered. The concentration gradient introduced by the moving interface exerts a mean Brownian force $\boldsymbol{f}^{\mathrm{B}}$ on the particles, which in turn move at a mean Brownian velocity $\boldsymbol{u}^{\mathrm{B}} = \boldsymbol{f}^{\mathrm{B}}/\zeta$. The Brownian force arises from the chemical potential gradient, *i.e.*, $\boldsymbol{f}^{\mathrm{B}} = -\boldsymbol{\nabla}\mu$, and the change of μ follows $\mathrm{d}\mu = v\mathrm{d}\Pi$ for isothermal systems, where $v = n^{-1} = \frac{4}{3}\pi a^3/\phi$ is the particle specific volume, and Π is the local osmotic pressure. With the assumption of local thermal equilibrium, the osmotic pressure $\Pi(\phi) = Z(\phi)n(\phi)k_{\mathrm{B}}T$ with $Z(\phi)$ the compressibility. The Brownian velocity is therefore $\boldsymbol{u}^{\mathrm{B}} = -d_0\phi^{-1}[\phi Z(\phi)]'\boldsymbol{\nabla}\phi$ and the volumetric flux is $\boldsymbol{j}_\phi = \phi\boldsymbol{u}^{\mathrm{B}}$, with the prime denoting derivative. Conservation of local flux in the z-direction leads to an equation of $\phi(z,t)$,

$$\frac{\partial\phi}{\partial t} = \frac{\partial}{\partial z}\left\{d_0\frac{\mathrm{d}}{\mathrm{d}\phi}[\phi Z(\phi)]\frac{\partial\phi}{\partial z}\right\}. \tag{5.13}$$

The boundary conditions are

$$\frac{\partial\phi}{\partial z} = 0 \text{ at } z = 0, \tag{5.14}$$

$$-d_0\frac{\mathrm{d}}{\mathrm{d}\phi}[\phi Z(\phi)]\frac{\partial\phi}{\partial z} - \phi\frac{\mathrm{d}L}{\mathrm{d}t} = 0 \text{ at } z = L(t), \tag{5.15}$$

where the interface motion $L(t)$ is determined by its movement profile. The initial condition is $\phi(z,0) = \phi_s$, *i.e.*, a uniform starting density in the gap between $z = 0$ and $z = L(0) = L_0$. Note that L in the model refers to the gap spacing accessible to the particles, and H in the simulations is the distance between the two confining boundaries. In the appendix, we discuss the conversion between H and L for proper comparison between the model and the simulations. When the interface moves at a constant velocity U_w,

$$L(t) = L_0 - U_w t, \tag{5.16}$$

and when the interface is subject to a constant external stress Σ_e, the change in $L(t)$ follows Eq. (5.4), as

$$\zeta\alpha_m\frac{\mathrm{d}L}{\mathrm{d}t} = \frac{3k_{\mathrm{B}}T\phi Z(\phi)}{4\pi a} - a^2\Sigma_e, \tag{5.17}$$

with ϕ evaluated at $z = L(t)$.

Here, we choose the Le Fevre equation of state [61] for $Z(\phi)$,

$$Z(\phi) = \frac{1+\alpha_3\phi}{(1+\alpha_1\phi)(1+\alpha_2\phi)(1+\beta_1\phi+\gamma_1\phi^2)(1+\beta_2\phi+\gamma_2\phi^2)}, \tag{5.18}$$

with the coefficients α_k, β_k and γ_k (k = 1,2,3) presented in Table 5.1. Eq. (5.18) has a simple pole at $\phi = -\alpha_1^{-1} = 0.6366$ and is reasonably accurate at both low and

Table 5.1: The coefficients associated with the Le Fevre equation of state in Eq. (5.18) from Le Fevre [61].

k	α_k	β_k	γ_k
1	−1.5708	−2.9552	2.5521
2	1.0232	−1.3795	2.1339
3	−0.8824		

high densities [62]. Selecting a single equation of state for all densities implies that the model ignores phase transitions and greatly simplifies the solution procedure. Further details on solving the continuum model are also presented in the appendix.

5.3 Results and Discussions

To investigate the colloidal film drying process, we carry out a series of BD simulations using the EMPF algorithm with constant velocity and constant normal stress interface movement. Each simulation contains $N = 1000$ particles, and starts with an initial gap width $H_0 = 30a$ and an initial volume fraction $\phi_0 = 0.1$. For constant normal stress interface movement, the interface resistance coefficient $\alpha_m = 1$. In the simulations, we scale the length with a and the time with a^2/d_0 when $\mathrm{Pe}_U \leq 1$ and $\mathrm{Pe}_\Sigma \leq 1$, and with a/U_w for $\mathrm{Pe}_U > 1$ and $\zeta/(a\Sigma_e)$ for $\mathrm{Pe}_\Sigma > 1$. The dimensionless step size is 10^{-4}. The simulations terminate after 20 successive solver failures. We perform 300 simulations for each Péclet number and present the averaged results unless otherwise stated. In what follows, we present the results with constant velocity and constant normal stress together and highlight their differences.

Interface movement

When the interface moves at a constant velocity U_w, Fig. 5.2 shows the average gap width H at which the simulations terminate as a function of Pe_U. Here, a simulation terminates because the suspension structures created by the approaching confining boundaries cannot be relaxed by the particle thermal or mechanical fluctuations, *i.e.*, the suspension jams, leading to repeated solver failures. In Fig. 5.2, the terminal H increases with the growing Pe_U, and is more sensitive to Pe_U when $\mathrm{Pe}_U \gg 1$. Meanwhile, the variations among different simulations also grow significantly with Pe_U. The inset of Fig. 5.2 presents the terminal H as a function of ϕ on the drying operating curve $H(\phi)$ over the phase diagram of Fortini and Dijkstra [30] for confined hard-sphere suspensions. The phase diagram outlines the boundaries of different crystalline structures in the H-ϕ plane. For example, $4\triangle$ means four-layer crystalline

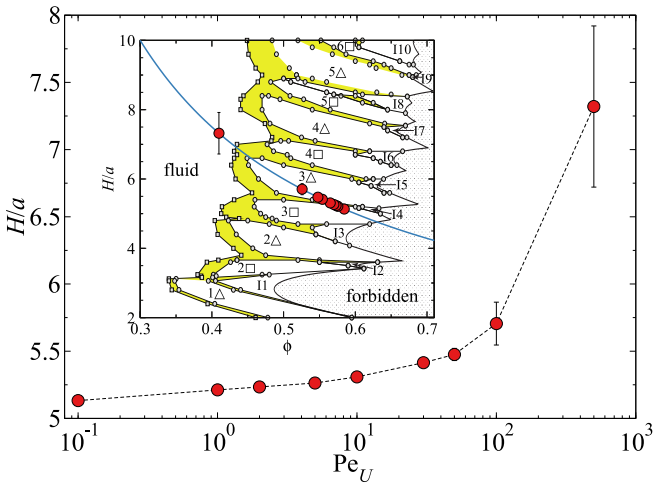

Figure 5.2: (Color online) The terminal gap width H as a function of Péclet number Pe_U for constant velocity interface movement. The error bars corresponds to variations in 300 independent simulations. The inset shows the gap width H as a function of the volume fraction ϕ for the initial H_0 and ϕ_0 in the simulations. The $H(\phi)$ operating curve is superimposed over the H-ϕ equilibrium phase diagram of confined hard-sphere systems from Fortini and Dijkstra [30] (with permission). The terminal gap widths in the simulations are also shown as circles in the inset.

structures with triangular symmetry. In the phase diagram, regions with crystalline-fluid coexistence are shown in yellow, and intermediate structures are tagged with letter 'I' followed by an integer. On the right, the shaded areas are geometrically inaccessible for any configurations. The operating curve is a hyperbola determined by the initial conditions H_0 and ϕ_0, satisfying $H\phi = H_0\phi_0$. Note that the $H(\phi)$ operating curves are identical for both modes of interface movement. As mentioned in the introduction, traversing the operating curve on the phase diagram provides valuable information on the film structures in the near equilibrium, $\mathrm{Pe}_U \ll 1$, limit.

When $\mathrm{Pe}_U \ll 1$, Brownian motion readily relaxes structural heterogeneities due to the moving interface, and gives rise to a roughly uniform structure across the gap. In the quasi-equilibrium limit ($\mathrm{Pe}_U \to 0$), we expect the simulation to terminate in the geometric limit, which, according to the inset of Fig. 5.2, is $H \approx 4.8a$. In the simulations, however, the terminal H at $\mathrm{Pe}_U = 0.1$, $H = 5.13a$, is far from the geometric limit and is closer to the phase transition between the $3\triangle$ phase and the $3\square$ phase. The slow interface movement at $\mathrm{Pe}_U = 0.1$ still disrupts the structural transitions, and eventually terminates the simulation by creating geometric frustrations. At $\mathrm{Pe}_U \sim 1$, the terminal H is also close to the $3\triangle$ and $3\square$ transition in

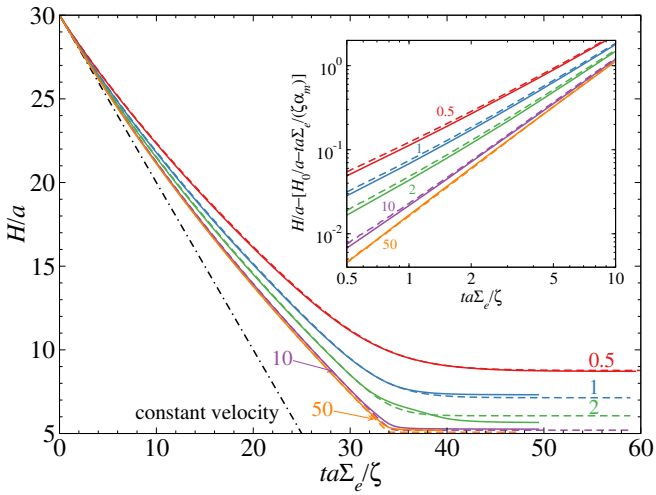

Figure 5.3: (Color online) The interface position H/a as functions of the scaled time $ta\Sigma_e/\zeta$ for constant normal stress interface movement with Pe_Σ = 0.5, 1, 2, 10, and 50, annotated in the figure with the same color as the curve. Solid lines are simulation results and dashed lines are from the continuum model. The dash-dotted line refers to the constant velocity interface movement $H_0 - ta^2\Sigma_e/(\zeta\alpha_m)$. The inset shows the the deviation from the constant velocity interface movement, $H - [H_0 - ta^2\Sigma_e/(\zeta\alpha_m)]$, at short times. The corresponding Pe_Σ are also shown.

Fig. 5.2. However, in this case the structural heterogeneity is also important. When $\mathrm{Pe}_U \gg 1$, the Brownian relaxation becomes ineffective, and the structural change is dominated by the moving boundary, which sweeps the particles into its vicinity and forms a growing particle front. As the particle front comes to contact with the stationary substrate, the resulting heterogeneous structure is easily jammed and quickly ends the simulation. At $\mathrm{Pe}_U = 500$, the compression on average terminates at $H = 7.3a$, well before any solid phase formation in the phase diagram. Moreover, the large variations in the terminal H at high Pe_U suggest that the jammed structures are quite different from each other, as any particle network in contact with both boundaries may force the simulation to stop.

With constant imposed normal stress Σ_e, the interface movement may be slowed down by the suspension stress build-up, allowing more time for structural relaxation. The interface stops moving when the external suspension osmotic pressure matches the normal stress, and fluctuates around an equilibrium position afterwards. Meanwhile, the suspension evolves towards the equilibrium structures at the corresponding H and ϕ in the phase diagram of Fig. 5.3 inset. In this case, the simulations are stopped manually. Unlike the interface motion with constant velocity, where a

higher Pe_U corresponds to a larger terminal H, a higher Pe_Σ corresponds to a smaller terminal H as relaxation is allowed. As indicated in Eq. (5.3) and (5.4), each Pe_Σ corresponds to a continuous change of Pe_U from 0 to $\mathrm{Pe}_\Sigma/\alpha_m$.

The changes of the interface location H as functions of the dimensionless time $ta\Sigma_e/\zeta$ at different Pe_Σ are shown in Fig. 5.3. Measurements from the simulations are shown in solid lines and numerical solutions of the continuum model are shown in dashed lines. Moreover, a dash-dotted line shows the interface positions evolution if $\Sigma_m = 0$, *i.e.*, the interface moves at a constant velocity as $H = H_0 - ta^2\Sigma_e/(\alpha_m\zeta)$ because $\mathrm{Pe}_U = \mathrm{Pe}_\Sigma/\alpha_m$. At the start of the interface movement, the interface movement asymptotes to constant velocity motion due to the small suspension stress on the interface Σ_m. In this case, the condition $\mathrm{Pe}_U = \mathrm{Pe}_\Sigma/\alpha_m$ roughly holds. Continuing the compression lead to an increase in Σ_m, which slows down and eventually stops the interface movement at the equilibrium position. In Fig. 5.3, the transition to the equilibrium position is smooth for small Pe_Σ, *e.g.*, at $\mathrm{Pe}_\Sigma = 0.5$, but becomes more abrupt at higher Pe_Σ, *e.g.*, at $\mathrm{Pe}_\Sigma = 50$ a sharp corner is observed near $ta\Sigma_e/\zeta = 32$. In addition, the results from the continuum model compare well with the simulation measurements, especially at $\mathrm{Pe}_\Sigma = 0.5$. Discrepancies between the model and the simulation become more apparent at higher Pe_Σ. For example, the model underestimates the equilibrium interface position at $\mathrm{Pe}_\Sigma = 1$, 10, and 50, but overestimates at $\mathrm{Pe}_\Sigma = 2$. after $ta\Sigma_e/\zeta = 34$. From later structural observations, these differences arise from using an equation of state [Eq. (5.18)] without phase transitions in the continuum model.

The inset of Fig. 5.3 presents the difference between the interface movement and the constant velocity motion $H_0 - ta^2\Sigma_e/(\alpha_m\zeta)$ at various Pe_Σ at small t. Deviation from the constant velocity movement decreases with increasing Pe_Σ, and the difference is apparent at $ta\Sigma_e/\zeta = 0.5$ even for $\mathrm{Pe}_\Sigma = 50$. The continuum model (dashed lines) captures the simulation measurements (solid lines). At small Pe_Σ, the differences between simulation and continuum model are noticeable. However, the differences become indistinguishable at $\mathrm{Pe}_\Sigma = 50$.

Suspension microstructures

We distinguish particles in crystalline and liquid-like environment using the correlational solid identification method [37, 63] based on the bond order parameters [64]. Parameters used by Marechal et al. [37] for hard-sphere sedimentation processes are suitable for the drying processes here. Identifying whether a particle i is solid

or liquid involves several steps. First, we find $N_b(i)$ neighbors within a critical distance of $r_c = 2.6a$ and compute the unnormalized bond order parameter $q^u_{l,m}(i) = N_b(i)^{-1} \sum_{j=1}^{N_b(i)} Y_{l,m}(\theta_{ij}, \phi_{ij})$, where θ_{ij} and ϕ_{ij} are the polar and azimuthal angles between particle i and its neighbor j relative to a fixed axis, and $Y_{l,m}$ is the spherical harmonic function of degree l and order m. We then normalize the bond order parameter with respect to all orders, *i.e.*, $q_{l,m}(i) = q^u_{l,m}(i)/\sqrt{\sum_{m=-l}^{l} |q^u_{l,m}(i)^2|}$. This leads to the spatial correlation $d_l(i,j) = \Re[\sum_{m=-l}^{l} q_{l,m}(i) q^*_{l,m}(j)]$ for two neighboring particles i and j, with $\Re[\cdot]$ extracting the real part of a complex number, and $*$ indicating complex conjugate. For particle i, a crystalline connection is formed with particle j if the spatial correlation $d_6(i,j) > d_c$, with $d_c = 0.7$ and symmetry index $l = 6$, and the particle has $n_{\text{con}}(i)$ crystalline connections. Finally, particle i is part of a solid structure if its crystalline connection number $n_{\text{con}}(i) > n_c$ with $n_c = 4$. We further define an overall order parameter Ξ for the suspension as the fraction of crystalline particles in the simulation cell, such that $\Xi = 1$ corresponds to an entirely crystalline structure.

Fig. 5.4 presents the overall order parameter Ξ as a function of the gap width H/a for various Péclet numbers in both interface movement modes. Combining Fig. 5.4 and the inset of Fig. 5.2 reveals the influence of the moving interface on the structural evolution of the drying process. Overall, Ξ grows with reducing H, but the details differ at high and low Péclet numbers in different interface movement modes.

Beginning with the constant interface velocity film drying process in Fig. 5.4a, with $\text{Pe}_U \ll 1$, Ξ remains close to zero for the majority of H and suddenly increases rapidly towards $\Xi = 1$. Taking $\text{Pe}_U = 0.1$ for example, Ξ suddenly grows almost vertically at $H \approx 6.5a$, corresponding to a fluid-3$\triangle$ phase transition in Fig. 5.2 inset. Here, the Ξ measurement is consistent with the phase diagram prediction. Therefore, the compression is quasi-equilibrium, and the structural rearrangement is thermodynamic-driven. However, the growth in Ξ slows down significantly at $H \approx 5.8a$ after the initial jump, *i.e.*, near the 3$\triangle$-3$\square$ transition in the phase diagram. In the denser 3$\triangle$ phase, the structural rearrangement takes place slowly, and is easily disrupted by the moving boundary. This leads to the slower Ξ growth and the eventual simulation termination.

When $\text{Pe}_U \gg 1$, Ξ exhibits qualitatively different behaviors with decreasing H in Fig. 5.4a. Taking the Ξ evolution at $\text{Pe}_U = 50$ for example, Ξ grows slowly at large H, in contrast to the sudden growth of Ξ at small H in the $\text{Pe}_U \ll 1$ limit. When $H \approx 13a$, far from any phase boundaries in the inset of Fig. 5.2, more than 10%

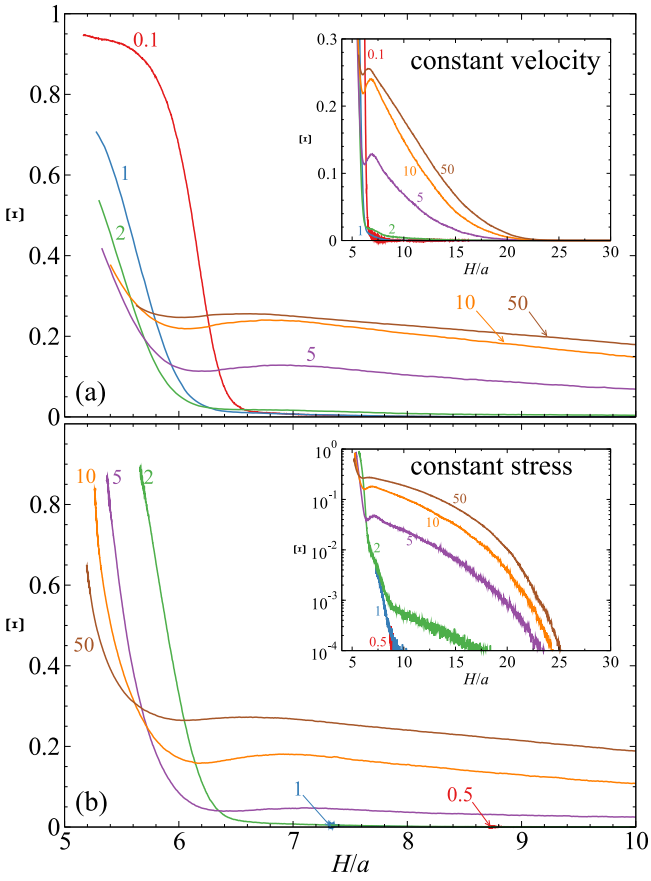

Figure 5.4: (Color online) The overall order parameter Ξ as a function of gap width H/a with (a): constant velocity interface motion with Pe_U = 0.1, 1, 2, 5, 10, and 50, and (b) constant normal stress interface motion with Pe_Σ = 0.5, 1, 2, 5, 10, and 50. The main figure and the inset show the same data with different axis scaling.

of the particles are already ordered, suggesting a heterogeneous mixture of ordered and disordered structures. More interestingly, when $H \approx 6.6a$, Ξ reaches a local maximum, decreases slightly before increasing again. We explain this observation via the growth of particle front near the moving boundary. At large H, the density next to the moving interface is high enough for crystallization, which contributes to the early increase of Ξ. As the front grows, subsequent crystallization proceeds epitaxially, *i.e.*, it uses the first layer crystals as a template for growth. Meanwhile, the particle front has to rearrange itself as it comes into contact with the stationary boundary, and this rearrangement eventually causes the "dip" in Ξ. Finally, the continued increase in Ξ suggests ordered structures are preferred at smaller H, but its formation is disrupted by the fast moving interface, leading to smaller terminal Ξ.

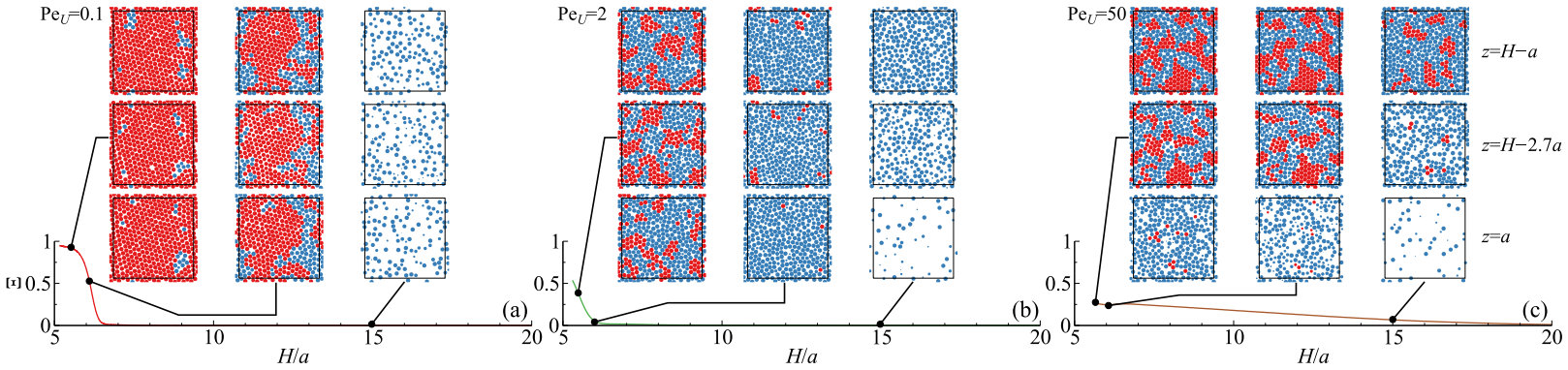

Figure 5.5: (Color online) Cut-plane views of the simulation cells at $z = H - a$, $z = H - 2.7a$, and $z = a$ at different gap locations H for (a): $\mathrm{Pe}_U = 0.1$, (b): $\mathrm{Pe}_U = 2$, and (c): $\mathrm{Pe}_U = 50$. The crystalline particles are colored red, and amorphous particles are colored blue. The corresponding evolution of Ξ as functions of H is also presented.

The evolution of Ξ in Fig. 5.4a demonstrates that the moving boundary alters the suspension structure via different mechanisms: when $\mathrm{Pe}_U \ll 1$, it induces spontaneous crystallization at small H by (almost) uniformly increasing the suspension density, and when $\mathrm{Pe}_U \gg 1$, it directly introduces localized solidification at larger H. The moving boundary also disrupts the spontaneous crystallization process when the thermodynamic time scale is comparable with the convective time scale a/U_w. This means that the least ordered structure for a given H is expected at a moderate $\mathrm{Pe}_U \sim 1$. In Fig. 5.4a, taking $H = 6a$ as an example, the minimum Ξ takes place at $\mathrm{Pe}_U = 2$, when the wall movement is too slow for localized order formation but too fast for spontaneous crystallization.

For structural evolution at constant normal stress compression in Fig. 5.4b, the Ξ evolution is qualitatively similar to the case of constant interface velocity in Fig. 5.4a. The effects of the moving interface on the suspension structures are weaker as the interface can be slowed down by the suspension pressure build-up. Here, as we manually stop the simulations shortly after the equilibrium H has been reached, the structural evolution may be incomplete, *i.e.*, the terminal Ξ in Fig. 5.4b for $\mathrm{Pe}_\Sigma > 1$ could be higher should the simulations last longer. For $\mathrm{Pe}_\Sigma = 0.5$ and 1, however, the overall Ξ is vanishingly small throughout the compression because the equilibrium position is in the liquid phase.

Fig. 5.5 shows cut-plane views of the simulation cell at, from top to bottom, $z = H-a$, $z = H - 2.7a$, and $z = a$, corresponding the particle center positions of the immediate particle layer next to the moving interface, the immediate second particle layer adjacent to a close-packed first layer, and the first layer next to the stationary boundary, respectively, at different H during the constant interface velocity film drying process. The corresponding Ξ evolution as a function of H is also presented. The particle intersections are shown as discs in the cut-plane views, with crystalline particles colored red and amorphous particles colored blue. Fig. 5.5a, 5.5b, 5.5c respectively presents the results at $\mathrm{Pe}_U = 0.1$, 2, and 50. These cut-plane views provide direct qualitative assessment of the suspension structural evolution.

The first feature revealed in Fig. 5.5 is the particle distributions during the compression. At $\mathrm{Pe}_U = 0.1$, Fig. 5.5a shows that the densities in the cut-plane views at different z-positions are approximately the same, suggesting an almost homogeneous suspension during the drying process. On the other hand, at $\mathrm{Pe}_U = 50$, Fig. 5.5c shows large density variations with respect to z. At $H = 15a$, the densities at all three cut-plane views are already quite different. At smaller H, differences

between views at $z = H - a$ and $z = H - 2.7a$ becomes less apparent, but their densities are still visibly higher than those at $z = a$. With an intermediate $\mathrm{Pe}_U = 2$ in Fig. 5.5b, at $H = 15a$ the density at $z = a$ is lower than the the density near the moving interface. However, the differences are less evident when $H = 6a$ and $5.5a$.

The second feature shown in Fig. 5.5 is the crystalline structures along with the Ξ evolution. At $\mathrm{Pe}_U = 0.1$, the suspension becomes crystalline with the Ξ increase, evidenced by the red discs in Fig. 5.5a. From the cut-plane views at $H = 6a$ and $5.5a$, the crystallization process takes place uniformly across the gap. At $H = 5.5a$, almost all particles in the suspension are crystalline. The few amorphous particles are due to defects such as stacking faults. For fast interface movement at $\mathrm{Pe}_U = 50$ in Fig. 5.5c, patches of crystalline structures emerge as early as $H = 15a$ next to the moving interface. The size of the crystal patches grow with continued compression. Moreover, using the existing crystalline structures next to the moving boundary as a template, a second layer of crystalline structures also start to grow epitaxially. Before the simulation stops at $H = 5.7a$, the crystalline structures remains patchy, as the fast moving interface does not permit further structural rearrangement. The structural evolution at $\mathrm{Pe}_U = 2$ in Fig. 5.5b shows a competition between the thermodynamic-driven crystallization process at low Pe_U and the kinetic crystallization process at high Pe_U. The net result is deferred crystallization onset. At $H = 6a$, the suspension remains mostly amorphous despite nearly uniform densities across the gap. Here, Brownian motion is strong enough to redistribute particles, but too weak relative to the boundary movement to organize local ordering. Patchy crystals are only observed at $H = 5.5a$. Therefore, the structures of the colloidal film can be controlled by carefully adjusting the interface speed U_w. Crystallization at high Pe_U in Fig. 5.5c explains the recent success of fast colloidal crystal fabrication with high drying rate [27]. Moreover, the amorphous structures at moderate Pe_U may find applications in angle independent photonic materials[2].

Further characterization of the thin film structures next to the moving boundary at $z = H - a$ with the gap spacing $H = 6a$ is presented in Fig. 5.6 using the two-dimensional radial distribution function in the xy-plane, $g_{xy}(r_{xy})$, averaged over all simulations. For clarity, $g_{xy}(r_{xy})$ at $\mathrm{Pe}_U = 2$ and 50 are shifted upwards by 2 and 4, respectively. The inset of Fig. 5.6 also show the planar pair distribution function corresponding to the cut-plane views in Fig. 5.5. At $\mathrm{Pe}_U = 0.1$, the radial distribution function $g_{xy}(r_{xy})$ shows a mild double peak near $r_{xy} = 4a$, suggesting crystalline structures with relatively low density. The crystalline structure is further

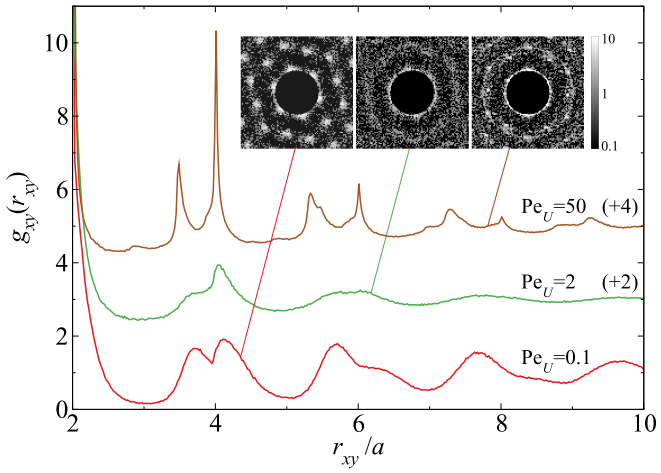

Figure 5.6: (Color online) The average planar radial distribution function in the xy-plane, $g_{xy}(r_{xy})$, measured at $z = H - a$ for $\mathrm{Pe}_U = 0.1$, 2, and 50 when the gap width $H = 6a$. The results at $\mathrm{Pe}_U = 2$ and 50 are shifted up by 2 and 4, respectively, for clarity. The insets show the 2D planar pair distribution function corresponding to the top snapshot in the middle column in Fig. 5.5a, 5.5b, and 5.5c.

confirmed by the hexagonal patterns in the corresponding pair distribution function. At $\mathrm{Pe}_U = 2$, the double peak for $g_{xy}(r_{xy})$ around $r_{xy} = 4a$ vanishes, suggesting amorphous suspension structure. The overall features in $g_{xy}(r_{xy})$ is less pronounced comparing to other Pe_U, and the pair distribution function is almost isotropic. At $\mathrm{Pe}_U = 50$, the peaks in $g_{xy}(r_{xy})$ becomes much sharper comparing to those at lower Pe_U, suggesting the particles are more densely packed. The split peaks near the second coordinate layer are at $3.5a$ and $4.0a$, closely correspond to closely packed hexagons, which show peaks at $2\sqrt{3}a$ and $4a$. The pair distribution function is a mixture of amorphous and crystalline structures, consistent with the qualitative observations in Fig. 5.5c.

The structural features for constant normal stress compression are qualitatively similar to those in Fig. 5.5 and 5.6, except for the weaker influences of the interface. The suspension is in general more ordered. For the particle layer immediately next to the moving interface, at $\mathrm{Pe}_\Sigma = 2$ and $H = 6a$, the second peak of $g_{xy}(r_{xy})$ is less pronounced and located at larger r compared to the constant velocity counterpart. Due to the similarity, these results are not presented.

Normal stress profiles

We measure the normal stress profile in the z-direction, $\Sigma_{zz}(z)$, using the method of Todd et al. [65], which, although derived for Hamiltonian systems, is also applicable for dissipative Brownian systems without hydrodynamic interactions. The stress components related to the z-direction at position z' is

$$\langle \Sigma_{z\alpha}(z') \rangle = -\langle n(z') \rangle k_{\mathrm{B}} T \delta_{z\alpha} - \frac{1}{2A} \left\langle \sum_{i=1}^{N} f_{i\alpha}^{\mathrm{P}} \mathrm{sgn}(z_i - z') \right\rangle, \ \alpha \in \{x, y, z\}, \quad (5.19)$$

where $\langle \cdot \rangle$ denotes an ensemble average, $n(z')$ is the local particle number density, $A = L^2$ is the xy area of the simulation cell, and $F_{i\alpha}^{\mathrm{P}}$ is the *interparticle* force in the α direction of particle i. Eq. (5.19) suggests that the local stress is intimately related to the total force across the plane. The first term on the right hand side of Eq. (5.19) is simplified from the original formulation for the isothermal Brownian suspensions. Note that the *interparticle* force $\boldsymbol{f}_i^{\mathrm{P}}$ for particle i excludes the forces from the confining boundaries, $\boldsymbol{f}_i^{\mathrm{W}}$. Since Eq. (5.19) involves all particles in the simulation box, it provides better local stress resolution comparing to spatial binning, which is susceptible to large noises at small bin widths [65]. The EMPF algorithm also eliminates the ambiguous stress definition from multiple overlaps.

To avoid inaccuracies from contact density measurement next to the wall—an inherent drawback of the time discretization algorithms—the contact stresses on the moving interface, Σ_m, and on the stationary substrate, Σ_s, are directly computed as

$$\Sigma_m = -\frac{1}{2A\Delta t} \sum_{r=1}^{l^+} \lambda_r^+ \quad \text{and} \quad \Sigma_s = -\frac{1}{2A\Delta t} \sum_{t=1}^{l^-} \lambda_t^-, \quad (5.20)$$

where λ_r^+ and λ_t^- are the wall confinement Lagrange multiplier defined in the appendix, and their values divided by Δt are twice the force exerted by the wall on particle r or t.

Fig. 5.7 and 5.8 present the suspension normal stress profiles $\Sigma_{zz}/(n_0 k_{\mathrm{B}} T)$, with $n_0 = \frac{3}{4}\phi_0/(\pi a^3)$, along with the moving interface stresses at different Péclet numbers for, respectively, the constant velocity and the constant normal stress drying processes. In both figures, the simulation measurements are presented on the left column while the continuum model results on the right. For constant velocity interface movement in Fig. 5.7, Σ_{zz} on the moving boundary eventually diverges, and the stress difference between the two boundaries increases with Pe_U. On the other hand, for drying process with constant imposed normal stress in Fig. 5.8, Σ_{zz} does not diverge, and near the equilibrium wall position, the stress profile eventually becomes

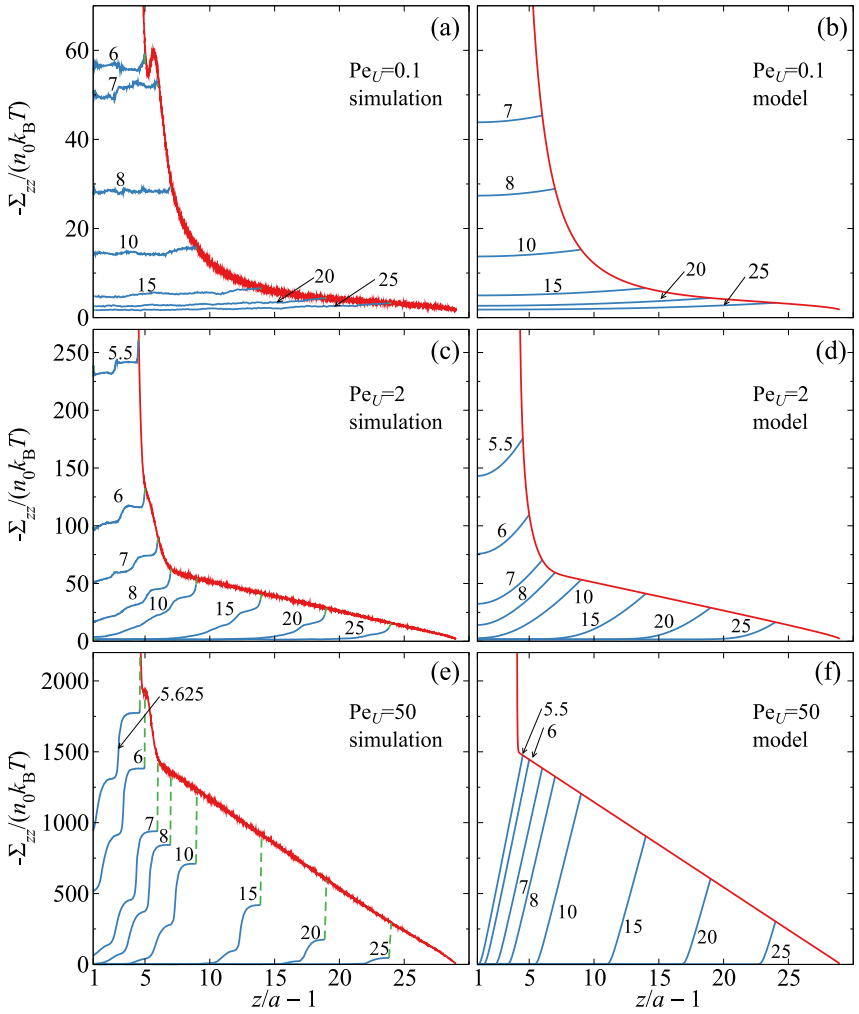

Figure 5.7: (Color online) The normal stress profiles $\Sigma_{zz}/(n_0 k_B T)$ in drying processes with constant velocity interface movement at (a), (b): $\mathrm{Pe}_U = 0.1$, (c), (d): $\mathrm{Pe}_U = 2$, and (e), (f): $\mathrm{Pe}_U = 50$. Simulation measurements are shown in (a), (c), and (e), and continuum model results are shown in (b), (d), and (f). To reduce noise, simulation stress measurements are averaged over $0.01a$. The normal stresses on the moving interface are shown in red, and the stress profiles at the denoted H/a are shown in blue. Near the boundaries, the contact stress and the suspension stress are connected by green dashed lines, visible only at high Pe_U due to stress concentration.

uniform across the gap, and suspension stress on the boundary eventually matches the imposed stress Σ_e.

Let us begin with the normal stress measurements in Fig. 5.7a, 5.7c, 5.7e for constant velocity interface movement. For $\mathrm{Pe}_U \ll 1$, the stress distribution across the gap reflects Brownian motion dominance. For example, at $\mathrm{Pe}_U = 0.1$ (Fig. 5.7a), the

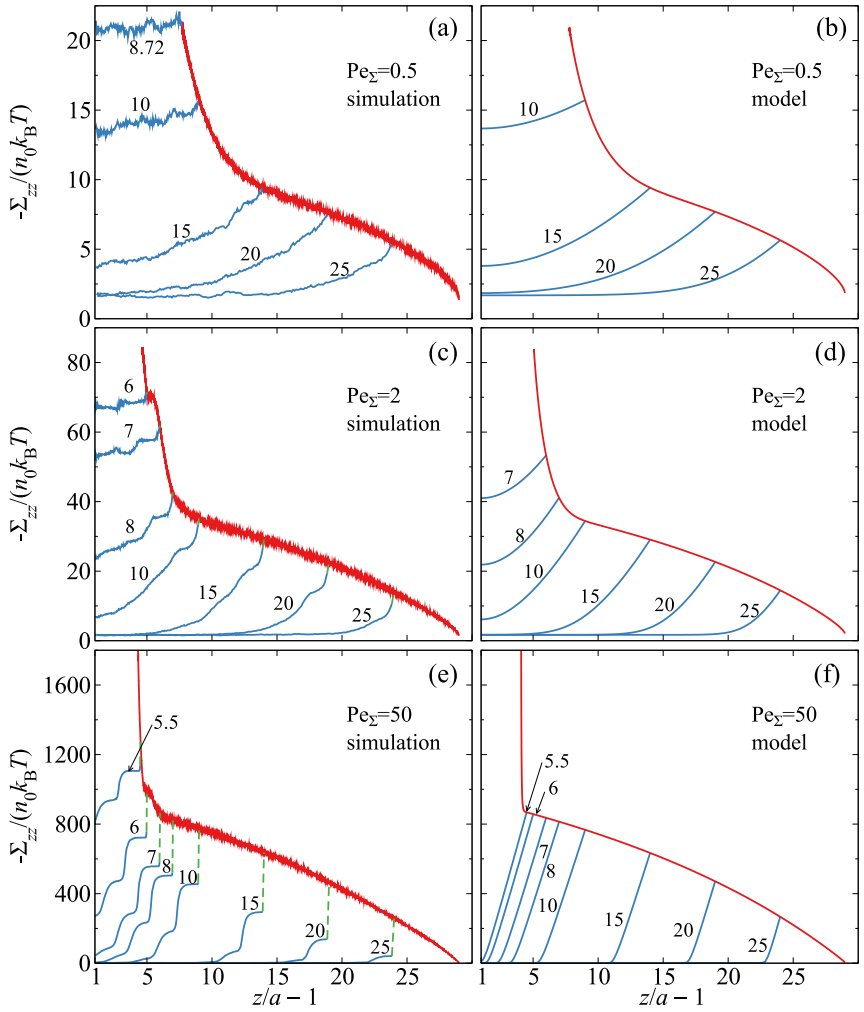

Figure 5.8: (Color online) The normal stress profiles $\Sigma_{zz}/(n_0k_BT)$ in drying processes with constant normal stress interface movement at (a), (b): $\mathrm{Pe}_\Sigma = 0.5$, (c), (d): $\mathrm{Pe}_\Sigma = 2$, and (e), (f): $\mathrm{Pe}_\Sigma = 50$. Simulation measurements are shown in (a), (c), and (e), and continuum model results are shown in (b), (d), and (f). Other arrangements are identical to Fig. 5.7.

stresses on the moving boundary increase with decreasing H, except a reduction between $H \approx 6.6a$ and $6.1a$. This reduction coincides with the abrupt increase of Ξ in Fig. 5.4a due to crystallization to the $3\triangle$ phase in the phase diagram. Therefore, the stress is reduced by the thermodynamic structural rearrangement. From the almost uniform stress distribution across the gap, the stress differences between the stationary and the moving boundaries are small due to strong Brownian motion. In addition, the stress profile becomes more inhomogeneous near the structural transition, *i.e.*, at $H = 7a$. Here, the higher stress on the moving boundary suggests the higher local density, which initiates the spontaneous crystallization.

At $\mathrm{Pe}_U \gg 1$, the structural heterogeneity leads to strong stress heterogeneity. On the moving boundary, the normal stress evolution with reducing H can be divided into four stages. Using the case of $\mathrm{Pe}_U = 50$ in Fig. 5.7e as an example, they are: (*i*) linear normal stress increase from the beginning to $H \approx 7a$. This reflects the normal stress required to carry the growing particle front at a constant velocity. The linearity implies linear particle front growth as the initial particle distribution is uniform. (*ii*) Abrupt stress increase over a short distance between $H \approx 7a$ and $6a$. The particle front begins to be in contact with the stationary boundary and is compressed, giving rise to a local Ξ maximum in Fig. 5.4a. (*iii*) Slower stress increase near $H/a = 6$. This slower stress growth is consistent with the onset of Ξ increase after the "dip" in Fig. 5.4a, *i.e.*, the tendency for crystallization in a dense and heterogeneous structure is strong enough to slow down the stress increase. (*iv*) Continued stress increase until simulation stops from compressing a jammed structure. Clearly, the stress on the moving interface is consistent with the suspension structural evolution. For moderate Pe_U, *e.g.*, $\mathrm{Pe}_U = 2$ in Fig. 5.7c, stage (*iii*) disappears completely together with the Ξ "dip" in Fig. 5.4a due to a lack of order in the suspension. Moreover, the stress distribution across the gap at large Pe_U is more complicated. Near the moving interface, the stresses measured in the suspensions from Eq. (5.19) are different from the stress measured on the interface via Eq. (5.20), suggesting boundary-layer-like stress variation in this region. Away from the boundaries, the stress exhibits a step-like profile, and remains inhomogeneous during the drying process. The stress profiles here are consistent with the structural heterogeneity.

The normal stress profiles for interface movement with constant imposed normal stress, shown in Fig. 5.8a, 5.8c, and 5.8e, share many similarities with those of constant velocity compression. As indicated earlier, in this compression mode the normal stress no longer diverges, and eventually matches the imposed stress. In the $\mathrm{Pe}_\Sigma \ll 1$ limit, qualitative features of the stress profile remain unchanged, but in the $\mathrm{Pe}_\Sigma \gg 1$ limit, the slowdown of the moving interface changes the linear $\Sigma_{zz}/(n_0 k_\mathrm{B} T)$ growth in stage (*i*) of the $\mathrm{Pe}_U \gg 1$ case to a curve, *e.g.*, the case of $\mathrm{Pe}_\Sigma = 50$ in Fig. 5.8e. Other stages of stress development discussed earlier remain similar. Stress concentration in the stress boundary layer remains at the beginning of the compression for $\mathrm{Pe}_\Sigma \gg 1$. However, with decreasing H, the stress boundary layer vanishes and the stress difference between the two boundaries diminishes, again due to relaxation from the slowing moving interface.

In Fig. 5.7 and 5.8, the normal stress computed from the continuum model, $\Sigma_{zz}(z) =$

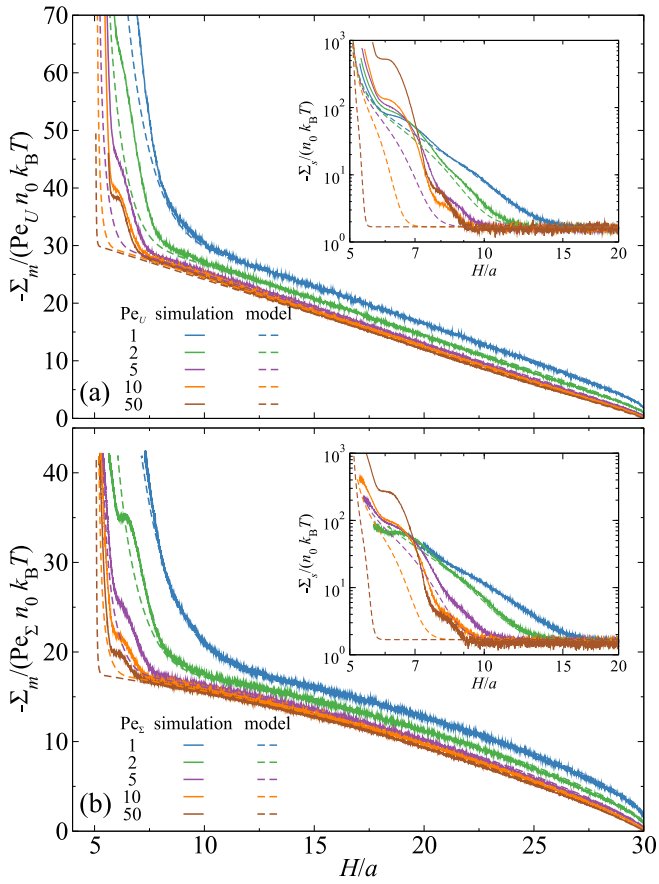

Figure 5.9: (Color online) The scaled suspension stress on the moving interface as functions of the gap width H/a for (a): $\Sigma_m/(\mathrm{Pe}_U n_0 k_\mathrm{B} T)$ for drying with an interface at constant velocity at (from right to left) $\mathrm{Pe}_U = 1$, 2, 5, 10, and 50 and (b): $\Sigma_m/(\mathrm{Pe}_\Sigma n_0 k_\mathrm{B} T)$ for drying with an interface subject to constant normal stress at (from right to left) $\mathrm{Pe}_\Sigma = 1$, 2, 5, 10, and 50. The insets show the stress on the stationary boundary $\Sigma_s/(n_0 k_\mathrm{B} T)$ as functions of gap spacing for the same Pe_U or Pe_Σ. The simulations results are shown in solid lines and model computations are shown in dashed lines.

$\frac{3}{4} k_\mathrm{B} T \phi Z(\phi)/(\pi a^3)$, not only captures the qualitative, but also some quantitative aspects of the simulation results, particularly the normal stresses evolution on the boundaries. The continuum model agrees excellently with the simulation until the onset of solidification in the simulation when $\mathrm{Pe}_U \ll 1$, *i.e.*, comparing Fig. 5.7a and 5.7b at $\mathrm{Pe}_U = 0.1$, the model agrees with the simulations up to $H \approx 7a$. Without crystallization, *e.g.*, in Fig. 5.8a and 5.8b at $\mathrm{Pe}_\Sigma = 0.5$ with constant normal stress interface movement, the agreement between the model and the simulation is present over the entire drying process. At larger Pe_U and Pe_Σ, the model can predict

the boundary normal stresses in both interface movement modes until significant structural rearrangement takes place in the simulation. However, the continuum model is unable to capture the complex, step-like, stress profiles. For example, at $\mathrm{Pe}_U = 50$ and $\mathrm{Pe}_\Sigma = 50$, the model can only capture the moving wall normal stress during stage (*i*) and (*ii*) of the stress evolution. Considering how simple the parameter-free model is, *i.e.*, ignoring the structural transitions and non-local effects, this agreement is remarkable.

Finally, Fig. 5.9 presents the moving stress evolution during the compression scaled with the corresponding Péclet number, $-\Sigma_m/(\mathrm{Pe}_U n_0 k_\mathrm{B} T)$ in Fig. 5.9a for $\mathrm{Pe}_U \geq 1$ and $-\Sigma_m/(\mathrm{Pe}_\Sigma n_0 k_\mathrm{B} T)$ in Fig. 5.9b for $\mathrm{Pe}_\Sigma \geq 1$. The stress evolution at different Péclet number collapses onto a master curve for different interface movement profile during stage (*i*) of the stress evolution in the high Péclet number limit. The collapse suggests that with $\mathrm{Pe}_U \gg 1$ or $\mathrm{Pe}_\Sigma \gg 1$, the stress on the moving interface is dominated by convection: at constant velocity interface movement, the faster the moving interface pushes the growing particle front, the larger the stress required; and with constant imposed normal stress, the growing particle front slows down the moving interface in a way that is proportional to the imposed stress. Furthermore, all data in Fig. 5.9b share the same maximum $\Sigma_m/(\mathrm{Pe}_\Sigma n_0 k_\mathrm{B} T)$, because $\Sigma_{zz}/(\mathrm{Pe}_\Sigma n_0 k_\mathrm{B} T) = (\Sigma_{zz}/\Sigma_e)(\frac{4}{3}\pi/\phi_0)$ and at equilibrium $\Sigma_{zz} = \Sigma_e$. Therefore, the scaled stress maximum is 41.9 for $\phi_0 = 0.1$, consistent with Fig. 5.9b. Here, the continuum model in dashed line agrees excellently with the simulation when $H > 7a$. At smaller gap width, structural rearrangement drives the model prediction away from the simulation data. The discrepancy is especially apparent at higher Pe_U or Pe_Σ.

The inset of Fig. 5.9 presents the stress on the stationary boundary, $\Sigma_s/(n_0 k_\mathrm{B} T)$, as functions of the gap spacing H in the corresponding compression mode at different Péclet numbers. The $\Sigma_s/(n_0 k_\mathrm{B} T)$ behaviors are similar between different interface movement modes, but do not collapse with the Péclet numbers like the stresses on the moving interface. For $\mathrm{Pe}_U \geq 1$ and $\mathrm{Pe}_\Sigma \geq 1$, the growth of $\Sigma_s/(n_0 k_\mathrm{B} T)$ is deferred, *e.g.*, Σ_s only begins to grow at $H \approx 15a$ with $\mathrm{Pe}_U = 1$ and at $H \approx 10a$ with $\mathrm{Pe}_U = 10$ in Fig. 5.9a. Prior to the growth, the stationary boundary stress remains a constant. The growth of $\Sigma_s/(n_0 k_\mathrm{B} T)$ takes place at smaller H with increasing Pe_U or Pe_Σ. This is because, physically, Σ_s only begins to change when the particle front becomes in contact with the stationary boundary. The continuum model captures the behaviors of Σ_s at low Pe_U and Pe_Σ, but underestimates the gap width where Σ_s

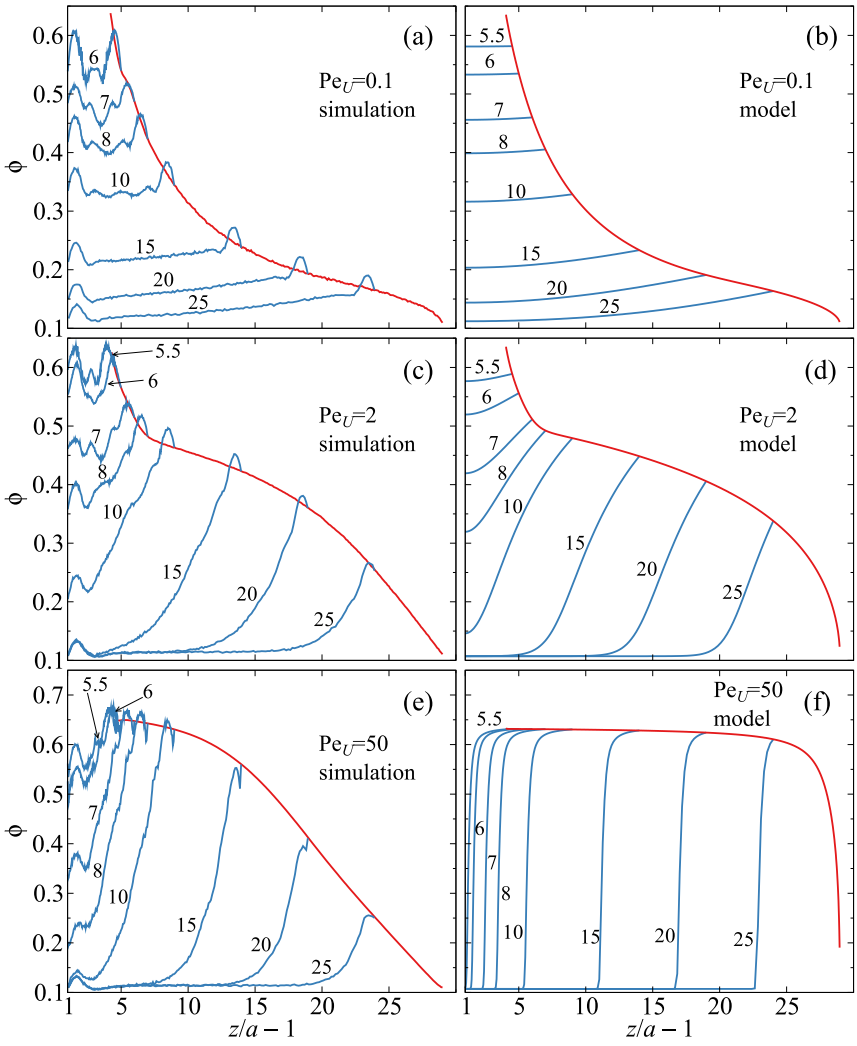

Figure 5.10: (Color online) Local volume fraction profile $\phi(z)$ in drying process with constant velocity interface movement at (a), (b): $\mathrm{Pe}_U = 0.1$, (c), (d): $\mathrm{Pe}_U = 2$, and (e), (f): $\mathrm{Pe}_U = 50$. Simulation measurements are shown in (a), (c), and (e), and continuum model results are shown in (b), (d), and (f). The local volume fractions next to the moving interface are shown in red, and the volume fraction profiles at the denoted H/a are shown in blue.

begins to grow, as the continuum model cannot resolve the structural evolution of the particle front.

Volume fraction profiles

Measuring the local volume fraction ϕ within the gap provides a direct comparison between the simulation and the continuum model. Unlike the number density n which can be sensitive to the measurement resolution near the fast moving interface,

the volume fraction is always bounded. The local volume fractions are computed by partitioning the simulation cell using Voronoi tessellation [66] with periodic boundary conditions in the x- and y-directions. In the z-direction, the part of the simulation cell that is inaccessible to particles is omitted, *i.e.*, the tessellation is limited between $z = a$ and $z = H - a$. For each particle i, the ratio of the particle volume $V_{p,i}$ to the tessellation cell volume $V_{c,i}$ defines the local volume fraction of the particle $\phi_i = V_{p,i}/V_{c,i}$. The volume fraction profile $\phi(z)$ is obtained by sorting and averaging ϕ_i based on their z-position. Comparing to other coarse-grained approaches [39], this is parameter-free and provides satisfactory spatial resolution.

Fig. 5.10 shows the simulation and the continuum model local volume fraction $\phi(z)$ across the gap at various H during the constant interface velocity drying process at $\mathrm{Pe}_U = 0.1$ (Fig. 5.10a, 5.10b), $\mathrm{Pe}_U = 2$ (Fig. 5.10c, 5.10d), and $\mathrm{Pe}_U = 50$ (Fig. 5.10e, 5.10f). The local volume fractions next to the moving interface are also shown. The simulation measurements are presented in the left and the computation from the continuum model on the right. Results from constant imposed normal stress are almost identical and therefore are not shown. That the almost identical ϕ profiles produce distinct stress development in two interface movement modes suggests the sensitivity of the local stress $\Sigma_{zz}(z)$ to the local volume fraction $\phi(z)$.

The measured local volume fraction is bounded by the Voronoi tessellation. For example, in Fig. 5.10a at $\mathrm{Pe}_U = 0.1$, the maximum ϕ from the simulations is ~ 0.65 despite extensive solidification, significantly lower than the bulk maximum $\phi \sim 0.74$ for fcc solids. Fluctuations in the ϕ measurements near the boundaries are due to measurement protocol, and the fluctuations at small H arises from crystallization. With $\mathrm{Pe}_U = 0.1$ in Fig. 5.10a, the ϕ profile is almost linear across the gap for $H \geq 15a$, and the ϕ difference between the moving interface and the stationary boundary is small. Therefore, the particle flux is almost constant across the gap due to abundant thermal fluctuations. At smaller H, the ϕ distribution becomes more symmetric due to crystallization. For $\mathrm{Pe}_U = 50$ in Fig. 5.10e, the ϕ profile shows more variations across the gap. The ϕ profile for $H \geq 15a$ clearly indicates the formation of a particle front with an advancing interface. When $H \approx 10a$, the particle front is in contact with the stationary boundary and begins to rearrange. The rearrangement is localized, causing significant ϕ increase near the stationary boundary, but not much change near the moving interface. The larger ϕ fluctuations near $H = 6a$ are due to crystallization. Qualitatively, the ϕ profiles at $\mathrm{Pe}_U = 2$ and $\mathrm{Pe}_U = 50$ from the simulations are similar.

The continuum model accurately predicts the ϕ profile at $\mathrm{Pe}_U \ll 1$ with $H > 7a$, but fails to capture the ϕ fluctuations at small H from the crystallization process. At higher Pe_U, the continuum model disagrees with the simulation measurements on the changes in ϕ next to the moving interface. This is especially pronounced at $\mathrm{Pe}_U = 50$: the model predicts that ϕ near the moving interface becomes almost constant when $H < 20a$. However, the corresponding simulation measurements show a much slower ϕ growth. Moreover, the simulation shows a more diffusive particle front near the moving wall, in contrast to the sharp interface predicted by the model. This "diffusive" front, however, is not due to the Brownian motion, but the finite particle size—an aspect not captured by the model.

Improving the continuum model is challenging. For example, incorporating the effects of convection on the particle mobility, *i.e.*, changing d_0 in Eq. (5.13) and (5.15) to collective diffusivity $d_c(\phi) = (1 + \mathrm{Pe}_U b)$ or $d_c(\phi) = (1 + \mathrm{Pe}_U b\phi)$—with b a fitting parameter—did not yield qualitative improvement. It should be recalled that the particle size does not enter the continuum model and therefore non-local, particle-scale effects similar to those proposed by Kamrin and Koval [51] for particle mobility may be helpful. Nonetheless, the existing continuum model successfully captures the ϕ evolution at small Péclet numbers and large H in both interface movement modes. The success of the model may be that the equation of state, Eq. (5.18), accurately captures the behaviors of the amorphous suspensions under confinement.

5.4 Concluding Remarks

We presented a simulation and modeling investigation on the colloidal film drying process with the interface moving at constant velocity or subject to constant imposed stresses. For the simulations, we developed a new EMPF algorithm to address the unique challenges in the drying process. The simulation results are compared with a continuum model, also developed in this work, to understand their validity.

At low Péclet numbers, the drying dynamics are dominated by Brownian motion up to small gap widths. Changes in suspension structures and stresses can be succinctly summarized by constructing an operating curve on the confined suspension phase diagram [30]. At high Péclet numbers, a growing particle front emerges next to the moving interface, which leads to structural heterogeneity. As a result, the stress profiles exhibit a stress boundary layer next to the moving interface, and step like stress profiles within the gap. Our simulations show that different suspension

structures from amorphous to crystalline can be obtained by adjusting interface motion. Interestingly, for a given H, the most amorphous structures are found at moderate Péclet numbers as the moving interface promotes localized crystallization and disrupts spontaneous phase transition. With constant imposed normal stress, the influence of the moving interface is weaker as the interface velocity can be reduced. The simple continuum model successfully captures the dynamics of the suspension at low Péclet numbers, but shows limited success at high Péclet numbers. The model predicts the interface stress and position in both compression modes, but cannot describe the stress and volume fraction profiles, suggesting the importance of phase transitions and non-local effects in the model construction.

This work provides an in-depth structural and mechanical characterization of the colloidal film drying process. It also sheds light on the non-equilibrium, boundary-driven transport processes of confined systems in general. It shows that film structure may be controlled by changing the interface movement, demonstrating the unexpectedly important role of convective transport on the film formation process and the colloidal self-assembly processes in general. The comparison between the continuum model and the simulation also show the need for new model developments that properly account for the convection effects.

A possible extension of this work is the incorporation of hydrodynamic interactions. Hydrodynamics profoundly affect the dynamics and transport of the confined colloidal suspensions [12, 15]. The influences of hydrodynamic interactions on the drying process are unknown, including the structural consequences of the reduced particle mobility and the long-range correlated particle motion. Their effects can only be assessed via detailed hydrodynamic simulations.

5.A Cost functions for confined systems

Additional cost functions to account for the interactions between the boundary and the clusters are necessary to use the EMPF algorithm for the film drying process. We assume that the boundaries are reflective in the z-direction and perfectly slip in the x- and y-directions. With constant interface velocity, the wall motion is deterministic. However, when the interface is subject to constant normal stress, the interface position also changes by interacting with the overlapping particles.

For the deterministic interface movement, the boundaries impose new geometric constraints, and remove the force-free constraints in the z-direction. Given an n-particle cluster with m overlapping particle pairs, l_+ and l_- particles overlapped with

the boundary at $z = H$ and $z = 0$, respectively, the cost function for particles with radii a is

$$\begin{aligned} f_c^{fw}(\boldsymbol{y}) = &\sum_{i=1}^{n} \epsilon_i + \sum_{s=1}^{m} \lambda_s^p [\|(\boldsymbol{x}_p + \Delta \boldsymbol{x}_p^{\mathrm{P}}) - (\boldsymbol{x}_q + \Delta \boldsymbol{x}_q^{\mathrm{P}})\|^2 - 4a^2] \\ &+ \sum_{r=1}^{l_+} \lambda_r^+ [(H - a) - (z_r + \Delta z_r^{\mathrm{P}})] + \sum_{t=1}^{l_-} \lambda_t^- [(z_t + \Delta z_t^{\mathrm{P}}) - a] \\ &+ \lambda_x^f \sum_{i=1}^{n} f_{i,x}^{\mathrm{P}} + \lambda_y^f \sum_{i=1}^{n} f_{i,y}^{\mathrm{P}}, \end{aligned} \tag{5.21}$$

where z_r and Δz_r^{P} are respectively the z-position and displacement of particle r overlapped with the boundary at $z = H$, and z_t and Δz_t^{P} are similar quantities with the boundary at $z = 0$, and the unknown vector is

$$\boldsymbol{y} = (\{\Delta \boldsymbol{x}_i^{\mathrm{P}}\}_n, \{\lambda_s^p\}_m, \{\lambda_r^+\}_{l_+}, \{\lambda_t^-\}_{l_-}, \lambda_x^f, \lambda_y^f). \tag{5.22}$$

When the interface is subject to a constant normal stress, its position change due to particle overlaps has to be solved as part of the problem. From Eq. (5.4), the force required to move the boundary a distance ΔH^{P} in z-direction is $f_m^{\mathrm{P}} = \zeta \alpha_m (L^2/a^2)(\Delta H^{\mathrm{P}}/\Delta t)$, and the energy associated with such motion is $\epsilon_m = f_m^{\mathrm{P}} \Delta H^{\mathrm{P}}$. If the cluster only overlaps with the moving boundary at $z = H$, the wall is treated as a large particle, and the cost function is augmented from Eq. (5.11):

$$\begin{aligned} f_c^{mw}(\boldsymbol{y}) = &\sum_{i=1}^{n} \epsilon_i + \epsilon_m + \sum_{s=1}^{m} \lambda_s^p [\|(\boldsymbol{x}_p + \Delta \boldsymbol{x}_p^{\mathrm{P}}) - (\boldsymbol{x}_q + \Delta \boldsymbol{x}_q^{\mathrm{P}})\|^2 - 4a^2] \\ &+ \sum_{r=1}^{l_+} \lambda_r^+ [(H + \Delta H^{\mathrm{P}} - a) - (z_r + \Delta z_r^{\mathrm{P}})] \\ &+ \boldsymbol{\lambda}^f \cdot (\sum_{i=1}^{n} \boldsymbol{f}_i^{\mathrm{P}} + f_m^{\mathrm{P}} \mathbf{1}_z), \end{aligned} \tag{5.23}$$

where $\mathbf{1}_z$ is the z-direction unit vector. In addition, the cluster may overlap with both boundaries, and the cost function is augmented from Eq. (5.21) as,

$$\begin{aligned} f_c^{tw}(\boldsymbol{y}) = &\sum_{i=1}^{n} \epsilon_i + \epsilon_m + \sum_{s=1}^{m} \lambda_s^p [\|(\boldsymbol{x}_p + \Delta \boldsymbol{x}_p^{\mathrm{P}}) - (\boldsymbol{x}_q + \Delta \boldsymbol{x}_q^{\mathrm{P}})\|^2 - 4a^2] \\ &+ \sum_{r=1}^{l_+} \lambda_r^+ [(H + \Delta H^{\mathrm{P}} - a) - (z_r + \Delta z_r^{\mathrm{P}})] \\ &+ \sum_{t=1}^{l_-} \lambda_t^- [(z_t + \Delta z_t^{\mathrm{P}}) - a] + \lambda_x^f \sum_{i=1}^{n} f_{i,x}^{\mathrm{P}} + \lambda_y^f \sum_{i=1}^{n} f_{i,y}^{\mathrm{P}}. \end{aligned} \tag{5.24}$$

The set of cost functions in Eq. (5.11), (5.21), (5.23) and (5.24) covers all possible scenarios of interface movement in this work.

5.B Solving the continuum model and mapping to simulations

The moving boundary problems in Eq. (5.13) and (5.15) and their auxiliary equations are transformed to a fixed domain of $0 \leq \xi \leq 1$ through the coordinate transformation $\xi(t) = z/L(t)$ [67]. Since particle size does not explicitly appear in the model, it is more convenient to scale the length with the initial gap width L_0. For constant velocity interface movement, we introduce a new dimensionless time $\tau = tU_w/L_0$ and a wall velocity Péclet number $\mathrm{Pe_{WU}} = U_w L_0/D_0 = \mathrm{Pe}_U(L_0/a)$, which leads to

$$\frac{\partial \phi}{\partial \tau} = \frac{1}{\mathrm{Pe_{WU}}(1-\tau)^2}\frac{\partial}{\partial \xi}\left\{\frac{\mathrm{d}}{\mathrm{d}\phi}[\phi Z(\phi)]\frac{\partial \phi}{\partial \xi}\right\} - \frac{\xi}{1-\tau}\frac{\partial \phi}{\partial \xi} \tag{5.25}$$

with boundary conditions

$$\frac{\partial \phi}{\partial \xi} = 0 \text{ at } \xi = 0, \tag{5.26}$$

$$\frac{\mathrm{d}}{\mathrm{d}\phi}[\phi Z(\phi)]\frac{\partial \phi}{\partial \xi} - \mathrm{Pe_{WU}}(1-\tau)\phi = 0 \text{ at } \xi = 1. \tag{5.27}$$

For constant normal stress interface movement, we define $\tau = (\zeta/\Sigma_e)(L_0/a^2)$, and the wall stress Péclet number $\mathrm{Pe_{W\Sigma}} = a^2 L_0 \Sigma_e/(k_\mathrm{B}T) = \mathrm{Pe}_\Sigma(L_0/a)$. With $\bar{L} = L(t)/L_0$, we have

$$\frac{\partial \phi}{\partial \tau} = \frac{1}{\mathrm{Pe_{W\Sigma}}}\frac{1}{\bar{L}^2}\left[\frac{\mathrm{d}^2 f}{\mathrm{d}\phi^2}\left(\frac{\partial \phi}{\partial \xi}\right)^2 + \frac{\mathrm{d}f}{\mathrm{d}\phi}\frac{\partial^2 \phi}{\partial \xi^2}\right] + \frac{\xi}{\bar{L}\alpha_m}\frac{\partial \phi}{\partial \xi}(-1+\beta f), \tag{5.28}$$

with boundary conditions

$$\frac{\partial \phi}{\partial \xi} = 0 \text{ at } \xi = 0, \tag{5.29}$$

$$\frac{1}{\bar{L}}\frac{\mathrm{d}f}{\mathrm{d}\phi}\frac{\partial \phi}{\partial \xi} + \frac{\phi \mathrm{Pe_{W\Sigma}}}{\alpha_m}(-1+\beta f) = 0 \text{ at } \xi = 1, \tag{5.30}$$

and the wall motion auxiliary equation

$$\frac{\mathrm{d}\bar{L}}{\mathrm{d}\tau} = \frac{-1+\beta f}{\alpha_m}, \tag{5.31}$$

where $f = \phi Z(\phi)$, and $\beta = 3/(4\pi)(L_0/a)\mathrm{Pe}_{\mathrm{W\Sigma}}^{-1}$. These non-linear partial differential equations can be converted to a set of ordinary differential equations by spatial discretization and solved numerically.

A subtlety for comparing the simulations with the continuum models is that in the simulations the confining boundaries reduce the particle accessible volume. For a simulation starting with H_0 and ϕ_0, the corresponding continuum model has an initial gap width $L_0 = H_0 - 2a$ and a starting volume fraction $\phi_s = \phi_0 H_0/(H_0 - 2a)$. The wall position $L(t)$ in the model corresponds to $H(t) = L(t)H_0/(H_0 - 2a)$ in the simulations. Furthermore, when comparing the stress and volume fraction profiles, the simulation position z_s with $H(t)$ and the model position z_m with $L(t)$ are related as

$$\frac{z_s - a}{H(t) - 2a} = \frac{z_m}{L(t)}. \tag{5.32}$$

References

[1] S.-H. Kim, S. Y. Lee, S.-M. Yang, and G.-R. Yi, "Self-assembled colloidal structures for photonics", NPG Asia Mater. **3**, 25 (2011).

[2] I. Lee, D. Kim, J. Kal, H. Baek, D. Kwak, D. Go, E. Kim, C. Kang, J. Chung, Y. Jang, S. Ji, J. Joo, and Y. Kang, "Quasi-amorphous colloidal structures for electrically tunable full-color photonic pixels with angle-independency", Adv. Mater. **22**, 4973 (2010).

[3] J. J. Guo and J. A. Lewis, "Aggregation effects on the compressive flow properties and drying behavior of colloidal silica suspensions", J. Am. Ceram. Soc **89**, 2345 (1999).

[4] D. M. Holms, F. Tegeler, and W. J. Clegg, "Stresses and strains in colloidal films during lateral drying", J. Eur. Ceram. Soc. **28**, 1381 (2008).

[5] J. Kim, K. Cho, S. Ryu, S. Y. Kim, and B. M. Weon, "Crack formation and prevention in colloidal drops", Sci. Rep. **5**, 13166 (2015).

[6] J. L. Keddie, "Film formation of latex", Mater. Sci. Eng. R-Rep. **21**, 101 (1997).

[7] D. D. Brewer, T. Shibuta, L. Francis, S. Kumar, and M. Tsapatsis, "Coating process regimes in particulate film production by forced-convection-assisted drag-out", Langmuir **27**, 11660 (2011).

[8] Y. K. Koh, C. H. Yip, Y.-M. Chiang, and C. C. Wong, "Kinetic stages of single-component colloidal crystallization", Langmuir **24**, 5245 (2008).

[9] A. F. Routh, "Drying of thin colloidal films", Rep. Prog. Phys. **76**, 046603 (2013).

[10] W. B. Russel, D. A. Saville, and W. R. Schowalter, *Colloidal dispersions* (Cambridge University Press, 1991).

[11] J. K. G. Dhont, *An introduction to dynamics of colloids* (Elsevier, Amsterdam, 1996).

[12] J. W. Swan and J. F. Brady, "The hydrodynamics of confined dispersions", J. Fluid Mech. **687**, 254 (2011).

[13] A. Q. Shen and P. Cheung, "The freedom of confinement in complex fluids", Phys. Today **63**, 30 (2010).

[14] A. W. C. Lau and T. C. Lubensky, "State-dependent diffusion: thermodynamic consistency and its path integral formulation", Phys. Rev. E **76**, 011123 (2007).

[15] H. Diamant, "Hydrodynamic interaction in confined geometries", J. Phys. Soc. Jpn. **78**, 041002 (2009).

[16] Y. Reyes and Y. Duda, "Modeling of drying in films of colloidal particles", Langmuir **21**, 7057 (2005).

[17] Q. Liao, L. Chen, X. Qu, and X. Jin, "Brownian dynamics simulation of film formation of mixed polymer latex in the water evaporation stage", J. Colloid Interface Sci. **227**, 84 (2000).

[18] M. Fujita and Y. Yamaguchi, "Multiscale simulation method for self-organization of nanoparticles in dense suspension", J. Comput. Phys. **223**, 108 (2007).

[19] M. Fujita and Y. Yamaguchi, "Drying simulation of nanoparticle suspension film on substrate", in International society of coating science and technology conference (2005).

[20] S. Ohta, S. Inasawa, O. Koike, M. Fujita, and Y. Yamaguchi, "Formation of well-aligned thin films of rod-like nanoparticles via solvent evaporation: a simulation study", Appl. Phys. Express **2**, 065002 (2009).

[21] D. R. Foss and J. F. Brady, "Brownian dynamics simulation of hard-sphere colloidal dispersions", J. Rheol. **44**, 629 (2000).

[22] N. Koumakis, M. Laurati, S. U. Egelhaaf, J. F. Brady, and G. Petekidis, "Yielding of hard-sphere glasses during start-up shear", Phys. Rev. Lett. **108**, 098303 (2012).

[23] N. Koumakis, J. F. Brady, and G. Petekidis, "Complex oscillatory yeilding of model hard-sphere glasses", Phys. Rev. Lett. **110**, 178301 (2013).

[24] J.-P. Gorce, D. Bovey, P. J. McDonald, P. Palasz, D. Taylor, and J. L. Keddie, "Vertical water distribution during the drying of polymer films cast from aqueous emulsions", Eur. Phys. J. E Soft Matter **8**, 421 (2002).

[25] T. Narita, P. Hebraud, and F. Lequeux, "Effects of the rate of evaporation and film thickness on nonuniform drying of film-forming concentrated colloidal suspensions", Eur. Phys. J. E Soft Matter **17**, 69 (2005).

[26] C. M. Cardinal, Y. D. Jung, K. H. Ahn, and L. F. Francis, "Drying regime maps for particulate coatings", AIChE J. **56**, 2769 (2010).

[27] A. Utgenannt, R. Maspero, A. Fortini, R. Turner, M. Florescu, C. Jeynes, A. G. Kanaras, O. L. Muskens, S. R. P., and J. L. Keddie, "Fast assembly of gold nanoparticles in large-area 2d nanogrids using a one-step, near-infrared radiation-assisted evaporation process", ACS Nano **10**, 2232 (2016).

[28] P. Pieranski, L. Strzelecki, and B. Pansu, "Thin colloidal crystals", Phys. Rev. Lett. **50**, 900 (1983).

[29] M. Schmidt and H. Löwen, "Phase diagram of hard spheres confined between two parallel plates", Phys. Rev. E **55**, 7228 (1997).

[30] A. Fortini and M. Dijkstra, "Phase behaviour of hard spheres confined between parallel hard plates: manipulation of colloidal crystal structures by confinement", J. Phys.: Condens. Matter **18**, L371 (2006).

[31] J. P. Hansen and I. R. McDonald, *Theory of simple liquids* (Academic Press, 2006).

[32] K. E. Davis, W. B. Russel, and W. J. Glantschnig, "Disorder-to-order transition in settling suspensions of colloidal silica: x-ray measurements", Science **245**, 507 (1989).

[33] J. P. Hoogenboom, P. Vergeer, and A. van Blaaderen, "A real-space analysis of colloidal crystallization in a gravitational field at a flat bottom wall", J. Chem. Phys. **119**, 3371 (2003).

[34] C. P. Royall, J. Dzubiella, M. Schmidt, and A. van Blaaderen, "Nonequilibrium sedimentation of colloids on the particle scale", Phys. Rev. Lett. **98**, 188304 (2007).

[35] T. Biben, R. Ohnesorge, and H. Löwen, "Crystallization in sedimentation profiles of hard spheres", Europhys. Lett. **28**, 665 (1994).

[36] M. Marechal and M. Dijkstra, "Crystallization of colloidal hard spheres under gravity", Phys. Rev. E **75**, 061404 (2007).

[37] M. Marechal, M. Hermes, and M. Dijkstra, "Stacking in sediments of colloidal hard spheres", J. Chem. Phys. **135**, 034510 (2011).

[38] Z.-Q. Li, Z.-Y. Sun, L.-J. An, and Z.-G. Wang, "Heterogeneity in structurally arrested hard spheres", Europhys. Lett. **84**, 26005 (2008).

[39] R. S. Fishman, E. F. Hill, T. K. Storsved, and G. P. Bierwagen, "Density fluctuations in hard-sphere systems", J. Appl. Phys. **79**, 729 (1996).

[40] P. N. Segrè, F. Liu, P. Umbanhowar, and D. A. Weitz, "An effective gravitational temperature for sedimentation", Nature **409**, 594 (2001).

[41] J. N. Israelachvili, "Adhesin forces between surfaces in liquids and condensable vapours", Surf. Sci. Rep. **14**, 109 (1992).

[42] P. A. Thompson and M. O. Robbins, "Origin of stick-slip motion in boundary lubrication", Science **250**, 792 (1990).

[43] J.-C. Wang and K. A. Fichthorn, "A method for molecular dynamics simulation of confined fluids", J. Chem. Phys. **112**, 8252 (2000).

[44] H. Eslami, F. Mozaffari, J. Moghadasi, and F. Müller-Plathe, "Molecular dynamics simulation of confined fluids in isosurface-isothermal-isobaric ensemble", J. Chem. Phys. **129**, 194702 (2008).

[45] T. Gruhn and P. A. Monson, "Molecular dynamics simulations of hard sphere solidification at constant pressure", Phys. Rev. E **64**, 061703 (2001).

[46] M. Schoen, D. J. Diestler, and J. H. Cushman, "Shear melting of confined solid monolayer films", Phys. Rev. B **47**, 5603 (1993).

[47] M. Schoen, S. Hess, and D. J. Diestler, "Rheological properties of confined thin films", Phys. Rev. E **52**, 2587 (1995).

[48] A. F. Routh and W. B. Zimmerman, "Distribution of particles during solvent evaporation from films", Chem. Eng. Sci. **59**, 2961 (2004).

[49] G. J. Kynch, "A theory of sedimentation", Trans. Faraday Soc. **48**, 166 (1952).

[50] K. E. Davis and W. B. Russel, "An asymptotic description of transient settling and ultrafiltration of colloidal dispersions", Phys. Fluids A **1**, 82 (1989).

[51] K. Kamrin and G. Koval, "Nonlocal constitutive relation for steady granular flow", Phys. Rev. Lett. **108**, 178301 (2012).

[52] P. Strating, "Brownian dynamics simulation of a hard-sphere suspension", Phys. Rev. E **59**, 2175 (1999).

[53] A. Scala, T. Voigtmann, and C. De Michele, "Event-driven brownian dynamics for hard spheres", J. Chem. Phys. **126**, 134109 (2007).

[54] D. M. Heyes and J. R. Melrose, "Brownian dynamics simulations of model hard-sphere suspensions", J. Non-Newtonian Fluid Mech. **46**, 1 (1993).

[55] B. Cichocki and K. Hinsen, "Dynamic computer simulation of concentrated hard sphere suspensions: i. simulation technique and mean square displacement data", Physica A **166**, 473 (1990).

[56] W. Schaertl and H. Sillescu, "Brownian dynamics simulations of colloidal hard spheres. effects of sample dimensionality on self-diffusion", J. Stat. Phys. **74**, 687 (1994).

[57] D. L. Ermak and J. A. McCammon, "Brownian dynamics with hydrodynamic interactions", J. Chem. Phys. **69**, 1352 (1978).

[58] H. Goldstein, C. P. Poole Jr., and J. L. Safko, *Classical mechanics* (Addison-Wesley, 2001).

[59] C. S. O'Hern, L. E. Silbert, A. J. Liu, and S. R. Nagel, "Jamming at zero temperature and zero applied stress: the epitome of disorder", Phys. Rev. E **68**, 011306 (2003).

[60] E. A. J. F. Peters and T. M. A. O. M. Barenbrug, "Efficient brownian dynamics simulation of particles near walls. i. reflecting and absorbing walls", Phys. Rev. E **66**, 056701 (2002).

[61] E. J. Le Fevre, "Equation of state for hard-sphere fluid", Nature Physical Science **235**, 20 (1972).

[62] A. Mulero, ed., *Theory and simulation of hard-sphere fluids and related systems* (Springer, 2008).

[63] P. R. ten Wolde, M. J. Ruiz-Montero, and D. Frenkel, "Numerical evidence for bcc ordering at the surface of a critical fcc nucleus", Phys. Rev. Lett. **75**, 2714 (1995).

[64] P. J. Steinhardt, D. R. Nelson, and M. Ronchetti, "Bond-orientational order in liquids and glasses", Phys. Rev. B **28**, 784 (1983).

[65] B. D. Todd, D. J. Evans, and P. J. Daivis, "Pressure tensor for inhomogeneous fluids", Phys. Rev. E **52**, 1627 (1995).

[66] C. H. Rycroft, "Voro++: a three-dimensional voronoi cell library in c++", Chaos **19**, 041111 (2009).

[67] J. Crank, *Free and moving boundary problems* (Oxford University Press, 1984).

Chapter 6

CONSTANT STRESS AND PRESSURE RHEOLOGY OF COLLOIDAL SUSPENSIONS

[1] M. Wang and J. F. Brady, "Constant stress and pressure rheology of colloidal suspensions", Physical Review Letters **115**, 158301 (2015) doi:10.1103/PhysRevLett.115.158301,

6.1 Introduction

Amorphous materials such as metallic glasses, granular matter, and colloidal suspensions exhibit a range of flow behaviors including shear-thickening [1], particle migration [2], shear banding [3], *etc*. The most fundamental and universal aspect of their rheology is a flow-arrest transition that takes place at either increased density or reduced temperature and is summarized by various 'jamming diagrams', pioneered by Liu & Nagel [4–6]. Extensive computational and experimental investigations reveal that the flow-arrest transition is affected by the interplay among thermal fluctuations [6–10] and particle geometry and interactions [11–14]. Distinct behaviors have been observed for strong and weak thermal fluctuations, but the connection between the two limits is an open question.

In this chapter we present a unified perspective on the flow-arrest transition spanning the entire range between the thermal and athermal limits. For simplicity, our study focuses on hard-sphere colloidal dispersions. Experiments and simulations at fixed volume (fraction) have found the suspension viscosity to diverge algebraically at a critical volume fraction: $\eta_s \propto (\phi_c - \phi)^{-\delta}$, where ϕ is the volume fraction and δ is the exponent. With strong thermal fluctuations the colloidal glass transition is observed: $\phi_c \approx 0.58$–0.60 and $\delta \approx 2.2$–2.6 [7, 15–17]. In the limit of the jamming transition where thermal fluctuations are weak: $\phi_c \approx 0.585$–0.64 and $\delta \approx 2.0$ [9, 18, 19]. Moreover, ϕ_c is sensitive to the particle size polydispersity [20], particle surface asperity [5], and even the sample preparation protocol [21]. Traditionally, the different exponents are interpreted as signatures of distinct physical processes—the colloidal glass vs. the jamming transition [9]. Here we show that when the suspension pressure, instead of the volume, is held fixed under shear a universal exponent and behavior emerges.

A challenge to dense suspension rheology is the divergence of properties such as viscosity and yield stress near ϕ_c. We overcome this in two ways. First, we impose a constant shear stress rather than shear rate, which allows the system to flow or not, and the yield stress—the stress below which the material does not flow—can be identified. Second, we impose a constant confining pressure rather than a fixed volume, which allows the system to dilate (or compact)—to change its volume fraction—as necessary under flow. In this way we are able to approach the critical point along trajectories at fixed shear stress and pressure, rather than, as is traditional, along paths of fixed shear rate and volume fraction.

It proves revealing to discuss the behavior from a perspective often used in the granular flow community. Although both the shear and normal stresses diverge at the critical point, their ratio does not. For viscous suspensions the behavior can be described in terms of the friction coefficient μ, a *macroscopic*, effective property of the material, and the viscous flow number I_v [19],

$$\mu = \sigma/\Pi \quad \text{and} \quad I_v = \eta_0\dot{\gamma}/\Pi, \tag{6.1}$$

where σ is the shear stress, Π is the particle (or osmotic) pressure, η_0 is the solvent viscosity, and $\dot{\gamma}$ is the strain rate. Using the viscous flow number I_v—the ratio of an internal suspension time scale η_0/Π to the flow time scale $\dot{\gamma}^{-1}$—Boyer *et al.* [19] successfully unified the rheology of viscous non-Brownian suspensions and inertial-driven granular materials.

For rapid granular flows both the shear and normal stresses scale inertially (as $\sim \rho a^2\dot{\gamma}^2$) and their ratio, the friction coefficient, is independent of the strain rate, which has led to the claim that a rate-independent friction coefficient is a signature of (dry) friction-dominated material and flow. However, in viscous non-Brownian suspensions (any colloidal suspension at high shear rates) both σ and Π scale linearly with the strain rate (as $\sim \eta_0\dot{\gamma}$) and the friction coefficient is independent of $\dot{\gamma}$ even though the material behaves as a liquid.

Liquid-like colloidal dispersions are not normally discussed in terms of μ because at low shear rates (strong thermal motion) the shear stress is proportional to $\dot{\gamma}$, but the normal stress is dominated by the equilibrium osmotic pressure and thus $\mu \sim \dot{\gamma}$ as $\dot{\gamma} \to 0$. However, near the flow-arrest point, the material has a dynamic yield stress, and μ may approach a constant as $\dot{\gamma} \to 0$. The friction coefficient perspective therefore enables a natural connection between Brownian suspensions and granular materials.

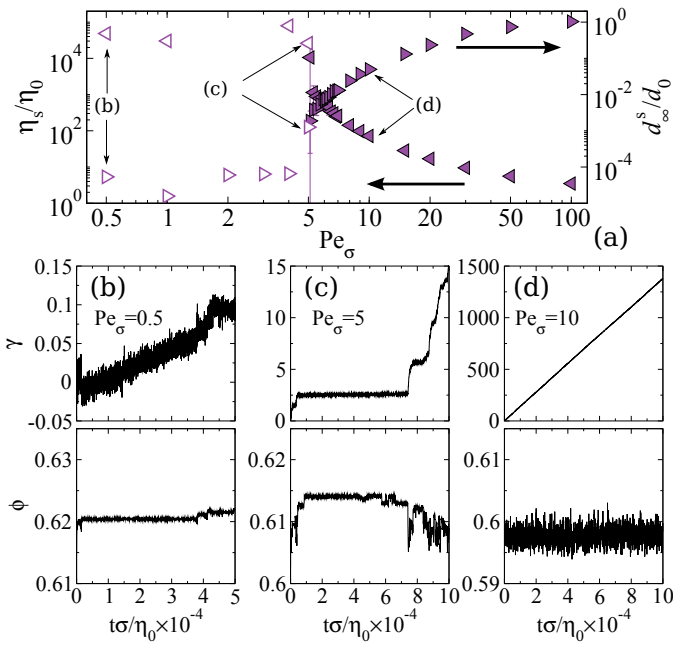

Figure 6.1: (a): The suspension steady shear viscosity η_s/η_0 (left triangles) and the long-time self-diffusivity d^s_∞/d_0 (right triangles), with $d_0 = k_\mathrm{B}T/(6\pi\eta_0 a)$, as functions of Pe_σ in constant shear stress and pressure simulations at an imposed pressure $\Pi a^3/k_\mathrm{B}T = 5$. The filled (open) symbols represent the flowing (arrested) states. Typical accumulated strain γ (top) and volume fraction ϕ (bottom) at Pe_σ = 0.5 (b), 5 (c), and 10 (d) as functions of dimensionless time $t\sigma/\eta_0$ are also presented, with the corresponding Pe_σ annotated in (a).

6.2 Method

We study the suspension rheology using Brownian dynamics (BD) simulations without hydrodynamic interactions (HIs). In the simulations, we enforce the hard-sphere interactions via the 'potential free' algorithm [22–25], and compute ϕ and $\dot\gamma$ from the imposed σ and Π, which, when scaled with the thermal energy $k_\mathrm{B}T$, give, respectively, the stress Péclet number $\mathrm{Pe}_\sigma = 6\pi a^3\sigma/k_\mathrm{B}T$ and the dimensionless pressure $\bar\Pi = \Pi a^3/k_\mathrm{B}T$, with a the mean particle radius. The particle dynamics follow the overdamped Langevin equation,

$$\zeta(\dot{\boldsymbol{x}} - \dot\gamma x_2 \boldsymbol{e}_1 - \tfrac{1}{3}\dot e \boldsymbol{x}) = \boldsymbol{f}_p + \boldsymbol{f}_b, \tag{6.2}$$

where $\boldsymbol{x} = (x_1, x_2, x_3)$ is the particle position in the 1-(velocity), 2-(velocity gradient), and 3-(vorticity) directions, $\zeta = 6\pi\eta_0 a$ is the Stokes resistance, $\dot e$ is the expansion rate, $\boldsymbol{e}_1$ is the unit vector in 1-direction, $\boldsymbol{f}_p$ is the interparticle force [25], and $\boldsymbol{f}_b$ is the Brownian force, which has a mean of zero and a variance of $2k_\mathrm{B}T\zeta$. We impose periodic boundary conditions in 1- and 3-directions and the Lees-Edwards

boundary condition in 2-direction. The strain ($\dot{\gamma}$) and expansion ($\dot{e}$) rates are computed from:

$$\sigma = (1 + \tfrac{5}{2}\phi)\eta_0\dot{\gamma} + \sigma_{12}^p, \tag{6.3}$$

$$\Pi = -(\kappa_0 + \tfrac{4}{3}\phi\eta_0)\dot{e} - \tfrac{1}{3}\boldsymbol{\sigma}^p : \mathbf{I}, \tag{6.4}$$

where κ_0 is the bulk viscosity of the compressible solvent [1], and $\boldsymbol{\sigma}^p = -nk_BT\mathbf{I} - n\left\langle \boldsymbol{x}\boldsymbol{f}_p \right\rangle$ is the particle stress contribution, with $n = N/V$ the number density. The simulation box size L is then adjusted isotropically as $\dot{L} = \frac{1}{3}\dot{e}L$. The novelty of our method is that, through a compressible solvent, the constant pressure constraint for the overdamped system is satisfied without introducing permeable boundaries.

For each $(\mathrm{Pe}_\sigma, \bar{\Pi})$ pair we perform at least three independent simulations, each contains $N = 200$ particles with 10% particle size polydispersity [8]. The simulation lasts at least 10^4 dimensionless time units with step size 10^{-4}, where the time is scaled with $6\pi\eta_0 a^3/k_BT$ when $\mathrm{Pe}_\sigma < 1$ and with η_0/σ when $\mathrm{Pe}_\sigma \geq 1$. In the appendices, we describe the computation of $\boldsymbol{f}_p$, and show that the selected parameters adequately capture the physics of flow-arrest transitions.

6.3 Results and discussions

Typical rheological responses from constant stress and pressure simulations at an imposed pressure $\bar{\Pi} = 5$ are shown in Fig. 6.1. The Pe_σ dependence of the shear viscosity $\eta_s = \sigma/\dot{\gamma}$ and the long-time self-diffusivity (LTSD) d_∞^s, measured from the slope of the mean-square displacement in the vorticity direction, $d_\infty^s = \lim_{t\to\infty} \frac{1}{2}\mathrm{d}\langle(\Delta x_3)^2\rangle/\mathrm{d}t$, are presented in Fig. 6.1a. The suspension exhibits a flow-arrest transition at $\mathrm{Pe}_\sigma \approx 5$, with the flowing data shown as filled symbols and the arrested data as open symbols. When $\mathrm{Pe}_\sigma \gtrsim 5$, the shear viscosity increases sharply with decreasing Pe_σ, reaching $\eta_s/\eta_0 \approx 2 \times 10^4$ at $\mathrm{Pe}_\sigma \approx 5$. Accompanying the growth in η_s is an abrupt reduction in d_∞^s. At lower Pe_σ, the shear viscosity remains high and the LTSD low. Fig. 6.1b–6.1d show behaviors of the accumulated strain $\gamma = \int_0^t \dot{\gamma}\mathrm{d}t$ and the volume fraction ϕ at different Pe_σ. The accumulated strain grows linearly with time in the flowing state, but changes little in the arrested state. At $\mathrm{Pe}_\sigma = 5$ in Fig. 6.1c, γ exhibits instability and switches between the flowing and arrested states. Correspondingly, ϕ fluctuates around a mean value for both the flowing and arrested suspensions, but becomes unstable at the flow-arrest point. We

[1] Treating the solvent as a compressible fluid allows the periodic unit cell to be expanded isotropically without violating the physics of Brownian particles in Stokes flow, c.f. Ref. [26]. Thus, a physical permeable boundary, which can cause local ordering, etc., is not necessary.

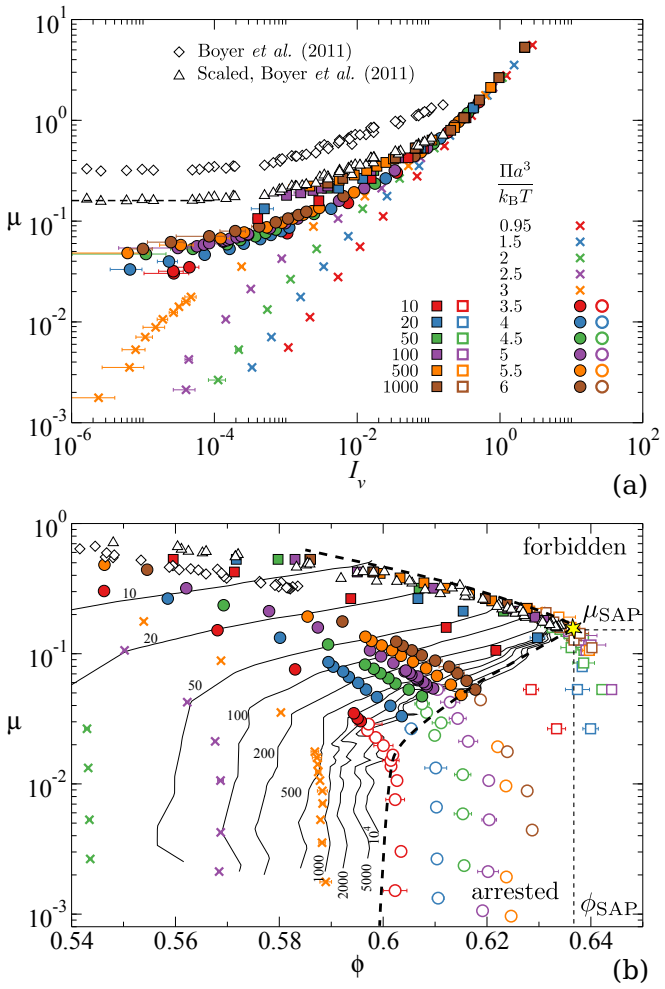

Figure 6.2: (Color online) The steady shear rheology of hard-sphere colloidal suspensions with constant shear stress and pressure, (a): $\mu = \sigma/\Pi$ as a function of $I_v = \eta_0\dot{\gamma}/\Pi$ and (b): μ as a function of ϕ. Simulations at the same imposed pressure $\Pi a^3/k_BT$ are shown in the same symbols. For suspensions exhibiting flow-arrest transitions, the filled (open) symbols represent the flowing (arrested) states. The raw and the scaled data of Boyer *et al.* [19] are shown in diamonds and triangles, respectively. In (b), the dashed lines outline the boundary of the flowing region, and the solid lines are contours of the shear viscosity η_s/η_0. The *Shear Arrest Point* (ϕ_{SAP}, μ_{SAP}) is shown as a star.

found that the suspensions is arrested when $\eta_s/\eta_0 > 2 \times 10^4$ over a wide range of imposed pressures. Consequently, this is adopted as a criterion for the flow-arrest transition in this work.

Fig. 6.2 presents the overall steady shear rheology at constant stress and pressure near the flow-arrest transition. Fig. 6.2a shows the friction coefficient as a function

of the viscous number, and Fig. 6.2b shows the corresponding volume fraction. The symbols of the same color are at the same confining pressure (shown in the figure legend) and trace out 'isobars'. Full symbols are flowing liquid-like systems, while unfilled symbols denote arrested states.

Starting with solid ×'s at low confining pressures, *e.g.*, at $\bar{\Pi} = 0.95$ in Fig. 6.2a, μ grows linearly with I_v at low and high I_v with different slopes; the suspension does not arrest. The ratio of μ and I_v is the shear viscosity, $\eta_s/\eta_0 = \mu/I_v$. At high I_v, the suspension viscosity η_s asymtotes to the solvent viscosity η_0. With increasing $\bar{\Pi}$, the μ-I_v curve flattens as I_v decreases, but eventually turns down such that $\mu \sim \dot{\gamma}$ as $\dot{\gamma} \to 0$. The suspension flows as a liquid with an increasing zero shear-rate viscosity corresponding to the larger ϕ seen in Fig. 6.2b.

When the confining pressure $\bar{\Pi} \geq 3.5$, the suspension arrests and flows only if μ exceeds a limiting value $\mu_m(\bar{\Pi})$, and the minimum shear rate (I_v) increases. The imposed stress corresponding to μ_m is the dynamic yield stress at the imposed pressure. Moreover, μ_m increases with $\bar{\Pi}$ and, as $\bar{\Pi} \to \infty$, μ_m asymptotes to a constant value of 0.16. At high $\bar{\Pi}$ (and high I_v for low $\bar{\Pi}$) all data collapse onto a single curve corresponding to the limiting behavior of non-Brownian viscous suspensions.

Fig. 6.2b shows the corresponding μ-ϕ curves. At low confining pressures (the ×'s) the volume fraction increases as the shear stress (μ) decreases. When arrested, $\bar{\Pi} \geq 3.5$ (open symbols), dilation always precedes flow as the shear stress is increased and the maximum flowable volume fraction ϕ_m is always lower than the zero-shear value. As a point of reference, the zero-shear volume fraction at $\bar{\Pi} = 3.5$ is $\phi = 0.60$ for our system. As $\bar{\Pi} \to \infty$, ϕ_m asymptotes to a constant value and the non-Brownian limit emerges as the μ-ϕ curves collapse. The flowing region in Fig. 6.2b is bounded from below by the arrested region and from above by the non-Brownian behavior.

The rightmost point of the flowing region, highlighted as a star in Fig. 6.2b, corresponds to the flow-arrest transition in the viscous non-Brownian limit. This point is referred to as the *Shear Arrest Point* (SAP):

$$(\phi_{\mathrm{SAP}}, \mu_{\mathrm{SAP}}) = \lim_{\bar{\Pi}\to\infty} (\phi_m, \mu_m) \approx (0.635, 0.16)\,, \tag{6.5}$$

which represents a limit beyond which the suspension is unable to flow regardless of the imposed pressure and shear stress. The SAP is uniquely determined from the constant stress and pressure rheology protocol and therefore may differ from other

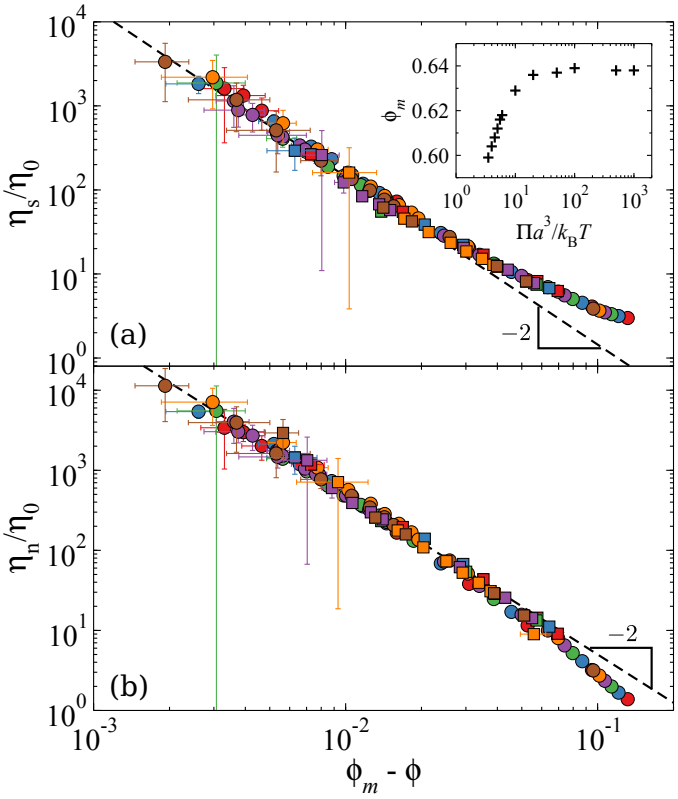

Figure 6.3: (Color online) Universal viscosity divergences (a): the shear viscosity η_s/η_0 and (b): the incremental normal viscosity η_n/η_0 as functions of $(\phi_m - \phi)$, the volume fraction difference from arrest, for flowing suspensions with $\bar{\Pi} \geq 3.5$. The inset of (a) shows ϕ_m as a function of $\bar{\Pi}$. The legends are identical to those in Fig. 6.2.

'jamming' points [5, 6]. In fact, ϕ_{SAP} is lower than the maximum random jammed (MRJ) density of the corresponding polydisperse packing $\phi_{\mathrm{MRJ}} \approx 0.645$.

Also presented in Fig. 6.2b are the shear viscosity contours up to $\eta_s/\eta_0 = 10^4$. Horizontal traversal near $\mu = 0$ recovers the equilibrium suspension behavior near the glass transition. The viscosity diverges at $\phi_g \approx 0.6$, which is also found experimentally in similar systems [16, 17, 27]. Vertical crossing corresponds to the constant volume rheology and the viscosity exhibits shear-thinning. Near the SAP, the range of μ in the flowing region reduces drastically for constant volume rheology. On the other hand, constant stress and pressure rheology allows the suspension to dilate and to find the SAP dynamically, a key merit of our approach.

In the flowing region near the flow-arrest transition both the shear viscosity η_s and the incremental normal viscosity η_n diverge as shown in Fig. 6.3. The incremental

normal viscosity η_n characterizes the flow contribution to the osmotic pressure,

$$\eta_n = (\Pi - \Pi^{eq})/\dot{\gamma}, \tag{6.6}$$

where Π^{eq} is the zero-shear equilibrium osmotic pressure at the same volume fraction. Both η_s and η_n diverge algebraically when approaching the flow-arrest transition: $(\eta_s, \eta_n) \sim (\phi_m - \phi)^{-2}$; the exponent 2 is independent of the imposed pressure and thus valid for both strong and weak thermal fluctuations. The same viscosity divergence exponents were found in experiments [19] and simulations [28] of non-Brownian systems, suggesting the physics of jamming is the most important and universal aspect of the flow-arrest transition. Thermal fluctuations only affect the arrest volume fraction ϕ_m, as shown in the inset of Fig. 6.3a.

Note that the divergence of the shear viscosity with an exponent of 2 is not inconsistent with exponent 2.2–2.6 reported for the colloidal glass transition. For the glass transition, one approaches the arrested region in Fig. 6.2b horizontally by varying the volume fraction at low μ, whereas the divergences observed here are for approaching arrest at fixed pressure. Both where the viscosity starts to diverge, ϕ_m, and how steep is the rise, the exponent α, depend on how the 'mountain' (the viscosity contours) is approached.

The data collapse in Fig. 6.3 can be explained by the internal structural relaxations in colloidal dispersions. The inherent relaxation from thermal fluctuations is characterized by $d_\infty^{s,0}$, and for glassy materials $\phi > \phi_g$, $d_\infty^{s,0} \to 0$. Comparing the shear to the inherent Brownian forces defines a zero-shear Péclet number $\dot{\gamma}a^2/d_\infty^{s,0}$ and shows that, in the glassy or arrested state, any finite shear rate gives a *large* Péclet number. The system is driven far from equilibrium and therefore shows universal behaviors. Indeed, this is seen in η_n: linear response would dictate that $\eta_n \propto \dot{\gamma}$ as $\dot{\gamma} \to 0$ [29], rather than be independent of $\dot{\gamma}$ as seen in Fig. 6.3b. There is no linear response regime near a flow-arrest point. This may explain why the inherently non-equilibrium isobaric flow-arrest transition of colloidal dispersions has features in common with the athermal granular jamming transitions [30–32].

Finally, we compare our simulations to the experiments of Boyer *et al.* [19], whose results are shown as diamonds in Fig. 6.2. The experimental data qualitatively agree with the simulation results in the non-Brownian limit ($\bar{\Pi} \to \infty$); however, their flow-arrest critical point $(\phi_c, \mu_c) = (0.585, 0.32)$ is quite different. We can achieve quantitative agreement by scaling the experimental data from (ϕ, μ) to (ϕ', μ') as

$$\frac{\mu'}{\mu} = \frac{\phi_{\mathrm{SAP}} - \phi'}{\phi_c - \phi} = \frac{\mu_{\mathrm{SAP}}}{\mu_c}, \tag{6.7}$$

which are shown as triangles in Fig. 6.2 and match the simulation results. The scaling of Eq. (6.7) implies that the fundamental physics behind the viscous non-Brownian arrest does not change with the HIs or the possible frictional contact forces in the experiments. Our simulations clearly capture the physics of the flow-arrest transition.

That $\mu_c > \mu_{\mathrm{SAP}}$ can be understood from the lack of HIs in the simulations. Hydrodynamics give an additional contribution to the shear stress via the high-frequency dynamic viscosity, which increases σ and therefore μ. However, they do not explain the difference in the computational ϕ_{SAP} and the experimental ϕ_c seen in Fig. 6.2b. One interpretation is that frictional contact forces in the experiments reduce the arrest volume fraction [5, 12]. Yet, there is a simpler explanation. In the experiments near suspension arrest, the minimum suspension height in the shear cell (8.8 mm) is not much larger than the particle diameter (1.1 mm) [19, 33]. There is a region of order the particle size a adjacent to the apparatus walls that is inaccessible to the particles. Using the accessible volume rather than the total volume can increase the volume fraction by as much as 11% and account for the difference between ϕ_{SAP} and ϕ_c. Clearly, extreme care is needed when studying dense suspensions as seemingly unimportant details can drastically affect the results.

6.4 Conclusions

This chapter demonstrates that constant stress and pressure rheology is an effective approach to study the flow-arrest transitions of dense amorphous materials and provides a unique perspective to distinguish the most fundamental physics in this transition. We found the viscous non-Brownian *Shear Arrest Point* (SAP) of hard-sphere colloidal suspensions from the collapse of the flow curves. The results strongly suggest that the jamming and glass transitions are different facets of the same phenomenon, offering the hope for a unified understanding.

6.A Computing the interparticle force

In BD the overdamped Langevin equation [Eq. (6.2)] is integrated with respect to time. Since the interactions in hard-sphere suspensions are singular, particle overlap is unavoidable regardless of the step size Δt. In the 'potential free' algorithm, the overlap-free condition is maintained in a predictor-corrector fashion: in the predictor step, the dynamics are evolved without the hard-sphere potential, and in the corrector step, the algorithm checks the particle overlap that violates the hard-sphere potential and moves the overlapping particles back to contact pairwise along the line that

connects the particle centers until the suspension is overlap-free. If particle i at $\boldsymbol{r}_i$ overlaps particle j at $\boldsymbol{r}_j$, *i.e.*, $|\boldsymbol{r}_{ij}| > (a_i + a_j)$, where $\boldsymbol{r}_{ij} = \boldsymbol{r}_i - \boldsymbol{r}_j$ and a_i and a_j are the particle radii, the particles are moved along $\boldsymbol{r}_{ij}$ according to

$$\Delta\boldsymbol{r}_i = a_j\boldsymbol{\Delta}_{ij} \text{ and } \Delta\boldsymbol{r}_j = -a_i\boldsymbol{\Delta}_{ij}, \tag{6.8}$$

where $\boldsymbol{\Delta}_{ij} = \boldsymbol{r}_{ij}[|\boldsymbol{r}_{ij}|^{-1} - (a_i + a_j)^{-1}]$. The interparticle force on particle i is computed according to Stokes law,

$$\boldsymbol{f}_{p,i} = 6\pi\eta_0 a_i \Delta\boldsymbol{r}_i/\Delta t, \tag{6.9}$$

and here the Newton's third law is satisfied $\boldsymbol{f}_{p,i} + \boldsymbol{f}_{p,j} = 0$.

6.B System size dependence

Fig. 6.4 presents the system size dependence on the suspension shear viscosity η_s, the long-time self-diffusivity d^s_∞, and the maximum of the dynamic susceptibility $\max(\chi_4)$ as functions of Pe_σ with different system sizes N. The imposed pressure is $\bar{\Pi} = 5$. The dynamic susceptibility χ_4 for an N-particle system is defined as [34],

$$\chi_4(\boldsymbol{k}, t) = N[\langle F_s(\boldsymbol{k}, t)^2\rangle - \langle F_s(\boldsymbol{k}, t)\rangle^2], \tag{6.10}$$

where $F_s(\boldsymbol{k}, t) = N^{-1}\sum_i e^{\imath\boldsymbol{k}\cdot[\boldsymbol{x}_i(t) - \boldsymbol{x}_i(0)]}$ is the self-intermediate scattering function, $\boldsymbol{k}$ is the wave vector, $\imath = \sqrt{-1}$, and $\boldsymbol{x}_i(t)$ is the particle position at time t. In Fig. 6.4c the wave vector $\boldsymbol{k}$ is in the vorticity direction and $|\boldsymbol{k}|a = 3.72$, near the first peak of the static structure factor. When $\mathrm{Pe}_\sigma > 5$, η_s/η_0, d^s_∞/d_0, and $\max(\chi_4)$ show little N-dependence for flowing suspensions. Near the flow-arrest transition, there are quantitative differences at different N. For example, with increasing N, the Pe_σ corresponding to the flow-arrest point shifts slightly towards lower Pe_σ, and the suspensions can achieve higher $\max(\chi_4)$ and lower d^s_∞. However, the qualitative behaviors in Fig. 6.4 remain consistent. Using a modest system size of $N = 200$ captures the physics behind the flow-arrest transition with only small quantitative differences in the $N \to \infty$ limit, and allows us to explore a wide range of parameters in a reasonable amount of time.

6.C Initial condition dependence

To investigate the effect of initial conditions on the BD simulation results, we performed simulations at $N = 200$ for a few $(\bar{\Pi}, \mathrm{Pe}_\sigma)$ pairs near the flow-arrest transitions. Each $(\bar{\Pi}, \mathrm{Pe}_\sigma)$ pair corresponds to 50 independent runs with distinct initial configurations generated from the Lubachevsky-Stillinger algorithm [35], which is also used in this work. Each run lasts 5×10^3 dimensionless time units

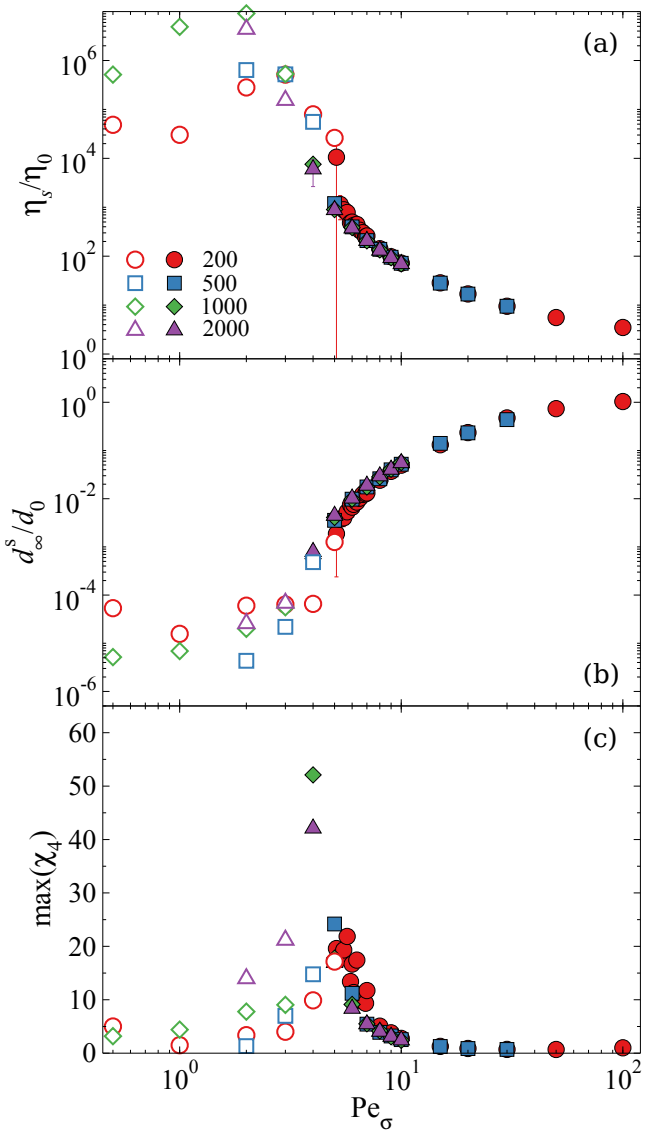

Figure 6.4: (Color online) The system size dependence on (a): the suspension shear viscosity η_s/η_0, (b): the long-time self-diffusivity d^s_∞/d_0. and (c): the maximum of the dynamic susceptibility max(χ_4) as functions of Pe_σ for constant stress and pressure simulations at $\Pi a^3/k_BT = 5$. The filled (open) symbols represent the flowing (arrested) suspension states.

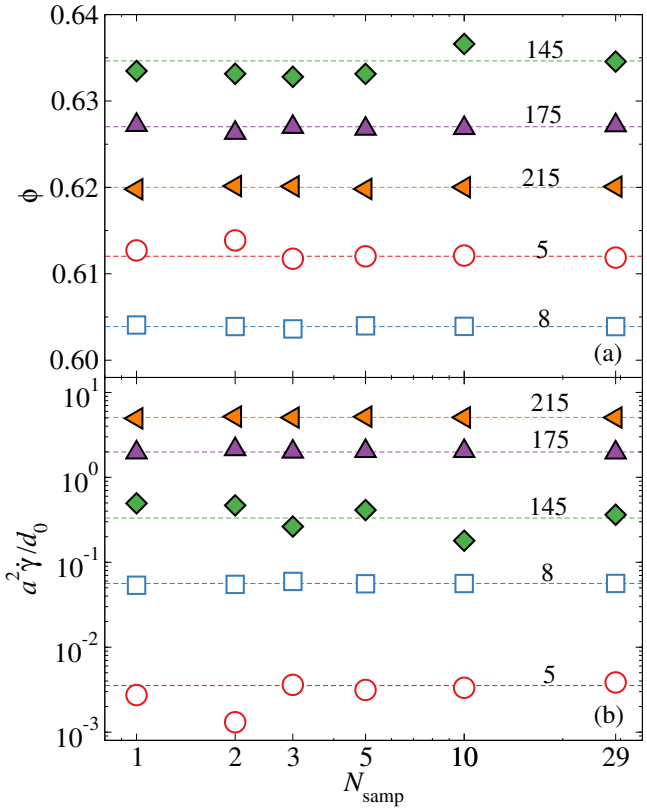

Figure 6.5: (Color online) The initial condition dependence on (a): the average volume fraction ϕ and (b): the average strain rate $\dot{\gamma}a^2/d_0$, with $d_0 = k_{\mathrm{B}}T/(6\pi\eta_0 a)$, as functions of the number of independent simulations in the group N_{samp}. The simulations are performed at $\Pi a^3/k_{\mathrm{B}}T = 5$ (open symbols) and 50 (filled symbols). The stress Péclet number Pe_σ are annotated in on the graph. The dashed lines show the overall average of all 50 independent runs.

with a step size 10^{-3}. Further decreasing the step size to the value used in this work (10^{-4}) does not alter the results. To quantify the initial condition dependence, we randomly partitioned the results to independent groups of $N_{\mathrm{samp}} = 1$, 2, 3, 5, 10, and 29 runs and compute the group average of the volume fraction ϕ and the scaled strain rate $a^2\dot{\gamma}/d_0$ (after the initial transient). Fig. 6.5 presents the results at $\bar{\Pi} = 5$ (open symbols) and 50 (filled symbols), representing the behaviors at low and high imposed pressures, as functions of the group size N_{samp}. The average from the entire 50 runs are shown dashed lines in the corresponding color. For reference, the flow-arrest transition takes place at $\mathrm{Pe}_\sigma \approx 5$ for $\bar{\Pi} = 5$ and $\mathrm{Pe}_\sigma \approx 130$ for $\bar{\Pi} = 50$.

Fig. 6.5 shows the group size N_{samp} does not affect the average ϕ and $\dot{\gamma}$ when Pe_σ is higher than the yield Péclet number. Here, the suspension flows as liquid and the

thermal and mechanical fluctuations erase any influences of the initial conditions. However, close to the flow-arrest transitions, *i.e.*, $(\bar{\Pi}, \mathrm{Pe}_\sigma) = (50, 145)$ and $(5, 5)$, the results are more sensitive to N_{samp}: both ϕ and $\dot{\gamma}$ fluctuates around the mean value without a definite trend. This fluctuation is also reflected in the large error bars in Fig. 6.3. Fig. 6.5 further demonstrates that $N_{\mathrm{samp}} \geq 3$ adequately reflects the system behavior and justifies the computational protocol of this work. It also validates that our results and conclusions are independent of the initial conditions.

References

[1] N. J. Wagner and J. F. Brady, "Shear thickening in colloidal dispersions", Phys. Today **62**, 27 (2009).

[2] J. F. Morris and F. Boulay, "Curvilinear flows of noncolloidal suspensions: the role of normal stresses", J. Rheo. **43**, 1213 (1999).

[3] F. Varnik, L. Bocquet, J.-L. Barrat, and L. Berthier, "Shear localization in a model glass", Phys. Rev. Lett. **90**, 095702 (2003).

[4] A. J. Liu and S. R. Nagel, "Nonlinear dynamics: jamming is not just cool any more", Nature **396**, 21 (1998).

[5] D. Bi, J. Zhang, B. Chakraborty, and R. P. Behringer, "Jamming by shear", Nature **480**, 355 (2011).

[6] T. K. Haxton, M. Schmiedeberg, and A. J. Liu, "Universal jamming phase diagram in the hard-sphere limit", Phys. Rev. E **83**, 031503 (2011).

[7] A. Ikeda, L. Berthier, and P. Sollich, "Unified study of glass and jamming rheology in soft particle systems", Phys. Rev. Lett. **109**, 018301 (2012).

[8] N. Koumakis, M. Laurati, S. U. Egelhaaf, J. F. Brady, and G. Petekidis, "Yielding of hard-sphere glasses during start-up shear", Phys. Rev. Lett. **108**, 098303 (2012).

[9] A. Ikeda, L. Berthier, and P. Sollich, "Disentangling glass and jamming physics in the rheology of soft materials", Soft Matter **9**, 7669 (2013).

[10] P. Olsson and S. Teitel, "Athermal jamming versus thermalized glassiness in sheared frictionless particles", Phys. Rev. E **88**, 010301(R) (2013).

[11] N. Estrada, E. Aźema, F. Radjai, and A. Taboada, "Identification of rolling resistance as a shape parameter in sheared granular media", Phys. Rev. E **84**, 011306 (2011).

[12] R. Seto, R. Mari, J. F. Morris, and M. M. Denn, "Discontinuous shear thickening of frfriction hard-sphere suspensions", Phys. Rev. Lett. **111**, 218301 (2013).

[13] R. Mari, R. Seto, J. F. Morris, and M. M. Denn, "Discontinuous shear thickening in brownian suspensions by dynamic simulation", arXiv: 1508.01243 (2015).

[14] C. Heussinger, "Shear thickening in granular suspensions: interparticle friction and dynamically correlated clusters", Phys. Rev. E **88**, 050201(R) (2013).

[15] W. van Megen, T. C. Mortensen, S. R. Williams, and J. Müller, "Measurement of the self-intermediate scattering function of suspensions of hard spherical particles near the glass transition", Phys. Rev. E **58**, 6073 (1998).

[16] G. Brambilla, D. El Masri, M. Pierno, L. Berthier, L. Cipelletti, G. Petekidis, and A. Schofield, "Probing the equilibrium dynamics of colloidal hard spheres above the mode-coupling glass transition", Phys. Rev. Lett. **102**, 085703 (2009).

[17] J. Reinhardt, F. Weysser, and M. Fuchs, "Comment on "probing the equilibrium dynamics of colloidal hard spheres above the mode-coupling glass transition"", Phys. Rev. Lett. **105**, 199604 (2010).

[18] W. B. Russel, N. J. Wagner, and J. Mewis, "Divergence in the low shear viscosity for brownian hard sphere dispersions: at random close packing or the glass transition?", J. Rheo. **57**, 1555 (2013).

[19] F. Boyer, E. Guazzelli, and O. Pouliquen, "Unifying suspension and granular rheology", Phys. Rev. Lett. **107**, 188301 (2011).

[20] W. C. K. Poon, E. R. Weeks, and C. P. Royall, "On measuring colloidal volume fractions", Soft Matter **8**, 21 (2012).

[21] P. Chaudhuri, L. Berthier, and S. Sastry, "Jamming transitions in amorphous packings of frictionless spheres occur over a continuous range of volume fractions", Phys. Rev. Lett. **104**, 165701 (2010).

[22] D. M. Heyes and J. R. Melrose, "Brownian dynamics simulations of model hard-sphere suspensions", J. Non-Newtonian Fluid Mech. **46**, 1 (1993).

[23] W. Schaertl and H. Sillescu, "Brownian dynamics simulations of colloidal hard spheres. effects of sample dimensionality on self-diffusion", J. Stat. Phys. **74**, 687 (1994).

[24] P. Strating, "Brownian dynamics simulation of a hard-sphere suspension", Phys. Rev. E **59**, 2175 (1999).

[25] D. R. Foss and J. F. Brady, "Brownian dynamics simulation of hard-sphere colloidal dispersions", J. Rheo. **44**, 629 (2000).

[26] J. F. Brady, A. S. Khair, and M. Swaroop, "On the bulk viscosity of suspensions", J. Fluid Mech. **554**, 109 (2006).

[27] D. El Masri, G. Brambilla, M. Pierno, G. Petekidis, A. Schofield, L. Berthier, and L. Cipelletti, "Dynamic light scattering measurements in the activated regime of dense colloidal hard spheres", J. Stat. Mech. Theor. Exp. **2009**, P07015 (2009).

[28] M. Trulsson, B. Andreotti, and P. Claudin, "Transition from the viscous to inertial regime in dense suspensions", Phys. Rev. Lett. **109**, 118305 (2012).

[29] J. F. Brady and M. Vicic, "Normal stresses in colloidal dispersions", J. Rheo. **39**, 545 (1995).

[30] E. Lerner, G. Düring, and M. Wyart, "A unified framework for non-brownian suspension flows and soft amorphous solids", Proc. Natl. Acad. Sci. USA **109**, 4798 (2012).

[31] M. Bouzid, M. Trulsson, P. Claudin, E. Clément, and B. Andreotti, "Nonlocal rheology of granular flows across yield conditions", Phys. Rev. Lett. **111**, 238301 (2013).

[32] B. Andreotti, J.-L. Barrat, and C. Heussinger, "Shear flow of non-brownian suspensions close to jamming", Phys. Rev. Lett. **109**, 105901 (2012).

[33] F. Boyer, "Suspensions concentrées : expériences originales de rhéologie", PhD thesis (Aix-Marseille Université, 2011).

[34] C. Toninelli, M. Wyart, L. Berthier, G. Biroli, and J.-P. Bouchaud, "Dynamical susceptibility of glass formers: contrasting the predictions of theoretical scenarios", Phys. Rev. E **71**, 041505 (2005).

[35] B. D. Lubachevsky and F. H. Stillinger, "Geometric properties of random disk packings", J. Stat. Phys. **60**, 561 (1990).

Chapter 7

CONSTANT STRESS AND PRESSURE RHEOLOGY OF COLLOIDAL SUSPENSIONS: STEADY STATE BEHAVIOR AND DYNAMICS NEAR THE FLOW-ARREST TRANSITIONS

7.1 Introduction

Colloidal suspensions are ubiquitous in nature and have found widespread applications in many industrial and technological processes [1, 2]. However, our understanding in the mechanics and dynamics of *dense* suspensions remains limited. Even the simplest hard-sphere colloidal suspensions, formed by dispersing micron-sized spherical particles in a Newtonian solvent, exhibit surprisingly rich behaviors including a glass transition [3–5], yielding [6, 7], shear thinning [8, 9], and shear thickening [9–11]. These behaviors arise from Brownian motion, hydrodynamic interactions (HIs), and excluded volume effects [12]. Quantitative understanding of suspension behavior is crucial for developing novel materials, for example, "smart" materials that autonomously respond to changes in the external environment.

In this work we focus on the suspension dynamics and rheology near the flow-arrest transition, where the suspension resists continuous deformation like a solid unless the imposed stress exceeds a yield stress. The flow-arrest transition is closely related to the thermal glass transition [5] and the athermal jamming transition [13]. Their relations are succinctly summarized by the "jamming diagram" [14]: when the thermal fluctuations dominate, the suspension behavior is controlled by the glass transition, and when the flow dominates, the dynamics follow the jamming transition. Although investigations in either limit are extensive [13, 15, 16], few works are dedicated to the behavior between these limits. Moreover, considering colloidal suspensions as a model system, the implications of our work are broad, as flow-arrest transitions are also common to granular matter [17], polymer melt [18], and metallic glass [19].

Recently, we [20] discovered a universal perspective that connects the glass and jamming transitions of colloidal suspensions using constant shear stress and pressure rheology. With constant confining pressure, the suspension shear viscosity η_s and the incremental normal viscosity η_n' were found to diverge algebraically with the

volume fraction ϕ as

$$\{\eta_s, \eta_n'\} \approx \{k_s, k_n\} \times (\phi_m - \phi)^{-\alpha}, \tag{7.1}$$

where α, k_s, and k_n are constants, ϕ_m is the arrest volume fraction at the confining pressure Π, and $\alpha = 2$. Here, the incremental normal viscosity $\eta_n' = (\Pi - \Pi^{\text{eq}})/\dot{\gamma}$ with Π^{eq} the equilibrium osmotic pressure at the corresponding ϕ, and $\dot{\gamma}$ the strain rate. For weakly polydisperse suspensions, Eq. (7.1) is valid when $\phi_G \leq \phi_m \leq \phi_{\text{SAP}}$, where $\phi_G \approx 0.60$ is the glass transition volume fraction and $\phi_{\text{SAP}} \approx 0.635$ is the (protocol dependent) Shear Arrest Point (SAP) volume fraction, similar to the jamming density [20]. The only pressure dependent quantity in Eq. (7.1) is $\phi_m(\Pi)$, suggesting that the physics of jamming dominates the behavior of flow-arrest transitions, and that thermal fluctuations only play a secondary role. The key to discovering Eq. (7.1) is to hold the confining pressure constant. Indeed, were the volume, instead of the pressure, held constant, the viscosity divergence $\eta_s \sim (\phi_c - \phi)^{-\delta}$ shows different exponents δ in different limits: near the glass transition ($\phi_c = \phi_G$), the exponent $\delta \approx 2.2$–2.6 [21–24], and near the jamming transition ($\phi_c = \phi_J$), $\delta \approx 2.0$ [25–27].

However, the limitations of Ref. [20] include neglecting Hydrodynamic Interactions (HIs) in the simulations, and only addressing the basic mechanical characterization of the colloidal suspensions. We address the first limitation in the next chapter using hydrodynamic simulations. In this work we focus on the second limitation and present a comprehensive study on the suspension mechanics, structures, and diffusive dynamics that complements and extends the our earlier work [20]. The role of HIs can be revealed by comparing this chapter with the next chapter.

The second goal of this work is to investigate the granular perspective on the rheological, structural, and dynamical features of colloidal suspensions using constant shear stress and pressure rheology. Recent advances in the constitutive modeling of granular rheology highlight the importance of the granular pressure [17, 28]. In the inertial driven granular flows with particle size a and density ρ, the rheology is characterized by the inertial number $I = \dot{\gamma} a \sqrt{\rho/\Pi}$, which is the ratio of an internal time scale $a\sqrt{\rho/\Pi}$ to the flow time scale $\dot{\gamma}^{-1}$. For viscous non-Brownian suspensions, Boyer et al. [26] introduced the viscous number I_v,

$$I_v = \eta_0 \dot{\gamma}/\Pi, \tag{7.2}$$

adapting the internal time scale to η_0/Π, emphasizing the importance of viscosity.

A combination of I and I_v characterizes the flow behaviors of, for example, wet granular materials [29]

Regardless of the origin of particle interactions, the granular rheology characterizes the mechanical response using the *macroscopic* friction coefficient,

$$\mu = \sigma/\Pi, \tag{7.3}$$

i.e., the ratio of the shear stress σ to the pressure Π. This quantity remains finite as the material becomes arrested, where both Π and σ diverge. Experiments and simulations suggest that the limiting friction coefficient at arrest ($\{I, I_v\} \to 0$), μ_c, depends on the interaction details of the materials such as presence of contact friction, etc. For non-Brownian viscous suspensions, the experiments of Boyer et al. [26] show that $(\phi_c, \mu_c) = (0.585, 0.32)$. For colloidal suspensions without HIs, Wang and Brady [20] found from the μ-ϕ flow map that suspensions arrest over a yield surface from the glass transition to the non-Brownian limit at the SAP, where $(\phi_{\text{SAP}}, \mu_{\text{SAP}}) = (0.635, 0.16)$.

Although particle interactions change the arrest location, theories of dense amorphous materials [30, 31] suggest that, for non-Brownian materials, the suspension behavior away from the arrest location is less sensitive to the interactions. The incremental friction coefficient and volume fraction, $\delta\mu = \mu - \mu_c$ and $\delta\phi = \phi_c - \phi$, change as power laws of I or I_v, e.g., for dry granular materials $\delta\mu \sim I^{\alpha_\mu}$ and $\delta\phi \sim I^{\alpha_\phi}$. For example, scaling theories predict that $\alpha_\mu = \alpha_\phi = 0.35$ regardless of the particle interactions and the system dimensions [31]. The theories highlight the importance of pressure and the power of the μ-I or μ-I_v rheology in characterizing the flow behaviors of non-Brownian materials. However, the influence of thermal fluctuations are not well understood.

A key aspect in the μ-I or μ-I_v rheology of non-Brownian systems is that the pressure and the stress, instead of the volume and the strain rate, are held constant. For materials with flow-arrest transitions, specifying a stress allows the material to explore the intrinsic material response (the flowing or the arrested states) without assumptions on the macroscopic flow behaviors, and holding the pressure constant allows the material to explore the corresponding volume without assuming a maximum volume fraction [32]. This approach enabled Boyer et al. [26] to determine a critical arrest point for non-Brownian suspensions, and allowed us to construct a flow map for Brownian suspensions [20].

Another focus of the present work is the diffusive dynamics of flowing colloidal suspensions across various length scales. The most common characterization of the diffusive dynamics is the long-time self-diffusivity, which measures the diffusion on a single particle level and is extracted from the particle mean-square displacements. As ϕ increases, the self-diffusivity decreases as the particle movements are hindered by its neighbors. On the other hand, the suspension also exhibits a *collective* diffusivity, describing the collective diffusion on the length scale of suspensions in response to a weak concentration gradient [33, 34]. For dilute suspensions at equilibrium, the collective diffusivity increases with ϕ, and without HIs, is proportional to the osmotic compressibility of the suspension. Investigations on the collective diffusivity of dense suspensions are not yet available, and existing works focus on dilute systems [35, 36]. Here, we approximate the collective diffusivity by measuring the decay of the temporal correlations of the density fluctuations at vanishing wave lengths. Also, we show that the dynamic susceptibility is crucial for characterizing the collective particle motions near the flow-arrest transition [15, 37].

In constant stress and pressure rheology, when the imposed shear stress is slightly higher than the yield stress, the suspension becomes unstable and switches between flowing and arrested states. This instability provides a unique opportunity to explore the dynamic aspects of the flow-arrest transition. Here, the flow-arrest transitions are spontaneous without changing the external forcing. This is distinct from earlier start-up/cessation investigations where the stress or the flow are suddenly changed [6, 7]. Comparing to the stress fluctuations [38] with a fixed strain rate, the strain rate fluctuations are more convenient for analysis, as large stress fluctuations near the flow-arrest transitions at fixed $\dot{\gamma}$ is equivalent to fluctuations near zero strain rate with a constant σ. Spatially, the flow arrest transition often involves changes in correlation lengths both near the glass [37] and the jamming [39, 40] transitions, suggesting the emergence of cooperative particle motions. In this work, we also study the temporal and the spatial characteristic of the flow-arrest transitions.

The close connections among the suspension rheology, dynamics, and microstructures are also investigated. For example, the Stokes-Einstein-Sutherland (SES) relation states that the self-diffusivity of a single particle, d_0, is proportional to the solvent thermal fluctuations, $k_\mathrm{B}T$, and inversely proportional to the solvent viscosity η_0. The SES relation is a fluctuation-dissipation relation. Although derived from a continuum perspective involving a single particle [41], the SES relation

holds surprisingly well for the diffusion of a tagged solvent particle in equilibrium simple liquids [42], and its breakdown is often considered as a signature of the departure from the equilibrium state [43]. In non-equilibrium systems, an effective temperature is often introduced as a device to use concepts of equilibrium statistical physics [44–46]. In these systems, the choice of the effective temperature is crucial to the physical description of the system. The possibility of using an effective temperature to connect the rheology and diffusion in dense colloidal suspensions is considered in this study.

This chapter is arranged as follows: In Sec. 7.2 we describe our simulation algorithm. The general rheology, structural, and dynamical features of the constant shear stress and pressure rheology are presented in Sec. 7.3. In Sec. 7.4 we focus on both the temporal and the spatial features of suspensions near the flow-arrest transition. In Sec. 7.5, we study the behavior of flowing suspensions using a granular perspective, and model how the suspensions move away from arrested states. Sec. 7.6 connects the diffusion, rheology, and structural features, and presents the universal features using a generalized SES relation. We summarize and conclude this work in Sec. 7.7.

7.2 Simulation Method

We consider N neutrally buoyant hard-sphere particles, with radius a_i for particle i, suspended in a compressible solvent with shear viscosity η_0 and bulk viscosity κ_0, occupying a total volume V. The particle radii follow the log-normal distribution characterized by the volume averaged radius a such that $a^3 = N^{-1}\sum_{i=1}^{N} a_i^3$, and the size polydispersity defined as p.d. $= \sigma_a/\bar{a}$ with $\bar{a} = N^{-1}\sum_{i=1}^{N} a_i$ and $\sigma_a^2 = N^{-1}\sum_{i=1}^{N}(a_i^2 - \bar{a}^2)$. In the thermodynamic limit, both N and V diverge to infinity but the number density $n = N/V$ and the volume fraction $\phi = \frac{4}{3}\pi a^3 n$ remain constant. Note that, particle size polydispersity is necessary to prevent spontaneous crystallization at high density.

Without HIs, particles in the suspension follow the overdamped Langevin equation. For particle i under a linear flow characterized by the velocity gradient tensor $\mathbf{G}$, this is,

$$\zeta_i \left(\frac{\mathrm{d}\boldsymbol{x}_i}{\mathrm{d}t} - \mathbf{G} \cdot \boldsymbol{x}_i \right) = \boldsymbol{f}_i^{\mathrm{B}} + \boldsymbol{f}_i^{\mathrm{P}}, \tag{7.4}$$

where, $\boldsymbol{x}_i$ is the particle position, $\boldsymbol{f}_i^{\mathrm{P}}$ and $\boldsymbol{f}_i^{\mathrm{B}}$ are, respectively, the interparticle and the Brownian forces acting on the particle, and $\zeta_i = 6\pi\eta_0 a_i$ is the Stokes resistance for a single particle from the solvent. The velocity gradient tensor $\mathbf{G}$ is a linear combination of an isotropic extensional flow characterized by the expansion rate $\dot{e}$

and a simple shear flow characterized by the strain rate $\dot{\gamma}$, i.e.,

$$\mathbf{G} = \tfrac{1}{3}\dot{e}\mathbf{I} + \dot{\gamma}\mathbf{e}_1 \otimes \mathbf{e}_2, \tag{7.5}$$

where $\mathbf{I}$ is the idem tensor, $\otimes$ is the open product, and $\mathbf{e}_1$, $\mathbf{e}_2$, and $\mathbf{e}_3$ are respectively the unit vectors in the velocity (1), the velocity gradient (2), and the vorticity (3) directions of the simple shear flow.

The Brownian force $\boldsymbol{f}_i^{\mathrm{B}}$ satisfies the fluctuation-dissipation relation,

$$\overline{\boldsymbol{f}_i^{\mathrm{B}}} = 0 \;\text{ and }\; \overline{\boldsymbol{f}_i^{\mathrm{B}}(t)\boldsymbol{f}_i^{\mathrm{B}}(0)} = 2k_{\mathrm{B}}T\zeta\mathbf{I}\delta(t), \tag{7.6}$$

where $\delta(x)$ is the Dirac delta function, and $k_{\mathrm{B}}T$ is the thermal energy scale. The interparticle force is computed pairwise as

$$\boldsymbol{f}_i^{\mathrm{P}} = \sum_{j=1}^{N} \boldsymbol{f}_{ij}^{\mathrm{P}}, \tag{7.7}$$

where the force from particle j on particle i, $\boldsymbol{f}_{ij}^{\mathrm{P}} = -\partial V_{ij}/\partial \boldsymbol{x}_i$, with the hard-sphere potential $V_{ij} = H(a_i + a_j - r_{ij})$. Here, $r_{ij} = \|\boldsymbol{x}_i - \boldsymbol{x}_j\|$ and $H(x)$ is the Heaviside function. Note that for a hard-sphere potential, $\boldsymbol{f}_i^{\mathrm{P}}$ diverges at particle contact, and is zero everywhere else. Moreover, we impose periodic boundary condition in the 1- and 3-directions and the Lees-Edwards boundary condition in the 2-direction. The simulation box size L is also adjusted isotropically based on $\dot{e}$ as $\mathrm{d}L/\mathrm{d}t = \frac{1}{3}\dot{e}L$.

To impose the constant stress and pressure constraints on the suspension, we consider the macroscopic stress balance on the suspension. Without HIs, the bulk stress of a suspension with compressible solvent is [47],

$$\langle\boldsymbol{\Sigma}\rangle = (\kappa_0 + \tfrac{4}{3}\eta_0\phi)(\mathbf{G} : \mathbf{I})\mathbf{I} + 2\eta_0(1 + \tfrac{5}{2}\phi)\mathbf{E} + \boldsymbol{\sigma}^{\mathrm{P}}, \tag{7.8}$$

where the rate of strain tensor $\mathbf{E} = \frac{1}{2}(\mathbf{G} + \mathbf{G}^{\dagger}) - \frac{1}{3}(\mathbf{G} : \mathbf{I})\mathbf{I}$, where $\dagger$ is the transpose, and the stress due to particle interactions,

$$\boldsymbol{\sigma}^{\mathrm{P}} = -nk_{\mathrm{B}}T\mathbf{I} - n\left\langle \boldsymbol{x}\boldsymbol{f}^{\mathrm{P}} \right\rangle, \tag{7.9}$$

containing contributions from thermal fluctuations and the spacial moment of interparticle forces [48], i.e., $n\left\langle \boldsymbol{x}\boldsymbol{f}^{\mathrm{P}} \right\rangle = V^{-1}\sum_{i=1}^{N} \boldsymbol{x}_i\boldsymbol{f}_i^{\mathrm{P}}$. Note that $\boldsymbol{\sigma}^{\mathrm{P}}$ depends only on the instantaneous particle configuration due to the overdamped suspension dynamics. Therefore, one can specify the imposed shear stress $\sigma = \langle\boldsymbol{\Sigma}\rangle : (\mathbf{e}_1 \otimes \mathbf{e}_2)$ and the imposed pressure $\Pi = -\frac{1}{3}\langle\boldsymbol{\Sigma}\rangle : \mathbf{I}$ and solve for $\dot{\gamma}$ and $\dot{e}$ according to Eq. (7.8):

$$\sigma = (1 + \tfrac{5}{2}\phi)\eta_0\dot{\gamma} + \boldsymbol{\sigma}^{\mathrm{P}} : (\mathbf{e}_1 \otimes \mathbf{e}_2), \tag{7.10}$$

$$\Pi = -(\kappa_0 + \tfrac{4}{3}\phi\eta_0)\dot{e} - \tfrac{1}{3}\boldsymbol{\sigma}^{\mathrm{P}} : \mathbf{I}, \tag{7.11}$$

assuming that the imposed linear flow can be described by $\mathbf{G}$ in Eq. (7.5). In addition, Eq. (7.11) shows that a compressible solvent with bulk viscosity κ_0 allows isotropic compression to be imposed without violating the physics of Brownian particles in Stokes flow, and avoids using physical permeable boundaries which may cause complications such as local ordering. This is indeed the novelty of our method: through a compressible solvent, the constant pressure constraint is satisfied without introducing boundaries.

In Brownian dynamics (BD) simulations, Eq. (7.4) is integrated with respect to time. To resolve the singular hard-sphere potential, we adopt the "potential-free" algorithm [49–52]. In this method, the interparticle force and the non-overlapping conditions are maintained in a predictor-corrector fashion: at time t, the particle configuration is first progressed according to Eq. (7.4) without considering $\boldsymbol{f}_i^{\mathrm{P}}$ to $t + \Delta t$. In the corrector step, the algorithm checks particle overlap and moves the overlapping particles back to contact pairwise along the line that connects the particle centers until the suspension is overlap-free. Specifically, if $r_{ij} < (a_i + a_j)$ for particles i at j, the particles are moved along $(\boldsymbol{x}_i - \boldsymbol{x}_j)$ according to

$$\Delta\boldsymbol{x}_i = a_j\boldsymbol{\Delta}_{ij} \text{ and } \Delta\boldsymbol{x}_j = -a_i\boldsymbol{\Delta}_{ij}, \tag{7.12}$$

where $\boldsymbol{\Delta}_{ij} = (\boldsymbol{x}_i - \boldsymbol{x}_j)[r_{ij}^{-1} - (a_i + a_j)^{-1}]$. The interparticle force for the pair is calculated based on the Stokes relation,

$$\boldsymbol{f}_{ij}^{\mathrm{P}} = \zeta_i\Delta\boldsymbol{x}_i/\Delta t. \tag{7.13}$$

Here, the Newton's third law, $\boldsymbol{f}_{ij}^{\mathrm{P}} + \boldsymbol{f}_{ji}^{\mathrm{P}} = 0$, is satisfied. Despite its simplicity, the potential-free algorithm has been extensively used to investigate systems with hard-sphere interactions such as start-up [6, 53] and oscillatory [54] bulk rheology, steady and transient microrheology [55, 56], osmotic propulsion [57], and active materials [58]. It has also been used to validate studies in dilute [59] and dense [60] suspensions, and compares favorably with molecular dynamics simulations [61].

Using the above algorithm, we perform constant shear stress and pressure rheology simulations with imposed shear stress σ and imposed pressure Π. Scaling σ and Π with the thermal energy $k_{\mathrm{B}}T$ leads to two key simulation parameters, the stress Péclet number Pe_σ and the scaled pressure $\bar{\Pi}$, defined as

$$\mathrm{Pe}_\sigma = \frac{6\pi a^3\sigma}{k_{\mathrm{B}}T} \text{ and } \bar{\Pi} = \frac{a^3\Pi}{k_{\mathrm{B}}T}. \tag{7.14}$$

As pointed out by Swan and Brady [62], Pe_σ is trivially connected to the strain rate Péclet number $\mathrm{Pe}_{\dot\gamma} = 6\pi a^3\eta_0\dot\gamma/(k_\mathrm{B}T)$ through

$$\mathrm{Pe}_{\dot\gamma} = (\eta_0/\eta_s)\mathrm{Pe}_\sigma, \tag{7.15}$$

where $\eta_s = \sigma/\dot\gamma$ is the suspension shear viscosity. The simulation time is scaled with a^2/d_0, with the Stokes-Einstein-Sutherland diffusivity $d_0 = k_\mathrm{B}T/(6\pi\eta_0 a)$, when $\mathrm{Pe}_\sigma \le 1$, and with η_0/σ when $\mathrm{Pe}_\sigma > 1$. The stress-scaled time automatically adjusts the resolution of configuration evolution with respect to the strain rate $\dot\gamma$. That is, because the dimensionless time step $\Delta\tau = \sigma\Delta t/\eta_0 = \dot\gamma\Delta t(\eta_s/\eta_0)$, for a fixed $\Delta\tau$, the higher the suspension shear viscosity, the smaller the dimensionless time step with respect to strain rate, $\dot\gamma\Delta t$. Therefore, with a fixed $\Delta\tau$, the constant stress and pressure rheology improves the temporal resolution of the configuration evolution for suspensions with large η_s.

We explore a wide range of Π and σ combinations to map out the flow behaviors using dynamic simulations. Each simulation contains $N = 200$ particles with a particle size polydispersity p.d. $= 0.1$. For convenience, the number of particle species with different radii is limited to 20. Increasing N does not qualitatively alter the results. A simulation begins with an random, non-overlapping polydisperse hard-sphere configuration generated by a modified Lubachesvky-Stillinger algorithm [63, 64] at an estimated starting volume fraction ϕ_0, and lasts for 5000 dimensionless time with a step size 10^{-3}. When computing the results, the first 1000 time units are discarded. In this work, the suspension is considered flowing when the shear viscosity $\eta_s < 2000$, and such that the suspensions have flown at least 2 strains. Moreover, the solvent bulk viscosity κ_0 affects how the suspension respond to the imposed pressure by controlling the rate at which the simulation cell changes its volume. If κ_0 is too large, the suspension cannot reach the steady state volume fraction by the end of the simulation, and if κ_0 is too small, the suspension may experience large density fluctuations. Once reaching the steady state, the suspension rheology becomes independent of κ_0. We found that with $\kappa_0/\eta_0 = 2000$, the suspensions can reach the steady state sufficiently fast for low $\bar\Pi$ without becoming unstable at high $\bar\Pi$. The volume control mechanism is slightly different from Ref. [20], where the bulk viscosity that controls the cell volume changes depends on the instantaneous volume fraction ϕ. Furthermore, for each (Π, σ) pair, we perform at least three independent runs to eliminate the dependence on initial configurations.

To validate the simulation method, Fig. 7.1 presents the osmotic pressure Π for polydisperse suspensions with p.d. $= 0.1$ as a function of ϕ using constant pressure

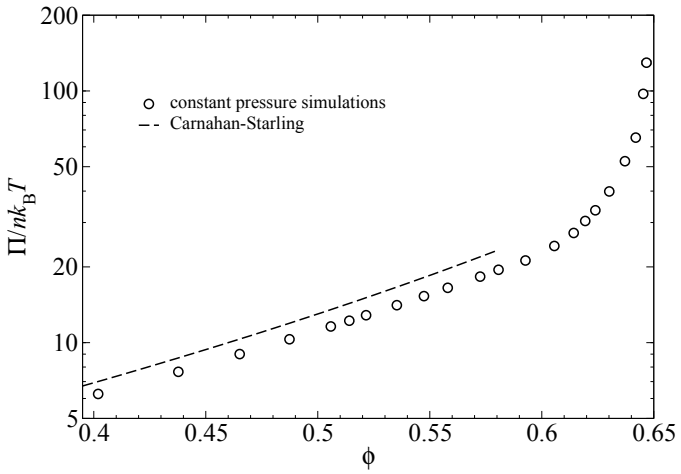

Figure 7.1: The suspension equilibrium osmotic pressure $\Pi/(nk_BT)$ as a function of the volume fraction ϕ, computed using constant pressure Brownian Dynamics simulations. The suspension size polydispersity p.d. = 0.1. The dashed line is the osmotic pressure from Carnahan-Starling equation of state for monodisperse suspensions. The error in ϕ is smaller than the symbol size.

simulations with $\dot{\gamma} = 0$. The error in ϕ is smaller than the symbol size even at the highest imposed pressure. Fig. 7.1 also shows, in dashed line, the Carnahan-Starling (CS) equation of state for monodisperse suspensions,

$$\frac{\Pi}{nk_BT} = \frac{1 + \phi + \phi^2 - \phi^3}{(1-\phi)^3}, \tag{7.16}$$

valid up to $\phi \approx 0.49$. The osmotic pressure diverges near $\phi \approx 0.65$. The particle size polydispersity effectively disrupts the spontaneous crystallization, evidenced by the continuous pressure increase with respect to ϕ and by the suspension microstructures. The size polydispersity also reduces the osmotic pressure comparing to the monodisperse systems, and increases the jamming volume fraction where the pressure diverges.

7.3 General features of flowing suspensions

Shear viscosity and volume fraction

The principle outputs of the constant stress and pressure simulations are the suspension strain rate $\dot{\gamma}$ and the volume fraction ϕ. At each time step, the instantaneous strain rate $\dot{\gamma}$ is from solving Eq. (7.10), and the instantaneous volume fraction ϕ is from monitoring the size of the simulation cell L. Fig. 7.2a presents the Pe_σ dependence of the steady state shear viscosity η_s and normal viscosity η_n for flowing

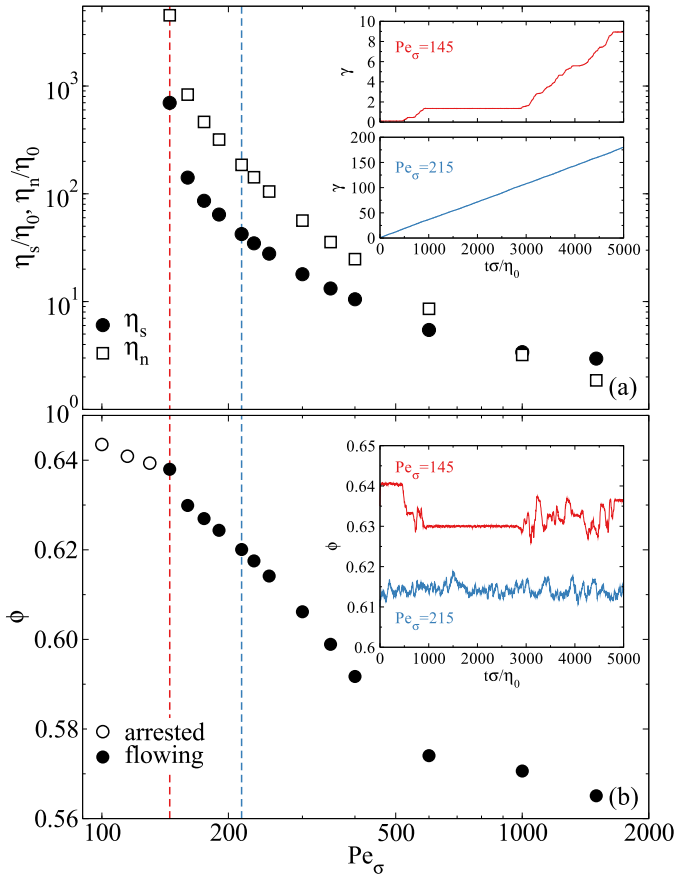

Figure 7.2: (Color online) Simulation results as functions of the stress Péclet number $\mathrm{Pe}_\sigma = 6\pi\sigma a^3/k_\mathrm{B}T$ at an imposed pressure $\bar{\Pi} = \Pi a^3/k_\mathrm{B}T = 50$. (a): the shear and the normal viscosities, η_s and η_n, respectively, and (b): the volume fraction ϕ. In (b), the arrested results are shown as open symbol. The insets of (a) show the time evolution of the accumulated strain γ at $\mathrm{Pe}_\sigma = 145$ and 215. The inset of (b) presents the corresponding time evolution of ϕ at the same Péclet numbers.

suspensions at an imposed pressure $\bar{\Pi} = 50$. Here, the normal viscosity,

$$\eta_n = \Pi/\dot{\gamma}, \tag{7.17}$$

accounts for the effect of the flow on the suspension pressure. At this imposed pressure, the suspension exhibits a yield stress, and is only able to flow when the stress Péclet number $\mathrm{Pe}_\sigma \geq 145$. For flowing suspensions, both η_s and η_n reduce several orders of magnitude with increasing Pe_σ from 145 to 10^3. The normal viscosity η_n is higher than the shear viscosity η_s when $\mathrm{Pe}_\sigma < 10^3$, and becomes lower afterwards as η_s approaches the solvent viscosity η_0 as $\mathrm{Pe}_\sigma \to \infty$, but η_n does not have a limiting value at high Pe_σ. Clearly, with a finite $\bar{\Pi}$, in the high

Pe_σ limit the particle interaction contributes negligibly to η_s due to dilation. If the volume fraction ϕ were fixed, the pressure $\Pi \sim \eta_0\dot{\gamma}$ as $\mathrm{Pe}_\sigma \to \infty$, and with fixed $\bar{\Pi} = \Pi a^3/k_\mathrm{B}T$, $\Pi \sim k_\mathrm{B}T$. Therefore, to keep $\bar{\Pi}$ constant with increasing Pe_σ, suspension dilation, i.e., a decrease in ϕ, is necessary, leading to vanishing particle viscosity contribution. Therefore, in the $\mathrm{Pe}_\sigma \to \infty$ limit, the confining pressure is too weak to "confine" the suspension. This is different from the constant volume hard-sphere suspension rheology [51], where the particle interactions' contribution to η_s is finite as $\mathrm{Pe}_\sigma \to \infty$, due to the formation of a particle accumulation boundary layer near contact [65].

The insets of Fig. 7.2a show the time evolution of the accumulated strain $\gamma(t) = \int_0^t \dot{\gamma}(\tau)\mathrm{d}\tau$ at $\mathrm{Pe}_\sigma = 145$ and 215. At $\mathrm{Pe}_\sigma = 215$, the suspension flows, and γ grows linearly with $t\sigma/\eta_0$, suggesting that the suspension flows continuously. The slope of the γ-t curve is inversely proportional to η_s. Close to the flow-arrest transition at $\mathrm{Pe}_\sigma = 145$, however, the accumulated strain does not grow linearly with time and is unstable: the suspension can become arrested before flowing again. These insets illustrates how the flow-arrest transitions can profoundly affect the suspension dynamics. In Sec. 7.4, we further study the suspension dynamics near the flow-arrest transitions.

Fig. 7.2b shows the average suspension volume fraction ϕ as a function of Pe_σ. Here, the arrested states are shown in open circles and the flowing states in filled circles. The suspension dilates (decreasing ϕ) with increasing Pe_σ both in the flowing and the arrested states. Not shown in this figure is that at even lower Pe_σ, ϕ approaches a constant zero-flow value. That ϕ decreases with increasing Pe_σ in both the arrested and the flowing states suggests that dilation precedes flowing in constant stress and pressure rheology, as the onset of flow requires more space among neighboring particles. For flowing suspensions, the strong shear thinning in η_s and η_n is consistent with the reduction in ϕ. Furthermore, when $\mathrm{Pe}_\sigma \gtrsim 500$, ϕ decreases much slower with growing Pe_σ compared to the case at lower Pe_σ, suggesting that the suspension undergoes qualitative changes, which are revealed in Fig. 7.3 as the formation of string-phase structures. However, such changes are not visible in the viscosity results of Fig. 7.2a.

The inset of Fig. 7.2b shows the time evolution of ϕ, also at $\mathrm{Pe}_\sigma = 145$ and 215. For flowing suspensions at $\mathrm{Pe}_\sigma = 215$, the volume fraction fluctuates with time about its mean value. Near the flow arrest transition ($\mathrm{Pe}_\sigma = 145$), similarly to γ in Fig. 7.2a, ϕ is also unstable. In this case, when the suspension is flowing (γ

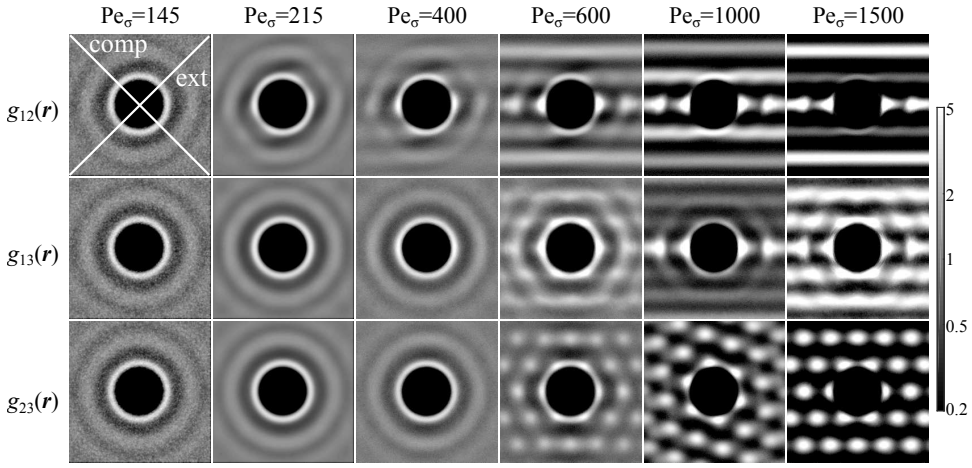

Figure 7.3: Equatorial slices of pair distribution function in the velocity-velocity gradient $g_{12}(\boldsymbol{r})$, velocity-vorticity $g_{13}(\boldsymbol{r})$, and velocity gradient-vorticity $g_{23}(\boldsymbol{r})$ planes at various Pe_σ with an imposed pressure $\bar{\Pi} = 50$. The slice width is $0.7a$. On the panel for $g_{12}(\boldsymbol{r})$ at $\mathrm{Pe}_\sigma = 145$ the compressional and the extensional axis are also highlighted.

increases with time), the corresponding ϕ exhibits more fluctuations compared to arrested suspensions. The volume fractions corresponding to the arrested states are not necessarily higher than the flowing states. This suggests that the suspension structure, not the volume fraction, is the deciding factor in the flow behaviors.

Real- and wave-space structural features

Next we examine the suspension microstructures. A common real-space structural characterization is the pair distribution function

$$g(\boldsymbol{r}) = \frac{V}{N^2}\left\langle \sum_{i,j}{}' \delta(\boldsymbol{r} - \boldsymbol{x}_i + \boldsymbol{x}_j)\right\rangle, \tag{7.18}$$

where the prime on the summation excludes the case of $i = j$. Fig. 7.3 presents the equatorial slices of $g(\boldsymbol{r})$ in the velocity-velocity gradient (12-), velocity-vorticity (13-), and velocity gradient-vorticity (23-) planes with a width of $0.7a$ at various Pe_σ and $\bar{\Pi} = 50$. Also shown in Fig. 7.3 are the compressional and the extensional axis in the shear plane.

The most striking feature of Fig. 7.3 is the formation of a "string phase" in suspensions when $\mathrm{Pe}_\sigma \geq 600$. This is evidenced by the lines in the velocity direction in $g_{12}(\boldsymbol{r})$ and $g_{13}(\boldsymbol{r})$, and nearly hexagonal crystalline structures in $g_{23}(\boldsymbol{r})$. The orientation of the hexagonal structures in $g_{23}(\boldsymbol{r})$ can shift with different simulations. Although the particle size polydispersity effectively disrupts the suspension crystal-

lization at low Pe_σ, it does not prevent the string phase formation at higher Pe_σ. The string phase also persists with increasing Pe_σ because HIs are absent. As is shown in the next chapter, HIs lead to a reentrant of amorphous structures at higher Pe_σ.

The suspension structure remains homogeneous when $\mathrm{Pe}_\sigma < 600$. In the shear plane, $g_{12}(\boldsymbol{r})$ exhibits increasing distortion towards the extensional axis with increasing Pe_σ. At $\mathrm{Pe}_\sigma = 400$, the homogeneous structural distortion is the most pronounced in Fig. 7.3. For two nearby particles in the shear flow, they are most likely to form a pair of close contact in the velocity direction, shown by the high probability of $g_{12}(\boldsymbol{r})$. The pair rotates from the compressional quadrant towards the extensional quadrant, and then disengages near the extensional axis. Meanwhile, at this Pe_σ, the structures of $g_{13}(\boldsymbol{r})$ and $g_{23}(\boldsymbol{r})$ remain isotropic. Note that the structural distortion in $g_{12}(\boldsymbol{r})$ is not apparent until $\mathrm{Pe}_\sigma = 215$, where the suspension flows appreciably.

The structural distortion shown in Fig. 7.3 is intimately related to the suspension rheology. For monodisperse systems without HIs, the structural distortion contributes to the suspension stress as [51, 66]:

$$n\left\langle \boldsymbol{x}\boldsymbol{f}^{\mathrm{P}}\right\rangle + \Pi^{\mathrm{eq}}\mathbf{I} = \frac{27}{2\pi}\eta_0\dot{\gamma}\phi^2\frac{g^{\mathrm{eq}}(2)}{\hat{d}}\int \hat{\boldsymbol{r}}\hat{\boldsymbol{r}}\hat{f}(2;\Omega)\mathrm{d}\Omega, \tag{7.19}$$

where Ω is the solid angle, and the suspension structure is decomposed to an equilibrium contribution $g^{\mathrm{eq}}(\boldsymbol{r})$ and a flow contribution $\hat{f}(\boldsymbol{r})$ as $g(\boldsymbol{r}) = g^{\mathrm{eq}}(\boldsymbol{r})[1 + (\mathrm{Pe}_{\dot{\gamma}}/\hat{d})\hat{f}(\boldsymbol{r})]$, where $\hat{d}$ is a characteristic diffusion scale describing the suspension relaxation process. With an appropriate choice of $\hat{d}$, the suspension rheology entirely depends on the structural distortion $\hat{f}$. In the constant ϕ study of Foss and Brady [51], the structural distortion $\hat{f}$ contribute positively to the shear viscosity, leading to a viscosity decrease slower than a $\mathrm{Pe}_{\dot{\gamma}}^{-1}$ decay.

From Eq. (7.19), the structural distortion in the compressional and the extensional axis contributes most significantly to the shear viscosity. Fig. 7.4 presents the peak values of $g(\boldsymbol{r})$ in these two axis, $\max(g_{\mathrm{comp}})$ and $\max(g_{\mathrm{ext}})$, as functions of Pe_σ at the same imposed pressure of $\bar{\Pi} = 50$. Note that, due to symmetry, both the accumulation in the compressional axis and the depletion in the extensional axis contribute positively to Eq. (7.19) [6], and therefore, the difference $\max(g_{\mathrm{comp}}) - \max(g_{\mathrm{ext}})$ qualitatively captures the structural contributions to the suspension viscosity.

Comparing to Fig. 7.3, the most distinguishing feature in Fig. 7.4 is that the behaviors in $\max(g_{\mathrm{comp}})$ and $\max(g_{\mathrm{ext}})$ are qualitatively different between the homogeneous and the string phase suspensions, which occurs around $\mathrm{Pe}_\sigma = 500$. With $\mathrm{Pe}_\sigma < 500$,

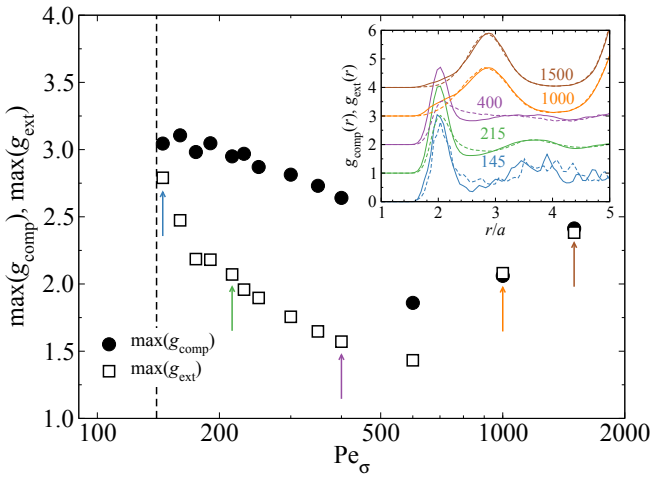

Figure 7.4: (Color online) The peak values of the pair distribution function in the compressional and the extensional axes, $\max(g_{\text{comp}})$ and $\max(g_{\text{ext}})$ as functions of Pe_σ at the imposed pressure $\bar{\Pi} = 50$. The vertical dashed line represents the estimated yield Pe_σ beyond which the suspension begins to flow. The inset presents the radial variation of $g_{\text{comp}}(r)$ (solid line) and $g_{\text{ext}}(r)$ (dashed line) at various Pe_σ, which are also pointed out by arrows in the main figure with their corresponding color. The curves are shifted for clarity when $\text{Pe}_\sigma \geq 215$.

both $\max(g_{\text{comp}})$ and $\max(g_{\text{ext}})$ decrease with increasing Pe_σ due to suspension dilation. With fixed volume, $\max(g_{\text{comp}})$ is expected to increase with increasing Péclet number [6]. The difference, $\max(g_{\text{comp}}) - \max(g_{\text{ext}})$, increases with Pe_σ, suggesting that the suspension structure becomes increasingly distorted. On the other hand, for $\text{Pe}_\sigma > 500$, both $\max(g_{\text{comp}})$ and $\max(g_{\text{ext}})$ grow with Pe_σ, and their difference disappears when $\text{Pe}_\sigma \geq 1000$ due to the formation of aligned string structures in the suspension.

The inset of Fig. 7.4 shows the $g_{\text{comp}}(r)$ in solid lines and $g_{\text{ext}}(r)$ in dashed lines at different Pe_σ; the results for $\text{Pe}_\sigma \geq 215$ are shifted for clarity. For $\text{Pe}_\sigma = 1000$ and 1500, the difference between $g_{\text{comp}}(r)$ and $g_{\text{ext}}(r)$ is almost indistinguishable due to the formation of the string phase. On the other hand, for homogeneous suspensions, the difference between $g_{\text{comp}}(r)$ and $g_{\text{ext}}(r)$ grows with increasing Pe_σ. With increasing Pe_σ, the first peaks in $g_{\text{comp}}(r)$ and $g_{\text{ext}}(r)$ become narrower, and the features beyond the first peak vanish, i.e., the distribution functions at $\text{Pe}_\sigma = 145$ show more pronounced undulations beyond the first peaks compared to those at $\text{Pe}_\sigma = 400$. Evidently, the microstructures of the homogeneous suspension are distinctly different from those of the string phase.

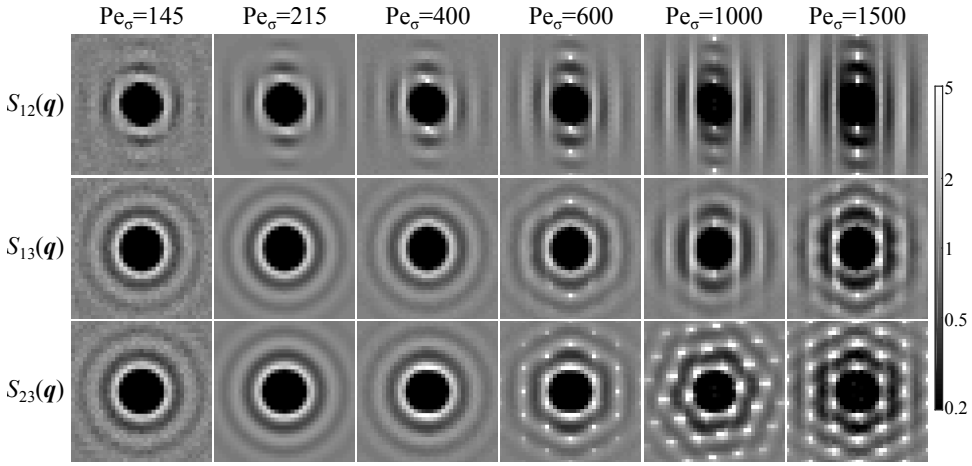

Figure 7.5: The static structure factors $S_{12}(\boldsymbol{q})$, $S_{13}(\boldsymbol{q})$, and $S_{23}(\boldsymbol{q})$ at various Pe_σ with an imposed pressure $\bar{\Pi} = 50$. Each panel depicts the structure factor $S(\boldsymbol{q})$ in the wave space from $-10qa$ to $10qa$ in both directions.

Complementary to real-space characterizations such as the pair-distribution function $g(\boldsymbol{r})$, the suspension structures are also frequently assessed via wave-space characterizations such as the static structure factor $S(\boldsymbol{q})$ [67, 68]. Defining the instantaneous wave-space density fluctuations [69],

$$n_{\boldsymbol{q}}(t) = \frac{1}{\sqrt{N}} \sum_{i=1}^{N} \exp[i\boldsymbol{q} \cdot \boldsymbol{x}_i(t)], \tag{7.20}$$

where $\boldsymbol{q}$ is the wave vector, the static structure factor is the instantaneous correlation, defined as

$$S(\boldsymbol{q}) = \left\langle n_{\boldsymbol{q}}(0) n_{-\boldsymbol{q}}(0) \right\rangle. \tag{7.21}$$

Fig. 7.5 presents the 2D static structure factors $S(\boldsymbol{q})$ in different wave-space planes. Here, the fundamental lattice vectors for the periodic simulation box corresponding to the 1-, 2-, and 3-directions are respectively $\mathbf{b}_1$, $\mathbf{b}_2$, and $\mathbf{b}_3$, and the wave vectors in, for example, $S_{12}(\boldsymbol{q})$, are $\boldsymbol{q} = i\mathbf{b}_1 + j\mathbf{b}_2$ with integers i and j. The wave-number in each direction in Fig. 7.5 is limited from $-10qa$ to $10qa$. In simulations with periodic boundary conditions, the maximum wave-space resolution is $2\pi/L$, strongly affected by the system size.

The structural information from $S(\boldsymbol{q})$ in Fig. 7.5 is consistent with the $g(\boldsymbol{r})$ characterizations in Fig. 7.3. In fact, $S(\boldsymbol{q})$ strongly resembles the $g(\boldsymbol{r})$ slices rotated counterclockwise by 90°. The wave-space characterization confirms the string phase formation with $\mathrm{Pe}_\sigma \geq 600$, which is especially evident with the regular hexagonal patterns in $S_{23}(\boldsymbol{q})$, and otherwise homogeneous suspension structures at lower Pe_σ.

In addition, the wave-space characterization is more sensitive to structural distortions, i.e., at $\mathrm{Pe}_\sigma = 145$, the structural distortion is already evident in $S_{12}(\boldsymbol{q})$, but appears isotropic in $g_{12}(\boldsymbol{r})$. Moreover, at $\mathrm{Pe}_\sigma = 400$, $S_{23}(\boldsymbol{q})$ distorts towards the velocity gradient direction, suggesting stronger structural correlations, which is not captured in $g_{23}(\boldsymbol{r})$. Otherwise, $S_{23}(\boldsymbol{q})$ and $S_{13}(\boldsymbol{q})$ are isotropic for homogeneous suspensions.

Suspension diffusion

Fig. 7.6 presents various dynamic characterization of suspensions as functions of Pe_σ at $\bar{\Pi} = 50$. The estimated flow-arrest boundary is shown as dash-dotted line. Fig. 7.6a shows the long-time self-diffusivity in the velocity gradient direction, $d^s_{\infty,22}$ (open symbols), and the vorticity direction, $d^s_{\infty,33}$ (filled symbols). In the k-direction, the long-time self-diffusivity is defined as

$$d^s_{\infty,kk} = \frac{1}{2}\lim_{t\to\infty}\frac{\mathrm{d}}{\mathrm{d}t}\left\langle \Delta x_k^2 \right\rangle, \tag{7.22}$$

where $\left\langle \Delta x_k^2 \right\rangle$ is the k-direction mean-square displacement averaged over all available times of particle trajectories. The mean-square displacements $\left\langle \Delta x_2^2 \right\rangle$ (dashed line) and $\left\langle \Delta x_3^2 \right\rangle$ (solid line) at selected Pe_σ are shown in the inset of Fig. 7.6a. The corresponding Pe_σ for flowing suspensions are are pointed out by arrows in the main figure, and a dash-dotted line is present at $\mathrm{Pe}_\sigma = 115$ for the arrested suspension.

In Fig. 7.6a, the scaled diffusivity $d^s_{\infty,33}/d_0$ emerges from a infinitesimal value as the imposed stress exceeds the yield stress to cause the suspension to flow, suggesting that the particle inherent thermal fluctuations contribute little to the dynamics. After the suspension begins to flow, further increasing Pe_σ also increases $d^s_{\infty,33}/d_0$ as the flow drives the particle diffusion. The increase in the diffusivity is significant, partly due to the suspension dilation. When the suspension forms a string phase at $\mathrm{Pe}_\sigma > 500$, the diffusivity stops to grow and decreases with increasing Pe_σ, as the string structure limits the diffusive movements. The diffusivity in the velocity gradient direction $d^s_{\infty,22}/d_0$ is consistent with its vorticity direction counterpart except for small quantitative differences. When the suspension is amorphous $\mathrm{Pe}_\sigma < 500$, $d^s_{\infty,22} > d^s_{\infty,33}$ due to the linear shear flow, and in the string phase, $d^s_{\infty,33} > d^s_{\infty,22}$.

The inset of Fig. 7.6a shows the time evolution of the mean-square displacement up to a diffusive time of $2a^2/d_0$. Within this time frame, at $\mathrm{Pe}_\sigma = 115$, the suspension is arrested, and the particles are confined to the cage formed by their neighbors. However, at $\mathrm{Pe}_\sigma = 145$, the suspension becomes flowing and the

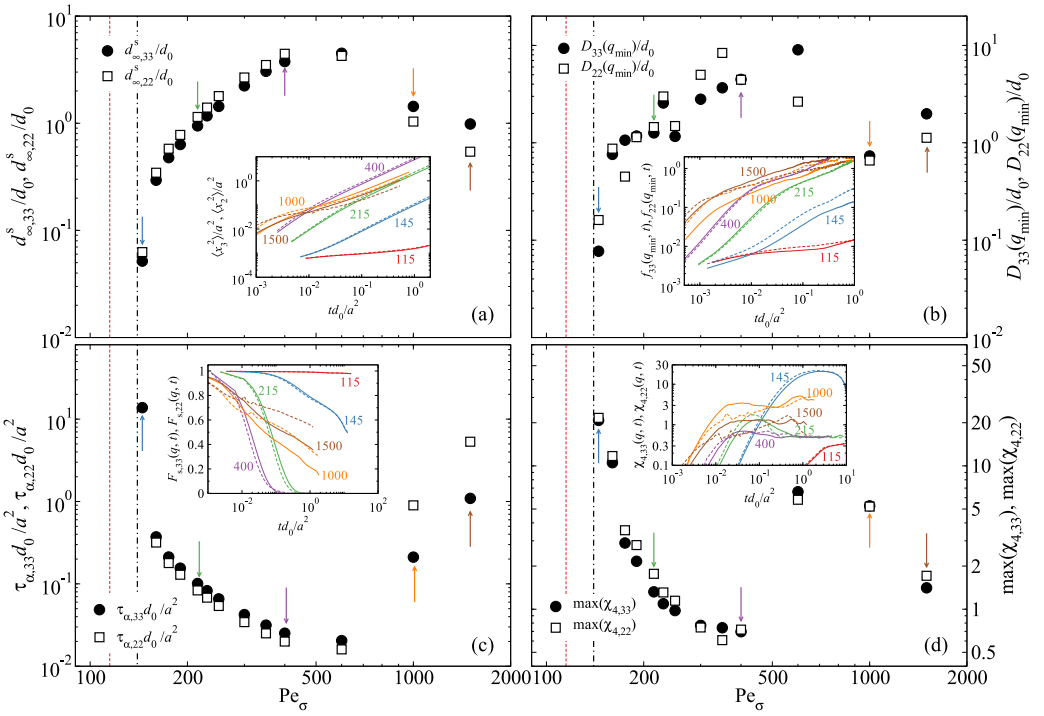

Figure 7.6: (Color online) Diffusive dynamics of suspensions as functions of Pe_σ at $\bar{\Pi} = 50$. The dash-dotted vertical lines represent the estimated arrest Pe_σ. The measurements in the vorticity direction, denoted by subscript 33, are shown as filled symbols in the main figures and solid lines in the insets. In the velocity gradient direction, denoted by subscript 22, the results are shown as open symbols and dashed lines. (a): The scaled long-time self-diffusivities, $d^s_{\infty,33}/d_0$ and $d^s_{\infty,22}/d_0$. The inset shows the time evolution of the mean-square displacement in the 3- and 2-directions, $\langle x_3^2 \rangle$ and $\langle x_2^2 \rangle$, at various Pe_σ, which are highlighted by arrows for flowing suspensions, and by vertical dashed lines for arrested suspensions in corresponding colors. (b): The scaled wave-number dependent diffusivities, $D_{33}(q_{\min})/d_0$ and $D_{22}(q_{\min})/d_0$, where $q_{\min}$ is the smallest measurable wave number in the unit cell. The inset shows the time evolution of the functions $f_{33}(q,t)$ and $f_{22}(q,t)$ defined in Eq. (7.25) at various Pe_σ. (c): The scaled α-relaxation times, $\tau_{\alpha,33}d_0/a^2$ and $\tau_{\alpha,22}d_0/a^2$, measured from the decay of the self-intermediate scattering function $F_s(q,t)$ at $qa = 3.5$. The inset shows the time evolution of the corresponding $F_s(q,t)$ in different directions at various Pe_σ. (d): The maximum of the dynamic susceptibilities, max($\chi_{4,33}$) and max($\chi_{4,22}$), measured at wave number $qa = 3.5$ in different directions. The inset shows the time evolution of the corresponding dynamic susceptibilities $\chi_{4,\alpha\alpha}(q,t)$ in different directions at various Pe_σ.

particle movement becomes diffusive, characterized by the linear growth of the mean-square displacement at large times. Increasing Pe_σ also changes the transition to the long-time diffusive behavior. At $\mathrm{Pe}_\sigma = 145$, the particle becomes diffusive

from a subdiffusive regime, consistent with the cage-breaking process in sheared suspensions. On the other hand, at $\mathrm{Pe}_\sigma = 215$ and 400, before entering long-time diffusive regime, the suspension is superdiffusive, i.e., $\left\langle \Delta x^2 \right\rangle \propto t^2$, suggesting that diffusion arises from strong particle interactions. Finally, in the string phase ($\mathrm{Pe}_\sigma =$ 1000 and 1500), the particles enter a sub-diffusive regime from the superdiffusive behavior before becoming diffusive. This is because the structural formation hinders the diffusion process, leading to much lower diffusivities in Fig. 7.6a. For amorphous suspensions, the difference between the 2- and 3- directions is small, but with string formation, the difference becomes more significant.

Another characterization of the suspension diffusive behavior is the wave-number dependent diffusivity $\boldsymbol{D}(\boldsymbol{q})$ which characterize the suspension diffusion over different length scales. From a small-wave length expansion of the Smoluchowski equation which describes the suspension dynamics [35, 36], it can be shown that in directions perpendicular to the 1-direction, the time-dependent structure factor,

$$S(\boldsymbol{q}, t) = \left\langle n_{\boldsymbol{q}}(t) n_{-\boldsymbol{q}}(0) \right\rangle, \tag{7.23}$$

decays as

$$S(\boldsymbol{q}, t) = S(\boldsymbol{q}) \exp[-\boldsymbol{q} \cdot \boldsymbol{D}(\boldsymbol{q}) \cdot \boldsymbol{q} t], \tag{7.24}$$

where, recall, $S(\boldsymbol{q})$ is the static structure factor. Eq. (7.24) shows that the temporal decay of $S(\boldsymbol{q}, t)$ from $S(\boldsymbol{q})$ is exponential and is characterized by $\boldsymbol{D}(\boldsymbol{q})$. Eq. (7.24) is identical for equilibrium suspensions [33, 70, 71]. Note that the zero wave-number limit of $\boldsymbol{D}(\boldsymbol{q})$ is the suspension collective diffusivity, describing how particles migrate in a weak concentration gradient, i.e., $\boldsymbol{d}_c = \lim_{|\boldsymbol{q}| \to 0} \boldsymbol{D}(\boldsymbol{q})$. At the wave number q_m corresponding to the peak of the static structure factor $S(\boldsymbol{q})$, the wave number dependent diffusivity is believed to describe the cage dynamics in the suspension [34, 72]. At length scale smaller than a single particle, i.e., $|q| \to \infty$, $\boldsymbol{D}$ approaches the long-time self-diffusivity.

In this work, we are interested in the collective diffusion behaviors. However, reaching the limit of $|\boldsymbol{q}| \to 0$ is challenging as the accessible wave numbers are integer multiples of $q_{\min} = 2\pi/L$. Alternatively, we focus on the diffusivities along the 2- and 3-direction with the minimum accessible wave number, $D_{kk}(q_{\min})$ with $k = 2, 3$. We define

$$f_{kk}(q, t) = -q^{-2} \ln[S_{kk}(q, t)/S_{kk}(q)], \tag{7.25}$$

and

$$D_{kk}(q) = \lim_{t \to \infty} \frac{\mathrm{d}}{\mathrm{d}t} f_{kk}(q, t). \tag{7.26}$$

The diffusivities $D_{kk}(q_{\min})$ approximate the suspension collective behavior on the scale of the simulation box.

Fig. 7.6b shows $D_{22}(q_{\min})/d_0$ (open symbols) and $D_{33}(q_{\min})/d_0$ (filled symbols) as functions of Pe_σ at $\bar{\Pi} = 50$. The results are more scattered compared to the long-time self-diffusivities in Fig. 7.6a due to the difficulties associated with the measurement. Compared to d^s_∞ in Fig. 7.6a, $D(q_{\min})$ is in general slightly higher at the same Pe_σ, but shares the same pattern with respect to changes in Pe_σ: grows with Pe_σ for amorphous flowing suspensions, and decreases with Pe_σ in the string phase, suggesting that the diffusive behaviors of dense suspensions are consistent at different length scales. Note that, for equilibrium suspensions at low to moderate concentration, d^s_∞ decreases while d_c grows with increasing ϕ.

The inset of Fig. 7.6b presents the time evolution of the function f_{kk} with $k = 2$ (dashed lines) and 3 (solid lines) in Eq. (7.25). As expected, at a time scale comparable to a^2/d_0, f_{kk} becomes linear in time for flowing suspensions in both the 2- and 3-directions. In the string phase, f_{kk} is qualitatively different. In particular, the difference between f_{22} and f_{33} are more significant, suggesting that the anisotropic string structures influence the collective diffusion differently in different directions. Moreover, for arrested suspensions, f_{kk} is not diffusive within the observation time frame. Indeed, the temporal evolution of f_{kk} shares strong similarity with $\left\langle \Delta x_k^2 \right\rangle$ in Fig. 7.6a.

A third characterization of the suspension dynamics, usually from dynamic light scattering experiments, is the self-intermediate scattering function $F_s(\boldsymbol{q}, t)$, averaged over all the available time. The function F_s is defined as

$$F_s(\boldsymbol{q}, t) = \frac{1}{N} \sum_i \left\langle \exp\{i\boldsymbol{q} \cdot [\boldsymbol{x}_i(t) - \boldsymbol{x}_i(0)]\} \right\rangle . \tag{7.27}$$

For dilute suspensions, $F_s \sim \exp(-d_0 q^2 t)$ due to the particle Brownian motion [1]. The decay of F_s characterizes how fast a particle in the suspension "forgets" where it has been, and, as is customary, characterized by the α-relaxation time τ_α when $F_s = e^{-1}$ [4]. Fig. 7.6c presents the α-relaxation times $\tau_{\alpha,kk}$ with $k = 2$ (open symbols) and 3 (filled symbols) as functions of Pe_σ at $\bar{\Pi} = 50$. Here, τ_α is computed at $qa = 3.5$, corresponding to a wave number near the peak of the static structure factor. This relaxation time characterizes the suspension "cage-breaking" dynamics.

The relaxation time $\tau_{\alpha,22}$ and $\tau_{\alpha,33}$ are similar to each other, with only quantitative differences in the string phase. As soon as the suspension becomes flowing, τ_α be-

comes finite, and quickly reduces with increasing stress for amorphous suspensions. When the suspension enters the string phase at $\mathrm{Pe}_\sigma > 500$, τ_α in both directions grows significantly, suggesting that the structural formation qualitatively affects the cage relaxation process. In fact, the changes in τ_α with respect to Pe_σ are consistent with those of d^s_∞, and Fig. 7.6a and 7.6c resemble top-down mirror images of each other.

The inset of Fig. 7.6c shows the self-intermediate scattering function F_s for extracting τ_α at selected Pe_σ. For an arrested suspension at $\mathrm{Pe}_\sigma = 115$, F_s does not decay significantly over an extended period of time. For flowing suspensions, on the other hand, the decay becomes faster with increasing Pe_σ. Note that with the formation of the string phase, the decay of F_s becomes qualitatively different.

Further information on the suspension dynamics can be extracted from the dynamic susceptibility, χ_4 [37],

$$\chi_4(\boldsymbol{q},t) = N\left[\left\langle\left(\frac{1}{N}\sum_i \exp\{i\boldsymbol{q}\cdot[\boldsymbol{x}_i(t)-\boldsymbol{x}_i(0)]\}\right)^2\right\rangle - \left\langle\frac{1}{N}\sum_i \exp\{i\boldsymbol{q}\cdot[\boldsymbol{x}_i(t)-\boldsymbol{x}_i(0)]\}\right\rangle^2\right] \tag{7.28}$$

which is closely related to the 4-point correlations in the suspension. The peak height of χ_4, $\max(\chi_4)$, is an important indication of dynamic heterogeneities in dense systems [4]. For glassy systems without imposed shear [22, 37, 73], $\max(\chi_4)$ is found to grow significantly near the glass transition. For sheared athermal systems interacting with soft potentials [39, 40], a real-space counterpart of $\max(\chi_4)$ is also found to grow near the jamming point. Therefore, $\max(\chi_4)$ may effectively characterize the flow-arrest transitions of dense systems regardless of underlying driving mechanisms. Fig. 7.6d shows $\max(\chi_4)$ in the 2- (open symbols) and the 3-directions (filled symbols) as functions of Pe_σ with $\bar{\Pi} = 50$. The inset of Fig. 7.6d shows the temporal evolution of χ_4 in both directions.

The peak of the dynamic susceptibility, $\max(\chi_4)$ decreases significantly with increasing Pe_σ in both the 2- and the 3-direction. The reduction in $\max(\chi_4)$ suggests the heterogeneities and fluctuations in the suspension become less significant. The flow-arrest transitions in our systems are similar to the glass and the jamming transitions in other systems. However, as the suspension enters the string phase, $\max(\chi_4)$ increases drastically again and then decreases. This shows that near the

amorphous-string transition, another dynamic heterogeneity emerges in the suspension dynamics.

Moreover, the temporal evolution of χ_4, shown in Fig. 7.6d inset, suggests that for arrested suspensions, e.g., at $\mathrm{Pe}_\sigma = 115$, χ_4 does not grow within the simulation time frame as the particles are essentially locked in place and are unable to organize large-scale fluctuations. For suspensions at $\mathrm{Pe}_\sigma = 145$, χ_4 exhibits a prominent peak at time $\sim a^2/d_0$. However, with increasing Pe_σ, the corresponding χ_4 reaches the peak at an earlier time, and the height of the peak is much lower, because as the suspension begins to flow, the particles do not need large-scale coordination to achieve diffusive motion. In the string phase at $\mathrm{Pe}_\sigma = 1000$ and 1500, the peak of χ_4 increases again, and the qualitative features of χ_4 are different, with more prominent difference between the 2- and the 3-directions comparing to amorphous phase results.

Fig. 7.6 shows the different facets of suspension dynamics in constant stress and pressure rheology. The various characterizations are consistent for flowing suspensions, and the differences between the 2- and 3-directions are negligible. However, structural development qualitatively changes the diffusive dynamics. To study the influence of pressure on the suspension rheology, we focus only on the amorphous suspensions, and from Fig. 7.6, we also focus only on the dynamics in the vorticity direction.

7.4 Dynamics near flow-arrest transitions

Here we investigate the suspension dynamics near the flow-arrest transitions. We focus on a few $(\bar{\Pi}, \mathrm{Pe}_\sigma)$ pairs with $\bar{\Pi} = 50$ and 5 by performing at least 50 independent simulations with distinct initial conditions for analysis.

Temporal heterogeneity

Fig. 7.7 shows the accumulated strain γ from different simulations at $(\bar{\Pi}, \mathrm{Pe}_\sigma) = (50, 145)$, illustrating the unstable suspension behaviors near flow-arrest transitions. The qualitative features of γ in each simulation is similar to those in the inset of Fig. 7.2a: the suspension switches between the flowing and the arrested states, leading to the intermittent growth and stagnation of γ with respect to time. In some cases, the suspension is completely stuck and is unable to flow. These unstable behaviors lead to distinct γ trajectories in each simulation. The average γ trajectory over 50 simulations is shown as a dashed line in Fig. 7.7. In an average sense, $\gamma \propto t$, and only reaches $\gamma \approx 12$ at $t\sigma/\eta_0 = 5000$, suggesting a highly viscous suspension.

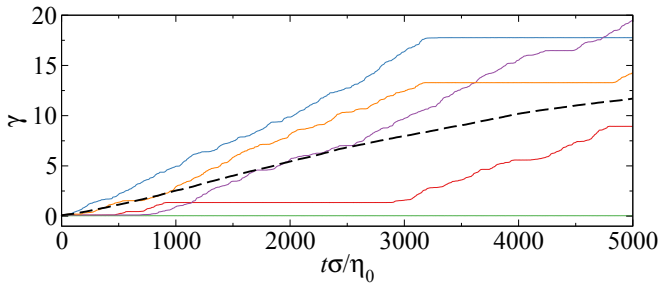

Figure 7.7: (Color online) The time evolution of the accumulated strain γ with $(\bar{\Pi}, \mathrm{Pe}_\sigma) = (50, 145)$. Different solid lines represent results from different runs. The dashed lines are averaged from 50 independent runs.

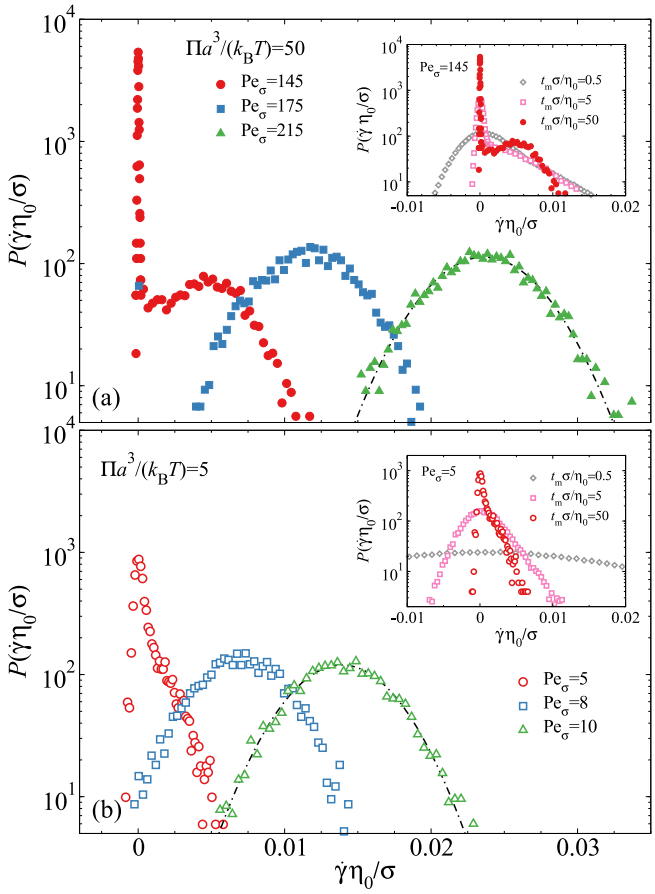

Figure 7.8: (Color online) The probability distribution of the strain rate $\dot{\gamma}\eta_0/\sigma$ at various Pe_σ with the averaging time $t_m\sigma/\eta_0 = 50$. The imposed pressures are $\bar{\Pi} = 50$ (a) and $\bar{\Pi} = 5$ (b). The inset shows the strain rate distribution with different averaging time t_m at the annotated Pe_σ.

Assuming that the unstable dynamics in Fig. 7.7 arises from a stationary process,

the temporal heterogeneity can be analyzed by populating the strain rate probability distribution, $P(\dot{\gamma})$, at different imposed pressures and stresses. However, directly populating the instantaneous strain rate $\dot{\gamma}$ leads to an uninteresting broad, Gaussian-like distribution. Although the instantaneous $\dot{\gamma}$ is strongly affected by noise, the smooth accumulated strain γ suggests that the noise in $\dot{\gamma}$ strongly cancels each other in consecutive times. Therefore, we average the strain rate over an intermediate time t_m, and populate the probability distribution of the average strain rate $\dot{\gamma}$ from independent segments of t_m. For example, the inset of Fig. 7.8a shows the probability $P(\dot{\gamma})$ averaged over time intervals $t_m\sigma/\eta_0 = 0.5$, 5, and 50 at $(\bar{\Pi}, \mathrm{Pe}_\sigma) = (50, 145)$. With increasing t_m, $P(\dot{\gamma})$ becomes narrower and develops split peaks. At $t_m\sigma/\eta_0 = 0.5$, the distribution $P(\dot{\gamma})$ is asymmetric, with a positive peak close to $\dot{\gamma} = 0$, and a tail skewed towards positive $\dot{\gamma}$, leading to an overall positive average $\dot{\gamma}$. Increasing $t_m\sigma/\eta_0$ to 5, the peak near $\dot{\gamma} = 0$ becomes significantly narrower, and a skewed tail remains for $\dot{\gamma} > 0$. When $t_m\sigma/\eta_0 = 50$, $P(\dot{\gamma})$ shows two contributions: a narrow distribution around $\dot{\gamma} = 0$, and a wide distribution with a different peak at $\dot{\gamma} > 0$. At this t_m, the noise is suppressed to reveal the origin of the asymmetry in $P(\dot{\gamma})$ at smaller t_m. The strain rate distribution shows that, near the flow-arrest transition, the suspensions switches between an arrested state with a narrow strain rate distribution centered at $\dot{\gamma} = 0$ and a flowing state with a wider $\dot{\gamma}$ distribution centered at $\dot{\gamma} > 0$. Switching between the flowing and the arrest states leads to the γ instability in Fig. 7.7. Approximating both contributing distributions as normal distribution $\mathcal{N}(\mu, \sigma)$ with mean μ and variance σ^2, we have

$$P(\dot{\gamma}) \approx w_A \mathcal{N}(0, \sigma_A) + (1 - w_A)\mathcal{N}(\dot{\gamma}_F, \sigma_F), \tag{7.29}$$

with $\sigma_F \gg \sigma_A$, $\dot{\gamma}_F > 0$, and w_A the proportion of the arrested states. In Fig. 7.8, w_A can be estimated by integrating over the peak centered at $\dot{\gamma} = 0$. Eq. (7.29) suggests that the suspension dynamics might be modeled as a reaction system with distinct flowing and arrested states via non-equilibrium statistical physics [74]. However, this is beyond the scope of the current work.

The main figure of Fig. 7.8a also presents $P(\dot{\gamma})$ at $\mathrm{Pe}_\sigma = 175$ and 215. The contributions from the arrested state quickly diminishes, i.e., $w_A \to 0$ as the imposed stress exceeds the yield stress $\sigma \gg \sigma_m$. A small arrest peak in $P(\dot{\gamma})$ remains visible at $\mathrm{Pe}_\sigma = 175$, but it completely vanishes at $\mathrm{Pe}_\sigma = 215$. Indeed the strain rate distribution at $\mathrm{Pe}_\sigma = 215$ can be fitted to a normal distribution, which is shown in dashed-dotted line in Fig. 7.8. Away from the flow-arrest transition, the strain rate distribution in the flowing state appears to follow a random Gaussian process.

To highlight the influences of $\bar{\Pi}$, Fig. 7.8b presents $P(\dot{\gamma})$ at $\bar{\Pi} = 5$ with the same t_m. Although the qualitative features are similar to Fig. 7.8a, reducing $\bar{\Pi}$ shows an increase in the fluctuations. Near the flow-arrest transition, i.e., at $\mathrm{Pe}_\sigma = 5$, $P(\dot{\gamma})$ has two contributions, and can be approximated via Eq. (7.29). Compared to the $P(\dot{\gamma})$ at $(\bar{\Pi}, \mathrm{Pe}_\sigma) = (50, 145)$, the most distinguishing feature here is that σ_A associated with the arrested state is larger, and σ_F associated with the flowing state is smaller. Consequently, the instability between the flowing and the arrested states in $\gamma(t)$ is less evident compared to $\bar{\Pi} = 50$. At higher Pe_σ, $P(\dot{\gamma})$ becomes broader due to the stronger thermal fluctuations. Furthermore, the inset of Fig. 7.8b presents the effect of t_m on $P(\dot{\gamma})$ near the flow-arrest transition. Increasing t_m show similar effects on $P(\dot{\gamma})$ as the case of $\bar{\Pi} = 50$, but the lower confining pressure leads to stronger thermal fluctuations at small t_m.

Fig. 7.8 shows that the instability in γ near the flow-arrest transition arises from the suspension switching between a flowing state and an arrested state. These behaviors are present at both low and high confining pressures, but are more pronounced at high $\bar{\Pi}$ due to the weaker thermal fluctuations. The strain rate distribution is sensitive to the averaging time t_m, and can be approximated using Eq. (7.29) with sufficiently large t_m. The weight w_A in Eq. (7.29) rapidly vanishes as the suspension leaves the flow-arrest transition. However, understanding how Eq. (7.29) is affected by the imposed stresses and pressures from a first principle perspective remains a challenge.

Fig. 7.8 also reveals that each $(\bar{\Pi}, \mathrm{Pe}_\sigma)$ pair covers a strain rate range which reduces with increasing averaging time t_m. Therefore, the suspension behaviors over the a range of $\dot{\gamma}$ can be analyzed with the same imposed stress and pressure. This is different from the start-up or the cessation studies, where the suspension responses at different $\dot{\gamma}$ is found through a sudden change in the external forcing. The results from the two approaches are equivalent in the linear response regime, but their relation for non-equilibrium systems is unclear.

We analyze the suspension behaviors at different $\dot{\gamma}$ for each $(\bar{\Pi}, \mathrm{Pe}_\sigma)$ pair with $t_m = 50\eta_0/\sigma$, which is long enough to suppress the thermal noises, but is also short enough for adequately sampling the suspension responses at each $\dot{\gamma}$. The suspension properties are computed from different simulation segments with same average $\dot{\gamma}$. Fig. 7.9a and 7.9b show the volume fraction ϕ and long-time self-diffusivity in the vorticity direction d^s_∞, respectively, as functions of the strain rate $\dot{\gamma}\eta_0/\sigma$ for $\mathrm{Pe}_\sigma = 145$, 175, and 215 at $\bar{\Pi} = 50$ and $\mathrm{Pe}_\sigma = 5$, 8, and 10 at $\bar{\Pi} = 5$. The diffusivity

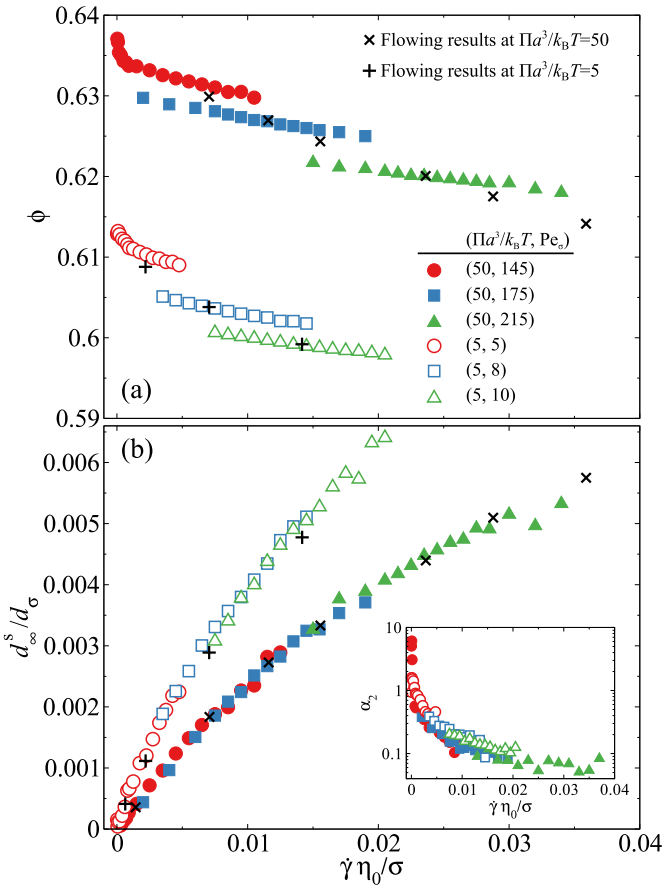

Figure 7.9: (Color online) The volume fraction, ϕ (a), and the stress scaled long-time self-diffusivity in the vorticity direction, $d^s_\infty \eta_0/(a^2\sigma)$ (b), as functions of the time-averaged strain rate $\dot{\gamma}\eta_0/\sigma$ in simulations at Pe_σ = 145, 175, and 215 for $\bar{\Pi}$ = 50 and at Pe_σ = 5, 8, 10 for $\bar{\Pi}$ = 5. The averaging time $t_m\sigma/\eta_0$ = 50. The crosses and pluses symbols are results averaged from the entire simulations at these pressures. The inset of (b) presents the corresponding non-Gaussian parameter α_2 as a function of $\dot{\gamma}\eta_0/\sigma$ measured at $t_m\sigma/\eta_0$ = 50.

in Fig. 7.9b is scaled with the stress diffusion scale,

$$d_\sigma = a^2\sigma/\eta_0, \tag{7.30}$$

to highlight the influence of the imposed stress. In Fig. 7.9, the scaled strain rate is the inverse shear viscosity, $\dot{\gamma}\eta_0/\sigma = \eta_0/\eta_s$. Also presented in Fig. 7.9 are ϕ and d^s_∞ averaged over the multiple simulations from Fig. 7.13b and Fig. 7.16a, shown as crosses for $\bar{\Pi}$ = 50 and pluses for $\bar{\Pi}$ = 5. Near the flow-arrest transitions, the ϕ and d^s_∞ curves can assess the suspension properties at much lower $\dot{\gamma}\eta_0/\sigma$ comparing to direct simulation-wide averages. Therefore, the analysis here is suitable for studying suspension dynamics near the flow-arrest transitions.

In Fig. 7.9a, each $(\bar{\Pi}, \mathrm{Pe}_\sigma)$ pair corresponds to a unique $\phi(\dot{\gamma})$ curve that does not overlap each other. In general, increasing $\dot{\gamma}$ leads to a ϕ decrease due to suspension dilation. Close to the flow arrest transition $\dot{\gamma} = 0$, the volume fraction ϕ becomes sensitive to $\dot{\gamma}$, and increases rapidly with diminishing $\dot{\gamma}$. This is particularly obvious at $(\bar{\Pi}, \mathrm{Pe}_\sigma) = (50, 145)$. At lower imposed pressure, the arrest volume fraction is reduced. The simulation-wide averages are always on the $\phi(\dot{\gamma})$ curves, except near the flow-arrest transitions due to the arrested states. On the other hand, in Fig. 7.9b, the dimensionless diffusivity d^s_∞/d_σ at different Pe_σ collapses to a master curve at the same $\bar{\Pi}$. The results also agree with the simulation-wide averages shown in the crosses and pluses at $\bar{\Pi} = 50$ and 5, respectively, justifying the adopted time frame $t_m = 50\eta_0/\sigma$.

We further characterize the suspension dynamics by computing the non-Gaussian parameter $\alpha_2(t)$ [75, 76] in the vorticity direction,

$$\alpha_2(t) = \frac{\left\langle \Delta x_3(t)^4 \right\rangle}{3\left\langle \Delta x_3(t)^2 \right\rangle^2} - 1, \tag{7.31}$$

which is presented in the inset of Fig. 7.9b at $t = t_m$. The non-Gaussian parameter α_2 becomes non-zero when the particle movement Δx_3 deviates from being fully diffusive, and is the real space equivalence of the dynamic susceptibility $\chi_4(t)$. A high α_2 suggests strong collective particle motions [75].

The inset of Fig. 7.9b shows that α_2 decreases from a large value at $\dot{\gamma}\eta_0/\sigma \approx 0$ with increasing $\dot{\gamma}$. Near the flow-arrest transition, the low d^s_∞ and the high α_2 suggests that the particles are locked by their neighbors and can only move around with collective motion. When $\dot{\gamma}\eta_0/\sigma \gg 0$, $\alpha_2 \ll 1$ and d^s_∞ is well defined, suggesting that the particles can diffuse in the 3-direction. Moreover, the non-Gaussian parameter α_2 at different $(\bar{\Pi}, \mathrm{Pe}_\sigma)$ pairs almost collapses, suggesting that the higher order particle dynamics are similar despite the different d^s_∞, and are principally determined by the strain rate.

Fig. 7.9 shows that, at a fixed imposed pressure Π, the volume fraction is a function of both the strain rate and the shear stress, $\phi = \phi(\dot{\gamma}, \sigma; \Pi)$, but the dimensionless diffusivity $\varrho = d^s_\infty/d_\sigma$ is only a function of the strain rate, $\varrho = \varrho(\dot{\gamma}; \Pi)$. Therefore, in constant stress and pressure rheology, the dimensionless diffusivity q does not have explicit dependence on the shear stress σ and the volume fraction ϕ, and can only be affected by changing $\dot{\gamma}$ and Π. With constant imposed stress, the average volume fraction $\langle\phi\rangle$ and the average diffusivity $\langle d^s_\infty\rangle$ are computed using the strain rate probability $P(\dot{\gamma})$ as $\langle\phi\rangle = \int \phi(\dot{\gamma}, \sigma; \Pi) P(\dot{\gamma}) \mathrm{d}\dot{\gamma}$ and

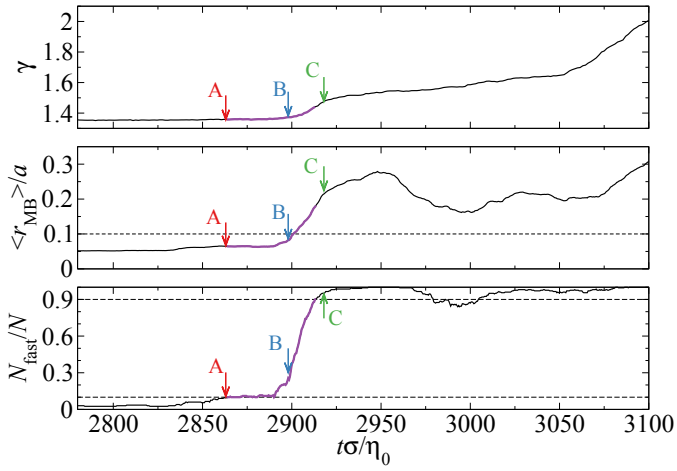

Figure 7.10: (Color online) Typical time evolution of a suspension at $\mathrm{Pe}_\sigma = 145$ and $\bar{\Pi} = 50$ near an arrest-event transition: (top) the accumulated strain γ; (center) the average radius of the minimum enclosing circle of the particle trajectory $\langle r_{\mathrm{MB}} \rangle$; (bottom) the fraction of the fast particles N_{fast}/N. In computing r_{MB}, the trajectory of the past $50\eta_0/\sigma$ time units in the velocity gradient-vorticity plane are considered. The transition from the flowing to the arrested states are highlighted, with the arrows pointing out three time instances A, B, and C. The horizontal dashed lines highlight the cutoff radius r_c in the middle panel and the lower and upper limiting fast particle fractions.

$\langle d_\infty^s \rangle = d_\sigma \int \varrho(\dot{\gamma}; \Pi) P(\dot{\gamma}) \mathrm{d}\dot{\gamma}$. For constant strain rate rheology with the corresponding stress distribution $\hat{P}(\sigma)$, the average volume fraction is similar to the case of constant stress, $\langle \phi \rangle = \int \phi(\dot{\gamma}, \sigma; \Pi) \hat{P}(\sigma) \mathrm{d}\sigma$. However, the average diffusivity becomes $\langle d_\infty^s \rangle = a^2 \varrho(\dot{\gamma}; \Pi) \langle \sigma \rangle / \eta_0$, allowing a direct connection between the suspension mechanics $\langle \sigma \rangle$ and the particle diffusion $\langle d_\infty^s \rangle$.

Spatial heterogeneity

The flow-arrest instability in the accumulated strain $\gamma(t)$ in Fig. 7.7 provides a unique opportunity to study the particle-level details of the *spontaneous* arrest-flow events, which, as we have mentioned, are distinct from the transient response in start-up or cessation studies. Here, the imposed stresses and pressures are fixed and the events entirely arise from the fluctuations of the system.

An arrest-flow event is defined as the shortest continuous time where the suspension changes from an arrested state to a flowing state. These states are based on the fraction of fast particles in the suspension, N_{fast}/N, i.e., in an arrested state $N_{\mathrm{fast}}/N \leq 10\%$ and in a flowing state $N_{\mathrm{fast}}/N \geq 90\%$. Fig. 7.10 illustrates a typical event from

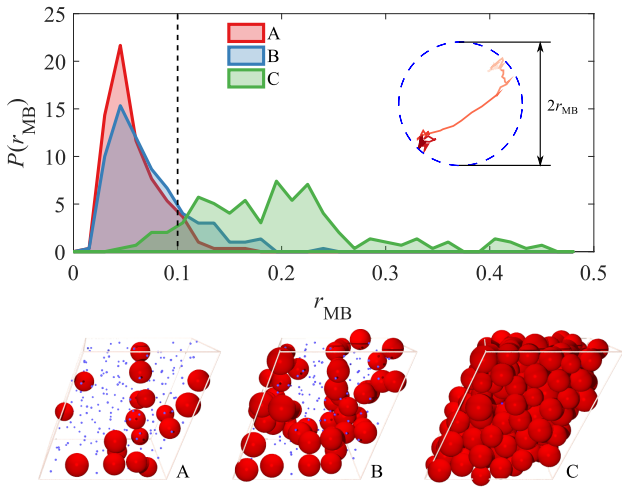

Figure 7.11: (Color online) (Top panel) The probability distribution of the radius of the minimum enclosing circle r_{MB} at time instances A, B, and C highlighted in Fig. 7.10. The cutoff radius r_c is shown in the vertical line. Also shown are the definition of r_{MB} and a typical particle trajectory, with more recent positions in darker color. (Bottom panel) The suspension snapshots at instances A, B, and C. The "fast" particles are shown in red in their full size, and the remainder are shown as blue dots.

point A to point C at $(\bar{\Pi}, \mathrm{Pe}_\sigma) = (50, 145)$, with the bottom panel showing the time evolution of N_{fast}/N. The exact choice of the cutoff fractions (10% and 90%) does not affect the spatial features of the event, but must ensure sufficient samples for analysis.

To determine N_{fast}, we analyze the particle trajectory projected to the 23-plane (velocity gradient-vorticity plane) over the past t_m time and compute the radius of the minimum enclosing circle r_{MB}, such that the distance between any two points in the trajectory does not exceed $2r_{MB}$. We consider a particle *fast* if its corresponding r_{MB} is larger than a cutoff radius r_c. Here, we choose the past time duration $t_m = 50\eta_0/\sigma$, and $r_c = 0.1a$. A typical particle trajectory projected into the 23-plane is shown in the top panel of Fig. 7.11. The current location at time t is red, and the color on the trajectory gradually fades to white at time $t - t_m$. The computed minimum enclosing circle [77] is shown in the dashed circle. Note also that the exact choice of r_c does not affect the results significantly.

The middle panel of Fig. 7.10 presents the time evolution of $\langle r_{MB} \rangle$ averaged over all particles as a function of time during the arrest-flow event. The dashed line represents the cutoff radius r_c. As the suspension changes from the arrested state

to the flowing state, $\langle r_{\mathrm{MB}} \rangle$ increase from below r_c to above. In addition, the top panel of Fig. 7.10 shows the accumulated strain γ as a function of time, which grows appreciably as the suspension becomes flowing. Changes in γ and $\langle r_{\mathrm{MB}} \rangle$ during the arrest-flow event are consistent with the N_{fast}/N evolution. However, defining the arrest-flow event using N_{fast}/N provides a clear duration for the event.

Characterizing the arrest-flow event using *fast* particles is inspired by experiments in colloidal glasses [75], where "mobile" particles move together in clusters as the suspension approaches the glass transition—a direct manifestation of dynamic heterogeneity. The length scale associated with the cluster, ℓ_c, diverges as the system approaches glass transition, because moving one particle out of its neighboring cage requires structural rearrangement in the entire system [15, 78, 79]. Therefore, studying clustering behaviors of mobile particles requires large system sizes to observe the diverging length scale and to eliminate the artifacts from periodic simulation box.

During an arrest-flow event, the fast particles in the suspension grow from a few to the entire system during a short period of time similarly to glassy dynamics. Taking points A, B, and C in Fig. 7.10 as an example, the top panel of Fig. 7.11 shows the corresponding probability distribution of r_{MB}, $P(r_{\mathrm{MB}})$, with the cutoff radius r_c shown as a vertical dashed line. At the beginning of the event (A), $P(r_{\mathrm{MB}})$ is peaked below r_c, as the majority of the particles are arrested and are confined to their neighboring cages. As the suspension starts flowing (B), the distribution shifts its tail towards higher r_{MB}. At at the end of the event (C), for the flowing suspension $P(r_{\mathrm{MB}})$ becomes much broader, and the majority of $P(r_{\mathrm{MB}})$ lies beyond r_c. The probability distributions at A and C illustrate the distinct flowing and arrested states. The corresponding simulation snapshots are shown in the bottom panel of Fig. 7.11. The fast particles are shown in full sizes and in red, and the other particles are shown as blue dots. Not clear in Fig. 7.11 is how the new fast particles appear.

The spatial organization of fast particles during an arrest-flow event has two possibilities: (1) the fast particles appear randomly in an uncorrelated fashion, suggesting that the flow-arrest transition is structurally independent, and is dominated by the thermal fluctuations; or (2) an arrested particle can only become mobile if its neighbors are also mobile. In this case, the suspension becomes flowing by propagating fast particles, and the arrest-flow event strongly depends on the structure of the fast particle cluster. In this sense, it is similar to the dynamic heterogeneity in a glass: in the thermodynamic limit, the suspension becomes flowing if the correlation length

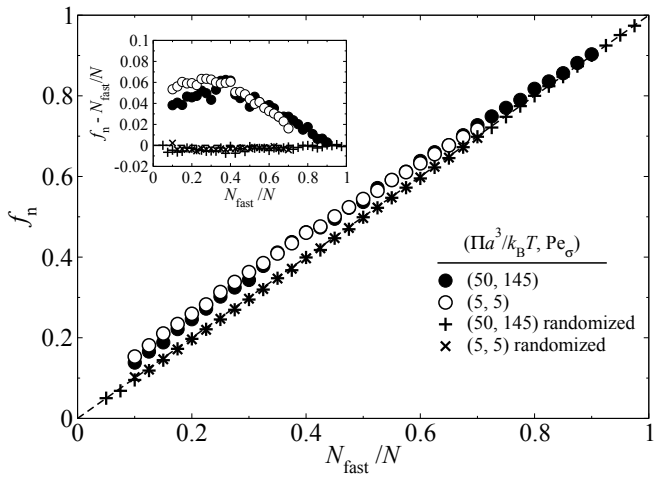

Figure 7.12: The fraction of the neighboring particles of a fast particle that are also fast, f_n, as a function of the fraction of fast particles in the suspension, N_{fast}/N, near the flow-arrest transitions at $(\bar{\Pi}, Pe_\sigma) = (50, 145)$ (filled symbols) and $(5, 5)$ (open symbols). The plus and cross symbols are the results when the fast particles are randomly selected. The inset highlights the difference $f_n - N_{fast}/N$.

of the fast particle cluster $\ell_c \to \infty$.

We analyze the structural details of the arrest-flow events to characterize the emergence of fast particles. The modest system size $N = 200$ makes analyzing the correlation length ℓ_c ineffective. Instead, we compare local behaviors of fast particles to the suspension-wide results. If a fast particle is enclosed by N_n neighboring particles, and N_{nf} of them are also fast moving particles, we define,

$$f_n = N_{nf}/N_n, \tag{7.32}$$

as the fraction of fast neighbors, which inherently depends on the suspension structure. If fast particles appear randomly, we expect $f_n = N_{fast}/N$. Otherwise, fast particles prefer to be next to each other if $f_n > N_{fast}/N$, while avoid each other if $f_n < N_{fast}/N$.

Fig. 7.12 presents f_n, defined in Eq. (7.32), as a function of the fraction of fast particles in the suspension, N_{fast}/N, which also gauges the progression of the arrest-flow events since the time duration of these events varies. The results are averaged over all available events at $(\bar{\Pi}, Pe_\sigma) = (50, 145)$ and $(5, 5)$. The neighboring particles are identified using radical tessellation [80], and the fast particles are found using their trajectories on the 23-plane. At $(\bar{\Pi}, Pe_\sigma) = (5, 5)$, the arrest-flow event is defined as the transition between $N_{fast}/N = 0.1$ and 0.7 due to stronger thermal

fluctuations. Fig. 7.12 also shows the "randomized" results by randomly assigning fast particles within the same sequences of particle configurations. As expected, the randomized results satisfy $f_{\mathrm{n}} = N_{\mathrm{fast}}/N$ as the emergence of the fast particles are independent of the existing fast particle configuration. On the other hand, for actual fast particles, $f_{\mathrm{n}} > N_{\mathrm{fast}}/N$: during an arrest-flow event, fast particles are more likely to appear next to each other. However, the result does not indicate whether a new fast moving particles prefers to appear next to an existing one, as the presence of a fast particle itself is dynamical: it appears and disappears during the arrest-flow event. Furthermore, as the fraction of fast particles becomes large ($N_{\mathrm{fast}}/N > 0.7$), the difference between f_{n} and N_{fast}/N diminishes due to the finite system size.

The emergence of fast particles is similar at different $\bar{\Pi}$, suggesting a universal suspension behavior in arrest-flow events. The inset of Fig. 7.12 quantifies this similarity by showing $f_{\mathrm{n}} - N_{\mathrm{fast}}/N$, which reaches a maximum of ~ 0.06 at $N_{\mathrm{fast}}/N \approx 0.4$. Clearly, when N_{fast}/N is small, the fast particles appear randomly due to mechanical or thermal fluctuations. As N_{fast}/N increases, the fast particles prefer to appear in clusters: the neighbor of a fast particle is more likely to be fast. Although it is difficult to quantify the correlation length from f_{n}, the results do show that cooperative particle rearrangement is necessary for arrest-flow events. The cooperation reaches a maximum at $N_{\mathrm{fast}}/N \approx 0.4$. Beyond that point, $f_{\mathrm{n}} - N_{\mathrm{fast}}/N$ decreases, and the fast moving particles emerge more randomly since a significant portion of the suspension is already fast. However, the cooperative rearrangement is still evident as the differences are higher than the randomized results.

7.5 A granular perspective on Brownian suspension rheology

Adopting a granular perspective, we characterize different aspects of suspension behavior using the viscous number. Focusing on amorphous systems, we exclude from the discussions the results showing string order structures, which exhibit qualitatively different structural and mechanical responses.

Mechanical responses

Fig. 7.13 presents the suspension shear viscosity $\eta_s = \sigma/\dot{\gamma}$, the volume fraction ϕ, and the *macroscopic* friction coefficient $\mu = \sigma/\Pi$ as functions of the viscous number $I_v = \dot{\gamma}\eta_0/\Pi$ for colloidal suspensions under constant imposed shear stress σ and confining pressure Π. In Fig. 7.13, the dimensionless imposed pressure $\bar{\Pi} = \Pi a^3/k_{\mathrm{B}}T = 1$ to 1000, and $I_v < 1$ due to the string order formation at higher I_v.

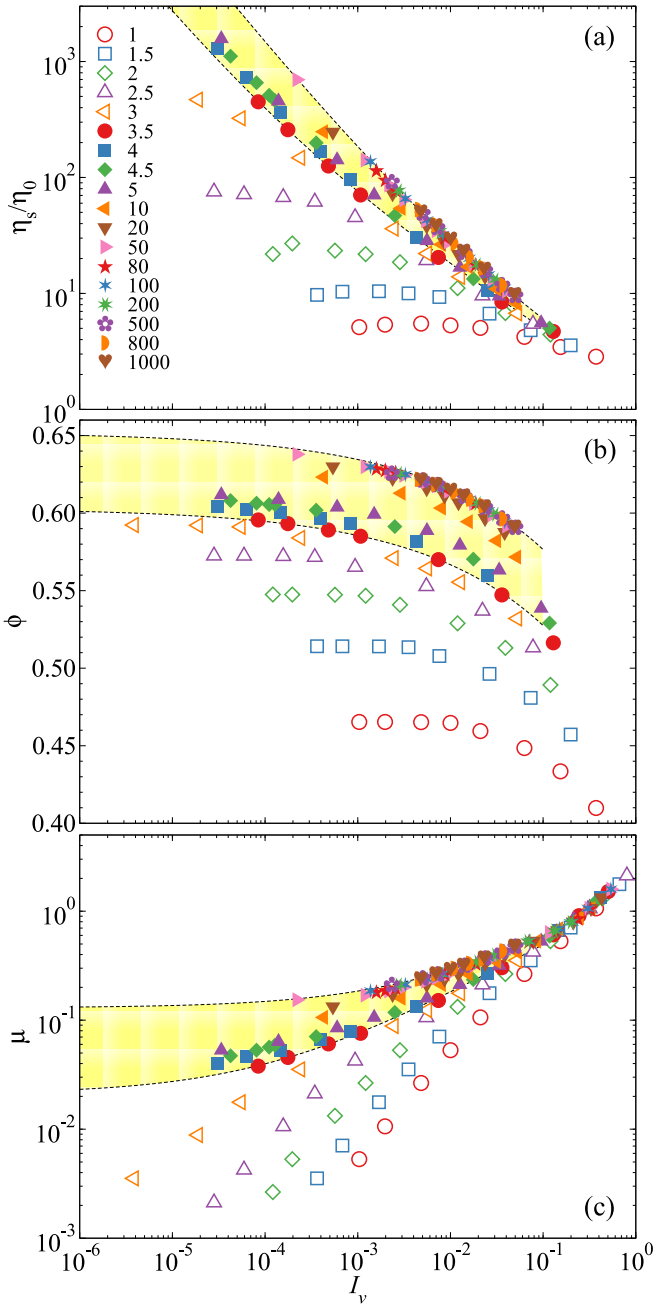

Figure 7.13: (Color online) The suspension shear viscosity η_s/η_0 (a), the volume fraction ϕ (b), and the *macroscopic* friction coefficient μ as functions of the viscous number I_v over a wide range of the imposed pressure $\bar{\Pi}$. The shaded area bounded by dashed lines are from the rheological model in Sec. 7.5, outlining the boundary of glassy suspensions.

The shear viscosity η_s in Fig. 7.13a shows two distinct behaviors in the $I_v \ll 1$ limit: with low imposed pressures $\bar{\Pi} < 3.5$, η_s asymptotes a finite value corresponding to

the at-rest viscosity of the equilibrium suspension with the same osmotic pressure Π. And when $\bar{\Pi} \geq 3.5$, the viscosity diverges $\eta_s \to \infty$ as $I_v \to 0$, suggesting the suspension arrests and becomes solid-like. For convenience, we call the former suspension behaviors liquid-like and the latter glassy, and show liquid-like suspensions as open symbols and glassy suspensions as filled symbols. The shear viscosity η_s decreases with growing I_v, i.e., the suspension shear thins in constant stress and pressure rheology. For both liquid-like and glassy suspensions, η_s at different $\bar{\Pi}$ collapse at high I_v, approaching the solvent viscosity η_0 due to suspension dilation. For glassy suspensions, increasing $\bar{\Pi}$ also show a data collapse at $\bar{\Pi} > 50$, suggesting the emergence of a non-Brownian limiting behavior. The shear viscosity η_s of glassy suspensions at lower $\bar{\Pi}$ are parallel to the collapsed results at small I_v.

Fig. 7.13b presents the volume fraction ϕ as a function of I_v for various $\bar{\Pi}$. At different $\bar{\Pi}$, the behaviors of ϕ are similar and are almost parallel to each other: the suspension dilates with increasing I_v, and approaches an at-rest value in the $I_v \ll 1$ limit. For liquid-like suspensions, this corresponds to the density of an equilibrium suspension with an osmotic pressure of the imposed pressure Π. Unlike the shear viscosity in Fig. 7.13a, ϕ does not collapse at high I_v at different $\bar{\Pi}$, but exhibits distinct limits. The volume fraction does show a high-pressure non-Brownian collapse when $\bar{\Pi} > 20$. The high-pressure limiting behaviors outline a ϕ boundary with respect to I_v corresponding to non-Brownian suspensions. Therefore, for a given viscous number I_v, there is a maximum volume fraction that decreases with increasing I_v. The double limit of $I_v \to 0$ and $\bar{\Pi} \to \infty$ defines the Shear Arrest Point (SAP) [20], where the highest volume fraction in Fig. 7.13b is attained at ϕ_{SAP}.

The *macroscopic* friction coefficient $\mu = \sigma/\Pi$ as a function of the viscous number I_v at different $\bar{\Pi}$ is shown in Fig. 7.13c. Since $\mu = I_v \eta_s/\eta_0$, for liquid-like suspensions with $\bar{\Pi} < 3.5$, the friction coefficient μ grows linearly with I_v in the $I_v \ll 1$ limit, with the slope corresponding to the equilibrium suspension viscosity. For glassy suspensions, as $I_v \to 0$ the friction coefficient approaches a constant μ_m characterizing the ratio of the yield stress σ_m to the imposed pressure. The magnitude of μ_m increases with growing I_v, and approaches the SAP friction coefficient μ_{SAP} as $\bar{\Pi} \to \infty$. When I_v is increased from the $I_v \to 0$ limit, μ emerges from the arrested value μ_m, and the difference $(\mu - \mu_m)$ appears to grow sublinearly with respect to I_v. Further increasing I_v leads to linear μ growth. The friction coefficients μ at different $\bar{\Pi}$ collapses with as the suspension viscosity approaches the solvent viscosity η_0 in Fig. 7.13a.

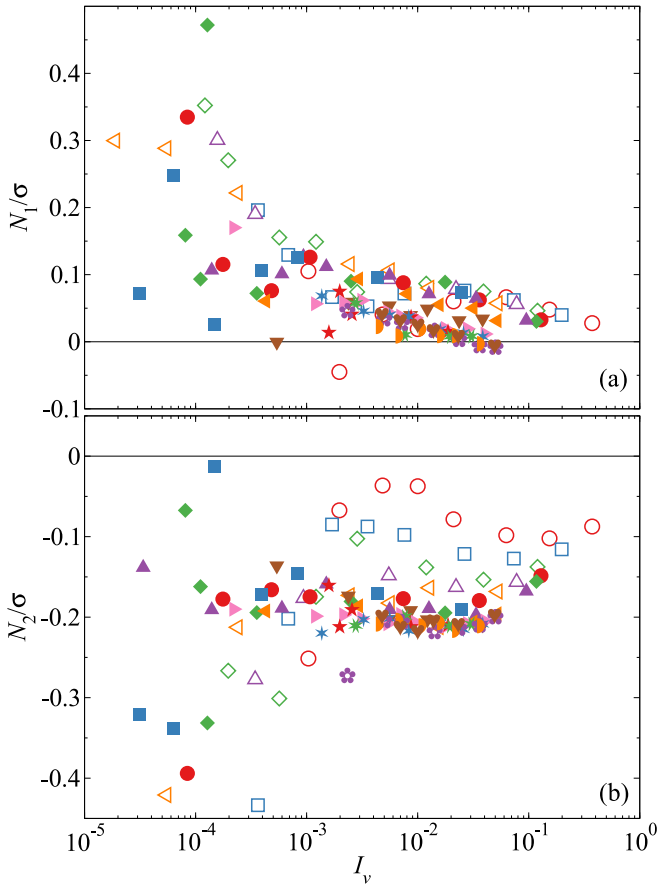

Figure 7.14: (Color online) The stress-scaled normal stress differences N_1/σ (a) and N_2/σ (b) as functions of viscous number I_v for a wide range of imposed pressure $\bar{\Pi}$. The symbols are identical those in Fig. 7.13.

Normal stress differences are another important characterization of the suspensions rheology. The first and the second normal stress differences, N_1 and N_2, defined as,

$$N_1 = \langle \Sigma_{11} \rangle - \langle \Sigma_{22} \rangle \quad \text{and} \quad N_2 = \langle \Sigma_{22} \rangle - \langle \Sigma_{33} \rangle, \tag{7.33}$$

are presented in Fig. 7.14 over a wide range of $\bar{\Pi}$. Consistent with earlier BD studies, N_1 is positive and N_2 is negative. For a simple isotropic material, N_1 and N_2 should emerge from zero as the material is deformed [81, 82]. In simulations, the departure of N_1 or N_2 from zero was not observed due to the difficulties associated with stress differences with significant fluctuations. Scaling the normal stress differences with the imposed stress σ, the results decreases with increasing I_v as the suspension dilates.

In Fig. 7.14a, N_1 appears scattered when $I_v < 0.005$, but the general trend is

deceasing with growing I_v. The positive N_1 is a signature of the dominance of interparticle or Brownian forces in suspensions [51]. If HIs dominant particle interactions, the first normal stress difference $N_1 < 0$ as HIs resist particle pairs to separate. On the other hand, repulsive interparticle forces promotes the pair separation. At higher I_v, N_1 approaches zero as the string-ordered phase formation establishes the fore-aft symmetry in $g(\boldsymbol{r})$ in Fig. 7.3. Moreover, at larger I_v the results at high $\bar{\Pi}$ collapse, showing a universal, non-Brownian N_1 limit.

The second normal stress difference N_2 is negative for all imposed pressures in Fig. 7.14b. For liquid-like suspensions, N_2/σ variation with $I_v < 10^{-3}$ is scattered. The general trend is that the magnitude of N_2/σ decreases. With increasing I_v, the magnitude $|N_2|/\sigma$ reaches a minimum, increases slightly before decreasing again. For glassy suspensions, the results for $I_v > 10^{-3}$ collapses to the non-Brownian limit, where $|N_2|/\sigma$ increases before decreasing again. With increasing $\bar{\Pi}$, $|N_2|/\sigma$ increases, but $|N_1|/\sigma$ decreases, and as $\bar{\Pi} \to \infty$, in general $|N_1| \lesssim |N_2|$. This is consistent with the suspension structural features in Eq. (7.19): for example, in Fig. 7.3, the structural differences near the 1- and 2-axis in g_{12} are more sensitive to Pe_σ relative to those between the 2- and 3-axis in g_{23}. Therefore, the normal stress differences are direct reflection of the suspension structures.

Suspension structures

The suspension structural features, $\max(g_{\mathrm{comp}})$ and $\max(g_{\mathrm{ext}})$, respectively, are presented in Fig. 7.15a and 7.15b for various imposed pressures. According to Eq. (7.19), they are related to the structural contributions to the suspension rheology. Recall that only amorphous suspensions—no string phases—are considered. Beginning with the peak height of g_{comp} in Fig. 7.15a, $\max(g_{\mathrm{comp}})$ is insensitive to I_v due to suspension dilation at low $\bar{\Pi}$, and with increasing I_v, it only increases slightly before decreasing again. At higher $\bar{\Pi}$, $\max(g_{\mathrm{comp}})$ grows but the qualitative features remain unchanged for liquid-like suspensions with $\bar{\Pi} < 3.5$ at low I_v. The peak height $\max(g_{\mathrm{comp}})$ decreases further at higher I_v and collapses with the results at lower $\bar{\Pi}$. For glassy suspensions, $\max(g_{\mathrm{comp}})$ collapses and a high pressure limiting behavior emerges. In this case, $\max(g_{\mathrm{comp}})$ first increases slightly, and then decreases with increasing I_v. Note that $\max(g_{\mathrm{comp}})$ remains finite at finite I_v even as $\bar{\Pi} \to \infty$. In contrast, for monodisperse hard-sphere systems, the contact value of pair distribution function diverges as the system acquires rigidity [83].

The peak values of g_{ext}, presented in Fig. 7.15b, significantly reduce with increasing

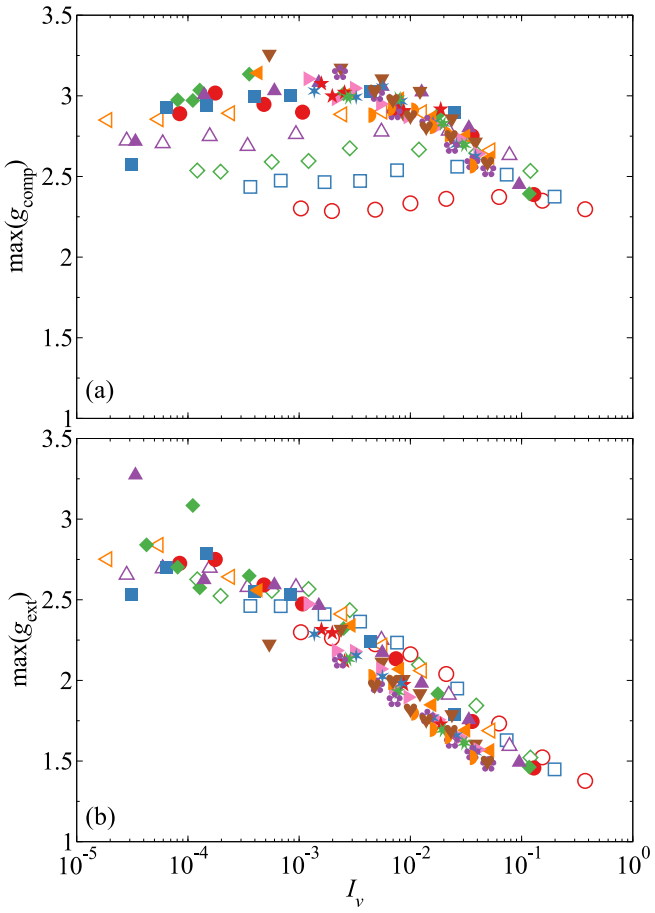

Figure 7.15: (Color online) The peak values of the pair distribution function along the compressional and extensional axes, $\max(g_{\text{comp}})$ (a) and $\max(g_{\text{ext}})$ (b), as functions of the viscous number I_v over a wide range of imposed pressures $\bar{\Pi}$. The symbols are identical to those in Fig. 7.13.

I_v for all $\bar{\Pi}$. In contrast to $\max(g_{\text{comp}})$, $\max(g_{\text{ext}})$ is more sensitive to I_v but less sensitive to $\bar{\Pi}$. This sensitivity grows with increasing I_v, as $\max(g_{\text{ext}})$ reduces faster with higher I_v, and at low I_v, $\max(g_{\text{ext}})$ is almost constant. Furthermore, at the same I_v, increasing $\bar{\Pi}$ in general increases $\max(g_{\text{comp}})$ but reduces $\max(g_{\text{ext}})$. Fig. 7.15 shows the structural features of non-Brownian suspensions in the $\bar{\Pi} \to \infty$ limit: the suspension structural features in the extensional axis, $\max(g_{\text{ext}})$, are more sensitive to I_v, and less sensitive in the compressional axis for $\max(g_{\text{comp}})$.

Diffusive dynamics

Fig. 7.16 presents several suspension diffusive behaviors for various $\bar{\Pi}$, including the long-time self-diffusivity d^s_∞ in Fig. 7.16a, the wave-number dependent diffusivity

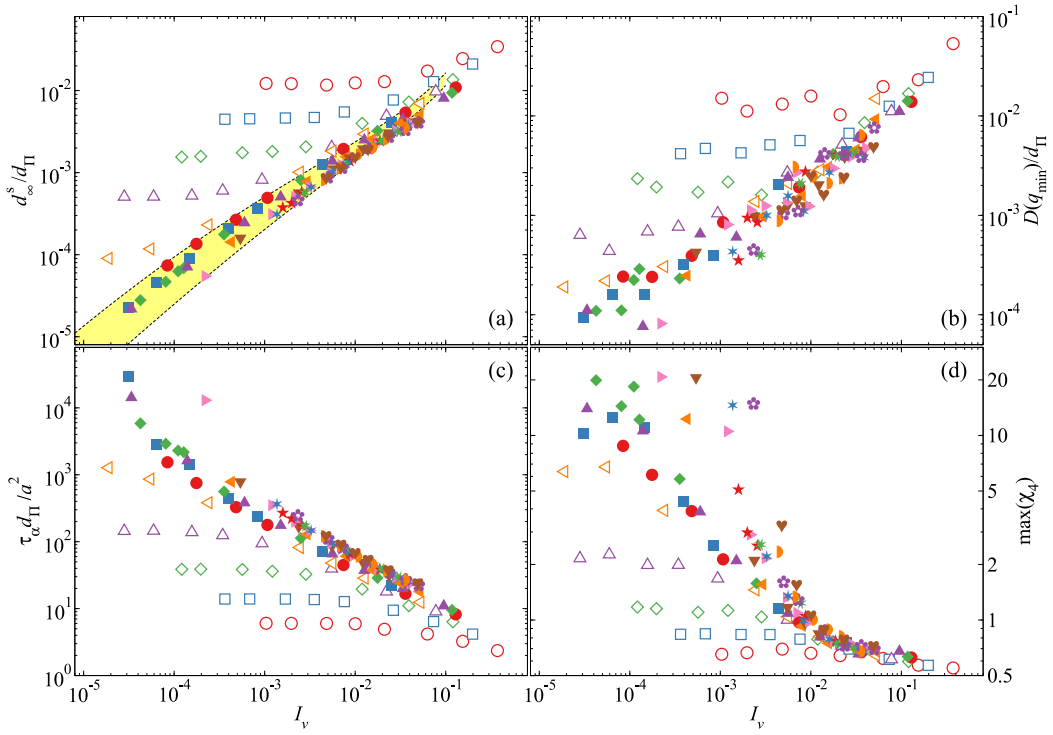

Figure 7.16: (Color online) Different characterizations of suspension dynamics as functions of the viscous number I_v over a wide range of imposed pressures $\bar{\Pi}$. The symbols are identical to those of Fig. 7.13. In (a)–(c) the diffusive quantities are characterized by the pressure diffusion scale $d_\Pi = \Pi a^2/\eta_0$. All the measurements are taken in the vorticity direction. (a): the long-time self-diffusivity d_∞^s/d_Π; (b): the wave-number dependent diffusivity measured at $q_{\min}$, $D(q_{\min})/d_\Pi$; (c): the α-relaxation time $\tau_\alpha d_\Pi/a^2$ from the self-intermediate scattering function at $qa = 3.5$; (d): the peak of the dynamic susceptibility $\max(\chi_4)$. In (a), the shaded area bounded by dashed lines highlights the glassy suspension behaviors from Eq. (7.43).

at the lowest wave number $D(q_{\min})$ in Fig. 7.16b, the α-relaxation time near peak of the static structure factor τ_α in Fig. 7.16c, and peak of the dynamic susceptibility in Fig. 7.16d. Here, we focus on the dynamics in the vorticity direction, since Fig. 7.6 indicated that the dynamics measured from the velocity gradient direction are qualitatively similar. For simplicity, we drop the 33 subscripts in the diffusive quantities. To accommodate the wide range of Brownian and non-Brownian suspension behaviors over a wide range of imposed pressures, we scale the diffusive behaviors with a confining pressure diffusion scale

$$d_\Pi = \dot{\gamma}\eta_0/\Pi. \tag{7.34}$$

Unlike the single-particle diffusivity d_0, the diffusion scale d_Π does not correspond to the diffusivity of an actual diffusion process.

Fig. 7.16a shows the long-time self-diffusivity d^s_∞ as functions of I_v. For liquid-like suspensions, e.g., at $\bar{\Pi} = 1.5$, d^s_∞ grows with I_v from a plateau, which arises from the at-rest suspension diffusion process. Further increasing I_v makes the flow stronger, which eventually overcomes the particle thermal fluctuations, leading to the diffusivity increases with I_v and scales linearly with $\dot{\gamma}$. Upon increasing $\bar{\Pi}$, both the plateau diffusivity and the viscous number where the suspension departs the plateau decrease, e.g., the plateau regimes ends at $I_v \approx 0.005$ for $\bar{\Pi} = 1.5$, and at $I_v \approx 0.0003$ for $\bar{\Pi} = 2.5$. Therefore, the suspension diffusive behaviors are becoming less affected by the at-rest particle dynamics and more affected by the imposed flow. With the emergence of the flow-arrest transition, the diffusivity plateau vanishes, and d^s_∞ only grows with I_v. Further increasing $\bar{\Pi}$ reduces the diffusivity, and the results in the $\bar{\Pi} \gg 1$ limit collapse to a non-Brownian limiting behavior. The high-pressure d^s_∞ are almost parallel to each other, suggesting that the particle diffusion is driven by the external flow, and the at-rest particle dynamics contribute little. The results at high I_v for different $\bar{\Pi}$ also collapse to the dilute diffusion behaviors. Also presented in Fig. 7.16a as yellow shade is the glassy diffusive behaviors predicted by Eq. (7.43), with the dashed lines representing the glass and the jamming limiting behaviors. The predicted diffusion boundary agrees well with the simulation results.

Fig. 7.16b presents the collective suspension diffusive behaviors in the vorticity direction, $D(q_{\min})$, for various $\bar{\Pi}$. Although at different ϕ the corresponding $q_{\min}$ are different, such differences do not affect the qualitative results. With respect to I_v, $D(q_{\min})$ is similar to d^s_∞ in Fig. 7.16a despite stronger data scattering as $D(q_{\min})$ is more difficult to measure. For liquid-like suspensions, $D(q_{\min})$ exhibits equilibrium plateaus in the $I_v \to 0$ limit, and increases with I_v afterwards. For glassy suspensions with $\bar{\Pi} \geq 3.5$, the collective diffusivity is lower than the liquid-like suspensions, and in the $\bar{\Pi} \to \infty$ limit, a non-Brownian limit emerges, suggesting the weak influences of thermal fluctuations. The similarity between $D(q_{\min})$ and d^s_∞, which represents the diffusion process at disparate suspension length scales, suggests that the same underlying mechanism drives the suspension diffusive dynamics at various imposed pressures.

Fig. 7.16c shows the α-relaxation time in the vorticity direction, τ_α, defined as the time for the self-intermediate scattering function to decay to $1/e$, for various imposed pressures. The wave number for F_s is taken at $qa = 3.5$, close to the first peak of the static structure factor, and therefore the corresponding τ_α characterizes

the dynamics of nearest neighboring particle cage. Fig. 7.16c is almost an up-down mirror image of d^s_∞ in Fig. 7.16a, showing that a high d^s_∞ corresponds to a low τ_α. Therefore, the suspension dynamics at the length scale of the cages and the single-particle length scale are similar. For liquid-like suspensions, τ_α decreases from a plateau with increasing I_v, and for glassy suspensions, the plateau vanishes. The crossover between the plateau and the decay occurs at different $\bar{\Pi}$. For glassy suspensions, the results at high $\bar{\Pi}$ also collapse in the non-Brownian limit.

Fig. 7.16d characterizes the suspension dynamic heterogeneity via the peak of the dynamic susceptibility $\max(\chi_4)$ in the vorticity direction, with χ_4 defined in Eq. (7.28), also measured at $qa = 3.5$. The dynamic heterogeneity $\max(\chi_4)$ is qualitatively different from other dynamic characterizations in Fig. 7.16a–7.16c. For liquid-like suspensions, $\max(\chi_4)$ decreases from a low I_v plateau with increasing I_v. The value of the low I_v plateau grows with increasing $\bar{\Pi}$, suggesting that the at-rest dynamic heterogeneity grows with $\bar{\Pi}$. With the emergence of the flow-arrest transitions, $\max(\chi_4)$ at low I_v can reach high value, and the low I_v plateau disappears altogether. In this case, the flow of the suspension is dominated by transient large-scale fluctuations in dynamic heterogeneity. For $I_v > 0.01$, $\max(\chi_4)$ at different $\bar{\Pi}$ collapses and quickly decreases below 1, suggesting that the flowing suspensions in this limit lack large-scale fluctuations.

We further explore the quantitative similarity among d^s_∞, $D(q_{\min})$, and τ_α in Fig. 7.17a and 7.17b by showing $D(q_{\min})$ and τ_α, respectively, as functions of the corresponding d^s_∞. Fig. 7.17a presents the diffusivity on the suspension scale, $D(q_{\min})$, as functions of the corresponding diffusivity on the particle scale, d^s_∞, with both along the vorticity direction. The dashed line indicates that $D(q_{\min}) = d^s_\infty$. In general, $D(q_{\min})$ grows linearly with d^s_∞, and $D(q_{\min})$ is slightly higher, suggesting similar diffusion behaviors at different length scales for flowing suspensions. At low d^s_∞, $D(q_{\min})$ does not follow d^s_∞ linearly and is much higher, most likely because the suspension develops large scale fluctuations to help structural rearrangement while at the single-particle level, the particle movement is still limited by the neighboring particle cage. The inset of Fig. 7.17a presents the ratio $D(q_{\min})/d^s_\infty$ as a function of I_v. Although the results scatters due to the difficulties in measuring $D(q)$, they confirm that $D(q_{\min})$ is in generally higher than d^s_∞ for almost all I_v. The diffusivity ratio becomes higher, up to $D(q_{\min})/d^s_\infty \approx 5$, at low I_v, and reduces with growing I_v. The high diffusivity ratio most likely arises from the emergence of flow-arrest transitions. The most significant data scattering is found in glassy suspensions.

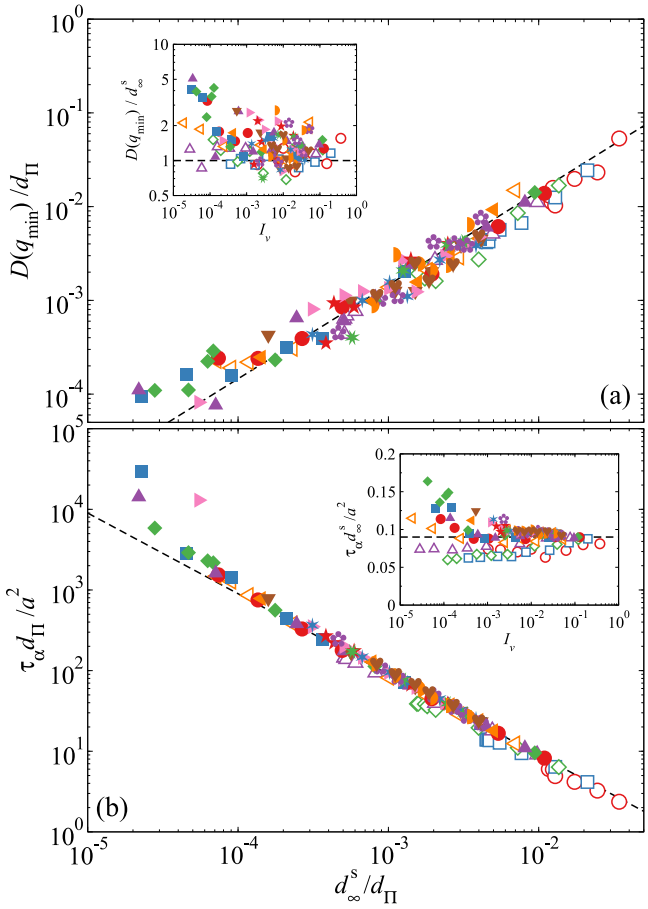

Figure 7.17: (Color online) The wave-number dependent diffusivity measured at $q_{\min}$, $D(q_{\min})$ (a), and the α-relaxation time τ_α (b), as functions of the corresponding long-time self-diffusivity d^s_∞ over a wide range of imposed pressures $\bar{\Pi}$. The symbols are identical to those of Fig. 7.13. The solid line in (a) represents $D(q_{\min}) \propto d^s_\infty$ and in (b) represents $\tau_\alpha^{-1} \propto d^s_\infty$. In the insets, the ratio, $D(q_{\min})/d^s_\infty$ (a), and the product, $\tau_\alpha d^s_\infty$ (b), are presented as functions of I_v. The solid lines in the insets are horizontal. All measurements are taken in the vorticity direction.

Fig. 7.17b presents the connection between τ_α and d^s_∞ in the vorticity direction, with the dashed line outlining $\tau_\alpha^{-1} \propto d^s_\infty$. Fig. 7.17b confirms that τ_α is inversely proportional to d^s_∞, and the results for various $\bar{\Pi}$ collapse onto a single curve. The quality of the collapse is better comparing to Fig. 7.17a, since both d^s_∞ and τ_α describe single-particle behaviors, but $D(q_{\min})$ quantifies the collective suspension behaviors beyond the single-particle level. The relaxation time τ_α deviates from being inversely proportional to d^s_∞ at low d^s_∞, and becomes higher than the dashed line. The inset of Fig. 7.17b shows the product $\tau_\alpha d^s_\infty/a^2$ as functions of I_v over a wide range of $\bar{\Pi}$. At moderate to high I_v, the product is almost a constant insensitive

to I_v. At lower I_v, where the suspensions show an increase in $\max(\chi_4)$, the product becomes more sensitive to I_v. This is especially true for glassy suspensions at higher $\bar{\Pi}$, where the product becomes much higher than the results at high I_v, suggesting longer τ_α, i.e., the diffusion on the cage scale is slower than the single-particle diffusion, consistent with the dynamic heterogeneity description of glass transition [15]. Unlike the glass transition, however, the dynamic heterogeneity arises from both the imposed flow and the particle thermal fluctuations.

Fig. 7.17 quantitatively demonstrates that the diffusion processes at different length scales are consistent for homogeneous flowing suspensions. Unexpected differences arise when the suspensions are near the flow-arrest transitions, because, in this case, the dynamics at various length scales are different.

A model for glassy rheology

The rheology of glassy suspensions at different imposed pressures $\bar{\Pi}$ in Fig. 7.13 shares great similarity in the behaviors near the flow-arrest transitions despite different arrest volume fractions ϕ_m and arrest friction coefficients μ_m. The similarity is especially evident from the almost parallel volume fractions in Fig. 7.13b and the viscosity divergence in Fig. 7.13a. A convenient way to model the suspension behaviors is to express ϕ and μ as,

$$\phi = \phi_m - \delta\phi \quad \text{and} \quad \mu = \mu_m + \delta\mu, \tag{7.35}$$

where the arrest point is (ϕ_m, μ_m). The changes from the arrest point can be expressed as a power law in the viscous number,

$$\delta\phi = K_\phi I_v^{\alpha_\phi} \quad \text{and} \quad \delta\mu = K_\mu I_v^{\alpha_\mu}, \tag{7.36}$$

where the "constants" K_ϕ and α_ϕ characterize $\delta\phi$ and K_μ and α_μ characterize $\delta\mu$: they may, in general, change with the imposed pressure Π. The power law expressions of $\delta\phi$ and $\delta\mu$ in I_v have long been used to characterize the flow of granular materials and non-Brownian suspensions in experiments and in simulations. For example, constant stress and pressure experiments on non-Brownian suspension found that $\alpha_\mu = \alpha_\phi = 0.5$ [26], and experiments in granular matter identified $\alpha_\mu = 1$ [28]. These expressions have been generalized to tensorial forms for continuous modeling the flow behaviors [17]. Moreover, mean-field theories have been developed to predict α_μ and α_ϕ [31].

If the physics of jamming dominates the flow behaviors of the suspensions, Eq. (7.36) should be a reasonable description of the glassy suspension behavior. The weak in-

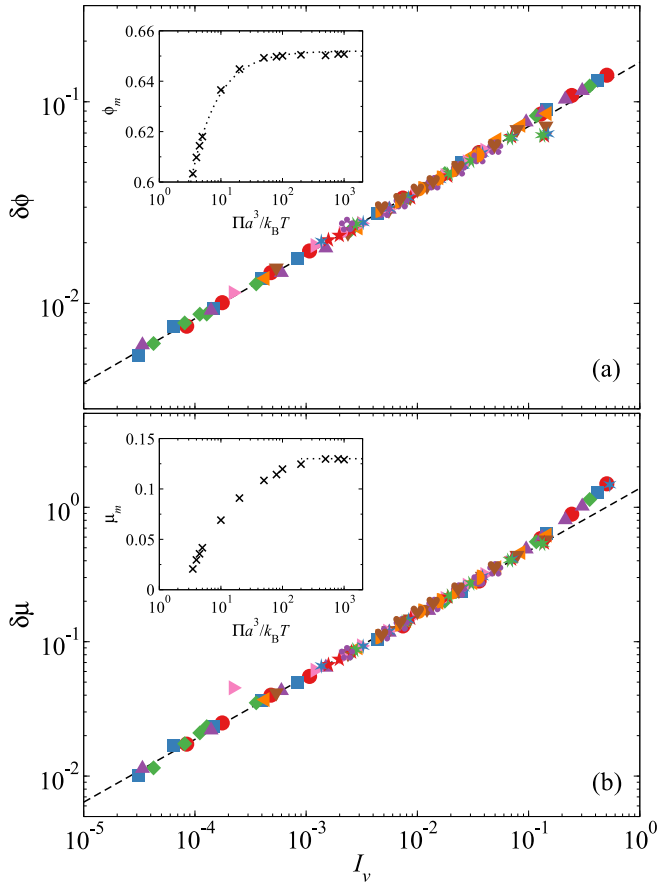

Figure 7.18: (Color online) The incremental volume fraction $\delta\phi = \phi_m - \phi$ (a) and the incremental friction coefficient $\delta\mu = \mu - \mu_m$ (b) as functions of the viscous number I_v for glassy suspensions with $\bar{\Pi} \geq 3.5$. The dashed lines in the main figures highlight the power law relation of Eq. (7.36). The insets show the limiting volume fraction ϕ_m (a) and the limiting friction coefficient μ_m (b) as functions of the imposed pressure $\bar{\Pi}$. The dashed line in the inset of (a) shows Eq. (7.37), and the dashed line in the inset of (b) is the non-Brownian μ_{SAP}. The legends are identical to those in Fig. 7.13.

fluences of thermal fluctuations on the *flow* behaviors also suggests that the constants K_μ, K_ϕ, α_μ, and α_ϕ should be independent of the imposed pressure $\bar{\Pi}$. On the other hand, the arrest point (ϕ_m, μ_m) is affected by thermal fluctuations at low imposed pressure and approaches the SAP at high pressures. We use non-linear regression to simultaneously solve for the constants in Eq. (7.36) as well as the arrest points in Eq. (7.35) that best describe the rheological data in Fig. 7.13 for $I_v < 0.1$.

Fig. 7.18 presents the incremental volume fraction $\delta\phi$ and the incremental friction coefficient $\delta\mu$ as functions of the viscous number I_v from the non-linear regression

Table 7.1: The parameters for the model of glassy suspension rheology in Eq. (7.35)–(7.38) and Eq. (7.42).

K_μ	1.38	μ_G	0.021	$\bar{\Pi}_G$	3.5
α_μ	0.467	ϕ_G	0.603	c_m	0.168
K_ϕ	0.157	μ_{SAP}	0.13	β_y	0.552
α_ϕ	0.32	ϕ_{SAP}	0.652	K_d	0.037

for glassy suspensions with $\bar{\Pi} \geq 3.5$. The constants in Eq. (7.36) are given in Table 7.1. The results show impressive collapse of $\delta\phi$ and $\delta\mu$ at imposed pressures ranging from $\bar{\Pi} = 3.5$ to 1000. Moreover, for $I_v < 0.1$ the data follow the power law relation of Eq. (7.36), shown as dashed lines in Fig. 7.18. With $I_v > 0.1$, the incremental friction coefficient $\delta\mu$ becomes higher than the power relation at lower I_v, suggesting that Eq. (7.35) needs additional terms to captures the suspension behavior.

Fig. 7.18 demonstrates that the flow behavior of glassy suspensions can be described using Eq. (7.36) with constants K_μ, K_ϕ, α_μ, and α_ϕ independent of the imposed pressure $\bar{\Pi}$, and therefore confirms that the physics of jamming dominates the suspension dynamics. This is because the at-rest diffusive process in glassy suspensions, characterized by a diffusivity $d_T(\phi)$, is extremely slow as the particles are locked by their neighbors, i.e., $d_T(\phi)/d_0 \ll 1$. As a result, the suspension effective Péclet number $\text{Pe}_T = \dot{\gamma}a^2/d_T \gg 1$ for any finite strain rate $\dot{\gamma} > 0$, and therefore the suspension dynamics is always effectively in the non-Brownian limit and dominated by jamming.

The exponent $\alpha_\mu = 0.467$, that characterizes the behaviors of the incremental friction coefficient as $\delta\mu \sim I_v^{\alpha_\mu}$, is close to the experimental exponent of 0.5 [26]. This explains the good agreement between the shifted experimental data and the Brownian dynamics simulation results in Ref. [20]. Moreover, fitting the results from hydrodynamic simulations leads to $\alpha_\mu = 0.485$ [84], which is also close to the $\delta\mu$ behaviors here, suggesting weak influences of HIs. On the other hand, that the exponent $\alpha_\phi = 0.32$ that characterizes the volume fraction behaviors $\delta\phi \sim I_v^{\alpha_\phi}$ is 25% smaller than the exponent from hydrodynamic simulations [84], 0.40, suggests stronger influences of HIs.

The insets of Fig. 7.18 show the arrest volume fractions ϕ_m, in Fig. 7.18a, and the arrest friction coefficient μ_m, in Fig. 7.18b, as functions of the imposed pressure $\bar{\Pi}$. Both μ_m and ϕ_m increases with $\bar{\Pi}$ and approaches constant values corresponding

to the SAP. Since the imposed pressure is sufficiently high, we can directly identify the non-Brownian SAP $(\phi_{\mathrm{SAP}}, \mu_{\mathrm{SAP}}) = (0.652, 0.13)$. This is slightly different from the SAP in our previous study [20] due to the differences in the simulation protocol described in Sec. 7.2, and more importantly, the suspension rheology model. In Appendix 7.A we discuss the connection between the model here and the earlier universal viscosity divergence model [20]. Moreover, the arrest volume fractions ϕ_m and the imposed pressures Π are connected via

$$\bar{\Pi} = c_m/(\phi_{\mathrm{SAP}} - \phi_m), \tag{7.37}$$

where the constant c_m is shown in Table 7.1. Eq. (7.37) is a well-known relation for jammed packings [85], and arises from the diverging radial distribution function at contact near jamming. We also found that the μ_m and ϕ_m are well connected via

$$\frac{\mu_{\mathrm{SAP}} - \mu_m}{\mu_{\mathrm{SAP}} - \mu_G} = \left(\frac{\phi_{\mathrm{SAP}} - \phi_m}{\phi_{\mathrm{SAP}} - \phi_G}\right)^{\beta_y}, \tag{7.38}$$

where the constants β_y is also in Table 7.1, and the glass point $(\phi_G, \mu_G) = (0.603, 0.021)$ corresponds to the fitting results at the glassy pressure $\bar{\Pi}_G = 3.5$. The form of Eq. (7.38) also highlights the importance of the physics of jamming, as μ_m is determined as a distance from μ_{SAP} using the volume fraction distance from ϕ_{SAP}. Implicit to Eq. (7.38) is that the glassy state emerges abruptly as soon as the imposed pressure exceed $\bar{\Pi}_G$, and the arrest friction coefficient μ_m suddenly becomes finite. This critical behavior is consistent with the mode-coupling theory picture of the glass transition.

In Fig. 7.13, the yellow shaded area shows the glassy suspension boundary from Eq. (7.35)–(7.38) using the parameters in Table 7.1, and the dashed lines outline the glass limit $\bar{\Pi} = \bar{\Pi}_G$ and the jamming limit $\bar{\Pi} \to \infty$. Comparing to the simulations, the model appropriately outlines the glassy response ($\bar{\Pi} > 3.5$), and matches the simulation rheological outputs including η_s, ϕ, and μ with respect to I_v. However, the rheology model cannot follow the results for $I_v > 0.1$, especially for ϕ and μ, since more terms are required to capture the $\delta\phi$ and $\delta\mu$ behavior.

Fig. 7.19 presents the friction coefficient μ as a function of the volume fraction ϕ. The flow map is qualitatively similar to our earlier work [20]. The flowing suspension behaviors are divided to liquid-like and glassy, with the glassy suspensions near the flow-arrest transitions shown in yellow shaded region following the rheology model. Each symbol represents an isobar in the flow map. For liquid-like suspensions, the isobar becomes vertical and approaches the corresponding equilibrium fraction as

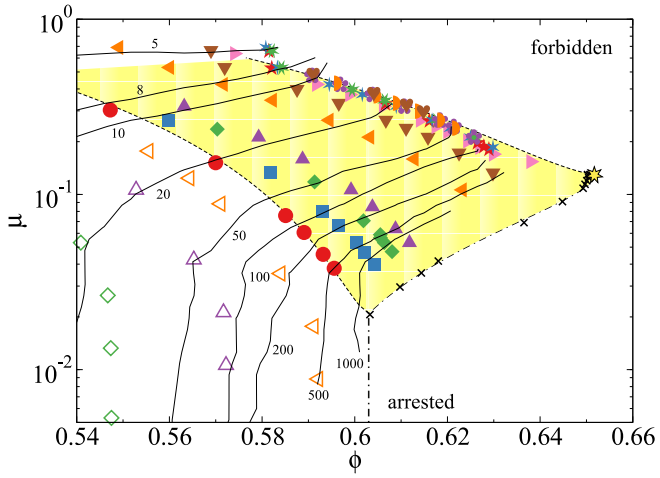

Figure 7.19: (Color online) The *macroscopic* friction coefficient $\mu = \sigma/\Pi$ as functions of the volume fraction ϕ for different imposed pressures $\bar{\Pi}$ for constant stress and pressure simulations. The legends are identical to Fig. 7.13. The shaded region bounded by the dashed lines are from the rheology model outlining the region of glassy behavior. The viscosity contours up to $\eta_s/\eta_0 = 10^3$ are shown in solid lines with annotated viscosity. The crosses show the arrest location (μ_m, ϕ_m) at different imposed pressure, and the dash-dotted line outlines the yield surface from Eq. (7.38). The Shear Arrest Point (SAP) is highlighted as a star at the intersection of the arrested, the forbidden, and the flowing region.

$\mu \to 0$. The glassy suspensions become flowing only if the imposed stress exceeds the yield stress. Therefore, an arrest region emerges at the lower half of Fig. 7.19. The volume fraction at the glassy pressure $\bar{\Pi}_G$ is $\phi_G = 0.603$, consistent with the mode-coupling glass transition point from the experiments on equilibrium colloidal suspensions with similar size polydispersity [22]. Further pressure increase leads to the collapsed non-Brownian behavior, and outlines a non-Brownian limiting behavior. A friction coefficient higher than non-Brownian limiting value is not physical for the given system. Consequently, a forbidden region emerges in the upper corner of the flow map. The intersection of the flowing, the forbidden, and the arrest region defines the SAP $(\phi_{\text{SAP}}, \mu_{\text{SAP}})$, the non-Brownian limit for sheared suspensions. The arrest points for the imposed pressures (ϕ_m, μ_m) are shown as crosses, and the model prediction from Eq. (7.38) is shown as a dash-dotted line. Note that at the glass transition density ϕ_G, our model assumes that the yield stress emerges abruptly.

Also presented in Fig. 7.19 are the suspension viscosity contours up to $\eta_s/\eta_0 = 10^3$. The qualitative features are identical our earlier work [20]. Without HIs, the

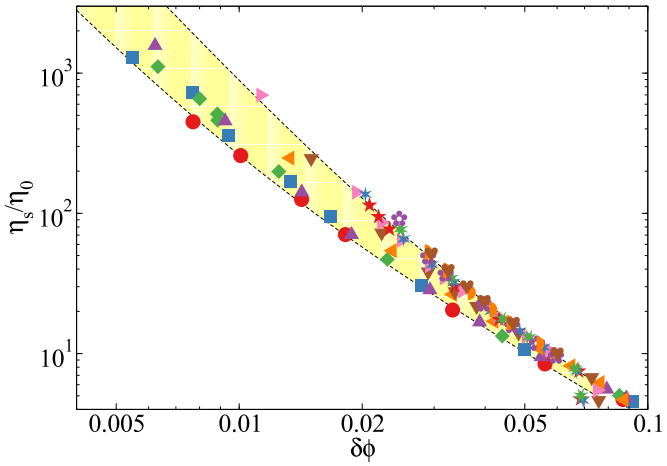

Figure 7.20: (Color online) The shear viscosity η_s/η_0 as a function of the volume fraction distance to the arrest $\delta\phi = (\phi_m - \phi)$ for glassy suspensions with $\bar{\Pi} \geq 3.5$. The yellow shaded region bounded by dashed lines are predictions from Eq. (7.39). The legends are identical to those in Fig. 7.13.

suspension viscosity at constant ϕ continues to decrease to a non-Brownian limiting value at all volume fractions. From linear response theory, the shear stress grows linearly with $\dot{\gamma}$, but the normal stress is increasing proportional to $\dot{\gamma}^2$. Therefore, it is always possible to find $\mu \ll 1$ such that the shear stress is non-zero but osmotic pressure changes little. Therefore, horizontally traversing the flow map in the limit of $\mu \to 0$ access the viscosity of equilibrium suspensions, and one approaches the viscosity divergence at ϕ_G differently from the constant pressure contours. Therefore, the viscosity divergence of equilibrium suspensions is expected to be different from the constant pressure viscosity divergence. Moreover, the rheology model does not describe the viscosity divergence of equilibrium suspensions near the glass transition since μ_m is finite. Near the boundary of the flow-arrest transitions, the viscosity contours are largely parallel to the arrest boundary shown as a dash-dotted line.

Fig. 7.20 explores the shear viscosity divergence of glassy suspensions as a function of the incremental volume fraction $\delta\phi$. The model in Sec. 7.5 shows that η_s changes with $\delta\phi$ as

$$\frac{\eta_s}{\eta_0} = \mu_m \left(\frac{\delta\phi}{K_\phi}\right)^{-\frac{1}{\alpha_\phi}} + K_\mu \left(\frac{\delta\phi}{K_\phi}\right)^{\frac{\alpha_\mu - 1}{\alpha_\phi}} . \tag{7.39}$$

The two-exponent divergence of the shear viscosity is evident in Fig. 7.20, and Eq. (7.39) with $\mu_m = \mu_G$ in the glass limit and $\mu_m = \mu_{\text{SAP}}$ in the jamming limit

describes the glassy suspensions results well in the yellow shaded region. Since μ_m changes from μ_G to μ_{SAP}, the viscosity divergence does not collapse to a universal curve presented in our earlier study [20]. In Appendix 7.A, we show that it is possible to shift the arrest volume fraction to $\hat{\phi}_m$ to recover the earlier universal viscosity divergence. Note that Fig. 7.18a shows the divergence of the normal viscosity $\eta_n \sim \delta\phi^{-1/\alpha_\phi}$, since the viscous number is the inverse normal viscosity, $I_v = \eta_0/\eta_n$.

An interesting corollary from the rheology model is that the strain rate Péclet number $\text{Pe}_{\dot{\gamma}} = \dot{\gamma}a^2/d_0$ at the non-Brownian limit SAP depends on how the SAP is approached. From Eq. (7.36) and (7.37), and the definition of I_v, the strain rate $\dot{\gamma} \sim \Pi(\delta\phi)^{1/\alpha_\phi} \sim \Delta_m^{-1}(\delta\phi)^{1/\alpha_\phi}$ where $\Delta_m = \phi_{\text{SAP}} - \phi_m$. The SAP is the double limit where $\delta\phi \to 0$ and $\Delta_m \to 0$, and the way the double limit is reached affects the value of $\dot{\gamma}$ at the SAP. For the general case of $\Delta_m \sim \delta\phi^p$ with $p > 0$, the strain rate at the SAP scales as $\dot{\gamma} \sim \text{Pe}_{\dot{\gamma}} \sim \delta\phi^{1/\alpha_\phi - p}$. Therefore, if $p > \alpha_\phi^{-1}$, approaching the SAP ($\delta\phi \to 0$) $\text{Pe}_{\dot{\gamma}} \to \infty$, the SAP corresponds to a true non-Brownian limit. If $p < \alpha_\phi^{-1}$, approaching the SAP leads to $\text{Pe}_{\dot{\gamma}} \to 0$. Here, the SAP corresponds to a vanishing $\text{Pe}_{\dot{\gamma}}$, suggesting that a non-Brownian limit with $\text{Pe}_{\dot{\gamma}} \to \infty$ does not exist [86]. Furthermore, when $p = \alpha_\phi^{-1}$, the strain rate Péclet number $\text{Pe}_{\dot{\gamma}}$ is finite at the SAP.

7.6 Connecting rheology, diffusion, and structure

Here we present the connections among the suspension rheology, diffusion, and structures beyond the granular perspective discussed in Sec. 7.5.

A diffusion-rheology flow map

To illustrate the connection between the suspension rheology and diffusion, Fig. 7.21 presents the stress scaled diffusivity d_∞^s/d_σ as functions of the inverse shear viscosity or the scaled strain rate, $\eta_0/\eta_s = \dot{\gamma}\eta_0/\sigma$, for different imposed pressures $\bar{\Pi}$. Scaling the diffusivity with d_σ in Eq. (7.30) leads to distinct behaviors for glassy and liquid-like suspensions. For liquid-like suspensions, the finite zero-shear viscosity and diffusivity lead to the divergence of d_∞^s/d_σ at finite η_0/η_s. Slightly increasing the stress does not significantly change the suspension viscosity, leading to rapid d_∞^s/d_σ reduction. Further stress increase causes the suspension viscosity to decrease due to suspension dilation and shear thinning. That d_∞^s/d_σ decreases with increasing η_0/η_s suggests that the diffusivity d_∞^s is not proportional to $\dot{\gamma}$, a relation commonly found in constant ϕ studies [51]. In the $\sigma \to \infty$ limit, $\phi \to 0$ due to dilation,

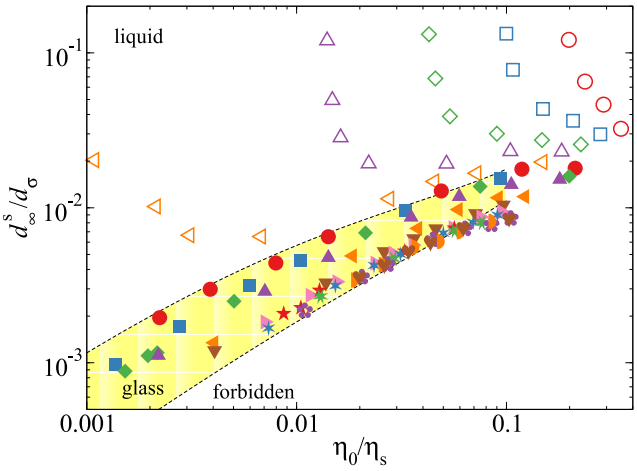

Figure 7.21: (Color online) The stress scaled long-time self-diffusivity in the vorticity direction, d^s_∞/d_σ, with the stress diffusion scale $d_\sigma = (a^2\sigma)/\eta_0$, as functions of the inverse viscosity $\eta_0/\eta_s = \dot{\gamma}\eta_0/\sigma$ over a wide range of imposed pressures $\bar{\Pi}$. The symbols are identical to those of Fig. 7.13. The shaded region bounded dash lines outlines the glassy suspension state from the model.

and therefore $\eta_0/\eta_s \to 1$. The stress-scaled diffusivity $d^s_\infty/d_\sigma \to 0$ as particles do not have neighbors to interact with and only move with the flow due to weak Brownian motions and low suspension volume fractions. However, this behavior can be disrupted by the string formation, which is excluded in Fig. 7.21.

With increasing Π, liquid-like suspensions begin to develop flow-arrest transitions. At $\bar{\Pi} = 3$, the stress-scaled diffusivity diverges at $\eta_0/\eta_s \approx 10^{-3}$. With increasing stress, d^s_∞/d_σ reaches a minimum, increases again to a maximum, and approaches zero as $\eta_0/\eta_s \to 1$. The growth of d^s_∞/d_σ with respect to η_0/η_s shows that the effect of flow overcomes the effect of dilation. With further increasing Π, the suspension enters the glass regime and d^s_∞/d_σ becomes qualitatively different. The divergence of d^s_∞/d_σ vanishes since, for glassy suspensions, the at-rest diffusivity approaches zero and the at-rest viscosity diverges. In Fig. 7.21, the stress-scaled diffusivity emerges from zero at $\eta_0/\eta_s \to 0$ for glassy suspensions. Further increase in Π slows down the growth of the stress-scaled diffusivity with respect to η_0/η_s, and the results begin to collapse as $\Pi \to \infty$, forming a jamming/granular limit. The suspension behavior beyond this limit is not physical regardless of the imposed stresses and pressures.

Fig. 7.21 highlights the distinct behaviors of liquid-like and glassy suspensions, and can be divided into the liquid-like region, the glass region, and the forbidden region.

Here, we present the glass region shaded yellow with dashed lines outlining the liquid-glass boundary and the jamming limit. As is demonstrated in Fig. 7.9b, for an imposed pressure, d^s_∞/d_σ depends only on the strain rate, and is not directly affected by the imposed stress σ. For constant strain rate rheology, Fig. 7.21 provides the connection between suspension mechanics and the dynamics. Moreover, the ratio of d^s_∞/d_σ to η_0/η_s is the strain rate scaled diffusivity $d^s_\infty/(a^2\dot\gamma)$. Fig. 7.21 shows that, for glassy suspensions, there is an upper limit of $d^s_\infty/(a^2\dot\gamma)$ taking place at the flow-arrest transition for each imposed pressure, and further increase in the stress reduces the diffusivity $d^s_\infty/(a^2\dot\gamma)$. Increasing Π reduces the maximum $d^s_\infty/(a^2\dot\gamma)$, and in the non-Brownian jamming limit ($\Pi \to \infty$), the at-rest diffusivity $d^s_\infty/(a^2\dot\gamma)$ reaches a minimum. In non-Brownian suspensions with hydrodynamic interactions, increasing flow also leads to decreasing scaled diffusivity $d^s_\infty/(a^2\dot\gamma)$ [87]. Clearly, this behavior does not originate from HIs.

Emerging Stokes-Einstein-Sutherland relation

To understand the suspension dynamics, comparing the time scale of particle diffusion, a^2/d^s_∞, to the time scale of flow, $\dot\gamma^{-1}$, defines a long-time Péclet number $\overline{\mathrm{Pe}}$,

$$\overline{\mathrm{Pe}} = \dot\gamma a^2/d^s_\infty. \tag{7.40}$$

The particle behaviors are driven by flow if $\overline{\mathrm{Pe}} \gg 1$ and by diffusion if $\overline{\mathrm{Pe}} \ll 1$. To account for particle interactions, we define the interaction friction coefficient

$$\mu^{\mathrm{I}} = \mu - (1 + \tfrac{5}{2}\phi)I_v, \tag{7.41}$$

which arises from the interparticle stress $\sigma^{\mathrm{I}} = \sigma - (1 + \frac{5}{2}\phi)\eta_0\dot\gamma$, and is identical to ${\sigma_{12}}^{\mathrm{P}}$ in Eq. (7.9) for systems without HIs. Accordingly, the interaction viscosity is defined as $\eta^{\mathrm{I}} = \mu^{\mathrm{I}}/I_v$. In the limit of vanishing flow, $I_v \to 0$, the interaction quantities approach the suspension quantities, $\mu^{\mathrm{I}} \to \mu$ and $\eta^{\mathrm{I}} \to \eta_s$.

Fig. 7.22a presents μ^{I} as a function of $\overline{\mathrm{Pe}}$ for a wide range of imposed pressures. Surprisingly, *all* the results for liquid-like and glassy suspensions collapse on to a single master curve, showing a universal connection between the suspension rheology and dynamics. Liquid-like suspensions can achieve both $\overline{\mathrm{Pe}} < 1$ and $\overline{\mathrm{Pe}} > 1$. For liquid-like suspensions, with weak imposed flow $\overline{\mathrm{Pe}} \ll 1$, the diffusion process is dominated by thermal fluctuations characterized by the zero-shear diffusivity. On the other hand, glassy suspensions can only reach $\overline{\mathrm{Pe}} \gtrsim 1$, showing that the diffusion process follows the imposed flow, as the at-rest diffusion is zero.

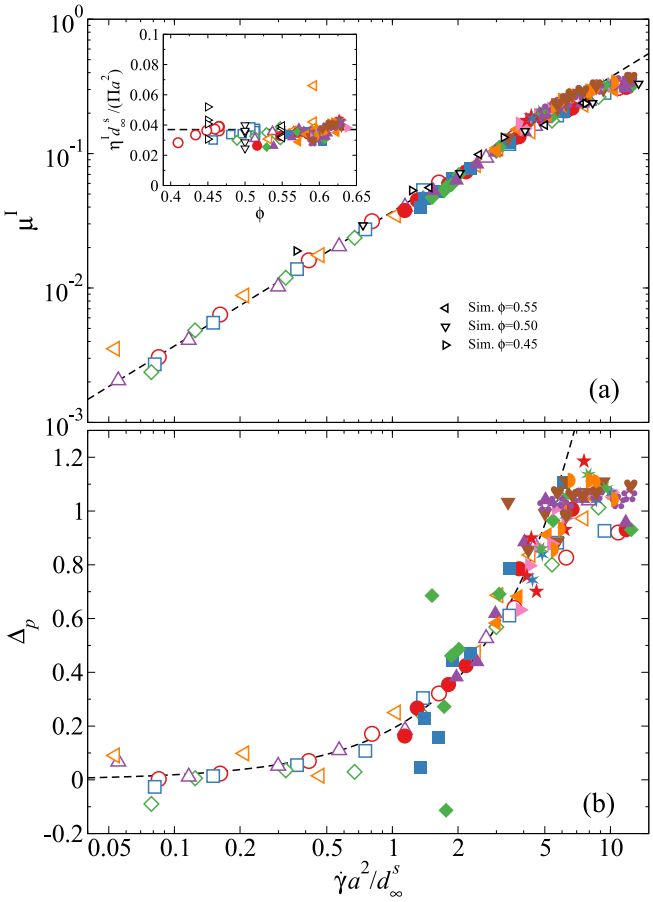

Figure 7.22: (Color online) (a) The interaction friction coefficient, $\mu^{\mathrm{I}} = \mu - (1 + \frac{5}{2}\phi)I_v$, as a function of the long-time Péclet number $\dot{\gamma}a^2/d^s_\infty = \overline{\mathrm{Pe}}$ over a wide range of imposed pressure $\bar{\Pi}$. The dashed line shows the linear relation of Eq. (7.42). The inset shows the scaled product $\eta^{\mathrm{I}} d^s_\infty/(\Pi a^2)$ as a function of the volume fraction ϕ, with the interaction viscosity $\eta^{\mathrm{I}} = \mu^{\mathrm{I}}/I_v$. Also presented are the constant volume Brownian Dynamics simulation results [51] at different ϕ. (b) The peak difference $\Delta_p = \max(g_{\mathrm{comp}}) - \max(g_{\mathrm{ext}})$ as a function of $\overline{\mathrm{Pe}}$. The dashed line represents the linear relation $\Delta_p = K_p\overline{\mathrm{Pe}}$ with $K_p = 0.19$. In (a) and (b), the symbols are identical to those of Fig. 7.13.

The following equation describes the data collapse in Fig. 7.22a for $\overline{\mathrm{Pe}} \lesssim 5$:

$$\mu^{\mathrm{I}} = K_d\overline{\mathrm{Pe}}, \tag{7.42}$$

where the constant $K_d = 0.037$. This is confirmed by the dashed line in Fig. 7.22. Rearranging Eq. (7.42) leads to

$$\eta^{\mathrm{I}} d^s_\infty/(\Pi a^2) = K_d. \tag{7.43}$$

The inset of Fig. 7.22a presents $\eta^{\mathrm{I}} d^s_\infty/\Pi$ as a function of the volume fraction ϕ. As expected, $\eta^{\mathrm{I}} d^s_\infty/\Pi \approx 0.037$ regardless of the volume fraction, the imposed stresses, and the confining pressures. Introducing an effective temperature $k_{\mathrm{B}}T_{\mathrm{eff}} = \Pi a^3$, Eq. (7.43) resembles an SES relation with T_{eff}. For $\overline{\mathrm{Pe}} \gtrsim 5$, the interaction friction coefficient μ^{I} becomes lower than the expected linear relation in Fig. 7.22. Here, the dynamics of flow become significantly faster than the diffusive dynamics. In this limit, the suspension begins to develop string phase structures that further suppresses the particle diffusion, leading to this deviation. Fig. 7.22a shows that the suspension pressure is a crucial aspect for modeling the dynamics of dense suspensions. Indeed, this is also apparent in Eq. (7.19) for weakly sheared suspensions, where the contact value $g^{\mathrm{eq}}(2)$ is proportional to the suspension pressure. Our results extend this insight to dense and strongly sheared suspensions.

In Fig. 7.22, for glassy suspensions $\overline{\mathrm{Pe}} \gtrsim 1$, and the minimum $\overline{\mathrm{Pe}}$ takes place in the limit of the glass transition. This is consistent with the highest slope of in the liquid-glass boundary in Fig. 7.21. With $\overline{\mathrm{Pe}} \approx 1$, the corresponding $\mu^{\mathrm{I}} \approx 0.03$, is slightly higher than the glass transition friction coefficient μ_G in Table 7.1. Therefore, as the suspension becomes glassy, it abruptly attains a finite yield stress, consistent with the glassy dynamics in the mode-coupling theory [4]. On the other hand, in the non-Brownian SAP, the limiting friction coefficient $\mu_{\mathrm{SAP}} \approx 0.13$ corresponds to $\overline{\mathrm{Pe}} \approx 4.2$ in Fig. 7.22a. Here, as the volume fraction reaches ϕ_{SAP}, the particle diffusivity also approaches its maximum. This is also consistent with the findings of Fig. 7.21, suggesting that for non-Brownian suspensions, particle diffusion arises from particle interactions, which reaches maximum in the jamming limit.

Fig. 7.22a also presents the constant volume and constant strain rate simulations of Foss and Brady [51] in triangles at different volume fractions. Despite small differences, the earlier results agree with the constant stress and pressure simulations. The differences most likely arise from the monodisperse systems used by Foss and Brady [51], which is more prone to structural developments at low and high strain rates comparing to polydisperse systems here. The agreement shows that data collapse in Fig. 7.22 is not specific to the constant stress and pressure rheology, and is general for hard-sphere suspensions.

The universal SES relation revealed in Fig. 7.22a is a new discovery on the rheology and dynamics of dense colloidal suspensions. For dense systems without shear, the SES relation is generally violated due to dynamic heterogeneity [43], with the notable exception of systems with ultra soft potentials [88, 89]. The results demonstrates

the critical role of the suspension pressure in particle diffusive dynamics, and confirms the idea that pressure sets the internal time scale of system [28]. More specifically, the suspension pressure can be considered an effective temperature $T_{\text{eff}} \propto \Pi$. Comparing to other definitions of the effective temperatures [45, 46, 90], $T_{\text{eff}} \propto \Pi$ is rather simple. However, it satisfies the fluctuation-dissipation relation (the SES relation), and in the dilute limit, $T_{\text{eff}} \to T$. Distinct from other studies, in this work the base state is the infinitely dilute suspension, suggesting that both the imposed flow and the presence of particles drive the system away from the base state.

Structure, diffusion, and rheology

In Fig. 7.22b we adopt the structural peak difference,

$$\Delta_p = \max(g_{\text{comp}}) - \max(g_{\text{ext}}), \tag{7.44}$$

to characterize how the suspension microstructure connects to its diffusive and rheological behavior. The peak difference Δ_p illustrates the suspension structural distortions, and approximates the structural contributions to the hard-sphere Brownian stresses in Eq. (7.19). Fig. 7.22b shows Δ_p as a function of the long-time Péclet number $\overline{\text{Pe}}$ over a wide range of confining pressures $\bar{\Pi}$. Despite some data scattering due to difficulties in measuring the suspension structures near the flow-arrest transition, the peak difference Δ_p also collapses with respect to $\overline{\text{Pe}}$, illustrating the structural changes are in concert with the suspension rheology and dynamics in a universal way.

When $\overline{\text{Pe}} \lesssim 5$, the peak difference Δ_p is linear in $\overline{\text{Pe}}$ as,

$$\Delta_p = K_p \overline{\text{Pe}}, \tag{7.45}$$

where $K_p \approx 0.19$, The linear relation is illustrated in dashed line in Fig. 7.22b. Therefore, the structural distortion is independent of Π for dense suspensions even close to the SAP. With $\mu^{\text{I}} \propto \overline{\text{Pe}}$ in Eq. (7.42), we reach a stress-structure relation,

$$\sigma^{\text{I}} = (K_d/K_p)\Pi\Delta_p, \tag{7.46}$$

suggesting that the shear stress is only related to the structural distortion and the suspension pressure, and is also consistent with the linear response results of Eq. (7.19). For liquid-like suspensions, Δ_p emerges from zero and grows linearly with $\overline{\text{Pe}}$, suggesting that the structural distortion emerges smoothly from isotropic equilibrium

suspensions. For glassy suspensions, however, because $\overline{\mathrm{Pe}} \gtrsim 1$, the structural distortion is present even at the flow-arrest transition. Therefore, the glassy suspension structures are inherently distorted, and the distortion grows with the flow. In the high pressure limit ($\bar{\Pi} \to \infty$), Δ_p is a minimum at the SAP. Clearly, structural distortion proceeds flow in dense suspensions. The finite structural distortion also suggests that the SAP is inherently anisotropic, and is distinct from the isotropic jammed state obtained from protocols such as rapid compression [63] or energy minimization [91].

At higher $\overline{\mathrm{Pe}}$, Δ_p becomes insensitive to $\overline{\mathrm{Pe}}$ and reaches a plateau. For the same $\overline{\mathrm{Pe}}$ range, Fig. 7.22a shows that μ^{I} deviates from the linear relation $\mu^{\mathrm{I}} \propto \overline{\mathrm{Pe}}$. These behaviors show, as expected, that the suspension structures are intimately related to the stresses. Further increasing $\overline{\mathrm{Pe}}$ leads to string phase formation, which further suppresses the particle diffusion and reduces the peak difference Δ_p. Therefore, $\overline{\mathrm{Pe}} \gtrsim 5$ implies that the suspension enters a new regime, where the suspension structures and rheology are less sensitive to $\overline{\mathrm{Pe}}$, preceding the order formation.

7.7 Summary and Conclusions

In this work, we studied the constant shear stress and pressure rheology of dense hard-sphere colloidal suspensions using Brownian Dynamics simulations without HIs. We particularly focused on the mechanical response, structural features, and diffusive dynamics of suspensions exhibiting flow-arrest transitions. Mechanically, comparing to constant volume rheology, fixing the confining pressure leads to dilation and stronger shear thinning in the shear and normal viscosities, η_s and η_n. With increasing confining pressure, the suspension changes from liquid-like to glassy, and flows only if the imposed stress exceeds the yield stress. Structurally, the suspension develops string phase at high imposed stress. For amorphous suspensions, the structural distortion increases with increasing stress. Dynamically, different characterizations of the suspension diffusion, including the long-time self-diffusivity d^s_∞, the wave-space diffusivity at the minimum wave number $D(q_{\min})$, the α-relaxation time τ_α near the first peak of the static structure factor, and the dynamic susceptibility χ_4, exhibit similar behaviors in the velocity gradient and the vorticity directions. The formation of a string phase qualitatively alters the suspension diffusive dynamics.

We analyzed the temporal and spatial dynamics of glassy suspensions near the flow-arrest transitions. By temporal coarse graining, we found that that the strain

rate distribution $P(\dot{\gamma})$ near the flow-arrest transition consists of a sharp peak in the arrested state and a broader peak at finite strain rate. Increasing the imposed stress eliminates the peak in the arrested state, and shifts $P(\dot{\gamma})$ towards a Gaussian. The stress-scaled diffusivity d^s_∞/d_σ is independent of σ and ϕ and is only directly controlled by the $\dot{\gamma}$ and Π. In addition, by analyzing particle trajectories, we found that the immediate neighbors of a *fast* particle are more likely to be fast, suggesting that the emergence of flow from an arrested state involves cooperative motions of fast particles in a dynamically heterogeneous fashion.

We characterized the suspension rheology using the viscosity number $I_v = \dot{\gamma}\eta_0/\Pi$, emphasizing the importance of pressure. In the limit of $\Pi \to \infty$, the suspension approaches the non-Brownian limit, and with vanishing I_v the friction coefficient reaches a minimum and the volume fraction reaches a maximum known as the SAP, $(\phi_{\text{SAP}}, \mu_{\text{SAP}})$ [20]. For normal stress differences, $N_1 > 0$ and $N_2 < 0$ for all imposed pressures. The suspension structural distortion, characterized by the peak values of the pair distribution function in the compressional and the extensional axes, $\max(g_{\text{comp}})$ and $\max(g_{\text{ext}})$, decreases with I_v and collapses in the $\Pi \to \infty$ limit. Moreover, suspension diffusion behaviors over different length scales show consistent behaviors, and reveal the non-Brownian high-pressure limiting behaviors when scaled with pressure.

We found that glassy suspensions begin to flow from an arrest point (ϕ_m, μ_m), which asymptotes the SAP in the $\Pi \to \infty$ limit. Away from the arrest point, the incremental friction coefficient $\delta\mu$ and the incremental volume fraction $\delta\phi$ change with the viscous number following power laws in Eq. (7.36), with the same constants for all pressures of glassy suspensions. The results show that the physics of jamming dominates the glassy suspension behavior, and thermal fluctuations only affect the arrest location. The results also show that the behavior of glassy suspensions can be succinctly summarized in a simple rheology model.

We discovered connections in the suspension structure, dynamics, and mechanics. We first constructed a diffusion-rheology map of the stress-scaled diffusivity and the inverse shear viscosity, with distinct liquid-like and glassy suspension behaviors. Since the stress-scaled diffusivity is only directly affected by Π and $\dot{\gamma}$, this flow map provides a direct connection between the suspension diffusion and rheology. We also found that the interaction friction coefficient μ^{I} as a function of $\dot{\gamma}a^2/d^s_\infty$ collapses for all imposed pressures and stresses, and that $\mu^{\text{I}} \propto \dot{\gamma}a^2/d^s_\infty$ when $\dot{\gamma}a^2/d^s_\infty \lesssim 5$. This leads to a non-equilibrium SES relation between η^{I} and d^s_∞

with an effective temperature proportional to the pressure, $T_{\text{eff}} \propto \Pi$. In addition, the suspension structural distortions, characterized by the peak difference Δ_p, also collapses as functions of $\dot{\gamma}a^2/d_\infty^s$, illustrating the close connection between the suspension structure and rheology.

This work is a comprehensive investigation of the constant stress and pressure rheology of dense colloidal suspensions. The results demonstrate the critical role of suspension pressure, and show that the granular perspective based on the viscous number is effective in connecting the behaviors of Brownian and non-Brownian suspensions. Our work also provides new perspectives in the mean-field modeling of colloidal suspensions using an effective temperatures proportional to the pressure. Moreover, the rheology and diffusion model is useful for predicting macroscopic suspension behaviors including particle migration and mixing in complex geometries and flow conditions [92].

7.A Universal viscosity divergences

The rheology of glassy suspensions in Sec. 7.5 can also be described using the universal divergence of the shear viscosity $\eta_s = \sigma/\dot{\gamma}$ and the incremental normal viscosity $\eta_n' = (\Pi - \Pi^{\text{eq}})/\dot{\gamma}$ in Eq. (7.1) with $\alpha = 2$ using a different set of arrest volume fractions $\hat{\phi}_m$. Fig. 7.23 presents η_s and η_n' as functions of the incremental volume fraction $\delta\hat{\phi} = \hat{\phi}_m - \phi$. With the new set of $\hat{\phi}_m$, both η_s and η_n' collapse and $\{\eta_s, \eta_n'\} \propto \delta\hat{\phi}^2$. The results are consistent with earlier findings [20]. The inset of Fig. 7.23 show the shift in $\hat{\phi}_m$ from the arrest volume fraction ϕ_m in Fig. 7.18a, $\Delta\phi = \hat{\phi}_m - \phi_m$ as a function of the imposed pressure $\bar{\Pi}$. The volume fraction difference $\Delta\phi$ in the glass limit, $\bar{\Pi} = \bar{\Pi}_G = 3.5$, is almost zero, and decreases to $\Delta\phi \approx -0.01$ in the $\Pi \to \infty$ limit, reducing the ϕ_{SAP} from 0.652 using models in Sec. 7.5 to 0.642 via Eq. (7.1), much closer to earlier results [20]. Clearly, the value of ϕ_{SAP} depends on the model selected to describe the data.

Moreover, the constants k_s and k_n in Eq. (7.1) can also be interpreted using the rheology model of Eq. (7.36), but the constant $K_\phi = K_\phi(\Pi)$ is also a function of the imposed pressure. Therefore, the universal viscosity divergence in Ref. [20] suggests that

$$k_s = \mu_m K_\phi^{\frac{1}{\alpha_\phi}} \quad \text{and} \quad k_n = \left(1 - \frac{\Pi^{\text{eq}}}{\Pi}\right) K_\phi^{\frac{1}{\alpha_\phi}} \tag{7.47}$$

are also constants. Note that at the flow-arrest transitions, the pressure is not the same as Π^{eq} since dilation precedes flow. The viscosity divergence description solely depends on the volume fraction behaviors and address changes in $\delta\mu$. Therefore,

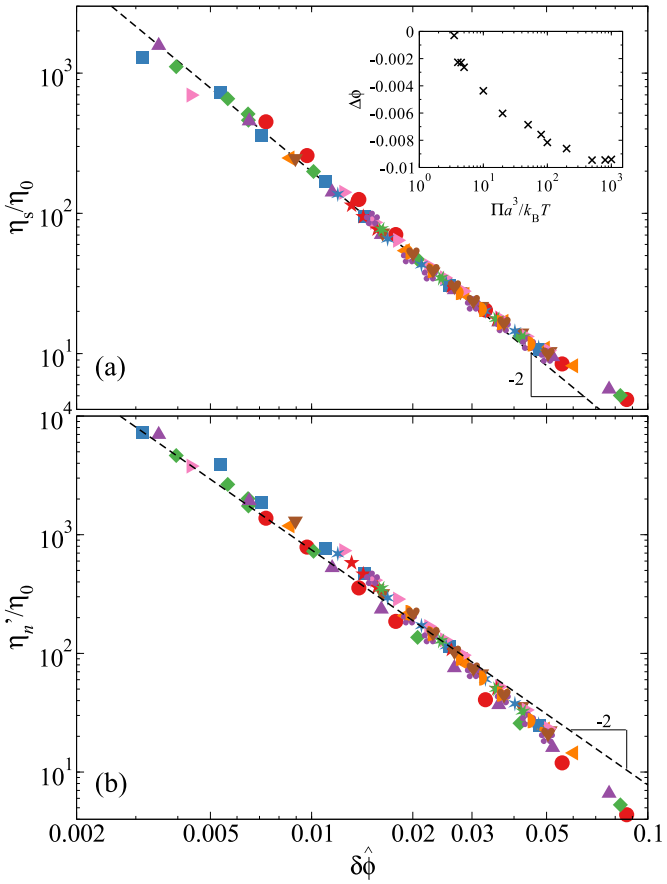

Figure 7.23: The shear viscosity η_s (a) and the incremental normal viscosity η_n' (b) as functions of the volume fraction distance from arrest $\delta\hat{\phi} = \hat{\phi}_m - \phi$. The dashed lines present the algebraic viscosity divergence $\{\eta_s, \eta_n'\} \propto \delta\hat{\phi}^2$. The inset shows the arrest volume fraction difference $\Delta\phi = \hat{\phi}_m - \phi_m$ as a function of the imposed pressure $\bar{\Pi}$, with ϕ_m from the inset of Fig. 7.18a. The legends are identical to those of Fig. 7.13.

despite the same physical interpretation of the suspension behaviors, the model in Sec. 7.5 have a wider range of applicability due to the additional descriptions on $\delta\mu$.

Another interpretation of Eq. (7.1) is based on the Herschel-Bulkley rheology of the pressure,

$$\Pi(\phi, \dot{\gamma}) = \Pi_m(\phi) + a(\phi)\dot{\gamma}^{\alpha_\gamma}, \tag{7.48}$$

and the existence of yield stress and pressure [93]. Expanding Eq. (7.48) at the flow-arrest transition with zero strain rate and the volume fraction ϕ_m to a flowing state with $(\phi, \dot{\gamma})$, we have

$$\Delta\Pi = -\partial\Pi/\partial\phi|_{(\phi_m,0)}\delta\phi + \partial\Pi/\partial(\dot{\gamma}^{\alpha_\gamma})|_{(\phi_m,0)}\dot{\gamma}^{\alpha_\gamma}. \tag{7.49}$$

Solving for $\dot{\gamma}$ in Eq. (7.49) with constant imposed pressure, $\Delta\Pi = 0$, leads to $\dot{\gamma} \propto \delta\phi^{1/\alpha_\gamma}$. Therefore, with finite yield stress σ_m and yield pressure difference $(\Pi_m - \Pi^{eq})$, Eq. (7.48) suggests the viscosities $\{\eta_s, \eta_n'\} \propto \delta\phi^{1/\alpha_\gamma}$. Note that $\Pi_m(\phi) > \Pi^{eq}(\phi)$ because dilation precedes flow in glassy suspensions. With $\alpha_\gamma = 0.5$, this interpretation connects our works to earlier constant volume studies with soft particle systems [21, 25, 32]. However, this interpretation also ignores changes in $\delta\mu$ and suffers similar limitations as Eq. (7.47).

References

[1] W. B. Russel, D. A. Saville, and W. R. Schowalter, *Colloidal dispersions* (Cambridge University Press, 1991).

[2] R. J. Hunter, *Foundations of colloid science* (Oxford University Press, 2001).

[3] P. N. Pusey and W. van Megen, "Phase behaviour of concentrated suspensions of nearly hard colloidal spheres", Nature **320**, 340 (1986).

[4] W. Götze, *Complex dynamics of glass-forming liquids: a mode-coupling theory* (Oxford University Press, 2008).

[5] G. L. Hunter and E. R. Weeks, "The physics of the colloidal glass transition", Rep. Prog. Phys. **75**, 066501 (2012).

[6] N. Koumakis, M. Laurati, S. U. Egelhaaf, J. F. Brady, and G. Petekidis, "Yielding of hard-sphere glasses during start-up shear", Phys. Rev. Lett. **108**, 098303 (2012).

[7] M. Ballauff, J. M. Brader, S. U. Egelhaaf, M. Fuchs, J. Horbach, N. Koumakis, M. Krüger, M. Laurati, K. J. Mutch, G. Petekidis, M. Siebenbürger, T. Voigtmann, and J. Zausch, "Residual stresses in glasses", Phys. Rev. Lett. **110**, 215701 (2013).

[8] H. M. Laun, "Rheological properties of aqueous polymer dispersions", Angewandte Makromolekulare Chemie **123/124**, 335 (1984).

[9] X. Cheng, J. H. McCoy, J. N. Israelachvili, and I. Cohen, "Imaging the microscopic structure of shear thinning and thickening colloidal suspensions", Science **333**, 1276 (2011).

[10] N. J. Wagner and J. F. Brady, "Shear thickening in colloidal dispersions", Phys. Today **62**, 27 (2009).

[11] C. D. Cwalina and N. J. Wagner, "Material properties of the shear-thickened state in concentrated near hard-sphere colloidal dispersions", J. Rheol. **58**, 949 (2014).

[12] J. Mewis and N. J. Wagner, *Colloidal suspension rheology* (Cambridge University Press, 2013).

[13] S. Torquato and F. H. Stillinger, "Jammed hard-particle packings: from kepler to bernal and beyond", Rev. Mod. Phys. **82**, 2633 (2010).

[14] A. J. Liu and S. R. Nagel, "Nonlinear dynamics: jamming is not just cool any more", Nature **396**, 21 (1998).

[15] L. Berthier and G. Biroli, "Theoretical perspective on the glass transition and amorphous materials", Rev. Mod. Phys. **83**, 587 (2011).

[16] A. J. Liu and S. R. Nagel, "The jamming transition and the marginally jammed solid", Annu. Rev. Condens. Matter Phys. **1**, 347 (2010).

[17] Y. Forterre and O. Pouliquen, "Flows of dense granular media", Annu. Rev. Fluid Mech. **40**, 1 (2008).

[18] M. Rubinstein and R. H. Colby, *Polymer physics* (Oxford University Press, 2003).

[19] P. Guan, M. Chen, and T. Egami, "Stress-temperature scaling for steady-state flow in metallic glasses", Phys. Rev. Lett. **104**, 205701 (2010).

[20] M. Wang and J. F. Brady, "Constant stress and pressure rheology of colloidal suspensions", Phys. Rev. Lett. **115**, 158301 (2015).

[21] A. Ikeda, L. Berthier, and P. Sollich, "Unified study of glass and jamming rheolgy in soft particle systems", Phys. Rev. Lett. **109**, 018301 (2012).

[22] G. Brambilla, D. El Masri, M. Pierno, L. Berthier, L. Cipelletti, G. Petekidis, and A. Schofield, "Probing the equilibrium dynamics of colloidal hard spheres above the mode-coupling glass transition", Phys. Rev. Lett. **102**, 085703 (2009).

[23] W. van Megen, T. C. Mortensen, S. R. Williams, and J. Müller, "Measurement of the self-intermediate scattering function of suspensions of hard spherical particles near the glass transition", Phys. Rev. E **58**, 6073 (1998).

[24] J. Reinhardt, F. Weysser, and M. Fuchs, "Comment on "probing the equilibrium dynamics of colloidal hard spheres above the mode-coupling glass transition"", Phys. Rev. Lett. **105**, 199604 (2010).

[25] A. Ikeda, L. Berthier, and P. Sollich, "Disentangling glass and jamming physics in the rheology of soft materials", Soft Matter **9**, 7669 (2013).

[26] F. Boyer, E. Guazzelli, and O. Pouliquen, "Unifying suspension and granular rheology", Phys. Rev. Lett. **107**, 188301 (2011).

[27] W. B. Russel, N. J. Wagner, and J. Mewis, "Divergence in the low shear viscosity for brownian hard sphere dispersions: at random close packing or the glass transition?", J. Rheo. **57**, 1555 (2013).

[28] P. Jop, Y. Forterre, and O. Pouliquen, "A constitutive law for dense granular flows", Nature **441**, 727 (2006).

[29] M. Trulsson, B. Andreotti, and P. Claudin, "Transition from the viscous to inertial regime in dense suspensions", Phys. Rev. Lett. **109**, 118305 (2012).

[30] E. Lerner, G. Düring, and M. Wyart, "A unified framework for non-brownian suspension flows and soft amorphous solids", Proc. Natl. Acad. Sci. U.S.A. **109**, 4798 (2012).

[31] E. DeGiuli, G. Düring, E. Lerner, and M. Wyart, "Unified theory of inertial granular flows and non-brownian suspensions", Phys. Rev. E **91**, 062206 (2015).

[32] T. Kawasaki, D. Coslovich, A. Ikeda, and L. Berthier, "Diverging viscosity and soft granular rheology in non-brownian suspensions", Phys. Rev. E **91**, 012203 (2015).

[33] J. K. G. Dhont, *An introduction to dynamics of colloids* (Elsevier, Amsterdam, 1996).

[34] A. J. Banchio and G. Nägele, "Short-time transport properties in dense suspensions: from neutral to charge-stabilized colloidal spheres", J. Chem. Phys. **128**, 104903 (2008).

[35] A. M. Leshansky and J. F. Brady, "Dynamic structure factor study of diffusion in strongly sheared suspensions", J. Fluid Mech. **527**, 141 (2005).

[36] A. M. Leshansky, J. F. Morris, and J. F. Brady, "Collective diffusion in sheared colloidal suspensions", J. Fluid Mech. **597**, 305 (2008).

[37] C. Toninelli, M. Wyart, L. Berthier, G. Biroli, and J.-P. Bouchaud, "Dynamical susceptibility of glass formers: contrasting the predictions of theoretical scenarios", Phys. Rev. E **71**, 041505 (2005).

[38] D. Lootens, H. Van Damme, and P. Hebraud, "Giant stress fluctuations at the jamming transition", Phys. Rev. Lett. **90**, 178301 (2003).

[39] C. Heussinger, L. Berthier, and J.-L. Barrat, "Superdiffusive, heterogeneous, and collective particle motion near the fluid-solid transition in athermal disordered materials", Europhys. Lett. **90**, 20005 (2010).

[40] C. Heussinger, P. Chaudhuri, and J.-L. Barrat, "Fluctuations and correlations during the shear flow of elastic particles near the jamming transition", Soft Matter **6**, 3050 (2010).

[41] A. Einstein, "Eine neue bestimmung der moleküldimensionen", Annalen der Physik **19**, 289 (1906).

[42] J. H. Simpson and H. Y. Carr, "Diffusion and nuclear spin relaxation in water", Phys. Rev. **111**, 1201 (1958).

[43] S. Kumar, G. Szamel, and J. F. Douglas, "Nature of the breakdown in the stokes-einstein relarelation in a hard sphere fluid", J. Chem. Phys. **124**, 214501 (2006).

[44] M. C. Miguel and J. M. Rubi, eds., *Jamming, yielding, and irreversible deformation in condensed matter* (Springer, 2006).

[45] L. F. Cugliandolo, "The effective temperature", J. Phys. A: Math. Theor. **44**, 483001 (2011).

[46] T. K. Haxton, "Ratio of effective temperature to pressure controls the mobility of sheared hard spheres", Physical Review E **85**, 011503 (2012).

[47] J. F. Brady, A. S. Khair, and M. Swaroop, "On the bulk viscosity of suspensions", J. Fluid Mech. **554**, 109 (2006).

[48] H. Goldstein, C. P. Poole Jr., and J. L. Safko, *Classical mechanics* (Addison-Wesley, 2001).

[49] D. M. Heyes and J. R. Melrose, "Brownian dynamics simulations of model hard-sphere suspensions", J. Non-Newtonian Fluid Mech. **46**, 1 (1993).

[50] W. Schaertl and H. Sillescu, "Brownian dynamics simulations of colloidal hard spheres. effects of sample dimensionality on self-diffusion", J. Stat. Phys. **74**, 687 (1994).

[51] D. R. Foss and J. F. Brady, "Brownian dynamics simulation of hard-sphere colloidal dispersions", J. Rheol. **44**, 629 (2000).

[52] P. Strating, "Brownian dynamics simulation of a hard-sphere suspension", Phys. Rev. E **59**, 2175 (1999).

[53] M. Laurati, K. J. Mutch, N. Koumakis, J. Zausch, C. P. Amann, A. B. Schofield, G. Petekidis, J. F. Brady, J. Horbach, M. Fuchs, and S. U. Egelhaaf, "Transient dynamics in dense colloidal suspensions under shear: shear rate dependence", J. Phys.: Condens. Matter **24**, 464104 (2012).

[54] N. Koumakis, J. F. Brady, and G. Petekidis, "Complex oscillatory yeilding of model hard-sphere glasses", Phys. Rev. Lett. **110**, 178301 (2013).

[55] I. C. Carpen and J. F. Brady, "Microrheology of colloidal dispersions by brownian dynamics simulations", J. Rheo. **49**, 1483 (2005).

[56] R. N. Zia and J. F. Brady, "Stress development, relaxation, and memory in colloidal dispersions: transient nonlinear microrheology", J. Rheo. **57**, 457 (2013).

[57] U. M. Córdova-Figueroa and J. F. Brady, "Osmotic propulsion: the osmotic motor", Phys. Rev. Lett. **100**, 158303 (2008).

[58] S. C. Takatori, W. Yan, and J. F. Brady, "Swim pressure: stress generation in active matter", Phys. Rev. Lett. **113**, 028103 (2014).

[59] B. Lander, U. Seifert, and T. Speck, "Mobility and diffusion of a tagged particle in a driven colloidal suspension", Europhys. Lett. **92**, 58001 (2010).

[60] H. Jin, K. Kang, K. H. Ahn, and J. K. G. Dhont, "Flow instability due to coupling of shear-gradients with concentration: non-uniform flow of (hard-sphere) glasses", Soft Matter **10**, 9470 (2014).

[61] D. M. Heyes and H. Sigurgeirsson, "The newtonian viscosity of concentrated stabilized dispersions: comparisons with the hard sphere fluid", J. Rheo. **48**, 223 (2004).

[62] J. W. Swan and J. F. Brady, "Colloidal dispersions deformed by a steady shear stress", Submitted (2013).

[63] B. D. Lubachevsky and F. H. Stillinger, "Geometric properties of random disk packings", J. Stat. Phys. **60**, 561 (1990).

[64] M. Skoge, A. Donev, F. H. Stillinger, and S. Torquato, "Packing hyperspheres in high-dimensional Euclidean spaces", Phys. Rev. E **74**, 041127 (2006).

[65] J. F. Brady and J. F. Morris, "Microstructure of strongly sheared suspensions and its impact on rheology and diffusion", J. Fluid Mech. **348**, 103 (1997).

[66] J. F. Brady, "The rheological behavior of concentrated colloidal dispersions", J. Chem. Phys. **99**, 567 (1993).

[67] A. K. Gurnon and N. J. Wagner, "Microstructure and rheology relationships for shear thickening colloidal dispersions", J. Fluid Mech. **769**, 242 (2015).

[68] F. Westermeier, D. Pennicard, H. Hirsemann, U. H. Wagner, C. Rau, H. Graafsma, P. Schall, M. P. Lettinga, and B. Struth, "Connecting structure, dynamics and viscosity in sheared soft colloidal liquids: a medley of anisotropic fluctuations", Soft Matter **12**, 171 (2016).

[69] G. Nägele, "On the dynamics and structure of charge-stabilized suspensions", Phys. Rep. **272**, 215 (1996).

[70] M. Wang, M. Heinen, and J. F. Brady, "Short-time diffusion in concentrated bidisperse hard-sphere suspensions", J. Chem. Phys. **142**, 064905 (2015).

[71] M. Wang and J. F. Brady, "Short-time transport properties of bidisperse suspensions and porous media: a stokesian dynamics study", J. Chem. Phys. **142**, 094901 (2015).

[72] G. Nägele, J. Bergenholtz, and J. K. G. Dhont, "Cooperative diffusion in colloidal mixtures", J. Chem. Phys. **110**, 7037 (1999).

[73] D. El Masri, G. Brambilla, M. Pierno, G. Petekidis, A. Schofield, L. Berthier, and L. Cipelletti, "Dynamic light scattering measurements in the activated regime of dense colloidal hard spheres", J. Stat. Mech. Theor. Exp. **2009**, P07015 (2009).

[74] R. Zwanzig, *Nonequilibrium statistical mechanics* (Oxford University Press, 2001).

[75] E. R. Weeks, J. C. Crocker, A. C. Levitt, A. Schofield, and D. A. Weitz, "Three-dimensional direct imaging of structural relaxation near the colloidal glass transition", Science **287**, 627 (2000).

[76] A. Rahman, "Correlations in the motion of atoms in liquid argon", Phys. Rev. A **136**, 405 (1964).

[77] B. Gärtner, "Fast and robust smallest enclosing balls", in Proceedings of the 7th annual european symposium on algorithms (1999), p. 325.

[78] G. Biroli and J. P. Garrahan, "Perspective: the glass transition", J. Chem. Phys. **138**, 12A301 (2013).

[79] L. Berthier, G. Biroli, L. Bouchaud J.-P.and Cipelletti, and W. van Saarloos, eds., *Dynamical heterogeneities in glasses, colloids, and granular media* (Oxford University Press, 2011).

[80] C. H. Rycroft, "Voro++: a three-dimensional voronoi cell library in c++", Chaos **19**, 041111 (2009).

[81] J. F. Brady and M. Vivic, "Normal ststress in colloidal dispersions", J. Rheol. **39**, 545 (1995).

[82] J. Bergenholtz, J. F. Brady, and M. Vivic, "The non-newtonian rheology of dilute colloidal suspensions", J. Fluid Mech. **456**, 239 (2002).

[83] S. Torquato, *Random heterogeneous materials microstructure and macroscopic properties* (Springer, 2002).

[84] M. Wang and J. F. Brady, "Constant stress and pressure rheology of colloidal suspensions: the effects of hydrodynamic interactions", In Preparation (2016).

[85] M. D. Rintoul and S. Torquato, "Metastability and crystallization in hard-sphere systems", Phys. Rev. Lett. **77**, 4198 (1996).

[86] M. Wang and J. F. Brady, "Wang and brady reply", Phys. Rev. Lett. **116**, 179802 (2016).

[87] A. Sierou and J. F. Brady, "Shear-induced self-diffusion in non-colloidal suspensions", J. Fluid Mech. **506**, 285 (2004).

[88] A. Ikeda and K. Miyazaki, "Glass transition of the monodisperse gaussian core model", Phys. Rev. Lett. **106**, 015701 (2011).

[89] A. Ikeda and K. Miyazaki, "Slow dynamics of the high density Gaussian core model", J. Chem. Phys. **135**, 054901 (2011).

[90] T. K. Haxton and A. J. Liu, "Activated dynamics and effective temperature in a steady state sheared glass", Phys. Rev. Lett. **99**, 195701 (2007).

[91] C. S. O'Hern, L. E. Silbert, A. J. Liu, and S. R. Nagel, "Jamming at zero temperature and zero applied stress: the epitome of disorder", Phys. Rev. E **68**, 011306 (2003).

[92] T. Dbouk, E. Lemaire, L. Lobry, and F. Moukalled, “Shear-induced particle migration: predictions from experimental evaluation of the particle stress tensor”, J. Non-Newtonian Fluid Mech. **198**, 78 (2013).

[93] A. Ikeda, L. Berthier, and P. Sollich, “Comment on "constant stress and pressure rheology of colloidal suspensions””, Phys. Rev. Lett **116**, 179801 (2016).

Chapter 8

CONSTANT STRESS AND PRESSURE RHEOLOGY OF COLLOIDAL SUSPENSIONS: THE EFFECTS OF HYDRODYNAMIC INTERACTIONS

8.1 Introduction

Dense colloidal suspensions are widely present in nature and in industry [1–3]. Their rich rheological behaviors, including yielding [4–6], shear thinning [7–9], and shear thickening [10, 11], lead to phenomena such as flow instability [12] and particle migration [13, 14]. These behaviors arise from the complex interplay among Brownian motion, hydrodynamic interactions (HIs), and interparticle forces at high particle concentrations. To develop novel materials and applications based on dense colloidal suspensions, a quantitative understanding of their structure, dynamics, and rheology is necessary.

An essential feature of dense colloidal suspensions is the emergence of solid-like behaviors, which is commonly found in amorphous materials including metallic glasses, granular matter, and polymer melts, with increasing density, decreasing temperature, or reducing imposed stress. The flow-arrest transitions of amorphous materials are succinctly summarized by the "jamming diagram", suggesting that the system behaviors are governed by a special point J in the zero-temperature, zero-inverse-density, and zero-stress limit [15–17]. In hard-sphere colloidal suspensions without shear, the flow-arrest transitions are controlled by the volume fraction ϕ and the thermal fluctuations, as the singular interaction potential eliminates temperature. In the non-Brownian limit without thermal fluctuations, the flow-arrest transition occurs near the hard-sphere jamming point at $\phi_J \approx 0.64$, and in the Brownian limit, it takes place at the glass transition density $\phi_G \approx 0.58$ [18, 19]. Near flow-arrest transitions, the shear viscosity η_s apparently diverges as $\eta_s \sim (\phi_m - \phi)^{-\alpha}$, with $\alpha \in [2.2, 2.7]$ in the Brownian limit [20–23] and $\alpha \approx 2.0$ in the non-Brownian limit [18, 24]. Do different arrest points ϕ_m and divergence exponents α imply different underlying physics between the glass and the jamming transitions, as opposed to the unifying view from the jamming diagram?

Part of the answer was revealed in our recent simulation study on the constant stress and pressure rheology of dense colloidal suspensions without HIs [25]. We

found that by imposing constant shear stress σ and pressure Π, instead of fixing the volume fraction ϕ, both the shear viscosity η_s and the incremental normal viscosity η_n' diverge as

$$\{\eta_s, \eta_n'\} = \{k_s, k_n\} \times (\phi_m - \phi)^{-\alpha}, \tag{8.1}$$

where the imposed pressure only affects ϕ_m, and k_s, k_n, and α are constant with $\alpha = 2$. With increasing pressure, the arrest volume fraction ϕ_m increases from ϕ_G towards a point close to the jamming point, defined as the Shear Arrest Point (SAP), $\phi_{\text{SAP}} \approx \phi_J$. Here, $\eta_s = \sigma/\dot{\gamma}$ and $\eta_n' = (\Pi - \Pi^{\text{eq}})/\dot{\gamma}$, with $\dot{\gamma}$ the strain rate and Π^{eq} the equilibrium suspension osmotic pressure at the corresponding ϕ. The results suggested that the physics of jamming dominates the suspension behaviors near the flow-arrest transition, and that thermal fluctuations only affect the arrest point when the pressure, instead of the volume, is held constant. Moreover, although the simulations did not consider HIs, the numerical results agreed well with scaled experimental data [24], implying that the HIs do not qualitatively alter the rheology near flow-arrest transitions, and act in a mean-field fashion. In that study, we did not consider in detail the suspension microstructures and diffusive dynamics.

In this work, we investigate the constant stress and pressure rheology of dense colloidal suspensions near the flow-arrest transition using hydrodynamic simulations. By explicitly computing HIs, we can directly evaluate the influences of HIs on the suspension rheology, structure, and dynamics. Note that the present work and the previous chapter [26] are both motivated by our earlier study [25], with this work focusing on systems with HIs and the other one without HIs.

Hydrodynamic interactions are ubiquitous in colloidal suspensions and can profoundly affect their behavior. For equilibrium suspensions, the dissipative HIs cannot alter the suspension structure, but do strongly affect the short-time transport properties of colloidal suspensions. For instance, in the dilute limit where only pairwise interactions are considered, HIs significantly reduce the short-time self-diffusivity [27] and the instantaneous sedimentation velocity [28]. At higher concentrations, HIs significantly increase the high-frequency dynamic shear viscosity, which diverges near the close packing density due to the diverging near-field lubrication interactions [29, 30].

For sheared suspensions, the influence of HIs is even more profound as they also participate the suspension structural evolution. Rheologically, the structural distortion in sheared suspensions may activate the strong near-field lubrication interactions, which, in turn, increase the hydrodynamic stresses and lead to continuous shear

thickening, i.e., the mild increase in shear viscosity with increasing strain rate, in moderately dense colloidal suspensions [8, 31–33]. Structurally, HIs keep the suspension homogeneous and prevent particles from forming strings aligned in the flow direction at high strain rates [33]. The string phases are always present in simulations without HIs [34, 35], and are also observed in some experiments on hard-sphere suspensions [36, 37]. Moreover, recent confocal microscopy experiments in confined suspensions and scattering experiments in bulk suspensions have found that particles in sheared suspensions align along the vorticity direction and move in a "log-rolling"-like fashion [7, 38–40]. Numerical simulations in confined systems reveal the necessary conditions for such vorticity alignment including HIs and freedom to exchange particles in the velocity gradient direction [38, 41]. However, vorticity alignment has not been observed in simulations with unconfined suspensions. Finally, HIs also affect particle dynamics by introducing chaotic particle trajectories, leading to shear-induced self and collective diffusion even in non-Brownian suspensions [42–44].

Despite their importance in sheared suspension rheology, structure, and dynamics, HIs are difficult to compute because they are long-range and non-pairwise-additive for distant particles and are singular for close particles [45]. Further complications include computing the Brownian forces that satisfy the fluctuation-dissipation relation [46], and introducing size polydispersity to avoid spontaneous crystallization [47, 48]. As a result, existing studies rely on varying degrees of simplification. For example, many studies [5, 49] based on repulsive dense systems assumed that HIs are mean-field-like and completely ignored them [50, 51]. However, for particles in close contact, HIs are distinct from repulsive interactions. Considering two particles separating from each other: the repulsive interaction promotes their departure, while the HIs resist their relative motion away from each other. Others used simplified HIs. For instance, Ando and Skolnick [52] truncated the multipole expansion to the force and torque levels and their simulation method is unsuitable for rheological simulations. Mari et al. [53] completely ignored the far-field HIs in their studies on discontinuous shear thickening. With full HIs, many investigations are limited to monodisperse non-Brownian systems [54, 55]. Dynamic rheology simulations of dense polydisperse colloidal suspensions with the long-range HIs have not therefore been performed.

In this work we use a variant of the Spectral Ewald Accelerated Stokesian Dynamics (SEASD) method [56] as the tool for the computation investigation. The SEASD

is based on the Stokesian Dynamics framework, which captures both the far-field and the near-field HIs by exploiting both the mobility and the resistance formalism of Stokes flow [57]. Features of the SEASD algorithm include $O(N \log N)$ computation scaling via the spectral Ewald method [58, 59], graphic processing unit (GPU) acceleration, and incorporation of particle size polydispersity. To meet the challenges in dynamic simulations of dense suspensions up to the jamming density, we further adopt the near-field Brownian approximation [60], which evaluates Brownian related quantities by assuming mean-field-like far-field HIs, and imposes constant shear stresses and pressures in simulations.

Imposing constant stress and pressure, instead of fixing the strain rate and the volume fraction, is especially suitable for investigating the rheology of dense suspensions. It allows direct assessment of the suspension mechanical responses without a priori assumptions on material behaviors. For suspensions with yield stresses, both the solid-like and liquid-like responses can be accessed. In contrast, imposing a constant strain rate implicitly assumes that the material deforms like a fluid, and therefore can only measure the liquid-like behavior. In addition, increasing the imposed pressures directly identifies the athermal limiting volume fraction without assumptions on the flow-arrest transition. Constant stress and pressure experiments on non-Brownian suspensions identified the limiting volume fraction $\phi_c = 0.585$ [24], which is significantly lower than the jamming density, $\phi_c < \phi_J$. However, analysis on the experimental set up shows that the small gap, of the order of 10 particle diameters, may alter the suspension structures in the shear cell and likely contribute to the low ϕ_c [25, 61]. In the non-Brownian limit, fixing the pressure also reduces the stress fluctuations in the system [62].

Computational realization of the constant stress and pressure rheology requires special considerations, as the dissipative nature of colloidal suspensions prevents the use of many extended ensemble methods in non-equilibrium molecular dynamics [63]. The constraints can be imposed by either introducing physical boundaries with anisotropic volume adjustment, which is often used in studies involving granular materials [64], or by introducing compressibility in the solvent, a new method adopted in our earlier investigation [25]. In this work, we continue with this latter approach, which, for suspensions with HIs, relies on resolving particle interactions in compressible flows [65]. Here, we develop a new algorithm to impose these constraints in hydrodynamic simulations by exploiting the instantaneous nature of HIs. The new algorithm reduces to the constant stress algorithm of Swan and Brady

[66] with fixed volume.

A unifying perspective is emerging on the rheology of both inertia driven granular matter and viscous driven non-Brownian suspensions [24, 67–69]. Despite distinct particle interactions, their rheology is qualitatively similar when the mechanical responses are characterized by a *macroscopic* friction coefficient,

$$\mu = \sigma/\Pi, \tag{8.2}$$

and a flow number defined by the ratio of an internal time scale associated with the system pressure and an external flow time scale $\dot{\gamma}^{-1}$ [70]. Near the jamming transitions, both shear stress σ and particle pressure Π diverge but their ratio μ remain finite. For dry granular materials, the flow number is the inertial number $I = \dot{\gamma} a \sqrt{\rho_p/\Pi}$ with a the particle radius and ρ_p the particle density. The viscous number I_v characterizes the dynamics of non-Brownian viscous suspensions,

$$I_v = \dot{\gamma}\eta_0/\Pi, \tag{8.3}$$

with η_0 the solvent viscosity [24]. For systems exhibiting both the inertial and the viscous driven dynamics, their behaviors can be characterized by combining I and I_v, suggesting a smooth crossover between these two regimes [67]. The similarity between μ-I and μ-I_v rheology means that developments in one system can be applied to both. For example, the non-local formalism of granular rheology [64, 71, 72] can also be used for non-Brownian suspensions. However, it is unclear how particle Brownian motion changes the "granular" perspective. If such an extension were possible, a unified perspective can be established in the Brownian and non-Brownian rheology, allowing significant improvement in the modeling of colloidal suspensions.

In Ref. [25], we adopted the granular perspective to construct a μ-ϕ flow map and identified the SAP $(\phi_{\text{SAP}}, \mu_{\text{SAP}}) = (0.635, 0.16)$ as an intersection between the arrested states and the inaccessible states and discovered the universal viscosity divergences in Eq. (8.1). In this work we continue to use the granular perspective to further characterize the suspension rheology beyond the flow-arrest transitions, hoping to establish a unifying perspective between the Brownian and the non-Brownian rheology, but now with full HIs.

Another focus of this work is on the connection between the suspension macroscopic mechanical response and the diffusive particle dynamics. Perhaps the most obvious connection is the Stokes-Einstein-Sutherland (SES) relation for dilute suspensions,

relating the particle diffusivity to the viscosity and the thermal energy, i.e., $d_0\eta_0/T$ is a constant. This is derived by combining the Einstein relation connecting the single particle diffusivity d_0 and the mobility m_0, $d_0 = k_\mathrm{B}Tm_0$, with $k_\mathrm{B}T$ the thermal energy, and the Stokes drag law for the single particle mobility $m_0 = 6\pi\eta_0 a$ with the particle radius a.

Although derived from the single-particle limit, the SES relation holds well for systems beyond the dilute regime. For equilibrium molecular liquids, the SES relation holds over a wide range of temperatures down to near the glass transition [73, 74]. For equilibrium colloidal suspensions up to the glass transition density, the SES relation remains valid with generalization to the the suspension shear viscosity η_s and the short-time self-diffusivities d_s. For long-time diffusion, mode coupling theory predicts the SES relation remains valid [75, 76], but different interpretations on the experimental results have lead to controversy [48, 77]. Furthermore, the SES relation has also been generalized to viscoelastic medium for microrheology experiments [78, 79]. Near the glass transition, the SES relation breaks down due to the development of dynamic heterogeneity [80]. For systems interacting with very soft potentials, the dynamic heterogeneity is suppressed and the SES relation remains valid at higher density [81–83].

An extended SES relation for non-equilibrium sheared suspensions means that the product of the diffusivity and the suspension shear viscosity is linear to an effective temperature T_eff for *all* volume fractions and *all* strain rates. The existence of such a powerful relation relies on the appropriate choice of T_eff, a concept pioneered by Edwards in the statistical mechanics of granular matter [84]. The effective temperature provides the critical connection between experiments and mean-field theories of dense amorphous systems, such as the soft-glass rheology theory and its mode-coupling variants [85, 86] and the shear-transformation zone theory [87, 88]. Recently, the concept of an effective temperature receives support from the generalized fluctuation-dissipation relations [89], and is consistent among different definitions in athermal [90, 91] and thermal [92–94] systems.

In this work, we explore whether such an extended SES relation exists for sheared suspensions by connecting the suspension diffusive dynamics to its rheology. Existing results are mixed. For sheared amorphous systems, simulations suggest an effective temperature defined from the osmotic compressibility does not lead to the desired data collapse [95]. Experiments on colloidal glasses show that the particle long-time self-diffusivity $d^s_\infty \propto \dot{\gamma}^\beta$ with the exponent $\beta = 1$ [96] or 0.8 [97, 98],

suggesting that $T_{\text{eff}} \propto \sigma\dot{\gamma}^{1-\beta}$. However, these experiments focused on very limited volume fractions and are strongly affected by structural heterogeneity such as shear banding.

This chapter is arranged as follows: After briefly describing our simulation algorithm in Sec. 8.2, we first focus on the features of constant stress and pressure rheology in Sec. 8.3. We then present the rheology of colloidal suspensions from a unifying granular perspective in Sec. 8.4. In Sec. 8.5, we explore the connection among the suspension rheology, structure, and particle diffusion. We summarize and conclude in Sec. 8.6.

8.2 Method

Hydrodynamic interactions in colloidal suspensions

We consider N neutrally-buoyant hard-sphere colloidal particles of different radius a_i located at $\boldsymbol{r}_i$ suspended in a viscous solvent of viscosity η_0 and density ρ_0, occupying a total volume V. The particle radii follow a log-normal distribution, characterized by the volume averaged radius a, such that $a^3 = N^{-1}\sum_i a_i^3$, and a size polydispersity p.d. $= \sigma_a/\overline{a}$, with $\overline{a} = N^{-1}\sum_i a_i$ and $\sigma_a^2 = N^{-1}\sum_i(a_i^2 - \overline{a}^2)$. The radii are sorted into M bins, with an average radius a_α, $\alpha \in \{1, \ldots, M\}$, in each bin. In the thermodynamic limit, both N and V grow unbounded but the number density $n = N/V$ and the volume fraction $\phi = \frac{3}{4}\pi\sum_i a_i^3/V$ remain unchanged.

The dynamics of colloidal particles evolve on a time scale, say t_s, much longer than the particle momentum relaxation time scale τ_I and the hydrodynamic time scale τ_H. The former, $\tau_I = \frac{2}{9}\rho_p a^2/\eta_0$ with ρ_p the particle density, characterizes the time required for the *particle* momentum to dissipate a distance of order the particle size a, and that $t_s \gg \tau_I$ suggests the particle acceleration is negligible over the time scale t_s and the dynamics are overdamped. The hydrodynamic time scale, $\tau_H = \rho_0 a^2/\eta_0$, describes the time required for the *solvent* momentum to diffusive the same distance, and that $t_s \gg \tau_H$ means the Reynolds number $\text{Re} = \tau_H/t_s \ll 1$. Therefore, the HIs among the particles are dominated by the viscous stresses, and the fluid velocity $\boldsymbol{v}(\boldsymbol{x})$ and the pressure $p(\boldsymbol{x})$ are governed by Stokes equation,

$$\boldsymbol{\nabla} p(\boldsymbol{x}) = \eta_0 \nabla^2 \boldsymbol{v}(\boldsymbol{x}) \text{ and } \boldsymbol{\nabla}\cdot\boldsymbol{v}(\boldsymbol{x}) = 0, \tag{8.4}$$

supplemented by no-slip boundary conditions $\boldsymbol{v} = \boldsymbol{U}_i + \boldsymbol{\Omega}_i \times (\boldsymbol{x} - \boldsymbol{r}_i)$ at the surface of particle i with velocity $\boldsymbol{U}_i$ and angular velocity $\boldsymbol{\Omega}_i$.

Because of the linearity of Eq. (8.4), the fluid forces and their moments, i.e., the force $\boldsymbol{F}^{\text{H}}$, torque $\boldsymbol{T}^{\text{H}}$, and stresslets $\boldsymbol{S}^{\text{H}}$, are linear to the particle kinematics including

the velocity $\boldsymbol{U}$ and the angular velocity $\boldsymbol{\Omega}$. This leads to the resistance formalism,

$$\begin{bmatrix} \boldsymbol{\mathcal{F}}^{\mathrm{H}} \\ \boldsymbol{S}^{\mathrm{H}} \end{bmatrix} = -\boldsymbol{\mathcal{R}} \cdot \begin{bmatrix} \boldsymbol{\mathcal{U}} - \boldsymbol{\mathcal{U}}^{\infty} \\ -\boldsymbol{E}^{\infty} \end{bmatrix} \tag{8.5}$$

where $\boldsymbol{\mathcal{F}}^{\mathrm{H}} = (\boldsymbol{F}^{\mathrm{H}}, \boldsymbol{T}^{\mathrm{H}})^{\dagger}$ is the generalized force, $\boldsymbol{\mathcal{U}} - \boldsymbol{\mathcal{U}}^{\infty} = (\boldsymbol{U} - \boldsymbol{U}^{\infty}, \boldsymbol{\Omega} - \boldsymbol{\Omega}^{\infty})^{\dagger}$ is the generalized velocity difference with respect to $\boldsymbol{U}^{\infty}$, $\boldsymbol{\Omega}^{\infty}$, and $\boldsymbol{E}^{\infty}$ from the imposed velocity field $\boldsymbol{v}^{\infty}$, *i.e.*, for particle i, $\boldsymbol{U}_i^{\infty} = \boldsymbol{v}^{\infty}(\boldsymbol{r}_i)$, $\boldsymbol{\Omega}_i^{\infty} = \frac{1}{2}\boldsymbol{\nabla}\times\boldsymbol{v}^{\infty}|_{\boldsymbol{r}_i}$, and $\boldsymbol{E}_i^{\infty} = \frac{1}{2}[\boldsymbol{\nabla}\boldsymbol{v}^{\infty} + (\boldsymbol{\nabla}\boldsymbol{v}^{\infty})^{\dagger}]_{\boldsymbol{r}_i}$. Here, the dagger represents transpose and symbols without subscript suggest the entire suspension, *e.g.*, $\boldsymbol{U} = (\boldsymbol{U}_1, \boldsymbol{U}_2, \ldots, \boldsymbol{U}_N)^{\dagger}$. The grand resistance tensor $\boldsymbol{\mathcal{R}}$ depends only on the suspension configuration $\boldsymbol{r}$, and can be conveniently partitioned as

$$\boldsymbol{\mathcal{R}}(\boldsymbol{r}) = \begin{bmatrix} \boldsymbol{R}_{\mathcal{F}\mathcal{U}} & \boldsymbol{R}_{\mathcal{F}\mathrm{E}} \\ \boldsymbol{R}_{\mathrm{S}\mathcal{U}} & \boldsymbol{R}_{\mathrm{SE}} \end{bmatrix}, \tag{8.6}$$

where, for example, $\boldsymbol{R}_{\mathcal{F}\mathcal{U}}$ describes the coupling between the generalized force $\boldsymbol{\mathcal{F}}$ to the generalized velocity difference $\boldsymbol{\mathcal{U}} - \boldsymbol{\mathcal{U}}^{\infty}$.

The overdamped Langevin equation describes the dynamics of colloidal particles,

$$0 = \boldsymbol{\mathcal{F}}^{\mathrm{H}} + \boldsymbol{\mathcal{F}}^{\mathrm{P}} + \boldsymbol{\mathcal{F}}^{\mathrm{B}}, \tag{8.7}$$

where $\boldsymbol{\mathcal{F}}^{\mathrm{P}}$ is the generalized force from interparticle conservative potentials, and $\boldsymbol{\mathcal{F}}^{\mathrm{B}}$ is the stochastic Brownian force satisfying the fluctuation-dissipation relation

$$\overline{\boldsymbol{\mathcal{F}}^{\mathrm{B}}(t)} = 0 \text{ and } \overline{\boldsymbol{\mathcal{F}}^{\mathrm{B}}(t)\boldsymbol{\mathcal{F}}^{\mathrm{B}}(0)} = 2k_{\mathrm{B}}T\boldsymbol{R}_{\mathcal{F}\mathcal{U}}\delta(t). \tag{8.8}$$

With Eq. (8.5), the suspension configuration change $\Delta\boldsymbol{\mathcal{X}}$, including both the translational and rotational degrees of freedom, over a small time Δt, can be solved by integrating Eq. (8.7) as

$$\Delta\boldsymbol{\mathcal{X}} = \left[\boldsymbol{\mathcal{U}}^{\mathrm{E}} + \boldsymbol{\mathcal{U}}^{\mathrm{B}} + \boldsymbol{\mathcal{U}}^{\mathrm{P}}\right]\Delta t + \Delta\boldsymbol{\mathcal{X}}^{\mathrm{B}}, \tag{8.9}$$

where $\Delta\boldsymbol{\mathcal{X}}^{\mathrm{B}}$ is the stochastic Brownian displacement satisfying

$$\overline{\Delta\boldsymbol{\mathcal{X}}^{\mathrm{B}}} = 0 \text{ and } \overline{\Delta\boldsymbol{\mathcal{X}}^{\mathrm{B}}\Delta\boldsymbol{\mathcal{X}}^{\mathrm{B}}} = 2k_{\mathrm{B}}T\Delta t\boldsymbol{R}_{\mathcal{F}\mathcal{U}}^{-1}, \tag{8.10}$$

and $\boldsymbol{\mathcal{U}}^{\mathrm{E}}$, $\boldsymbol{\mathcal{U}}^{\mathrm{P}}$, and $\boldsymbol{\mathcal{U}}^{\mathrm{B}}$ are, respectively, the deterministic velocity contributions from the imposed flow, the interparticle force, and the Brownian drift:

$$\boldsymbol{\mathcal{U}}^{\mathrm{E}} = \boldsymbol{\mathcal{U}}^{\infty} + \boldsymbol{R}_{\mathcal{F}\mathcal{U}}^{-1} \cdot \boldsymbol{R}_{\mathcal{F}\mathrm{E}} \cdot \boldsymbol{E}^{\infty}, \tag{8.11}$$

$$\boldsymbol{\mathcal{U}}^{\mathrm{P}} = \boldsymbol{R}_{\mathcal{FU}}^{-1} \cdot \boldsymbol{\mathcal{F}}^{\mathrm{P}}, \tag{8.12}$$

$$\boldsymbol{\mathcal{U}}^{\mathrm{B}} = k_{\mathrm{B}}T\boldsymbol{\nabla} \cdot \boldsymbol{R}_{\mathcal{FU}}^{-1}. \tag{8.13}$$

Note that $\boldsymbol{\mathcal{U}}^{\mathrm{B}}$ arises due to the configuration dependent Brownian force $\boldsymbol{\mathcal{F}}^{\mathrm{B}}$, and the divergence operator in Eq. (8.13) acts on the last index of $\boldsymbol{R}_{\mathcal{FU}}^{-1}$.

Spatially averaging the Cauchy stress in the suspension leads to the suspension total stress without the fluid thermodynamic pressure [99, 100],

$$\begin{aligned}\langle \boldsymbol{\Sigma} \rangle =& 2\eta_0 \langle (\boldsymbol{E}^{\infty})' \rangle + (\kappa_0 - \tfrac{2}{3}\eta_0) E^{\infty} \boldsymbol{I} \\ & - nk_{\mathrm{B}}T\boldsymbol{I} + n(\langle \boldsymbol{S}^{\mathrm{E}} \rangle + \langle \boldsymbol{S}^{\mathrm{P}} \rangle + \langle \boldsymbol{S}^{\mathrm{B}} \rangle),\end{aligned} \tag{8.14}$$

where the average operator $\langle \cdot \rangle = V^{-1} \sum_i (\cdot)_i$, the traceless strain rate $(\boldsymbol{E}^{\infty})'$ and the rate of expansion E^{∞} satisfy $(\boldsymbol{E}^{\infty})' + \frac{1}{3}E^{\infty}\boldsymbol{I} = \boldsymbol{E}^{\infty}$, κ_0 is the solvent bulk viscosity, and the superscripts in $\langle \boldsymbol{S}^{\mathrm{E}} \rangle$, $\langle \boldsymbol{S}^{\mathrm{P}} \rangle$, and $\langle \boldsymbol{S}^{\mathrm{B}} \rangle$ have the same meaning as those in Eq. (8.10). Here, the solvent is compressible for imposing the constant pressure constraint. The stresslets are computed from the resistance tensors,

$$\langle \boldsymbol{S}^{\mathrm{E}} \rangle = -\langle \boldsymbol{R}_{\mathrm{S}\mathcal{U}} \cdot \boldsymbol{R}_{\mathcal{FU}}^{-1} \cdot \boldsymbol{R}_{\mathcal{F}\mathrm{E}} - \boldsymbol{R}_{\mathrm{SE}} \rangle : \langle \boldsymbol{E}^{\infty} \rangle, \tag{8.15}$$

$$\langle \boldsymbol{S}^{\mathrm{P}} \rangle = -\langle (\boldsymbol{R}_{\mathrm{S}\mathcal{U}} \cdot \boldsymbol{R}_{\mathcal{FU}}^{-1} + r\mathbf{l}) \cdot \boldsymbol{F}^{\mathrm{P}} \rangle, \tag{8.16}$$

$$\langle \boldsymbol{S}^{\mathrm{B}} \rangle = -k_{\mathrm{B}}T\langle \boldsymbol{\nabla} \cdot (\boldsymbol{R}_{\mathrm{S}\mathcal{U}} \cdot \boldsymbol{R}_{\mathcal{FU}}^{-1}) \rangle, \tag{8.17}$$

where the divergence operator in Eq. (8.17) acts on the last index in the parenthesis. Accordingly, the suspension shear viscosity is decomposed as

$$\eta_s = \eta_0 + \eta^{\mathrm{E}} + \eta^{\mathrm{B}} + \eta^{\mathrm{P}}. \tag{8.18}$$

Note that for hard-sphere colloidal suspensions, the first and the second terms in Eq. (8.16) cancel exactly, and therefore interparticle force contribution to the stresslet is zero [99].

The constant stress and pressure dynamics

In a simple shear flow, the imposed velocity field $\boldsymbol{v}^{\infty} = (\dot{\gamma}x_2, 0, 0)$, where $\dot{\gamma}$ is the strain rate and $\boldsymbol{x} = (x_1, x_2, x_3)$ is the position in the 1- (the velocity), 2- (the velocity gradient), and 3- (the vorticity) direction. The suspension dynamics and mechanics can be respectively solved from Eq. (8.9) and (8.14).

For simulations with constant imposed shear stress σ and pressure Π, we solve for the corresponding strain rate $\dot{\gamma}$ and expansion rate $\dot{e}$, which lead to $\boldsymbol{v}^{\infty}(\boldsymbol{x})$ and the configuration evolution in Eq. (8.9). The computation exploits the instantaneous

nature of the Stokes equations and proceeds as follows: At each time t with the suspension configuration $\boldsymbol{r}(t)$, the resistance tensors in Eq. (8.6) are known. We first evaluate the velocity and stress contributions from the interparticle force, $\boldsymbol{S}^{\mathrm{P}}$ and $\boldsymbol{\mathcal{U}}^{\mathrm{P}}$, and the Brownian motion, $\boldsymbol{S}^{\mathrm{B}}$, $\boldsymbol{\mathcal{U}}^{\mathrm{B}}$, and $\Delta\boldsymbol{\mathcal{X}}^{\mathrm{B}}$. The suspension is then subjected to two unit test flows, $\hat{\boldsymbol{v}}_{\gamma}^{\infty} = (x_2, 0, 0)$ and $\hat{\boldsymbol{v}}_{e}^{\infty} = \frac{1}{3}(x_1, x_2, x_3)$. From the linearity of Stokes flow, with an imposed flow $\boldsymbol{v}^{\infty} = \dot{\gamma}\hat{\boldsymbol{v}}_{\gamma}^{\infty} + \dot{e}\hat{\boldsymbol{v}}_{e}^{\infty}$, the flow stresslet

$$\boldsymbol{S}^{\mathrm{E}} = \dot{\gamma}\hat{\boldsymbol{S}}_{\gamma}^{\mathrm{E}} + \dot{e}\hat{\boldsymbol{S}}_{e}^{\mathrm{E}}, \tag{8.19}$$

where, $\hat{\boldsymbol{S}}_{\gamma}^{\mathrm{E}}$ is from $\hat{\boldsymbol{v}}_{\gamma}^{\infty}$ and $\hat{\boldsymbol{S}}_{e}^{\mathrm{E}}$ is from $\hat{\boldsymbol{v}}_{e}^{\infty}$. From Eq. (8.14), the suspension shear stress and pressure balances are

$$\sigma = \dot{\gamma}\eta_0 + n(\dot{\gamma}\hat{S}_{\gamma,12}^{\mathrm{E}} + \dot{e}\hat{S}_{e,12}^{\mathrm{E}} + S_{12}^{\mathrm{P}} + S_{12}^{\mathrm{B}}), \tag{8.20}$$

$$-\Pi = \kappa_0\dot{e} - nk_{\mathrm{B}}T + \tfrac{1}{3}n(\dot{\gamma}\hat{S}_{\gamma}^{\mathrm{E}} + \dot{e}\hat{S}_{e}^{\mathrm{E}} + S^{\mathrm{P}} + S^{\mathrm{B}}), \tag{8.21}$$

where, for example, S_{12}^{B} is the 12-component of $\left\langle \boldsymbol{S}^{\mathrm{B}} \right\rangle$ and $S^{\mathrm{B}} = \boldsymbol{I} : \left\langle \boldsymbol{S}^{\mathrm{B}} \right\rangle$. Therefore, we solve for $\dot{\gamma}$ and $\dot{e}$ from Eq. (8.20) and (8.21), and reconstruct $\boldsymbol{S}^{\mathrm{E}}$ from Eq. (8.19). To advance the particle dynamics, we use Eq. (8.9) with

$$\boldsymbol{\mathcal{U}}^{\mathrm{E}} = \dot{\gamma}\,\hat{\boldsymbol{\mathcal{U}}}_{\gamma}^{\mathrm{E}} + \dot{e}\,\hat{\boldsymbol{\mathcal{U}}}_{e}^{\mathrm{E}}, \tag{8.22}$$

where $\hat{\boldsymbol{\mathcal{U}}}_{\gamma}^{\mathrm{E}}$ is from $\hat{\boldsymbol{v}}_{\gamma}^{\infty}$ and $\hat{\boldsymbol{\mathcal{U}}}_{e}^{\mathrm{E}}$ is from $\hat{\boldsymbol{v}}_{e}^{\infty}$. The size of the simulation box L, with $V = L^3$, is adjusted according to $\mathrm{d}L/\mathrm{d}t = \frac{1}{3}\dot{e}L$.

The constant stress and constant pressure method above is an extension of the method of Wang and Brady [25] for simulations without HIs. Our method reduces to the constant stress and fixed volume method of Swan and Brady [66] when $\dot{e} = 0$.

In this work, we focus on polydisperse suspensions with size polydispersity p.d. = 0.1, particle number $N = 100$, and the species number $M = 10$. In the constant stress and pressure simulations, the suspension dynamics are controlled by the stress Péclet number Pe_{σ} and the dimensionless pressure $\bar{\Pi}$,

$$\mathrm{Pe}_{\sigma} = \sigma a^2/(\eta_0 d_0) \quad \text{and} \quad \bar{\Pi} = \Pi a^3/(k_{\mathrm{B}}T), \tag{8.23}$$

with the single particle diffusivity $d_0 = k_{\mathrm{B}}T/(6\pi\eta_0 a)$. The stress Péclet number Pe_{σ} is connected to the strain rate Péclet number $\mathrm{Pe}_{\dot{\gamma}}$ as

$$\mathrm{Pe}_{\dot{\gamma}} = (\eta_0/\eta_s)\mathrm{Pe}_{\sigma} = \dot{\gamma}a^2/d_0. \tag{8.24}$$

To resolve the dynamics, the time is scaled with a^2/d_0 when $\mathrm{Pe}_{\sigma} \le 1$ and with η_0/σ when $\mathrm{Pe}_{\sigma} > 1$. For each combination of (σ, Π), we perform a long simulation at

the corresponding $(\mathrm{Pe}_\sigma, \bar{\Pi})$ with a dimensionless time $\tau = 5000$ and a step size $\Delta\tau = 10^{-2}$ for $\bar{\Pi} < 100$ and $\Delta\tau = 2.5 \times 10^{-3}$ for $\bar{\Pi} \geq 100$. The simulations start with random configurations generated by the polydisperse Lubachevsky-Stillinger algorithm [101, 102]. When computing the results, the data from the first $\tau = 1000$ are discarded. In the appendix we describe the computation of HIs using the SEASD method with near-field Brownian approximation, and the algorithm validation using the constant stress computations.

A feature of the constant stress simulations is that, with a fixed time step at $\mathrm{Pe}_\sigma > 1$, the temporal resolution of the configuration evolution improves automatically with increasing suspension shear viscosity. This is because the step size $\Delta\tau = \Delta t\sigma/\eta_0 = \Delta\gamma(\eta_s/\eta_0)$, where the strain step $\Delta\gamma = \dot{\gamma}\Delta t$ characterizes the temporal resolution. Therefore, the same dimensionless time step $\Delta\tau$ may be used for both the solid-like and the liquid-like suspensions. In contrast, with fixed $\dot{\gamma}$, it is necessary to reduce the step size near the flow-arrest transitions to resolve the configuration evolution. In addition, larger time steps can be used in constant stress simulations. For example, when the shear viscosity $\eta_s/\eta_0 \approx 10$, typical for suspensions at $\phi \approx 0.45$ [33], $\Delta\tau = 10^{-2}$ with constant stress is equivalent to $\Delta\gamma = 10^{-3}$, a typical step size in constant strain rate studies [44, 54].

Furthermore, to prevent singular particle overlap in dynamic simulations with constant time step $\Delta\tau$, we introduce an additional excluded volume radius $b_i > a_i$ for each particle. Here, the excluded volume parameter $\delta = 1 - a_i/b_i = 5 \times 10^{-4}$, corresponding to a 1.5×10^{-3} change in volume fractions. From simulations on bidisperse suspensions [56], introducing δ does not change the suspension rheology at low to moderate $\mathrm{Pe}_{\dot{\gamma}}$, but slightly reduces the shear viscosity when $\mathrm{Pe}_{\dot{\gamma}} \gg 1$. In this work we enforce the excluded volume condition using the potential-free algorithm [34, 103], and monitor the stress contribution from the excluded volume effects. To minimize the impact of this procedure, a simulation is valid only if the excluded volume effect contributes less than 1% to the total stress.

8.3 Features of constant stress and pressure rheology

In this section we focus on the features of constant stress and pressure rheology at two imposed pressures, $\bar{\Pi} = 1.5$ and 50. At low imposed pressure, e.g., $\bar{\Pi} = 1.5$, colloidal suspensions flow like a liquid and do not exhibit a yield stress. With high imposed pressure, e.g., $\bar{\Pi} = 50$, the suspensions become glassy and develop a yield stress, i.e., they flow only if the imposed stress exceeds the yield stress.

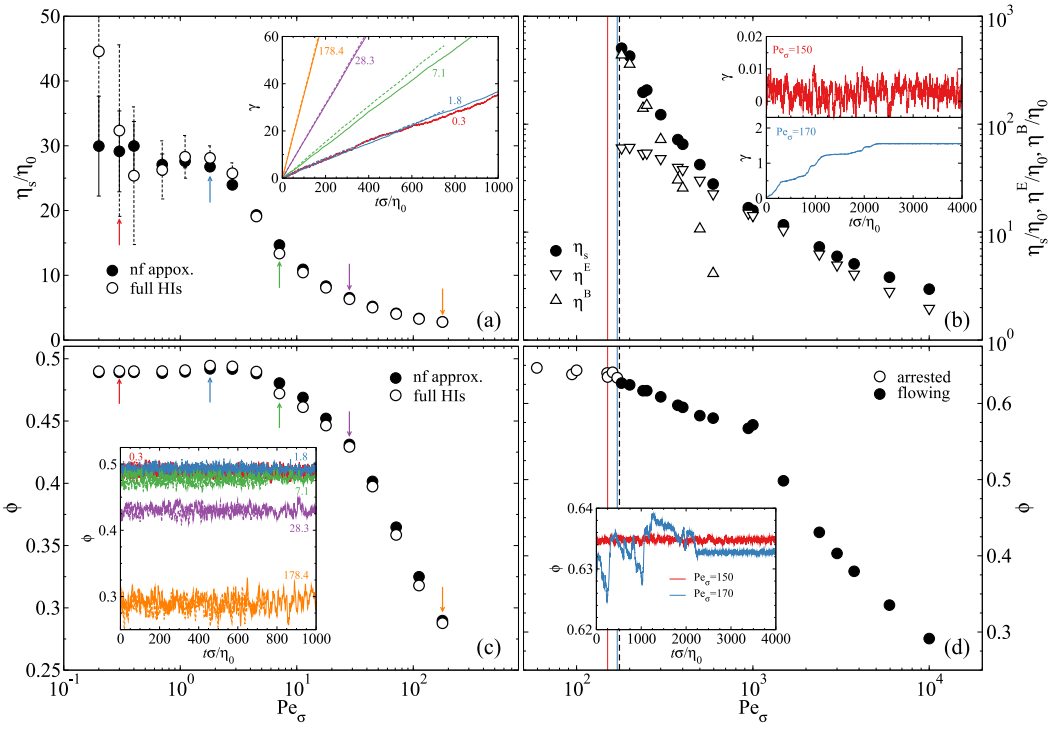

Figure 8.1: (Color Online) The constant stress and pressure rheology of a polydisperse suspension with polydispersity p.d. = 0.1 as functions of Pe_σ at $\bar{\Pi} = 1.5$ [(a), (c)] and at $\bar{\Pi} = 50$ [(b), (d)]. In (a) and (c), the results with full HIs are shown in open symbols in the main figure and dashed lines in the inset, and the results with near-field Brownian approximation are shown in filled symbols and solid lines. In (b) and (d), the thin lines indicate the Pe_σ for the insets with corresponding colors, and the black dashed line outlines the flow-arrest transition. (a) The suspension shear viscosity η_s/η_0. Inset: the time evolution of the accumulated strains γ at $\mathrm{Pe}_\sigma = 0.3$, 1.8, 7.1, 28.3, and 178.4. (b) The suspension shear viscosity η_s/η_0 (filled circle), the Brownian contribution η^{B}/η_0 (up triangle) and the flow contribution η^{E}/η_0 (down triangle). Insets: time trace of the accumulated strain γ at $\mathrm{Pe}_\sigma = 150$ and 170. (c) The steady state volume fraction ϕ. Inset: time traces of the instantaneous volume fraction at the same Pe_σ as (a). (d) The steady state volume fraction ϕ. The arrested results are shown in open circles and the flowing results in filled circles. Inset: time trace of the volume fraction ϕ at $\mathrm{Pe}_\sigma = 150$ and 170.

Rheology: shear viscosity and volume fraction

Fig. 8.1 presents the suspension rheological behaviors in shear viscosity η_s and volume fraction ϕ. The shear viscosity is the ratio of the imposed stress σ and the mean strain rate $\langle\dot{\gamma}\rangle$, i.e., $\eta_s = \sigma/\langle\dot{\gamma}\rangle$. The error bars in Fig. 8.1 are estimated by splitting the long simulations runs into independent segments of 500 dimensionless time units each. The liquid-like results at $\bar{\Pi} = 1.5$ are shown in Fig. 8.1a and 8.1c,

and the glassy results at $\bar{\Pi} = 50$ are shown in Fig. 8.1b and 8.1d.

We begin with liquid-like suspensions at $\bar{\Pi} = 1.5$. Fig. 8.1a shows the shear viscosity η_s/η_0 as a function of the stress Péclet number Pe_σ. Despite some fluctuations, in the $\mathrm{Pe}_\sigma \to 0$ limit, the shear viscosity η_s approaches a finite value corresponding to the zero-shear viscosity of an equilibrium suspension with the same osmotic pressure as the imposed pressure Π. With increasing Pe_σ, η_s decreases continuously, and quickly approaches the solvent viscosity, i.e., $\eta_s \to \eta_0$ as $\mathrm{Pe}_\sigma \to \infty$. The lack of shear-thickening and a finite high-shear viscosity are the key features of the constant stress and pressure rheology as the suspension dilates with growing Pe_σ. This is because the imposed pressure is scaled with $k_\mathrm{B}T$, but the suspension pressure scales as $f(\phi)\eta_0\dot{\gamma}$, with the function $f(\phi) \sim \phi^2$ at small ϕ, and therefore the suspension dilates so the pressure matches the imposed value.

The inset of Fig. 8.1a presents the time trace of the accumulated strain $\gamma(t) = \int_0^t \dot{\gamma}(\tau)d\tau$ for several Pe_σ. For continuously deforming, liquid-like suspensions, $\gamma(t)$ increases linearly with time. The inverse slope of the accumulated strain with respect to the dimensionless time $t\sigma/\eta_0$ is the suspension shear viscosity η_s/η_0. Therefore, the higher the suspension shear viscosity, the slower γ increases with time. For suspensions with similar shear viscosities, e.g., $\mathrm{Pe}_\sigma = 0.3$ and 1.8, their accumulated strains almost overlap. The accumulated strain $\gamma(t)$ exhibits more fluctuations at low Pe_σ relative to results at high Pe_σ due to stronger thermal fluctuations.

Fig. 8.1c shows the steady state volume fraction ϕ as a function of Pe_σ, and the inset presents the time trace of the instantaneous ϕ. When $\mathrm{Pe}_\sigma < 1$, changing Pe_σ does not significantly alter ϕ, and in the $\mathrm{Pe}_\sigma \to 0$ limit, the volume fraction ϕ corresponds that of an equilibrium suspension with an osmotic pressure equal to the imposed pressure. At higher Pe_σ, increasing Pe_σ reduces ϕ because the suspension dilates in response to the increase in suspension pressure from the growing imposed stress. The reduction in ϕ is drastic with respect to Pe_σ: at $\mathrm{Pe}_\sigma = 178$, the volume fraction has already decreased from ~ 0.49 to below 0.3. The inset of Fig. 8.1c shows that the volume fraction for all cases fluctuates around a constant value, confirming that the suspension is at steady sate. Moreover, the fluctuations in ϕ are more significant at lower ϕ, due to the lower suspension bulk viscosity [104]. As the bulk viscosity characterizes the suspension's resistance to expansion, lower volume fraction makes responding to an imposed pressure easier for the suspension, and therefore allows larger fluctuations.

Fig. 8.1a and 8.1c also compare the results from full hydrodynamic computations (open symbols and dashed lines) and near-field Brownian approximations (filled symbols and solid lines). Despite small quantitative differences, the two methods agree well with each other. This is consistent with the results in constant ϕ and $\dot{\gamma}$ simulations in bidisperse suspensions [56]. Considering the tremendous time saving from the near-field Brownian approximation, it is adequate for the constant stress and pressure dynamic simulations of polydisperse suspensions in this work.

When the imposed pressure $\bar{\Pi} > 3$, the colloidal suspension becomes glassy and a yield stress emerges without apparent structural signatures. Note that at equilibrium, $\bar{\Pi} = 3$ corresponds to $\phi \approx 0.56$. Therefore, the suspension shear viscosity η_s diverges at low imposed stress. Determining the exact value of the yield stress is difficult as it depends on the observation time scale—the longer one waits, the more likely for one to observe flow [16]. In practice, however, the flow-arrest transition can be determined by a viscosity threshold, beyond which the suspension is considered arrested. Here, the threshold viscosity is $\eta_s/\eta_0 = 2000$. For typical simulations with dimensionless time $\tau = 5000$, this viscosity threshold corresponds to a minimum strain $\gamma \approx 2.5$ for the flowing suspensions at $\mathrm{Pe}_\sigma > 1$.

Fig. 8.1b and 8.1d illustrate the constant stress and pressure rheology of glassy suspensions at $\bar{\Pi} = 50$. Fig. 8.1b presents the various components of the shear viscosity. From the simulations, the yield stres corresponding to $\mathrm{Pe}_\sigma \approx 175$ is shown as a dashed vertical line in the figures. When the imposed stress is lower than the yield stress, the suspension is arrested and unable to flow. This is confirmed in the time traces of the accumulated strain γ at $\mathrm{Pe}_\sigma = 150$ and 170 in the inset of Fig. 8.1b. When close to the yield stress, e.g., at $\mathrm{Pe}_\sigma = 170$, the suspension appears unstable, switching between flowing and arrested behaviors. In this case, the computed viscosity exhibits large fluctuations. Further reducing the imposed stress, the suspension becomes completely arrested. In the inset of Fig. 8.1b, the accumulated strain cannot exceed 0.01 at $\mathrm{Pe}_\sigma = 150$ even over an extended period time of $t\sigma/\eta_0 = 4000$.

The shear viscosity η_s/η_0 in flowing suspensions shows strong shear thinning in Fig. 8.1b. Over two decades of Pe_σ the viscosity reduces more than three orders of magnitude. The Brownian viscosity η^{B}, shown as up triangles, is responsible for the strong shear-thinning behaviors near the flow-arrest transition. The flow viscosity η^{E}, shown as down triangles, changes more slowly compared to η^{B} near the flow arrest transition. At higher Pe_σ, η^{E} also decreases with increasing Pe_σ, and the

shear thinning of η^{E} with growing Pe_σ is much weaker comparing to η^{B}. Unlike the constant volume simulations where η^{E} reaches a high-shear rate limiting value, the decrease in η^{E} in constant stress and pressure rheology results from dilation of the suspension.

Fig. 8.1d presents the suspension volume fraction ϕ as functions of Pe_σ at $\bar{\Pi} = 50$. Here, the volume fractions at the arrest state are shown in open symbols and the flowing state in filled symbols. In Fig. 8.1d, with increasing Pe_σ, the suspension always dilates regardless of flowing or not from $\phi \approx 0.645$ at $\mathrm{Pe}_\sigma \approx 60$ to less than 0.3 at $\mathrm{Pe}_\sigma = 10^4$. The dilation before flow is necessary in order for the suspension to rearrange its structure and to allow two particles to pass each other. Furthermore, the volume fraction shows a kink near $\mathrm{Pe}_\sigma = 10^3$ at $\phi \approx 0.57$. After $\mathrm{Pe}_\sigma = 10^3$, the dilation becomes stronger with increasing Pe_σ. The kink in ϕ at $\mathrm{Pe}_\sigma = 10^3$ is not observed for suspensions at lower imposed pressures, e.g., in Fig. 8.1c at $\bar{\Pi} = 1.5$. From the structural examinations in Sec. 8.3, we found that this kink is related to the shear-induced string formation in polydisperse suspensions.

The time traces of the ϕ for arrested suspensions, also at $\mathrm{Pe}_\sigma = 150$ and 170, are shown in the inset of Fig. 8.1d. Far from the flow-arrest transition, i.e., at $\mathrm{Pe}_\sigma = 150$, ϕ fluctuates with small variation. Near the flow-arrest transition, i.e., at $\mathrm{Pe}_\sigma = 170$, ϕ also show intermittent behaviors and becomes unstable when the corresponding accumulated strain γ exhibits significant increases in the inset of Fig. 8.1b. The unstable behaviors stop when γ stops growing at $t\sigma/\eta_0 \gtrsim 2200$.

Structures: the pair distribution function

We investigate the suspension structure by computing the steady state pair distribution function

$$g(\boldsymbol{r}) = \frac{V}{N^2}\left\langle \sum_{i,j}{}' \delta(\boldsymbol{r} - \boldsymbol{r}_i + \boldsymbol{r}_j)\right\rangle, \tag{8.25}$$

where the prime on the summation excludes the case of $i = j$, and $\delta(x)$ is the Dirac delta function. It is the conditional probability of finding a second particle at location $\boldsymbol{r}$ given the first particle. Fig. 8.2 shows the equatorial slices of $g(\boldsymbol{r})$ with width $0.7a$ on the velocity-velocity gradient (12), velocity-vorticity (13), and velocity gradient-vorticity (23) planes for suspensions with $\bar{\Pi} = 1.5$ at selected Pe_σ. Changing the width of the slice has little qualitative influences on the results. With HIs, the suspension remains homogeneous for all Pe_σ. This is distinct from simulations without HIs, where the particles spontaneously align in the velocity direction, forming string-like structures at high Pe_σ. In the shear plane, $g_{12}(\boldsymbol{r})$ is

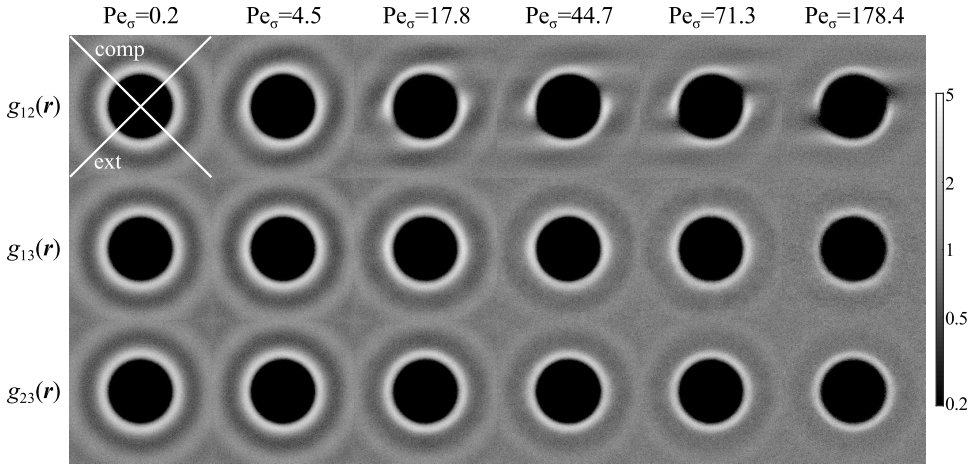

Figure 8.2: Equatorial slices of the pair distribution function $g(\boldsymbol{r})$ on the velocity-velocity gradient (12), velocity-vorticity (13), and velocity gradient-vorticity (23) planes of suspensions with an imposed pressure $\bar{\Pi} = 1.5$ at various Pe_σ. The suspension size polydispersity p.d. = 0.1. The width of the slice is $0.7a$. The compression and the extension axes are also highlighted.

almost isotropic at $\mathrm{Pe}_\sigma = 0.2$. With increasing Pe_σ, for example, at $\mathrm{Pe}_\sigma = 17.8$, the neighboring particles begin to accumulate at the particle front in the flow direction, suggesting the formation of a particle pair. The pair then rotates, first quickly in the compressional quadrant, as indicated by the lower probability density near the compressional axis, and then slowly in the extensional quadrant. Near the extensional axis, the particle pair disengages. Further increase in Pe_σ compresses the first ring of $g_{12}(\boldsymbol{r})$, suggesting a boundary layer formation [105]. However, the overall intensity of $g_{12}(\boldsymbol{r})$ decreases with increasing Pe_σ due to the suspension dilation. Moreover, a particle depletion wake emerges near the extensional axis when $\mathrm{Pe}_\sigma > 44.7$ because, compared to the flow, the diffusion is too weak to drive the particles towards the low density region.

In Fig. 8.2, the $g(\boldsymbol{r})$ slices in the 13-plane, $g_{13}(\boldsymbol{r})$, exhibit weaker anisotropy compared to $g_{12}(\boldsymbol{r})$. Starting from an isotropic structure at $\mathrm{Pe}_\sigma = 0.2$, $g_{13}(\boldsymbol{r})$ first show particle accumulation in the velocity direction (left-right in the figure) relative to the vorticity direction (up-down in the figure) with increasing Pe_σ. This is especially pronounced at $\mathrm{Pe}_\sigma = 44.7$. However, at higher Pe_σ, this trend is reversed along with the formation of depletion wake in $g_{12}(\boldsymbol{r})$. For example, at $\mathrm{Pe}_\sigma = 178$, slightly more particles are present in the vorticity direction compared to the velocity direction, suggesting the a weak particle alignment in the vorticity direction. Finally, the $g(\boldsymbol{r})$ slice in the 23-plane, $g_{23}(\boldsymbol{r})$, is always isotropic. At $\bar{\Pi} = 1.5$, the principle influence

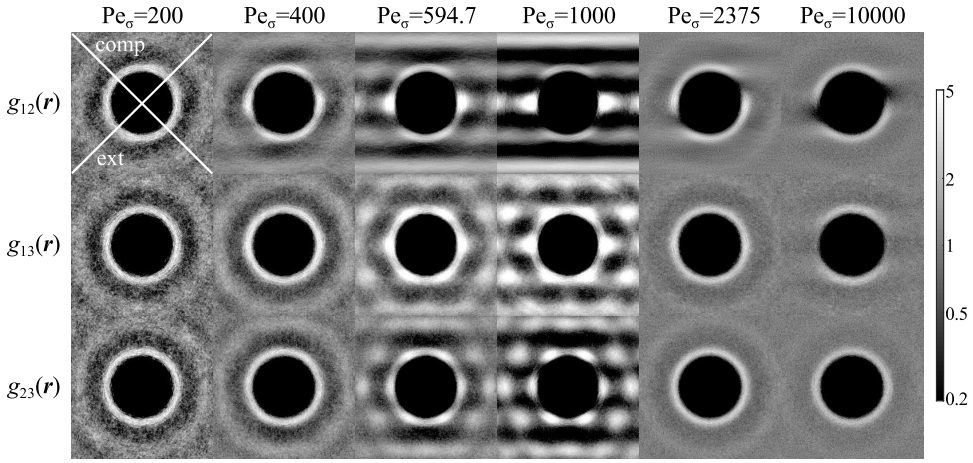

Figure 8.3: Equatorial slices of pair distribution function $g(\boldsymbol{x})$ on the 12-, 13-, and 23-planes of suspensions with imposed pressure $\bar{\Pi} = 50$ at various Pe_σ. Other parameters are identical to Fig. 8.2.

of increasing Pe_σ on $g_{23}(\boldsymbol{r})$ is the reducing suspension structural features beyond the nearest neighbors and the decreasing peak values associated with the nearest neighbors.

Fig. 8.3 presents the equatorial slices of $g(\boldsymbol{r})$ for suspensions at $\bar{\Pi} = 50$. As indicated in Fig. 8.1d, the at-rest volume fraction at this imposed pressure is well above the monodisperse fluid-solid phase transition, and therefore the colloidal suspension is prone to crystallization. At the lowest Pe_σ in Fig. 8.3, the suspension structure is isotropic without indications of structural formation, suggesting that introducing a small size polydispersity effectively suppresses the spontaneous crystallization.

Increasing Pe_σ reveals that the size polydispersity p.d. = 0.1 is not sufficient to prevent formation of string phases at intermediate Pe_σ, i.e., at $\mathrm{Pe}_\sigma = 595$ and 1000 in Fig. 8.3, the particles align in the flow direction and organize to hexagonal structures in the 23-plane. The string phase is less sensitive to the particle size polydispersity compared to the equilibrium crystallization, i.e., a size polydispersity sufficient to prevent spontaneous crystallization is not enough to prevent string order formation.

Even in the string phase the stress is dominated by HIs, as the stress contribution from the excluded volume effects is only 0.6% of the total stress at $\mathrm{Pe}_\sigma = 595$ and 0.3% at $\mathrm{Pe}_\sigma = 1000$. The Péclet numbers with the string phase in Fig. 8.3 correspond to the location of the volume fraction "kink" in Fig. 8.1d. At other imposed pressures, the string phase formation is observed when $\bar{\Pi} \geq 20$ with volume fractions between

$\phi = 0.56$ and 0.58. Similar string phases are found in non-hydrodynamic Brownian dynamics simulations [34], in Accelerated Stokesian Dynamics simulations of non-Brownian monodisperse suspensions at $0.5 < \phi < 0.6$ [54], and in experiments [36, 37]. Their formation is commonly attributed to the the repulsive interparticle forces. It is unlikely the case here as the stress contribution from interparticle forces is low. Another interpretation is that HIs are localized and dominated by the pairwise lubrication interactions for very dense systems. The localized HIs may behave similarly to repulsive forces in non-hydrodynamic systems, and promote the string phase formation. On the other hand, at higher ϕ the limited available space cannot geometrically accommodate the string formation in suspensions.

Surprisingly, the string phase in Fig. 8.3 melts at higher Pe_σ. This is different from simulations without HIs, where the string order persists at higher Pe_σ [26]. A possible explanation is suspension dilation, as suspensions at lower ϕ are dominated by the long-range, non-pairwise-additive aspect of the HIs, which disrupts the string order formation. This explanation is also consistent with the observations in Fig. 8.2.

Beyond the melting of the string phase structures, the structural evolution of amorphous suspensions at $\bar{\Pi} = 50$ in Fig. 8.3 is similar to those at $\bar{\Pi} = 1.5$ in Fig. 8.2 with more pronounced structural features. For example, in the 12-plane, the particle depletion wake also approaches the velocity axis with increasing Pe_σ. In the 13-plane, the anisotropy in $g_{13}(\boldsymbol{r})$ at $\mathrm{Pe}_\sigma = 10^4$ is evident and clearly suggests a strong preference for the particles to align in the vorticity direction.

We have found that the vorticity alignment is present for all imposed pressures $\bar{\Pi}$ with high Pe_σ. Experimentally, the vorticity particle alignment was first discovered in sheared suspensions with strong confinement [7, 38], and was also recently found in experiments of sheared bulk suspensions [39, 40]. Numerical evidence, however, has been limited to simulations in confined systems [38, 41]. This work is the first numerical study for bulk suspensions that exhibits such alignment. Our results suggest that the vorticity particle alignment does not require confinement, high volume fractions, or Brownian motion. Therefore, it must originate from pairwise HIs. Indeed, the vorticity particle alignment is a consequence of the periodic particle trajectory in simple shear flow. Batchelor and Green [106] showed that the particle trajectories in simple shear flows contain a region of closed trajectories extending to infinity in the vorticity direction, and in this region, a particle pair undergoes periodic motion. As a result, when a particle enters the closed trajectory region of another particle, it is effectively locked in a periodic orbit until it encounters another particle.

Such hydrodynamic "trapping" increases the probability of particle presence in the vorticity direction, and therefore leads to the preferred vorticity alignment.

Quantitative details of the pair distribution function $g(\boldsymbol{r})$ significantly affect the suspension stress. In the $\mathrm{Pe}_{\dot{\gamma}} \gg 1$ limit, the dominant hydrodynamic stresslet $\boldsymbol{S}^{\mathrm{E}}$ can be approximated from the boundary-layer approximation [33, 107]

$$\boldsymbol{S}^{\mathrm{E}}_{\mathrm{b.l.}} \sim \eta'_{\infty}(\phi)\dot{\gamma}\phi^2 g^{\infty}(2;\phi)\times \int_{\hat{\boldsymbol{r}}\cdot\boldsymbol{E}\cdot\hat{\boldsymbol{r}}<0} \hat{\boldsymbol{r}}\hat{\boldsymbol{r}}(\hat{\boldsymbol{r}}\cdot\boldsymbol{E}\cdot\hat{\boldsymbol{r}})\bar{g}(\theta,\varphi)d\Omega, \tag{8.26}$$

where $\hat{\boldsymbol{r}}$ is the unit vector in the radial direction, η'_{∞} is the high-frequency dynamic shear viscosity, $g^{\infty}(2;\phi)$ is the pair distribution function outside the boundary layer, $\bar{g}(\theta,\varphi)$ is the $O(1)$ angular variation within the boundary layer, and Ω is the solid angle. From a radial-balance approximation, $\bar{g}(\theta,\varphi) \propto -\hat{\boldsymbol{r}}\cdot\boldsymbol{E}\cdot\hat{\boldsymbol{r}}$ [107]. In the $\mathrm{Pe}_{\dot{\gamma}} \ll 1$ limit, on the other hand, the deviatoric part of the Brownian stresslet $\boldsymbol{S}^{\mathrm{B}}$ is estimated as [33, 50]

$$n\left\langle \boldsymbol{S}^{\mathrm{B}}\right\rangle + \Pi^0\boldsymbol{I} = -\frac{27}{2\pi}\eta_0\dot{\gamma}\phi^2\frac{g^0(2,\phi)}{\hat{d}(\phi)}\times \int \hat{\boldsymbol{r}}\hat{\boldsymbol{r}}\,\hat{f}(2;\theta,\varphi)d\Omega, \tag{8.27}$$

where Π^0 is the equilibrium osmotic pressure, $g^0(2,\phi)$ is the equilibrium contact value of the pair distribution function, $\hat{d}(\phi)$ is a characteristic diffusion scale relative to the single particle value, and $\hat{f}(\boldsymbol{r})$ is the distortion of the equilibrium pair distribution function $g(\boldsymbol{r})/g^0(\boldsymbol{r}) = 1+[\mathrm{Pe}_{\dot{\gamma}}/\hat{d}(\phi)]\hat{f}(\boldsymbol{r})$. Eq. (8.26) and (8.27) are derived for monodisperse suspensions, and are helpful for formulating scaling arguments to collapse the rheology results in the liquid-like regime [33, 54]. In addition, they also reveal that the most significant structural contributions are from the extensional and the compressional axes indicated in Fig. 8.2 and 8.3. Furthermore, Eq. (8.26) and (8.27) show that both the extensional and the compressional quadrant contribute positively to η^{B} and η^{E} in their respective regimes.

Fig. 8.4 presents the peak values of the of the pair distribution on the compressional axis, $\max(g_{\mathrm{comp}})$ (filled symbols), and on the extensional axis, $\max(g_{\mathrm{ext}})$ (open symbols), as functions of Pe_{σ} at $\bar{\Pi} = 1.5$ and $\bar{\Pi} = 50$. The insets of Fig. 8.4 also show $g_{\mathrm{comp}}(r)$ (solid lines) and $g_{\mathrm{ext}}(r)$ (dashed lines) as selected Pe_{σ}. Here, the data at different Pe_{σ} are shifted for clarity. For liquid-like suspensions at $\bar{\Pi} = 1.5$ in Fig. 8.4a, at $\mathrm{Pe}_{\sigma} = 0.2$, $\max(g_{\mathrm{comp}})$ and $\max(g_{\mathrm{ext}})$ are almost identical, consistent

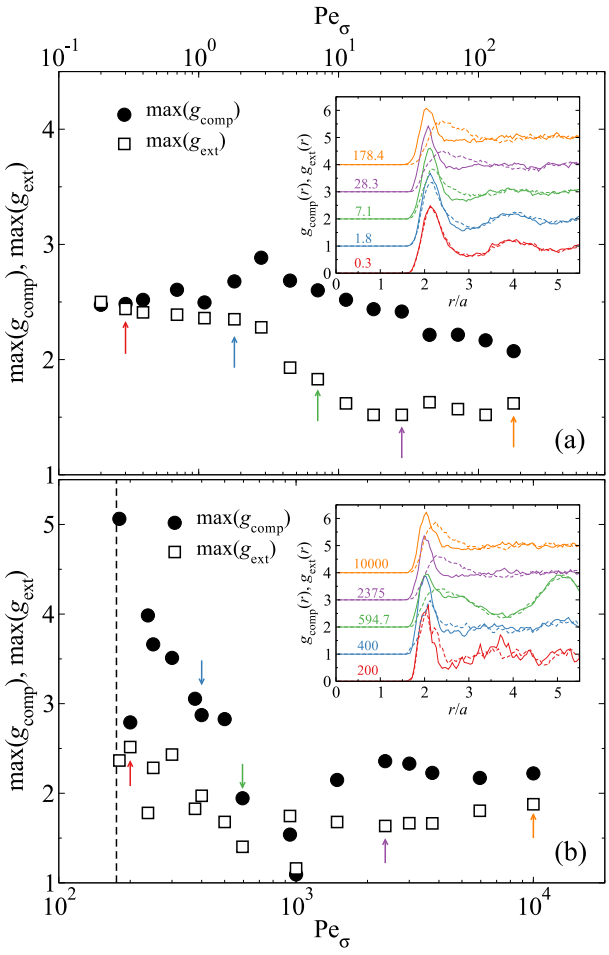

Figure 8.4: (Color online) The maximum value of the pair distribution functions on the compressional and the extensional axes, $\max(g_{\text{comp}})$ (filled symbols) and $\max(g_{\text{ext}})$ (open symbols), respectively, as functions of Pe_σ at (a) $\bar{\Pi} = 1.5$ and (b) $\bar{\Pi} = 50$. The insets show $g_{\text{comp}}(r)$ (solid lines) and $g_{\text{ext}}(r)$ (dashed lines), obtained from the equatorial slices of $g(\boldsymbol{r})$ in the 12-plane with a width of $0.7a$, at selected Pe_σ annotated by arrows in the main figure. The $g_{\text{comp}}(r)$ and $g_{\text{ext}}(r)$ results are shifted for clarity. In (b) the estimated flow-arrest transition Pe_σ is shown in the vertical dashed line.

with the almost isotropic suspension structure in Fig. 8.2. With increasing Pe_σ, $\max(g_{\text{comp}})$ first increases, reaches a maximum at $\text{Pe}_\sigma = 2.8$, and then decreases. On the other hand, $\max(g_{\text{ext}})$ first decreases slowly when $\text{Pe}_\sigma < 2.8$, and reduces more quickly with respect to Pe_σ until $\text{Pe}_\sigma = 28.3$, where $\max(g_{\text{ext}})$ grows mildly with Pe_σ again. These rich structural features arise from the HIs in the constant stress and pressure rheology. The inset of Fig. 8.4a provides further insights to the structural changes. Increasing Pe_σ reduces the width of the first peak of $g_{\text{comp}}(r)$ and

flattens the undulation of $g_{\text{comp}}(r)$ beyond the first peak, suggesting a compression of neighboring particles and the dominance of pair interactions in this direction with high imposed stresses. On the other hand, increasing Pe_σ shifts the location of the $g_{\text{ext}}(r)$ maximum away from the particle surface, reduces the undulations beyond the first peak, and also qualitatively changes the shape of $g_{\text{ext}}(r)$, e.g., $g_{\text{ext}}(r)$ at $\text{Pe}_\sigma = 28.3$ is notably different from the near-equilibrium structure at $\text{Pe}_\sigma = 0.3$. Comparing to Fig. 8.2, the changes in $g_{\text{ext}}(r)$ is associated with the development of the particle depletion wake in the extensional quadrant.

The structural features in the compressional and the extensional axes at $\bar{\Pi} = 50$ are presented in Fig. 8.4b. Despite slightly scattered data, $\max(g_{\text{comp}})$ and $\max(g_{\text{ext}})$ are different from the onset of flow near the flow-arrest transition, suggesting that the flow of glassy suspensions is inherently far from equilibrium. With increasing Pe_σ up to $\text{Pe}_\sigma = 1000$, both $\max(g_{\text{comp}})$ and $\max(g_{\text{ext}})$ decrease, and their difference is also diminishing. In fact, $\max(g_{\text{comp}})$ and $\max(g_{\text{ext}})$ become almost identical with the string phase formation. After the dissolution of the string phase at $\text{Pe}_\sigma > 10^3$, $\max(g_{\text{comp}})$ first increases and then decreases, and $\max(g_{\text{ext}})$ increases mildly with growing Pe_σ, similarly to the high Pe_σ behaviors at $\bar{\Pi} = 1.5$. In the inset of Fig. 8.4b, $g_{\text{comp}}(r)$ and $g_{\text{ext}}(r)$ at $\text{Pe}_\sigma = 200$ and 400 exhibit fluctuations due to the slow suspension structural evolution. At $\text{Pe}_\sigma = 594.7$, the formation of string order phase qualitatively changes $g_{\text{comp}}(r)$ and $g_{\text{ext}}(r)$ from amorphous suspensions at other Pe_σ, including the formation of significant undulations beyond the first peak. The structural features of $g_{\text{comp}}(r)$ and $g_{\text{ext}}(r)$ at $\text{Pe}_\sigma = 2375$ and 10^4 are similar to those at $\text{Pe}_\sigma = 28.3$ and 178.4 at $\bar{\Pi} = 1.5$ in Fig. 8.4a.

Dynamics: long-time self-diffusivity

The diffusive dynamics of the suspension are characterized by the long-time self-diffusivities in the velocity gradient direction $d^s_{\infty,22}$ and the vorticity direction $d^s_{\infty,33}$. The diffusivity in direction k is calculated as

$$d^s_{\infty,kk} = \frac{1}{2} \lim_{t\to\infty} \frac{\mathrm{d}\left\langle \Delta x_k^2 \right\rangle}{\mathrm{d}t}, \tag{8.28}$$

where $\left\langle \Delta x_k^2 \right\rangle$ is the particle mean-square displacement computed from all available data.

Fig. 8.5a present $d^s_{\infty,33}$ as functions of Pe_σ at $\bar{\Pi} = 1.5$. At this imposed pressure, the zero-shear diffusivity is finite, and $d^s_{\infty,33}$ increases with Pe_σ. The inset of Fig. 8.5 shows the mean square displacement $\left\langle \Delta x_3^2 \right\rangle$ as functions of the dimensionless time

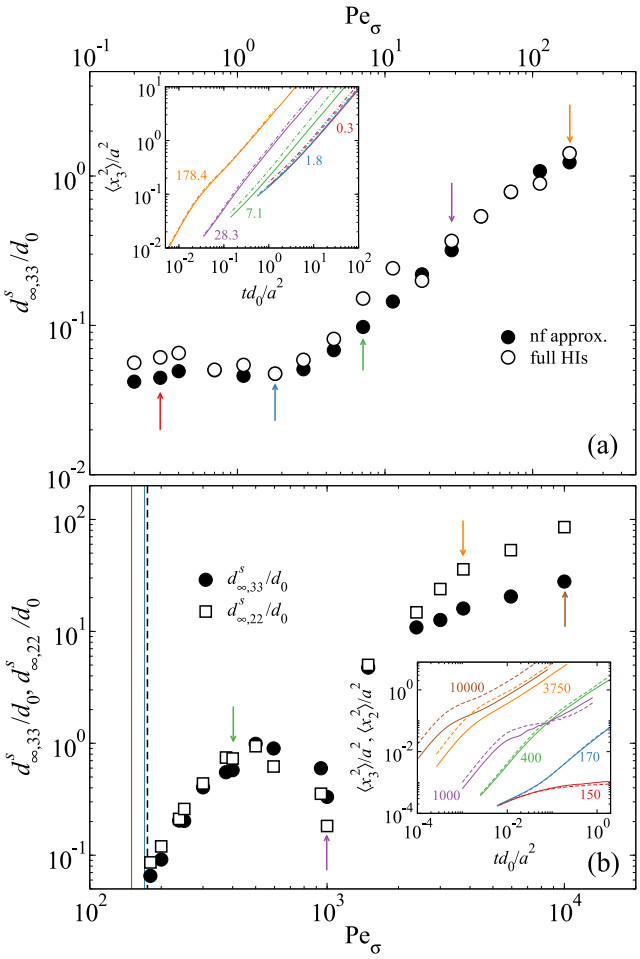

Figure 8.5: (Color online) Long-time self-diffusivity in the vorticity (3-) and the velocity gradient (2-) direction, $d^s_{\infty,33}/d_0$ and $d^s_{\infty,22}/d_0$, respectively, at (a) $\bar{\Pi} = 1.5$ and (b) $\bar{\Pi} = 50$. (a): $d^s_{\infty,33}/d_0$ computed with full HIs (open symbols) and with the near-field Brownian approximation (filled symbols). Inset: the time trace of the mean-square displacement in the 3-direction, $\left\langle \Delta x_3^2 \right\rangle$ at different Pe_σ. The solid lines are from the near-field Brownian approximation and the dash-dotted lines are from full calculations. (b): $d^s_{\infty,33}/d_0$ (filled circles) and $d^s_{\infty,22}/d_0$ (open squares) from near-field Brownian approximation as functions of Pe_σ. Inset: the time trace of the mean-square displacement in the 3-direction $\left\langle \Delta x_3^2 \right\rangle$ (solid lines) and the 2-direction $\left\langle \Delta x_2^2 \right\rangle$ (dashed lines) at different Pe_σ.

ta^2/d_0: at small Pe_σ, $\left\langle \Delta x_3^2 \right\rangle$ is observed to first grow sublinearly, and then linearly with time. Since the particle dynamics in the $\mathrm{Pe}_\sigma \ll 1$ limit are dominated by Brownian motion, $\left\langle \Delta x_3^2 \right\rangle$ is expected to grow linearly with time at a smaller time scale not captured in the figure, and its rate of growth characterizes the translational short-time self-diffusivity d^t_s. With $\mathrm{Pe}_\sigma \gg 1$, e.g. $\mathrm{Pe}_\sigma = 178.4$, $\left\langle \Delta x_3^2 \right\rangle$ grows

linearly with time at long times, but proportional to t^2 when $td_0/a^2 < 0.02$. This is because in the short-time limit, the particle dynamics are dominated by the flow, i.e., $\left\langle \Delta x^2 \right\rangle \sim (\dot{\gamma} t)^2$. However, at larger time scale, the extensive interaction with neighboring particles restores the diffusive motion. Moreover, Fig. 8.5a also compares the results from full hydrodynamic computations and from the near-field Brownian approximation. Their agreement is satisfactory despite small quantitative differences.

The suspension dynamics at $\bar{\Pi} = 50$ are shown in Fig. 8.5b, where both $d^s_{\infty,33}$ and $d^s_{\infty,22}$ are presented in the main figure and $\left\langle \Delta x_2^2 \right\rangle$ and $\left\langle \Delta x_3^2 \right\rangle$ in the inset. There are several noteworthy features. First, when the imposed stress is much smaller than the yield stress, e.g. at $\mathrm{Pe}_\sigma = 150$, the suspension arrests and the long-time self-diffusivities vanish. At this Pe_σ, the mean square displacement does not grow linearly with time, but rather reaches a constant value characterizing the size of the confining cage. Close to the flow-arrest transition, e.g., at $\mathrm{Pe}_\sigma = 170$, the suspension becomes activated and there is a small but finite diffusivity. Unlike the liquid-like suspensions at $\bar{\Pi} = 1.5$ in Fig. 8.5a, the suspensions do not exhibit a zero-shear diffusivity. As the imposed stress exceeds the yield stress, the diffusivities grow with Pe_σ, and exhibit little anisotropy, i.e., $d^s_{\infty,33} \approx d^s_{\infty,22}$. At higher Pe_σ, however, the diffusivities decrease due to the string order formation seen in Fig. 8.3. The qualitative influences of structural formation in the suspension dynamics are also evidenced by the distinct $\left\langle \Delta x_2^2 \right\rangle$ and $\left\langle \Delta x_3^2 \right\rangle$ at $\mathrm{Pe}_\sigma = 10^3$ in Fig. 8.5b inset. Moreover, with the dissolution of the string order phase at higher Pe_σ, $d^s_{\infty,22}$ becomes much higher than $d^s_{\infty,33}$, suggesting anisotropy in the suspension dynamics. From the inset, the particles move more easily in the 2-direction due to the enhanced velocity fluctuations in the non-Brownian limit [43].

8.4 A granular perspective on colloidal rheology

Here we examine the constant stress and pressure rheology of dense colloidal suspensions using a granular perspective. The results with string order formation are not included because, as is shown in Sec. 8.3, the string order phase introduces qualitatively different suspension behaviors.

Mechanical responses

Fig. 8.6 presents the shear viscosity η_s/η_0, the volume fraction ϕ, and the *macroscopic* friction coefficient $\mu = \sigma/\Pi$ as functions of the viscous number $I_v = \dot{\gamma}\eta_0/\Pi$ defined in Eq. (8.3) over a wide range of imposed pressures $\bar{\Pi}$ from the constant

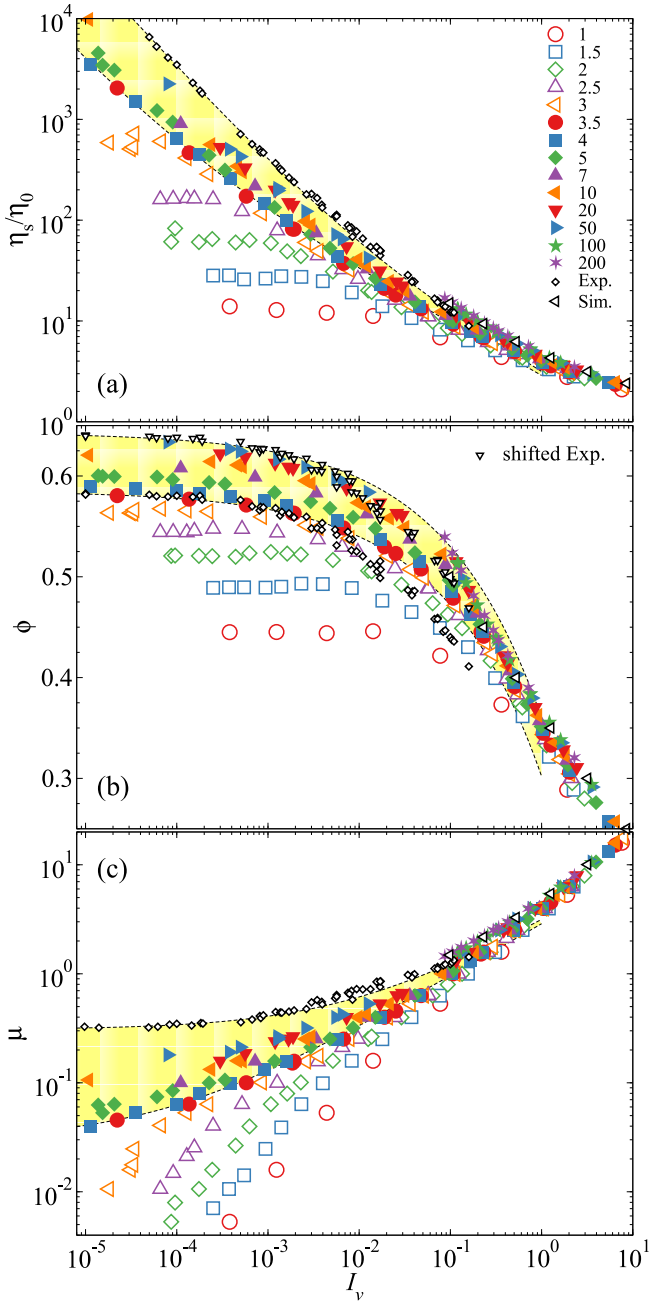

Figure 8.6: (Color online) The suspension shear viscosity η_s/η_0 (a), the volume fraction ϕ (b), and the *macroscopic* friction coefficient $\mu = \sigma/\Pi$ as functions of the viscous number $I_v = \dot{\gamma}\eta_0/\Pi$ with different imposed pressures $\bar{\Pi}$. Also presented are the non-Brownian results from experiments [24] (black open diamonds) and Accelerated Stokesian Dynamics (ASD) simulations at fixed strain rate $\dot{\gamma}$ and volume fraction ϕ [54] (black open left triangles). The shaded area bounded by dashed lines are from the rheological model outlining the boundary of glassy suspensions. The experimental results shifted upwards to ϕ_{SAP} are also presented in (b) (black open down triangles).

stress and pressure simulations. In Fig. 8.6 the liquid-like suspensions, which do not develop a yield stress, are shown as open symbols, and glassy suspensions, which exhibit flow-arrest transitions, are shown as filled symbols. Using I_v highlights the importance of pressure on the suspension rheology. Consistent with Fig. 8.1, with constant imposed pressure, η_s/η_0 and ϕ decrease, and μ increases with increasing I_v. In the limit $I_v \to \infty$, the shear viscosity η_s approaches the solvent viscosity η_0, the volume fraction ϕ asymptotes zero, and the friction coefficient μ grows without bound due to suspension dilation. Fig. 8.6 is similar to the results without HIs [25, 26] with quantitative differences. In addition, for comparison Fig. 8.6 also present results from the experiments of Boyer et al. [24] and the Accelerated Stokesian Dynamics (ASD) simulations of Sierou and Brady [54] on non-Brownian suspensions.

Fig. 8.6a shows the suspension shear viscosity η_s/η_0. Liquid-like suspensions occur at low imposed pressures $\bar{\Pi} < 3.5$, and they exhibit a zero-shear viscosity in the $I_v \to 0$ limit, which grows with increasing $\bar{\Pi}$. At higher confining pressures, $\bar{\Pi} \geq 3.5$, the zero-shear viscosity disappears as the suspension develops yield stresses. When $I_v \gg 1$, the data collapse towards the solvent viscosity η_0 at all imposed pressures due to suspension dilation. For small I_v, the differences among the isobaric η_s decrease with increasing $\bar{\Pi}$. As $\bar{\Pi} \to \infty$, a non-Brownian limit is expected to emerge. However, the highest pressure with $I_v < 0.1$ in our simulations is $\bar{\Pi} = 50$. At higher imposed pressure, reaching a low I_v without significant stress contributions from the interparticle forces is computationally difficult. Reducing the dimensionless time step $\Delta\tau$ from 0.01 to 0.0025 only marginally reduces the viscous number I_v where the interparticle force stress contribution is less than 1%. Therefore, despite an evident tendency, the imposed pressures $\bar{\Pi}$ in the simulations is not high enough to achieve the limiting non-Brownian viscosity.

In Fig. 8.6a the suspension viscosity in the non-Brownian limit is established from the non-Brownian experiments [24] and ASD simulations [54], shown in open diamonds and triangles in black, respectively. The experiments and simulations complement the entire I_v range with $I_v \lesssim 0.1$ from the experiments and $I_v \gtrsim 0.1$ from the simulations. At $I_v \approx 0.1$, the experimental and the numerical results overlap and agree well, showing consistent non-Brownian suspension behaviors. The small difference between the non-Brownian experiments and simulations may arise from different interparticle forces [54]. The suspension viscosity from the constant stress and pressure simulation agree well with the non-Brownian simulation

data for $I_v \gtrsim 0.1$. At $I_v < 0.1$, the experiments suggest that the viscosities at $\bar{\Pi} = 50$ have not yet reached the non-Brownian limit.

Fig. 8.6b presents the volume fraction ϕ as a function of I_v at various imposed pressures. Consistent with Fig. 8.1, the results show that, for a given I_v, increasing the imposed pressure compresses the suspension, and at fixed pressure, increasing I_v dilates the suspension. For $I_v \ll 1$, the volume fraction asymptotes a value corresponding to the $I_v \to 0$ limit. When $I_v > 1$, the volume fractions collapse to a non-Brownian limiting behavior with $\phi < 0.35$ for all imposed pressures $\bar{\Pi}$. With $I_v < 1$, only a tendency for data collapse is found with $\bar{\Pi} \geq 10$. Similarly to Fig. 8.6a, our imposed pressure $\bar{\Pi}$ is not high enough for the non-Brownian limiting behavior to be reached in the double limit $I_v \to 0$ and $\bar{\Pi} \to \infty$.

The non-Brownian results from earlier simulations and experiments are also presented in Fig. 8.6b. At the common I_v range covered by both the experiments and the simulations, the volume fraction results are inconsistent. At $I_v \approx 0.1$, ϕ from the ASD simulations [54] are significantly higher than the experimental data, due to the significantly lower maximum volume fraction $\phi_c \approx 0.585$ in the experiments. Simply shifting the experimental ϕ upwards by an amount of $(\phi_{\text{SAP}} - \phi_c)$ restores the consistency in the non-Brownian results. In Fig. 8.6b, the shifted experimental data are shown in down triangles. The SAP volume fraction ϕ_{SAP} is independently determined from the constant stress and pressure simulation data without the knowledge of earlier non-Brownian results, and is described in later. When $I_v > 0.1$, the shifted non-Brownian ϕ is slightly lower than the collapsed data from the constant stress and pressure simulations, most likely due to the particle size polydispersity in the latter. On the other hand, in the $I_v \ll 1$ limit, the volume fraction behaviors at $\bar{\Pi} = 50$ is close to the shifted non-Brownian results.

Fig. 8.6c presents the *macroscopic* friction coefficient μ as a function of I_v. For liquid-like suspensions with $\bar{\Pi} < 3.5$, μ increases linearly with I_v when $I_v \ll 1$ because the ratio $\mu/I_v = \eta_s/\eta_0$, and the initial linear increase in μ characterizes the suspension's zero-shear viscosity. For glassy suspensions with $\bar{\Pi} \geq 3.5$, the suspensions develop a yield stress, as μ asymptotes a constant, finite value in the limit $I_v \to 0$. Similar to Fig. 8.6a and 8.6b, the friction coefficient data collapse for all imposed pressures when $I_v \gg 1$, and a tendency of data collapse is evident with $\bar{\Pi} \geq 10$ when $I_v \ll 1$. The results from earlier non-Brownian experiments and ASD simulations are also presented in Fig. 8.6c. The non-Brownian experiments and simulations agree for the overlapping viscous numbers near $I_v \approx 0.1$, suggesting

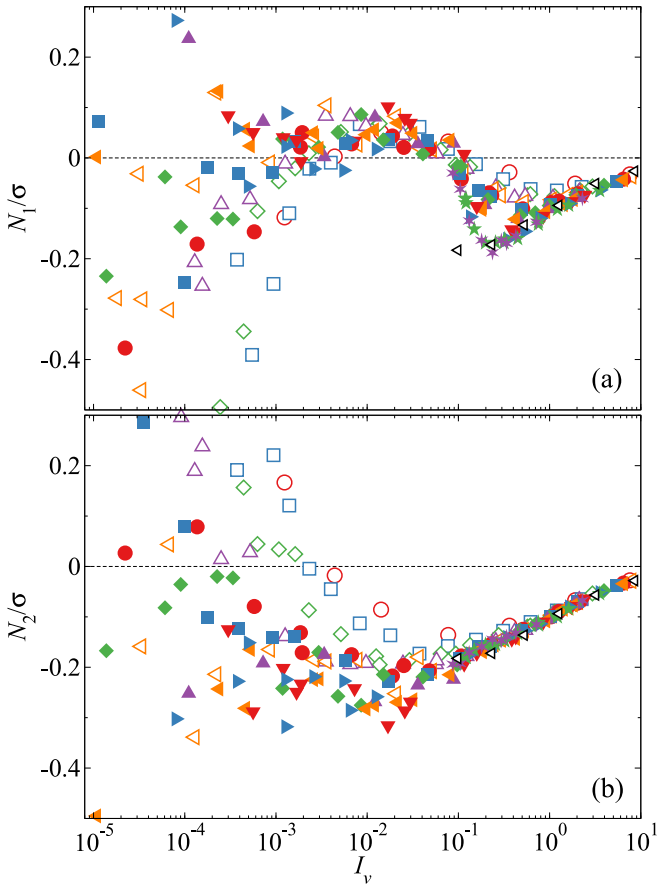

Figure 8.7: (Color online) The first and the second normal stress differences scaled with the shear stress, N_1/σ (a) and N_2/σ (b), as functions of the viscous number I_v at various imposed pressures $\bar{\Pi}$. Also presented are the non-Brownian ASD simulation results [54]. The legends are identical to those of Fig. 8.6.

a consistent behavior similar to the consistent viscosity in Fig. 8.6a. The non-Brownian friction coefficient μ with $I_v \gtrsim 0.1$ agree well with the collapsed constant stress and pressure simulation results. When $I_v \lesssim 0.1$, however, the experiments of Boyer et al. [24] show a higher limiting friction coefficient compared to the limiting μ at $\bar{\Pi} = 50$. Our results suggest that, the expected μ from simulations in the $\bar{\Pi} \to \infty$ and $I_v \to 0$ limits should be consistent with the non-Brownian experimental results here.

The first and the second normal stress differences, N_1 and N_2, are computed from the total stress $\langle \boldsymbol{\Sigma} \rangle$ as,

$$N_1 = \langle \Sigma_{11} \rangle - \langle \Sigma_{22} \rangle , \tag{8.29}$$

$$N_2 = \langle \Sigma_{22} \rangle - \langle \Sigma_{33} \rangle . \tag{8.30}$$

Fig. 8.7a and 8.7b respectively present the scaled normal stress differences, N_1/σ and N_2/σ, as functions of the viscous number I_v at different imposed pressures $\bar{\Pi}$. In the high I_v regime ($I_v > 0.5$ for N_1 and $I_v > 0.1$ for N_2), both N_1 and N_2 are negative, and collapse to non-Brownian limiting behaviors at different $\bar{\Pi}$. The negative N_1 is the signature of HIs in the suspensions, because, to separate a particle pair, the HIs pull the pair together, while the interparticle forces push it apart. The former lead to negative N_1, while the latter to positive [33, 54, 56]. The magnitude of N_1/σ and N_2/σ decreases with increasing I_v due to suspension dilation. This is in contrast to the fixed volume rheology where N_1 and N_2 asymptote high-shear limiting values [33, 56]. The non-Brownian ASD simulation results [54] are also presented in Fig. 8.7, and they agree well with the collapsed constant stress and pressure simulations, except for N_1 at $I_v = 0.1$. The first normal stress difference N_1 near $I_v = 0.1$ are close to zero for all imposed pressures, and with $I_v > 0.1$, they first reach a negative minimum before increasing again. The non-Brownian simulation results only show increase in N_1 with growing I_v, as fluctuations in ϕ about its average value for $I_v \approx 0.1$ may reduce $|N_1|$ compared to the corresponding fixed ϕ simulations.

In the low shear limit, dilute theories [105, 108] predict that N_1 increases and N_2 decreases from zero in a fashion proportional $\dot{\gamma}^2$. The simulation results in Fig. 8.7 do not reveal such behaviors, suggesting that I_v is not sufficiently low. On the other hand, N_1 and N_2 behave distinctly in the low I_v regime. In Fig. 8.7a, N_1 is largely negative when $I_v < 10^{-3}$. The general trend is that, with increasing $\bar{\Pi}$, N_1 at $I_v < 10^{-5}$ shifts from negative to positive. In the range $10^{-3} < I_v < 0.1$, N_1 becomes loosely collapsed. It first becomes slightly positive and decreases after reaching a maximum. The second normal stress difference N_2 in Fig. 8.7b reduces from the lower I_v limit and reaches a local minimum before collapsing to the high I_v behaviors. The N_2 values at $I_v < 10^{-5}$ decrease from positive to negative with increasing $\bar{\Pi}$, and become increasingly noisy. The low I_v behaviors in Fig. 8.7a and 8.7b demonstrate the complex interplay of between Brownian motion and HIs in polydisperse suspensions.

Structural peaks

The peak values of pair distribution function along the compressional and the extensional axes, $\max(g_{\text{comp}})$ and $\max(g_{\text{ext}})$, are key suspension structural features. As discussed in Sec. 8.3, they are closely related to the suspension rheology, and are strongly affected by the particle Brownian motion and HIs. Fig. 8.8 presents

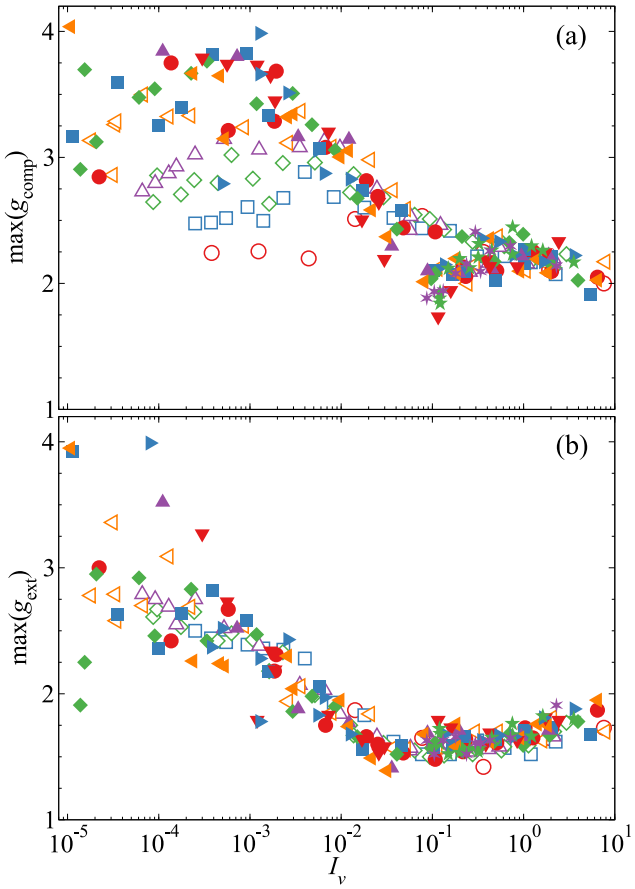

Figure 8.8: (Color online) The peak values of the pair distribution function along the compressional and the extensional axes, max(g_{comp}) (a) and max(g_{ext}) (b), as functions of the viscous number I_v at various imposed pressures $\bar{\Pi}$. The legends are identical to those of Fig. 8.6.

max(g_{comp}) and max(g_{ext}) as functions of the viscous number I_v over different imposed pressures $\bar{\Pi}$.

Fig. 8.8a focuses on the peak value of the pair distribution function along compressional axis, max(g_{comp}). For liquid-like suspensions with $\bar{\Pi} < 3.5$, max(g_{comp}) first increases and then decreases with increasing I_v. The decrease of max(g_{comp}) at different $\bar{\Pi}$ largely collapse. With increasing $\bar{\Pi}$ the peak value max(g_{comp}) in the equilibrium limit also grows, and joins the collapsed max(g_{comp}) decrease at a smaller I_v. For glassy suspensions with $\bar{\Pi} \geq 3.5$, max(g_{comp}) also collapses at small I_v: the initial increase takes place at $I_v < 10^{-4}$, followed by a plateau until $I_v \approx 10^{-3}$. Further increase in I_v lead to decrease in max(g_{comp}). With $I_v \gtrsim 0.1$, max(g_{comp}) discontinuously drops to max(g_{comp}) ≈ 2, reaches a maximum, and decreases again

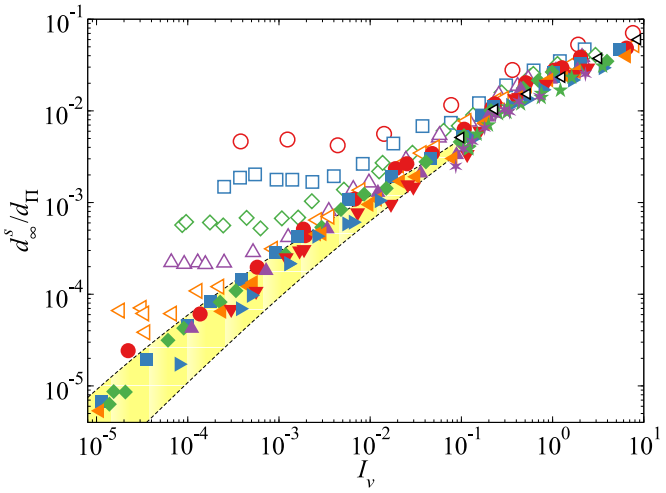

Figure 8.9: (Color online) The long-time self-diffusivity in the vorticity direction scaled with the pressure diffusion scale d^s_∞/d_Π, where $d_\Pi = a^2\Pi/\eta_0$, as functions of the viscous number I_v at various imposed pressures $\bar{\Pi}$. Also presented are the non-Brownian ASD simulation results [43, 54]. The yellow shaded region bounded by dashed liens are predictions from Eq. (8.43). The legends are identical to those of Fig. 8.6.

along with the lower $\bar{\Pi}$ results. The discontinuous behavior of $\max(g_{\text{comp}})$ is likely associated with the string phase structures in Fig. 8.3.

Fig. 8.8b shows the changes of $\max(g_{\text{ext}})$ with respect to I_v at various I_v. In the extensional axis, the peak values of g_{ext} collapse better compared to $\max(g_{\text{comp}})$ in Fig. 8.8a: with increasing I_v, $\max(g_{\text{ext}})$ first decreases, reaching a minimum at $I_v \approx 0.1$, and then increases slightly. The data in the $I_v \to 0$ limit are somewhat scattered, but unlike $\max(g_{\text{comp}})$, they do not show different low I_v limiting values at different $\bar{\Pi}$. Moreover, the range of I_v corresponding to $\max(g_{\text{ext}})$ increases is also the I_v range where $\max(g_{\text{comp}})$ becomes discontinuous, suggesting that they are caused by the same mechanism, possibly due to the stronger HIs among particles. Fig. 8.8 highlights the importance of the compressional quadrant on the structural contributions to the suspension rheology in the low I_v limit.

Long-time self-diffusivity

We characterize the particle diffusive dynamics using the long-time self-diffusivity in the vorticity direction, $d^s_{\infty,33}$, and for simplicity refer to it as d^s_∞ in the following discussion. Usually, the diffusion of Brownian suspensions is compared with the single-particle Stokes-Einstein-Sutherland diffusivity d_0, as is the case of Fig. 8.5.

However, for strongly driven suspensions far from equilibrium, a different diffusion scale may necessary as thermal fluctuations may be irrelevant for the suspension dynamics. For the constant stress and pressure simulations in this work, we choose the pressure diffusion scale,

$$d_\Pi = a^2\Pi/\eta_0, \tag{8.31}$$

for the characterization of the diffusivity d^s_∞.

Fig. 8.9 presents the scaled diffusivity d^s_∞/d_Π as functions of the viscous number for different $\bar{\Pi}$, with liquid-like suspensions ($\bar{\Pi} < 3.5$) in open symbols and glassy suspensions ($\bar{\Pi} \geq 3.5$) in filled symbols. For liquid-like suspensions, d^s_∞/d_Π increases with I_v from a plateau corresponding to the equilibrium at-rest value. Increasing $\bar{\Pi}$ reduces the at-rest diffusivity d^s_∞/d_Π, as both the equilibrium self-diffusivity decreases with the volume fraction ϕ and the pressure increases with ϕ. In addition, increasing $\bar{\Pi}$ also reduces the viscous number I_v where d^s_∞/d_Π departs from the at-rest values, e.g., at $\bar{\Pi} = 1$, d^s_∞ departs the plateau at $I_v \approx 10^{-2}$, and at $\bar{\Pi} = 2.0$, the departure viscous number is $I_v \approx 10^{-3}$. With $I_v > 0.1$, the difference in d^s_∞/d_Π between different $\bar{\Pi}$ reduces significantly.

For glassy suspensions, d^s_∞/d_Π does not show a plateau and always increases with increasing I_v. The lack of a plateau suggests that the at-rest diffusion vanishes, i.e., as $d^s_\infty/d_\Pi \to 0$ as $I_v \to 0$. Therefore, in the glassy regime, particles are frozen by their neighbors at $\dot{\gamma} = 0$, and the diffusion process is restored with flow ($\dot{\gamma} \neq 0$). The pressure scaled diffusivity d^s_∞/d_Π for glassy suspensions is lower than its liquid-like counterpart and decreases with further pressure increase. In the non-Brownian high-pressure limit $\Pi \to \infty$, d^s_∞/d_Π collapses to a jamming limit as evidenced by the data collapse trend in Fig. 8.9. In this limit, d^s_∞/d_Π remains finite despite diverging pressure, and grows with I_v. Fig. 8.9 highlights the importance of pressure in suspension dynamics, an frequently overlooked aspect in studies at lower Π or ϕ. Note that Eq. (8.31) is similar to the single-particle d_0 by replacing the thermal energy scale $k_\mathrm{B}T$ with a pressure energy scale $a^3\Pi$. The collapse of d^s_∞/d_Π in the high pressure limit suggests that the pressure may be considered a measure of the internal fluctuations in the system, which are explored in Sec. 8.5.

Fig. 8.9 also presents the non-Brownian ASD simulation results [43, 54] (in black open left triangles) for comparison, as they are the only rheology studies with appropriate normal stress and diffusion characterizations. The non-Brownian results agree well with the high pressure results with $I_v > 0.1$, providing an independent validation for the constant stress and pressure simulations. The shaded region

bounded by dashed lines in Fig. 8.9 is the glassy regime predicted by the model presented Sec. 8.4 together with the universal collapse found in Sec. 8.5. The non-Brownian limit from the model, shown as the lower dashed line in Fig. 8.9, can only achieved with simulations at higher imposed pressures.

A model for glassy rheology

Fig. 8.6 shows that the rheological behavior of glassy suspensions ($\bar{\Pi} \geq 3.5$ in filled symbols) is similar to the non-Brownian limiting behavior. For example, all glassy suspensions exhibit a viscosity divergence and the emergence of yield stress as $I_v \to 0$. Physically, as the suspensions become glassy with sufficiently high imposed pressure, its at-rest dynamics become extremely slow and its flow behavior becomes dominated by the external forcing. In other words, if we characterize the at-rest dynamics of suspensions using a diffusivity d_T, in the glassy state, the particles are effectively locked by their neighbors, and therefore d_T/d_0 vanishes. Therefore, as soon as the suspension begins to flow, the effective Péclet number $\mathrm{Pe}_T = \dot{\gamma}a^2/d_T \gg 1$ as long as $\dot{\gamma}$ is finite. Consequently, it is clear that the non-Brownian dynamics dominate the behavior of glassy suspensions. This is one of the principle conclusions of our earlier work [25].

The rheology of non-Brownian suspensions beyond the flow-arrest transition can be characterized by the departure of ϕ and μ from their arrest values,

$$\phi = \phi_m - \delta\phi \quad \text{and} \quad \mu = \mu_m + \delta\mu, \tag{8.32}$$

where μ_m and ϕ_m are the limiting arrest friction coefficient and volume fraction, and $\delta\mu$ and $\delta\phi$ characterize how the suspension departures from the arrested state. For non-Brownian systems, $\delta\mu$ and $\delta\phi$ depends only on the viscous number, and assuming a power law,

$$\delta\phi = K_\phi I_v^{\alpha_\phi} \quad \text{and} \quad \delta\mu = K_\mu I_v^{\alpha_\mu}, \tag{8.33}$$

where K_ϕ, α_ϕ, K_μ, and α_μ are constants. Eq. (8.33) describes a wide range of experiments and simulations of non-Brownian systems, and is also suggested from theoretical investigations [68, 69].

We characterize the glassy rheology for $I_v < 1$ in Fig. 8.6 using Eq. (8.32) and (8.33). Since the physics of jamming dominates the glassy suspension behavior, we speculate that the power law relations in Eq. (8.33) are unaffected by thermal fluctuations and are independent of the imposed pressure $\bar{\Pi}$. Meanwhile, the arrest

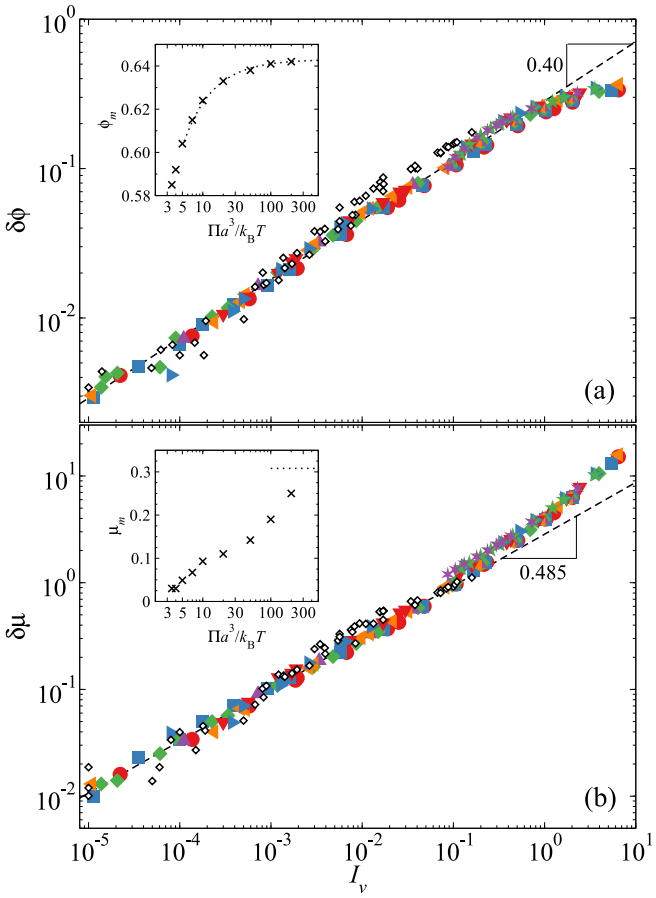

Figure 8.10: (Color online) The incremental volume fraction $\delta\phi = \phi_m - \phi$ (a) and friction coefficient $\delta\mu = \mu - \mu_m$ (b) as functions of the viscous number I_v for glassy suspensions with $\bar{\Pi} \geq 3.5$. The dashed lines in the main figures show Eq. (8.33) with parameters in Table 8.1. The insets show the limiting volume fraction ϕ_m (a) and the limiting friction coefficient μ_m (b) as functions of the imposed pressure $\bar{\Pi}$. The dashed line in the inset of (a) shows Eq. (8.34), and the dashed line in the inset of (b) is the non-Brownian μ_{SAP}. Also presented are the non-Brownian experimental results [24] in open black diamonds. The legends are identical to those in Fig. 8.6.

volume fraction ϕ_m and friction coefficient μ_m change with the imposed pressure. We find the optimal parameters that best describe the results in Fig. 8.6 using non-linear regression. Note that the non-Brownian limiting results from experiments [24] and simulations [54] are *not* considered in the regression process, and can be used as an independent check.

Fig. 8.10 presents $\delta\phi$ and $\delta\mu$ as functions of I_v for glassy suspensions with $\bar{\Pi} \geq 3.5$. The parameters for Eq. (8.33) from the regression analysis are shown in the first two columns of Table 8.1. Here, the volume fraction exponent $\alpha_\phi = 0.40$ is close to

the theoretical prediction of 0.35 [68], and is consistent with simulations of inertial systems [109] and non-Brownian viscous systems without HIs in the zero-pressure limit [62], where both studies have found $\alpha_\phi = 0.39$. The friction coefficient exponent $\alpha_\mu = 0.485$ is close to the non-Brownian experiments of Boyer et al. [24] which have a value of 0.5. The fitted ϕ_m and μ_m as functions of the imposed pressure $\bar{\Pi}$ are presented in the corresponding insets. The excellent data collapse suggests that Eq. (8.33) adequately describes the glassy suspension behavior for imposed pressures $\bar{\Pi}$ from 3.5 to 200. Also presented in Fig. 8.10 are the non-Brownian experimental results [24]. The simulation results agree with the experiment when the experimental critical friction coefficient μ_c is shifted from 0.32 to 0.308 with the original critical volume fraction $\phi_c = 0.585$. Here, Eq. (8.33) also satisfactorily describes the non-Brownian experimental data, which are not considered in the regression analysis. Fig. 8.10 shows that Eq. (8.33) with a single set of parameters describes glassy suspension behavior for $\bar{\Pi} \geq 3.5$ including the non-Brownian limit. It confirms our assertion that the dynamics of glassy dynamics are dominated by jamming, and that thermal fluctuations only affect the location of the flow-arrest transitions.

The insets of Fig. 8.10 show the locations of the flow-arrest transitions, (μ_m, ϕ_m), at different imposed pressures $\bar{\Pi} \geq 3.5$. In constant stress and pressure rheology, the smallest pressure where the suspension begins to exhibit flow-arrest transitions is called the glass transition pressure $\bar{\Pi}_G$, and in this work $\bar{\Pi}_G = 3.5$, with the corresponding glassy arrest location $(\mu_G, \phi_G) = (0.03, 0.585)$ from Fig. 8.10. The volume fraction ϕ_G is consistent with the hard-sphere colloidal glass transition, which is often marked by the divergence of the viscosity or the relaxation time [18, 22]. The finite μ_G at the glass transition suggests the sudden appearance of a yield stress, consistent with mode-coupling theory predictions [110]. To find the flow-arrest transition location in the $\bar{\Pi} \to \infty$ limit—the SAP—it is necessary to consider the non-Brownian experimental results [24], as the maximum imposed pressures for $I_v \ll 1$ are not sufficiently high. From the excellent collapse of $\delta\mu$ in Fig. 8.10b, we adopt the adjusted experimental limiting friction coefficient $\mu_c = 0.308 = \mu_{\text{SAP}}$. Determining ϕ_{SAP} is more subtle, because, as is shown in Fig. 8.6b, the original experimental ϕ is incompatible with the numerical results. Here, we found that the arrest volume fractions $\phi_m > 0.60$ with $\bar{\Pi} \leq 50$ satisfy the expression,

$$\bar{\Pi} = c_m/(\phi_{\text{SAP}} - \phi_m), \tag{8.34}$$

and the fitting shows that $\phi_{\text{SAP}} = 0.643$. Eq. (8.34) is appropriate here as it also

Table 8.1: The parameters for the model of glassy suspension rheology in Eq. (8.32)–(8.35) and Eq. (8.43).

K_μ	2.85	μ_G	0.03	$\bar{\Pi}_G$	3.5
α_μ	0.485	ϕ_G	0.585	c_m	0.202
K_ϕ	0.283	μ_{SAP}	0.308	β_y	0.211
α_ϕ	0.40	ϕ_{SAP}	0.643	K_d	0.037

describes the pressure of nearly jammed hard-sphere systems [111]. A check for the validity of ϕ_{SAP} is that, by shifting the experimental data upwards by $(\phi_{\mathrm{SAP}} - \phi_c)$ in Fig. 8.6b, the shifted results smoothly connect the non-Brownian ASD simulations near $I_v \approx 0.1$. Therefore, with non-Brownian experimental results and extrapolation, the $\bar{\Pi} \to \infty$ limit of the flow-arrest point, the SAP, is $(\mu_{\mathrm{SAP}}, \phi_{\mathrm{SAP}}) = (0.308, 0.643)$.

Finally, the following expression describes the relation between ϕ_m and μ_m in the inset of Fig. 8.10:

$$\frac{\mu_{\mathrm{SAP}} - \mu_m}{\mu_{\mathrm{SAP}} - \mu_G} = \left(\frac{\phi_{\mathrm{SAP}} - \phi_m}{\phi_{\mathrm{SAP}} - \phi_G}\right)^{\beta_y}, \tag{8.35}$$

with $\beta_y = 0.211$. Eq. (8.32)–(8.35) present a simple model for the rheology glassy suspensions valid for imposed pressure $\bar{\Pi} > \bar{\Pi}_G$. Table 8.1 summarizes the model parameters. In Fig. 8.6 the model results in the glassy limit at $\bar{\Pi} = \bar{\Pi}_G$ and the jamming limit at $\bar{\Pi} \to \infty$ are shown in dashed lines and the region bounded by these lines are colored yellow to show the glassy region. Fig. 8.6 shows that the simple model is valid near the flow arrest transitions for $I_v \lesssim 0.1$. At higher I_v, the model underestimates μ, and cannot capture the qualitative trend of the changes in ϕ when $\phi < 0.4$. Compared to models based on volume fractions [21, 112], the rheology model in Eq. (8.32)–(8.35) is simple yet powerful, with Eq. (8.32) and (8.33) highlighting the dominance of jamming physics, and Eq. (8.34) and (8.35) describing the adjustments from thermal fluctuations.

The flow map

Fig. 8.11 presents the μ-ϕ flow map at various imposed pressures $\bar{\Pi}$. The flow map is qualitatively similar to the results without HIs [25]. At a given $\bar{\Pi}$, the suspension dilates with increasing μ. The zero shear limit corresponds to $\mu \to 0$ in Fig. 8.11. For liquid-like suspensions, ϕ in the zero shear limit asymptotes the equilibrium value corresponds to the imposed pressure $\bar{\Pi}$. At $\bar{\Pi} \geq 3.5$, the glassy suspensions stops to flow when $\mu < \mu_m$ as the imposed stress is less than the yield stress σ_m. In Fig. 8.11, a region of arrested states emerges at the bottom right corner. The boundary for the arrested region, i.e., the yield surface, is shown in

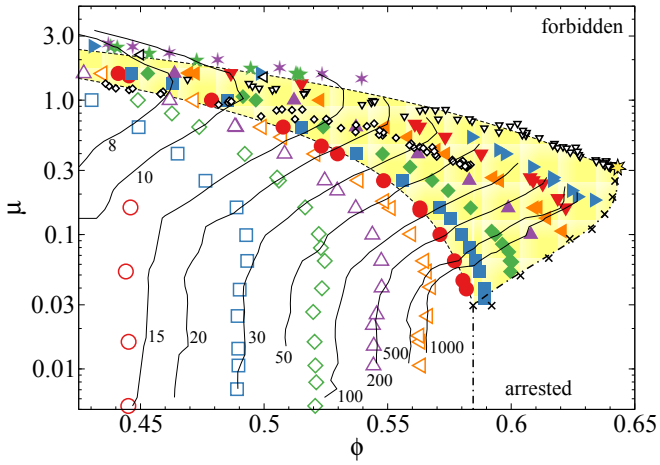

Figure 8.11: (Color online) The *macroscopic* friction coefficient $\mu = \sigma/\Pi$ as functions of the volume fraction ϕ over a wide range of imposed pressures $\bar{\Pi}$ for constant stress and pressure simulations. Also shown are the original and shifted non-Brownian experiments Boyer et al. [24], and the ASD simulations of Sierou and Brady [54]. The shifted experimental results shift the volume fraction data by $(\phi_{\text{SAP}} - \phi_c)$ with $\phi_c = 0.585$. The legends are identical to Fig. 8.6. The shaded region bounded by the dashed lines are from the rheology model outlining the region of glassy behavior. The viscosity contours up to $\eta_s/\eta_0 = 10^3$ are shown as solid lines with annotated viscosity. The crosses show the arrest location (μ_m, ϕ_m) at different imposed pressures, and the dash-dotted line outlines the yield surface from Eq. (8.35). The Shear Arrest Point (SAP) is highlighted as a star at the intersection of the arrested, the inaccessible, and the flowing region.

crosses in Fig. 8.11. With increasing imposed pressure $\bar{\Pi}$, the limiting friction coefficient μ_m increases until reaching the non-Brownian limit μ_{SAP}. That μ_m grows with increasing imposed pressure suggests that $\delta\sigma_m/\delta\Pi \geq \mu_m$, with the equal sign established at the SAP. That is, increasing the imposed pressure causes a larger increase in the yield stress $\delta\sigma_m$ predicted by the current limiting friction coefficient $\mu_m\delta\Pi$ until reaching the non-Brownian limit. In the $\bar{\Pi} \to \infty$ limit, the suspension dynamics are expected to collapse to the non-Brownian behaviors. With $\phi \leq 0.55$, the high-pressure data collapse is evident for $\bar{\Pi} = 100$ and $\bar{\Pi} = 200$. However, at larger ϕ, the constant stress and pressure simulation results only show a tendency to collapse. In Fig. 8.11, the non-Brownian limit is established by the ϕ-shifted experimental results. Since the hydrodynamic simulations can capture the suspension behaviors with HIs, unlike simulations without HIs [25], shifting the experimental friction coefficient is not necessary. This also confirms the mean-field hydrodynamic arguments in our earlier work. In the μ-ϕ flow map, the region beyond

the non-Brownian limit is physically inaccessible, and is shown as "forbidden" in Fig. 8.11. At the intersection of the forbidden, the arrested, and the flowing regions, the SAP emerges at the highest volume fraction attainable in the flowing suspensions.

In Fig. 8.11, the glassy suspension behaviors from the rheology model are shaded in yellow. The regions are bounded by three curves: two outline the $\mu(\phi)$ behaviors at $\bar{\Pi} = \bar{\Pi}_G$ and $\bar{\Pi} \to \infty$, one from the yield surface in Eq. (8.35). Note that at ϕ_G, the yield surface is vertical up to the glassy friction coefficient μ_G as we assume a physical scenario predicted by the mode-coupling theory [110, 113]: that as soon as the volume fraction exceeds ϕ_G, the suspension develops a finite static yield stress corresponding to μ_G. The glassy region predicted by the rheology model agrees well with the simulation and experimental results near the flow-arrest transitions.

Fig. 8.11 also shows the shear viscosity contours up to $\eta_s/\eta_0 = 10^3$. The contours show that, at a constant volume fraction $\phi \leq 0.57$, the shear viscosity first decreases and then increases with increasing μ, suggesting continuous shear thickening, which is also observed in constant volume simulations [8, 32, 33]. Continuous shear thickening arises from HIs among particles by forming "hydroclusters" in the suspensions. However, with $\phi > 0.57$, shear thickening behaviors disappear from the viscosity contours. One may argue that in the constant stress and pressure simulations, the strain rates at high volume fractions are not high enough to reveal the shear thickening behaviors. For example, at $\phi = 0.60$, the strain rate Péclet number corresponding to an impose pressure $\bar{\Pi} = 50$ is $\mathrm{Pe}_{\dot{\gamma}} \approx 6.1$, as in Fig. 8.1b and 8.1d, $\phi = 0.60$ corresponds to $\mathrm{Pe}_\sigma = 400$ and $\eta_s/\eta_0 = 65$, and $\mathrm{Pe}_{\dot{\gamma}}$ can be obtained from Eq. (8.24). However, for dense suspensions, experiments [114] and simulations [33] also show that the onset $\mathrm{Pe}_{\dot{\gamma}}$ of shear thickening behaviors decreases with increasing volume fractions, and $\mathrm{Pe}_{\dot{\gamma}} \approx 6$ may not be low at this volume fraction. Another possibility is that the continuous shear thickening disappears at high ϕ, as the decreasing Brownian viscosity contribution η^{B} from a high value masks the increase in the flow viscosity η^{E}, and that η^{E} cannot grow without bound as any small steric effects may significantly limit its value.

To understand the lack of shear thickening in Fig. 8.11 at high ϕ, we performed constant stress and *volume* simulations over a wide range of imposed stresses at $\phi = 0.6$. Fig. 8.12 presents the resulting shear viscosity η_s and its flow and Brownian contributions, η^{E} and η^{B}, as functions of Pe_σ ranging from 10 to 10^5. The strain rate Péclet number $\mathrm{Pe}_{\dot{\gamma}}$ corresponding to $\mathrm{Pe}_\sigma = 10^5$ is $\mathrm{Pe}_{\dot{\gamma}} = 1537$. With increasing Pe_σ, η^{B} decreases drastically towards zero. However, η^{E} increases

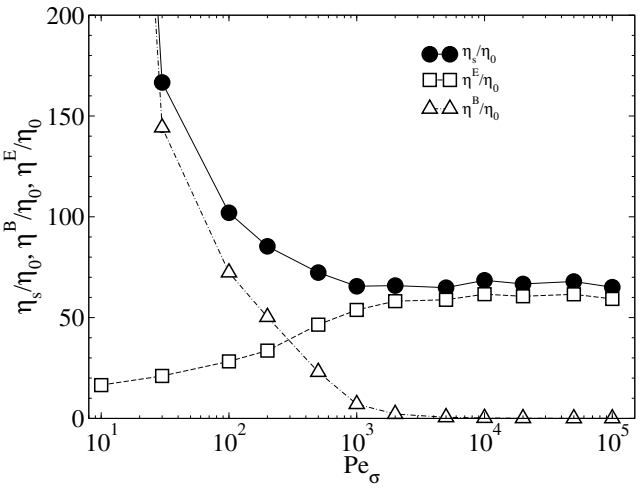

Figure 8.12: The shear viscosity η_s/η_0 and its flow and Brownian contributions, η^{E}/η_0 and η^{B}/η_0 as functions of stress Péclet number in constant stress and *volume* simulations at $\phi = 0.60$ with the particle size polydispersity p.d. = 0.1. The duration of each simulation is $\tau = 2000$ with a step size $\Delta\tau = 0.01$.

mildly, and reaches a high Pe_σ limiting value. Because the excluded volume radius is slightly larger than the hydrodynamic radius in the simulations, η^{E} cannot not continuously grow with Pe_σ. The effect of this interparticle force is evident from the difference between η^{E} and η_s in the $\mathrm{Pe}_\sigma \to \infty$ limit. The net result is that η_s exhibits only shear thinning with increasing Pe_σ until reaching the high Pe_σ viscosity. The increase in η^{E} is masked by the strong reduction of η^{B}. Therefore, in hydrodynamic simulations, even weak excluded volume effects can make the shear thickening disappear at high ϕ.

Fig. 8.11 and 8.12 also suggest that the experimentally observed discontinuous shear thickening [114, 115] cannot occur in hard-sphere suspensions with pure HIs. Other mechanisms must be operative. A popular interpretation of the discontinuous shear thickening is the frictional contact mechanism [53, 116, 117]. Although appealing for its simplicity and effectiveness, this interpretation directly uses the *macroscopic* concept of frictional interactions in granular materials to colloidal particles, which are several orders of magnitude smaller.

The viscosity contours in Fig. 8.11 near flow-arrest transitions are almost parallel to the arrest boundary shown in dash dotted line. From Eq. (8.32) and (8.33), the

suspension viscosity η_s can be expressed in $\delta\phi$ as,

$$\frac{\eta_s}{\eta_0} = \mu_m \left(\frac{\delta\phi}{K_\phi}\right)^{-\frac{1}{\alpha_\phi}} + K_\mu \left(\frac{\delta\phi}{K_\phi}\right)^{\frac{\alpha_\mu - 1}{\alpha_\phi}} . \tag{8.36}$$

Since both exponents α_μ and α_ϕ are positive, η_s exhibits a two-exponent divergence with respect to $\delta\phi$. At small $\delta\phi$, the divergence is characterized by the exponent $-1/\alpha_\phi$, and at large $\delta\phi$, the divergence is characterized by $(\alpha_\mu - 1)/\alpha_\phi$. Equating the first and the second terms in Eq. (8.36) leads to the crossover the volume fraction difference $\delta\phi_c$ and the crossover shear viscosity η_{sc} separating the two divergence regimes:

$$\delta\phi_c = K_\phi \left(\frac{\mu_m}{K_\mu}\right)^{\frac{\alpha_\phi}{\alpha_\mu}} \quad \text{and} \quad \frac{\eta_{sc}}{\eta_0} = 2\mu_m \left(\frac{\mu_m}{K_\mu}\right)^{-\frac{1}{\alpha_\mu}} . \tag{8.37}$$

With the parameters in Table 8.1, the crossover point in the glass limit is $(\delta\phi_c, \eta_{sc}/\eta_0) = (0.0066, 718)$ and in the jamming limit is $(0.045, 60.5)$. Since there is an observation window of $\delta\phi$ and η_s, the crossover is more apparent with large $\delta\phi_c$ and small η_{sc}. For example, the crossover point for non-Brownian soft-potential systems in the zero-pressure limit [62] is $(0.0183, 6.3)$, making the two-exponent behaviors apparent.

For non-Brownian suspensions, Boyer et al. [24] found $\alpha_\phi = 0.5$, leading to a leading order viscosity divergence $\eta_s \propto \delta\phi^{-2}$. In simulations without HIs, a similar viscosity divergence was discovered as in Eq. (8.1), with k_s and k_n independent of $\bar{\Pi}$, suggesting the dominance of the jamming physics. In fact, the universal viscosity divergence in Eq. (8.1) can also be interpreted using Eq. (8.32) and (8.33). Assuming that in Eq. (8.33), K_ϕ is now a function of the imposed pressure Π, and with a new set of limiting volume fractions ϕ_m, the volume fraction difference $\delta\phi = K_\phi(\Pi) I_v^{\alpha_\phi}$. Therefore, the universal shear viscosity η_s and the incremental normal viscosity η_n' divergences in Ref. [25] suggests that the constants k_s and k_n in Eq. (8.1) are

$$k_s = \mu_m K_\phi^{\frac{1}{\alpha_\phi}} \quad \text{and} \quad k_n = \left(1 - \frac{\Pi^{\text{eq}}}{\Pi}\right) K_\phi^{\frac{1}{\alpha_\phi}}, \tag{8.38}$$

also with $\alpha_\phi = 0.5$. Here, $\Pi^{\text{eq}}(\phi) \neq \Pi$ at the flow arrest transitions as the suspensions have to dilate before flowing. This interpretation relies on the existence of a yield stress and yield pressure, and does not reveal K_μ and α_μ in Eq. (8.33). Recently, the exponent $\alpha_\phi = 0.5$ is also discussed using the Herschel-Bulkley rheology of the osmotic pressure [118]. Despite the same underlying physical messages, the model in Sec. 8.4 is more general due to the additional description on the friction

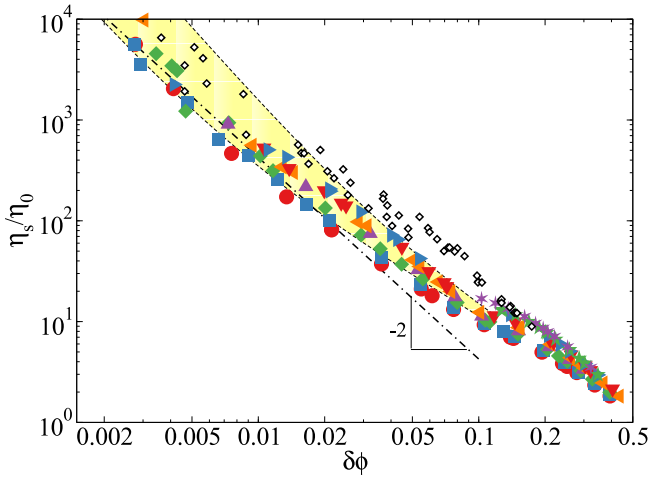

Figure 8.13: (Color online) The shear viscosity η_s/η_0 as a function of the volume fraction distance to the arrest $\delta\phi = (\phi_m - \phi)$ for glassy suspensions with $\bar{\Pi} \geq 3.5$. The non-Brownian experimental results of Boyer et al. [24] are also presented as black open diamonds. The yellow shaded region bounded by dashed lines are predictions from Eq. (8.36). The dash-dotted line shows an alternative viscosity divergence $\propto \delta\phi^{-2}$. The legends are identical to Fig. 8.6.

coefficient μ. More importantly, although the model associated with Eq. (8.1) works for simulations without HIs, it does not fit the SEASD results well.

Fig. 8.13 examines the viscosity divergence near the flow-arrest transition, and presents the shear viscosity η_s as functions of the the volume fraction difference from the arrest $\delta\phi = \phi_m - \phi$ for glassy suspensions with $\bar{\Pi} \geq 3.5$. The glass and the jamming limits of Eq. (8.36) are also presented in Fig. 8.13 in dashed lines. The constant stress and pressure simulation results agree with Eq. (8.36), and generally lie in an area bounded by the glass and the jamming limits highlighted in yellow. However, the non-Brownian experimental results [24] are rather scattered, as the small discrepancies in Fig. 8.10 are amplified in Fig. 8.13. Due to the disparate crossover points in the glass and in the jamming limits, near $\delta\phi = 0.01$ the viscosity appears to diverge at two different exponents. Moreover, by focusing on the data with $\eta_s/\eta_0 > 100$, the dash-dotted line Fig. 8.13 suggests that a divergence of $\delta\phi^{-2}$ also loosely describes the simulation results. That the data are close to the crossover viscosity η_{sc} leads to the ambiguity in the divergence exponent, i.e., any exponent between $-1/\alpha_\phi$ and $(\alpha_\mu - 1)/\alpha_\phi$ may appear reasonable.

Finally, the divergence of the the normal viscosity, $\eta_n = \Pi/\dot{\gamma}$ [24], is shown in Fig. 8.6a, as the inverse scaled normal viscosity is the viscous number $I_v = \eta_0/\eta_n$.

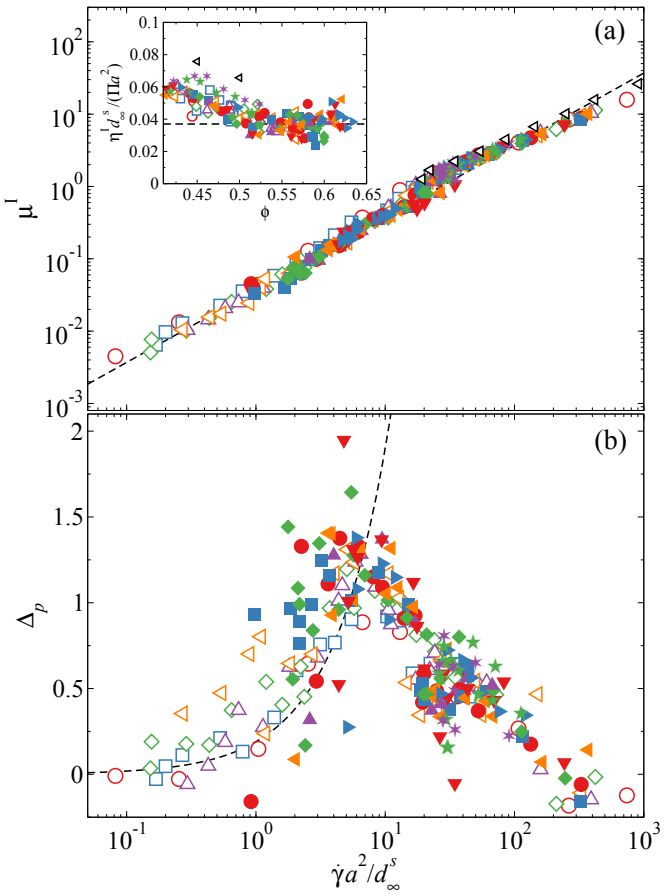

Figure 8.14: (Color online) (a) The interaction friction coefficient $\mu^{\rm I} = \mu - (1 + \frac{5}{2}\phi)I_v$ as functions of the strain rate scale $\dot{\gamma}a^2/d_\infty^s$. The dashed line indicates the linear relation $\mu^I = K_d\dot{\gamma}a^2/d_\infty^s$ with K_d in Table 8.1. The black open left triangles are the non-Brownian ASD simulation results [43, 54]. Inset: the product $(\eta^{\rm I}d_\infty^s/(\Pi a^2)$ as functions of volume fraction ϕ. The interaction viscosity $\eta^{\rm I} = \mu^{\rm I}/I_v$. (b) The peak difference $\Delta_p = \max(g_{\rm comp}) - \max(g_{\rm ext})$ as functions of the strain rate scale $\dot{\gamma}a^2/d_\infty^s$. The dashed lines represents a linear relation $\Delta_p = K_p\dot{\gamma}a^2/d_\infty^s$ with $K_p = 0.19$. In (a) and (b), the legends are identical to those of Fig. 8.6.

Therefore, from Eq. (8.33) we have $\eta_n/\eta_0 = (\delta\phi/K_\phi)^{-1/\alpha_\phi}$ with the constants from Table 8.1.

8.5 Universal behaviors for dense suspensions

Here we explore the universal connection among suspension structure, diffusion, and rheology for *all* imposed pressures. These relations are valid regardless of the way the external forces are imposed, and reveal the fundamental suspension behaviors.

An effective Stokes-Einstein-Sutherland relation

The pressure scaled diffusivity d^s_∞/d_Π in Fig. 8.6a and the suspension shear viscosity η_s/η_0 in Fig. 8.9 are close to up-down mirror images of each other with respect to the viscous number I_v, i.e., where η_s/η_0 is high, the corresponding d^s_∞/d_Π is low, suggesting that the product $\eta_s d^s_\infty/(\eta_0 d_\Pi)$ may be constant. The exception is the $I_v \gg 1$ limit, where the shear viscosity η_s/η_0 collapses stronger than d^s_∞/d_Π, as in the dilute limit $\eta_s \to \eta_0$, but d^s_∞ does not approach d_Π. To eliminate this exception, we introduce an interaction stresses σ^{I} that removes the single-particle contributions, i.e., $\sigma^{\mathrm{I}} = \sigma - (1 + \frac{5}{2}\phi)\eta_0\dot{\gamma}$. This stress definition leads to the interaction friction coefficient μ^{I} and the interaction viscosity η^{I},

$$\mu^{\mathrm{I}} = \mu - (1 + \tfrac{5}{2}\phi)I_v \quad \text{and} \quad \eta^{\mathrm{I}}/\eta_0 = \mu^{\mathrm{I}}/I_v. \tag{8.39}$$

In the $I_v \ll 1$ limit, $\mu^{\mathrm{I}} \to \mu$ and $\eta^{\mathrm{I}} \to \eta_s$. The inset of Fig. 8.14a shows the product $\eta^{\mathrm{I}} d^s_\infty/(\eta_0 d_\Pi) = \eta^{\mathrm{I}} d^s_\infty/(\Pi a^2)$ as functions of the volume fraction ϕ for *all* imposed pressures $\bar{\Pi}$.

The combination $\eta^{\mathrm{I}} d^s_\infty/(\Pi a^2)$ collapses impressively without any fitting parameters over a wide parameter space with over 5 orders of magnitude in Pe_σ and over 2 orders of magnitude in $\bar{\Pi}$. The collapsed results decrease slightly from 0.06 to 0.038 with increasing ϕ up to $\phi \approx 0.52$, and become approximately constant afterwards. Consistent with the observation of the up-down mirror images in Fig. 8.6a and Fig. 8.9, the inset of Fig. 8.14a suggests an effective SES relation for $\phi \gtrsim 0.52$, i.e.,

$$d^s_\infty = \frac{k_{\mathrm{B}} T_{\mathrm{eff}}}{6\pi\eta^{\mathrm{I}} a_z}, \tag{8.40}$$

with the effective temperature

$$k_{\mathrm{B}} T_{\mathrm{eff}} = \Pi a_z^3 \tag{8.41}$$

and the characteristic length scale $a_z \approx 0.8a$. Eq. (8.40) explicitly confirms the idea of effective temperature discussed in Sec. 8.4. It is valid for non-equilibrium sheared suspensions with both strong and weak thermal fluctuations, and, as is shown in the companion paper [26], is not affected by HIs. The characteristic scale a_z is close to the size of the activation zone in the shear transformation zone interpretation of hard-sphere rheology [119]. In the high shear limit, the effective temperature is proportional to the strain rate, $T_{\mathrm{eff}} \propto \dot{\gamma}$, consistent with other definitions of effective temperatures [13, 96]. In particular, the effective temperature defined in the experiments of Eisenmann et al. [96] is proportional to the shear stress,

since they focused on only one volume fraction at low strain rate. As is shown in Fig. 8.6c, with $I_v \to 0$, $\sigma = \mu_m \Pi$, i.e., both σ and Π are suitable for defining an effective temperature near the flow-arrest transitions. However, for a universal collapse shown in the inset of Fig. 8.14a, $T_{\text{eff}} \propto \Pi$ is necessary. In the limit of dilute equilibrium suspensions, the effective temperature is restored to the actual temperature $T_{\text{eff}} \to T$ and $a_z \to a$. Unlike other studies [90, 92, 95], here the base state is the infinitely dilute equilibrium suspension. Both the imposed flow and the presence of particles drive the system from the base state. The effective SES relation in Eq. (8.40) suggests a novel mean-field perspective on the rheology of non-equilibrium colloidal suspensions, highlighting the importance of osmotic pressure.

The main figure of Fig. 8.14a shows another perspective of the effective SES relation, and presents the interaction friction coefficient μ^{I} as a function of the long-time Péclet number,

$$\overline{\text{Pe}} = \dot{\gamma} a^2 / d^s_\infty = I_v d_\Pi / d^s_\infty, \tag{8.42}$$

i.e., the strain rate scaled by the vorticity direction long-time self-diffusivity. In the high shear limit, the long-time diffusivity with fixed ϕ becomes proportional to the strain rate, $d^s_\infty \propto \dot{\gamma}$ [33, 96], and $\overline{\text{Pe}}$ becomes a constant. In contrast, a larger $\overline{\text{Pe}}$ range can be accessed using constant stress and pressure rheology due to suspension dilation.

Without any fitting parameters, *all* simulation data collapse onto a universal curve in Fig. 8.14a. The collapsed μ^{I} is linear to the scaled strain rate up to $\overline{\text{Pe}} \approx 10$, becomes slightly scattered at $\overline{\text{Pe}} \approx 20$, and collapses again. The collapsed data are adequately described by the following linear relation,

$$\mu^{\text{I}} = K_d \overline{\text{Pe}}, \tag{8.43}$$

where the constant $K_d = 0.037$. Scaling the strain rate with the diffusivity in the velocity gradient direction gives similar results. The diffusivity prediction from Eq. (8.43) in the glass and the jamming limit are presented in Fig. 8.9.

For liquid-like suspensions, the particles can diffuse even without flow, and therefore $\overline{\text{Pe}}$ can reach low values. In Fig. 8.14a, the minimum is reached at $\bar{\Pi} = 1$ with $\overline{\text{Pe}} \approx 0.08$. However, for glassy suspensions, Fig. 8.14a shows that only $\overline{\text{Pe}} \gtrsim 1$ is possible. Therefore, the rate of dispersion, d^s_∞ / a^2, is at most as fast as the rate of convection, characterized by $\dot{\gamma}$, i.e., the particle diffusion is driven by the flow, not by the thermal fluctuations. This is because for glassy suspensions, the at-rest

diffusivity $d_T/d_0 \ll 1$ leading to an effective Péclet number $\mathrm{Pe}_T \gg 1$ for any finite $\dot{\gamma}$, and therefore the physics of non-Brownian jamming dominates the suspension dynamics [25]. Moreover, the collapsed results also suggest that the volume fraction ϕ is unimportant.

The lowest imposed pressure corresponds to $\overline{\mathrm{Pe}} \approx 1$ in glassy suspensions is $\bar{\Pi} = 3.5$, and the corresponding friction coefficient $\mu^{\mathrm{I}} \approx 0.03$ in Fig. 8.14a. Therefore, Fig. 8.14a suggests that as soon as the suspension becomes glassy, a finite yield stress emerges discontinuously, consistent with the mode-coupling theory predictions [113] and the rheology model presented in Sec. 8.4. At this limit, since the suspension only begins to flow, $I_v \ll 1$ and therefore $\mu^{\mathrm{I}} \to \mu$. Therefore, Fig. 8.14a independently validates the glass transition friction coefficient, $\mu_G = 0.03$, in the rheology model of Sec. 8.4.

Fig. 8.14a also predicts the suspension diffusion near the athermal jamming limit. The non-Brownian ASD simulation results up to $\phi = 0.50$ [43, 54] are presented in black open left triangles and agree well with simulations at finite $\bar{\Pi}$ along the same master curve of Eq. (8.43). The long-time Péclet number $\overline{\mathrm{Pe}}$ increases with decreasing ϕ. Therefore, the diffusivity at the SAP can be read from the figure. With the experimental SAP friction coefficient $\mu_{\mathrm{SAP}} = 0.308$, the corresponding $\overline{\mathrm{Pe}} \approx 8.3$ in Fig. 8.14a, suggesting a long-time self-diffusivity $d^s_\infty = 0.12\dot{\gamma}a^2$. Surprisingly, the maximum diffusivity in non-Brownian suspensions is found at the highest volume fraction near the SAP due to strong interactions with neighboring particles.

Structure, rheology, and dynamics

Fig. 8.14b explores the connection between the suspension structures and dynamics by plotting the compressional and extensional axes pair distribution function peak difference,

$$\Delta_p = \max(g_{\mathrm{comp}}) - \max(g_{\mathrm{ext}}), \tag{8.44}$$

as functions of $\overline{\mathrm{Pe}}$. The peak difference Δ_p approximates the structural integral $\int \hat{r}\hat{r}g(2,\Omega)\mathrm{d}\Omega$. Despite some data scattering, a trend in how Δ_p changes with $\overline{\mathrm{Pe}}$ is evident: with increasing $\overline{\mathrm{Pe}}$, Δ_p first increases, reaches a maximum at $\overline{\mathrm{Pe}} \approx 7$, and then decreases. With fixed ϕ, the peak difference Δ_p grows with the suspension structural anisotropy, and constant Π and σ, the influences of suspension dilation is also important.

When $\overline{\mathrm{Pe}} \lesssim 7$, the growth of Δ_p with $\overline{\mathrm{Pe}}$ is roughly linear, shown in a dashed line in

Fig. 8.14b,

$$\Delta_p = K_p \overline{\mathrm{Pe}}, \tag{8.45}$$

with the constant $K_p = 0.19$. Combining with Fig. 8.14a, the results suggests that the suspension interaction shear stress $\sigma^{\mathrm{I}} \propto \Delta_p \Pi$, i.e., the suspension shear stress contains multiplicative contributions from the osmotic pressure and the structural anisotropy. Moreover, for liquid-like suspensions, the structural anisotropy increases from 0 at low $\overline{\mathrm{Pe}}$. However, for glassy suspensions, at the onset of flow $\overline{\mathrm{Pe}} \approx 1$, the structural anisotropy is already finite, confirming that the structural change precedes flow as is shown in Fig. 8.1d.

At a critical $\overline{\mathrm{Pe}}$, the anisotropy reaches a maximum before the suspension begins to dilate, leading to Δ_p reduction. Here, the critical $\overline{\mathrm{Pe}}$ is roughly the same for all $\bar{\Pi}$, as particle diffusion is intimately connected to the suspension structures. Since $\overline{\mathrm{Pe}}$ is the inverse of the diffusivity, Fig. 8.14b suggests that the structural change is due to the limited diffusion comparing to the flow. Further reduction in Δ_p appears branched near $\overline{\mathrm{Pe}} \approx 20$, where μ^I also becomes more scattered in Fig. 8.14a. Here, the two branches exhibit different Δ_p reduction with respect to $\overline{\mathrm{Pe}}$. Since results with apparent string formation are not considered in Fig. 8.14b, the more sensitive branch may arise from the formation of subtle structures not as obvious as the strings. The less sensitive branch, on the other hand, arises from suspension dilation in the high shear limit. From Fig. 8.2 and 8.3, this reduction is also related to the vorticity direction particle alignment.

8.6 Summary and Conclusions

We studied the rheology, structure, and dynamics of the constant stress and pressure rheology of dense colloidal suspensions over a wide parameter space including 5 decades of imposed stresses and 2 decades of imposed pressures with HIs. To achieve this, we developed a computational method based on the SEASD method to impose the constant stress and pressure constraint by solving the instantaneous suspension mechanical balance. To further improve the computational speed, we adopted the near-field Brownian approximation, which used a mean-field approximation for the far-field part of the Brownian forces.

With fixed pressure, the suspension dilates and continues to shear thin with increasing imposed stresses. The suspension behaviors can be broadly divided to the liquid-like and glassy. Liquid-like suspensions do not exhibit flow-arrest transitions at low imposed stresses, but glassy suspensions do. Structurally, liquid-like

suspensions are homogeneous at all imposed stresses, and high pressure glassy suspensions show string order formation with increasing imposed stresses. Further stress increase melts the string structures. At high imposed stress, the particles exhibit preferential alignment in the vorticity direction due to the closed trajectory of particle pairs in simple shear flows. The particle long-time self-diffusivity of colloidal exhibits little anisotropy at low imposed stress. The diffusivity decreases drastically with string order formation. At high imposed stresses after string melting, the diffusivity show increasing anisotropy in the vorticity and the velocity gradient directions.

We examined the flow behaviors of amorphous suspensions using a granular perspective, and characterized the rheology using the macroscopic friction coefficient μ and the viscous number I_v. Our simulation results agree well with the non-Brownian experiments [24] and ASD simulations [43, 54] including the shear viscosity η_s, the normal stress differences N_1 and N_2, and the long-time self-diffusivity d^s_∞. By constructing a μ-ϕ flow map, we also found that shear thickening occurs when the volume fractions are held constant with $\phi < 0.57$.

We discovered universal connections among the suspension rheology, diffusion, and diffusion in parameter-free data collapses. By introducing an interaction friction coefficient μ^I, we discovered that $\mu^I \propto \dot{\gamma}a^2/d^s_\infty$, suggesting that the suspension dynamics are controlled by an effective temperature proportional to the osmotic pressure, $T_{\text{eff}} \propto \Pi$, and the diffusivity can be predicted via an effective SES relation. Moreover, the structural features of the suspension, characterized by the peak difference Δ_p, also collapse for different imposed pressures. Our discoveries here suggests that the suspension dynamics can be described in a mean-field fashion using the concept of effective temperature T_{eff}. Our novelty in this work is that the effective temperature is connected to pressure, and is based on a base state with both $\dot{\gamma} \to 0$ and $\phi \to 0$.

Based on the simulation results, we developed a model for glassy suspensions near the flow-arrest transitions. We found that the friction coefficient and the volume fraction changes from the arrest value following universal power laws of I_v regardless of the imposed pressures $\bar{\Pi}$, suggesting that physics of jamming dominates the glassy suspension behaviors, and that the thermal fluctuations only affect the arrest locations. Our model is the only available model that can simultaneously predict the rheological and the diffusive behaviors of glassy suspensions. With a complementary model for liquid-like suspensions, we can completely describe the

suspension behaviors. However, the development of a rheology model for liquid-like suspension is deferred to future works.

This study is the first comprehensive hydrodynamic investigations on the behaviors of dense suspensions, and demonstrate that the influences of HIs are quantitative for amorphous systems. Our work suggests that the flowing behaviors of dense suspensions should be described in a mean-field fashion using the concept of effective temperatures. Our work also points out that pressure is an extremely crucial quantity in understanding the behaviors of non-equilibrium flowing systems.

8.A Computing hydrodynamic interactions

We compute HIs in polydisperse hard-sphere Brownian suspensions using the SEASD method with near-field Brownian approximation [56]. The framework of Stokesian Dynamics [57] resolves the long-range non-pairwise-additive far-field and diverging near-field lubrication interactions in suspension hydrodynamics by combining the mobility and the resistance formalism. It computes the grand resistance tensor $\boldsymbol{\mathcal{R}}$ as

$$\boldsymbol{\mathcal{R}} = (\boldsymbol{\mathcal{M}}^{\infty})^{-1} + (\boldsymbol{\mathcal{R}}_{2\mathrm{B}} - \boldsymbol{\mathcal{R}}^{\infty}_{2\mathrm{B}}), \tag{8.46}$$

with $\boldsymbol{\mathcal{M}}^{\infty}$ the far-field grand mobility tensor and $(\boldsymbol{\mathcal{R}}_{2\mathrm{B}} - \boldsymbol{\mathcal{R}}^{\infty}_{2\mathrm{B}})$ the pairwise grand resistance tensor from the exact solutions of two-body hydrodynamic problems with the far-field contribution removed. The far-field resistance contribution $\boldsymbol{\mathcal{R}}^{\infty}_{2\mathrm{B}}$ is the inversion of $\boldsymbol{\mathcal{M}}^{\infty}$ for two particles. Inverting $\boldsymbol{\mathcal{M}}^{\infty}$ captures the long-range non-pairwise-additive aspect of the HIs, and $(\boldsymbol{\mathcal{R}}_{2\mathrm{B}} - \boldsymbol{\mathcal{R}}^{\infty}_{2\mathrm{B}})$ recovers the near-field diverging lubrication interactions. In the SEASD method, the action of $\boldsymbol{\mathcal{M}}^{\infty}$ on a vector is computed using Spectral Ewald method [58, 59], and $(\boldsymbol{\mathcal{R}}_{2\mathrm{B}} - \boldsymbol{\mathcal{R}}^{\infty}_{2\mathrm{B}})$ is constructed pairwise with cutoff distance, currently set at $2(a_i + a_j)$ for each pair due to the short-range lubrication interactions.

The near-field Brownian approximation adopts a mean-field approach to treat the far-field HIs for $\boldsymbol{\mathcal{U}}^{\mathrm{B}}$ [Eq. (8.13)], $\Delta\boldsymbol{\mathcal{X}}^{\mathrm{B}}$ [Eq. (8.10)], and $\boldsymbol{S}^{\mathrm{B}}$ [Eq. (8.17)], and retains the full hydrodynamic computations for other quantities. In computing the Brownian-related quantities, the far-field grand mobility tensor $\boldsymbol{\mathcal{M}}^{\infty}$ is approximated as a diagonal matrix, using $d_s^{\mathrm{t,ff}}$ for the elements corresponding to the velocity-force coupling, and $d_s^{\mathrm{r,ff}}$ for the elements corresponding to the angular velocity-torque coupling. For the strain rate-stresslet coupling, the single-particle relation $\boldsymbol{E}^{\infty} = \boldsymbol{S}^{\mathrm{H}}/(\frac{20}{3}\pi\eta_0 a^3)$ is used. Here, $d_s^{\mathrm{t,ff}}$ and $d_s^{\mathrm{r,ff}}$ are the far-field short-time translational and rotational diffusion coefficients of equilibrium suspensions at the same composition and vol-

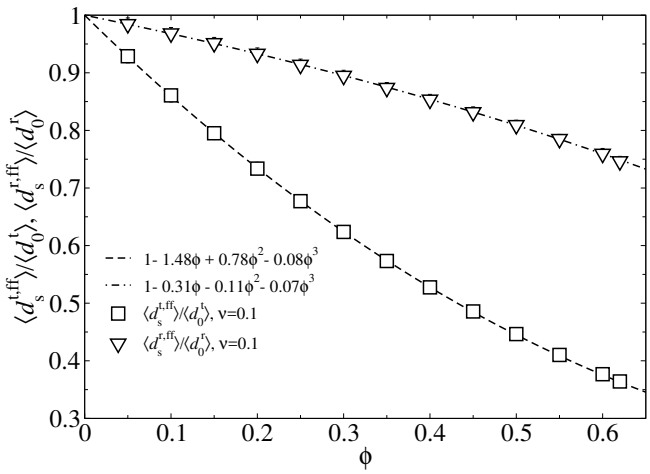

Figure 8.15: The mean far-field translational and rotational diffusion coefficients, $\left\langle d_s^{\mathrm{t,ff}}\right\rangle$ and $\left\langle d_s^{\mathrm{r,ff}}\right\rangle$, respectively, as functions of volume fraction ϕ for a polydisperse suspension with polydispersity p.d. = 0.1. The dashed and dash-dotted lines are cubic polynomial fit to the calculation results.

ume fractions. They can be obtained from static calculations without the near-field lubrication contributions.

In this work, we consider the polydisperse suspension an effective medium characterized by the mean single-particle translational and rotational diffusion coefficients $\left\langle d_0^{\mathrm{t}}\right\rangle = N^{-1}\sum_i d_{0,i}^{\mathrm{t}}$ and $\left\langle d_0^{\mathrm{r}}\right\rangle = N^{-1}\sum_i d_{0,i}^{\mathrm{r}}$, respectively, with $d_{0,i}^{\mathrm{t}} = k_{\mathrm{B}}T/(6\pi\eta_0 a_i)$ and $d_{0,i}^{\mathrm{r}} = k_{\mathrm{B}}T/(8\pi\eta_0 a_i^3)$, and compute a single effective far-field diffusion coefficient for all particle species. This approach eliminates the need to identify different particle species in the approximated far-field mobility tensor, and is consistent with the mean-field idea behind the near-field Brownian approximation.

Fig. 8.15 shows the mean far-field translational and rotational diffusion coefficients, $\left\langle d_s^{\mathrm{t,ff}}\right\rangle$ and $\left\langle d_s^{\mathrm{r,ff}}\right\rangle$, respectively, for polydisperse suspensions with polydispersity p.d. = 0.1 as functions of volume fraction ϕ. The configurations are generated by a polydisperse Lubachevsky-Stillinger algorithm [101, 102] followed by a brief equilibration [30]. The system size $N = 800$ and the species number $M = 10$, and each point in Fig. 8.15 is averaged over 500 independent configurations. Note that $\left\langle d_s^{\mathrm{t,ff}}\right\rangle$ exhibits a strong system size dependence proportional to $N^{\frac{1}{3}}$, and this effect has been corrected in Fig. 8.15 with the far-field high-frequency dynamic viscosity [56]. The finite size effect in $\left\langle d_s^{\mathrm{r,ff}}\right\rangle$ is negligible. The simulation results can be satisfactorily fit by a cubic polynomial in ϕ up to the close packing density. These fitted polynomials are used in the dynamic simulations for computing Brownian

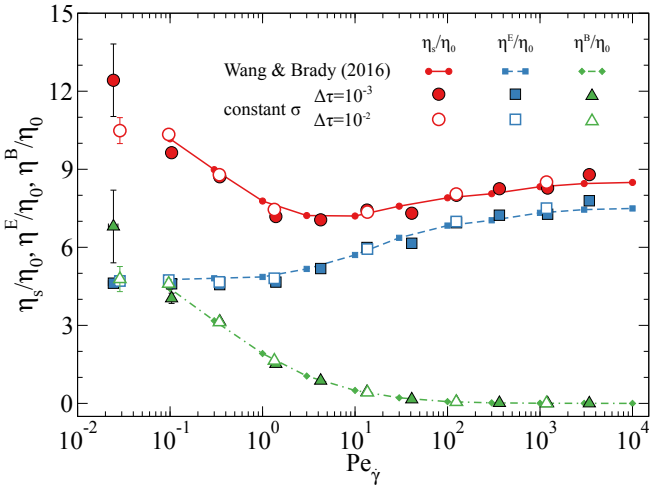

Figure 8.16: (Color online) The total suspension viscosity η_s/η_0 and its flow and Brownian contributions, η^{E}/η_0 and η^{B}/η_0, respectively, as functions of the strain rate Péclet number $\mathrm{Pe}_{\dot\gamma}$ for a bidisperse suspension with size ratio 2 and equal volume ratio at $\phi = 0.45$. All computations are from SEASD method with full hydrodynamic interactions. The lines are from constant strain rate simulations [56]. The symbols are from constant stress simulations with dimensionless step size $\Delta\tau = 10^{-3}$ (filled symbols) and $\Delta\tau = 10^{-2}$ (open symbols).

related quantities.

8.B Validation via constant stress simulations

As indicated in Sec. 8.2, with $\dot e = 0$, the constant stress and pressure algorithm reduces to the constant stress, fixed volume algorithm of Swan and Brady [66]. For homogeneous suspensions below the glass transition, imposing a constant stress is equivalent to imposing a corresponding strain rate at steady state. Therefore, the constant stress and pressure algorithm can be partially validated by comparing results from constant stress simulations with known constant strain rate data.

We performed constant stress simulations at different dimensionless time steps $\Delta\tau$ for bidisperse colloidal suspensions of size ratio 2 and equal volumes for both species at a total volume fraction $\phi = 0.45$ with full HIs. Fig. 8.16 compares the constant stress suspension shear viscosity, η_s, and its flow and Brownian contributions, η^{E} and η^{B}, respectively, with the constant strain rate results [56]. The constant stress results, originally expressed as functions of Pe_σ, are converted to functions of $\mathrm{Pe}_{\dot\gamma}$ using Eq. (8.24). Note that, for hard-sphere suspensions, the interparticle force does not contribute to the stress, and therefore $\eta^{\mathrm{P}} = 0$. Qualitatively, increasing $\mathrm{Pe}_{\dot\gamma}$ leads to rapid reduction in η^{B} and slow growth in η^{E}. At high Pe_σ, the Brownian viscosity

η^B reduces to zero but the flow viscosity η^E asymptotes a constant. As a result, the suspension viscosity η_s first decreases and then increases mildly with growing $\mathrm{Pe}_{\dot{\gamma}}$. A key feature of the constant volume rheology is the existence of a high-shear viscosity as $\mathrm{Pe}_{\dot{\gamma}} \to \infty$.

In Fig. 8.16, the good agreement between the constant stress results, shown in symbols, and the constant strain rate data, shown in dots, at least partially validate the constant stress and pressure algorithm in Sec. 8.2. In addition, Fig. 8.16 also compares the effect of the dimensionless time step size with $\Delta\tau = 10^{-2}$ and 10^{-3}. In the low $\mathrm{Pe}_{\dot{\gamma}}$ limit, the Brownian viscosity η^B at $\Delta\tau = 10^{-3}$ show larger fluctuations, but the flow contribution η^E with different time steps agree well. In the high $\mathrm{Pe}_{\dot{\gamma}}$ limit, on the other hand, η^B agrees well, but η^E exhibit small differences at different $\Delta\tau$, suggesting subtle differences in particle configurations. Despite these small quantitative differences, different time steps lead to the same suspension rheology, justifying using $\Delta\tau = 10^{-2}$ in most dynamic simulations in this work.

References

[1] W. B. Russel, D. A. Saville, and W. R. Schowalter, *Colloidal dispersions* (Cambridge University Press, 1991).

[2] R. J. Hunter, *Foundations of colloid science* (Oxford University Press, 2001).

[3] J. Mewis and N. J. Wagner, *Colloidal suspension rheology* (Cambridge University Press, 2013).

[4] M. Ballauff, J. M. Brader, S. U. Egelhaaf, M. Fuchs, J. Horbach, N. Koumakis, M. Krüger, M. Laurati, K. J. Mutch, G. Petekidis, M. Siebenbürger, T. Voigtmann, and J. Zausch, "Residual stresses in glasses", Phys. Rev. Lett. **110**, 215701 (2013).

[5] N. Koumakis, M. Laurati, S. U. Egelhaaf, J. F. Brady, and G. Petekidis, "Yielding of hard-sphere glasses during start-up shear", Phys. Rev. Lett. **108**, 098303 (2012).

[6] T. Sentjabrskaja, E. Babaliari, J. Hendricks, M. Laurati, G. Petekidis, and S. U. Egelhaaf, "Yielding of binary colloidal glasses", Soft Matter **9**, 4524 (2013).

[7] X. Cheng, J. H. McCoy, J. N. Israelachvili, and I. Cohen, "Imaging the microscopic structure of shear thinning and thickening colloidal suspensions", Science **333**, 1276 (2011).

[8] G. Bossis and J. F. Brady, "The rheology of brownian suspensions", J. Chem. Phys. **91**, 1866 (1989).

[9] H. M. Laun, "Rheological properties of aqueous polymer dispersions", Angewandte Makromolekulare Chemie **123/124**, 335 (1984).

[10] N. J. Wagner and J. F. Brady, "Shear thickening in colloidal dispersions", Phys. Today **62**, 27 (2009).

[11] C. D. Cwalina and N. J. Wagner, "Material properties of the shear-thickened state in concentrated near hard-sphere colloidal dispersions", J. Rheol. **58**, 949 (2014).

[12] L. Isa, R. Besseling, A. N. Morozov, and W. C. K. Poon, "Velocity oscillations in microfluidic flows of concentrated colloidal suspensions", Phys. Rev. Lett. **102**, 058302 (2009).

[13] R. G. M. van der Sman and H. M. Vollebregt, "Effective temperature for sheared suspensions: a route towards closures for migration in bidisperse suspension", Adv. Colloid Interface Sci. **185–186**, 1 (2012).

[14] M. Hermes, B. M. Guy, G. Poy, M. E. Cates, M. Wyart, and W. C. K. Poon, "Unsteady flow and particle migration in dense, non-brownian suspensions", J. Rheol. **60**, 905 (2016).

[15] A. J. Liu and S. R. Nagel, "Nonlinear dynamics: jamming is not just cool any more", Nature **396**, 21 (1998).

[16] A. J. Liu and S. R. Nagel, "The jamming transition and the marginally jammed solid", Annu. Rev. Condens. Matter Phys. **1**, 347 (2010).

[17] T. K. Haxton, M. Schmiedeberg, and A. J. Liu, "Universal jamming phase diagram in the hard-sphere limit", Phys. Rev. E **83**, 031503 (2011).

[18] W. B. Russel, N. J. Wagner, and J. Mewis, "Divergence in the low shear viscosity for brownian hard sphere dispersions: at random close packing or the glass transition?", J. Rheol. **57**, 1555 (2013).

[19] P. N. Pusey and W. van Megen, "Phase behaviour of concentrated suspensions of nearly hard colloidal spheres", Nature **320**, 340 (1986).

[20] P. Olsson and S. Teitel, "Athermal jamming versus thermalized glassiness in sheared frictionless particles", Phys. Rev. E **88**, 010301(R) (2013).

[21] A. Ikeda, L. Berthier, and P. Sollich, "Unified study of glass and jamming rheology in soft particle systems", Phys. Rev. Lett. **109**, 018301 (2012).

[22] G. Brambilla, D. El Masri, M. Pierno, L. Berthier, L. Cipelletti, G. Petekidis, and A. Schofield, "Probing the equilibrium dynamics of colloidal hard spheres above the mode-coupling glass transition", Phys. Rev. Lett. **102**, 085703 (2009).

[23] W. van Megen, T. C. Mortensen, S. R. Williams, and J. Müller, "Measurement of the self-intermediate scattering function of suspensions of hard spherical particles near the glass transition", Physical Review E **58**, 6073 (1998).

[24] F. Boyer, E. Guazzelli, and O. Pouliquen, "Unifying suspension and granular rheology", Phys. Rev. Lett. **107**, 188301 (2011).

[25] M. Wang and J. F. Brady, "Constant stress and pressure rheology of colloidal suspensions", Phys. Rev. Lett. **115**, 158301 (2015).

[26] M. Wang and J. F. Brady, "Constant stress and pressure rheology of colloidal suspensions: steady state behavior and dynamics near the flow-arrest transitions", In Preparation (2016).

[27] G. K. Batchelor, "Brownian diffusion of particles with hydrodynamic interaction", J. Fluid Mech. **74**, 1 (1976).

[28] G. K. Batchelor, "Sedimentation in a dilute dispersion of spheres", J. Fluid Mech. **52**, 245 (1972).

[29] R. J. Phillips, J. F. Brady, and G. Bossis, "Hydrodynamic transport properties of hard-sphere dispersions. i. suspensions of freely mobile particles", Phys. Fluids **31**, 3462 (1988).

[30] M. Wang and J. F. Brady, "Short-time transport properties of bidisperse suspensions and porous media: a stokesian dynamics study", J. Chem. Phys. **142**, 094901 (2015).

[31] J. F. Brady and G. Bossis, "Stokesian dynamics", Annu. Rev. Fluid Mech. **20**, 111 (1988).

[32] T. N. Phung, J. F. Brady, and G. Bossis, "Stokesian dynamics simulation of brownian suspensions", J. Fluid Mech. **313**, 181 (1996).

[33] D. R. Foss and J. F. Brady, "Structure, diffusion and rheology of brownian suspensions by stokesian dynamics simulation", J. Fluid Mech. **407**, 167 (2000).

[34] D. R. Foss and J. F. Brady, "Brownian Dynamics simulation of hard-sphere colloidal dispersions", J. Rheol. **44**, 629 (2000).

[35] S. R. Rastogi, N. J. Wagner, and S. R. Lustig, "Rheology, self-diffusion, and microstructure of charged colloids under simple shear by massively parallel nonequilibrium brownian dynamics", J. Chem. Phys. **104**, 9234 (1996).

[36] B. J. Ackerson and P. N. Pusey, "Shear-induced order in suspensions of hard spheres", Phys. Rev. Lett. **61**, 1033 (1988).

[37] B. J. Ackerson, "Shear induced order and shear processing of model hard sphere suspensions", J. Rheol. **34**, 553 (1990).

[38] X. Cheng, X. Xu, S. A. Rice, A. R. Dinner, and I. Cohen, "Assembly of vorticity-aligned hard-sphere colloidal strings in a simple shear flow", Proc. Natl. Acad. Sci. U. S. A. **109**, 63 (2012).

[39] A. K. Gurnon and N. J. Wagner, "Microstructure and rheology relationships for shear thickening colloidal dispersions", J. Fluid Mech. **769**, 242 (2015).

[40] F. Westermeier, D. Pennicard, H. Hirsemann, U. H. Wagner, C. Rau, H. Graafsma, P. Schall, M. P. Lettinga, and B. Struth, "Connecting structure, dynamics and viscosity in sheared soft colloidal liquids: a medley of anisotropic fluctuations", Soft Matter **12**, 171 (2016).

[41] X. Xu, S. A. Rice, and A. R. Dinner, "Influence of interlayer exchanges on vorticity-aligned colloidal string assembly in a simple shear flow", J. Phys. Chem. Lett. **4**, 3310 (2013).

[42] D. Leighton and A. Acrivos, "The shear-induced migration of particles in concentrated suspensions", J. Fluid Mech. **181**, 415 (1987).

[43] A. Sierou and J. F. Brady, "Shear-induced self-diffusion in non-colloidal suspensions", J. Fluid Mech. **506**, 285 (2004).

[44] A. M. Leshansky and J. F. Brady, "Dynamic structure factor study of diffusion in strongly sheared suspensions", J. Fluid Mech. **527**, 141 (2005).

[45] S. Kim and S. J. Karrila, *Microhydrodynamics* (Dover, 2005).

[46] D. L. Ermak and J. A. McCammon, "Brownian dynamics with hydrodynamic interactions", J. Chem. Phys. **69**, 1352 (1978).

[47] A. Mulero, ed., *Theory and simulation of hard-sphere fluids and related systems* (Springer, 2008).

[48] W. C. K. Poon, E. R. Weeks, and C. P. Royall, "On measuring colloidal volume fractions", Soft Matter **8**, 21 (2012).

[49] N. Koumakis, "A study on the effects of interparticle interactions on the dynamics, rheology and aging of colloidal systems out of equilibrium", PhD thesis (University of Crete, 2011).

[50] J. F. Brady, "The rheological behavior of concentrated colloidal dispersions", J. Chem. Phys. **99**, 567 (1993).

[51] J. F. Brady, "The long-time self-diffusivity in concentrated colloidal dispersions", J. Fluid Mech. **272**, 109 (1994).

[52] T. Ando and J. Skolnick, "Crowding and hydrodynamic interactions likely dominate in vivo macromolecular motion", Proc. Natl. Acad. Sci. U. S. A. **107**, 18457 (2010).

[53] R. Mari, R. Seto, J. F. Morris, and M. M. Denn, "Discontinuous shear thickening in brownian suspensions by dynamic simulation", Proc. Natl. Acad. Sci. U. S. A. **112**, 15326 (2015).

[54] A. Sierou and J. F. Brady, "Rheology and microstructure in concentrated noncolloidal suspensions", J. Rheol. **46**, 1031 (2002).

[55] S. Gallier, E. Lemaire, F. Peters, and L. Lobry, "Rheology of sheared suspensions of rough frictional particles", J. Fluid Mech. **757**, 514 (2014).

[56] M. Wang and J. F. Brady, "Spectral ewald acceleration of stokesian dynamics for polydisperse suspensions", J. Comput. Phys. **306**, 443 (2016).

[57] L. Durlofsky, J. F. Brady, and G. Bossis, "Dynamic simulation of hydrodynamically interacting particles", J. Fluid Mech. **180**, 21 (1987).

[58] D. Lindbo and A.-K. Tornberg, "Spectrally accurate fast summation for periodic Stokes potentials", J. Comput. Phys. **229**, 8994 (2010).

[59] D. Lindbo and A.-K. Tornberg, "Spectral accuracy in fast Ewald-based methods for particle simulations", J. Comput. Phys. **230**, 8744 (2011).

[60] A. J. Banchio and J. F. Brady, "Accelerated Stokesian Dynamics: brownian motion", J. Chem. Phys. **118**, 10323 (2003).

[61] X. Bian, S. Litvinov, M. Ellero, and N. J. Wagner, "Hydrodynamic shear thickening of particulate suspension under confinement", J. Non-Newtonian Fluid Mech. **213**, 39 (2014).

[62] T. Kawasaki, D. Coslovich, A. Ikeda, and L. Berthier, "Diverging viscosity and soft granular rheology in non-brownian suspensions", Phys. Rev. E **91**, 012203 (2015).

[63] D. J. Evans and G. Morriss, *Statistical mechanics of nonequilibrium liquids* (Cambridge University Press, 2008).

[64] M. Bouzid, M. Trulsson, P. Claudin, E. Clément, and B. Andreotti, "Nonlocal rheology of granular flows across yield conditions", Phys. Rev. Lett. **111**, 238301 (2013).

[65] A. S. Khair, M. Swaroop, and J. F. Brady, "A new resistance function for two rigid spheres in a uniform compressible low-reynolds-number flow", Phys. Fluids **18**, 043102 (2006).

[66] J. W. Swan and J. F. Brady, "Colloidal dispersions deformed by a steady shear stress", Submitted (2013).

[67] M. Trulsson, B. Andreotti, and P. Claudin, "Transition from the viscous to inertial regime in dense suspensions", Phys. Rev. Lett. **109**, 118305 (2012).

[68] E. DeGiuli, G. Düring, E. Lerner, and M. Wyart, "Unified theory of inertial granular flows and non-brownian suspensions", Phys. Rev. E **91**, 062206 (2015).

[69] E. Lerner, G. Düring, and M. Wyart, "A unified framework for non-brownian suspension flows and soft amorphous solids", Proc. Natl. Acad. Sci. U.S.A. **109**, 4798 (2012).

[70] Y. Forterre and O. Pouliquen, "Flows of dense granular media", Annu. Rev. Fluid Mech. **40**, 1 (2008).

[71] K. Kamrin and G. Koval, "Nonlocal constitutive relation for steady granular flow", Phys. Rev. Lett. **108**, 178301 (2012).

[72] M. Bouzid, A. Izzet, M. Trulsson, E. Clément, P. Claudin, and B. Andreotti, "Non-local rheology in dense granular flows. revisiting the concept of fluidity", Eur. Phys. J. E **38**, 125 (2015).

[73] J. H. Simpson and H. Y. Carr, "Diffusion and nuclear spin relaxation in water", Phys. Rev. **111**, 1201 (1958).

[74] I. Chang and H. Sillescu, "Heterogeneity at the glass transition: translational and rotational self-diffusion", J. Phys. Chem. B **101**, 8794 (1997).

[75] A. J. Banchio, G. Nägele, and J. Bergenholtz, "Viscoelasticity and generalized stokes-einstein relations of colloidal dispersions", J. Chem. Phys. **111**, 8721 (1999).

[76] A. J. Banchio, J. Bergenholtz, and G. Nägele, "Rheology and dynamics of colloidal suspensions", Phys. Rev. Lett. **82**, 1792 (1999).

[77] D. Bonn and W. K. Kegel, "Stokes-Einstein relations and the fluctuation-dissipation theorem in a supercooled colloidal fluid", J. Chem. Phys. **118**, 2005 (2003).

[78] T. G. Mason, K. Ganesan, J. H. van Zanten, D. Wirtz, and S. C. Kuo, "Particle tracking microrheology of complex fluids", Phys. Rev. Lett. **79**, 3282 (1997).

[79] T. M. Squires and T. G. Mason, "Fluid mechanics of microrheology", Annu. Rev. Fluid Mech. **42**, 413 (2010).

[80] M. D. Ediger, "Spatially heterogeneous dynamics in supercooled liquids", Annu. Rev. Phys. Chem. **51**, 99 (2000).

[81] S. Gupta, J. Stellbrink, E. Zaccarelli, C. N. Likos, M. Camargo, P. Holmqvist, J. Allgaier, L. Willner, and D. Richter, "Validity of the Stokes-Einstein Relation in Soft Colloids up to the Glass Transition", Physical Review Letters **115**, 128302 (2015).

[82] A. Ikeda and K. Miyazaki, "Glass transition of the monodisperse gaussian core model", Phys. Rev. Lett. **106**, 015701 (2011).

[83] A. Ikeda and K. Miyazaki, "Slow dynamics of the high density Gaussian core model", J. Chem. Phys. **135**, 054901 (2011).

[84] S. F. Edwards and R. B. S. Oakeshott, "Theory of powders", Physica A **157**, 1080 (1989).

[85] P. Sollich, F. Lequeux, P. Hebraud, and M. E. Cates, "Rheology of soft glassy materials", Phys. Rev. Lett. **78**, 2020 (1997).

[86] P. Hébraud and F. Lequeux, "Mode-coupling theory for the pasty rheology of soft glassy materials", Phys. Rev. Lett. **81**, 2934 (1998).

[87] J. S. Langer, "Shear-transformation-zone theory of viscosity, diffusion, and stretched exponential relaxation in amorphous solids", Phys. Rev. E **85**, 051507 (2012).

[88] M. L. Falk and J. S. Langer, "Deformation and failure of amorphous, solidlike materials", Annu. Rev. Condens. Matter Phys. **2**, 353 (2011).

[89] L. F. Cugliandolo, "The effective temperature", J. Phys. A: Math. Theor. **44**, 483001 (2011).

[90] I. K. Ono, D. J. O'Hern C. S.and Durian, S. A. Langer, A. J. Liu, and S. R. Nagel, "Effective Temperatures of a Driven System Near Jamming", Physical Review Letters **89**, 095703 (2002).

[91] H. A. Makse and J. Kurchan, "Testing the thermodynamic approach to granular matter with a numerical model of a decisive experiment", Nature **415**, 614 (2002).

[92] L. Berthier and J.-L. Barrat, "Shearing a Glassy Material: Numerical Tests of Nonequilibrium Mode-Coupling Approaches and Experimental Proposals", Phys. Rev. Lett. **89**, 095702 (2002).

[93] L. Berthier and J.-L. Barrat, "Nonequilibrium dynamics and fluctuation-dissipation relation in a sheared fluid", J. Chem. Phys. **116**, 6228 (2002).

[94] M. Zhang and G. Szamel, "Effective temperatures of a driven, strongly anisotropic brownian system", Phys. Rev. E **83**, 061407 (2011).

[95] T. K. Haxton, "Ratio of effective temperature to pressure controls the mobility of sheared hard spheres", Physical Review E **85**, 011503 (2012).

[96] C. Eisenmann, C. Kim, J. Mattsson, and D. A. Wetiz, "Shear melting of a colloidal glass", Phys. Rev. Lett. **104**, 035502 (2010).

[97] T. Sentjabrskaja, P. Chaudhuri, M. Hermes, W. C. K. Poon, J. Horbach, S. U. Egelhaaf, and M. Laurati, "Creep and flow of glasses: strain response linked to the spatial distribution of dynamical heterogeneities", Sci. Rep. **5**, 11884 (2015).

[98] R. Besseling, E. R. Weeks, A. B. Schofield, and W. C. K. Poon, "Three-Dimensional Imaging of Colloidal Glasses under Steady Shear", Phys. Rev. Lett. **99**, 028301 (2007).

[99] J. F. Brady, "Brownian motion, hydrodynamics, and the osmotic pressure", J. Chem. Phys. **98**, 3335 (1993).

[100] J. F. Brady, A. S. Khair, and M. Swaroop, "On the bulk viscosity of suspensions", J. Fluid Mech. **554**, 109 (2006).

[101] B. D. Lubachevsky and F. H. Stillinger, "Geometric properties of random disk packings", J. Stat. Phys. **60**, 561 (1990).

[102] M. Skoge, A. Donev, F. H. Stillinger, and S. Torquato, "Packing hyperspheres in high-dimensional Euclidean spaces", Phys. Rev. E **74**, 041127 (2006).

[103] D. M. Heyes and J. R. Melrose, "Brownian dynamics simulations of model hard-sphere suspensions", J. Non-Newtonian Fluid Mech. **46**, 1 (1993).

[104] M. Swaroop, "The bulk viscosity of suspensions", PhD thesis (California Institute of Technology, 2010).

[105] J. Bergenholtz, J. F. Brady, and M. Vivic, "The non-newtonian rheology of dilute colloidal suspensions", J. Fluid Mech. **456**, 239 (2002).

[106] G. K. Batchelor and J. T. Green, "The hydrodynamic interaction of two small freely-moving spheres in a linear flow field", J. Fluid Mech. **56**, 375 (1972).

[107] J. F. Brady and J. F. Morris, "Microstructure of strongly sheared suspensions and its impact on rheology and diffusion", J. Fluid Mech. **348**, 103 (1997).

[108] J. F. Brady and M. Vivic, "Normal ststress in colloidal dispersions", J. Rheol. **39**, 545 (1995).

[109] P.-E. Peyneau and J.-N. Roux, "Frictionless bead packs have macroscopic friction, but no dilatancy", Phys. Rev. E **78**, 011307 (2008).

[110] D. Bonn, J. Paredes, M. M. Denn, L. Berthier, T. Divoux, and S. Manneville, "Yield stress materials in soft condensed matter", arXiv:1502.05281 (2015).

[111] M. D. Rintoul and S. Torquato, "Metastability and crystallization in hard-sphere systems", Phys. Rev. Lett. **77**, 4198 (1996).

[112] A. Ikeda, L. Berthier, and P. Sollich, "Disentangling glass and jamming physics in the rheology of soft materials", Soft Matter **9**, 7669 (2013).

[113] W. Götze, *Complex dynamics of glass-forming liquids: a mode-coupling theory* (Oxford University Press, 2008).

[114] B. M. Guy, M. Hermes, and W. C. K. Poon, "Towards a unified description of the rheology of hard-particle suspensions", Phys. Rev. Lett. **115**, 088304 (2015).

[115] A. Fall, N. Huang, F. Bertrand, G. Ovarlez, and D. Bonn, "Shear thickening of cornstarch suspensions as a reentrant jamming transition", Phys. Rev. Lett. **100**, 018301 (2008).

[116] R. Seto, R. Mari, J. F. Morris, and M. M. Denn, "Discontinuous shear thickening of frfriction hard-sphere suspensions", Phys. Rev. Lett. **111**, 218301 (2013).

[117] J. R. Royer, D. L. Blair, and S. D. Hudson, "Rheological signature of frictional interactions in shear thickening suspensions", Phys. Rev. Lett. **116**, 188301 (2016).

[118] A. Ikeda, L. Berthier, and P. Sollich, "Comment on "constant stress and pressure rheology of colloidal suspensions"", Phys. Rev. Lett **116**, 179801 (2016).

[119] C. K. C. Lieou and J. S. Langer, "Nonequilibrium thermodynamics in sheared hard-sphere materials", Phys. Rev. E **85**, 061308 (2012).

Chapter 9

CONCLUSION AND OUTLOOK

This thesis presented a comprehensive investigation on various aspects related to the constant stress and pressure rheology of polydisperse colloidal suspensions. Using bidisperse suspensions as a model system, we first investigated the effects of particle sizes on the suspension short-time transport properties. Our results showed that introducing a second species of different particle size leads to qualitative differences in the suspension transport properties such as the sedimentation velocity. However, in many cases, the influences of particle sizes are only quantitative. We found that the pairwise additive approximation with proper structural input is valid in most cases up to a volume fraction of $\phi = 0.1$, demonstrating the strong influences of many-body effects in transport properties. In contrast, the semi-analytical approximation scheme with partial resummation of the many-body hydrodynamic interactions is valid up to $\phi = 0.4$.

Our work on the short-time transport properties serves as a critical reference for future experiments and simulations on bidisperse systems, and provides insight and guidance on using particle sizes to tune the suspension transport properties. The approximation scheme on the hydrodynamic functions signficantly simplifies the interpretation of scattering experiments for bidisperse suspensions. The computational scheme can be straightforwardly extended to other systems such as charge-stabilized colloidal suspensions. In this case, in addition to the size differences, the charge differences also affect the transport properties by changing the suspension structures. With proper structure predictions, we can significantly extend our capability to predict transport properties in other colloidal systems.

We also developed the Spectral Ewald Accelerated Stokesian Dynamics (SEASD) for computing hydrodynamic interactions in polydisperse colloidal suspensions. The main advantages of the SEASD include the polydisperse capability, the flexible error control via the Spectral Ewald (SE) method, and the GPU acceleration. We extensively validated the SEASD, and found that SEASD-nf, the near-field Brownian approximation of the algorithm, can quantitatively capture the hydrodynamic interactions in the rheology of bidisperse suspensions.

Comparing to other Particle-Mesh-Ewald (PME) techniques, the SE method is

simple and allows full error controls. The SEASD method can be conveniently extended to compute the hydrodynamic interactions of active particles with surface velocities. By casting the swimming model with surface velocity [1] into a form independent of the reference frame [2], we can adapt the SEASD to study dynamics of swimming particles. Furthermore, an area for improvement in the current SEASD is the computation of Brownian force, which is the most time-consuming step in dynamic simulations of colloidal systems. A possibility is to exploit the symmetry of the computation kernel, similarly to the approach in fluctuating hydrodynamics [3].

Our investigations on the film drying process of colloidal suspensions revealed the critical role of the confining boundary on the stress and structures of the colloidal suspensions. Interestingly, both fast and slow boundary motion contribute to structural formation, and the most amorphous structures occurs at a moderate boundary velocity. The simple continuum model is surprisingly effective for predicting the structural and stress evolution, but cannot capture the boundary-layer-like stress distributions and the volume fraction distribution at fast boundary motion. The model can be improved by incorporating non-local effects in way similarly to Kamrin and Koval [4].

We exhaustively investigated the behaviors of dense colloidal suspensions including the suspension mechanics, structures, and diffusive dynamics with constant imposed stress and pressure, and evaluated the role of hydrodynamic interactions through non-hydrodynamic and hydrodynamic simulations. We found that hydrodynamic interactions profoundly affect the suspension structures, but only quantitatively changes the behaviors of amorphous and glassy suspensions. We devised a simple model to describe the rheology and diffusion of glassy suspensions, highlighting the role of jamming physics on the suspension dynamics. We also discovered an universal collapse of simulation data representing an effective Stokes-Einstein-Sutherland (SES) relation with an effective temperature proportional to the osmotic pressure. This revelation suggests that a mean-field description for the rheology and dynamics of dense suspensions is possible.

We can use the rheology model as a constitutive relation to predict macroscopic behaviors of glassy suspensions using the approach of Jop et al. [5]. An example is microrheology in glass: i.e., the structure and stress of the glassy suspensions in response to a moving probe. The model prediction can be compared with the simulations and Mode Coupling Theory predictions [6]. Another point of interest is the validity of the effective SES relation beyond the hard-sphere systems.

References

[1] J. R. Blake, "A spherical envelope approach to ciliary propulsion", J. Fluid Mech. **46**, 199 (1971).

[2] B. Delmotte, E. Keaveny, F. Plouraboue, and E. Climent, "Large-scale simulation of steady and time-dependent active suspensions with the force-coupling method", J. Comput. Phys. **302**, 524 (2015).

[3] S. Delong, F. B. Usabiaga, R. Delgado-Buscalioni, B. E. Griffith, and A. Donev, "Brownian dynamics without green's functions", J. Chem. Phys. **140**, 134110 (2014).

[4] K. Kamrin and G. Koval, "Nonlocal constitutive relation for steady granular flow", Phys. Rev. Lett. **108**, 178301 (2012).

[5] P. Jop, Y. Forterre, and O. Pouliquen, "A constitutive law for dense granular flows", Nature **441**, 727 (2006).

[6] M. Gruber, G. C. Abade, A. M. Puertas, and M. Fuchs, "Active microrheology in a colloidal glass", Phys. Rev. E **94**, 042602 (2016).